

Dissertation zur Erlangung des Doktorgrades
der Fakultät für Chemie und Pharmazie
der Ludwig-Maximilians-Universität München

**Tailoring of structure-property-relationships
in 2D carbon nitrides for photocatalytic
hydrogen evolution**

Julia Kröger

aus
München, Deutschland

2021

Erklärung

Diese Dissertation wurde im Sinne von § 7 der Promotionsordnung vom 28. November 2011 von Frau Professor Dr. Bettina V. Lotsch betreut.

Eidesstattliche Versicherung

Diese Dissertation wurde eigenständig und ohne unerlaubte Hilfe erarbeitet.

München, 29.06.2021

(Julia Kröger)

Dissertation eingereicht am:

01.07.2021

1. Gutachterin:

Prof. Dr. Bettina Lotsch

2. Gutachter:

Prof. Dr. Tom Nilges

Mündliche Prüfung am:

17.08.2021

„Überall geht ein frühes Ahnen dem späteren Wissen voraus.“

Alexander von Humboldt

H.-J. Quadbeck-Seeger, *Aphorismen und Zitate über Natur
und Wissenschaft*, John Wiley & Sons, **2013**.

Danksagung

Zu allererst möchte ich mich herzlich bei Prof. Dr. Bettina V. Lotsch für die Möglichkeit bedanken, die Dissertation in ihrem Lehrstuhl auf einem interessanten und spannenden Thema durchführen zu können, für ihre Betreuung, Unterstützung sowie die mir gewährte wissenschaftliche Freiheit.

Desweiteren danke ich Prof. Dr. Tom. Nilges für die Übernahme des Zweitgutachtens. Mein weiterer Dank gilt meiner Prüfungskommission- Prof. Dr. Konstantin Karaghiosoff, Prof. Dr. Thomas Bein, Prof. Dr. Wolfgang Schnick, und Prof. Dr. Ivana Ivanović-Burmazović für die Bereitschaft an meiner Doktorprüfung teilzunehmen.

Mein besonderer Dank gilt allen meinen Co-Autoren und Kollegen für die gute Zusammenarbeit, ohne deren Hilfe die Realisierung meiner vielschichtigen Forschungsprojekte nicht möglich gewesen wären. Hervorheben möchte ich hier: Dr. Filip Podjaski, Dr. Alberto Jimenez-Solano, Gökcen Savasci, Hendrik Schlomberg und Varun Sridhar für unzählige, inspirierende Gespräche und fachlichen Diskussionen. Ich danke auch den vielen exzellenten Wissenschaftler*innen, deren Expertise die Projekte bereichert haben: Dr. Igor Moudrakovski, Dr. Petra Rovó und Dr. Kathrin Küster, für die Durchführung zahlreiche NMR bzw. UPS und XPS Messungen, sowie Diskussionen zur Interpretation der Ergebnisse. Dr. Sebastian Bette und Dr. Maxwell Terban für vielzählige PDF und XRD-Messungen, Simulationen und Diskussionen zu deren Auswertungen. Viola Duppel und Marie-Luise Schreiber für SEM, TEM und ICP Messungen.

Für die alltägliche, immer herzliche und oft auch technische Unterstützung sowie ihre organisatorische Hilfe möchte ich mich außerdem bei Claudia Kamella, Sigrid Fuhrmann und Viola Duppel bedanken. Ferner möchte ich Dr. Vincent Lau für Einführung und Hilfestellung bei meinen ersten Versuchen am MPI danken.

Danken möchte ich auch der ganzen Arbeitsgruppe, derzeitigen und früheren Kolleg*innen, für das angenehme und sympathische Arbeitsklima, die fachlichen Diskussionen und die vielen schönen Momente innerhalb, aber auch außerhalb des Institutes, die wir zusammen erlebt haben. Danke auch für die Freundschaften, die während dieser Zeit entstanden sind. Mein besonderer Dank gilt hier Dr. Filip Podjaski. Meinen Praktikant*innen und Masteranden danke ich für ihre tatkräftige Unterstützung und ihre spannenden Beiträge zu unsere Forschung.

Mein Dank gilt auch Dr. Filip Podjaski und Dr. Takayoshi Oshima für das kritische Korrekturlesen dieser Arbeit.

Darüber hinaus bedanke ich mich bei Prof. Dr. R. Seshadri für die Möglichkeit eines spannenden Forschungsaufenthaltes in seiner Gruppe an der UCSB und den dabei erlangten Einblicken und Erkenntnissen. Besonders möchte ich mich hier auch bei Dr. Filip Podjaski, Andreas Gouder und Gökcen Savasci, Prof. Dr. Bettina V. Lotsch und Prof. Dr. Christian Ochsenfeld für die schöne und unvergessliche Zeit, die wir zusammen in Amerika verbracht haben, bedanken.

Der größte Dank gilt jedoch meiner Familie und Freunden, die mich auf dem Weg zur Promotion und insbesondere während der Zeit am MPI unterstützt haben und mir Rückhalt gaben.

Abstract

To address the increasing demand of energy in an environmentally friendly and renewable manner, a huge variety of new technologies are being developed and tested nowadays. One promising possibility to tackle a major part of those problems is the exploitation of sunlight to drive catalytic reactions, which enable the production of renewable fuels, like hydrogen and carbon-based fuels. For a sustainable application the catalysts employed should be renewable, inexpensive, easy to synthesize and chemically stable. Those requirements are fulfilled by the polymeric semiconductors carbon nitrides, a material class with building blocks consisting of strictly alternating nitrogen and carbon atoms and optical band gaps in the visible range. Especially the production of hydrogen from water, as a next generation fuel, is one key research area, which can be tackled by the photocatalyst carbon nitride.

In this thesis, a new generation of carbon nitrides – a truly two-dimensional (2D) carbon nitride called poly(heptazine imide) (PHI) – is investigated. PHI outperforms most of the other reported carbon nitrides in terms of photocatalytic hydrogen evolution rates. Since this multifunctional material is also known to enable time delayed hydrogen evolution in the dark, by intrinsically storing photo-generated electrons, the understanding of structure-property-relationships is vital to enable a transfer of the optoelectronic properties to other materials and allow a targeted photocatalyst design in future. Therefore, the structure of PHI is analyzed in detail by various diffraction and spectroscopy methods, revealing a trigonal symmetry of the polymer backbone with structural pores (Chapter 4). Due to the salt based synthesis, hydrated potassium ions are located in the pores, leading to a staggered stacking behavior of PHI layers. When exchanging the potassium ions by protons a higher degree of stacking faults is observed, enabling increased hydrogen evolution rates at the same time. In addition, the produced hydrogen amount is found to increase further when the crystallite size of PHI is reduced. To gain insights into the important structural features affecting photocatalysis, an analysis of the interwoven interplay of different parameters affecting the photocatalytic activity was performed in dependence of PHI particle size (Chapter 5). With decreasing particle size the amount of functional groups at the surface, mainly NH_2 , OH and C=O , is increasing, which leads to a higher suspension stability and enables more homogeneous Pt deposition. In parallel, the amount of trap states formed in the optical band gap increases, causing deeper trap states, which can be detrimental for charge transport when particles are too small. An optimal bulk to surface ratio, where the different parameters keep the balance, is found for particles in the range of 180-500 nm, which were sonicated for 2 hours. Even further enhancement in photocatalytic hydrogen evolution can be obtained by re-agglomerating those sonicated particles, probably due to more efficient inter-particle charge transport.

Since the particle surface is highly important for the catalytic process, the targeted exchange of peripheral groups can be used for specific catalytic reactions (Chapter 6). In this thesis, the first synthesis route for post-synthetic functionalization of chemically stable PHI by a triamino-s-triazine (melamine) group, leading to so called “Mel-PHI”, is demonstrated as well. The covalent

attachment of melamine to the polymer backbone causes a more hydrophobic surface of the carbon nitride, which is shown to significantly tune the interaction with the surfactant and electron donor. Due to these adapted interfacial properties an increase of the reaction rate by enhancing the hole transfer reaction can be enabled. This allows to address one key parameter in photocatalytic hydrogen evolution, which is the quenching of the light-induced holes. Consequently, increased charge transfer rates are observed which, prevent charge recombination, resulting in one of the highest reported photocatalytic hydrogen evolution rates for carbon nitrides of $5570 \mu\text{mol h}^{-1} \text{g}^{-1}$ with a comparably low Pt loading of 1.75 wt%. Nevertheless, the oxidation products of the electron donor also need to desorb quickly from the surface to not hinder the photocatalytic reaction kinetically on the long run, as observed with the oxidation products of triethanolamine on Mel-PHI.

Besides the surface, also the optoelectronic bulk properties of PHI are analyzed and optimized in this thesis (Chapter 7). As described before, PHI enables intrinsic electron storage after photoexcitation, a unique property, which was not observed in the heptazine-based 1D polymer structure. The major reason for this behavior is most likely the presence of mobile, hydrated alkali ions residing in the pores of PHI, which can also penetrate the material from the surrounding solution and stabilize photo-generated electrons on the polymer backbone. A predominantly ionic conductivity is found in PHI, with electronic conductivity being 2-3 orders of magnitude lower. The ionic mobility is highly dependent on the ion species, since not only the stacking of the 2D sheets and hence the pore channel geometry and effective pore size is affected by the size of the hydrated ions, but also the interaction strength between ion and polymer backbone. Besides the ion size, also the relative humidity (RH) influences the ionic transport. By increasing the RH from 0 to 42%, the overall conductivity can be enhanced by 4-5 orders of magnitude, which is attributed to the shielding of the attractive Coulombic interactions between the PHI backbone and the hydrated ions. An optimal combination of stacking faults, hydrated ion size and interaction strength is found for sodium ions in PHI pores, with conductivity values of $10^{-5} \text{ S cm}^{-1}$ at ambient conditions. Likewise, the most efficient stabilization of photo-generated electrons is observed for Na-PHI, which leads to a maximized photocatalytic hydrogen evolution rate. This clearly shows that bulk charge transfer also needs to be addressed when tuning photocatalytic reaction rates.

The insights gained in this thesis on the example of photocatalytic hydrogen evolution can be transferred easily to other light driven reactions and therefore, present general guidelines for studying and addressing different parameters affecting photocatalytic energy transfer processes and reactions. In addition, the described structure-property-relationships can be used as design concepts for various present and new organic based photocatalysts, hence not being restricted to the class of carbon nitrides. Besides, the intricacy of different properties that are important in light driven processes are highlighted, to raise the awareness that simple structural changes affect photocatalytic efficiency on multiple levels. Each parameter has to be studied in detail, to find the maximal efficiency of each material for the targeted reaction.

Table of Contents

1. General introduction to photocatalysis	1
1.1. Potential of solar based renewable energy.....	1
1.2. Light driven processes in a semiconductor.....	4
1.3. Photocatalytic water splitting.....	10
1.4. Use of sacrificial reagents and related aspects	14
1.5. Bibliography.....	16
2. Introduction to carbon nitrides.....	20
2.1. Crystal structure.....	20
2.2. Photocatalytic water splitting with carbon nitrides.....	24
2.3. Photophysical properties.....	28
2.4. Strategies to enhance photocatalytic hydrogen evolution rate.....	30
2.4.1. Defects, vacancies and functional groups.....	31
2.4.2. Particle size and surface area.....	34
2.4.3. Stacking distance.....	36
2.4.4. Heterojunctions and donor-acceptor structure.....	38
2.5. Light-induced charge storage in poly(heptazine imide).....	39
2.6. Other light driven reactions enabled by carbon nitrides.....	41
2.7. Bibliography.....	44
3. Research Objective.....	51
4. Structural insights into 2D poly(heptazine imide) (PHI).....	53
4.1. Introduction.....	54
4.2. Results and discussion	55
4.3. Conclusion.....	65
4.4. Bibliography.....	66
5. Morphology control in PHI: impact on optoelectronic properties and photocatalysis.....	68
5.1. Introduction.....	69
5.2. Results and discussion	71
5.3. Conclusion.....	82
5.4. Bibliography.....	83
6. Interfacial engineering of PHI for improved photocatalysis.....	86
6.1. Introduction.....	87
6.2. Results and discussion	89
6.3. Conclusion.....	100

6.4.	Bibliography	101
7.	Conductivity insights and correlation to photocatalytic hydrogen evolution in ionic PHI	104
7.1.	Introduction	105
7.2.	Results and discussion	107
7.3.	Conclusion	119
7.4.	Bibliography	120
8.	Conclusion and outlook	123
9.	Appendix	130
9.1.	Supporting information of chapter 4 “Structural insights into 2D poly(heptazine imide) (PHI)”	130
9.1.1.	Experimental details	130
9.1.2.	Instrumental details	132
9.1.3.	Transmission electron microscopy (TEM)	135
9.1.4.	Fourier-transform infrared spectrum	138
9.1.5.	X-ray powder diffraction (XRD) and size estimations	139
9.1.6.	Electron paramagnetic resonance (EPR)	143
9.1.7.	Solid-state nuclear magnetic resonance (ssNMR)	144
9.1.8.	Quantum-chemical calculations	149
9.1.9.	XRD and PDF experiments combined with structure modeling	158
9.1.10.	Protonation with different acids/concentrations	180
9.1.11.	Base treated H-PHI	182
9.1.12.	Elemental analysis	184
9.1.13.	Water sorption	185
9.1.14.	Raman spectroscopy	186
9.1.15.	Bibliography	187
9.2.	Supporting information of chapter 5 “Morphology control in PHI: impact on optoelectronic properties and photocatalysis”	189
9.2.1.	Instrumental details	189
9.2.2.	Experimental details	191
9.2.3.	Quantum-chemical calculations	193
9.2.4.	Particle size and morphology analysis	194
9.2.5.	Structural analysis	201
9.2.6.	Photocatalysis and optical characterization	210
9.2.7.	Analysis of PHI after photocatalysis	215
9.2.8.	PL analysis	219

9.2.9.	Electrochemical measurements.....	224
9.2.10.	Quantum-chemical calculations.....	225
9.2.11.	Bibliography	232
9.3.	Supporting information of chapter 6 “Interfacial engineering of PHI for improved photocatalysis”	234
9.3.1.	Experimental Section	234
9.3.2.	Proposed mechanism of Mel-PHI formation.....	241
9.3.3.	Alternative synthesis conditions	242
9.3.4.	Side phase analysis.....	247
9.3.5.	Composition and structural analysis.....	250
9.3.6.	Optical band gap analysis.....	265
9.3.7.	Photocatalysis.....	271
9.3.8.	Mel-PHI analysis after photocatalysis.....	280
9.3.9.	PL analysis	288
9.3.10.	Appendix quantum-chemical calculations.....	293
9.3.11.	Bibliography	295
9.4.	Supporting information of chapter 7 “Conductivity insights and correlation to photocatalytic hydrogen evolution in ionic PHI”.....	298
9.4.1.	Experimental procedure.....	298
9.4.2.	Instrumental setup	299
9.4.3.	Structural analysis of PHI with different counterions.....	304
9.4.4.	Electrochemical measurements	317
9.4.5.	Humidity dependent electrochemical analysis.....	328
9.4.6.	NMR analysis.....	333
9.4.7.	Quantum-chemical calculations	340
9.4.8.	Photocatalytic activity.....	344
9.4.9.	PL and electrochemical analysis under illumination	346
9.4.10.	Bibliography	349
9.5.	List of abbreviation.....	352
9.6.	List of figures	354
9.7.	List of publications	357
9.8.	International conference presentations	359

1. General introduction to photocatalysis

1.1. Potential of solar based renewable energy

The constantly increasing demand of energy in our society, along with the challenges brought about by global warming require alternatives for our dominantly fossil fuel based energy production. In 2019 the global energy generation world wide was mainly based on fossil fuels and only based by 5% on renewable energies (mainly wind energy) and 6% hydroelectricity.^[1, 2] A huge variety of different renewable energy sources are studied and optimized to compete with the current energy production, including the exploitation of wind, solar and water energy as well as biomass. One of the most promising technologies is the usage of solar energy, since it easily can cover the world's energy demand. The solar energy reaching the earth each hour amounts to around 15 TW (4.6×10^{20} J), which is more or less equal to the energy demand on earth in one year (in the year 2011). Hence, every year an energy amount of 120,000 TW (3.9×10^{25} J a⁻¹) is freely available in principle, which surpassed ~10,000 times the current energy demand on earth and is still 3,000 times more than the expected energy consumption of 43 TW in 2100.^[3-7] Even when using the already commercially existing solar cells, with an efficiency of around 12%, an area of approximately 680,000 km² (~ 7.5% of the Sahara desert) with 300 W m⁻² irradiation, would be enough to tackle the current energy demand on Earth.^[8]

Since the irradiation power differs with global tilt and depends on the weather, several key figures were defined to describe the average light intensity and hence the power correlated to it. First, the value of direct horizontal incident light at a surface perpendicular to the incident sunlight is recorded by the direct normal irradiation (DNI). Second, the value of global horizontal irradiation (GHI) is a description of the total solar flux that is incident on a horizontal surface at the earth surface. This includes reflected or scattered light by e.g. clouds, which is taken into account in addition to the direct illumination.^[9] The data in Figure 1.1a and b show the average yearly GHI and DNI from the last 20 years, which illustrates the huge potential of using sunlight on earth for energy generation. However, those values are dependent on the sky conditions^[10] and to introduce a standard, which allows a comparison between different places or laboratories, the air mass 1.5 global (AM 1.5 G) light condition is used. This describes the penetration of 1.5 atmospheres by sunlight, which is equal to a tilting degree of the incident light on the earth surface at sea level by 48.2° (relative to the sun's zenith), including reflected light.^[11] This corresponds to solar irradiation on the surface of the earth at mid latitude on a sunny day, where the light intensity is 100 mW cm⁻² (100 W m⁻²). The resulting solar spectrum is defined by The American Society for Testing and Materials (ASTM-G173-03).^[12] The peaks in this spectrum, depicted in Figure 1.1c, is caused by absorption of H₂O, and O₂ molecules in the atmosphere.^[11, 13]

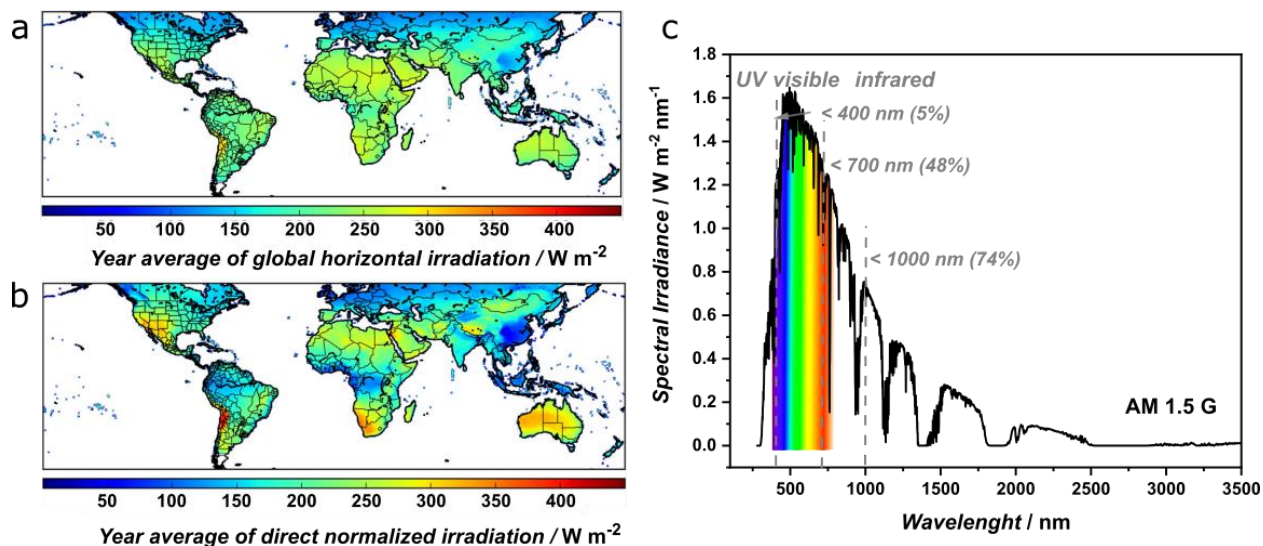


Figure 1.1: a) Depiction of average irradiation over a year, which reaches the earth surface when looking at the global horizontal irradiation and b) the direct normalized irradiation.^[14] Taken and adapted with permission from ^[14] Copyright 2020 Elsevier. c) Solar spectrum at atmospheric condition; air mass 1.5 global (AM 1.5 G) at 48.2° tilted surface. Numbers in brackets describe the percentage amount of light up to the specific wavelength in comparison to the total light intensity.^[12, 15]

To tap the full potential of the renewable source sunlight, the efficient conversion of light energy into electricity or chemical energy carriers is a major research topic today. However, some applications are already used on an industrial scale, such as in photovoltaic facilities or the production of electrical energy in photothermal electricity transformations.^[2] The conversion of sunlight into chemical energy, which is then also storable directly, is still under investigation (Figure 1.2). Nevertheless, this approach is very promising, since one of the most abundant, sustainable and renewable resource to drive (catalytic) reactions is solar energy.^[7] In general, two different types of photo-sensitized reactions can be distinguished, as suggested by Osterloh.^[16] First photocatalysis, which describes an energetically downhill reaction ($\Delta G < 0$) when comparing the energy of the starting materials with the energy of the product, and second, photosynthesis for energetically uphill ($\Delta G > 0$) reactions.^[16] Photosynthetic reactions are especially known from nature, but an increasing number of publications have proved ample evidence that also artificial systems are capable of such reactions.^[17] In the literature the distinction between photocatalytic and photosynthetic reactions is typically not invoked, especially when analyzing only one half reaction, while the respective other reaction is driven by sacrificial reagents.

In the field of photocatalysis a further distinction can be made between true photocatalysts and photosensitizers with a co-catalysts. A photocatalysts is a semiconductor with an optical band gap, absorbing the photon and acting as an electrocatalyst on its own at the same time by transferring an electron or proton. Alternatively, a photosensitizer, only absorbing the photon and transferring the energy, can be combined with a co-catalyst/ electrocatalyst, where the actual catalytic reaction takes place.^[18] Nevertheless, it is dependent on the field, which of the terms is used, since they are closely related.^[18, 19]

One particular photosynthetic reaction, namely water splitting, has the potential, in principle, to replace currently used energy production in many different applications also due to the storability of the produced gases. One of the reasons why hydrogen gas is not used today is a comparably expensive production, mostly from natural gas or by electrolysis.^[20, 21] It is therefore a key challenge to find an easy, cheap and efficient way to produce hydrogen gas without emitting CO₂.^[20, 22, 23] A possible hydrogen based infrastructure from its solar production to its consumption is shown in Figure 1.2. Photocatalysis is the direct way of producing hydrogen from water with the power of sunlight. In contrast, the indirect way for hydrogen generation via electrolysis would be based on electricity obtained from renewable energies, which is possible from an electrochemical perspective and a mature technology already. The power-to-gas conversion is only limited by the development of suitable catalysts as well as the infrastructure it requires to enable a stable supply. Another benefit of a hydrogen based energy supply is the storability of the gas, which allows electricity or power production on demand, by using the well-established fuel cell technology.^[24] Particularly for transportation, renewable energy technologies like fuel cells are in the focus of research at the moment. However, hydrogen based energy supply is also conceivable for powering houses or power plants for heating and electricity. The huge advantage of hydrogen fuel cells over other energy conversion technologies is the formation of the nontoxic and environmentally friendly product water.^[23] For this reason and due to a comparably easy and well established set-up of a hydrogen infrastructure, which is supported by the German government,^[25] hydrogen and fuel cells are among the most promising concepts for our future energy supply, if costs can be reduced to be competitive with current power supply technologies.^[23]

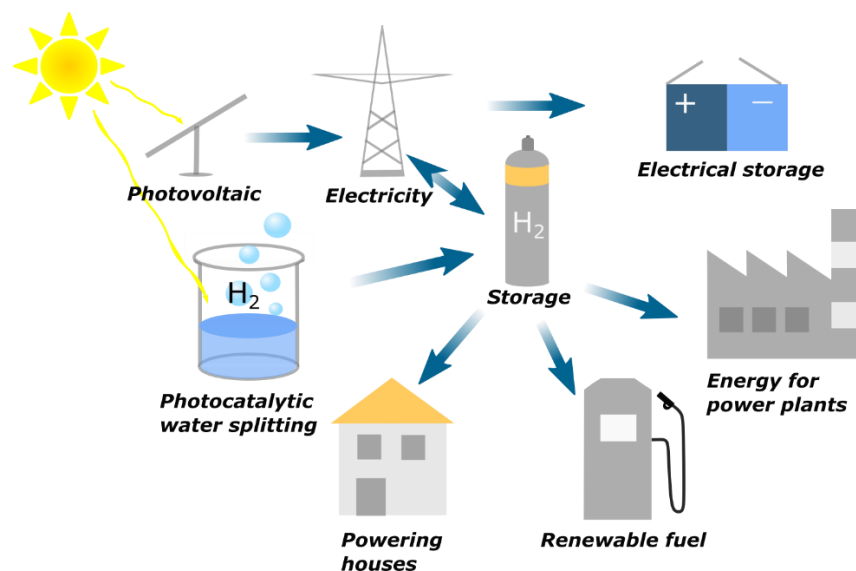


Figure 1.2: Infrastructure of solar driven hydrogen evolution on a direct way in photocatalysis and indirect via photovoltaics producing electricity, which can be transferred into hydrogen by electrolysis. Hydrogen gas can be used to power up power plants, houses or vehicles for transport by fuel cell technology, converting hydrogen either directly into power, or via fuel cells into electricity.^[22, 26-28]

1.2. Light driven processes in a semiconductor

When a semiconductor is illuminated to drive a photocatalytic reaction or differently stated, to catalyze a redox reaction, multiple steps occur on different time scales. All those processes together influence the overall efficiency, so that each of these steps should be understood, tuned and optimized.^[19] First, the photon is absorbed by the photocatalysts on the femtosecond time scale (I) so that an electron is excited from the valence band (VB) into the conduction band (CB) and a hole remains in the VB (Figure 1.3).^[19] This gives rise to exciton (electron-hole pair) formation within a few fs,^[29] which need to be separated into free charge carriers (II) by overcoming the exciton binding energy, to prevent recombination.^[19] Subsequently, while the charges diffuse or are transported to (the co-catalyst at) the surface (III), bulk or surface recombination (IV) of charges can occur. Those charge separation and transport process are normally taking place in the nano- to microsecond time regime, whereas recombination can happen on all timescales.^[19, 29] After charge transport and transfer to the co-catalysts the redox reaction can take place if sufficient driving force is provided^[19] and can be understood as electrocatalytic process.^[19, 30] In addition, also trapping of electrons in trap states (V), which are located within the optical band gap can take place on the ps to μ s timescale, which can lead to enhanced recombination or more efficient charge separation, depending on the depth of the trap state.^[31] In the following, a closer look at each of these steps will be taken.

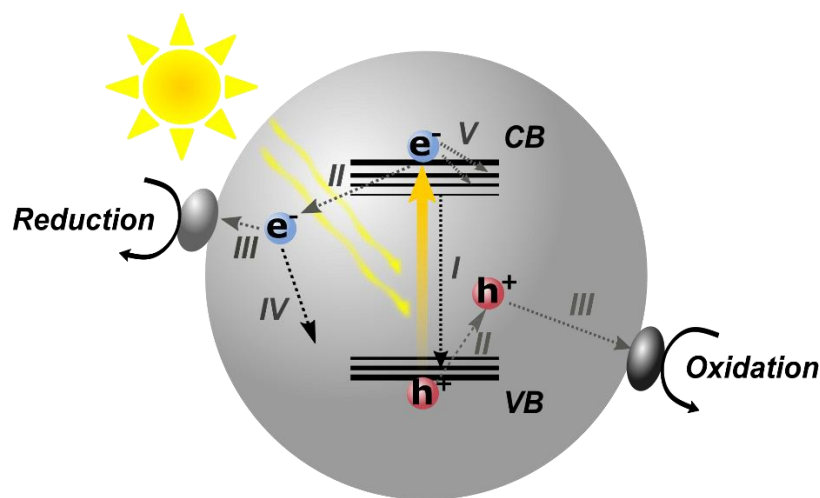


Figure 1.3: Light-induced charge separation and recombination in a semiconductor. I, Photo-induced charge generation and possible immediate recombination, II, charge carrier separation, III, transport of electrons and holes to the surface and transfer to a co-catalyst where the oxidation or reduction reaction is taking place, IV, bulk or surface recombination during charge transport, V, electron trapping in trap states located within the optical band gap.^[32, 33]

In the following, the term “photocatalysis” is used for a light driven redox process, independent of the overall energetic landscape (uphill or downhill), a terminology slightly different from the definition presented by Osterloh^[16] in the introduction. To enable photocatalytic reactions, the semiconductor must feature an optical band gap to absorb the energy of photons. The width of the band gap in a semiconductor combined with the absorbance defines the respective amount

of light that is absorbed by the semiconductor. Here not only the excitation from the VB in the CB is possible, but also excitations above the band gap. These so called “hot” charge carriers (or out-of-equilibrium charge carriers) usually undergo ultrafast intra-band relaxation to the band edges.^[34, 35] Nevertheless, not all of the incident light (I) is absorbed by a semiconductor, since different interactions are possible. The sum of the absorptance ($A_{\%}$), light that is transmitted (T), specular-reflected (R_s) and scattered forward (S) and back-scattered or diffuse-reflected (R_d) is equivalent to the incident light (Equation 1):

$$I = A_{\%} + T + R_s + S + R_d \quad (1)$$

The absorptance describes the effectiveness of the material to absorb light.^[36] Those parameters can be used to calculate the absorption coefficient, which further gives rise to the absorption depth, describing how far the light can penetrate into the material. The penetration depth is defined as the distance where the light intensity is reduced by $1/e$ (around 36%) compared to the incident light.^[36] By using well dispersed powder samples in a suspension for photocatalysis the incident light that is scattered by the particles, can be absorbed further, thereby enhancing overall light absorption.^[36] Since for powder samples the absorption coefficient (α) is difficult to obtain, diffuse reflectance (R) measurements can be performed to describe the absorption by the Kubelka-Munk function ($f(R)$), which is based on the reflectance (Equation 2):

$$f(R) = \frac{(1 - R)^2}{2R} = \frac{\alpha}{s} \quad (2)$$

where s is the scattering coefficient. However, the Kubelka-Munk function is based on certain assumptions, like no surface reflection occurring, the sample being homogeneously illuminated, the sample surface being composed of an isotropic and plane layer, and only scattering and absorption of light is taken into account.^[37] Nevertheless, this function can be used to estimate the optical band gap (E_g) of a semiconductor via the Tauc plot, using the following equation (Equation 3):

$$\alpha h\nu \propto (h\nu - E_g)^{\frac{1}{n}} \quad (3)$$

with the photon energy ($h\nu$ with h the Planck constant and ν the frequency of the light). Depending on the electronic structure n can take values of 3, 2, 3/2 and 1/2 for an indirect forbidden, indirect allowed, direct forbidden and direct allowed transition, respectively.^[36, 37]

In the photo-generated excited state excitons can form, as mentioned before. Two different types of such excitons are described for loosely and strongly bound charge carriers, namely Mott-Wannier and Frenkel excitons, which are typically characterized by a high and low dielectric constant, respectively. For an easy and hence efficient separation of excitons the binding energy of excitons should be lower than the thermal energy at room temperature (25 meV).^[19, 38] In the

case of Mott-Wannier excitons the binding energy largely fulfils these criteria, with binding energy being smaller than 10 meV and a binding radius of roughly 10 nm. Frenkel excitons on the other hand can have binding energies higher than 1 eV with a radius of only 1 nm, which are mostly found in organic systems.^[19, 39] For systems with such a high binding energy charge separation commonly takes place at the molecular level, at separated highest occupied molecular orbitals (HOMO) and lowest unoccupied molecular orbitals (LUMO) rather than at extended valence and conduction bands as in most inorganic systems.^[40] For inorganic or hybrid systems, such as (hybrid) perovskites, the dielectric constant is high, and so are the exciton diffusion lengths and charge carrier mobility, which hence can enhance photocatalytic efficiency.^[19, 41, 42]

An exciton cannot only dissociate into free charge carriers but can also form polarons, which describe a reorganization of the structure due to the additional charges generated during illumination.^[43, 44] The formation of polarons usually slows down the dynamics of charge carriers, which might also limit charge transfer and hence the subsequent photocatalytic process.^[43, 45] In general for an efficient charge carrier transport to take place, the diffusion coefficient and the lifetime of the charge carriers are important parameters, which should be as high as possible. The carrier conductivity can be enhanced by increasing the temperature, by introducing an electric field gradient, or by changing the dopant concentration.^[36] In inorganic materials the unbound electrons and holes are transported in the conduction or valence bands, respectively, where the conductivity is determined by the concentration of dopants.^[46] In many organic systems, such as carbon nitrides, the charge transfer processes are better described by hopping rather than by band-like transport.^[34, 44, 47] Especially in such systems, particle size or film thickness is crucial for photocatalysis, since the photo-generated charge should reach the surface within its diffusion length to prevent recombination.^[19, 48] So for organic materials often a suspension of well-dispersed particles with a high surface area is used.^[49]

Besides a diffusion based charge transport, driven by concentration gradients, also a potential gradient can be used for transportation. In inorganic systems such gradient can be achieved by junctions formed at interfaces such as the interface of semiconductor-metal, semiconductor-electrolyte, or with other semiconductors.^[19, 50] The absolute position of the band edges is therefore crucial for the thermodynamic driving force of the catalyzed reaction to take place at the surface.^[36, 42]

When the semiconductor is not in contact with an electrolyte or a metal, its average electron energy is described by the Fermi level (E_F). The energy of an electron rich system, such as a metal or the electrolyte, is given by the work function or the redox-potential, which is usually different from the potential of the semiconductor in vacuum. When the semiconductor is brought into contact with a metal or the electrolyte, mobile charge carriers flow from one side to the other lowering their energy and consequently both chemical potentials align and equilibrate. This then results in a band bending at the semiconductor surface (Figure 1.4b),^[51, 52] which also affects the

thermodynamics of charge carriers in the bulk, assists charge separation, and helps driving charge carriers to the surface.^[37, 53]

Depending on the conductivity type of the semiconductor, the direction of the band bending in the space charge layer is usually different. For n-type semiconductors, where electrons are the dominant charge carriers and hence the Fermi energy is typically above the redox-potential of the electrolyte, an upwards band bending results within the space charge layer on contact. This upwards bending drives holes to the surface and electrons towards the bulk (Figure 1.4b). For p-type materials (opposite case for the Fermi level as in n-type semiconductors) the bands are commonly bent downwards. A similar layer mirroring the charges missing in the semiconductor, due to band alignment, is formed at the interface in the electrolyte, which is called Helmholtz layer and consists of ions with the opposite charge to the charge induced in the semiconductor. Besides, the type of the semiconductor affects also the surface states and functionalization can contribute to band bending or even dominate it.^[37, 42, 52] Hence, the interface of the metal or electrolyte and semiconductor can on the one hand be described as ohmic contact, without charge transport barrier due to band bending, which hence is favorable for charge transfer. On the other hand, Schottky barriers can form, where the charges have to overcome potential energy barriers arising from band bending before they can be transferred from one side to another. For the formation of such Schottky barriers at the interface of the semiconductor and the electrolyte, the position of the semiconductor E_F relative to the $E_{F(\text{redox})}$ of the electrolyte is important, since it can create potential gradients enhancing charge carrier transport due to surface band bending.^[53, 54]

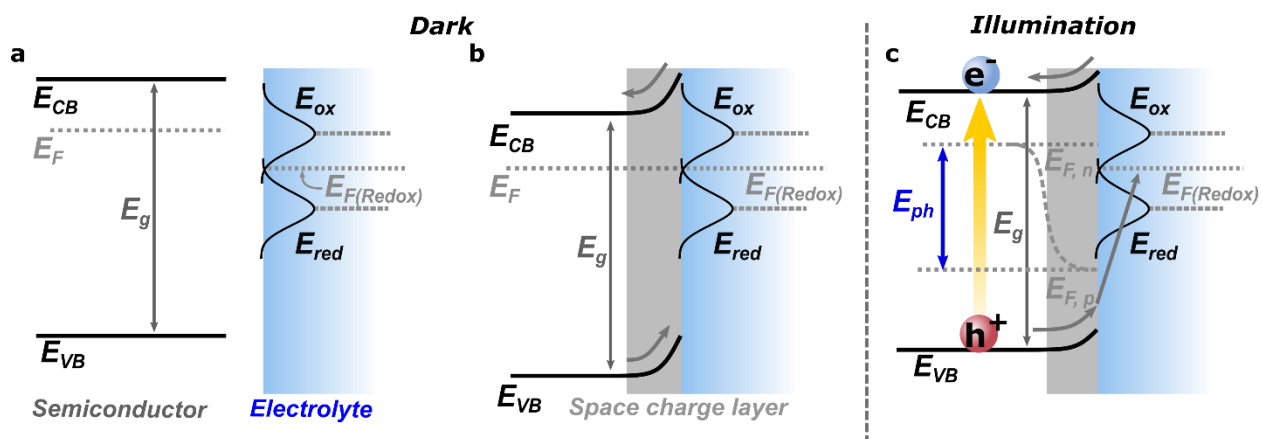


Figure 1.4: a) Band alignment of a semiconductor-electrolyte interface in the dark. Here an n-type semiconductor is shown, which is not in contact with the electrolyte. b) When semiconductor and electrolyte are brought in contact a space charge layer is formed with bands upward bending and the Fermi-level (E_F) of the semiconductor is aligned with the redox-potential ($E_{F(\text{redox})}$) of the electrolyte. c) During illumination E_F is modified and better described by quasi-Fermi levels of electrons ($E_{F,n}$) and holes ($E_{F,p}$) that are continuously formed. Their difference describes the photopotential (E_{ph}).^[36, 52, 55, 56]

During illumination E_F of the n-type semiconductor is rising, since charges are added to the conduction band (Figure 1.4c). Therefore, the Fermi level can be considered to consist of quasi-Fermi levels related to the average electron occupancy energy ($E_{F,n}$) and the hole energy ($E_{F,p}$). Their difference describes the photopotential (E_{ph}), which practically defines how much energy these charge carriers can provide.^[52, 56]

The band bending described is not necessarily present in an extended manner in organic materials, due to small crystallite sizes, high grain boundary resistance, a small polarizability and low mobile charge concentrations, as well as energetically high charge transfer barriers from the electrolyte to the material, or vice versa.^[42] This often leads to assumptions, for example in Mott-Schottky plots where a band bending is assumed, since band bending is difficult to measure. Nevertheless, it was reported for organic polymer semiconductors that only free charge carriers can contribute to the space charge layer, resulting in surface band bending for materials only when charge carriers are sufficiently mobile.^[57-59] If the mobile charge carrier concentration in the semiconductor is too low to align its energy with the surroundings, a rather flat band scenario is expected, such as for very small particles, which are too small to sustain spatially extended space charge regions. In these cases, charge generation and separation should occur near the surface, since charges are largely localized and not transported further by a potential gradient.^[60]

When considering nanostructured materials or materials with very high surface areas, the contribution of the surface states to the interfacial energetics and hence, the charge carrier lifetime and transport becomes more significant relative to the bulk, or even dominant. Out of this reason surface functional groups, often labeled as defects, can be used to tune the charge transport, especially in organic systems. On the one hand they can create electronically active states, which are vital for photocatalytic activity by acting as a charge carrier reservoir and may also be beneficial for exciton dissociation.^[19] On the other hand defects can add recombination centers or inter-band gap states (trap states), which are detrimental for photocatalysis. Depending on how deep the trap states reach into the band gap, shallow and deep trap states are distinguished (Figure 1.5a). In addition, the probability of the trapped electron to take part in photocatalytic reactions is smaller in deeper trap states, since such states normally cannot be de-trapped easily.^[31, 61, 62]

Charge carrier lifetimes in combination with quantum yield measurements can be used to describe the efficiency of charge separation within one system. The longer the lifetimes the higher the possibility of charge carriers being used for the redox process at the surface, before they recombine. In general, three different types of recombination in a homogeneous material can be distinguished (Figure 1.5b). First, the (non)-radiative band-to-band recombination, sometimes also called geminate recombination, from CB into VB (I) can occur, which is often dominant in direct band gap semiconductors and happens at timescales of femto- to nanoseconds.^[29, 63] For radiative recombination, an electron and a hole annihilate by emitting a photon, for non-radiative decays the release of energy during annihilation happens via e.g. temperature increase. Second,

Auger recombination (II) can occur, where an electron and hole recombine by band-to-band recombination, transferring the energy to another charge carrier. Third, a non-radiative defect or trap state mediated Shockley-Read-Hall (III) recombination is possible, mainly occurring in indirect semiconductors. This recombination process can also be described as a two-step recombination process (Figure 1.5b). Alternatively, also the emission of trapped electrons into the CB by de-trapping can cause recombination.^[36, 64, 65]

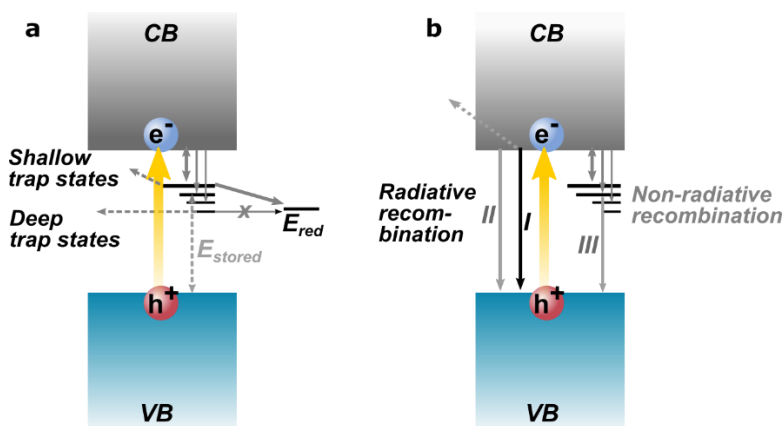


Figure 1.5: a) Charge trapping in semiconductors after photoexcitation.^[31, 61] b) Possibilities of radiative (black, error) or non-radiative (grey errors) charge carrier recombination after photoexcitation of the semiconductor. I) Direct radiative recombination, II) Auger recombination, III) Non-radiative trap-assisted recombination (Shockley-Read-Hall).^[64, 66, 67]

Once the charges are generated, separated and transported to the interface of semiconductor and electrolyte or metal, they also need to be transferred to the place where the actual catalytic reaction takes place. The charge transfer at such interfaces can significantly be hindered, due to potential barriers and trap states, which can cause charge recombination.^[68, 69] Since in most of the studied systems co-catalysts (or electrocatalysts) are used to drive the catalytic reaction more efficiently, also mass transfer at their surface is a key parameter, which is often neglected in photocatalysis. Here, the knowledge gained from thermodynamic and kinetic analysis performed in electrocatalysis can be helpful. This includes e.g. local changes in pH value, which can reduce the probability of mass transfer,^[36] or ion transport in the solution, which can create additional concentration overpotentials reducing the overall efficiency.^[19]

1.3. Photocatalytic water splitting

As described before, the energy of photons can be used to drive and catalyze a large variety of different chemical reactions. In terms of renewable energy supply, the production of hydrogen and oxygen from water is one of the main and probably most impactful research areas. In the 1970's, the first report about a semiconductor being able to drive water splitting in a photoelectrochemical cell during illumination was published by Fujishima and Honda.^[70] In this cell TiO_2 acts as photoanode driving the oxygen evolution reaction (OER), while Pt as counter-electrode and cathode material drives the hydrogen evolution reaction (HER) with an electrical bias being applied. Afterwards, it has been shown that also suspended semiconductors, acting as heterogeneous photocatalysts, can drive these water splitting reactions when decorated with co-catalysts.^[71] Nowadays, a huge variety of different materials is reported for photocatalytic water splitting, while being illuminated with UV or visible light in the presence (photoelectrocatalysis), but also in the absence (photocatalysis) of an additional external electrical bias. The systems using light and an external bias at the same time to drive photocatalytic reactions are more precisely called photo-assisted electrocatalytic processes, which will not be discussed in the following.^[72]

Overall water splitting into hydrogen and oxygen requires a thermodynamic driving force of 1.23 eV and is a four-electron reaction. Due to energetic losses at both half-reactions, which are usually summarized as overpotentials, more energy is required in reality. This overpotential depends on the catalytically active surface and should be as low as possible.^[73] Hence, the semiconductors require a band gap that absorb photons with energies larger than 1.23 eV (Figure 1.6).^[36, 72] For a single photocatalyst system the actual required band gap is assumed to be between 1.6 and 2.4 eV to provide a sufficient driving force for photocatalytic water splitting.^[73, 74] Furthermore, the band position of the photocatalyst have to straddle the electrochemical redox potentials for the hydrogen and oxygen evolution reactions, respectively.

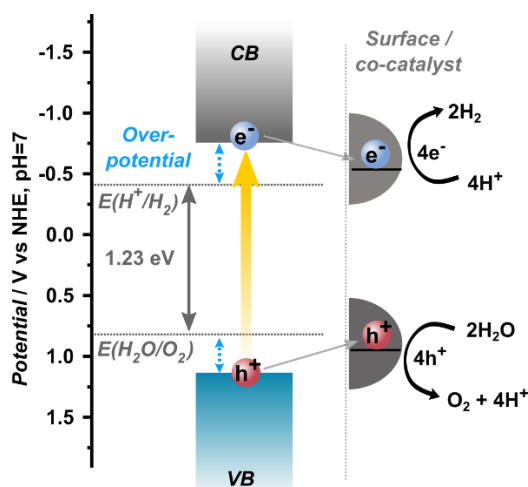


Figure 1.6: Energy scheme of required potentials for water splitting at pH 7. Blue arrows show the overpotentials, describing the additional energy required to drive the reactions, which depend on the material used.^[75, 76]

It is difficult to run both half reactions, HER and OER, at the same time on a suspended photocatalyst, since photo-generated charge carriers need to percolate to the reactive surface separately without recombining again. Therefore, in most cases only one of the half reactions is studied.^[73] The respective other redox reaction is then bypassed and performed by the addition of sacrificial agents. These can act as electron donor (e.g. alcohols) or acceptor (e.g. Ag^+ , Fe^{3+}), hence extracting one of the charges by an energetically favorable and fast one electron process, while being irreversible to avoid back-reactions.^[42, 77, 78] Often, such sacrificial reagents are used to overcome high dissociation energies of excitons in the photocatalytic material, which otherwise would present a bottleneck due to charge recombination.^[42] Even though sacrificial agents are consumed during the photocatalytic process, they are not detrimental *per se*, since they can also lead to the formation of value-added products.^[79] In addition, co-catalysts are used to drive the actual catalysis at its surface, by acting as energetic sink for electrons or holes, enhancing charge carrier separation.^[73]

Until now, only a few reports can be found about efficient overall water splitting, without the usage of a sacrificial agent or additive.^[80] One reason for this is the back reaction of hydrogen and oxygen forming water as an undesired decay reaction, slowing down the gas production, when not separated efficiently.^[75, 80, 81] Possibilities to overcome this problem is a kinetic control of the reaction to suppress the backward reaction, e.g. by surface coating^[75, 82, 83] or by surface functionalization or interface design, which specifically allows only one molecule (the one being oxidized or reduced) to adsorb.^[84] However, the problems of the simultaneous production of oxygen and hydrogen in suspensions remains, so that the reactive gas mixture has to be separated afterwards, adding additional costs.^[80] Furthermore, corrosion of the semiconductor can be a problem, which might cause a high photocurrent contribution that can be falsely interpreted as photocatalytic activity.^[80, 85] Photoelectrochemical devices based on multi-junction solar cells with gaseous products formed in different reaction compartments are a solution for such problems. Besides, they allow for the use of different and specifically tailored materials for the locally separate generation of hydrogen and oxygen. In so called Z-schemes, a two-step photoexcitation approach is used, where the photocatalytic system components also can be improved individually, while a redox mediator between them shuttles the charges, akin to nature's photosynthesis (Figure 1.7). Nevertheless, the kinetic alignment in such Z-schemes is more challenging than in a single material system, since more back or quenching reactions are possible.^[75]

Since the hydrogen evolution is only a two electron transfer process, it is easier to achieve than the four-electron transfer for oxygen evolution. Having a closer look at HER on the surface of an electrocatalyst or co-catalyst, three rate limiting processes with two surface reaction mechanisms, each having different kinetics, can be distinguished. Initially, one proton from the solution adsorbs at the catalysts surface by the first electron transfer. This reaction step is called Volmer mechanism, which is followed by the Heyrowsky or Tafel reaction describing the formation of H_2 .

In case of a good hydrogen affinity of the catalyst, two such surface adsorbed hydrogen atoms combine, forming H_2 (Volmer-Tafel mechanism). The kinetically even faster process is described by the direct reaction of the first adsorbed hydrogen with another proton from solution, forming H_2 directly if the second electron is transferred (Volmer-Heyrowsky mechanism).^[86-88] This mechanism takes place at the most efficient metal catalysts such as Pt.^[73] Besides, the adsorption energy of hydrogen is an important factor for describing the surface normalized specific activity, called exchange current density in electrochemistry studies.

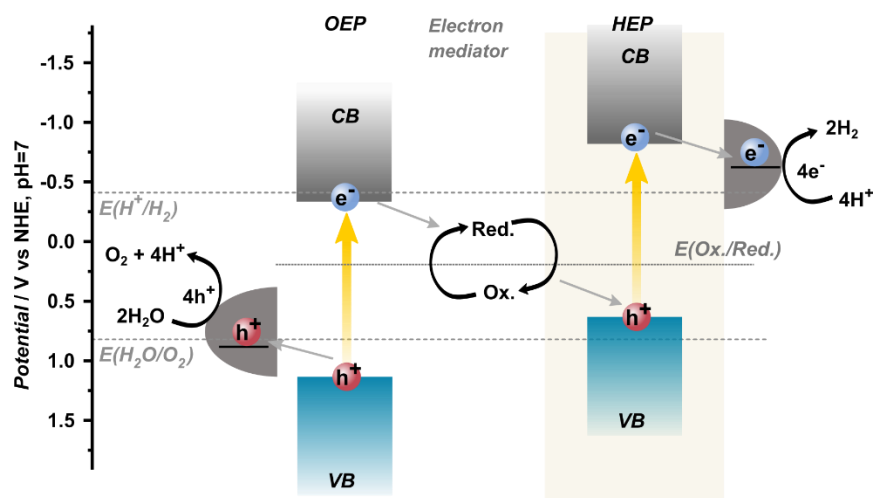


Figure 1.7: Two compartment photocatalysis reaction with redox-mediator for overall water splitting, with an oxygen evolution photocatalytic system (OEP), electron mediator, and hydrogen evolution photocatalytic system (HEP).^[75, 89]

Based on the Sabatier's principle the strength of the metal-hydrogen bond should be strong enough for adsorption, but weak enough to also desorb the hydrogen atom again without a large energy penalty.^[90, 91] This property results in a so called Volcano relation. In the optimal case, when the adsorption of hydrogen is slightly favored, the highest intrinsic activity is observed. However, good electrocatalyst have even higher exchange current densities and surface reaction kinetics when a driving force (potential) is applied.

When photocatalytic systems are compared, hydrogen evolution activities are used as benchmark. Nevertheless, these numbers rely on many material-independent factors, including the light intensity and spectral shape, the optical density of the suspension, its colloidal stability, the donors used, and the amount and type of co-catalysts employed. The hydrogen evolution rate itself is therefore strongly dependent on the specific setup, and not easily applicable for comparison. Mass normalized activities are not necessarily helpful, since photocatalytic activity does not scale linearly with the mass in a wide concentration range (Figure 1.8). Recommendations on best practice suggest that the reaction rate should be measured at the optimal photocatalyst concentration, at the onset of the plateau (II), normalized to the catalyst amount. If the concentration is too high, the light penetration depth can decrease (III), which can cause a reduction in product formation, or the rate remains constant (IV).^[92] So either the

concentration of the plateau onset has to be used, or other values should be used for comparison, which will be discussed in the following.

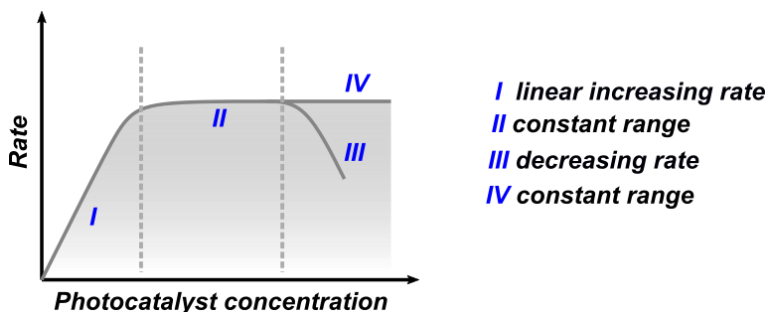


Figure 1.8: Dependence of photocatalyst concentration on photocatalytic rate. I) linear increase of rate; II) constant rates with optimal concentration range at the onset of the plateau; III) decrease of reaction rate, due to light penetration depth reduction or IV) reaction rates remain constant.^[92] Adapted with permission from ^[92]. Copyright 2015 John Wiley and Sons.

Therefore, the efficiency of a photocatalyst for hydrogen evolution is typically measured in terms of solar-to-hydrogen (STH) efficiency or described by a quantum yield (vide infra), which are more comparable between different setups.^[75, 93] The most accurate value would be the internal quantum yield, accounting for absorbed photons only, but these are difficult to extract for dispersed and scattering systems. The STH describes the relation between the output energy to that of the incident light (Equation 4):

$$STH = \frac{r_{H_2} \times \Delta G}{P_{sun} \times A_{geo}} \quad (4)$$

where r_{H_2} is the hydrogen production rate, ΔG is the Gibbs free energy (237 kJ mol^{-1}), P_{sun} is the energy flux (= number of photons of incident light at a given spectral distribution, per second; standardized to 100 mW cm^{-1})^[92, 94, 95] of the sunlight and A_{geo} is the area, which is illuminated.^[15, 36] The STH values are difficult to measure in low ranges and often inaccurate values are reported, so that all values given in the following should only be understood as rough estimates.^[96] An overall solar to hydrogen efficiency of 25% is estimated as target to be competitive with the currently used hydrogen production from natural gas, which was already reported to be possible for a multi-junction photovoltaic-electrolysis system.^[97-99] However, particle based, dispersed systems have much lower fixed costs and are more practical, lowering the efficiency requirements.^[98] In general, a minimum STH efficiency of 5-10% is required, to achieve reasonable costs.^[15, 75, 93]

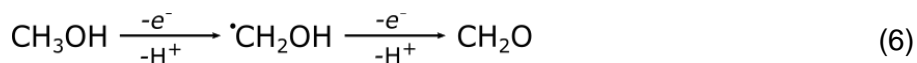
The second value, which is often used as comparison for hydrogen evolution efficiency, is apparent quantum yield. The apparent quantum yield ($\zeta_p(\lambda)$) at a given wavelength of a reaction is the rate of the product formation (r_{H_2}) over the intensity of the incident light at a given wavelength ($I_0(\lambda)$) (Equation 5).

$$\zeta_p(\lambda) = \frac{r_{H_2}}{I_o(\lambda)} \quad (5)$$

This number can only be used for comparison between materials, where the light is absorbed, scattered and reflected identically.^[92] Since this is rarely the case the production rates of hydrogen can only be compared when the same measurement geometry and reactor is used (which essentially restricts comparison to values generated within one research group). If not only the activity at one specific wavelength is studied, but rather at polychromatic light, the value is called quantum efficiency rather than quantum yield.^[93] Ideally the internal quantum efficiency or yield should be measured, since this value is devoid of light scattering or reflection and hence more comparable between different laboratories.^[93]

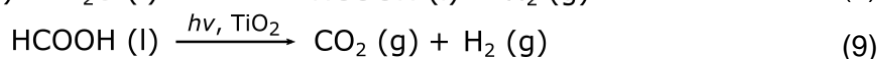
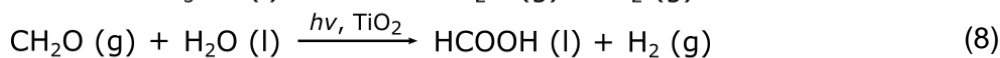
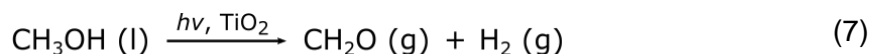
1.4. Use of sacrificial reagents and related aspects

To study the desired photocatalytic reaction in more detail, sacrificial reagents can be used to drive the respective other half reaction. Sacrificial reagents enhance the kinetics of the reaction, which can be a rate limiting factor, or the exciton dissociation. Instead of studying the overall water splitting, often only the hydrogen evolution is analyzed and electron donors are used to overcome the sluggish four-electron transfer process of water oxidation. However, several problems can arise by using sacrificial reagents. For the commonly used electron donors in photocatalytic hydrogen evolution studies current doubling effects must be considered as well. Current doubling describes the process when a single photon leads to the creation of a hydrogen molecule, although this is a two-electron transfer process and would normally require two photons. The first light-induced electron transfer process from the donor, e.g. methanol, to the photocatalyst, yields the formation of an α -hydroxyalkyl radical (e.g. $\bullet\text{CH}_2\text{OH}$). By an electron transfer from the radical into the conduction band of the photocatalyst, which is possible without photon energy, the respective aldehyde is formed (Equation 6). Besides this direct mechanism, where photo-generated holes are involved, also an indirect methanol oxidation via $\bullet\text{OH}$ radicals is possible.^[77, 100] During photocatalytic reaction these $\bullet\text{OH}$ radicals can be formed, which react with methanol forming methoxy radicals. Those radicals react further with methanol to $\bullet\text{CH}_2\text{OH}$, which can react to an aldehyde by transferring an additional electron to the photocatalyst.^[101-106]



Similar current doubling effects were shown for other alcohol electron donors as well, which have a hydrogen atom at the α -position to the alcohol group.^[77, 107] In an analogous way, formates as well as sulfides and sulfites can cause current doubling, since they form strongly reducing radical anions.^[77] However, a direct evidence of such current doubling processes and an estimation of the amount has not been shown so far.^[100] Although reports exist where more hydrogen is produced than oxidation products of methanol could be observed, they cannot be used as clear

evidence for current doubling, since carbonates as product of CO₂ dissolved in water were not included in the analysis.^[101] CO₂ formation after several hours of reaction time is possible, since the proposed mechanism for methanol oxidation at the surface of a band gap excited TiO₂ is (Equation 7-9):^[77]



The first two reaction steps are thermodynamically unfavorable at room temperature, so that the photon energy is used to raise the chemical potential of the reactants, which will then drive the reaction.^[77]

Also for the analysis of the water oxidation half reaction, the commonly used electron acceptors Ag⁺ and Fe³⁺ should be considered critically, since they can also produce small amounts of oxygen, artificially increasing the product yield and might have detrimental effects on the light absorption of the photocatalyst once deposited. Alternatives for those sacrificial reagents can be nitroaromatic compounds, which form aniline derivate, or carbon tetrachloride, CCl₄, which is reduced to CCl₂ in water, as they cannot be oxidized further, and hence do not form oxygen as a side reaction.^[108-111] Nevertheless, electron donor based studies help to provide fundamental insights into the electron transfer process from the semiconductor to the metal and, hence, the proton reduction. For overall water splitting, especially for systems with two different compartments or those that use redox-mediators to decouple both half-reactions, the understanding of such electron transfer mechanisms is important to enable efficient systems.^{[80,}

112, 113]

1.5. Bibliography

- [1] B. Statistical Review of World Energy, *Statistical review of world energy*, Vol. 69, BP, **2020**.
- [2] A. K. Azad, *Advances in Clean Energy Technologies*, Elsevier Science, **2020**.
- [3] L. Zhou, H. Zhang, H. Sun, S. Liu, M. O. Tade, S. Wang, W. Jin, *Catal. Sci. Technol.* **2016**, 6 (19), 7002-7023.
- [4] K. H. Solangi, M. R. Islam, R. Saidur, N. A. Rahim, H. Fayaz, *Renew. Sust. Energy Rev.* **2011**, 15 (4), 2149-2163.
- [5] H. Sun, S. Wang, *Energy Fuels* **2014**, 28 (1), 22-36.
- [6] R. Wegenmayr, Powerhouse Earth, https://www.mpg.de/6348886/W005_Environment-climate_070-077.pdf (accessed 2020, September).
- [7] N. S. Lewis, D. G. Nocera, *Proc. Natl. Acad. Sci. U. S. A.* **2006**, 103 (43), 15729-15735.
- [8] O. Kruse, J. Rupprecht, J. H. Mussnug, G. C. Dismukes, B. Hankamer, *Photoch. Photobio. Sci.* **2005**, 4 (12), 957-970.
- [9] A. Sayigh, *Photovoltaics for Sustainable Electricity and Buildings*, Springer, **2016**.
- [10] P. Blanc, B. Espinar, N. Geuder, C. Gueymard, R. Meyer, R. Pitz-Paal, B. Reinhardt, D. Renné, M. Sengupta, L. Wald, S. Wilbert, *Sol. Energy* **2014**, 110, 561-577.
- [11] S. Karathanasis, *Solar Radiation*. In *Linear Fresnel Reflector Systems for Solar Radiation Concentration: Theoretical Analysis, Mathematical Formulation and Parameters' Computation using MATLAB*, Springer International Publishing, Cham, **2019**, 13-72.
- [12] U. S. Department of Energy, Reference Air Mass 1.5 Spectra, <https://www.nrel.gov/grid/solar-resource/spectra-am1.5.html> (accessed 2020, September).
- [13] K. Dornelles, M. Roriz, V. Roriz, R. Caram, *Thermal performance of white solar-reflective paints for cool roofs and the influence on the thermal confort and building energy use in hot climates* **2011**.
- [14] E. Dupont, R. Koppelaar, H. Jeanmart, *Appl. Energy* **2020**, 257.
- [15] Q. Wang, K. Domen, *Chem. Rev.* **2020**, 120 (2), 919-985.
- [16] F. E. Osterloh, *ACS Energy Lett.* **2017**, 2 (2), 445-453.
- [17] B. Zhang, L. Sun, *Chem. Soc. Rev.* **2019**, 48 (7), 2216-2264.
- [18] C. Michelin, N. Hoffmann, *ACS Catal.* **2018**, 8 (12), 12046-12055.
- [19] K. Takanabe, *ACS Catal.* **2017**, 7 (11), 8006-8022.
- [20] S. Bashir, J. L. Liu, *Hydrogen-driven Economy and Utilization*. In *Nanostructured Materials for Next-Generation Energy Storage and Conversion: Hydrogen Production, Storage, and Utilization*, Springer Berlin, **2017**, 291-339.
- [21] S. E. Hosseini, M. A. Wahid, *Int. J. Energy Res.* **2020**, 44 (6), 4110-4131.
- [22] B. Zhu, R. Zou, Q. Xu, *Adv. Energy Mater.* **2018**, 8 (24), 1801193.
- [23] I. Staffell, D. Scamman, A. Velazquez Abad, P. Balcombe, P. E. Dodds, P. Ekins, N. Shah, K. R. Ward, *Energ. Environ. Sci.* **2019**, 12 (2), 463-491.
- [24] X. Ren, Y. Wang, A. Liu, Z. Zhang, Q. Lv, B. Liu, *J. Mater. Chem. A* **2020**, 8 (46), 24284-24306.
- [25] B. f. V. u. d. I. (BMVI), *Gesamtkonzept klimafreundliche Nutzfahrzeuge*, BMVI, **2020**.
- [26] N. B. Rasmussen, P. Enevoldsen, G. Xydis, *Int. J. Energy Res.* **2020**, 44 (5), 3990-4007.
- [27] T. Hisatomi, K. Domen, *Nat. Catal.* **2019**, 2 (5), 387-399.
- [28] S. Bourne, *Fuel Cells Bull.* **2012**, 2012 (1), 12-15.
- [29] M. Z. Rahman, K. Davey, S.-Z. Qiao, *J. Mater. Chem. A* **2018**, 6 (4), 1305-1322.
- [30] A. J. Bard, L. R. Faulkner, *Electrochemical Methodes: Fundaments and Application*, Vol. 2, John Wiley & Sons, Inc., **2001**.
- [31] R. Godin, Y. Wang, M. A. Zwiijnenburg, J. Tang, J. R. Durrant, *J. Am. Chem. Soc.* **2017**, 139 (14), 5216-5224.
- [32] R. Li, C. Li, *Chapter One - Photocatalytic Water Splitting on Semiconductor-Based Photocatalysts*. In *Advances in Catalysis*, Vol. 60, Song, C., Ed. Academic Press, **2017**, 1-57.
- [33] W.-J. Ong, L.-L. Tan, Y. H. Ng, S.-T. Yong, S.-P. Chai, *Chem. Rev.* **2016**, 116 (12), 7159-7329.
- [34] H. Wang, S. Jin, X. Zhang, Y. Xie, *Angew. Chem. Int. Ed.* **2020**, 132 (51), 23024-23035.
- [35] Y. Dubi, Y. Sivan, *Light Sci. Appl.* **2019**, 8 (1), 89.
- [36] K. Takanabe, *Solar Water Splitting Using Semiconductor Photocatalyst Powders*. In *Solar Energy for Fuels*, Tüysüz, H.; Chan, C. K., Eds. Springer International Publishing, Cham, **2016**, 73-103.

- [37] Z. Chen, H. Dinh, E. Miller, *Photoelectrochemical Water Splitting: Standards, Experimental Methods, and Protocols*, **2013**.
- [38] T. Le Bahers, M. Rérat, P. Sautet, *J. Phys. Chem. C* **2014**, *118* (12), 5997-6008.
- [39] S. Melissen, T. Le Bahers, S. N. Steinmann, P. Sautet, *J. Phys. Chem. C* **2015**, *119* (45), 25188-25196.
- [40] H. Bässler, A. Köhler, *Top. Curr. Chem.* **2012**, *312*, 1-65.
- [41] K. M. Pelzer, S. B. Darling, *Mol. Syst. Des. Eng.* **2016**, *1* (1), 10-24.
- [42] T. Banerjee, F. Podjaski, J. Kröger, B. P. Biswal, B. V. Lotsch, *Nat. Rev. Mater.* **2021**, *6* (2), 168-190.
- [43] E. Pastor, J.-S. Park, L. Steier, S. Kim, M. Grätzel, J. R. Durrant, A. Walsh, A. A. Bakulin, *Nat. Commun.* **2019**, *10* (1), 3962.
- [44] C. Merschjann, S. Tschierlei, T. Tyborski, K. Kailasam, S. Orthmann, D. Hollmann, T. Schedel-Niedrig, A. Thomas, S. Lochbrunner, *Adv. Mater.* **2015**, *27* (48), 7993-7999.
- [45] J. Husek, A. Cirri, S. Biswas, L. R. Baker, *Chem. Sci.* **2017**, *8* (12), 8170-8178.
- [46] E. D. Jones, *Control of Semiconductor Conductivity by Doping*. In *Electronic Materials: From Silicon to Organics*, Miller, L. S.; Mullin, J. B., Eds. Springer US, Boston, **1991**, 155-171.
- [47] Y. Tamai, H. Ohkita, H. Bente, S. Ito, *J. Phys. Chem. Lett.* **2015**, *6* (17), 3417-3428.
- [48] W. H. Leng, P. R. F. Barnes, M. Juozapavicius, B. C. O'Regan, J. R. Durrant, *J. Phys. Chem. Lett.* **2010**, *1* (6), 967-972.
- [49] Y. Wang, A. Vogel, M. Sachs, R. S. Sprick, L. Wilbraham, S. J. A. Moniz, R. Godin, M. A. Zwijnenburg, J. R. Durrant, A. I. Cooper, J. Tang, *Nat. Energy* **2019**, *4* (9), 746-760.
- [50] H. Gerischer, *J. Phys. Chem-US* **1984**, *88* (25), 6096-6097.
- [51] H. Gerischer, *J. Electroanal. Chem.* **1975**, *58* (1), 263-274.
- [52] N. Guijarro, M. S. Prévot, K. Sivula, *Phys. Chem. Chem. Phys.* **2015**, *17* (24), 15655-15674.
- [53] J. Bisquert, P. Cendula, L. Bertoluzzi, S. Gimenez, *J. Phys. Chem. Lett.* **2014**, *5* (1), 205-207.
- [54] F. Williams, A. J. Nozik, *Nature* **1984**, *312* (5989), 21-27.
- [55] D. Zhang, S. Dong, *Prog. Nat. Sci.* **2019**, *29* (3), 277-284.
- [56] M. Malizia, B. Seger, I. Chorkendorff, P. C. K. Vesborg, *J. Mater. Chem. A* **2014**, *2* (19), 6847-6853.
- [57] D. S. Yang, D. Bilby, K. Chung, J. K. Wenderott, J. Jordahl, B. H. Kim, J. Lahann, P. F. Green, J. Kim, *Adv. Mater. Interfaces* **2018**, *5* (15), 1800471.
- [58] I. Lange, J. C. Blakesley, J. Frisch, A. Vollmer, N. Koch, D. Neher, *Phys. Rev. Lett.* **2011**, *106* (21), 216402.
- [59] J. K. Wenderott, B. X. Dong, P. F. Green, *J. Mater. Chem. C* **2017**, *5* (30), 7446-7451.
- [60] Z. Zhang, J. T. Yates, *Chem. Rev.* **2012**, *112* (10), 5520-5551.
- [61] S. Kohtani, A. Kawashima, H. Miyabe, *Catalysts* **2017**, *7* (10).
- [62] J. Xu, Y. Teng, F. Teng, *Sci. Rep.* **2016**, *6* (1), 32457.
- [63] Z. Mi, L. Wang, C. Jagadish, *Semiconductors for Photocatalysis*, Elsevier Science, **2017**.
- [64] M. Plakhotnyuk, *Nanostructured Heterojunction Crystalline Silicon Solar Cells with Transition Metal Oxide Carrier Selective Contacts*, DTU Nanotech, Denmark, **2018**.
- [65] T. Dittrich, *Materials Concepts For Solar Cells*, World Scientific Publishing Company, **2014**.
- [66] K. Moazzami, T. E. Murphy, J. D. Phillips, M. C. K. Cheung, A. N. Cartwright, *Semicond. Sci. Technol.* **2006**, *21* (6), 717-723.
- [67] Y. Tian, M. Peter, E. Unger, M. Abdellah, K. Zheng, T. Pullerits, A. Yartsev, V. Sundström, I. G. Scheblykin, *Phys. Chem. Chem. Phys.* **2015**, *17* (38), 24978-24987.
- [68] Z. Wang, W. Qiao, M. Yuan, N. Li, J. Chen, *J. Phys. Chem. Lett.* **2020**, *11* (12), 4644-4648.
- [69] Z. Wang, W. Qiao, M. Yuan, N. Li, J. Chen, *J. Phys. Chem. Lett.* **2020**, *11* (6), 2369-2373.
- [70] A. Fujishima, K. Honda, *Nature* **1972**, *238* (5358), 37-38.
- [71] A. J. Bard, *J. Photochem.* **1979**, *10* (1), 59-75.
- [72] D. J. Martin, *Introduction: Fundamentals of Water Splitting and Literature Survey*. In *Investigation into High Efficiency Visible Light Photocatalysts for Water Reduction and Oxidation*, Springer International Publishing, Cham, **2015**, 1-53.
- [73] K. Striegler, *Modified Graphitic Carbon Nitrides for Photocatalytic Hydrogen Evolution from Water: Copolymers, Sensitizers and Nanoparticles*, Springer Fachmedien Wiesbaden, **2015**.
- [74] J. R. Bolton, S. J. Strickler, J. S. Connolly, *Nature* **1985**, *316* (6028), 495-500.
- [75] S. Chen, T. Takata, K. Domen, *Nat. Rev. Mater.* **2017**, *2* (10), 17050.

- [76] H. Ahmad, S. K. Kamarudin, L. J. Minggu, M. Kassim, *Renew. Sust. Energy. rev.* **2015**, *43*, 599-610.
- [77] J. Schneider, D. W. Bahnemann, *J. Phys. Chem. Lett.* **2013**, *4* (20), 3479-3483.
- [78] J. Corredor, M. J. Rivero, C. M. Rangel, F. Gloaguen, I. Ortiz, *J. Chem. Technol. Biotechnol.* **2019**, *94* (10), 3049-3063.
- [79] L. I. Granone, F. Sieland, N. Zheng, R. Dillert, D. W. Bahnemann, *Green Chem.* **2018**, *20* (6), 1169-1192.
- [80] H. Idriss, *Catal. Sci. Technol.* **2020**, *10* (2), 304-310.
- [81] H. Yoshida, R. Yamada, T. Yoshida, *ChemSusChem* **2019**, *12* (9), 1958-1965.
- [82] Y. Inoue, *Energ. Environ. Sci.* **2009**, *2* (4), 364-386.
- [83] M. Yoshida, K. Takanabe, K. Maeda, A. Ishikawa, J. Kubota, Y. Sakata, Y. Ikezawa, K. Domen, *J. Phys. Chem. C* **2009**, *113* (23), 10151-10157.
- [84] B.-J. Ng, L. K. Putri, X. Y. Kong, Y. W. Teh, P. Pasbakhsh, S.-P. Chai, *Adv. Sci.* **2020**, *7* (7), 1903171.
- [85] M. A. Khan, P. Varadhan, V. Ramalingam, H.-C. Fu, H. Idriss, J.-H. He, *ACS Energy Lett.* **2019**, *4* (11), 2712-2718.
- [86] A. Ganguly, O. Anjaneyulu, K. Ojha, A. K. Ganguli, *CrystEngComm* **2015**, *17* (47), 8978-9001.
- [87] T. R. Cook, D. K. Dogutan, S. Y. Reece, Y. Surendranath, T. S. Teets, D. G. Nocera, *Chem. Rev.* **2010**, *110* (11), 6474-6502.
- [88] Y. Liang, Y. Li, H. Wang, H. Dai, *J. Am. Chem. Soc.* **2013**, *135* (6), 2013-2036.
- [89] M. A. Nadeem, M. A. Khan, A. A. Ziani, H. Idriss, *Catalysts* **2021**, *11* (1), 60.
- [90] A. R. Zeradjanin, A. Vimalanandan, G. Polymeros, A. A. Topalov, K. J. J. Mayrhofer, M. Rohwerder, *Phys. Chem. Chem. Phys.* **2017**, *19* (26), 17019-17027.
- [91] J. M. Jaksic, N. M. Ristic, N. V. Krstajic, M. M. Jaksic, *Int. J. Hydrogen Energy* **1998**, *23* (12), 1121-1156.
- [92] H. Kisch, D. Bahnemann, *J. Phys. Chem. Lett.* **2015**, *6* (10), 1907-1910.
- [93] H. A. Vignolo-González, S. Laha, A. Jiménez-Solano, T. Oshima, V. Duppel, P. Schützendübe, B. V. Lotsch, *Matter* **2020**, *3* (2), 464-486.
- [94] H. Dotan, N. Mathews, T. Hisatomi, M. Grätzel, A. Rothschild, *J. Phys. Chem. Lett.* **2014**, *5* (19), 3330-3334.
- [95] J. H. Kim, D. Hansora, P. Sharma, J.-W. Jang, J. S. Lee, *Chem. Soc. Rev.* **2019**, *48* (7), 1908-1971.
- [96] J. Yi, W. El-Alami, Y. Song, H. Li, P. M. Ajayan, H. Xu, *Chem. Eng. J.* **2020**, *382*, 122812.
- [97] J. Jia, L. C. Seitz, J. D. Benck, Y. Huo, Y. Chen, J. W. D. Ng, T. Bilir, J. S. Harris, T. F. Jaramillo, *Nat. Commun.* **2016**, *7* (1), 13237.
- [98] B. A. Pinaud, J. D. Benck, L. C. Seitz, A. J. Forman, Z. Chen, T. G. Deutsch, B. D. James, K. N. Baum, G. N. Baum, S. Ardo, H. Wang, E. Miller, T. F. Jaramillo, *Energ. Environ. Sci.* **2013**, *6* (7), 1983-2002.
- [99] T. A. Kistler, N. Danilovic, P. Agbo, *J. Electrochem. Soc.* **2019**, *166* (13), H656-H661.
- [100] J. Schneider, D. Bahnemann, J. Ye, G. L. Puma, D. D. Dionysiou, *Photocatalysis: Fundamentals and Perspectives*, Royal Society of Chemistry, **2016**.
- [101] T. A. Kandiel, R. Dillert, L. Robben, D. W. Bahnemann, *Catal. Today* **2011**, *161* (1), 196-201.
- [102] K. D. Asmus, H. Moeckel, A. Henglein, *J. Phys. Chem-US* **1973**, *77* (10), 1218-1221.
- [103] C. Sonntag, *Free-Radical-Induced DNA Damage and Its Repair: A Chemical Perspective*, Springer Berlin Heidelberg, **2006**.
- [104] C.-y. Wang, R. Pagel, D. W. Bahnemann, J. K. Dohrmann, *J. Phys. Chem. B* **2004**, *108* (37), 14082-14092.
- [105] J. Schneider, M. Matsuoka, M. Takeuchi, J. Zhang, Y. Horiuchi, M. Anpo, D. W. Bahnemann, *Chem. Rev.* **2014**, *114* (19), 9919-9986.
- [106] J. Zhao, R. Shi, Z. Li, C. Zhou, T. Zhang, *Nano Select* **2020**, *1* (1), 12-29.
- [107] R. Gao, A. Safrany, J. Rabani, *Radiat. Phys. Chem.* **2002**, *65* (6), 599-609.
- [108] J. L. Ferry, W. H. Glaze, *J. Phys. Chem. B* **1998**, *102* (12), 2239-2244.
- [109] W. Kim, T. Tachikawa, T. Majima, W. Choi, *J. Phys. Chem. C* **2009**, *113* (24), 10603-10609.
- [110] X. Yang, Y. Li, A. Lu, Y. Yan, C. Wang, P.-K. Wong, *Sol. Energy Mater. Sol. Cells* **2011**, *95* (7), 1915-1921.
- [111] A. Hakki, R. Dillert, D. Bahnemann, *Catal. Today* **2009**, *144* (1), 154-159.

- [112] S. Tan, H. Feng, Y. Ji, Q. Zheng, Y. Shi, J. Zhao, A. Zhao, J. Yang, Y. Luo, B. Wang, J. G. Hou, *J. Phys. Chem. C* **2018**, 122 (50), 28805-28814.
- [113] K. Katsiev, G. Harrison, Y. Al-Salik, G. Thornton, H. Idriss, *ACS Catal.* **2019**, 9 (9), 8294-8305.

2. Introduction to carbon nitrides

2.1. Crystal structure

Carbon nitrides are a class of materials built up strictly from alternating carbon and nitrogen atoms, forming mostly either triazine or heptazine units (Figure 2.1).^[1, 2] These units can be interconnected via imide bridges to form layered carbon nitride polymers. Due to their structural similarity to graphene, they are also often called graphitic carbon nitrides (g-C₃N₄). The first compound of this material class was discovered already in 1834 by Berzelius and was named “melon” by J. v. Liebig without apparent reason.^[3] In the late 1980th carbon nitrides have attracted significant attention, because a three-dimensional interconnected compound (the so-called crystalline phase β -C₃N₄) was predicted, which is assumed to be potentially even harder than diamond.^[4, 5] The structure of β -C₃N₄ is similar to the tetrahedral β -Si₃N₄, where carbon atoms are in a sp³ and nitrogen atoms in a sp² hybridization state. Nevertheless, despite decades of efforts, the successful synthesis of such a compound has not yet been unambiguously verified.^[6] The true revival of carbon nitrides came with totally different properties enabling novel applications using them as photocatalytic semiconductors. In 2009, Wang *et al.*^[7] calculated and demonstrated the semiconducting properties of polymeric carbon nitrides as well as their appropriate band positions to drive photocatalytic water splitting. Ever since this report, this material class has been in the focus of research with diverse applications, most of which being based on their semiconducting nature, in catalysis^[8] or energy related purposes, including energy storage^[9], sensing^[10], and autonomous systems.^[11] The main advantage of carbon nitrides with respect to other, mostly inorganic semiconductors, lies in their sustainability due to the organic nature, low toxicity, ease of synthesis and, their molecular backbone, as well as the optical band gap, which allows excitation with visible light.

The synthesis of carbon nitride requires mostly solid-state chemistry techniques. Polymeric carbon nitrides are formed when heating either urea, thiourea, cyanamide, dicyandiamide, ammonium cyanamide, melamine or 5-aminotetrazol to 500-600°C.^[12] Both triazine or heptazine based compounds can be obtained by slightly varying the synthesis conditions. Heating for example dicyandiamide in an eutectic mixture of LiX/KX (X= Cl, Br) up to 600°C results in poly(triazine imide) (PTI) (Figure 2.1).^[13-15] Lower synthesis temperatures of 550°C in KCl melts result in poly(heptazine imide) (PHI).^[16] The pores of PTI are filled with LiCl or LiBr, depending on the salt mixture used. If no salt melt is present during the synthesis at 500-600°C, the 1D carbon nitride melon is the product.^[17, 18] At temperatures as high as 630 °C and under an autogenous ammonia pressure, 1D melon can be (partly) transformed into a 2D network called poly(heptazine imide) (PHI), which is templated by melamine (Figure 2.1).^[2, 19] Alternatively, potassium containing K-PHI can be obtained by heating 5-aminotetrazol in an eutectic LiCl/KCl salt melt to 550°C.^[20, 21] The precursor 5-aminotetrazol can also be synthesized from dicyandiamide directly.^[22, 23]

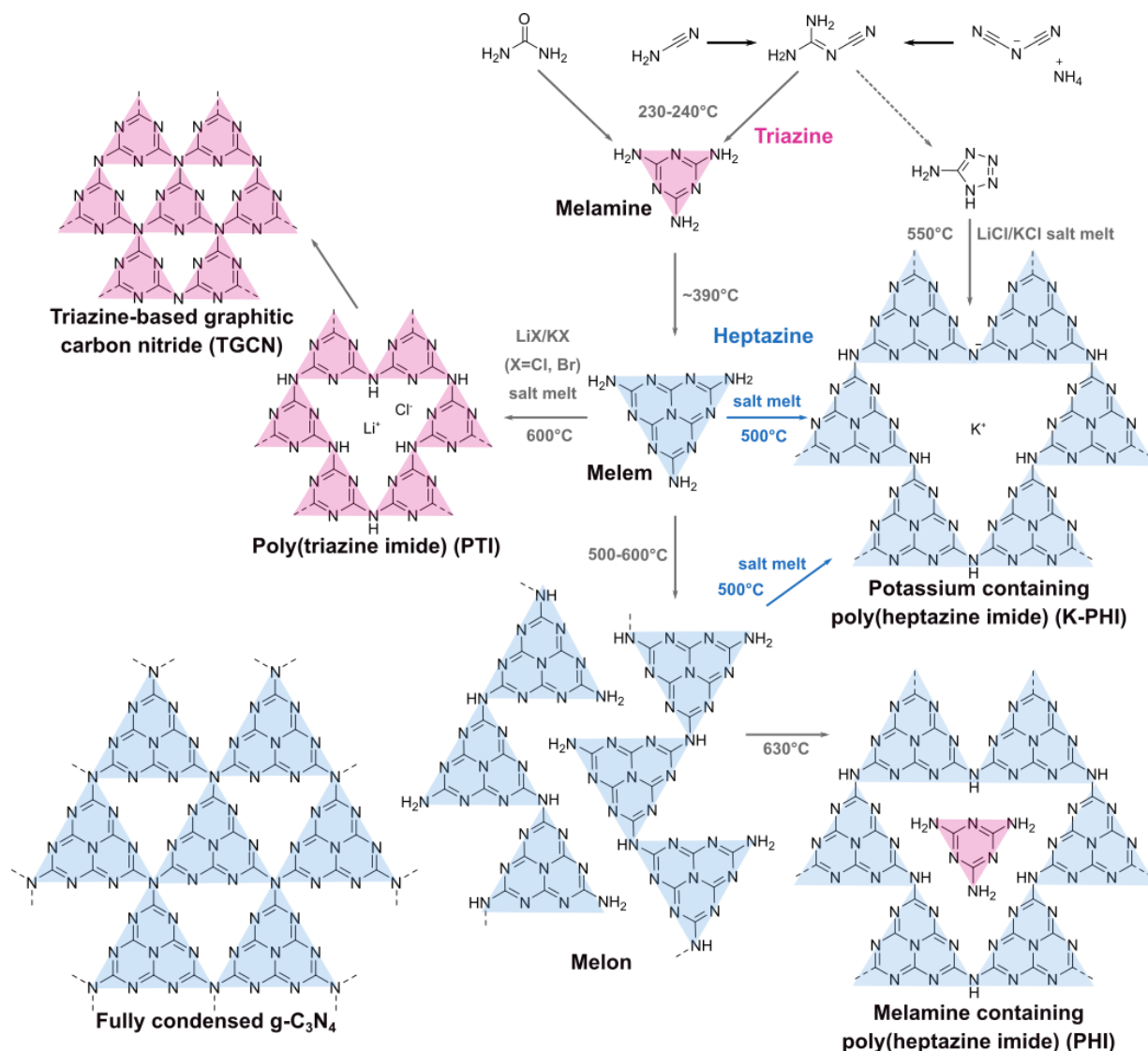


Figure 2.1: Synthesis procedure for various carbon nitrides. 1D melon^[17, 24] is obtained by heating the precursors (urea, dicyandiamide or cyanodiamide) to $500-600^\circ\text{C}$ in the absence of a salt melt. When a salt melt is present the 2D carbon nitrides PTI^[13, 25] or PHI^[20, 26] are formed, with pore fillings depending on the synthesis conditions.^[19] Besides, fully condensed structure of triazine-based systems (TGCN)^[2, 27, 28] and heptazine-based systems (g-C₃N₄)^[29] were reported, however, the existence of fully condensed g-C₃N₄ is still debated and lacking experimental evidence.^[17] Blue arrow highlights the synthesis routes, which will be discussed in more detail in Chapter 4 in combination with structural analysis.^[2]

Despite the numerous publications on carbon nitrides with various applications, the correct structural description of the different compounds is challenging, which primarily results from the lack of crystallinity of the compounds.^[30] Among the polymeric carbon nitrides, PTI is the best understood and structurally characterized compound. It consists of planar 2D layers that are stacked on top of each other in an AB manner with a distance of 3.36 \AA (in case of lithium and chloride ions), forming channels filled with lithium/protons and chloride/bromide ions (Figure 2.2a, b).^[13, 14] One chloride/bromide ion is located in the middle of the channel, whereas the lithium ions/protons are placed around the chloride ions, also interacting with nitrogen atoms from the

PTI backbone.^[13, 14, 25, 31] The unit cell of PTI crystals with a hexagonal space group ($P6_3cm$, $a=8.47$, $c=6.75$ Å) contains two layers of PTI with chloride/bromide ions between the layers and one third occupied lithium positions within the layer (Figure 2.2a, b). In 2019, an orthorhombic structure of PTI/Li⁺Cl⁻ was published (space group $Cmc2_1$, $a=14.73$, $b=8.47$, $c=6.64$ Å), which can be described as a superstructure of the hexagonal structure, as evidenced by synchrotron PXRD data.^[31] An alternative structure solution was found previously, based on NMR analysis. In each pore, one hydrogen atom is bound to a bridging nitrogen and most probably an additional one to a triazine ring. Two lithium ions are coordinated in the pores as well, interacting with two nitrogen atoms of two different triazine rings, respectively.^[32]

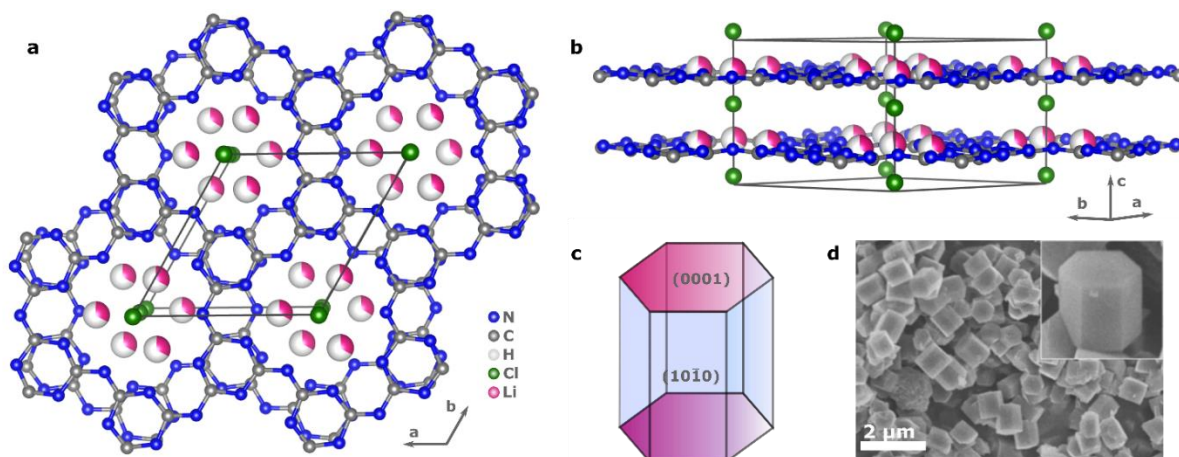


Figure 2.2: Structure of PTI/Li⁺Cl⁻: a) Crystal structure with unit cell of PTI/Li⁺Cl⁻ view along c -axis and b) view along a,b plane.^[32] c) Single crystal shape and facets of PTI/Li⁺Cl⁻ grown by ionothermal synthesis.^[33] d) SEM image of single crystals (adapted with permission from^[33]. Copyright 2020 Springer nature).

Recently, the synthesis of single crystals of PTI/Li⁺Cl⁻ was reported, grown by an ionothermal synthesis route.^[33] This procedure allowed a thorough characterization of the structure and also an investigations on their active facets for overall water splitting. The prismatic side planes (1010) were found to be the most active ones. This was also confirmed by quantum-chemical calculations, showing a preferred electron and hole transfer to this surface plane (Figure 2.2c, d). The co-catalysts Pt or Co, which were used for photocatalytic water splitting, were mainly deposited on the (1010) plane, where the active centers are found. Therefore, an enhancement ratio of (1010) / (0001) lead to an increase in photocatalytic water splitting activity. Additionally, the exciton binding energy was estimated by temperature dependent photoluminescence measurements. The observed value of 50.4 meV^[33] is smaller than most values obtained for conjugated polymers,^[34, 35] and only slightly larger than the thermal energy at room temperature (~ 26 meV).

Larger single-crystals of the polymeric heptazine-based structures melon and PHI could not be obtained so far, even though heptazine-based systems are predicted to be more thermally stable than triazine-based systems.^[36, 37] The 1D poly(aminoimino) heptazine, also known as melon, was characterized from a nanocrystalline material. This material is often called g-C₃N₄ in the literature

and typically a fully condensed 2D structure is assumed, the existence of which has not been unambiguously proven so far (Figure 2.1).^[2, 17] The in-plane structure of melon can best be described by a rectangular geometry using the plane group $p2gg$ ($a=16.7$, $b=12.4$ Å, $\gamma=90^\circ$) (Figure 2.3a). The 1D polymer chains of heptazine units are bridged by NH-groups. Each heptazine unit has a terminating NH_2 group that gives rise to the formation of hydrogen bonds with the neighboring polymer chain. In this way planar layers are formed, which are stacked on top of each other with a distance of ca. 3.2 Å. The stacking energy landscape is flat, which makes stacking displacements likely.^[17] However, another synthesis method, with slightly lower synthesis temperatures of 510-610 °C results in melon with a triclinic crystal structure ($P1$ or $P\bar{1}$, $a=16.2$, $b=12.1$, $c=3.26-3.28$ Å, $\alpha=\beta=90^\circ$, $\gamma=87-90^\circ$). Depending on the synthesis temperature, a denser packing along the c -axis and a larger γ angle was observed for higher temperatures. The most likely stacking type is an AB stacking or AA stacking with layer offset of flat or slightly buckled layers, which are energetically similar.^[38-40]

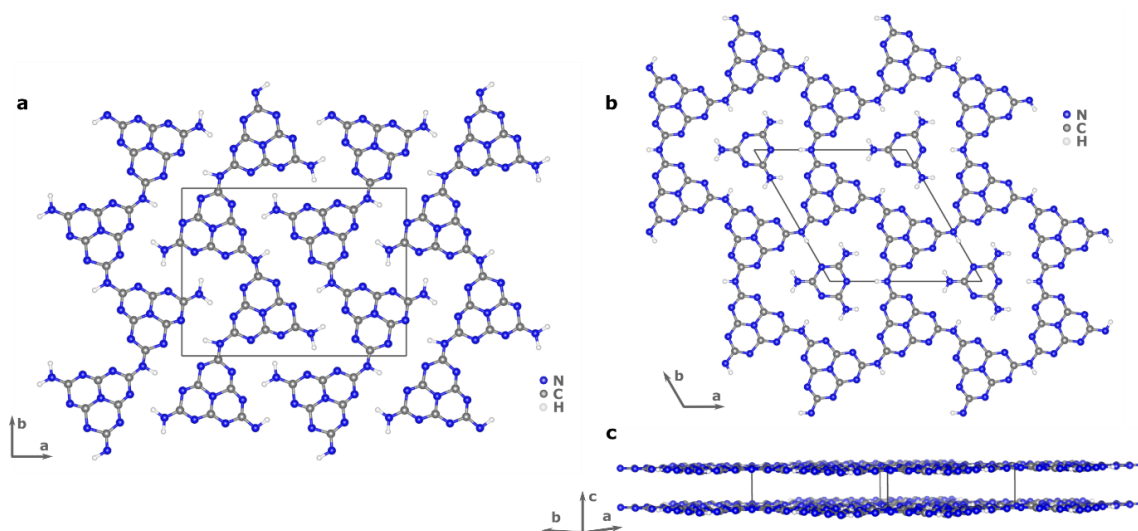


Figure 2.3: a) In-plane structure of melon viewed from the top^[17, 38] and b) PHI template by melamine, view along c -axis and c) along a,b plane.^[19]

The further condensed 2D polymer formed by heptazine units, PHI, was first reported in 2009 with incorporated melamine units and was characterized by transmission electron microscopy (TEM). From electron diffraction data of the nanocrystalline material, a hexagonal cell could be indexed ($a=12.4$ Å) with a stacking distance of 3.2 Å (Figure 2.3b, c). Six heptazine units form a pore, which is filled with melamine (Figure 2.1). The stacking behavior of the planar layers could not be identified conclusively.^[19] PHI can also be obtained by an ionothermal synthesis route using for example KCl/LiCl salt melts. The pores of PHI are then filled with potassium ions and the resulting material is called K-PHI. When synthesized from 5-amintetrazol, a structure similar to PHI filled with melamine was observed, which is called K-PHI and has a hexagonal unit cell ($a=12.64$ Å) (space group $P31m$).^[20, 41, 42] Similar to a publication of our group (Chapter 4), Savateev *et al.*^[42] described stacking faults in K-PHI as a reason for line broadening in PXRD data.

2.2. Photocatalytic water splitting with carbon nitrides

As mentioned above, the development of carbon nitrides as photocatalysts for water splitting started in 2009.^[7] Since then, the research interest in this material class increased exponentially, not only for photocatalytic hydrogen evolution. Overall water splitting with carbon nitrides (both water oxidation and reduction occurring simultaneously) enabled by one single material at the same time, however, has only been reported in few publications to date. In one of these publications, crystalline PTI/HCl was used, which was loaded with 1 wt% Pt and 3-12 wt% CoO_x via photo-deposition as co-catalysts for the hydrogen and oxygen evolution reactions, respectively, without the use of sacrificial reactants. A hydrogen evolution rate of around 650 μmol h⁻¹ g⁻¹ and 310 μmol h⁻¹ g⁻¹ for oxygen evolution was measured. The main problem, however, was the back reaction of hydrogen and oxygen forming water.^[25] Also for heptazine-based systems overall water splitting was reported. Among the highest ever reported STH with a suspended photocatalyst of 2% was reported for carbon nitride (g-C₃N₄) in combination with carbon quantum dots.^[43] The postulated mechanism for oxygen evolution assumed the formation of H₂O₂ on the carbon nitride, which is then further decomposed to O₂ by the carbon quantum dots.

To prevent the back reaction of hydrogen and oxygen forming water and to overcome the sluggish four-electron transfer at the oxidation site, hydrogen evolution reactions is typically reported using an electron donor as sacrificial agent. The most studied carbon nitride for photocatalytic hydrogen evolution is melon (g-C₃N₄ in literature). Of all the carbon nitride materials, melon is the one with the most negative conduction band and hence strongest driving force for hydrogen evolution from water. However, the lowest photocatalytic HER is observed for melon in experiments, which points to other effects being more important.^[1] Despite the large number of publications, some challenges remain in terms of efficient hydrogen evolution with carbon nitrides, which include interfacial design, mechanistic insights, back reaction with oxygen being present in air, and side reactions of the used electron donor.

Hydrogen evolution was reported with a huge variety of different co-catalysts ranging from Pt^[8] over Au,^[44] Ag,^[45] Rh,^[46] to Ni- or Co-based molecular catalysts,^[34, 47-49] also in combination with graphene.^[50] Nevertheless, most of the tested co-catalysts are not as efficient and stable as Pt, so that the most commonly used co-catalyst is still platinum.^[51] No matter which metal support or co-catalysts is used, its interface to the carbon nitride is crucial for charge transfer and hence must be studied in detail to enable fast and efficient charge transport and interfacial charge transfer. Important parameters which, influence this interface, are the shape of the particles and, hence, exposure of facets or active sites, defect and vacancy types and concentrations, as well as the absolute and relative band positions.^[30] Unlike in inorganic systems, for carbon nitrides it is still not fully clear if assumptions on band alignments with metals or the electrolyte are valid, which is challenging for interfacial design.^[1]

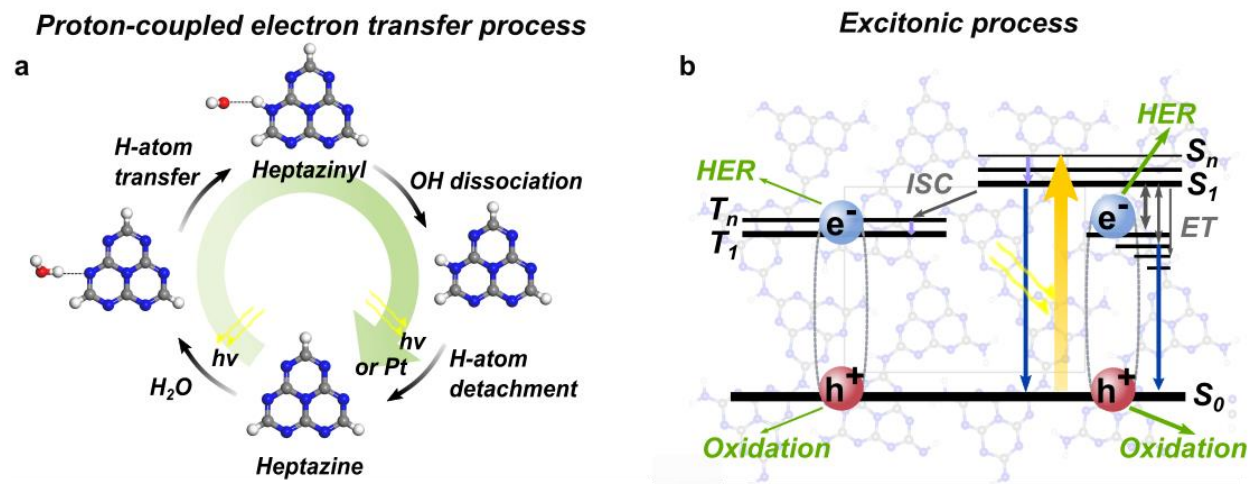


Figure 2.4: Schematic description of process in photocatalytic hydrogen evolution reactions on heptazine-based materials. a) Postulated proton-coupled electron transfer process for heptazine molecules.^[52, 53] b) Exciton based process for carbon nitrides with exciton formation after illumination. Light blue arrows depict internal conversion, dark blue arrows the exciton recombination possibilities and green arrows the exciton dissociation possibilities. ISC = inter system conversion, ET = exciton transfer into trap states, HER = hydrogen evolution reaction, S = singlet state and T = triplet state.^[54-56]

Not only the interaction with the co-catalyst is important, but also the interface between photocatalyst and electrolyte, as well as the organic molecules used in the study (as pollutant, sacrificial agent or reactant). Depending on the interaction strength of the starting materials, intermediates and products, the mechanism of the photocatalytic reaction can be changed or in the worst case, the reaction is prevented.^[57] Little is known about these interfacial interactions and also about the respective photocatalytic mechanism including its intermediates. For photocatalytic hydrogen evolution with carbon nitrides an excitonic process, which is similar to inorganic systems,^[54, 58] and a molecular approach is postulated in literature (Figure 2.4a, b). The assumed molecular mechanism is based on a proton-coupled electron transfer and was calculated for heptazine molecules.^[59] A favorable two-photon reaction (with wavelength shorter than 275 nm) is predicted where the first photon absorption causes an interaction between a water molecule with one nitrogen atom of the triazine or heptazine unit (Figure 2.4a). By hydrogen abstraction, an $\cdot\text{OH}$ radical and a heptazinyl/triazinyl radical is formed. A second photon or Pt is used to split the hydrogen atom off the ring again, so that overall four photons are required to form one H_2 molecule. This would lead to a bisection of the quantum efficiency in contrast to the normally assumed two-photon process. Alternatively, a recombination of two hydrogen radicals is postulated to form H_2 in the presence of Pt, without the requirement of light for this step, resulting in a two-photon H_2 production route, which is 4.4 eV more favorable than the first described route with four photons. Similar mechanisms were postulated in presence of electron donors.^[52] Recently this proton-coupled electron transfer mechanism was also supported experimentally by electron paramagnetic resonance measurements, showing the transfer of protons, hydrogen atoms and electrons from the carbon nitride surface to the Pt, where molecular hydrogen is formed.^[60] Based on this mechanistic hypothesis it was calculated that for donor free

hydrogen evolution a low-barrier proton transfer in the excited state is needed.^[59] This energy of the charge transfer state (in the hydrogen bonded complex) can be stabilized by 1.0-1.3 eV when electron-withdrawing groups (e.g. COOH, CN or NO₂) are attached at the heptazine unit,^[59] in contrast to electron donating groups like NH₂ or NHCN.^[52] However, further studies are necessary to confirm these findings also experimentally and to prove the existence of a proton-coupled electron transfer process in carbon nitrides.

As mentioned above excitonic processes in carbon nitride photocatalysis (Figure 2.4b) are often described to have a major impact on the photocatalytic performance.^[54] Due to light irradiation electrons are excited from the ground state (S₀) to a singlet excited state (S_n). After internal conversion a singlet exciton is formed and transferred to trap states. Alternatively the singlet exciton is transformed in a triplet (T_n) exciton via intersystem crossing. The exciton dissociation is most probably taking place at defect sites or interfaces and can be promoted by electron donors. The resulting free charge carriers are transferred to the co-catalyst and can eventually participate in the redox reaction.^[54] However, not only charge transfer, which is the main process in carbon nitrides,^[54, 55] but also resonant energy transfer of the exciton is possible in polymer based systems, as well as carbon nitrides, e.g. forming singlet oxygen while relaxing to the ground state again.^[56, 61] Both, charge carrier and excitonic aspects, coexist in polymer photocatalysts, but not to the same extent. Major excitonic effects are rather expected in materials with large exciton binding energies, while material with small binding energies rather emerge charge carrier effects.^[56, 62] In carbon nitrides exciton quenching is relatively fast for the electrons and quenching of the photo-generated holes is comparably slow.^[63] One report of a theoretical study of a combined mechanism of an excitonic interface proton-coupled electron transfer mechanism exists, which is still to be proven experimentally.^[64]

Another problem, which is often neglected, arises from the presence of oxygen in photocatalytic reaction solutions or suspensions. As reported for different materials for overall water splitting, the presence of oxygen and hydrogen can cause recombination of those two gases forming water, as naturally catalyzed by Pt.^[65] In 2019, the effect of Pt addition on the photocatalytic oxidation reaction in the presence of oxygen from the air was compared for carbon nitrides and the well-studied photocatalyst TiO₂ (which has a 0.5 eV more positive conduction band).^[66] Due to the addition of Pt, the charge separation is enhanced in both systems and shallow trap states may be formed, even though the effects are more pronounced in TiO₂/Pt. A similar trend was observed with other noble metals like Pd, Au and Ag, deposited on carbon nitrides.^[66] However, different mechanism for the formation of reactive oxygen species were found in Pt covered TiO₂ or carbon nitride. For TiO₂ the formation of ·OH radicals is possible via an oxidative pathway from water or via a reductive pathway from oxygen (via ·O₂⁻). Due to the more negative band edges of carbon nitride, the oxidative pathway is not possible. Once Pt is added the reductive pathway intermediate H₂O₂ is efficiently decomposed by the transition metal, so that the rate of ·OH radicals formed in Pt decorated carbon nitride is low in comparison to Pt loaded TiO₂.^[66] In line, for melon

in the absence of a co-catalyst selective H_2O_2 formation was described in the presence of an electron donor.^[67] The predicted mechanism assumes a two-electron transfer from the donor to a heptazine unit. After that, molecular oxygen is adsorbed at a carbon atom next to the imide bridge and forms a superoxide radical. Then, H_2O_2 is formed via a 1,4-endoperoxide species, which is suppressed if Pt is present, due to enhanced electron transfer to the metal.^[67] However, direct recombination of oxygen and hydrogen at the Pt surface is also possible, so that oxygen contamination should be avoided when studying hydrogen evolution. In addition, reports also exist, which describe an energy transfer rather than a charge transfer between carbon nitrides and oxygen, leading to the formation of singlet oxygen instead of radical generation.^[61]

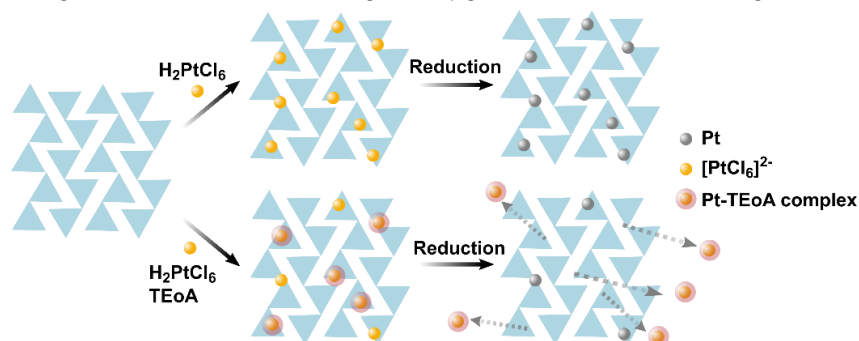


Figure 2.5: Effect of the addition of reaction components triethanolamine (TEoA) and H_2PtCl_6 in different orders to photo-deposit Pt on carbon nitrides (if no TEoA is present, the photo-deposition is conducted in absence of another electron donor). A complex formation of triethanolamine and Pt^{4+} is possible.^[68]

In addition, also the adsorption and desorption processes of the donor molecules at the photocatalytic surface should be considered, since reaction pathways and reaction efficiencies are severely affected by those as well.^[69, 70] Recently, it was reported that the choice of electron donor during photocatalytic hydrogen evolution is critical, since e.g. triethanolamine (TEoA) can form a complex with Pt (a tetra-TEoA Pt^{4+} complex), so that the platinum cannot be reduced by the carbon nitride anymore (Figure 2.5). Here, the interaction between Pt and the carbon nitride is weakened and less Pt is deposited on the material. A four times higher HER rate can be obtained when TEoA is added after Pt deposition, which is conducted without any electron donor.^[68] Nevertheless, the Pt deposition without any electron donor to be present is unlikely and the formation of the tetra-TEoA Pt^{4+} complex is yet to be proven.

2.3. Photophysical properties

The mechanistic analysis in photocatalysis is fundamentally connected to the knowledge of photophysical properties of the respective photocatalyst. Such properties include light-induced charge carrier generation, their stabilization, separation, or recombination. The photo-excited state of charge carriers in melon-type carbon nitrides was described to last only for nanoseconds (ns) to microseconds (μ s). Within this time frame, the electrons and holes have to be separated and extracted to avoid losses. So far, most insights into the underlying charge transfer and recombination processes were obtained by ultrafast spectroscopic measurement.^[71, 72] In the following, an overview of the processes is given that are involved in photocatalytic reactions with carbon nitrides.

After illuminating melon-type carbon nitrides, Frenkel-type excitons are generated, which have a high exciton binding energy (several 100 meV to 1 eV) with small radii of approximately 1.4 Å. These are linked to a low dielectric constant of 3-5.^[56, 72-75] The exciton binding energy describes the difference between the energy band gap of a material and the energetic reduction due to the Coulombic interaction upon electron-hole-pair formation.^[56, 72] To separate the charges, this energy has to be overcome so that a low exciton binding energy and large radius is needed for efficient photocatalytic reactions. When assuming a 2D extended, buckled, perfectly conjugated network, the binding energy can be reduced to 320-360 meV with a radius of the excitons of 2.9-3.0 Å for triazine- and heptazine-based systems.^[73] One of the lowest exciton binding energy reported so far for carbon nitrides was described for single crystalline PTI with only 50 meV,^[33] whereat a higher exciton binding energy of 840 meV was predicted.^[73] However, due to the generally high exciton binding energies and low dielectric constants in carbon nitrides, especially when compared to well-defined inorganic systems, excitonic effects for charge carrier separation play a major role in this class of materials. Those excitonic effects are difficult to measure and therefore are not fully understood so far.^[56, 72] One of the major problems is the not well defined molecular structure of carbon nitrides, which includes significant amounts of defects in the polymeric backbone and on terminal sites.^[61]

Excitons can dissociate within their lifetime (\sim 200 fs) into single polaron pairs, after overcoming the binding energy. The term polaron is used to describe the interaction of the charge carrier with the surrounding lattice or polymer backbone.^[76] The electron and hole polarons in melon can subsequently diffuse between the layers using overlapping molecular orbitals via a hopping mechanism.^[77] The imide bridges between the heptazine units were calculated to be insulating, so that the electron transport appears to be dominantly occurring in the stacking direction.^[63, 72, 77-79] Similar to these findings, conductivity analysis of oriented thin films of PTI/LiBr showed anisotropic behavior with a two order of magnitude higher out-of-plane conductivity (up to 1×10^{-4} S m^{-1}). In this study, also light-generated charges were found to relax towards a metastable polaronic state, which is transported via 1D (or better described as zig-zag) hopping along the

stacking direction. However, this behavior is opposite to other more conducting 2D materials like e.g. graphite or MoS₂, where higher in-plane conductivities have been observed.^[80]

The higher the mobility of such polarons and the higher the hopping rate in combination with low exciton recombination, the higher is the probability of charge carriers to reach the surface and promote photocatalysis.^[81, 82] Exciton dissociations and therefore suppression of recombination most likely happens in areas that have energetic inhomogeneity assisting this process.^[56, 83] In carbon nitrides, this can be achieved by interfaces of more and less ordered regions, as typically present in semicrystalline materials.^[84] Another way to enhance the exciton dissociation is the formation of heterojunctions within carbon nitrides, like in donor-acceptor structures, e.g. by introducing selenium atoms acting as donor sites and cyanamide groups as acceptors,^[8, 85] or by co-catalyst addition and interfacial design (between semiconductor and a solution or donor).^[72, 73, 86] Nevertheless, the excitons' lifetimes are at maximum around 1 ns in organic materials, and a diffusion length of those excitons of 20 nm can be assumed, so that the domain size of the particles should be on the same order of magnitude to allow an efficient exciton separation at interfaces to prevent their recombination.^[87]

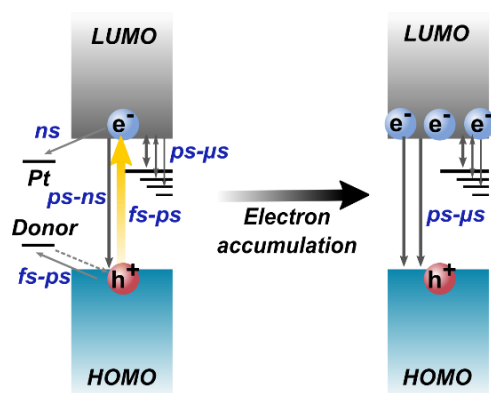


Figure 2.6: Timescales for different light-induced processes in carbon nitrides, analyzed by ultrafast spectroscopic measurements.^[48, 63]

In 2017, a publication reported that free charge carriers in melon are generated in the range of 200 fs, which are trapped within ps and can recombine on various timescales from ps to μ s, hinting to a trapping-detrapping process (Figure 2.6).^[55] The electron transfer from melon to the co-catalyst Pt also most likely happens on the ns time scale and therefore competes with charge trapping. Such trap states might be introduced by surface termination groups or defect sites such as urea, amines or hydroxyl groups. Depending on the concentration of these groups, trap states were found to reach up to 1 eV into the band gap, whereas at these deep levels, the electrons do not take part in reduction reactions anymore. One way of tuning carbon nitride materials is consequently the identification of groups and defects that are responsible for trapping electrons, and hence the intentional introduction shallow trap defects.^[55]

A fast hole extraction prevents charge recombination and is therefore required for high photocatalytic activities.^[63, 88] The hole extraction in melon-based systems was found to be in the

range of 100 fs depending on the electron donor employed (e.g. methanol or triethanolamine). Also an electron transfer from the carbon nitride back to the oxidized donor can occur in the range of 400 ps, which should be prevented.^[89] In general, a balance between electron and hole extraction is therefore one key parameter in photocatalysis.^[1, 72]

2.4. Strategies to enhance photocatalytic hydrogen evolution rate

In this paragraph, a summary of the factors that are commonly tuned in carbon nitrides to obtain efficient photocatalysts will be given, and compared to strategies used for inorganic systems. The measurement of intrinsic properties in organic materials, like bulk and grain boundary conductivity or band position of the material in contact with an electrolyte is challenging, based on not well controllable defects, homogeneous films or sufficiently large crystallite domains.^[1] However, compared to inorganic systems organic semiconductors offer different tuning possibilities on the molecular level, like the rational integration of internal donor-acceptor functions, covalent surface functionalization, or tuning of the crystallinity and the polymer chain length.^[1, 90] In Figure 2.7 the most common strategies are summarized that were individually reported already for carbon nitrides in order to enhance their hydrogen evolution rate. Among these are the introduction of donor-acceptor functions^[91], tuning of vacancies^[92], defects or functional groups^[93, 94], building of heterojunction or copolymerization^[95], reducing the stacking distance^[96] and nanostructuring the material, e.g. by reducing the particle size^[97]. Aim of such modifications is to enhance the hydrogen evolution rate, the charge carrier mobility or surface area, to reduce the excitation energy or to increase the absorption behavior, as well as to tune the electronic structure.^[51, 98] In the following, especially the effect of structural changes on the photophysical properties will be discussed, since this is still a very controversially discussed topic in carbon nitride chemistry, where detailed structural descriptions are still largely missing.

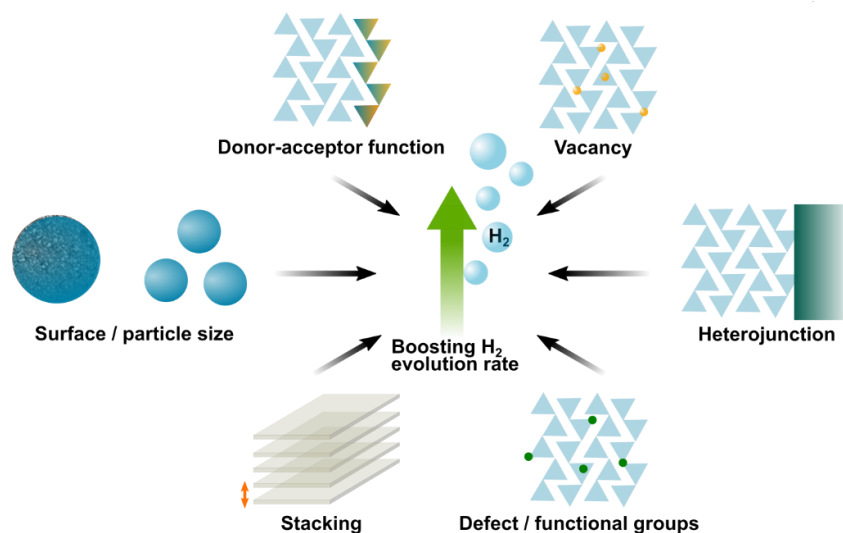


Figure 2.7: Reported tuning parameters on the molecular/structural and morphological level in the bulk and at the interface in order to boost photocatalytic hydrogen evolution with melon.^[91, 92, 95-97, 99]

2.4.1. Defects, vacancies and functional groups

The concentration and kind of surface states are important parameters to tune the photocatalytic activity^[100, 101] by acting as catalytically active centers, coordination sites for co-catalysts, or recombination centers.^[8, 92, 94, 102] Such surface states are often denoted as defects. Different types of defects can be distinguished, namely point defects, such as vacancies or atomic doping, line defects like edge dislocation, volume defects and planar defects (Figure 2.8).^[51] In the following mainly point defects will be discussed in more detail. However, a clear separation of influences of a single types of defects, vacancies and functional groups is difficult due to their simultaneous presence.

Point defects were studied intensively for carbon nitride-based systems, especially the effect of nitrogen vacancies. By introducing nitrogen vacancies the amount of cyano groups^[92, 103], OH groups^[104] or NH_x groups^[105] can increase at the same time, consequently causing a slight narrowing of the optical band gap or other changes in the electronic structure (Figure 2.8a).^[92, 103-105] Both negative or positive effects on the photocatalytic hydrogen evolution rate were described after introducing those defects, which were explained by shorter or longer lifetimes of photo-generated charges trapped in the defect-containing carbon nitride, and hence a reduced or enhanced charge separation efficiency.^[103-105] Often, enhanced photocatalytic activity is attributed to a better light absorption and lower radiative recombination rates arising from an increasing nitrogen vacancy concentration.^[106-108] The apparent contrary results can be explained by the formation of mid-gap states, which are more or less deep depending on the defects, and their concentration. Depending on the depth of trap states they can add Shockly-Read-Hall (non-radiative trap state mediated) recombination pathways, a higher amount of mobile electrons via the hopping mechanism, or reduced mobility of charges in deep trap states, leading to different results.^[103, 104, 109] Such trap states caused by vacancies in combination with functional groups can reside up to 0.5-1.0 eV below the conduction band, as predicted by DFT calculations.^[108, 110]

For post-synthetic introduction of nitrogen defects, which are mainly located at the particles' surface in contrast to vacancies introduced during a one-step synthesis, which are located in the bulk and at the surface, an enhancement in photocatalytic activity could be observed.^[51, 99] Surface defects are reported to be responsible for charge trapping and separation, due to slight changes in the electronic structure, whereas bulk defects can change the electronic structure detrimentally.^[51, 111] For this reason the exact analysis of nitrogen defects or vacancies is important.^[108] Most probably also the precise concentration of defects is crucial, since small amounts tend to increase the activity and higher concentrations of defects cause the filling of deeper trap states, having negative effects on the photocatalytic performance.^[104, 110] Hence, the defect concentration should be controlled and tuned with high precision. In general, also carbon vacancies can be formed, which are reported to cause a more negative conduction band of the carbon nitride^[112, 113] and are used for nitrogen or nitric oxide fixation, rather than HER.^[113, 114]

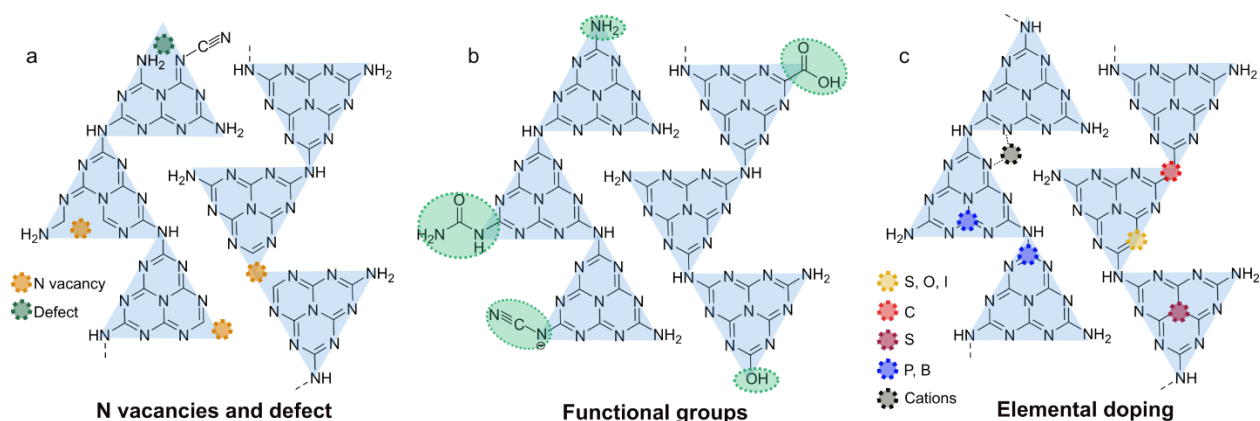


Figure 2.8: Defect-introducing strategies for carbon nitrides, including the formation of a) vacancies^[92, 109, 115] (here the most common N vacancies are shown), b) functional or termination groups^[94, 115-118] and c) elemental doping.^[119-125] The most commonly used elements for doping are depicted with their predicted position for replacing atoms in the heptazine backbone or by coordinating between heptazine units. Most defect studies were performed on melon-type carbon nitrides.

Since defects and functional groups are often linked, a negative impact on photocatalysis was also reported for specific functional groups (Figure 2.8b). Similar to nitrogen vacancies also the effect of such functional groups in carbon nitrides are controversially discussed in the literature especially in terms of charge separation efficiency.^[1, 126, 127] Particularly, in more crystalline carbon nitrides a faster electron transfer was reported than for amorphous materials, enabling a more efficient charge separation.^[128] In 2016, a synthesis route to remove or repair defects like amino and cyano groups in heptazine-based carbon nitrides was published^[93], akin to self-healing properties known for covalent organic frameworks.^[129] For this purpose, melamine was mixed with defect containing carbon nitrides and heated to 550 °C. The photocatalytic activity was enhanced by the healing process when less defects were present in the carbon nitride, which was attributed to reduced recombination rates.^[93] Likewise, in nanocrystalline materials with fewer defects it was reported that the vibrational relaxation is decreased, probably due to less and less deep trap states, as suggested by photoacoustic measurements. In addition, the adsorption energy of hydrogen atoms is minimized in crystalline materials and hence the reaction rates are increased by up to 16 times.^[107] The often neglected parameter of hydrogen atom transfer kinetic is likely severely influenced by the transfer pathway and the surface termination groups, as shown for hydrophilic functional groups, which enhance the proton transfer to Pt and hence the photocatalytic hydrogen efficiency.^[60]

Depending on the type of functional groups also beneficial effects with increasing concentration of functionalization were reported. This is for example the case for hydrophilic amine groups, where the photocatalytic activity in melon-based systems was shown to increase constantly with decreasing chain length down to dimers.^[130] This positive effect was explained by better exposure of the amine groups, which are possibly the active sides for HER, to the surrounding liquid.^[130, 131] DFT calculations have shown that such amine groups were more involved in the LUMO orbital in smaller oligomers (up to 0.5 eV), whereas the HOMO, located at the heptazine rings, is almost

not affected by changes in chain length.^[130, 132] Another explanation for the enhanced HER are amine-mediated proton-coupled electron transfer pathways enhancing charge transfer.^[130, 133] Most likely similar reasons resulted in the enhanced activity of amorphous PTI in comparison to a more crystalline compound.^[134]

Similarly, also the introduction of urea or cyanamide functional groups showed an enhanced hydrogen evolution rate (and quantum yields of 18% for urea and 9% for cyanamide functionalization) while having faster non-radiative decay rates.^[8, 94] By surface functionalization and defect engineering, the amount of active centers and hence the co-catalyst deposition can be tuned as well,^[51, 135] since e.g. amine, urea or cyanamide groups were suggested to better coordinate Pt and hence enable a more efficient electron transfer to the co-catalyst.^[8, 94, 130]

As mentioned above, elemental doping can also introduce point defects. Doping in melon-type carbon nitrides was used as a method to reduce the optical band gap and enhance the probability of efficient charge separation and transfer, similar as it is done for inorganic semiconductors.^[1, 30] To this end, various elements were used for doping, like sulphur^[119, 136], oxygen^[120, 137], phosphorous^[121, 138], boron^[122], iodine^[123, 139] or carbon^[124, 140], which are expected to replace either C atoms or N atoms in the heptazine rings (Figure 2.8c). In general, it appears like p-doping (electron removal) preserves the structure of the carbon nitride, whereas n-doping increases the structural disorder.^[2] The problem with doping in these organic materials however is the low control of targeted atom replacement and hence structural control and understanding. Furthermore, doping in organic based systems is better described by substitution or addition of atoms in the polymer backbone, which add defect states and also change the structure of the polymer.^[1] One way to overcome this problem by controlling the doping concentration was published for PTI. The defect concentration in PTI can be tuned by introducing 2,4,6-triaminopyrimidine or 4-amino-2,6-dihydroxypyrimidine into the synthesis.^[134, 141] Due to the additional carbon atom in the ring a distortion of the crystal structure can be observed, leading to enhanced light absorption and longer charge carrier lifetimes and, hence, higher photocatalytic activity with increasing concentration of defects.

Besides elemental replacement also the introduction or intercalation of cations like Fe³⁺, Ni²⁺, Cu²⁺, Co³⁺ or Mn³⁺ in the carbon nitride backbone was reported to change the light absorption behavior.^[142] Likewise, the intercalation of ions like Li, Na and K and small amount of Cl or salts such as NaCl, K₂SO₄, MgCl₂ in heptazine-based carbon nitrides were reported to enhance the conductivity and, hence, the photocatalytic activity by 5-35 times in comparison to the pristine material.^[143, 144] As a reason for the enhancement, also the formation of new electron transfer pathways were named.^[144] However, no analysis of the type of conductivity, possibly being ionic or electronic, nor charge transfer analysis by e.g. transient absorption spectroscopy was performed. As for all other defects, which are introduced into the system, a detailed structural understanding is important, especially to extract structure-property relationships to develop future for design strategies for optimized photocatalysts.

2.4.2. Particle size and surface area

Tuning the morphology of photocatalysts also effects the surface structure and several photophysical properties at the same time, including light absorption, concentration of accessible active centers, charge transport and separation^[92, 145] as well as probabilities of surface ^[145] and bulk recombination.^[146-148] With particle size reduction and hence increasing surface area, these properties change as follows: the probability of active sites being located at the surface is increased, more pronounced light scattering can be observed, which can be beneficial for light distribution in suspended systems,^[145, 147] reaction kinetics can be enhanced due to an increasing active area, which is in contact with the electrolyte,^[149] the optical band gap can increase,^[150] and the amount of band bending can be reduced, due to a smaller space charge layer, which becomes limited by the particle size and the available mobile charge carriers forming it, and thereby can affect the band positions in the bulk and reduce the efficiency of charge carrier separation.^[145, 151]

The so called quantum size or confinement effects describe changes in the density of electronic states in confined space that can lead to an increase in band gap. It has been described that the conduction band (or LUMO) potential becomes more reducing and the valence band (or HOMO) position more oxidizing, when particle size gets sufficiently small.^[145, 152] The resulting higher driving force of the generated electrons and holes can enhance redox reactions and hence, the photocatalysis process, as described e.g. for the proton reduction reaction with suspended CdSe nanoparticles. A logarithmic dependence between those particle size and activity was found.^[153] An analogous study for carbon nitrides is not reported so far, but a similar effect is postulated in the literature with reducing carbon nitride particle size or due to exfoliation (Chapter 2.4.3).^[154, 155]

Another approach affecting the particle morphology and activity is the introduction of mesoporosity in carbon nitrides. This can be achieved by bottom up strategies like soft^[156, 157] or hard templating.^[2, 158] Hard templating is describing a process where hard precursors like silica are included in the synthesis as structural templating features and subsequently are removed after product synthesis by strong bases or acids such as NaOH, HF or NH₄HF₂. Soft templating strategies do not require a removal of the template (e.g. NH₄Cl) anymore, since it is transformed or decomposed during synthesis, forming for example gas bubbles that nanostructure the product *in-situ*.^[148] With these strategies, the surface area can be increased up to values of 400 m² g⁻¹^[159], which is 8-40 times more than in the bulk carbon nitride material (10-50 m² g⁻¹).^[8, 105, 159] Furthermore, non-template based top down or bottom up synthesis routes can be used for morphology tuning of carbon nitrides, as will be described below. All these different techniques were used to synthesize various geometries for nanostructured carbon nitrides that allow to study light scattering and charge transport in structures with varying dimensionality, including 0D quantum dots^[160], 1D nanorods^[161, 162], nanowires^[163, 164] nanofibres^[165], or nanotubes^[166, 167], as well as 2D nanosheets^[154, 168] and nanoribbons^[169] and 3D porous materials^[170] (Figure 2.9).^[170, 171]

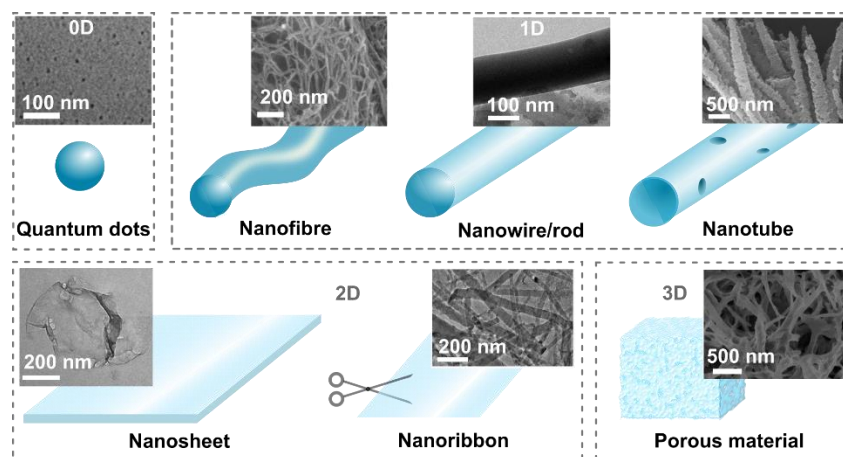


Figure 2.9: Morphology tuning used for melon-based carbon nitrides to boost photocatalysis. Ranging from 0D quantum dots^[160] (SEM image is adapted with permission from ^[160]. Copyright 2014, Royal Society of Chemistry), via 1D nanofibres^[163] (SEM image is adapted with permission from ^[163]. Copyright 2016, Elsevier), nanowires or nanorods^[161] (SEM image is adapted with permission from ^[161]. Copyright 2013, American Chemical Society), and nanotube^[167] (SEM image is adapted with permission from ^[167]. Copyright 2015, Royal Society of Chemistry), to 2D nanosheets^[154] (SEM image is adapted with permission from ^[154]. Copyright 2017, John Wiley and Sons.), and nanoribbons^[172] (SEM image is adapted with permission from ^[172]. Copyright 2014, John Wiley and Sons), and to 3D porous materials (SEM image is adapted with permission from ^[170]. Copyright 2016, Royal Society of Chemistry).^[170, 173]

Of special interest is the nanosheet formation that was reported in several publications to enhance the photocatalytic hydrogen evolution of carbon nitrides. The formation of single sheet carbon nitrides is still challenging, which might be caused by the chemical stability and insolubility of this material or due to the fact that most of the time, 1D melon is studied, which does not have a true 2D structure.^[2, 154] In addition, it was calculated that carbon nitrides have a three times more polar or polarizable surface than graphene, and hence a three times higher stacking interaction than graphene. This, in combination with a potentially high hydrogen bonding possibility^[174] of carbon nitrides might explain why these materials are more difficult to exfoliate, especially for monolayer fabrication.^[175, 176] Hence, it is key to brake the stacking interaction, which is described for solvothermal exfoliation routes, liquid ammonia assisted lithium intercalation^[97], reductive alkylation^[154], thermal exfoliation^[177, 178], acid exfoliation^[179, 180] and liquid exfoliation (with solvent enabling hydrogen bonding) methods.^[174, 181, 182] These methods may be assisted by ultrasonic treatments. In most of the publications an enhancement of photocatalytic activity was reported for particles with a decreased size.^[149] One of the highest HER of 8.5 mmol h⁻¹ g⁻¹ (3 wt% Pt and 10 vol% TEoA) was reported for an exfoliated melon-based carbon nitride, with a particle height of 0.5 nm only, corresponding to two layers being stacked on top of each other.^[168] In similar studies, the enhanced photocatalytic activity of exfoliated carbon nitride, obtained by a sonication method, was attributed to reduced hydrogen bonds and enhanced interlayer electron transfer.^[130, 183, 184] In addition, a higher charge density at specific carbon atoms, which were predicted to be the location for photo-generated electron trapping, and better exposure of nucleophilic sites, are named as additional reasons for activity enhancements due to nanostructuring.^[130, 184]

Nevertheless, an increased surface area is not necessary causing higher hydrogen evolution rates, since crystallinity can be reduced and a higher amount of defects or surface terminations with detrimental effects can be formed, as discussed before.^[185] Hence, the topic of exfoliation is also controversially discussed in the literature.^[30, 63, 168, 186] If the activity of nanostructured carbon nitrides is normalized to the surface area, materials with higher surface area often perform worse in comparison to the bulk material.^[185] Therefore, it was suggested that the limiting charge carrier mobility itself should be enhanced to overcome limitations in hydrogen evolution, and not necessarily the particle geometry.^[146, 187]

One way to overcome the problem of efficient charge separation is the combination of bulk and sheet material to form a hybrid. It was reported that the charge transfer kinetics can be enhanced in this case, since an electron transfer channel is formed from bulk material to nanosheets, also assisting charge separation and boosting photocatalysis.^[63] The bulk material is absorbing the light efficiently, separating the charge carriers and transporting the electrons to the nanosheets, within ns time scale. The transport mechanism is similar to diffusion processes expected in small molecule. Once the electrons reach the nanosheets, the larger amount of terminal and catalytically active groups at the surface is boosting the photocatalytic reaction.^[63] Further research is needed to understand those processes fully and to disentangle the different process, which are influenced by such morphological and structural changes.

2.4.3. Stacking distance

The formation of nanosheets is directly linked to changes in stacking distances in carbon nitrides. As described above, charge separation is mainly happening by a hopping mechanism between the layers in carbon nitride (Figure 2.10), so that a lower interlayer distance can lead to an enhanced charge transport and, hence, better charge separation and higher photocatalytic activity.^[77, 79, 105] The hopping rates of charges between the layers were found to be in the range of 10^9 s^{-1} when the stacking distance was reduced to 3.23 Å in comparison to carbon nitrides with stacking distances of 3.30 Å with one order of magnitude lower hopping rates.^[77] The dependence of stacking distance and hopping rate can be described best with an exponential function, which is also valid for samples being synthesized from different methods.^[75, 77] Consequently several layers must be stacked on top of each other to enable such charge separation at all.^[63, 77] Different strategies were reported so far, which allow to tune the interlayer stacking. By using e.g. ammonium chloride in a microwave assisted synthesis the layer distances in melon-type carbon nitride can be changed. The ammonium chloride is causing a partial exfoliation of the layered melon structure, resulting in sheets with a height of 15-25 nm, corresponding to 5-8 layers, with only slight denser packing of those few layers in comparison to the pristine materials. In addition, the optical band gap is reduced from 2.92 eV in the bulk material to 2.63 eV in the partially exfoliated one, which was described as the reason for enhanced photocatalytic hydrogen evolution by 5 times in comparison to the bulk carbon nitride.^[188] More significant changes in the

interlayer spacing in bulk material from 3.26 to 2.92 Å were reported for carbon nitrides where oxamide and KCl/LiCl were added to the synthesis. Material with closer packing have shown to enhance the exciton dissociation, charge transport between the layers and, hence, hydrogen evolution efficiency (and 57% AQY at 420 nm).^[96] Also the addition of tartaric acid to the precursors dicyandiamide before thermal polymerization results in a reduced stacking distance, which increases the photocatalytic activity by 8 times.^[105] Also by just increasing the synthesis temperature from 500 to 550°C or 600°C the layer stacking distance can be reduced, without additional reagents.^[189, 190] Nevertheless, it has to be stated that due to the addition of salt melts or higher synthesis temperature more structural parameter like the formation of 2D structure rather than a 1D structure and a higher amount of polymerization with lower concentration of defects were possibly changed simultaneously. A clear separation for purely stacking effects on photocatalysis is not possible to extract from these studies.

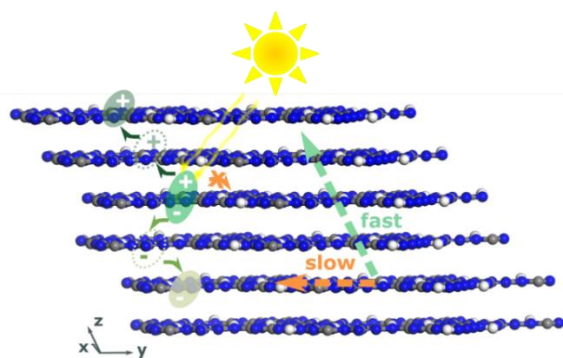


Figure 2.10: Exciton diffusion in between the layers is orders of magnitude faster than within one layer of melon.^[77, 80]

Another study points to an influence of the order of stacking on charge carrier lifetimes. When comparing crystalline samples to more amorphous ones, it was shown that the lifetimes of charge carriers are prolonged in samples with a higher order of stacking.^[191] This points to an enhanced interlayer migration of charges in crystalline samples. In line with a theoretical analysis of different stacking types in melon-type carbon nitride showed a higher mobility of charge carriers when the layers are stacked in an AA manner compared to AB stacking.^[192] This might be caused by a stronger coupling of the p_z orbitals in AA stacking in contrast to AB.^[79] Nevertheless, these studies were not conducted in a photocatalytic environment and no direct correlation between lifetime and photocatalytic activity is possible here.^[191]

2.4.4. Heterojunctions and donor-acceptor structure

Another way to increase the charge mobility and charge separation efficiency is by tuning the electronic structure due to the formation of a covalently attached intramolecular donor-acceptor function e.g. by copolymerizing or adding functional groups (Figure 2.11 a, b), since terminations groups were already describe in Chapter 2.4.1 to have a huge impact on the properties.^[91] In principle, two methods can be distinguished here to introduce such a functionalization: pre- and post-modification. Post-modification describes the heterojunction formation of carbon nitrides with energetically well matching semiconductors, molecules or polymers.^[95, 193] This modification approach allows to control functional groups while additional defect formation is prevented.^[194, 195] One example is the functionalization of electron donating primary amine groups at carbon nitrides with the electron accepting 2,5-thiophenedicarboxylic acid via an amide like linkage to extend the π -conjugation.^[196] For pre-modification of melon-type carbon nitrides, additives like e.g. quinolone as electron acceptor^[197] or hydrocarbons as donor^[198], are added to the educts in carbon nitride synthesis. However, the position of such molecule incorporation cannot be controlled well. In both cases, post and pre-modification, an additional electron transition mode can be obtained due to the formation of an interfacial charge transfer transition.^[196, 197]

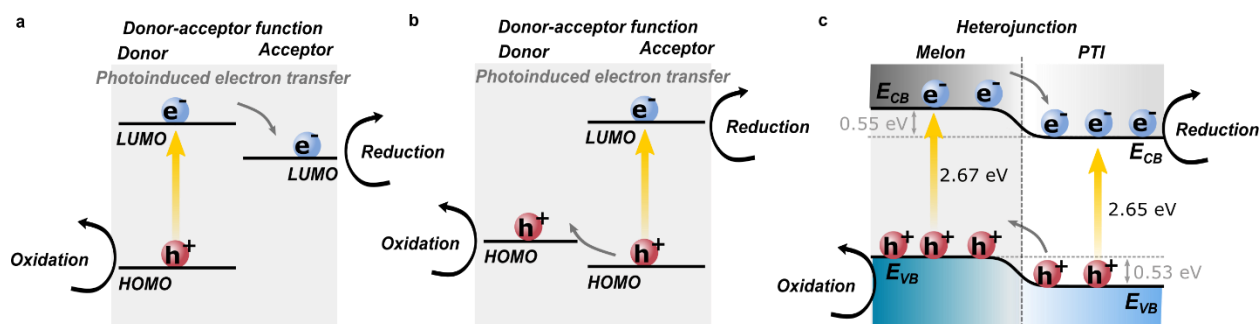


Figure 2.11: Donor-acceptor function of carbon nitrides, where only the a) donor or b) the acceptor is absorbing light and charge carriers are transferred to the respective other part.^[197-199] c) Heterojunction formed between melon-type carbon nitride and PTI, where both material absorb sun light and both charge carrier types are shuttled.^[200] (Adapted with permission from ^[200]. Copyright 2017, American Chemical Society).

Also the formation of heterojunctions or surface assemblies, without covalent attachment, can enhance the photocatalytic activity by increasing charge separation and extend the amount of solar light that can be used.^[51, 201] Such heterojunctions contain two semiconductors that both absorb light, so that the relative band alignment becomes an important parameter.^[51] Multiple heterojunctions with carbon nitrides are reported in literature, including covalent organic frameworks^[202], perylene^[203], metal organic frameworks^[204], graphene^[205], TiO_2 ^[206, 207] or MoS_2 ^[208]. As an example the heterojunction of PTI and heptazine-based carbon nitride is described here.^[200] By engineering the molten salt (eutectic mixture of KCl/LiCl) synthesis conditions (450-550°C) an *in situ* formation of a heptazine-triazine interface could be obtained (Figure 2.11c). This heterojunction enhances the charge separation and enables hydrogen evolution rates as high as $4800 \mu\text{mol h}^{-1} \text{g}^{-1}$, which is 12 time higher than melon or 4 times higher than PTI on their own.

2.5. Light-induced charge storage in poly(heptazine imide)

The truly 2D polymer PHI was found to have the unconventional property of simultaneously absorbing light and being able to store the photo-generated electrons.^[209] When PHI is illuminated with light above the band gap (<450nm) in aqueous suspension or as thin film on an electrode substrate, electrons and holes are generated. In presence of an electron donor, the holes are extracted and quenched. The electrons remain on the material and even accumulate due to the high overpotential for hydrogen evolution on bare PHI, changing the yellow color of the sample gradually to blue (Figure 2.12). The accumulation of these negative charges is assisted by alkaline ions that diffuse into the structural pores and screen the electrons. Such ions must have a suitable size to fit in the PHI pores including their hydration sphere. Partially, these are present in the pristine K-PHI structure, but the process can be assisted by ions originating from the surrounding electrolyte. In this blue, photo-reduced state PHI is stable for many days, as long as no electron acceptor or transfer process discharges the material. Therefore, charged PHI must be stored in oxygen free conditions^[209], similar to TiO₂^[210] or Cu-imidazolate complexes to prevent reactions with oxygen, forming superoxide radicals, which undergo further reactions.^[211]

The blue state can be used to produce hydrogen on demand by adding Pt^[209] or Ni-bis(diphosphine)^[50] to trigger HER via the co-catalyst. The storage process hence enables the so called “dark photocatalysis”^[209] i.e. production of solar fuels after illumination. This process of light absorption and subsequent use of the photo-generated charge for catalysis on demand is similar to the photosynthesis process in nature.^[209, 212] In plants the energy of sunlight is converted into chemical energy (sugars) in a coupled light and dark reaction. Due to illumination of chlorophyll an electron-hole pair is generated. The electron is transferred to an electron transport chain, which leads to the reduction of nicotinamide adenine dinucleotide phosphate (NADP) to NADPH. At the same time oxygen and protons are generated from water, building up a proton gradient that is used for the production of adenosine triphosphate (ATP). Both molecules NADPH and ATP are used in combination with CO₂ afterwards in the light independent Calvin-Benson cycle, to produce carbohydrates.^[212, 213] Similar to this system the hydrogen evolution reaction can be performed light-independently with PHI in the dark. After the co-catalysts is added hydrogen is produced for several hours from the stored electrons and the carbon nitride is transferred to the yellow ground state again, when those stored electrons are consumed.^[209] Besides hydrogen evolution, also organic synthesis of e.g. dibenzylsulfanes were reported in the dark.^[214]

Alternatively, direct discharge of the stored electrons is also possible electrically, provided a sufficiently good electronic contact and thin films.^[9] A direct solar batteries can be formed, thereby overcoming the intermittency of solar irradiation by a direct storage process in the photoabsorber, and bypassing the need of producing and storing energy externally while the sun is shining. For aqueous solar battery applications with K-PHI the blue state can be produced by electrical charging or by band gap illumination in presence of a donor.^[9] The behavior of K-PHI can be

described best as negative photoelectrode material, with the working principle of a pseudocapacitor. Prior to illumination, the material has an open circuit potential (OCP) in the range of +200 to -200 mV vs Ag/AgCl. Upon illumination, electrons accumulate in the conduction or intercalation band and the potential is increasing to -600 mV vs Ag/AgCl and more negative (-800 mV) when an electron donor assists hole extraction and charge accumulation. This allowed an overall charge storage of 43.7 C g^{-1} after 100 min illumination, corresponding roughly to one electron on every 9th to 10th heptazine unit. Both, pure illumination as well as the ion assisted photo-charging process increase the conductivity of the material (by a factor of 45). With these findings a simple, cheap and sustainable solution for simultaneous light absorption and storing in one material was enabled, which allows for time delayed use of solar energy. Similar capacitive behavior was also found for melon-based carbon nitrides. Analogous to alkaline ion intercalation in the volume of PHI, the cations from the electrolyte were reported to interact at the carbon nitride electrode surface.^[196] The properties, such as photocurrent and photo-response, of such a melon-based photoanode can also be tuned by introducing nitrogen vacancies and OH groups.^[104]

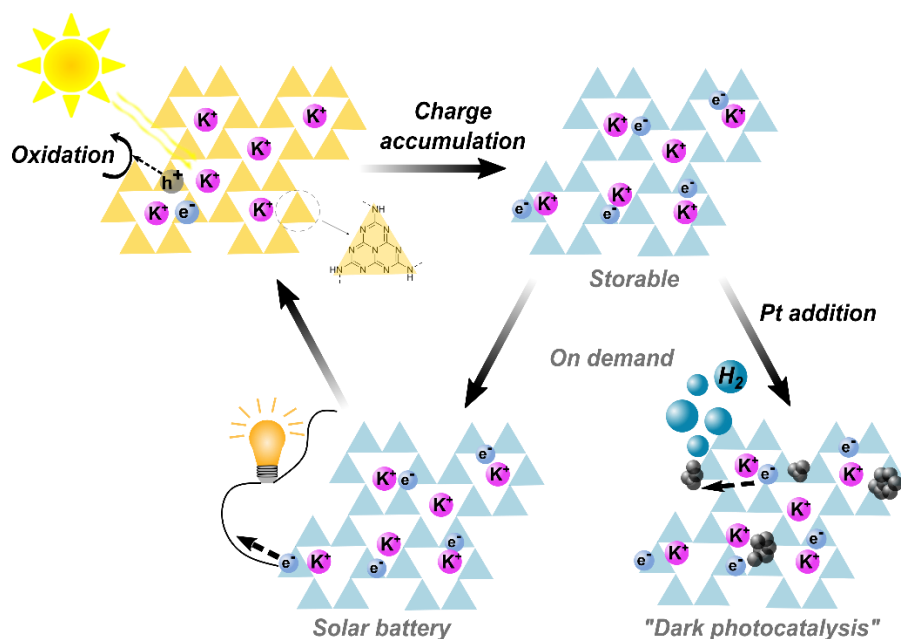


Figure 2.12: Solar battery^[9] and "dark photocatalysis"^[209] application enabled by K-PHI due to stable photo-reduced, blue state after illuminating K-PHI with light <450 nm. After discharging and prior to illumination, K-PHI is yellow and changes its color to blue during illumination.

Nevertheless, the increasing charge carrier concentration or more explicitly the electron accumulation, can also reach a critical level, where charge recombination upon photoexcitation and also the back reaction with oxidized electron donors becomes more likely. Thereby, a loss channel in charge carrier production is added, which is reducing the photocatalytic efficiency.^[48, 89] One way to overcome an excessive electron accumulation is the introduction of redox mediators as methyl viologen, as described by the groups of E. Reisner and J. R. Durrant.^[48] To better understand what is happening in PHI under photocatalytic conditions, the material was first investigated without any electron donor and co-catalyst being present. It was found that the higher

the excitation power the faster the bimolecular recombination. However, if an electron donor is added to quench the holes, a ~400 times faster recombination dynamics is observed in comparison to the system without added donor, which is due to excessive electron accumulation in PHI that increases the recombination rate of electron-hole pairs. When a redox mediator is added the photocatalytic activity can be increased by roughly 30 %, preventing the recombination partially.

Besides time delayed photocatalysis and solar battery applications, the electron storing property of PHI can also enable charging of PHI-based Janus particles used as microswimmers.^[11] Such Janus particles are composed of two or more particle sides, where the sides differ in their structure or physical property, enabling symmetry breaking and hence, propulsion due to (photo)catalytic reactions occurring on one or either side of the Janus particle.^[215, 216] PHI Janus particles capped on one side with Pt, Au or SiO₂ can be propelled under continuous illumination in the presence of an electron donor (methanol or H₂O₂) due to their high photocatalytic efficiency.^[11] However, to achieve a battery type propulsion, a synergistic charging effect is necessary and was enabled by using Pt caps in H₂O₂ only, due to different decomposition reactions and kinetics of H₂O₂ at the surface of Pt and PHI. The solar battery swimming process gets prolonged with increasing light charging duration, enabling half an hour of dark propulsion after only 30 s of illumination. It is anticipated that such behavior can be used also for responsive, autonomous micromachines.^[11, 217]

2.6. Other light driven reactions enabled by carbon nitrides

Besides photocatalytic hydrogen evolution a huge variety of light-induced reactions were reported for carbon nitrides, including photocatalytic nitrogen fixation, CO₂ reduction, pollutant degradation and organic coupling reactions (Figure 2.13), which will be discussed in more detail in the following. Starting with the CO₂ reduction reaction that was successfully reported for PHI and melon-type carbon nitrides in presence and absence of co-catalysts.^[30, 218, 219] Since CO₂ reduction is a multi-electron process, which is more complex than hydrogen evolution also because of the higher activation energy of carbon dioxide in comparison to water reduction,^[30, 220, 221] photocatalytic hydrogen evolution is a competitive reaction.^[222] Numerous strategies were tested to limit the hydrogen reaction kinetically by e.g. special co-catalysts^[223], morphology tuning^[219, 224], defect tailoring^[225] and the formation of heterojunctions.^[222, 226] One promising approach is the mixture of graphene or carbon with carbon nitrides to create a more hydrophobic substrate for CO₂ conversion in presence of water. When creating a gas-liquid-solid interface a faster CO₂ diffusion can be enabled, overcoming the CO₂ diffusion limitations normally being present in aqueous phases. The photosynthesis like reaction could be increased up to 415 $\mu\text{mol m}^2 \text{h}^{-1}$, with a quantum yield of 0.33%. Those values are already comparable to natural photosynthesis.^[222] This pinpoints that surface and interface engineering is not only a key parameter in photocatalytic hydrogen evolution, but also in other photocatalytic reactions.

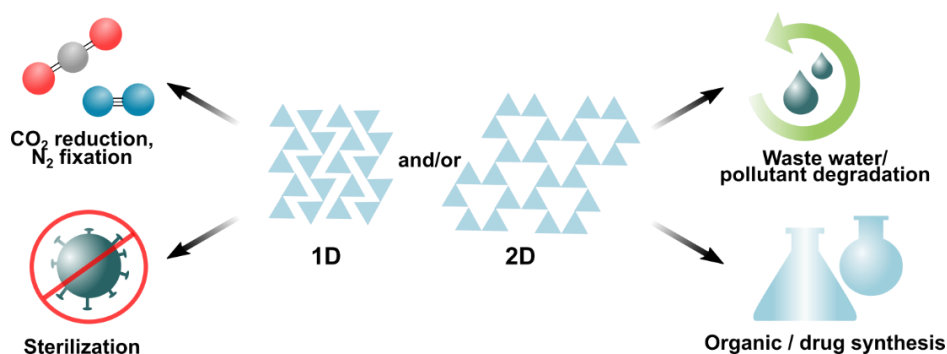


Figure 2.13: Photo-induced reactions catalyzed by carbon nitrides (1D melon-type and 2D PHI) including CO_2 reduction,^[218] N_2 fixation,^[227] antibacterial reactions,^[228] waste water treatment, pollutant degradation^[154, 229] and synthesis of organic molecules^[230] like e.g. drugs.

Similar problems arise when looking at N_2 fixation, since the activation energy of nitrogen is even high than of CO_2 due to a high bond dissociation energy (941 kJ mol^{-1}), low proton affinity and a huge ionization potential of nitrogen.^[231] Additionally, hydrogen evolution is again a side reaction and N_2 -fixation photocatalysts have to compete with the established Haber-Bosch process for NH_3 formation to become interesting for industrial applications. In principle, the photocatalytic formation of NH_3 from water and N_2 was reported for phosphorous doped carbon nitrides with nitrogen defects in the absence of co-catalysts with a solar-to-chemical conversion efficiency of 0.1 % already.^[227] Nitrogen vacancies are reported to act as nitrogen fixation location, where the molecule is dissociated via electron donation, forming a 1,4-endbridged $\text{N}=\text{N}$ species. The Lewis acid phosphorous atom adsorbs a water molecule, which is the electron donor in this reaction.^[231] However, further research in N_2 fixation is necessary, to understand and tailor the underlying mechanism further.

Since in many photocatalytic reactions a sacrificial reagent is required to enhance the limiting hole extraction kinetics for the aimed reaction, the respective oxidation reaction can also be used to intentionally create higher value chemicals or to degrade pollutants.^[229, 232, 233] For example, one electron donor, which is oxidized during photocatalytic hydrogen evolution to create a higher value chemical is e.g. bioactive 1,4-dihydro-2,6-dimethylpyridine-3,5-dicarboxylate that is studied as model systems for the natural NADH.^[93, 234] Besides such value added synthesis, also the degradation of micro-plastics as poly(ethylene terephthalate) or poly(lactic acid) and lignocellulose with simultaneous H_2 production were reported for K-PHI, while using a molecular Ni-co-catalyst.^[229, 235]

Moreover, light-induced pollutant degradation without the formation of hydrogen is described widely with carbon nitrides. Often, the *in situ* formed superoxide or hydroxyl radicals from molecular oxygen or hydroxyl ions, are used as active agent to degrade organic compounds. The degradation of pollutants is segmented in liquid and gas phase decontaminations. Commonly reported water (liquid phase) pollutants, which can be degraded by carbon nitrides are Rhodamine B^[154], methyl orange^[45] or methylene blue^[236] stemming from textile, plastic or dye industry^[237], as well as medical compounds like diclorfenac^[238], bisphenol A^[239], 5-sulfosalicylic

acid^[183] or antibiotic tetracycline hydrochloride.^[240] The insights gained from hydrogen evolution reactions can be transferred to such degradation reactions and can help to design more efficient catalytic processes. This is also applicable for gas phase pollutants such as NO_x in air.^[241-243] A more medical based approach for the use of carbon nitrides is based on the antibacterial effects of those materials when illuminated.^[228] In combination with CeO₂ or Ag it was shown that a high photocatalytic sterilization rate of *Staphylococcus aureus* or towards *E. coli*, *Staphylococcus aureus* or Gram-positive or negative was enabled, respectively.^[244]

The formed oxygen radicals can also be used for synthesis, e.g. for the coupling of oxamine and nitriles in a [3+2] cycloaddition to oxadiazoles or isoxazoles, which can be further used for the synthesis of drugs.^[20] As a second example, the photo-acetalization of aldehydes or ketons over carbon nitrides is using molecular oxygen as reaction partner to deprotonate the reagents.^[245] However, coupling reactions, catalyzed by carbon nitrides, are also reported in absence of oxygen. Such light driven reactions can be used among others to produce high value chemicals, including C-S coupling reaction between alkyl sulfonates and styrenes^[230], oxidative thiolations of methylarenes with elemental sulfur^[214] or addition of N-radicals to a C=C or C-H bond forming polycyclic molecules.^[26]

Those reports emphasize the large variety and the impact of photocatalytic reactions being possible with carbon nitrides, while having a huge potential to address environmental, medical and industrial problems. By gaining detailed insights in the light driven processes in carbon nitrides and how photo-generated charges are separated and transferred especially at different interfaces, a wide range of targeted designs can be enabled specifically for various applications and is therefore one key challenge in current carbon nitride research.

2.7. Bibliography

- [1] T. Banerjee, F. Podjaski, J. Kröger, B. P. Biswal, B. V. Lotsch, *Nat. Rev. Mater.* **2021**, 6 (2), 168-190.
- [2] F. K. Kessler, Y. Zheng, D. Schwarz, C. Merschjann, W. Schnick, X. Wang, M. J. Bojdys, *Nat. Rev. Mater.* **2017**, 2 (6), 17030.
- [3] J. Liebig, *Annalen der Pharmacie* **1834**, 10 (1), 1-47.
- [4] A. Y. Liu, M. L. Cohen, *Science* **1989**, 245 (4920), 841-842.
- [5] R. Riedel, *Adv. Mater.* **1992**, 4 (11), 759-761.
- [6] E. Stavrou, S. Lobanov, H. Dong, A. R. Oganov, V. B. Prakapenka, Z. Konôpková, A. F. Goncharov, *Chem. Mater.* **2016**, 28 (19), 6925-6933.
- [7] X. Wang, K. Maeda, A. Thomas, K. Takane, G. Xin, J. M. Carlsson, K. Domen, M. Antonietti, *Nat. Mater.* **2009**, 8 (1), 76-80.
- [8] V. W.-h. Lau, I. Moudrakovski, T. Botari, S. Weinberger, M. B. Mesch, V. Duppel, J. Senker, V. Blum, B. V. Lotsch, *Nat. Commun.* **2016**, 7 (1), 12165.
- [9] F. Podjaski, J. Kröger, B. V. Lotsch, *Adv. Mater.* **2018**, 30 (9), 1705477.
- [10] Z. Zhou, Y. Zhang, Y. Shen, S. Liu, Y. Zhang, *Chem. Soc. Rev.* **2018**, 47 (7), 2298-2321.
- [11] V. Sridhar, F. Podjaski, J. Kröger, A. Jiménez-Solano, B.-W. Park, B. V. Lotsch, M. Sitti, *Proc. Natl. Acad. Sci. U. S. A.* **2020**, 117 (40), 24748-24756.
- [12] B. V. Lotsch, J. Senker, W. Schnick, *Inorg. Chem.* **2004**, 43 (3), 895-904.
- [13] E. Wirnhier, M. Döblinger, D. Gunzelmann, J. Senker, B. V. Lotsch, W. Schnick, *Chem.– Eur. J.* **2011**, 17 (11), 3213-3221.
- [14] S. Y. Chong, J. T. A. Jones, Y. Z. Khimiyak, A. I. Cooper, A. Thomas, M. Antonietti, M. J. Bojdys, *J. Mater. Chem. A* **2013**, 1 (4), 1102-1107.
- [15] E. J. McDermott, E. Wirnhier, W. Schnick, K. S. Viridi, C. Scheu, Y. Kauffmann, W. D. Kaplan, E. Z. Kurmaev, A. Moewes, *J. Phys. Chem. C* **2013**, 117 (17), 8806-8812.
- [16] A. Savateev, S. Pronkin, M. G. Willinger, M. Antonietti, D. Dontsova, *Chem.– Asian J.* **2017**, 12 (13), 1517-1522.
- [17] B. V. Lotsch, M. Döblinger, J. Sehnert, L. Seyfarth, J. Senker, O. Oeckler, W. Schnick, *Chem.– Eur. J.* **2007**, 13 (17), 4969-4980.
- [18] W.-J. Ong, L.-L. Tan, Y. H. Ng, S.-T. Yong, S.-P. Chai, *Chem. Rev.* **2016**, 116 (12), 7159-7329.
- [19] M. Döblinger, B. V. Lotsch, J. Wack, J. Thun, J. Senker, W. Schnick, *Chem. Commun.* **2009**, (12), 1541-1543.
- [20] A. Savateev, S. Pronkin, J. D. Epping, M. G. Willinger, C. Wolff, D. Neher, M. Antonietti, D. Dontsova, *ChemCatChem* **2017**, 9 (1), 167-174.
- [21] B. Kurpil, Y. Markushyna, A. Savateev, *ACS Catal.* **2019**, 9 (2), 1531-1538.
- [22] C. Ye, J.-C. Xiao, B. Twamley, J. n. M. Shreeve, *Chem. Commun.* **2005**, (21), 2750-2752.
- [23] J. Thiele, J. T. Marais, *Liebigs Ann.* **1893**, 273 (2 - 3), 144-160.
- [24] L. Seyfarth, J. Seyfarth, B. V. Lotsch, W. Schnick, J. Senker, *Phys. Chem. Chem. Phys.* **2010**, 12 (9), 2227-2237.
- [25] L. Lin, C. Wang, W. Ren, H. Ou, Y. Zhang, X. Wang, *Chem. Sci.* **2017**, 8 (8), 5506-5511.
- [26] B. Kurpil, K. Otte, A. Mishchenko, P. Lamagni, W. Lipiński, N. Lock, M. Antonietti, A. Savateev, *Nat. Commun.* **2019**, 10 (1), 945.
- [27] G. Algara-Siller, N. Severin, S. Y. Chong, T. Björkman, R. G. Palgrave, A. Laybourn, M. Antonietti, Y. Z. Khimiyak, A. V. Krasheninnikov, J. P. Rabe, U. Kaiser, A. I. Cooper, A. Thomas, M. J. Bojdys, *Angew. Chem. Int. Ed.* **2014**, 53 (29), 7450-7455.
- [28] T. Suter, V. Brázdová, K. McColl, T. S. Miller, H. Nagashima, E. Salvadori, A. Sella, C. A. Howard, C. W. M. Kay, F. Corà, P. F. McMillan, *J. Phys. Chem. C* **2018**, 122 (44), 25183-25194.
- [29] T. S. Miller, A. B. Jorge, T. M. Suter, A. Sella, F. Corà, P. F. McMillan, *Phys. Chem. Chem. Phys.* **2017**, 19 (24), 15613-15638.
- [30] I. F. Teixeira, E. C. M. Barbosa, S. C. E. Tsang, P. H. C. Camargo, *Chem. Soc. Rev.* **2018**, 47 (20), 7783-7817.
- [31] C.-Z. Liao, V. W.-h. Lau, M. Su, S. Ma, C. Liu, C.-K. Chang, H.-S. Sheu, J. Zhang, K. Shih, *Inorg. Chem.* **2019**, 58 (23), 15880-15888.

- [32] M. B. Mesch, K. Bärwinkel, Y. Krysiak, C. Martineau, F. Taulelle, R. B. Neder, U. Kolb, J. Senker, *Chem.– Eur. J.* **2016**, *22* (47), 16878-16890.
- [33] L. Lin, Z. Lin, J. Zhang, X. Cai, W. Lin, Z. Yu, X. Wang, *Nat. Catal.* **2020**, *3* (8), 649-655.
- [34] S.-W. Cao, X.-F. Liu, Y.-P. Yuan, Z.-Y. Zhang, J. Fang, S. C. J. Loo, J. Barber, T. C. Sum, C. Xue, *Phys. Chem. Chem. Phys.* **2013**, *15* (42), 18363-18366.
- [35] B. Kippelen, J.-L. Brédas, *Energ. Environ. Sci.* **2009**, *2* (3), 251-261.
- [36] E. Kroke, M. Schwarz, E. Horath-Bordon, P. Kroll, B. Noll, A. D. Norman, *New J. Chem.* **2002**, *26* (5), 508-512.
- [37] J. Gracia, P. Kroll, *J. Mater. Chem.* **2009**, *19* (19), 3013-3019.
- [38] T. Tyborski, C. Merschjann, S. Orthmann, F. Yang, M. C. Lux-Steiner, T. Schedel-Niedrig, *J. Phys.: Condens. Matter* **2013**, *25* (39), 395402.
- [39] F. Fina, S. K. Callear, G. M. Carins, J. T. S. Irvine, *Chem. Mater.* **2015**, *27* (7), 2612-2618.
- [40] S. T. A. G. Melissen, T. Le Bahers, P. Sautet, S. N. Steinmann, *Phys. Chem. Chem. Phys.* **2021**, *23* (4), 2853-2859.
- [41] Z. Chen, A. Savateev, S. Pronkin, V. Papaefthimiou, C. Wolff, M. G. Willinger, E. Willinger, D. Neher, M. Antonietti, D. Dontsova, *Adv. Mater.* **2017**, *29* (32), 1700555.
- [42] A. Savateev, N. V. Tarakina, V. Strauss, T. Hussain, K. ten Brummelhuis, J. M. Sánchez Vadiño, Y. Markushyna, S. Mazzanti, A. P. Tyutyunnik, R. Walczak, M. Oschatz, D. M. Guldi, A. Karton, M. Antonietti, *Angew. Chem. Int. Ed.* **2020**, *59* (35), 15061-15068.
- [43] J. Liu, Y. Liu, N. Liu, Y. Han, X. Zhang, H. Huang, Y. Lifshitz, S.-T. Lee, J. Zhong, Z. Kang, *Science* **2015**, *347* (6225), 970-974.
- [44] Y. Di, X. Wang, A. Thomas, M. Antonietti, *ChemCatChem* **2010**, *2* (7), 834-838.
- [45] K. Sridharan, E. Jang, J. H. Park, J.-H. Kim, J.-H. Lee, T. J. Park, *Chem.– Eur. J.* **2015**, *21* (25), 9126-9132.
- [46] Y. Zhang, D. A. J. M. Ligthart, X.-Y. Quek, L. Gao, E. J. M. Hensen, *Int. J. Hydrogen Energy* **2014**, *39* (22), 11537-11546.
- [47] J. Dong, M. Wang, X. Li, L. Chen, Y. He, L. Sun, *ChemSusChem* **2012**, *5* (11), 2133-2138.
- [48] W. Yang, R. Godin, H. Kasap, B. Moss, Y. Dong, S. A. J. Hillman, L. Steier, E. Reisner, J. R. Durrant, *J. Am. Chem. Soc.* **2019**, *141* (28), 11219-11229.
- [49] Z. Pan, P. Niu, M. Liu, G. Zhang, Z. Zhu, X. Wang, *ChemSusChem* **2020**, *13* (5), 888-892.
- [50] H. Kasap, R. Godin, C. Jeay-Bizot, D. S. Achilleos, X. Fang, J. R. Durrant, E. Reisner, *ACS Catal.* **2018**, *8* (8), 6914-6926.
- [51] J. Yi, W. El-Alami, Y. Song, H. Li, P. M. Ajayan, H. Xu, *Chem. Eng. J.* **2020**, *382*, 122812.
- [52] W. Domcke, J. Ehrmaier, A. L. Sobolewski, *ChemPhotoChem* **2019**, *3* (1), 10-23.
- [53] J. Ehrmaier, T. N. V. Karsili, A. L. Sobolewski, W. Domcke, *J. Phys. Chem. A* **2017**, *121* (25), 4754-4764.
- [54] L. Tian, W. Xie, X. Wu, B. Guo, G. Xie, P. Cheng, X. Liu, J. R. Gong, *J. Phys. Chem. C* **2020**, *124* (45), 24667-24676.
- [55] R. Godin, Y. Wang, M. A. Zwijnenburg, J. Tang, J. R. Durrant, *J. Am. Chem. Soc.* **2017**, *139* (14), 5216-5224.
- [56] H. Wang, S. Jin, X. Zhang, Y. Xie, *Angew. Chem. Int. Ed.* **2020**, *132* (51), 23024-23035.
- [57] S. Zhu, D. Wang, *Adv. Energy Mater.* **2017**, *7* (23), 1700841.
- [58] M. Re Fiorentin, F. Risplendi, M. Palumbo, G. Cicero, *ACS Appl. Nano Mater.* **2021**, *4* (2), 1985-1993.
- [59] E. J. Rabe, K. L. Corp, X. Huang, J. Ehrmaier, R. G. Flores, S. L. Estes, A. L. Sobolewski, W. Domcke, C. W. Schlenker, *J. Phys. Chem. C* **2019**, *123* (49), 29580-29588.
- [60] Y. Zhang, Y. Dai, H. Li, L. Yin, M. R. Hoffmann, *Commun. Mater.* **2020**, *1* (1), 66.
- [61] H. Wang, S. Jiang, S. Chen, D. Li, X. Zhang, W. Shao, X. Sun, J. Xie, Z. Zhao, Q. Zhang, Y. Tian, Y. Xie, *Adv. Mater.* **2016**, *28* (32), 6940-6945.
- [62] N. J. Hestand, R. V. Kazantsev, A. S. Weingarten, L. C. Palmer, S. I. Stupp, F. C. Spano, *J. Am. Chem. Soc.* **2016**, *138* (36), 11762-11774.
- [63] K. L. Corp, C. W. Schlenker, *J. Am. Chem. Soc.* **2017**, *139* (23), 7904-7912.
- [64] A. Migani, L. Blancafort, *J. Am. Chem. Soc.* **2016**, *138* (49), 16165-16173.
- [65] S. Chen, T. Takata, K. Domen, *Nat. Rev. Mater.* **2017**, *2* (10), 17050.
- [66] J. Lim, H. Kim, J. Park, G.-H. Moon, J. J. M. Vequizo, A. Yamakata, J. Lee, W. Choi, *Environ. Sci. Technol.* **2020**, *54* (1), 497-506.

- [67] Y. Shiraishi, S. Kanazawa, Y. Sugano, D. Tsukamoto, H. Sakamoto, S. Ichikawa, T. Hirai, *ACS Catal.* **2014**, *4* (3), 774-780.
- [68] M. Liu, P. Xia, L. Zhang, B. Cheng, J. Yu, *ACS Sustain. Chem. Eng.* **2018**, *6* (8), 10472-10480.
- [69] J. Kou, C. Lu, J. Wang, Y. Chen, Z. Xu, R. S. Varma, *Chem. Rev.* **2017**, *117* (3), 1445-1514.
- [70] J. N. Muir, Y. Choi, H. Idriss, *Phys. Chem. Chem. Phys.* **2012**, *14* (34), 11910-11919.
- [71] M. Z. Rahman, C. B. Mullins, *Acc. Chem. Res.* **2019**, *52* (1), 248-257.
- [72] Y. Li, S. Jin, X. Xu, H. Wang, X. Zhang, *J. Appl. Phys.* **2020**, *127* (17), 170903.
- [73] S. Melissen, T. Le Bahers, S. N. Steinmann, P. Sautet, *J. Phys. Chem. C* **2015**, *119* (45), 25188-25196.
- [74] W. Wei, T. Jacob, *Phys. Rev. B* **2013**, *87* (8), 085202.
- [75] C. Merschjann, T. Tyborski, S. Orthmann, F. Yang, K. Schwarzburg, M. Lublow, M. C. Lux-Steiner, T. Schedel-Niedrig, *Phys. Rev. B* **2013**, *87* (20), 205204.
- [76] L. Yu, *Solitons & Polarons in Conducting Polymers*, World Scientific, **1988**.
- [77] C. Merschjann, S. Tschierlei, T. Tyborski, K. Kailasam, S. Orthmann, D. Hollmann, T. Schedel-Niedrig, A. Thomas, S. Lochbrunner, *Adv. Mater.* **2015**, *27* (48), 7993-7999.
- [78] M. N. Huda, J. A. Turner, *J. Appl. Phys.* **2010**, *107* (12), 123703.
- [79] Z. Ding, M. An, S. Mo, X. Yu, Z. Jin, Y. Liao, K. Esfarjani, J.-T. Lü, J. Shiomi, N. Yang, *J. Mater. Chem. A* **2019**, *7* (5), 2114-2121.
- [80] Y. Noda, C. Merschjann, J. Tarábek, P. Amsalem, N. Koch, M. J. Bojdys, *Angew. Chem. Int. Ed.* **2019**, *58* (28), 9394-9398.
- [81] H. Wang, S. Jiang, S. Chen, X. Zhang, W. Shao, X. Sun, Z. Zhao, Q. Zhang, Y. Luo, Y. Xie, *Chem. Sci.* **2017**, *8* (5), 4087-4092.
- [82] G. A. Meek, A. D. Baczewski, D. J. Little, B. G. Levine, *J. Phys. Chem. C* **2014**, *118* (8), 4023-4032.
- [83] L. Shi, C. K. Lee, A. P. Willard, *ACS Cent. Sci.* **2017**, *3* (12), 1262-1270.
- [84] H. Wang, X. Sun, D. Li, X. Zhang, S. Chen, W. Shao, Y. Tian, Y. Xie, *J. Am. Chem. Soc.* **2017**, *139* (6), 2468-2473.
- [85] H. Ou, X. Chen, L. Lin, Y. Fang, X. Wang, *Angew. Chem. Int. Ed.* **2018**, *57* (28), 8729-8733.
- [86] P. Guiglion, C. Butchosa, M. A. Zwijnenburg, *Macromol. Chem. Phys.* **2016**, *217* (3), 344-353.
- [87] Y. Tamai, H. Ohkita, H. Benten, S. Ito, *J. Phys. Chem. Lett.* **2015**, *6* (17), 3417-3428.
- [88] G. Peng, J. Albero, H. Garcia, M. Shalom, *Angew. Chem. Int. Ed.* **2018**, *57* (48), 15807-15811.
- [89] Z. Chen, Q. Zhang, Y. Luo, *Angew. Chem. Int. Ed.* **2018**, *57* (19), 5320-5324.
- [90] F. E. Osterloh, *ACS Energy Lett.* **2017**, *2* (2), 445-453.
- [91] D. K. Chauhan, S. Jain, V. R. Battula, K. Kailasam, *Carbon* **2019**, *152*, 40-58.
- [92] J. Zhang, J. Chen, Y. Wan, H. Liu, W. Chen, G. Wang, R. Wang, *ACS Appl. Mater. Inter.* **2020**, *12* (12), 13805-13812.
- [93] W. Wu, J. Zhang, W. Fan, Z. Li, L. Wang, X. Li, Y. Wang, R. Wang, J. Zheng, M. Wu, H. Zeng, *ACS Catal.* **2016**, *6* (5), 3365-3371.
- [94] V. W.-h. Lau, V. W.-z. Yu, F. Ehrat, T. Botari, I. Moudrakovski, T. Simon, V. Duppel, E. Medina, J. K. Stolarczyk, J. Feldmann, V. Blum, B. V. Lotsch, *Adv. Energy Mater.* **2017**, *7* (12), 1602251.
- [95] Z. Zhao, Y. Sun, F. Dong, *Nanoscale* **2015**, *7* (1), 15-37.
- [96] G. Zhang, G. Li, Z.-A. Lan, L. Lin, A. Savateev, T. Heil, S. Zafeirotos, X. Wang, M. Antonietti, *Angew. Chem. Int. Ed.* **2017**, *56* (43), 13445-13449.
- [97] Y. Yin, J. Han, X. Zhang, Y. Zhang, J. Zhou, D. Muir, R. Sutarto, Z. Zhang, S. Liu, B. Song, *RSC Adv.* **2014**, *4* (62), 32690-32697.
- [98] J. Zhang, J. Sun, K. Maeda, K. Domen, P. Liu, M. Antonietti, X. Fu, X. Wang, *Energ. Environ. Sci.* **2011**, *4* (3), 675-678.
- [99] X. Li, G. Hartley, A. J. Ward, P. A. Young, A. F. Masters, T. Maschmeyer, *J. Phys. Chem. C* **2015**, *119* (27), 14938-14946.
- [100] H. Yoneyama, *Crit. Rev. Solid State Mater. Sci.* **1993**, *18* (1), 69-111.
- [101] K. Takanebe, *ACS Catal.* **2017**, *7* (11), 8006-8022.
- [102] M. Z. Rahman, K. Davey, C. B. Mullins, *Adv. Sci.* **2018**, *5* (10), 1800820.
- [103] J. Xue, M. Fujitsuka, T. Majima, *Phys. Chem. Chem. Phys.* **2019**, *21* (5), 2318-2324.
- [104] Q. Ruan, T. Miao, H. Wang, J. Tang, *J. Am. Chem. Soc.* **2020**, *142* (6), 2795-2802.
- [105] H. Shi, S. Long, J. Hou, L. Ye, Y. Sun, W. Ni, C. Song, K. Li, G. G. Gurzadyan, X. Guo, *Chem.–Eur. J.* **2019**, *25* (19), 5028-5035.
- [106] P. Niu, G. Liu, H.-M. Cheng, *J. Phys. Chem. C* **2012**, *116* (20), 11013-11018.

- [107] Y. Dai, Q. Bu, R. Sooriyagoda, P. Tavadze, O. Pavlic, T. Lim, Y. Shen, A. Mamakhel, X. Wang, Y. Li, H. Niemantsverdriet, B. B. Iversen, F. Besenbacher, T. Xie, J. P. Lewis, A. D. Bristow, N. Lock, R. Su, *J. Phys. Chem. Lett.* **2019**, *10* (18), 5381-5386.
- [108] Y. Wang, P. Du, H. Pan, L. Fu, Y. Zhang, J. Chen, Y. Du, N. Tang, G. Liu, *Adv. Mater.* **2019**, *31* (40), 1807540.
- [109] B. Choudhury, K. K. Paul, D. Sanyal, A. Hazarika, P. K. Giri, *J. Phys. Chem. C* **2018**, *122* (16), 9209-9219.
- [110] J. Xue, M. Fujitsuka, T. Majima, *ACS Appl. Mater. Inter.* **2019**, *11* (43), 40860-40867.
- [111] A. Meng, Z. Teng, Q. Zhang, C. Su, *Chem.–Asian J.* **2020**, *15* (21), 3405-3415.
- [112] L. Wang, K. Wang, T. He, Y. Zhao, H. Song, H. Wang, *ACS Sustain. Chem. Eng.* **2020**, *8* (43), 16048-16085.
- [113] Y. Li, W. Ho, K. Lv, B. Zhu, S. C. Lee, *Appl. Surf. Sci.* **2018**, *430*, 380-389.
- [114] S. Cao, B. Fan, Y. Feng, H. Chen, F. Jiang, X. Wang, *Chem. Eng. J.* **2018**, *353*, 147-156.
- [115] P. Niu, M. Qiao, Y. Li, L. Huang, T. Zhai, *Nano Energy* **2018**, *44*, 73-81.
- [116] L. Chen, J. Song, *Adv. Funct. Mater.* **2017**, *27* (39), 1702695.
- [117] L. Pei, H. Tan, M. Liu, R. Wang, X. Gu, X. Ke, J. Jia, Z. Zheng, *Green Chem.* **2021**, *23* (10), 3612-3622.
- [118] J. Y. Bai, L. J. Wang, Y. J. Zhang, C. F. Wen, X. L. Wang, H. G. Yang, *Appl. Catal., B* **2020**, *266*, 118590.
- [119] G. Liu, P. Niu, C. Sun, S. C. Smith, Z. Chen, G. Q. Lu, H.-M. Cheng, *J. Am. Chem. Soc.* **2010**, *132* (33), 11642-11648.
- [120] J. Li, B. Shen, Z. Hong, B. Lin, B. Gao, Y. Chen, *Chem. Commun.* **2012**, *48* (98), 12017-12019.
- [121] Y. Zhang, T. Mori, J. Ye, M. Antonietti, *J. Am. Chem. Soc.* **2010**, *132* (18), 6294-6295.
- [122] Y. Wang, H. Li, J. Yao, X. Wang, M. Antonietti, *Chem. Sci.* **2011**, *2* (3), 446-450.
- [123] G. Zhang, M. Zhang, X. Ye, X. Qiu, S. Lin, X. Wang, *Adv. Mater.* **2014**, *26* (5), 805-809.
- [124] G. Dong, K. Zhao, L. Zhang, *Chem. Commun.* **2012**, *48* (49), 6178-6180.
- [125] L. Jiang, X. Yuan, Y. Pan, J. Liang, G. Zeng, Z. Wu, H. Wang, *Appl. Catal., B* **2017**, *217*, 388-406.
- [126] Y. Kang, Y. Yang, L.-C. Yin, X. Kang, G. Liu, H.-M. Cheng, *Adv. Mater.* **2015**, *27* (31), 4572-4577.
- [127] Y.-P. Yuan, L.-S. Yin, S.-W. Cao, L.-N. Gu, G.-S. Xu, P. Du, H. Chai, Y.-S. Liao, C. Xue, *Green Chem.* **2014**, *16* (11), 4663-4668.
- [128] S. Huang, Y. Xu, F. Ge, D. Tian, X. Zhu, M. Xie, H. Xu, H. Li, *J. Colloid Interface Sci.* **2019**, *556*, 324-334.
- [129] C. Liu, W. Zhang, Q. Zeng, S. Lei, *Chem.–Eur. J.* **2016**, *22* (20), 6768-6773.
- [130] V. W.-h. Lau, M. B. Mesch, V. Duppel, V. Blum, J. Senker, B. V. Lotsch, *J. Am. Chem. Soc.* **2015**, *137* (3), 1064-1072.
- [131] X. Li, I. V. Sergeev, F. Aussenac, A. F. Masters, T. Maschmeyer, J. M. Hook, *Angew. Chem. Int. Ed.* **2018**, *57* (23), 6848-6852.
- [132] P. Wu, J. Wang, J. Zhao, L. Guo, F. E. Osterloh, *J. Mater. Chem. A* **2014**, *2* (47), 20338-20344.
- [133] N. Ullah, S. Chen, Y. Zhao, R. Zhang, *J. Phys. Chem. Lett.* **2019**, *10* (15), 4310-4316.
- [134] K. Schwinghammer, B. Tuffy, M. B. Mesch, E. Wirnhier, C. Martineau, F. Taulelle, W. Schnick, J. Senker, B. V. Lotsch, *Angew. Chem. Int. Ed.* **2013**, *52* (9), 2435-2439.
- [135] N. Meng, W. Zhou, Y. Yu, Y. Liu, B. Zhang, *ACS Catal.* **2019**, *9* (12), 10983-10989.
- [136] X. Ma, Y. Lv, J. Xu, Y. Liu, R. Zhang, Y. Zhu, *J. Phys. Chem. C* **2012**, *116* (44), 23485-23493.
- [137] Z.-F. Huang, J. Song, L. Pan, Z. Wang, X. Zhang, J.-J. Zou, W. Mi, X. Zhang, L. Wang, *Nano Energy* **2015**, *12*, 646-656.
- [138] Y. Zhou, L. Zhang, J. Liu, X. Fan, B. Wang, M. Wang, W. Ren, J. Wang, M. Li, J. Shi, *J. Mater. Chem. A* **2015**, *3* (7), 3862-3867.
- [139] Q. Han, C. Hu, F. Zhao, Z. Zhang, N. Chen, L. Qu, *J. Mater. Chem. A* **2015**, *3* (8), 4612-4619.
- [140] G. Liu, M. Xue, Q. Liu, H. Yang, Y. Zhou, *J. Colloid Interface Sci.* **2019**, *552*, 728-734.
- [141] M. K. Bhunia, S. Melissen, M. R. Parida, P. Sarawade, J.-M. Basset, D. H. Anjum, O. F. Mohammed, P. Sautet, T. Le Bahers, K. Takanebe, *Chem. Mater.* **2015**, *27* (24), 8237-8247.
- [142] Z. Ding, X. Chen, M. Antonietti, X. Wang, *ChemSusChem* **2011**, *4* (2), 274-281.
- [143] H. Gao, S. Yan, J. Wang, Y. A. Huang, P. Wang, Z. Li, Z. Zou, *Phys. Chem. Chem. Phys.* **2013**, *15* (41), 18077-18084.
- [144] H. Gao, S. Yan, J. Wang, Z. Zou, *Dalton Trans.* **2014**, *43* (22), 8178-8183.
- [145] F. E. Osterloh, *Chem. Soc. Rev.* **2013**, *42* (6), 2294-2320.

- [146] X. Li, A. F. Masters, T. Maschmeyer, *ChemCatChem* **2015**, 7 (1), 121-126.
- [147] J. Zhang, M. Zhang, C. Yang, X. Wang, *Adv. Mater.* **2014**, 26 (24), 4121-4126.
- [148] Y. Li, X. Li, H. Zhang, Q. Xiang, *Nanoscale Horiz.* **2020**, 5 (5), 765-786.
- [149] Y. Xiao, G. Tian, W. Li, Y. Xie, B. Jiang, C. Tian, D. Zhao, H. Fu, *J. Am. Chem. Soc.* **2019**, 141 (6), 2508-2515.
- [150] A. D. Yoffe, *Adv. Phys.* **2001**, 50 (1), 1-208.
- [151] A. Hagfeldt, H. Lindström, S. Södergren, S.-E. Lindquist, *J. Electroanal. Chem.* **1995**, 381 (1), 39-46.
- [152] F. T. Rabouw, C. de Mello Donega, *Top. Curr. Chem.* **2016**, 374 (5), 58.
- [153] M. A. Holmes, T. K. Townsend, F. E. Osterloh, *Chem. Commun.* **2012**, 48 (3), 371-373.
- [154] X.-H. Song, L. Feng, S.-L. Deng, S.-Y. Xie, L.-S. Zheng, *Adv. Mater. Interfaces* **2017**, 4 (15), 1700339.
- [155] S. P. Pattnaik, A. Behera, S. Martha, R. Acharya, K. Parida, *J. Mater. Sci.* **2019**, 54 (7), 5726-5742.
- [156] Y. Wang, X. Wang, M. Antonietti, Y. Zhang, *ChemSusChem* **2010**, 3 (4), 435-439.
- [157] L. Xu, J. Xia, H. Xu, S. Yin, K. Wang, L. Huang, L. Wang, H. Li, *J. Power Sources* **2014**, 245, 866-874.
- [158] F. Goettmann, A. Fischer, M. Antonietti, A. Thomas, *Angew. Chem. Int. Ed.* **2006**, 45 (27), 4467-4471.
- [159] M. A. Wahab, J. Joseph, L. Atanda, U. K. Sultana, J. N. Beltramini, K. Ostrikov, G. Will, A. P. O'Mullane, A. Abdala, *ACS Appl. Energy Mater.* **2020**, 3 (2), 1439-1447.
- [160] W. Wang, J. C. Yu, Z. Shen, D. K. L. Chan, T. Gu, *Chem. Commun.* **2014**, 50 (70), 10148-10150.
- [161] X. Bai, L. Wang, R. Zong, Y. Zhu, *J. Phys. Chem. C* **2013**, 117 (19), 9952-9961.
- [162] X.-H. Li, J. Zhang, X. Chen, A. Fischer, A. Thomas, M. Antonietti, X. Wang, *Chem. Mater.* **2011**, 23 (19), 4344-4348.
- [163] M. Xie, W. Wei, Z. Jiang, Y. Xu, J. Xie, *Ceram. Int.* **2016**, 42 (3), 4158-4170.
- [164] J. Liu, J. Huang, D. Dontosova, M. Antonietti, *RSC Adv.* **2013**, 3 (45), 22988-22993.
- [165] M. Tahir, C. Cao, N. Mahmood, F. K. Butt, A. Mahmood, F. Idrees, S. Hussain, M. Tanveer, Z. Ali, I. Aslam, *ACS Appl. Mater. Inter.* **2014**, 6 (2), 1258-1265.
- [166] S. Wang, C. Li, T. Wang, P. Zhang, A. Li, J. Gong, *J. Mater. Chem. A* **2014**, 2 (9), 2885-2890.
- [167] Z. Huang, F. Li, B. Chen, G. Yuan, *RSC Adv.* **2015**, 5 (124), 102700-102706.
- [168] Q. Han, B. Wang, J. Gao, Z. Cheng, Y. Zhao, Z. Zhang, L. Qu, *ACS Nano* **2016**, 10 (2), 2745-2751.
- [169] X. Bu, Y. Bu, S. Yang, F. Sun, L. Tian, Z. Peng, P. He, J. Sun, T. Huang, X. Wang, G. Ding, J. Yang, X. Xie, *RSC Adv.* **2016**, 6 (113), 112210-112214.
- [170] Y. Zeng, C. Liu, L. Wang, S. Zhang, Y. Ding, Y. Xu, Y. Liu, S. Luo, *J. Mater. Chem. A* **2016**, 4 (48), 19003-19010.
- [171] M. Shalom, S. Inal, C. Fettkenhauer, D. Neher, M. Antonietti, *J. Am. Chem. Soc.* **2013**, 135 (19), 7118-7121.
- [172] Y. Zhao, F. Zhao, X. Wang, C. Xu, Z. Zhang, G. Shi, L. Qu, *Angew. Chem. Int. Ed.* **2014**, 53 (50), 13934-13939.
- [173] N. Tian, H. Huang, X. Du, F. Dong, Y. Zhang, *J. Mater. Chem. A* **2019**, 7 (19), 11584-11612.
- [174] M. Ayán-Varela, S. Villar-Rodil, J. I. Paredes, J. M. Munuera, A. Pagán, A. A. Lozano-Pérez, J. L. Cenis, A. Martínez-Alonso, J. M. D. Tascón, *ACS Appl. Mater. Inter.* **2015**, 7 (43), 24032-24045.
- [175] X. Zhang, X. Xie, H. Wang, J. Zhang, B. Pan, Y. Xie, *J. Am. Chem. Soc.* **2013**, 135 (1), 18-21.
- [176] J. Liu, H. Wang, M. Antonietti, *Chem. Soc. Rev.* **2016**, 45 (8), 2308-2326.
- [177] P. Niu, L. Zhang, G. Liu, H.-M. Cheng, *Adv. Funct. Mater.* **2012**, 22 (22), 4763-4770.
- [178] P. Qiu, H. Chen, C. Xu, N. Zhou, F. Jiang, X. Wang, Y. Fu, *J. Mater. Chem. A* **2015**, 3 (48), 24237-24244.
- [179] F. Cheng, H. Wang, X. Dong, *Chem. Commun.* **2015**, 51 (33), 7176-7179.
- [180] J. Tong, L. Zhang, F. Li, K. Wang, L. Han, S. Cao, *RSC Adv.* **2015**, 5 (107), 88149-88153.
- [181] S. Yang, Y. Gong, J. Zhang, L. Zhan, L. Ma, Z. Fang, R. Vajtai, X. Wang, P. M. Ajayan, *Adv. Mater.* **2013**, 25 (17), 2452-2456.
- [182] K. Schwinghammer, M. B. Mesch, V. Duppel, C. Ziegler, J. Senker, B. V. Lotsch, *J. Am. Chem. Soc.* **2014**, 136 (5), 1730-1733.
- [183] H. Lan, L. Li, X. An, F. Liu, C. Chen, H. Liu, J. Qu, *Appl. Catal., B* **2017**, 204, 49-57.
- [184] D. B. Nimbalkar, M. Stas, S.-S. Hou, S.-C. Ke, J.-J. Wu, *ACS Appl. Mater. Inter.* **2019**, 11 (21), 19087-19095.

- [185] L. Zhou, H. Zhang, H. Sun, S. Liu, M. O. Tade, S. Wang, W. Jin, *Catal. Sci. Technol.* **2016**, 6 (19), 7002-7023.
- [186] Q. Liang, Z. Li, Z.-H. Huang, F. Kang, Q.-H. Yang, *Adv. Funct. Mater.* **2015**, 25 (44), 6885-6892.
- [187] V. Coropceanu, J. Cornil, D. A. da Silva Filho, Y. Olivier, R. Silbey, J.-L. Brédas, *Chem. Rev.* **2007**, 107 (4), 926-952.
- [188] Q. Yang, S. Hu, Y. Yao, X. Lin, H. Du, Y. Yuan, *Chinese J. Catal.* **2021**, 42 (1), 217-224.
- [189] A. Thomas, A. Fischer, F. Goettmann, M. Antonietti, J.-O. Müller, R. Schlögl, J. M. Carlsson, *J. Mater. Chem.* **2008**, 18 (41), 4893-4908.
- [190] H. Zhang, A. Yu, *J. Phys. Chem. C* **2014**, 118 (22), 11628-11635.
- [191] J. Wu, X. Ji, X. Yuan, Z. Zhao, Y. Li, B. Wen, H. Zhang, D. Yu, Y. Zhao, Y. Tian, *Chem. Mater.* **2019**, 31 (21), 9188-9199.
- [192] A. H. Reshak, S. A. Khan, S. Auluck, *RSC Adv.* **2014**, 4 (14), 6957-6964.
- [193] P. Zhang, H. Li, Y. Wang, *Chem. Commun.* **2014**, 50 (48), 6312-6315.
- [194] J. Sun, R. Phatake, A. Azoulay, G. Peng, C. Han, J. Barrio, J. Xu, X. Wang, M. Shalom, *Chem.–Eur. J.* **2018**, 24 (56), 14921-14927.
- [195] B. Kumru, M. Antonietti, B. V. K. J. Schmidt, *Langmuir* **2017**, 33 (38), 9897-9906.
- [196] D. Vidyasagar, S. G. Ghugal, S. S. Umare, M. Banavoth, *Sci. Rep.* **2019**, 9 (1), 7186.
- [197] X. Fan, L. Zhang, R. Cheng, M. Wang, M. Li, Y. Zhou, J. Shi, *ACS Catal.* **2015**, 5 (9), 5008-5015.
- [198] N. Karjule, J. Barrio, J. Tzadikov, M. Shalom, *Chem.–Eur. J.* **2020**, 26 (29), 6622-6628.
- [199] C. Zhu, T. Wei, Y. Wei, L. Wang, M. Lu, Y. Yuan, L. Yin, L. Huang, *J. Mater. Chem. A* **2021**, 9 (2), 1207-1212.
- [200] A. Jin, Y. Jia, C. Chen, X. Liu, J. Jiang, X. Chen, F. Zhang, *J. Phys. Chem. C* **2017**, 121 (39), 21497-21509.
- [201] K. M. Alam, P. Kumar, P. Kar, U. K. Thakur, S. Zeng, K. Cui, K. Shankar, *Nanoscale Adv.* **2019**, 1 (4), 1460-1471.
- [202] M. Luo, Q. Yang, W. Yang, J. Wang, F. He, K. Liu, H. Cao, H. Yan, *Small* **2020**, 16 (20), 2001100.
- [203] C. Ye, J.-X. Li, H.-L. Wu, X.-B. Li, B. Chen, C.-H. Tung, L.-Z. Wu, *ACS Appl. Mater. Inter.* **2018**, 10 (4), 3515-3521.
- [204] R. Wang, L. Gu, J. Zhou, X. Liu, F. Teng, C. Li, Y. Shen, Y. Yuan, *Adv. Mater. Interfaces* **2015**, 2 (10), 1500037.
- [205] Q. Xiang, J. Yu, M. Jaroniec, *J. Phys. Chem. C* **2011**, 115 (15), 7355-7363.
- [206] M. Bledowski, L. Wang, A. Ramakrishnan, O. V. Khavryuchenko, V. D. Khavryuchenko, P. C. Ricci, J. Strunk, T. Cremer, C. Kolbeck, R. Beranek, *Phys. Chem. Chem. Phys.* **2011**, 13 (48), 21511-21519.
- [207] Z. Jiang, C. Zhu, W. Wan, K. Qian, J. Xie, *J. Mater. Chem. A* **2016**, 4 (5), 1806-1818.
- [208] Y. Hou, A. B. Laursen, J. Zhang, G. Zhang, Y. Zhu, X. Wang, S. Dahl, I. Chorkendorff, *Angew. Chem. Int. Ed.* **2013**, 52 (13), 3621-3625.
- [209] V. W.-h. Lau, D. Klose, H. Kasap, F. Podjaski, M.-C. Pignié, E. Reisner, G. Jeschke, B. V. Lotsch, *Angew. Chem. Int. Ed.* **2017**, 56 (2), 510-514.
- [210] H. H. Mohamed, C. B. Mendive, R. Dillert, D. W. Bahnemann, *J. Phys. Chem. A* **2011**, 115 (11), 2139-2147.
- [211] M. Schulz, N. Hagemeyer, F. Wehmeyer, G. Lowe, M. Rosenkranz, B. Seidler, A. Popov, C. Streb, J. G. Vos, B. Dietzek, *J. Am. Chem. Soc.* **2020**, 142 (37), 15722-15728.
- [212] K. C. VanMeter, R. J. Hubert, W. G. VanMeter, *Microbiology for the Healthcare Professional Elsevier Health Sciences*, **2013**.
- [213] A. Silverstein, V. B. Silverstein, L. S. Nunn, *Photosynthesis*, Twenty-First Century Books, **2007**.
- [214] A. Savateev, B. Kurpil, A. Mishchenko, G. Zhang, M. Antonietti, *Chem. Sci.* **2018**, 9 (14), 3584-3591.
- [215] H. Su, C. A. Hurd Price, L. Jing, Q. Tian, J. Liu, K. Qian, *Materials Today Bio* **2019**, 4, 100033.
- [216] Z. Ye, Y. Sun, H. Zhang, B. Song, B. Dong, *Nanoscale* **2017**, 9 (46), 18516-18522.
- [217] F. Podjaski, B. V. Lotsch, *Adv. Energy Mater.* **2021**, 11 (4), 2003049.
- [218] R. Kuriki, C. S. K. Ranasinghe, Y. Yamazaki, A. Yamakata, O. Ishitani, K. Maeda, *J. Phys. Chem. C* **2018**, 122 (29), 16795-16802.
- [219] G. Zhang, G. Li, T. Heil, S. Zafeirotos, F. Lai, A. Savateev, M. Antonietti, X. Wang, *Angew. Chem. Int. Ed.* **2019**, 58 (11), 3433-3437.
- [220] J. Fu, J. Yu, C. Jiang, B. Cheng, *Adv. Energy Mater.* **2018**, 8 (3), 1701503.

- [221] J. Hussain, H. Jónsson, E. Skúlason, *Faraday Discuss.* **2016**, 195 (0), 619-636.
- [222] Y. Xia, K. Xiao, B. Cheng, J. Yu, L. Jiang, M. Antonietti, S. Cao, *ChemSusChem* **2020**, 13 (7), 1730-1734.
- [223] S. Roy, E. Reisner, *Angew. Chem. Int. Ed.* **2019**, 58 (35), 12180-12184.
- [224] C. Bie, B. Zhu, F. Xu, L. Zhang, J. Yu, *Adv. Mater.* **2019**, 31 (42), 1902868.
- [225] P. Xia, M. Antonietti, B. Zhu, T. Heil, J. Yu, S. Cao, *Adv. Funct. Mater.* **2019**, 29 (15), 1900093.
- [226] S. Sorcar, J. Thompson, Y. Hwang, Y. H. Park, T. Majima, C. A. Grimes, J. R. Durrant, S.-I. In, *Energ. Environ. Sci.* **2018**, 11 (11), 3183-3193.
- [227] Y. Shiraishi, S. Shiota, Y. Kofuji, M. Hashimoto, K. Chishiro, H. Hirakawa, S. Tanaka, S. Ichikawa, T. Hirai, *ACS Appl. Energy Mater.* **2018**, 1 (8), 4169-4177.
- [228] P. Xia, S. Cao, B. Zhu, M. Liu, M. Shi, J. Yu, Y. Zhang, *Angew. Chem. Int. Ed.* **2020**, 59 (13), 5218-5225.
- [229] T. Uekert, H. Kasap, E. Reisner, *J. Am. Chem. Soc.* **2019**, 141 (38), 15201-15210.
- [230] A. U. Meyer, V. W.-h. Lau, B. König, B. V. Lotsch, *Eur. J. Org. Chem.* **2017**, 2017 (15), 2179-2185.
- [231] Z. Wang, X. Hu, Z. Liu, G. Zou, G. Wang, K. Zhang, *ACS Catal.* **2019**, 9 (11), 10260-10278.
- [232] A. Vijeta, E. Reisner, *Chem. Commun.* **2019**, 55 (93), 14007-14010.
- [233] M. A. Bajada, A. Vijeta, A. Savateev, G. Zhang, D. Howe, E. Reisner, *ACS Appl. Mater. Inter.* **2020**, 12 (7), 8176-8182.
- [234] D. Zhang, L.-Z. Wu, L. Zhou, X. Han, Q.-Z. Yang, L.-P. Zhang, C.-H. Tung, *J. Am. Chem. Soc.* **2004**, 126 (11), 3440-3441.
- [235] H. Kasap, D. S. Achilleos, A. Huang, E. Reisner, *J. Am. Chem. Soc.* **2018**, 140 (37), 11604-11607.
- [236] J. Xue, S. Ma, Y. Zhou, Q. Wang, *RSC Adv.* **2015**, 5 (107), 88249-88257.
- [237] M. Hassanpour, H. Safardoust-Hojaghan, M. Salavati-Niasari, *J. Mol. Liq.* **2017**, 229, 293-299.
- [238] W. Zhang, L. Zhou, H. Deng, *J. Mol. Catal. A: Chem.* **2016**, 423, 270-276.
- [239] C. Chang, Y. Fu, M. Hu, C. Wang, G. Shan, L. Zhu, *Appl. Catal., B* **2013**, 142-143, 553-560.
- [240] J. Xue, S. Ma, Y. Zhou, Z. Zhang, M. He, *ACS Appl. Mater. Inter.* **2015**, 7 (18), 9630-9637.
- [241] Y. Sun, T. Xiong, Z. Ni, J. Liu, F. Dong, W. Zhang, W.-K. Ho, *Appl. Surf. Sci.* **2015**, 358, 356-362.
- [242] Z.-Z. Lu, S.-Q. Li, J.-Y. Xiao, *Catal. Lett.* **2020**.
- [243] M. Zhou, G. Dong, J. Ma, F. Dong, C. Wang, J. Sun, *Appl. Catal., B* **2020**, 273, 119007.
- [244] W. Bing, Z. Chen, H. Sun, P. Shi, N. Gao, J. Ren, X. Qu, *Nano Res.* **2015**, 8 (5), 1648-1658.
- [245] M. Abdullah Khan, I. F. Teixeira, M. M. J. Li, Y. Koito, S. C. E. Tsang, *Chem. Commun.* **2016**, 52 (13), 2772-2775.

3. Research Objective

Despite an already huge and still increasing number of publications, many aspects concerning the correlation between the structure, the photophysical properties and the photocatalytic activity of carbon nitrides is still unclear. The major problem arises from a not yet sufficiently well characterized molecular structure of carbon nitrides, especially when considering the identification of active sites and surface functional groups. Therefore, it is difficult to extract fundamental information required for photocatalysis or to gain insights in structure-properties-relationships.^[1] To address these issues rationally, the structure of carbon nitrides need to be analyzed thoroughly. The truly 2D carbon nitride poly(heptazine imide) (PHI) is of special interest, since unlike the other carbon nitrides, this compound is highly photocatalytically active. At the same time, it enables time delayed “dark” photocatalysis due to its intrinsic electron storage ability. The aim of this thesis is therefore a fundamental investigation of PHI, to carve out the structural properties that enable and influence the photocatalytic activity on several levels. For this purpose, the effects of surface terminations, particle size as well as incorporated ions are studied to develop design strategies for efficient photocatalysts by trying to balance detrimental factors with beneficial properties for best performance. Here, the photocatalytic hydrogen evolution is regarded as model system for photocatalytic reactions, despite a generally huge variety of photocatalytic reactions being enabled by carbon nitrides.

At first, a new synthesis route is reported to yield crystalline PHI, which was thoroughly characterized (Chapter 4). With the chemical structure being solved, PHI was synthesized with different particle sizes, so that the structural and photophysical changes could be monitored as a function of gradually decreasing particle size. Each of the different steps, which are involved in photocatalysis will be studied in this thesis in detail. This includes light absorption, exciton separation and charge transport, the amount and depths of trap states, as well as charge transfer to the co-catalyst (Figure 3.1). The aim of a combined study, taking all of these steps into account, is to entangle the interwoven interplay of those factors on photocatalytic hydrogen evolution, when particle sizes are reduced and to enable a material optimization based on these findings (Chapter 5). Such a combined analysis is rarely reported and therefore serves as example for overall analysis of photocatalytic parameters that influence activity.

Once those interactions are understood, the next step is the targeted design or adaptation of surface functionalities in carbon nitrides to enable boosted activity and tailored applications. Especially since photocatalysis is mainly a surface process, the terminal groups play an important role in the interfacial design, which can affect for example the wettability or charge carrier transfer to the co-catalysts and electron donor. Therefore, new synthesis procedures are being identified, that for the first time allow for the functionalization of the thermally and chemically stable carbon nitride PHI. By this the bottleneck reaction, namely the hole extraction kinetic, is tackled. At the same time the charge separation, hydrophilicity, Pt interaction as well as electron donor ad- and

desorption properties, are affected, as will be discussed in Chapter 6. The insights gained from this interfacial design process, affecting the performance of suspended photocatalytic systems, can easily be extended to other molecular systems while providing a new perspective on treating and tuning the oxidation reaction.

Lastly, also the charge transport in PHI is being investigated. In photocatalysis or photo-induced processes, not only the charge carrier separation and extraction, but also their transport is a key parameter for efficient use of light energy, which is occurring in the bulk of the material and therefore is not necessarily influenced by surface functional groups and particle size. As result of the synthesis, hydrated potassium ions are located in the pores of K-PHI, which can be exchanged for other cations. Their fundamental influence on the underlying conductivity mechanism in PHI is studied in order to enlighten the dependence of the photocatalytic activity of PHI on charge transport properties arising from the presence of those ions (Chapter 7). The conductivity analysis is often neglected in organic based semiconductors, since they are believed to be rather isolating, making the extraction of such parameters challenging. Thereby, this analysis helps to gain insights into the required charge transport processes in organic materials, which can limit but also enhance the photocatalysis behavior of the material.

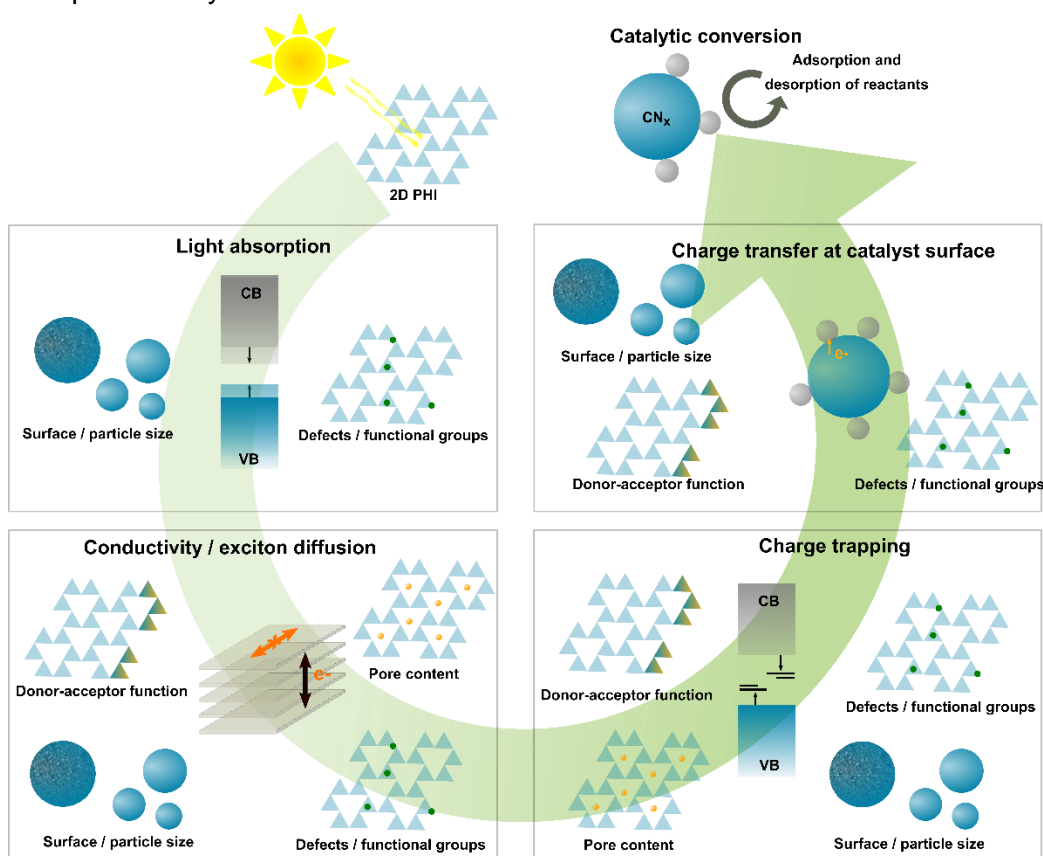


Figure 3.1: Structure-activity-relationships in 2D PHI are being studied for their individual contribution to the overall photocatalytic process. The detailed study of certain tuning parameters of carbon nitrides is used to optimize the catalyst design. The timescales on which those processes occur are increasing from light absorption, to exciton diffusion, charge separation and trapping, and finally, charge transfer at the surface and catalytic reaction (from left top to right top).

4. Structural insights into 2D poly(heptazine imide) (PHI)

The work in this chapter was published, reproduced and adapted from:

Structural insights into poly(heptazine imide): A light-storing carbon nitride material for dark photocatalysis

Hendrik Schlomberg,* [Julia Kröger](#),* Gökçen Savasci, Maxwell W. Terban, Sebastian Bette, Igor Moudrakovski, Viola Duppel, Filip Podjaski, Renée Siegel, Jürgen Senker, Robert E. Dinnebier, Christian Ochsenfeld, and Bettina V. Lotsch.

Chem. Mater. **2019**, *31*, (18), 7478-7486. DOI: 10.1021/acs.chemmater.9b02199

*equally contributed

Hendrik Schlomberg, and Bettina V. Lotsch conceived the project. Hendrik Schlomberg, Julia Kröger and Bettina V. Lotsch wrote the manuscript with input from all other authors. Hendrik Schlomberg and Julia Kröger synthesized the materials and performed most of the structural analysis and evaluated the data. Julia Kröger performed the photocatalysis experiments. Gökçen Savasci performed the quantum-chemical calculations with supervision of Christian Ochsenfeld. Maxwell W. Terban and Sebastian Bette performed PDF and XRD measurements, analysis and simulations with supervision of Robert E. Dinnebier. Igor Moudrakovski, Renée Siegel and Jürgen Senker performed solid state NMR measurements. Viola Duppel performed the TEM measurements. Filip Podjaski and Julia Kröger performed long-term charge storage tests. All authors assisted the analysis of their respective experiments and the overall discussion. Bettina V. Lotsch supervised the work.

Supporting information can be found in Chapter 9.1.

Abstract

Solving the structure of carbon nitrides has been a long-standing challenge due to the low crystallinity and complex structures observed within this class of earth-abundant photocatalysts. Herein, we report on two-dimensional layered potassium poly(heptazine imide) (K-PHI) and its proton-exchanged counterpart (H-PHI), obtained by ionothermal synthesis using a molecular

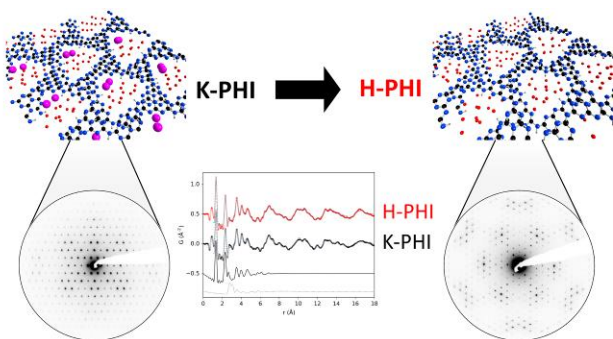


Figure 4.1: Table of content figure for structural insights into poly(heptazine imide).

precursor route. We present a comprehensive analysis of the in-plane and three-dimensional structure of PHI. Transmission electron microscopy and solid-state NMR spectroscopy, supported by quantum-chemical calculations, suggest a planar, imide-bridged heptazine backbone with trigonal symmetry in both K-PHI and H-PHI, whereas pair distribution function analyses and X-ray powder diffraction using recursive-like

simulations of planar defects point to a structure-directing function of the pore content. While the out-of-plane structure of K-PHI exhibits a unidirectional layer offset, mediated by hydrated potassium ions, H-PHI is characterized by a high degree of stacking faults due to the weaker structure directing influence of pore water. Structure–property relationships in PHI reveal that a loss of in-plane coherence, materializing in smaller lateral platelet dimensions and increased terminal cyanamide groups, correlates with improved photocatalytic performance. Size-optimized H-PHI is highly active toward photocatalytic hydrogen evolution, with a rate of $3363 \mu\text{mol g}^{-1} \text{h}^{-1}$ H_2 placing it on par with the most active carbon nitrides. K- and H-PHI adopt a uniquely long-lived photo-reduced polaronic state in which light-induced electrons are stored for more than 6 h in the dark and released upon addition of a Pt co-catalyst. This work highlights the importance of structure–property relationships in carbon nitrides for the rational design of highly active hydrogen evolution photocatalysts.

4.1. Introduction

A new class of (semi)crystalline two-dimensional (2D) carbon nitrides has emerged over the past few years, which exhibits outstanding photocatalytic performance^[1-3] along with intriguing photophysical properties, such as the potential for time-delayed fuel production (“dark photocatalysis”),^[4] which also make them attractive candidate materials for solar batteries.^[5] A hallmark of this carbon nitride family is its ability to store electrons in the form of a long-lived photo-reduced state,^[4, 6, 7] which allows for the separation of light absorption (the light reaction) and catalytic conversion (the dark reaction) akin to natural photosynthesis. This material has been postulated to exhibit a 2D poly(heptazine imide) (PHI)-based structure, but so far a comprehensive elucidation of its local and long-range structure is lacking. PHI has been synthesized by both, molecular precursor approaches^[8, 9] as well as top down strategies starting from the well-known melon polymer.^[2, 10] And yet, even though the synthesis procedures may vary widely, the use of salt melts, i.e., ionothermal synthesis, seems to be vital to all of these approaches.^[2, 8-10]

Ionothermal synthesis routes often yield fundamentally different products as compared to high-temperature solid-state approaches. A prominent example is the synthesis of melon, which is often referred to as graphitic carbon nitride, $\text{g-C}_3\text{N}_4$. Although the solid-state synthesis of melon yields a one-dimensional heptazine-based polymer, 2D networks are typically formed by a salt-melt approach using the same types of precursors. Under these conditions, the ionic flux and its components, typically alkali metal halides, serve as a high-temperature solvent and structure-directing agent at the same time.^[11-13] The structure-directing influence of alkali ions has been observed by Savateev *et al.* and is also known to be the governing factor during the formation of secondary building units in zeolites.^[9, 14] Interestingly, the composition of the melt also seems to have a profound influence on the type of carbon nitride backbone—triazine or heptazine-based—that is formed during the reaction.^[8]

Herein, we have used a molecular building block approach to synthesize highly crystalline potassium containing PHI terminated by cyanamide (NCN^-)-functional groups, abbreviated as potassium PHI (K-PHI), and its metal-free counterpart H-PHI. A comprehensive investigation of their local and long-range structures has been carried out through a combination of electron diffraction (ED) and transmission electron microscopy (TEM) imaging, solid-state nuclear magnetic resonance (ssNMR) spectroscopy, supported by quantum-chemical calculations, X-ray powder diffraction (PXRD), and pair distribution function analysis (PDF). We show that both materials feature an extended 2D network constituted by tri-*s*-triazine (heptazine) units connected via imide bridges. These layers assemble in either ordered or disordered long-range stacking relationships driven by interactions with the pore content, resulting in hitherto unknown structural modifications in this PHI family.

4.2. Results and discussion

The ionothermal bottom-up synthesis of PHI starts from the molecular precursors potassium melonate, dicyandiamide, and potassium thiocyanate (KSCN), which are heated under their autogenous pressure in an ampoule to yield highly crystalline potassium poly(heptazine imide) (K-PHI), terminated with NCN -functional groups. In contrast to other PHI-derived materials (mainly synthesized from LiCl/KCl eutectics), the herein discussed synthesis is based on KSCN as the salt component and hence flux. When K-PHI is treated with dilute acid, it is converted into the proton-bearing H-PHI, thus pointing to the Brønsted acid–base character of the polymer.^[9] Note that the reaction is insensitive to which acid (e.g., HCl , H_3PO_4 , H_2SO_4 , or HClO_4) is used for the transformation (Figures S1.50–S1.52). In the following text, we elucidate the local structure of K-PHI and H-PHI by solid-state NMR spectroscopy and characterize the 2D projection of the structure by means of TEM, whereas PXRD, PDF analyses, and recursive-like simulations of planar defects lead to the classification of the material in the third dimension.

TEM Analysis. The TEM image in Figure 4.2a reveals the sheet-like morphology of the crystallites and high crystallinity of the carbon nitride backbone over a large area of up to several 100 nm (for overview TEM images see Figures S1.1 and S1.3). The lattice fringes correspond to an interval of 11 Å within the layer planes, illustrated by the high-resolution (HR) TEM image in Figure 4.2a. The good agreement between the measured (Figure 4.2b) and simulated (4.2c) selected area electron diffraction (SAED) patterns along the [001] zone axis based on the structural model shown in Figure 4.2d indicates trigonal layer symmetry of the PHI backbone in H-PHI. The fast Fourier transformation (FFT) obtained from large crystallites (Figure 4.2a, inset) also fits the depicted SAED pattern. The 100 lattice spacing of 11 Å corresponds to the pore-to-pore distance of 12.8 Å and is consistent with a hexagonal arrangement of trigonal pores and a 2D network topology, similar to that found in the triazine analogue poly(triazine imide) (PTI).^[11, 12] The TEM data suggest that ideal H-PHI layers crystallize with trigonal symmetry, forming a “graphitic” 2D framework of imide-bridged heptazine building units akin to melamine-intercalated PHI, which crystallizes in the space group $P31m$.^[15] Particularly in the H-PHI case, slight intensity

deviations from the perfect hexagonal distribution of the electron diffraction spots (Figure 4.2b) and the fact that the diffraction data of H-PHI are relatively tolerant against tilting of the specimen for up to $\pm 10^\circ$ indicate structural disorder along the [001] zone axis. Intensity deviations might also arise from losing pore content (i.e., water) in ultra high vacuum and local heating through the electron beam, which may induce on-spot incipient degradation and enable the layers to shift to the eclipsed case, as also seen in thermogravimetric PXRD experiments in Figure S1.27. The diffraction spots of K-PHI (Figure 4.2f, [001] zone axis) imply that the material exhibits monoclinic layer symmetry. The SAED pattern can be reproduced by ED simulation with corresponding distances of 11 Å for the $\bar{1}10$ and 8.7 Å for the 100 reflection (Figure 4.2g). The HR-TEM image (Figure 4.2e) also points toward the existence of large crystalline domains, with the FFT (inset) reproducing the pattern obtained from the simulation in Figure 4.2g. The difference in symmetry suggests an altered stacking behavior of the PHI backbones in K-PHI and H-PHI, likely driven by the pore constituents (water in H-PHI or potassium ions in K-PHI). Note that the water content nearly doubles from 10 wt % for K-PHI to 20 wt % for H-PHI, determined by combustion analysis and inductively coupled plasma (Tables S1.8 and S1.9).

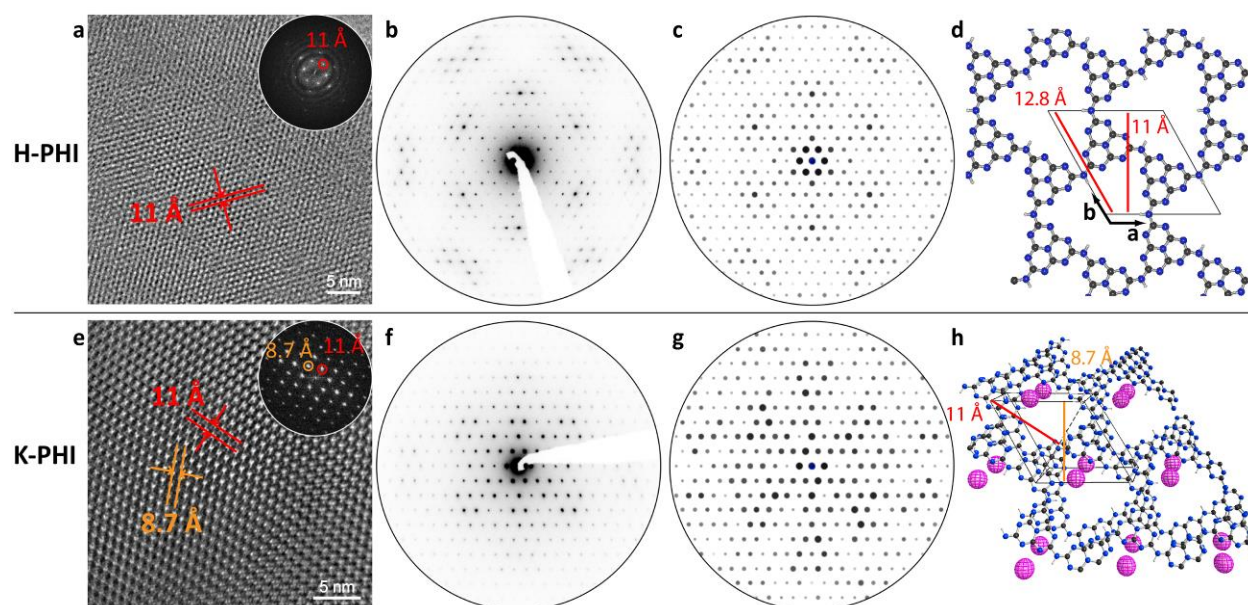


Figure 4.2: a) High-resolution TEM image of H-PHI clearly revealing lattice fringes over extended areas; (b) SAED pattern and c) simulated SAED pattern (c) of the [001] zone axis of H-PHI, based on a theoretical trigonal cell model depicted in d). e–g) cover the corresponding figures for K-PHI; Insets show the FFT confirming the 6-fold symmetry of the diffraction pattern for H-PHI and the reduced monoclinic layer symmetry for K-PHI, respectively. (h) Structural model obtained from Rietveld refinement for K-PHI (see Figure 4.4b); water molecules inside the pores were omitted for better visibility.

Solid-State NMR Spectroscopy. To probe the local structure of PHI, especially the intralayer connectivity and the distribution of cations within the pores, ^{13}C , ^{15}N , ^{14}N , and ^1H ssNMR spectra were recorded for K-PHI and compared with those of H-PHI. Figure 4.3a–i shows the ^{13}C direct excitation, ^{15}N cross-polarization (CP) and ^1H ssNMR spectra of K-PHI (top row) and H-PHI (middle row), as well as the ^{13}C – ^{15}N 2D heteronuclear correlation (HETCOR)^[16] spectrum of K-

PHI, the ^1H - ^{14}N 2D HETCOR, and 2D ^1H double-quantum–single-quantum (DQ–SQ)^[17] spectra of H-PHI (bottom row). Various model systems of single PHI pores with different substitution patterns and positions were designed and optimized on the PBE0-D3/def2-TZVP^[18-21] level of theory to then calculate NMR chemical shifts on the B97-2/pcsSeg-2^[22, 23] level of theory on optimized pore geometries (Figures S1.18–S1.24) to develop a better understanding of the experimental data and to support the assignment.

The direct excitation ^{13}C NMR experiment shows five distinct signals for K-PHI, which can be assigned according to the inset in Figure 4.3a. Like in melon,^[24] the central carbon atom (C1) in the heptazine unit exhibits a chemical shift of 157 ppm. The signal at 164 ppm is attributed to a peripheral carbon atom next to a NH-group (C2) as its signal is the most intense in the ^{13}C cross-polarization experiment confirming its proximity to a proton (Figure S1.12). Additionally, the ^{13}C - ^{15}N 2D HETCOR spectrum shows distinctly that C2 correlates with the NH-group at –242 ppm (Figure 4.3g), identifying this NH as the connecting bridge between two heptazine units. The ^{13}C NMR signal at 168 ppm arises from a carbon atom next to a deprotonated imide bridge (C3). Indeed, this C3 is only connected to nitrogen atoms with a chemical shift at –173 ppm (Figure 4.3g), a typical value for nonprotonated nitrogen. In the case of an attached NCN moiety, the neighboring heptazine carbon atom (C4) is shifted downfield to 172 ppm whereas the carbon atom of the terminal NCN-group (C5) is found at 120 ppm, which is likewise observed for cyanamide in molecular potassium melonate.^[25] However, according to the integrated intensities in NMR spectra, these cyanamide groups are only present in about every second to fifth (batch variations) heptazine ring in K-PHI. Assuming only terminating cyanamide groups at the edges of the crystallites, especially for large crystals in the range of 100 nm, the expected NCN content would be lower than the observed amount. However, additional cyanamide could have been introduced as point defects within the PHI sheet. Such a point defect is equivalent to a missing heptazine unit, leveraging additional internal NCN termini, since the former NH bridges become terminating NCN-groups inside the PHI layer. As discussed in more detail in the Supporting Information (SI) (Figure S1.9), the concentration of these defects has been estimated to be approx. 5–12%. The number of NCN-groups seems to be reduced upon the transformation to H-PHI, which can be attributed to partial hydrolysis of the functional group, resulting in an increased number of terminal NH_2 groups or urea terminations.

^{15}N CP MAS NMR of K-PHI confirms the presence of NH-groups at –242 ppm (N2, inset Figure 4.3b) bridging the heptazine units, as well as a small amount of terminal NH_2 groups at –273 ppm (N1) (note that the intensity of the NH_2 CP signal is grossly overestimated). The ^{15}N direct excitation spectra (Figure S1.11) show negligible (below detection limit) amounts of these NH_2 groups. The central nitrogen atom at –229 ppm (N3) has a very low intensity in the CP experiments, as the polarization transfer is very poor. This assignment is confirmed by the ^{13}C - ^{15}N 2D correlation experiment (Figure 4.3g) in which the central nitrogen is only connected to the carbon at 157 ppm (C1). The peripheral nitrogen atoms at –160 to –200 ppm (N4) lie in the typical

range of shifts known from heptazine-derived molecules.^[24] Interestingly, the best agreement with our quantum-chemical models is found by assuming the “naked” anionic N-bridge to be screened by a potassium ion (Figures S1.23). In this case, calculations suggest that the signal of the anionic bridge (N5) lies at -173 ppm and is thus beneath the shifts of the heptazine core. Placing the potassium ion in the center of the pore (Figure S1.24), a shift at >-140 ppm is calculated for the bridging nitrogen atom, which is not found in our measurements. Thus, our data suggest that K^+ , presumably with a partial hydration shell, is located off-center and moved toward the polymeric backbone.

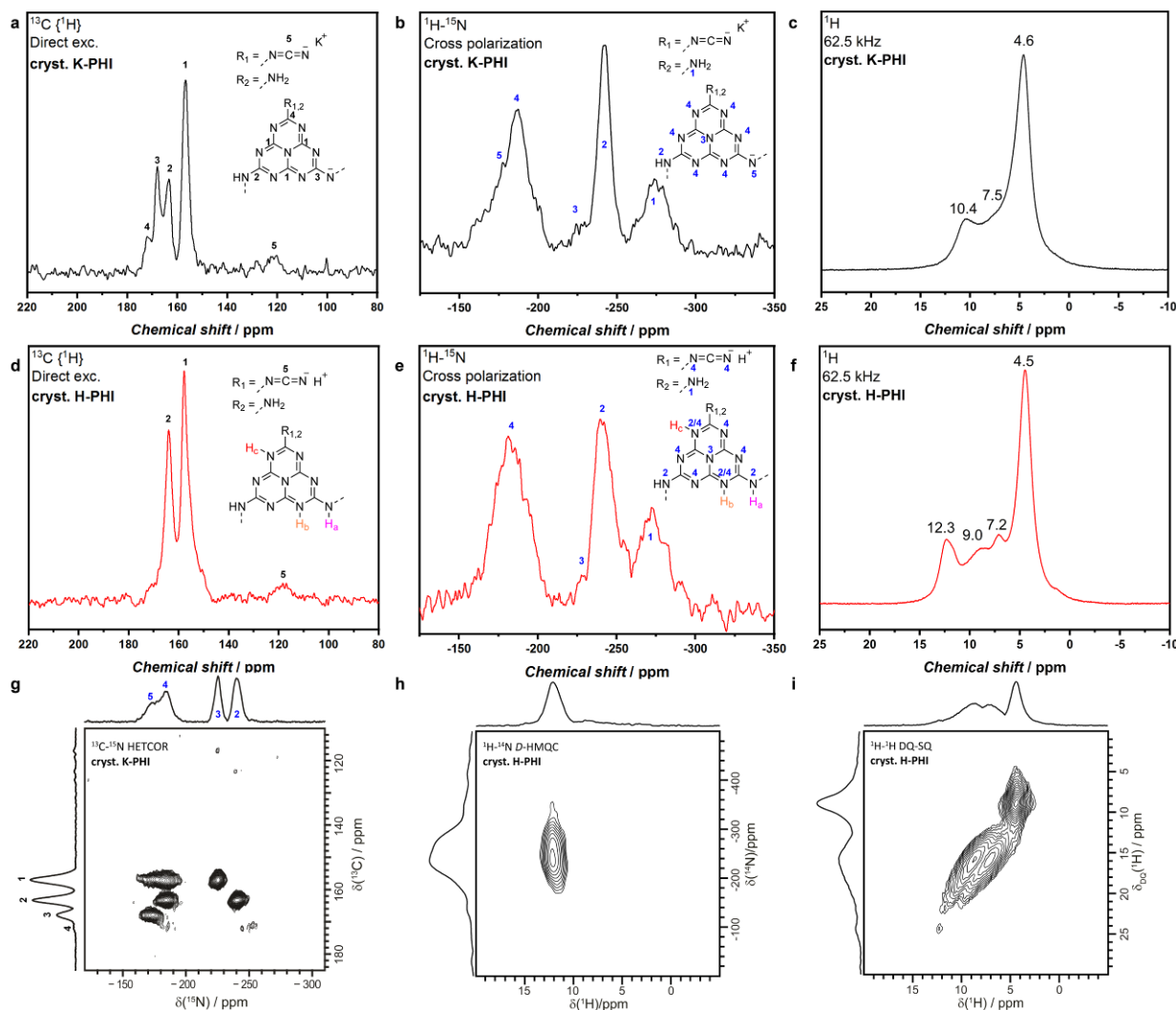


Figure 4.3: a, d) ^{13}C direct and b, e) ^{15}N cross-polarization and (c, f) ultrafast ^1H magic angle spinning (MAS) solid-state NMR spectra of K-PHI and H-PHI. The contact times of CP ^{15}N NMR spectra were both set to 4 ms. Insets show the proposed structures and their NMR assignments in black for carbon atoms and in blue for nitrogen atoms. In the case of H-PHI, the different possible protonation sites are labeled H_a, H_b, H_c; however, coexistence of several different tautomers is possible with the majority of NH-groups still located at bridges. g) ^{13}C - ^{15}N dynamic nuclear polarization (DNP) HETCOR NMR spectrum of K-PHI, ^1H - ^{14}N dipolar heteronuclear multiple-quantum coherence, and ^1H - ^1H DQ-SQ spectra of H-PHI h, i).

Although the structure of the acid-treated polymer H-PHI is largely similar, some distinct changes in the NMR spectra accompany the transformation. The NMR data of H-PHI support the assumption that protonation occurs predominantly at formerly negatively charged bridging nitrogen atoms (H_a , inset Figure 4.3d). Due to the conjugated charge in the network, however, protonation may also occur directly at the heptazine ring. Quantum-chemical calculations have identified H_b and H_c (inset Figure 4.3d) as potential protonation sites. The corresponding calculated chemical shift of these ring protonations are -247 and -261 ppm, respectively, which is in agreement with the upfield shift of the NH-group signal in Figure 4.3e. Molecular heptazine-based compounds such as cyameluric acid or protonated calcium melonate support this possibility, as they also bear the proton at the heptazine ring.^[26, 27] However, the overall low absolute amount of NH sites at the ring, along with the coexistence of different protonation sites and expected similar chemical shifts (see calculated pore models in Figures S1.18, S1.19, and S1.22) for this group compared with the bridging NH, does not allow for an unambiguous resolution of the protonation sites.

In direct excitation ^{13}C NMR of protonated samples (H-PHI), the previously visible signal C3 next to a deprotonated bridge now disappears, hinting that this nitrogen has been protonated, which would result in a chemical shift similar to that of C2. Indeed, the relative intensity of C2 increases for H-PHI in the directly detected ^{13}C spectrum. The resonance of C5 at 120 ppm slightly shifts upfield to 117 ppm as compared to that of K-PHI, which is also mapped by our calculations (Figure S1.18). The carbon atom next to the protonated NCN-group is now located beneath the signal of C2. The ^{15}N CP MAS experiment yields a picture for H-PHI very similar to that for K-PHI. However, the NH-group at -242 ppm is broadened toward higher fields in H-PHI and the central nitrogen in the heptazine unit is slightly upfield-shifted to -233 ppm as well. Additionally, a shoulder of the carbon signal at 157 ppm toward higher fields is also observed. These small changes could be related to interactions with protons of water in close proximity to nitrogen atoms on the *s*-heptazine ring and the possibility of NH located at the ring.

The ^1H NMR measurements of K-PHI and H-PHI (Figure 4.3c, f) help to give a clearer picture on the role of water and protons within those networks. Both spectra exhibit an intense signal at about 4.5 ppm, which is assigned to relatively free water inside the pores. Several additional overlapping peaks can be observed between 5 and 12.3 ppm for H-PHI. From the ^1H - ^{14}N 2D correlation spectra, the proton of the bridging NH can be assigned to a chemical shift of about 10.4 ppm for K-PHI (Figure S1.14b) and 12.3 ppm for H-PHI (Figure 4.3h), confirming that the majority of the bridging nitrogen atoms are protonated. Note that this low-field shifted resonance varies with the amount of water present in the sample. For a “dry” H-PHI sample (vacuum-dried at 120 °C for 2 days), this peak shifts upfield to about 7 ppm, as shown by its ^1H - ^{14}N 2D HETCOR spectrum (Figure S1.14a). This is in agreement with the calculations, hinting at water as a factor that significantly influences the proton NMR shifts. A calculated model pore with one water molecule interacting with an imide bridge leads to a shift of the NH proton from 8 ppm (without

water) to roughly 11 ppm (with water), which is close to the experimental results (cf. Figures S1.19 and S1.20). In H-PHI, this proton signal is downfield-shifted to 12.3 ppm compared to that of the potassium-containing anionic network (10.4 ppm), thus indicating more acidic protons for H-PHI. The ^1H NMR resonances between the free water and the NH-bridging peaks (between 5 and 12 ppm for H-PHI) reveal no strong bonding to the network and consequently show no correlation with any nitrogen in the ^1H - ^{14}N 2D HETCOR spectrum and hence are assigned to additional water inside the pore. The ^1H - ^1H 2D DQ-SQ spectrum of H-PHI (Figure 4.3i) provides both a higher resolution for ^1H and information on proximity between these protons. On the diagonal we observe the self-correlation peak of free water at 4.5 ppm and also the bridging NH self-correlation, although this second one is less intense due to a large distance between the NH units. In addition, we observe a quite intense correlation between one ^1H at 7.2 and one at 9.0 ppm. From the DQ-SQ experiment acquired with different recoupling times (Figure S1.15), these two protons are close to each other (their distance is similar to the ^1H - ^1H distance in water). This would hint at a water molecule with each of its two protons creating hydrogen bonds to nitrogen atoms on the heptazine ring. Similar protons are also observed in the case of K-PHI (Figure S1.16), i.e., also in close contact to the network. In general, ssNMR spectroscopy, in combination with our calculated pore models, corroborates the existence of a heptazine-based interconnected 2D network for K-PHI and H-PHI partially functionalized by NCN-groups. In both materials, the network strongly interacts with water and hydrated potassium, respectively. This interplay represents a key factor for explaining the three-dimensional (3D) structure, as presented in the following sections.

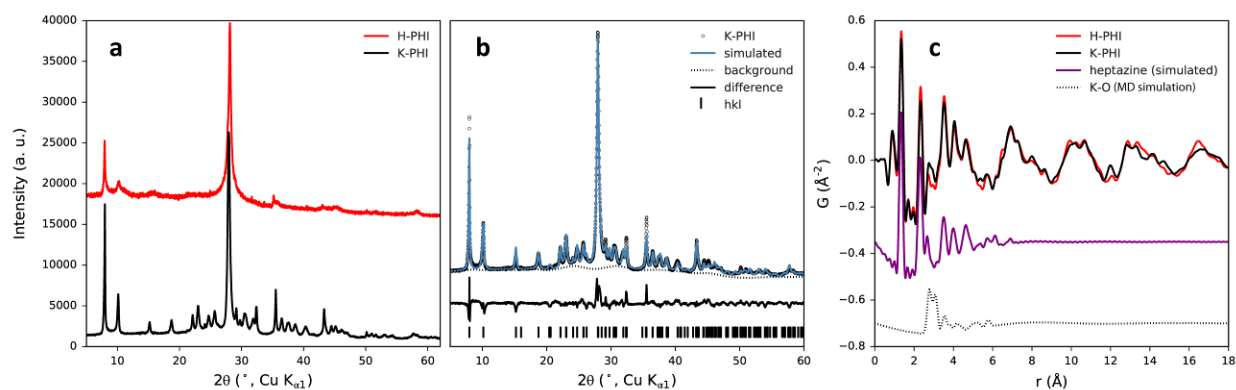


Figure 4.4: a) PXRD patterns of H-PHI and K-PHI measured using Cu $K\alpha_1$ radiation, b) Rietveld refinement for K-PHI, and c) experimental PDFs for K-PHI and H-PHI, and simulated ones from a single heptazine molecule and from a model of potassium–oxygen distances derived from molecular dynamics (MD) simulations.

X-Ray Powder Diffraction and PDF Analysis. PXRD patterns show significant peak broadening for H-PHI, whereas K-PHI exhibits higher crystallinity and was therefore used as the starting point for modeling (Figure 4.4a). In line with the TEM data, the Bragg peaks could be indexed with a triclinic unit cell, which was confirmed by Pawley refinement^[28] to be pseudo-hexagonal with $a = b = 12.78 \text{ \AA}$, $c = 4.31 \text{ \AA}$, $\alpha = \beta = 109.63^\circ$ and $\gamma = 120^\circ$, $R_{wp} = 3.87\%$. The structure model for the

Rietveld refinement^[29] (Figure 4.4b) was based upon the previously solved structure of PTI, reimagined for PHI sheets.^[11, 12] The cell metric indicates a single layer per cell, which is stacked in a slip-stacked fashion, given the non-90° α/β angles. A planar heptazine dimer was defined as a rigid body and oriented in the ab -plane, forming large triangular pores with two heptazine units on each side and an interlayer distance of approximately 3.2 Å, in agreement with the prominent 001 stacking reflection at ca. 28° 2 θ . Reasonable relative peak intensities could only be obtained by including K and O atoms (i.e., water molecules) representing the pore content, indicating that the pores are indeed filled. Further details on Pawley and Rietveld analyses can be found in Figures S1.28–S1.31.

H-PHI appears to be structurally related through well-defined $1\bar{1}0$, 010/100, 001, and $32\bar{1}/23\bar{1}$ reflections and could be indexed by Pawley refinement with a similar cell (Figure S1.29). However, a suitable Rietveld refinement for H-PHI was not possible due to significant peak broadening. Since NMR and TEM data suggest an intact layer constitution of H-PHI, this broadening is attributed to planar defects occurring as stacking fault disorder that developed during K⁺ removal, which is discussed in the next section.

To gain further insights into the local structure, PDFs (Figures S1.32, S1.33) were obtained from synchrotron X-ray total scattering data for H-PHI and K-PHI, in Figure 4.4c. A direct comparison shows highly similar local structures in both compounds. The heptazine units are present and conformationally rigid. Broad, interlayer peaks repeating with a wavelength of ~3.19 Å for K-PHI and ~3.17 Å for H-PHI indicate that the sheets are stacked with high fidelity, on the order of at least several hundred Angstroms, shown in Figures S1.32 and S1.33. The lack of longer wavelength modulations expected from periodic porous channels indicates that the pores are populated by uncorrelated electron density. Small differences in medium-range, low-amplitude features indicate possible differences in local ordering of pore content and neighboring layers, whereas more drastic long-range deviation in the behavior of the interlayer peaks provides additional evidence of differences in the stacking behavior. Model refinements to the K-PHI and H-PHI PDFs (Figures S1.34–S1.36) were consistent with the results from Rietveld refinements, as shown in Figures S1.30 and S1.31. In terms of short-range ordering, the most notable difference between H-PHI and K-PHI is the increase in peak intensity around 2.7–3.3 Å, which correlates with an increase in K⁺ (Figure S1.37) concentration. This feature is connected to potassium–oxygen distances found in water-solvated potassium ions observed via MD simulations (Figure S1.25), providing direct evidence of water–K⁺ coordination within the pores. Notably, in all Rietveld and PDF refinements, K⁺ ions consistently moved off center, in-plane, toward one corner of the triangular pore. Complexation of K⁺ ions with azines has previously been shown favorable (planar orientation/similar bond distances).^[30] It is reasonable that K⁺ could occupy both fully water-coordinated and partial nitrogen-coordinated positions.

Both TEM and PXRD data are consistent with the comparably high crystallinity of the carbon nitride backbone. The overall high in-plane order likely results from the use of molecular

precursors that have a higher mobility in the salt melt, which serves as a source for error correction during bond formation. The fact that the reflections in the PXRD pattern of H-PHI are particularly broadened will be discussed in the next section.

Stacking Fault Simulations. Information on the 3D structure of the bulk PHI is difficult to extract from electron diffraction patterns due to the local nature of the method and the pronounced 2D morphology of the crystallites. The structural coherence of the PHI materials in the third dimension is governed by the stacking order of the layers and in the case of H-PHI is vastly affected by planar defects occurring as stacking faults. Thus, systematic simulations^[31] of distinct faulting scenarios have been performed and compared qualitatively to the measured PXRD pattern, which yields information on all three dimensions of the bulk material. H-PHI in Figure 4.5a shows significant peak broadening and triangular, Warren-type line shapes,^[32] which are indicative of planar defects in the crystal structure. We therefore conclude that H-PHI has a higher degree of out-of-plane disorder compared with K-PHI.

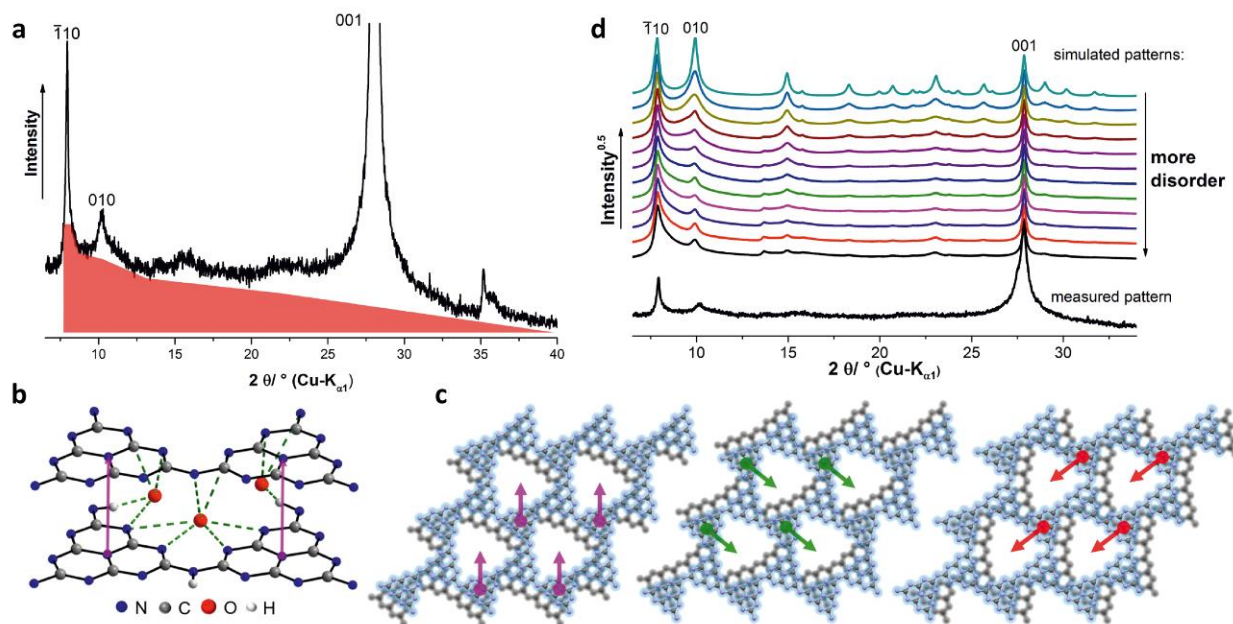


Figure 4.5: a) PXRD of H-PHI showing the triangular peak shape. b) Model with suggested influence of pore material (in this case, water, Figure S1.40), leading to indirect interactions between the layers as well as different stacking variants with respective colored stacking vectors. c) Possible equivalent stacking vectors for sheets of PHI; (d) simulation for faulting scenario IV (see chapter 9 of the appendix 9.1 and Figures S1.47–S1.49).

In Figure 4.5b, possible interactions of pore water with the poly(heptazine imide) backbone of H-PHI are depicted. These interactions direct the stacking of the layers and induce a layer offset; i.e., a layer is shifted toward the pore of the preceding layer. Due to the intrinsic trigonal symmetry of the heptazine subunit, this type of stacking exhibits three equivalent directions (Figure 4.5c). The eclipsed case was also considered for the simulations, i.e., layers stacked directly atop each other. Different faulting scenarios were developed using these four stacking relationships and used for qualitative simulations on the diffractive effect of structural disorder (detailed

information is given in chapter 9 of the appendix 9.1). The faulting scenario (“Faulting scenario IV”, Figures S1.47–S1.49) that was evaluated as the most suitable based on the match between simulated and measured patterns describes completely random transitions between all three pore directed stackings. This leads to a loss in the orientational coherence perpendicular to the layer planes and therefore to vast broadening of most reflections in the PXRD pattern in Figure 4.5d. Small sections of homogeneously stacked layers are, however, still apparent, as indicated by the presence of the remaining 010 reflection.

The combined approach of PDF and PXRD along with stacking fault simulations reveals the overall 3D structures of H-PHI and K-PHI. It has been shown that the stacking of the pores is governed by rather weak pore–water interactions in the case of H-PHI, resulting in highly defective stacking. Nevertheless, pore water clearly mediates interlayer interaction. When the water molecules are removed by heating H-PHI up to 400 °C under an inert, dynamic atmosphere in a TG-experiment, an *ex situ* PXRD analysis of the residue (Figure S1.27) reveals a significant decrease in the crystallite size perpendicular to the layer planes. The complete removal of pore water also shifts the layer arrangement toward an eclipsed stacking order. The presence of potassium within the pores leads to a more ordered stacking, which is indicated by much sharper reflections in the corresponding PXRD pattern (Figure 4.4a). Therefore, the range of the interlayer interaction is much larger in K-PHI than in H-PHI. This can be attributed both to the large ionic radius of the potassium cation and its more isolated positive charge. As potassium is located off-center in the pores, it interacts with the PHI framework. In addition, a partial hydration sphere is formed around the cation by the pore water molecules (Figure S1.25), which may indirectly mediate interactions to further distant layers.

Photocatalysis. Knowledge of the structure–property relationships in this class of carbon nitrides is key for the rational design of photocatalysts with improved properties. We therefore investigated the photocatalytic activity of H-PHI and K-PHI, obtained from ampoule synthesis, for the hydrogen evolution reaction (HER) with a focus on carving out those structural features that affect the activity the most. We find that H-PHI, like K-PHI, is active toward HER in the presence of a Pt co-catalyst and methanol as the sacrificial electron donor but shows only moderate activity (H-PHI: 88 $\mu\text{mol g}^{-1}\text{h}^{-1}$, K-PHI: 193 $\mu\text{mol g}^{-1}\text{h}^{-1}$). This can be directly traced back to the large crystallites that tend to form aggregates that disperse only weakly in aqueous solution, thus having less accessible surface area and a reduced number of edge sites available. The latter seems to be vital for the catalytic activity^[33] for co-catalyst-supported systems through the presence of cyanamide terminations at the edges of the platelets. These terminations can bind more efficiently to the Pt co-catalyst and provide a higher degree of ionicity and thus colloidal stability.^[2]

To test this hypothesis, we synthesized variants of H-PHI and K-PHI with smaller crystallite sizes (~20 nm) and an increased amount of external cyanamide groups accordingly, by using a mixture of melon and KSCN as precursors at ambient pressure under an argon flow, followed by treatment in diluted HCl. For the as-obtained, optimized K-PHI, we recorded a 3-fold increased activity of

600 $\mu\text{mol g}^{-1}\text{h}^{-1}$ compared to that of the highly crystalline sample, whereas we registered a 38-time increase in activity for H-PHI (3364 $\mu\text{mol g}^{-1}\text{h}^{-1}$, Figure 4.6b). This is well beyond the activity of the prototypical carbon nitride melon with an activity of just 25 $\mu\text{mol g}^{-1}\text{h}^{-1}$ measured under the same conditions. Note, however, that a quantitative comparison of the intrinsic photocatalytic activities of K-PHI and H-PHI is difficult since the observed hydrogen evolution rates depend on a complex interplay between various parameters, which, in addition, may scale differently with the particle size. These include exfoliation and agglomeration of the crystallites, the nature and amount of defects, or the amount of co-catalyst incorporated in the sample.

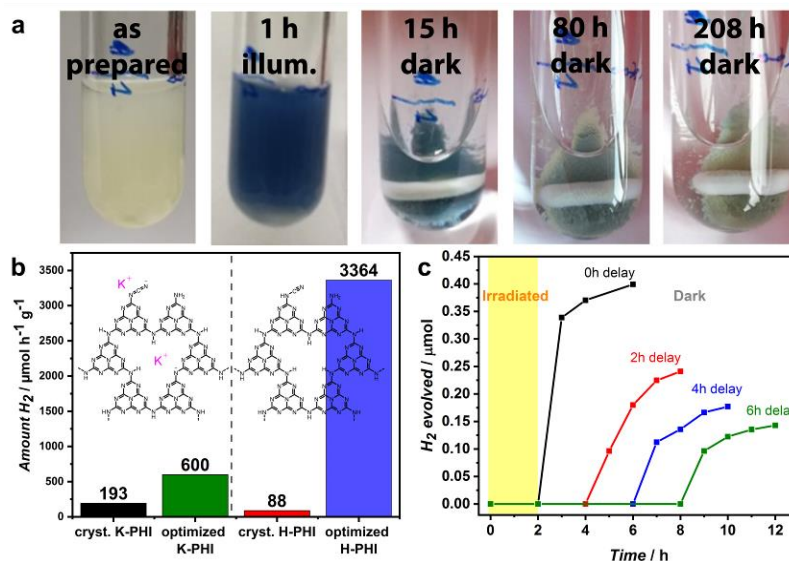


Figure 4.6: a) H-PHI before and after 1 h of illumination and after storing the material in the stable, photo-reduced “blue” state up to 208 h in the dark. A shade toward green is likely due to small amounts of oxygen leaking into the vessel. b) Comparison of photocatalytic rates for hydrogen evolution for K-PHI and H-PHI, respectively. c) Dark photocatalysis in phosphate buffer with various delay times for addition of platinum co-catalyst, i.e., 0, 2, 4, or 6 h.

For a more detailed structural characterization of these optimized compounds, see Figures S1.7 and S1.8. It is apparent that the optimized materials exhibit lower long-range in-plane order, as indicated by broad, diffuse reflections. In particular, both $\bar{1}10$ and the 010 reflections are vastly broadened, which is attributed to a loss of coherence within the layer plane, i.e., smaller platelets (Figure S1.5). By using the Scherrer equation from the PXRD data in Figure S1.8, the crystallite sizes in the lateral dimension have been estimated to be about 20 nm for the optimized samples and up to 100 nm (Table S1.1) for the most crystalline samples. The extension in *c*-direction remains fairly similar for all samples at approx. 20 nm. Small crystallites have a higher amount of accessible cyanamide groups at their surface and are suspended more easily in water, enabling them to participate more efficiently in the photocatalytic reaction.

While the HER activity observed for H-PHI puts it on par with the best carbon nitride photocatalysts,^[34-39] it bears another intriguing property, which has previously been documented for K-PHI;^[4, 6] under illumination and in the presence of an electron donor, H-PHI also forms a photo-reduced state that is exceptionally long-living, clearly visible by its blue color. Figure 4.6a

depicts the suspension during photo-reduction, which is yellow initially and then turns dark blue upon irradiation in the presence of 4-methyl benzylalcohol as the electron donor. Under an argon atmosphere, the photoexcited photocatalyst is reduced by the electron donor and remains in the photo-reduced state for over 200 h. The diminishing of the blue color is due to quenching of the anion radical by oxygen, which slowly diffuses into the solution over time (Figure 4.6a, right). The photo-reduced radical state was also monitored by electron magnetic resonance spectroscopy (EPR), which shows a photo-induced paramagnetic signal for both K-PHI and H-PHI with g-factors of ≈ 2.003 (Figure S1.10), indicative of a heptazine-centered π radical.^[4, 36, 40, 41] To test whether photo-reduced H-PHI is able to store the trapped electrons and release them upon addition of a hydrogen evolution catalyst after a time delay, 15 mg of the sample was irradiated under a Xenon lamp (100 mW cm⁻², AM 1.5 G) in phosphate buffer with 4-methylbenzyl alcohol as an electron donor for 2 h. Then, a colloidal platinum suspension was added in the dark (Figure 4.6c) either directly or 2, 4, or 6 h after illumination. Indeed, hydrogen was evolved for several hours (27 $\mu\text{mol g}^{-1}$, direct addition), which shows the ability of the system to separate the light (photoexcitation) from the dark reaction (catalysis) akin to the biological model of photosynthesis. Even after waiting for 6 h, 37% of the initial amount of H₂ could still be registered.

4.3. Conclusion

In conclusion, we have synthesized a 2D poly(heptazine imide) (PHI) polymer, which is comparable with PTI-LiCl^[11, 12] in terms of crystallinity but by far exceeds its photocatalytic performance.^[13, 42] Characterization of K-PHI and H-PHI provides insights into the structure–property– activity relationship of this new class of high-performance photocatalysts. By combining a suite of analytical techniques, including TEM, NMR spectroscopy, PXRD, PDF analysis, and quantum-chemical calculations, we were able to confirm the in-plane PHI-based 2D structure and derive a detailed picture of the out-of-plane structure. Our analysis not only suggests that ionothermal synthesis conditions likely support error correction, thus leading to extended crystallites of over 100 nm in lateral dimension, but also that metal ions can act as out-of-plane structure-directing agents, leading to a pronounced long-range order in the *c*-direction. Furthermore, water inside the pores has been found to have a major influence on the 3D stacking structure of PHI networks. Our work thus adds another structurally characterized member to the large yet ill-defined class of carbon nitrides, which is notoriously difficult to characterize. As such, this study provides synthetic and analytical tools that are crucial for the rational design of better photocatalysts and helps to carve out the structural features that are essential for observing an unusually long-lived charge separated state, enabling time-delayed photocatalysis in the dark.

4.4. Bibliography

- [1] A. Savateev, D. Dontsova, B. Kurpil, M. Antonietti, *J. Catal.* **2017**, *350*, 203-211.
- [2] V. W.-h. Lau, I. Moudrakovski, T. Botari, S. Weinberger, M. B. Mesch, V. Duppel, J. Senker, V. Blum, B. V. Lotsch, *Nat. Commun.* **2016**, *7* (1), 12165.
- [3] H. Ou, L. Lin, Y. Zheng, P. Yang, Y. Fang, X. Wang, *Adv. Mater.* **2017**, *29* (22), 1700008.
- [4] V. W.-h. Lau, D. Klose, H. Kasap, F. Podjaski, M.-C. Pignié, E. Reisner, G. Jeschke, B. V. Lotsch, *Angew. Chem. Int. Ed.* **2017**, *56* (2), 510-514.
- [5] F. Podjaski, J. Kröger, B. V. Lotsch, *Adv. Mater.* **2018**, *30* (9), 1705477.
- [6] Z. Zeng, X. Quan, H. Yu, S. Chen, Y. Zhang, H. Zhao, S. Zhang, *Appl. Catal., B* **2018**, *236*, 99-106.
- [7] A. Savateev, B. Kurpil, A. Mishchenko, G. Zhang, M. Antonietti, *Chem. Sci.* **2018**, *9* (14), 3584-3591.
- [8] Z. Chen, A. Savateev, S. Pronkin, V. Papaefthimiou, C. Wolff, M. G. Willinger, E. Willinger, D. Neher, M. Antonietti, D. Dontsova, *Adv. Mater.* **2017**, *29* (32), 1700555.
- [9] A. Savateev, S. Pronkin, M. G. Willinger, M. Antonietti, D. Dontsova, *Chem.– Asian J.* **2017**, *12* (13), 1517-1522.
- [10] L. Lin, W. Ren, C. Wang, A. M. Asiri, J. Zhang, X. Wang, *Appl. Catal., B* **2018**, *231*, 234-241.
- [11] E. Wirnhier, M. Döblinger, D. Gunzelmann, J. Senker, B. V. Lotsch, W. Schnick, *Chem.– Eur. J.* **2011**, *17* (11), 3213-3221.
- [12] M. B. Mesch, K. Bärwinkel, Y. Krysiak, C. Martineau, F. Taulelle, R. B. Neder, U. Kolb, J. Senker, *Chem.– Eur. J.* **2016**, *22* (47), 16878-16890.
- [13] Y. Ham, K. Maeda, D. Cha, K. Takanabe, K. Domen, *Chem.– Asian J.* **2013**, *8* (1), 218-224.
- [14] M. Iwama, Y. Suzuki, J. Plévert, K. Itabashi, M. Ogura, T. Okubo, *Cryst. Growth Des.* **2010**, *10* (8), 3471-3479.
- [15] M. Döblinger, B. V. Lotsch, J. Wack, J. Thun, J. Senker, W. Schnick, *Chem. Commun.* **2009**, (12), 1541-1543.
- [16] J. Schaefer, R. A. McKay, E. O. Stejskal, *J. Magn. Reson.* **1979**, *34* (2), 443-447.
- [17] M. H. Levitt, Symmetry-Based Pulse Sequences in Magic-Angle Spinning Solid-State NMR. In *eMagRes*, **2007**.
- [18] C. Adamo, V. Barone, *J. Chem. Phys.* **1999**, *110* (13), 6158-6170.
- [19] M. Ernzerhof, G. E. Scuseria, *J. Chem. Phys.* **1999**, *110* (11), 5029-5036.
- [20] S. Grimme, J. Antony, S. Ehrlich, H. Krieg, *J. Chem. Phys.* **2010**, *132* (15), 154104.
- [21] A. Schäfer, C. Huber, R. Ahlrichs, *J. Chem. Phys.* **1994**, *100* (8), 5829-5835.
- [22] P. J. Wilson, T. J. Bradley, D. J. Tozer, *J. Chem. Phys.* **2001**, *115* (20), 9233-9242.
- [23] F. Jensen, *J. Chem. Theory Comput.* **2015**, *11* (1), 132-138.
- [24] B. Jürgens, E. Irran, J. Senker, P. Kroll, H. Müller, W. Schnick, *J. Am. Chem. Soc.* **2003**, *125* (34), 10288-10300.
- [25] E. Horvath-Bordon, E. Kroke, I. Svoboda, H. Fuess, R. Riedel, *New J. Chem.* **2005**, *29* (5), 693-699.
- [26] A. Sattler, W. Schnick, *Z. Anorg. Allg. Chem.* **2006**, *632* (8-9), 1518-1523.
- [27] S. J. Makowski, D. Gunzelmann, J. Senker, W. Schnick, *Z. Anorg. Allg. Chem.* **2009**, *635* (15), 2434-2439.
- [28] G. S. Pawley, *J. Appl. Crystallogr.* **1981**, *14* (6), 357-361.
- [29] H. Rietveld, *J. Appl. Crystallogr.* **1969**, *2* (2), 65-71.
- [30] R. Amunugama, M. T. Rodgers, *Int. J. Mass spectrom.* **2000**, *195-196*, 439-457.
- [31] A. A. Coelho, J. S. O. Evans, J. W. Lewis, *J. Appl. Crystallogr.* **2016**, *49* (5), 1740-1749.
- [32] B. E. Warren, *Phys. Rev.* **1941**, *59* (9), 693-698.
- [33] D. M. Haiber, P. A. Crozier, *ACS Nano* **2018**, *12* (6), 5463-5472.
- [34] G. Liu, T. Wang, H. Zhang, X. Meng, D. Hao, K. Chang, P. Li, T. Kako, J. Ye, *Angew. Chem. Int. Ed.* **2015**, *54* (46), 13561-13565.
- [35] D. J. Martin, K. Qiu, S. A. Shevlin, A. D. Handoko, X. Chen, Z. Guo, J. Tang, *Angew. Chem. Int. Ed.* **2014**, *53* (35), 9240-9245.
- [36] J. Sun, J. Zhang, M. Zhang, M. Antonietti, X. Fu, X. Wang, *Nat. Commun.* **2012**, *3* (1), 1139.

- [37] B. Kurpil, A. Savateev, V. Papaefthimiou, S. Zafeiratos, T. Heil, S. Özenler, D. Dontsova, M. Antonietti, *Appl. Catal., B* **2017**, *217*, 622-628.
- [38] V. W.-h. Lau, V. W.-z. Yu, F. Ehrat, T. Botari, I. Moudrakovski, T. Simon, V. Duppel, E. Medina, J. K. Stolarczyk, J. Feldmann, V. Blum, B. V. Lotsch, *Adv. Energy Mater.* **2017**, *7* (12), 1602251.
- [39] L. Cui, J. Song, A. F. McGuire, S. Kang, X. Fang, J. Wang, C. Yin, X. Li, Y. Wang, B. Cui, *ACS Nano* **2018**, *12* (6), 5551-5558.
- [40] D. Dvoranová, M. Mazúr, I. Papailias, T. Giannakopoulou, C. Trapalis, V. Brezová, *Catalysts* **2018**, *8*, 47.
- [41] N. A. Rodríguez, A. Savateev, M. A. Grela, D. Dontsova, *ACS Appl. Mater. Inter.* **2017**, *9* (27), 22941-22949.
- [42] K. Schwinghammer, B. Tuffy, M. B. Mesch, E. Wirnhier, C. Martineau, F. Taulelle, W. Schnick, J. Senker, B. V. Lotsch, *Angew. Chem. Int. Ed.* **2013**, *52* (9), 2435-2439.

5. Morphology control in PHI: impact on optoelectronic properties and photocatalysis

The work in this chapter was published, reproduced and adapted from:

Morphology control in 2D carbon nitrides: impact of the particle size on optoelectronic properties and photocatalysis

Julia Kröger, Alberto Jiménez-Solano, Gökçen Savasci, Vincent-W.h. Lau, Viola Duppel, Igor Moudrakovski, Kathrin Küster, Tanja Scholz, Andreas Gouder, Marie-Luise Schreiber, Filip Podjaski, Christian Ochsenfeld, Bettina V. Lotsch

Adv. Funct. Mater. **2021**, *31*, (28), 2102468. DOI:10.1002/adfm.202102468

Julia Kröger and Filip Podjaski conceived the project. Julia Kröger wrote the manuscript with assistance of Filip Podjaski and Bettina V. Lotsch. Julia Kröger designed the experiments, performed the synthesis as well as photocatalysis and electrochemical experiment, all common analysis and evaluated the analytic data, with initial synthesis and experiments contribution of Vincent W.h. Lau. Alberto Jiménez-Solano performed PL measurements. Gökçen Savasci performed the quantum-chemical calculations with the supervision of Christian Ochsenfeld. Viola Duppel performed TEM and SEM measurements. Igor Moudrakovski carried out NMR measurements. Kathrin Küster performed XPS measurements. Tanja Scholz performed crystallite size calculations. Andreas Gouder conducted AFM measurements. Marie-Luise Schreiber carried out elemental analysis. All authors assisted the analysis of their respective experiments. Bettina V. Lotsch and Filip Podjaski supervised the work.

Supporting information can be found in Chapter 9.2.

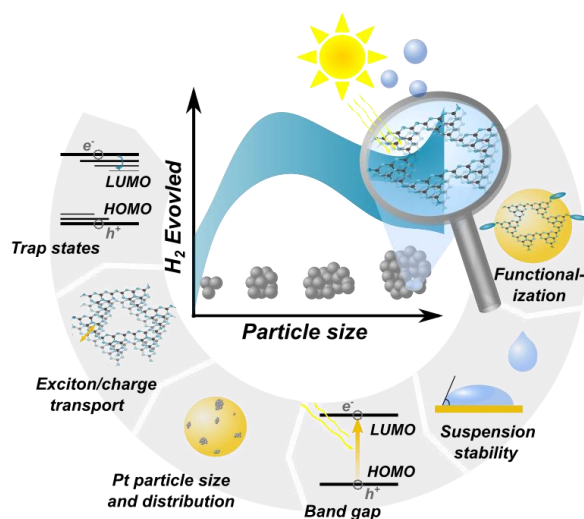


Figure 5.1: Table of content figure for morphology control of poly(heptazine imide) influencing multiple parameters, which are affecting photocatalysis jointly.

Abstract

The carbon nitride poly(heptazine imide), PHI, has recently emerged as a powerful 2D carbon nitride photocatalyst with intriguing charge storing ability. Yet, insights into how morphology, particle size and defects influence its photophysical properties are virtually absent. Here, ultrasonication is used to systematically tune the particle size as well as concentration of surface functional groups and study their impact. Enhanced photocatalytic activity correlates with an optimal amount of those defects that create shallow trap states in the optical band

gap, promoting charge percolation, as evidenced by time-resolved photoluminescence spectroscopy, charge transport studies, and quantum-chemical calculations. Excessive amounts of terminal defects can act as recombination centers and hence, decrease the photocatalytic activity for hydrogen evolution. Re-agglomeration of small particles can, however, partially restore the photocatalytic activity. The type and amount of trap states at the surface can also influence the deposition of the co-catalyst Pt, which is used in hydrogen evolution experiments. Optimized conditions entail improved Pt distribution, as well as enhanced wettability and colloidal stability. A description of the interplay between these effects is provided to obtain a holistic picture of the size–property–activity relationship in nanoparticulate PHI-type carbon nitrides that can likely be generalized to related photocatalytic systems.

5.1. Introduction

Carbon nitrides, of which the archetype material is known since the 19th century as the heptazine-based polymer “melon”, have recently re-entered the stage as an earth-abundant semiconductor system with potential applications ranging from photo/electrochemical redox catalysis for environmental remediation to chemical sensing.^[1, 2] These applications are based on the material’s favorable properties, including chemical and thermal stability, an optical band gap in the visible range and energy levels appropriately positioned for a number of key photocatalytic reactions, including water splitting.^[3] The class of carbon nitrides comprises triazine- and heptazine-based polymers, the dimensionality of which being determined by the synthesis procedure: whereas 1D heptazine-based polymers, which are called “melon” and often misleadingly referred to as “g-C₃N₄” in the literature are obtained by heating the precursors in a solid state reaction, ionothermal synthesis results in the 2D network poly(heptazine imide) (PHI) or poly(triazine imide) (PTI).^[4-6] For example, using a KSCN melt as a reaction medium, the PHI structure is obtained with hydrated potassium ions incorporated from the melt (K-PHI) and possessing cyanamide groups as defects; the potassium ions can be subsequently exchanged e.g. by protons, forming H-PHI.^[4, 7, 8] Besides high photocatalytic hydrogen evolution rates,^[7, 8] PHI exhibits the unusual ability to stabilize photo-generated electrons after the holes are quenched by suitable electron donors. This can be exploited afterward to temporally decouple the absorption of sunlight from its transformation into chemical fuels such as hydrogen for hours.^[4, 9, 10] This long-lived photo-reduced state can also be harvested for time-delayed electrical discharge after illumination in an aqueous solar battery anode.^[11] Unveiling the full potential of such “light-storage” properties necessitates a more thorough understanding of the structure–property–activity relationships in PHI. Even though the atomic-level structure of K- and H-PHI has recently been resolved,^[4] little is known about the impact of morphology, particle size, and surface terminations on the photocatalytic properties. In particular, surface terminations were recently described to have a significant impact on the photocatalytic behavior of PHI by enhancing its interaction with reactants.^[12]

For melon-type carbon nitrides, it was reported that morphology tuning, e.g. by exfoliation, can change the optical and electronic properties of the material, which then results in enhanced photocatalytic activity.^[13-16] Different reasons for this enhancement were listed, including increased surface area, higher amount of beneficial defects or surface functional groups for attaching the co-catalyst as well as higher porosity, leading to enhanced light absorption and charge transport, which results in a reduction of the recombination rate of photo-generated charges.^[16-18] This demonstrates the importance of morphology and surface properties for photocatalytic reactions and the need to understand their correlations. However, there are not only reports about enhanced photocatalytic behavior by reducing the particle size, but also about reduced charge carrier lifetimes in exfoliated carbon nitride, which then lead to a reduced hydrogen evolution rate.^[15, 19] Consistent with these findings, a more efficient charge carrier separation with longer lifetimes of photo-induced charges was reported for carbon nitrides, since the excitons were found to dissociate across the layers rather than within one layer, posing the question of whether excitons in carbon nitrides are inter- or intralayer excitons, or both.^[15, 20, 21] The above highlights the controversial nature and a lack of understanding of the size–activity relationship in carbon nitrides, which is influenced by many parameters. One possible explanation for these conflicting results may be found in the differences in synthesis and exfoliation of melon, the latter carried out e.g. by sonication, thermal treatment, mechanical treatment, ion intercalation, or chemical exfoliation by sulfuric acid.^[17, 22-26] During the exfoliation process, defects or vacancies can be generated, and new surface terminal groups may develop on the carbon nitride backbone. On the one hand, defects are discussed as facilitators in photocatalysis. They can form electronic states in the optical band gap, which can enhance visible light absorption and influence charge carrier transfer at the interface.^[27-31] On the other hand, defects can act as recombination centers or deep trap states, reducing the charge carriers' mobility and driving force for photocatalytic reactions, which counteracts photocatalytic performance.^[3, 32-35] A recently published work highlights the effect of functional groups and defects in melon-type carbon nitride being beneficial only up to a particular concentration, which also strongly depends on the type of functional group or defect.^[36] This ambiguity of structure and defect types warrants an in-depth analysis of the interplay and influence of morphology and structural changes on different optoelectronic properties and, consequently, photocatalytic activity. As photocatalysis is a complex process relying on intertwined structural, optoelectronic, and morphological properties, many of which are associated with different time scales,^[37] disentangling these factors is essential for understanding the overall photocatalytic activity.

Here, we study the effect of ultrasonic particle size reduction of K- and H-PHI on the photocatalytic hydrogen evolution reaction (HER) by analyzing multiple parameters. Central to our study is the size separation of PHI particles, based on differential centrifugation velocities. By breaking apart agglomerates, functional surface groups and defects are generated and, comprehensively analyzed by various techniques. With decreasing particle size and the correspondingly increase in surface area, the number of functional groups increases (especially NH₂, OH, and -C=O), while

at the same time, light absorption is slightly shifted. Besides, we find that with increasing amounts of functional groups, the distribution of photo-deposited Pt, used as co-catalyst for HER, becomes more uniformly distributed, and the Pt particle size is reduced. Simultaneously, the suspension stability is enhanced, which is beneficial for high photocatalytic activity, provided that the particles are not smaller than 180 nm. On the other hand, the amount and depth of trap states increases with the number of functional groups, influencing the accessibility of photo-excited electrons for transfer to the surface. Intriguingly, we observe that re-agglomeration of those particles causes a significant increase of the hydrogen evolution rate (up to 35%). This might be correlated with an enhanced crystallite interaction in the particle when the amount of functional groups increases, enabling better charge carrier separation. Photoluminescence (PL) and conductivity measurements hint to a multiple trapping and release model (MTR)^[38] for the electron transfer in PHI. This observation points to opposing effects of reduced charge carrier separation and enhanced dispersion stability with decreasing particle size. Therefore, hydrogen evolution as a function of particle size is found to be an interplay of all these parameters. Optimal performance is found for 2 h sonicated samples with particle sizes above 180 nm, ideally in a re-agglomerated material. Importantly, we find that the contribution of each parameter, depending on the particle size, is not as unambiguous as often reported in the literature.

5.2. Results and discussion

Morphology and structural analysis

Particle size reduction by an ultrasonication route involved the sonication of PHI in water for an extended duration of 2 h, followed by fractionated centrifugation of the aggregates. This yields a colloidal solution with a concentration of around 5 mg mL⁻¹ (Figure 5.2a), akin to procedures reported in the literature.^[5, 11] The first precipitate (P1) contains the largest particles (P1: 300-1500 nm), the second precipitate (P2) contains medium particle sizes (P2: 100-400 nm), with the third precipitate (P3) containing the smallest particles down to 40 nm (Figure S2.1-S2.3, Table S2.4). The particle sizes were analyzed by a combination of dynamic light scattering (DLS), atomic force microscopy (AFM), transmission electron microscopy (TEM), and scanning electron microscopy (SEM), as well as Brunauer–Emmett–Teller (BET) surface area analysis (Figure S2.1-S2.11). To reduce the particle sizes even further, H-PHI was sonicated for 24 h, and the supernatant (P4) was separated and precipitated at 500 relative centrifugal force (RCF) (Table S2.1). The resulting particle sizes are in the range of 20-350 nm (Figure S2.3, S2.6). Since K-PHI is protonated when storing in water for a long time, forming H-PHI, this 24 h sonication process was only performed on H-PHI (Figure S2.45). The suspension of PHI with small particles (below 200 nm) remained colloidally stable in water for months, with no indication of settling. This is also evident by their large zeta-potential (-23 mV to -45 mV) across all pH values measured for H-PHI sheets (Figure S2.9, Table S2.2). The colloidal suspensions can be dried to isolate PHI for further characterization (notated as “PHI re-agglomerate”).

The primary crystallite size obtained by TEM analysis of pristine particles is only in the range of 20-45 nm (Figure S2.4) when compared to SEM and AFM analyses, which show that larger particles are agglomerates of smaller crystallites. After 24 h sonication (P4), the primary crystallite size is reduced to 5-25 nm, as shown by TEM (Figure 5.2b, S2.5). In AFM, a minimal thickness of 3–5 nm (Figure 5.2c, d) for P4 particles could be measured. Based on the interlayer separation of 3.16 Å resulting from the PXRD analysis (vide infra), this corresponds to 9 to 16 PHI layers in the stacking direction. Crystallite sizes can also be estimated from PXRD data (Figure 5.3a) by using the Scherrer equation (Table S2.4), which gives a more representative value of the average domain size compared to the local information gained from TEM or AFM. For particles being sonicated for 24 h, the crystallite size is only slightly reduced (by 15% to 22 (± 1) nm in the vertical direction) with respect to the pristine material (lateral: 14 (± 1) nm and vertical: 26 (± 1) nm), proving that primary crystallites remain intact during sonication, but that the agglomerates break apart, forming smaller agglomerates or even single crystallite particles.

The measurement of the hydrodynamic diameter of the particles, estimated by DLS (Figure S2.10, Table S2.3), is in reasonable agreement with particle sizes of K-PHI and H-PHI obtained by microscopy techniques (Table S2.4), which also measure an average, effective size without directional preference. However, since DLS analysis assumes perfectly spherical particles, a direct relationship between the results of microscopy and DLS for 2D materials is yet to be accurately determined.^[39] Nevertheless, DLS measurements were used in the following for particle size estimation, since this measurement allows for fast and quantitative particle analysis.

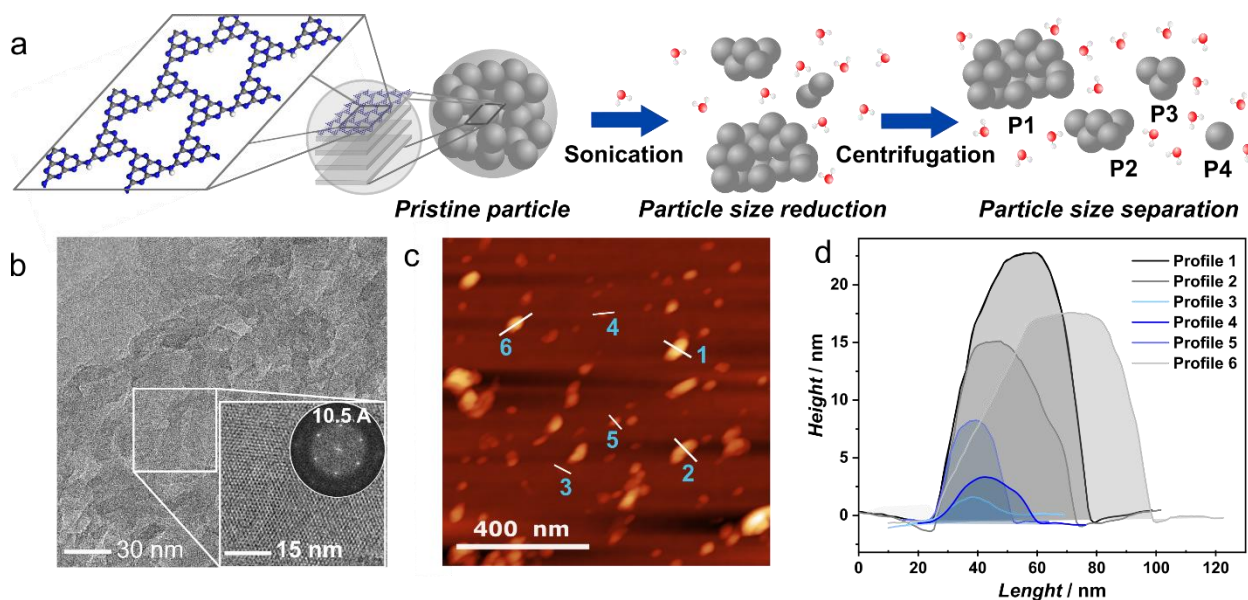


Figure 5.2: Morphology and particle size analysis of PHI. a) Schematic illustration of PHI sonication for breaking apart agglomerated particles, followed by stepwise centrifugation for separation of particle clusters with different sizes (blue: nitrogen, grey: carbon, white: hydrogen, red: oxygen). b) TEM image of H-PHI P4 (24 h sonicated), the inset showing a magnification of single P4 particles with the Fast Fourier Transformed (FFT) image showing the characteristic distances in PHI. c) AFM image of single H-PHI P4 particles (24 h sonicated). d) Corresponding representative height profiles.

The analysis of BET surface area and pore volume reveals a type IV isotherm, associated with condensation processes in mesopores, most probably located between agglomerated particles as textural pores (Figure S2.11).^[40] The surface area is slightly increased for H-PHI P4 ($70 \text{ cm}^3 \text{ g}^{-1}$) in comparison to the pristine material H-PHI ($60 \text{ cm}^3 \text{ g}^{-1}$) (Table S2.5). This finding is in line with the assumption of particles consisting of agglomerated crystallites, where the big agglomerated particles break apart during sonication, forming smaller agglomerates or even single crystallites.

Although considered a relatively harmless dispersion technique, acoustic bubbles formed by ultrasound are hot and can generate highly reactive radicals.^[41] Thus, the absence of chemical changes to the investigated materials must be ascertained. To verify that the mildly sonicated materials are chemically identical to the pristine PHI and to study the surface termination of small particles, the colloidal solution was evaporated to dryness. The residual powder was structurally characterized by ^{13}C and ^{15}N magic angle spinning solid state nuclear magnetic resonance spectroscopy (MAS NMR), Fourier transform infrared spectroscopy (FT-IR), powder X-ray diffraction (PXRD), elemental analysis, and X-ray photoelectron spectroscopy (XPS).

As stated above, the primary crystallite size is almost unchanged when the particle size is reduced by sonication. Therefore, in PXRD no significant changes are observed. The in-plane ($\bar{1}10$) and out-of-plane (001) reflections are at 7.9° (11.10 \AA) and 27.9° to 28.3° 2θ (3.19 \AA for H-PHI and 3.16 \AA for K-PHI), respectively, with the key difference being the slight isotropic broadening of the interlayer stacking reflection (Figure 5.3a, S2.12, S2.13) in smaller particles.^[4]

The FT-IR spectra of the colloidal H-PHI and K-PHI are basically identical to the pristine sample, showing all the signals corresponding to the heptazine moiety (Figure S2.14, S2.15). This points clearly to an intact PHI polymer network, which is further proven by elemental analysis (Table S2.8) as well as ^{13}C and ^{15}N {H} CP MAS NMR spectroscopy (Figure 5.3b, c). The signal positions in ^{13}C NMR at 156-157 ppm (heptazine-ring carbon) and 163-164 ppm (heptazine-ring carbon next to imide bridge) remain at the same position, but broadening of ^{13}C signals can be seen in all sonicated materials, likely due to surface functionalization or increased water interaction. The same trend can be observed in ^{15}N { ^1H } CP NMR for the two main signals around -176 to -190 ppm (heptazine-ring nitrogen atoms) and -237 to -244 ppm (imide bridges). The peaks at 166 ppm in the ^{13}C NMR and -267 ppm in the ^{15}N NMR of K-PHI P1 are more pronounced than those in the pristine material, which also hints to an increase in NH_2 groups, consistent with the literature (Figure 5.3b, c, S2.24).^[28] Additionally, an enhanced water interaction is visible in ^{15}N NMR, especially in smaller particles, which is observed by a shift of the NH-bridge nitrogen peak at -240 ppm to -238 ppm,^[4, 5, 42] in agreement with quantum-chemical calculations (Figure S2.20-S2.23). In line with this, the FT-IR analysis shows an increase in the O-H/N-H bond vibration at $3680\text{-}2220 \text{ cm}^{-1}$ in atmospheric conditions (up to 47% in P4) with decreasing particle size, being more pronounced when the average particle size gets smaller than 200 nm (Figure 5.3d, S2.14-S2.18, Table S2.6-S2.7).

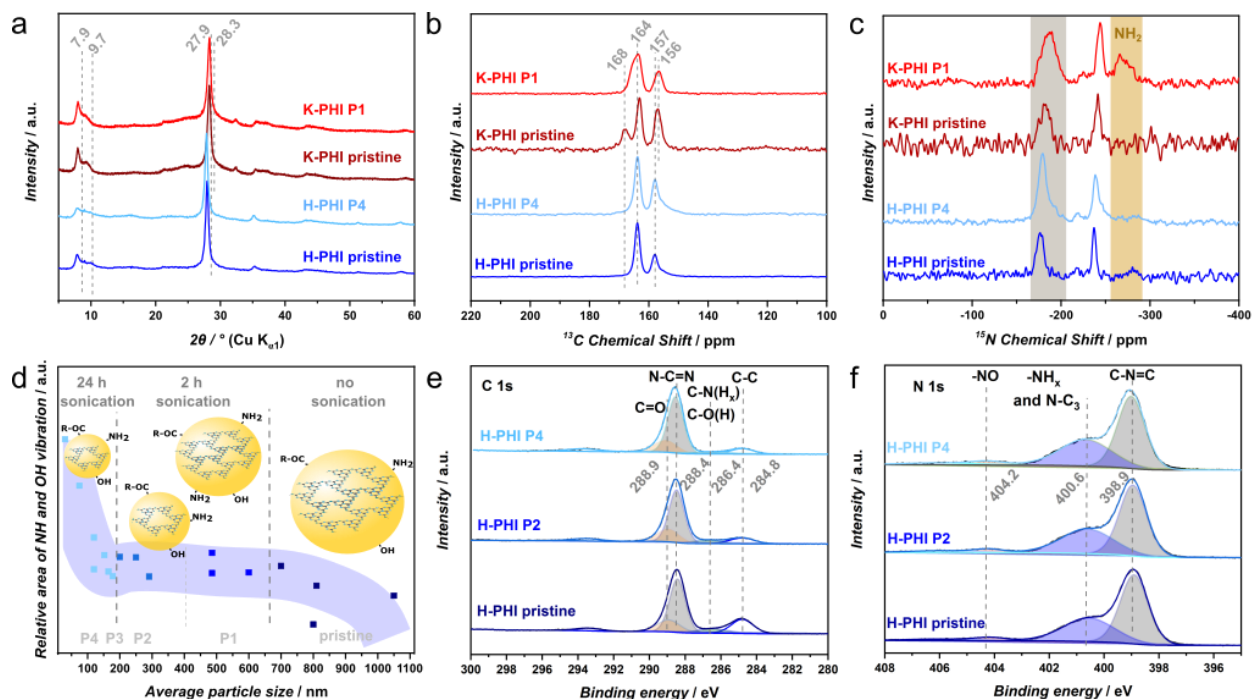


Figure 5.3: Characterization of structural defects of pristine PHI and small particles of PHI after sonication. a) PXRD of pristine K-PHI and K-PHI P1 as well as pristine H-PHI and H-PHI P4. b) ^{13}C $\{^1\text{H}\}$ CP MAS NMR experiments of pristine K-PHI and K-PHI P1 as well as pristine H-PHI and H-PHI P4. c) ^{15}N $\{^1\text{H}\}$ CP MAS NMR experiments of pristine K-PHI and K-PHI P1 as well as pristine H-PHI and H-PHI P4; d) Relative area of NH and OH vibrations (related to the heptazine vibration at $805\text{-}811\text{ cm}^{-1}$) of FT-IR of H-PHI as a function of particle size. R of carboxyl functionality = OH or NH_2 . e), f) XPS analysis of pristine H-PHI (average particle size $1500\text{-}1000\text{ nm}$) and H-PHI particles after 2 h (P2 with average particle size $400\text{-}350\text{ nm}$) and 24 h sonication (P4 with average particle size around 79 nm) e) C 1s spectra, and f) N 1s spectra. Grey areas depict bonds in the heptazine ring, blue areas the NH_x or OH bonds, and orange the NO or CO bonds.

XPS analysis of pristine H-PHI and a 2 h and 24 h sonicated sample was used to confirm the functional groups introduced into the system by sonication. In C 1s spectra, besides the typical heptazine ring signals two distinct signals are observed at 286.4 and 288.9 eV , which can be correlated to C-N(H_x) or C-O(H) (blue area) and C=O (orange), respectively, where the latter is assigned either to a carboxylic acid or $(\text{NH}_x)_y\text{C}=\text{O}$ ($x, y = 1, 2$) moiety (Figure 5.3e).^[7, 8, 43-49] The formation of vacancies due to sonication can be excluded or considered insignificant (Chapter 9.2.5, Table S2.9). To disentangle the C-N(H_x) and C-O(H) signals, N 1s and O 1s spectra were analyzed as well (Figure 5.3f, S2.19). The relative portion of NH_x (blue area in the N 1s XPS spectrum)^[7, 8, 45-47] increases by up to 13% with decreasing particle size (Chapter 9.2.5), akin to FT-IR and NMR analysis. However, the signal in the O 1s spectrum at 531.8 eV (OH groups)^[7, 8, 50] is reduced with decreasing particle size (to 64%), probably caused by evaporation of structural water in the vacuum chamber of XPS, which is more likely to happen for smaller particles.

In addition, a slight increase of N-O (orange) (up to 20%, extracted from N 1s spectrum) and C=O bonds (orange) (up to 8%, estimated from C 1s spectrum) can be found with decreasing particle size. The presence of these groups is also confirmed by O 1s XPS spectra, although the contributions from the substrate here may have a small influence (Chapter 9.2.5). The

concentration of N-O bonds is only around 10% of the C=O concentration (in COOH or CO(NH_x)_y), so that FT-IR spectroscopy shows a slight increase of C=O vibrations but no clear trend for N-O (Figure S2.16-S2.18, Table S2.7). Furthermore, a small peak in ¹³C NMR at 170-172 ppm (Figure 5.3b, S2.22) and additional vibrations at 2100 cm⁻¹ in FT-IR (Figure S2.15-S2.18) hint to a meagerly increased amount of C≡N in sonicated samples.^[4, 7] In comparison to the other functional groups, the concentration of N-C≡N groups in all fractions (pristine-P4) is small and does not significantly change with the particle size.

From these characterizations, we conclude that the ultrasound treatment is sufficiently mild such that the pristine and bath sonicated PHI are chemically identical in terms of their bulk polymer backbone after sonication to preserve the molecular backbone of PHI. Besides, the particle size reduction with increasing sonication time, the de-agglomeration of PHI crystallites in ambient to humid environment increases especially the amount of terminal OH and NH₂ groups (up to 47% in P4 compared to the pristine material). Besides the C=O groups, which rise up to 20% by particle size reduction from pristine PHI to P4, a small amount of C≡N and NO defects are formed, which are not severely affected in their concentration by particle size reduction.

Influence of functional groups on photocatalytic hydrogen evolution

Next, we investigated photocatalytic hydrogen evolution to study the influence of morphological and structural modifications induced by sonication. First, the effects of particle size on the absorption edge of the samples were analyzed. In the pristine material, the optical band gap estimated from several different batches for K-PHI is 2.73 (±0.01) eV, whereas for H-PHI a value of 2.92 (±0.01) eV was obtained. A slight increase in the optical band gap is observed for particle sizes below 200 nm by 0.09 (±0.01) eV (K-PHI) and 0.03 (±0.01) eV (H-PHI), respectively (Figure S2.25-S2.28, Table S2.10). When reducing the particle size, a pronounced Urbach tail is visible in the UV-Vis spectra. This is likely caused by excitations below the band gap, due to emerging intermediate states in the band gap associated with defects, in line with the findings of increasing amounts of surface groups.^[51]

All PHI materials were tested for the photocatalytic activity in hydrogen evolution reaction (HER) in a 1 mg mL⁻¹ suspension containing 10 vol% methanol as an electron donor and an optimized Pt loading of 2 wt% for H-PHI and 8 wt% for K-PHI,^[4, 7, 8] photo-deposited from hexachloroplatinic acid during illumination with simulated sunlight (AM 1.5 G). For pristine H-PHI, a maximum activity of 31 μmol h⁻¹ was measured, which increases to 35-41 μmol h⁻¹ (by 13-25%) when the average particle sizes are reduced down to 500-180 nm (P1, P2) (Figure S2.29). A further reduction in particle size causes a monotonous decrease in HER activity by 97% (1 μmol h⁻¹) for the 24 h sonicated particles P4 with an average size of 75 nm (Figure 5.4a, S2.29). Interestingly, the photocatalytic performance of P4 particles can be increased upon re-agglomeration prior to photo-deposition of Pt, which also works for re-agglomerated P1 particles (Figure 5.4a, S2.29-S2.31), vide infra. Due to drying, P4 particles agglomerate randomly, similar to the coiling process

described for carbon nitrides in the literature.^[52] The enhanced photocatalytic activity is contrary to the expectation that high dispersity and/or smaller particle sizes lead to a better catalytic rate.^[53, 54] For K-PHI, initially, a similar trend is observed (Figure 5.4b, S2.32, S2.33), although K-PHI is not stable during photocatalysis and transforms into H-PHI, which is assumed to take place faster for smaller particles, causing an increase in photocatalytic activity for small particles again (Figure S2.32-S2.34, S2.45). For this reason, the following analysis will mainly concentrate on the H-PHI results.

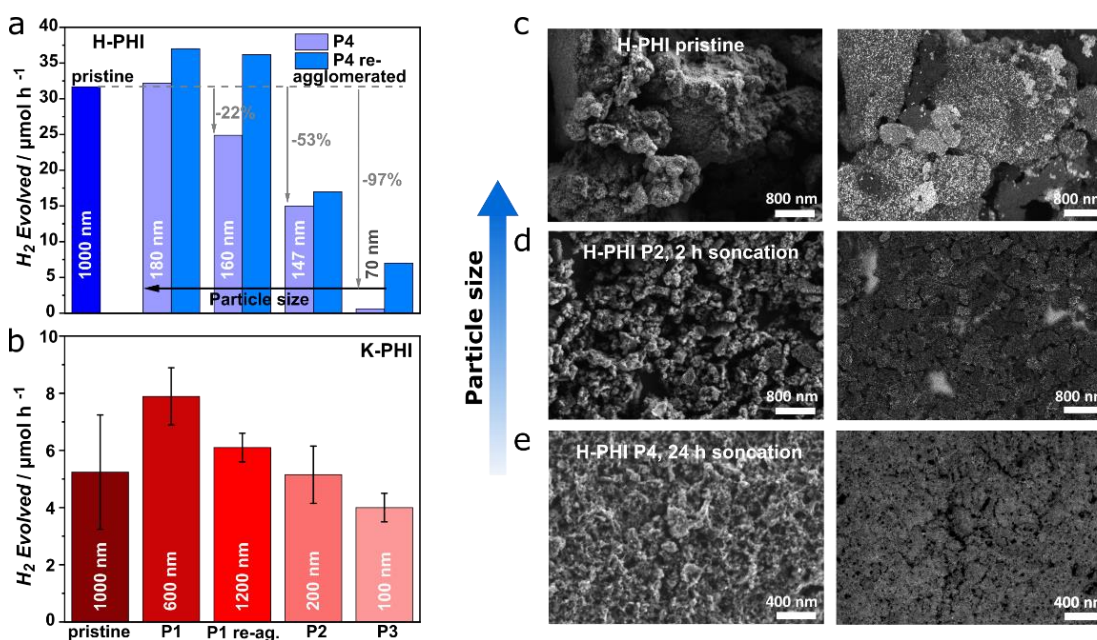


Figure 5.4: Photocatalytic hydrogen evolution of H-PHI and K-PHI in the presence of the electron donor methanol (10 vol%) and co-catalyst Pt (2 wt% for H-PHI and 8 wt% for K-PHI). a) Hydrogen evolution in the presence of H-PHI pristine and P4 (24 h sonication) as well as re-agglomerated P4 (20 mg of catalyst were used). b) Hydrogen evolution of K-PHI pristine, P1, P1 re-agglomerated, P2 and P3 (5 mg of catalyst were used). SEM images of H-PHI after photocatalysis (left) and back-scattered electron image with brighter spots displaying Pt (right) c) for pristine H-PHI, d) for 2 h sonicated (P2) H-PHI and e) for 24 h sonicated (P4) H-PHI.

Next, we investigated the influence of particle size on the distribution, size, and loading of the Pt co-catalyst, which typically is a “blind spot” in most reported photocatalytic experiments with carbon nitrides. As a general trend, we observe a decrease in the size of Pt nanoparticles, when the PHI particle size is reduced (Figure S2.37-S2.43). At the same time, the Pt particles are more homogeneously distributed (Figure 5.4c-e). For pristine H-PHI, the Pt particle size was estimated by SEM to be in the range of 8-38 nm (Figure 5.4c, S2.37) while it increases in P1 up to 40-68 nm. When decreasing the particle size further to P2-P4, the Pt particle size is reduced to 1-5 nm (Figure 5.4d, e, S2.37-S2.40). The different Pt particle sizes likely correlate with the nature and number of PHI functional groups: with decreasing particle size, the number of surface functional groups increases, which can act as Pt coordination-centers and nucleation sites (Figure S2.41-S2.43). In addition, the more Pt nucleation sites are present, the more homogeneous the Pt coverage, which has a positive effect on the photocatalytic activity, as has also been reported for

melon-based carbon nitrides, since charge carrier migration distances are very limited.^[3, 55-57] In line with this, a shift by 0.40-0.45 eV to lower binding energies can be observed for the Pt 4f XPS signals correlated with Pt²⁺ for P4 in comparison to pristine H-PHI, which is likely caused by stronger metal-support interactions via surface NH, OH, and CO groups (Figure S2.19, Chapter 9.2.5).^[7, 18, 58] The stronger the metal-carbon nitride interaction, the better the local charge transfer.^[18, 59] In addition, the XPS spectra showed a decreasing Pt²⁺/Pt⁰ ratio up to 20% for decreasing particle sizes (pristine material: 1.70; P4: 1.37) (Table S2.9), which points to an incomplete Pt reduction for bigger particles, possibly due to less efficient overall charge transfer.^[60]

Regarding the Pt loading, we found that with decreasing particle size (down to a particle size of ~250 nm), more Pt was photo-deposited on the material. While 2 wt% added Pt were deposited on particles of 250 nm in size, only 1 wt% Pt was found on pristine particles after photocatalysis (Table S2.11). At smaller sizes below 250 nm the Pt amount decreases again (1.4 wt% at 79 nm particle size) (Table S2.11, Figure S2.41-S2.44). The fact that less Pt is deposited on smaller particles despite the larger amount of functional groups and enhanced local metal-carbon nitride interaction points to a faster recombination process of photo-generated charges in smaller particles. Such enhanced recombination rates are detrimental for HER as observed for particle sizes < 180 nm, which are probably influenced by the amount and type of surface functional groups (especially NH₂, OH and C=O) (Figure S2.35). In the pristine material, however, the bulk-based charge separation across the 2D layers^[15, 20] appears to be hindered by the long diffusion lengths of the photo-generated charges to reach the catalytic surface, leading to decreased activity. The charge diffusion might be enhanced in re-agglomerated particles due to the nature and density of functional groups at their surface or interface,^[15, 61-65] which is resulting in an enhanced photocatalytic activity.

To study the influence of the surface functional groups and their possible role as trap states, which have already been suggested to be present by UV-vis spectroscopy, we used photoluminescence (PL) spectroscopy.^[32] PL experiments were performed on the pristine material in degassed water, degassed water and electron donor and under the same conditions as photocatalysis experiments, i.e. in the presence of an electron donor and co-catalyst (Figure S2.46). Figure 5.5a shows a representative emission spectrum of H-PHI P1 in degassed, O₂-free water, excited at 370 nm, where the maximum is located at around 450 nm (2.7 eV). The broad PL signal can be deconvoluted into two Gaussian contributions, similar to carbon nitride materials reported in the literature,^[32, 51] located at around 2.75 eV, stemming from the bulk, and at 2.45 eV, corresponding to mostly (surface) trap states (Figure 5.5a, S2.46-S2.49).^[32] Both emission peaks are smaller than the optical band gap of 2.9 eV for all studied environments, indicating that emissions are caused by states in the band gap. Although their spectral positions slightly vary with the particle size investigated, their energetic shifts are constant relative to the band gap, as shown in Figure 5.5b.

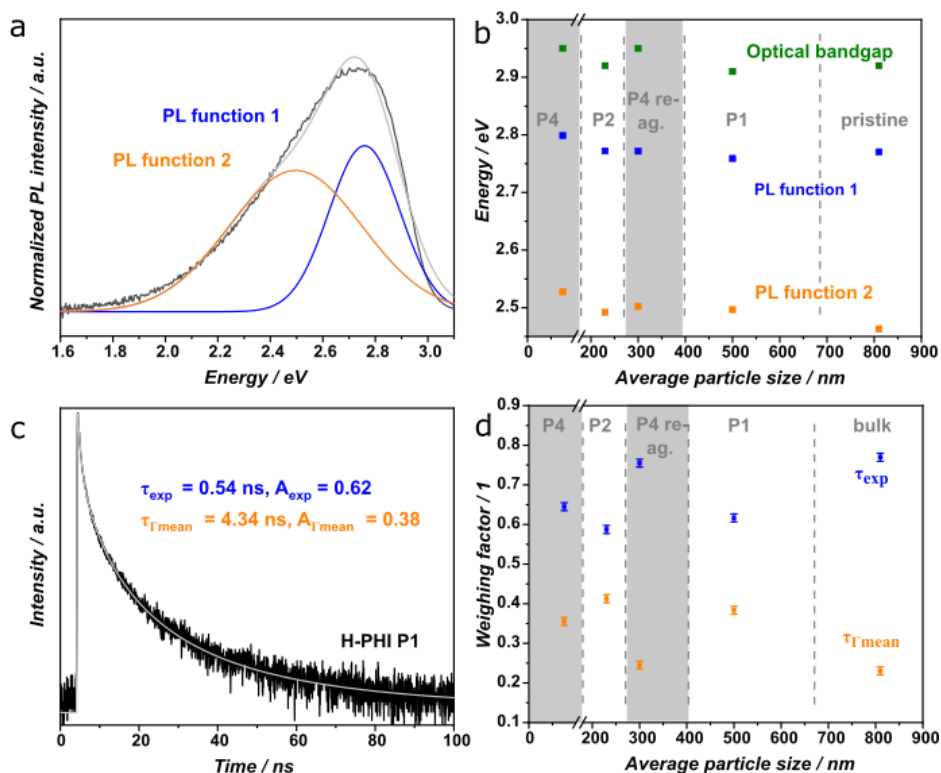


Figure 5.5: Photoluminescence (PL) analysis of H-PHI in degassed water. a) Deconvolution of the PL signal of H-PHI P1 based on two Gaussian functions to describe also shallow and deep states in the band gap. b) The optical band gap of H-PHI and center of the Gauss functions corresponding to the PL deconvolution depending on the particle size. Re-agglomerated particles are denoted as “re-ag.” c) Time-dependent PL analysis of H-PHI P1, which is fitted with one exponential and a Γ function. d) Contribution of the exponential and Γ -decay to the overall lifetime decay (errors included) as a function of the average batch particle size.

In order to extract more information about the influence of the trap states, time-resolved photoluminescence (TRPL) measurements were carried out, which contain information on both radiative and non-radiative decay types.^[66] These were fitted by a combination of an exponential and a Γ -function (Figure 5.5c, S2.50).^[12] *A priori*, both recombination types can show a distribution decay nature according to a Γ function.^[67] However, the best fit obtained in all cases is an exponential function attributed to the faster decay in the bulk (<0.54 ns). The distribution function (Γ), which accounts for all decays on longer time scale, is assigned to trap states induced by surface terminations.^[68, 69] The respective weight factors of both processes are compared for their contribution to the excited charge carrier decay process as a function of particle size (Figure 5.5d, S2.50, Table S2.12). In aqueous suspension, where the intrinsic properties are best visible (Figure 5.5b, d), an increase in the relative weight attributed to the traps (orange) is observed as PHI is sonicated. This finding is consistent with an increase of functional groups on the particle’s surface that can act as trap states. Additionally, shorter lifetimes were observed with smaller particle sizes (Table S2.12), probably due to enhanced formation and population of such trap states, yielding a higher degree of charge recombination or capturing the charges on longer timescales exceeding the time scale of the PL measurement. Under the conditions in which the

photocatalysis experiments take place, i.e. donor presence and photo-deposited Pt, the relative PL trends for the surface based processes are preserved (Figure S2.51, S2.52). However, the absolute numbers are changing. Charge trapping and recombination in the bulk is not affected by the addition of Pt.

The re-agglomeration of P4 particles prolongs the lifetime compared to that of the pristine material significantly (Table S2.12). The relative weight of the PL fit functions reaches similar values to that of the pristine material (Figure 5.5d). This can be rationalized by an enhanced exciton separation in the agglomerates.^[15] The transfer between crystalline areas might even be enhanced in the re-agglomerated samples due to more or different functional groups at the interface and hence possible hydrogen bonding between the agglomerated particles.^[38, 70, 71] As evidenced by electrochemical impedance spectroscopy, a grain-boundary based electron transport process is likely to be present, which hints to a multiple-trapping-and-release model (MTR)-like process in PHI (Figure S2.53). The electrons are transported across the layers in the crystallites, and once reaching an edge of the crystallite, charge hopping becomes necessary. The hopping is enhanced by shallow trap states formed at the interface and improves with well-interconnected interfaces.^[38] Similar results were reported for a melon-type carbon nitride, where enhanced exciton dissociation was reported at the interface between ordered and disordered carbon nitride structure.^[72]

To better estimate the energetics of the functional groups (NH_2 , OH , $\text{NHC}\equiv\text{N}$ and NHCOOH or NHCONH_2) and hence, trap states for different particle sizes, quantum-chemical calculations were performed, which provide insights into the nature of the trap states and their energetic depth. Three different model systems for PHI were designed as size-increasing computational models, consisting of 1, 7, and 19 pores to approach the different particle sizes that are actually observed under experimental conditions (Figure S2.54). When comparing the localization of highest occupied molecular orbital (HOMO) and lowest unoccupied molecular orbital (LUMO), no significant difference was found for the localization as a function of the size of the model system or functional group (Figure S2.55-S2.61, Table S2.13). Independent of the size of the pore model, orbitals are rather localized at single hepatize units than being delocalized over the entire system (Figure S2.55-S2.57, Table S2.13), hence revealing contributions from functional groups at the pore edges. Changes in orbital contributions by functional groups are also reflected in the calculated optical band gaps, where the largest values were found for primary amine terminations with 4.35 eV, followed by NHCONH_2 (4.31 eV), hydroxyl (4.30 eV), $\text{NHC}\equiv\text{N}$ (4.27 eV) and NHCOOH groups (4.25 eV), successively decreasing the band gap (Table S2.14). The smaller the experimentally analyzed PHI particles are, the more significant the influence of the functional groups. However, it is likelier that the functional groups form trap states, rather than a homogenous shifts of the band edges. This is reflected by both the Urbach tail seen in the UV-Vis spectra (Figure S2.26) and by spectral PL deconvolution (Figure S2.47). In addition, calculated ionization potentials (E_{IP}) and electron affinities (E_{EA}) for different model systems

(Chapter 9.2.10) were identified as proxies for the functional group contribution and band edge energies (Figure S2.62-S2.66).

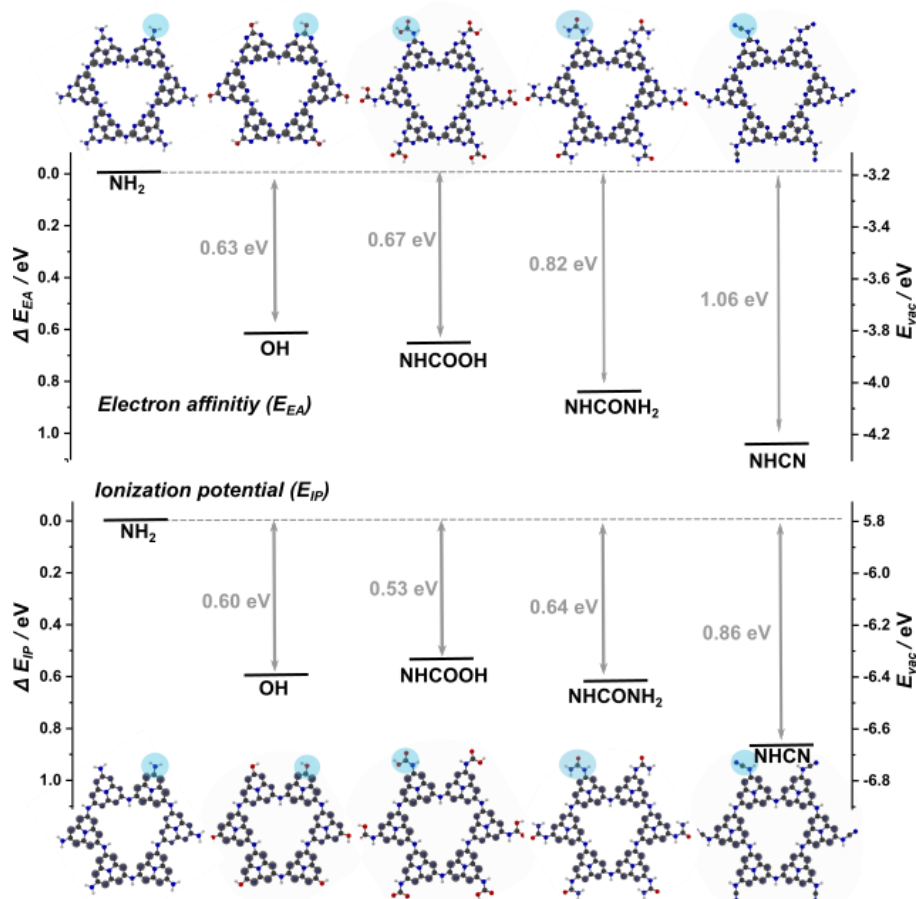


Figure 5.6: Quantum-chemical calculations of electron affinity (E_{EA}) and ionization potential (E_{IP}) of the one-pore PHI model system obtained on PBE0-D3/def2-TZVP^[73, 74]/RI-PBE-D3/def2-TZVP^[75-78] level of theory. Comparison of different terminal groups (NH_2 , OH, $NHCOOH$, $NHCONH_2$ and $NHC\equiv N$), with values referenced to the NH_2 terminal group.

Akin to the literature, it was found that relative to terminal NH_2 groups, the OH groups change the E_{IP} (by 0.60 eV) and E_{EA} (by 0.63 eV) in a similar way such that only shallow trap states are formed close to the LUMO (Figure 5.6, S2.67).^[32, 79] C=O and C \equiv N containing terminal groups reduce the optical band gap the most, which is also visible in a more pronounced shift of the E_{EA} in comparison to E_{IP} relative to the NH_2 terminated system (Figure S2.68-S2.70). This might be consistent with the formation of trap states that are located deeper in the optical band gap than for NH_2 and OH groups.^[30, 32, 33] For this reason $NHCOOH$, $NHCONH_2$ and $NHC\equiv N$ groups might influence the charge carrier energetics, and therefore the photocatalytic activity, most profoundly.

The higher the concentration of functional groups in general, the higher the amount of detrimental deeper trap states that would enhance recombination and hence reduce the hydrogen evolution rate.^[33, 69] In agreement with photocatalysis experiments and PL data, the highest photocatalytic activity was measured for P1 and P2 samples, with a slightly higher but not excessive amount of

functional groups as evidenced by structural analysis. Based on these findings, we conclude that it is possible to tune the light absorption properties and the amount and depth of trap states by introducing different functional groups intentionally, which has a pronounced influence on the availability of charge carriers for HER.

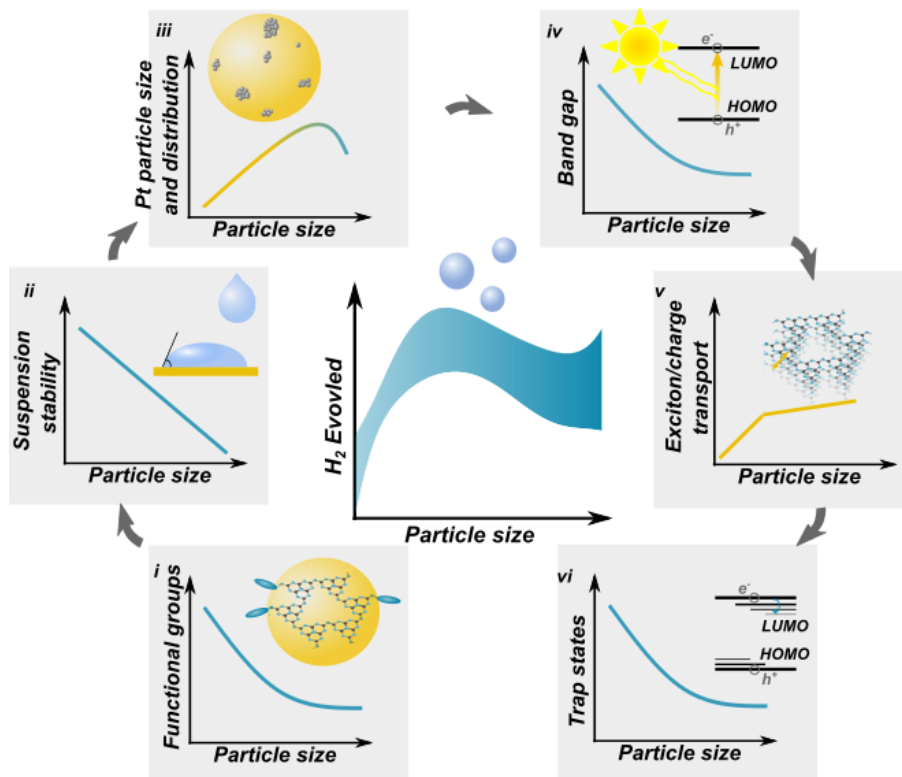


Figure 5.7: Overview of different contributions to hydrogen evolution, including the concentration of functional groups (i), suspension stability (ii), Pt particle size and distribution (iii), light absorption (iv), exciton separation and transport (v), and amount and depth of trap states (vi). With different effects on hydrogen evolution, a combination of these contributions is responsible for the observed hydrogen evolution trend.

Taking together the results for sonicated PHI and their effects on photocatalysis, it can be stated that photocatalysis is a process with multiple interwoven parameters.^[37] They act together on the hydrogen evolution activity in different and partly opposing ways. By changing the size of the photocatalyst, e.g. by sonication, the amount of functional groups, the particle dispersibility, the size, distribution and loading of the Pt co-catalyst, light absorption, exciton or charge separation, as well as the amount and depth of trap states are all changed, as summarized in Figure 5.7. Contrary to most published results, a non-linear trend for the actual measured photocatalytic activity as a particle size function was obtained. This is caused by an increased amount of functional groups (especially OH, NH₂, and C=O) at the surface with decreasing particle sizes (i), which leads to enhanced polarity/wettability and suspension stability (ii). As a result, the Pt deposition is more homogeneous, and the Pt particle size is reduced for smaller PHI particles (iii). However, the band gap increases for very small particles (iv), and the charge or exciton separation is decreased with too small particles due to restrictions in layer number and, therefore, carrier diffusion length (v). Higher levels of deep trap states are observed in the smallest size regime due

to a larger number of surface defects (vi). These deep lying surface defects reduce the hydrogen evolution activity, as long as bulk recombination is not the limiting factor for large particles. Despite how interwoven each of these factors are in the final photocatalytic activity, the increase of hydrogen evolution rate for particle sizes in the range of 180-500 nm and in re-agglomerated particles over pristine H-PHI suggests that it is possible to adjust individual parameters, so that beneficial properties become exposed while no limiting effects becomes detrimental. This approach provides a general template for future catalyst design.

5.3. Conclusion

In this work, we have used ultrasonication as a route to systematically study correlations between morphology-related properties and photocatalytic hydrogen evolution rates in the 2D carbon nitride poly(heptazine imide). By reducing the particle size of PHI down to 20 nm by de-agglomeration, this technique successfully yields stable colloidal solutions while preserving the structural integrity of the PHI primary crystallites in the in-plane as well as the out-of-plane directions. A combined structural analysis by NMR, FT-IR, PXRD, TEM, and XPS revealed that the polymer backbone remains unchanged when reducing particle size, and that the number of functional groups (mainly NH₂, OH, and C=O bearing) located at the periphery increases. As a result, the Pt distribution becomes more homogeneous. This highlights the intertwined effects resulting from size reduction and their impact on charge carrier localization, co-catalyst attachment, and consequently, charge transfer for HER. TRPL measurements in combination with electrochemical analysis and quantum-chemical calculations suggest that the increasing amount of functional groups creates trap states, which are only beneficial for photocatalytic hydrogen evolution as long as their influence is not excessive. Thus, an optimum activity is reached for 2 h sonicated samples with a particle size of 180-500 nm and re-agglomerated samples of those particles. The functional groups formed are also beneficial for charge transport at particle interfaces, consistent with a multiple-trapping-and-release (MTR) model known for semi-crystalline organic semiconductors. If particles are too small, an excess amount of recombination centers are introduced, likely caused by defects lying deep in the band gap. These trap states reduce the efficiency for Pt deposition and hence charge transfer, resulting in lower photocatalytic activity as evidenced by quantum-chemical calculations of ionization potentials and electron affinities. For particles below 180 nm, large optical band gaps and deep trap states adversely affect photocatalysis, whereas the remaining effects of size reduction such as increased wettability enhance photocatalytic efficiency. The results presented here are not only instrumental in the context of PHI thin film and device fabrication, but they might also help to tune the properties of photocatalytic carbon nitride-based microswimmers or solar battery applications.^[80] Disentangling the interdependent structural, morphological, and optoelectronic variables, which together define light-induced charge transport and transfer reactions is key to understand, address and optimize general photocatalyst design.

5.4. Bibliography

- [1] X. Wang, K. Maeda, A. Thomas, K. Takane, G. Xin, J. M. Carlsson, K. Domen, M. Antonietti, *Nat. Mater.* **2009**, *8* (1), 76-80.
- [2] J. Liu, H. Wang, M. Antonietti, *Chem. Soc. Rev.* **2016**, *45* (8), 2308-2326.
- [3] T. Banerjee, F. Podjaski, J. Kröger, B. P. Biswal, B. V. Lotsch, *Nat. Rev. Mater.* **2021**, *6* (2), 168-190.
- [4] H. Schlöberg, J. Kröger, G. Savasci, M. W. Terban, S. Bette, I. Moudrakovski, V. Duppel, F. Podjaski, R. Siegel, J. Senker, R. E. Dinnebier, C. Ochsenfeld, B. V. Lotsch, *Chem. Mater.* **2019**, *31* (18), 7478-7486.
- [5] K. Schwinghammer, M. B. Mesch, V. Duppel, C. Ziegler, J. Senker, B. V. Lotsch, *J. Am. Chem. Soc.* **2014**, *136* (5), 1730-1733.
- [6] Z. Chen, A. Savateev, S. Pronkin, V. Papaefthimiou, C. Wolff, M. G. Willinger, E. Willinger, D. Neher, M. Antonietti, D. Dontsova, *Adv. Mater.* **2017**, *29* (32), 1700555.
- [7] V. W.-h. Lau, I. Moudrakovski, T. Botari, S. Weinberger, M. B. Mesch, V. Duppel, J. Senker, V. Blum, B. V. Lotsch, *Nat. Commun.* **2016**, *7* (1), 12165.
- [8] V. W.-h. Lau, V. W.-z. Yu, F. Ehrat, T. Botari, I. Moudrakovski, T. Simon, V. Duppel, E. Medina, J. K. Stolarczyk, J. Feldmann, V. Blum, B. V. Lotsch, *Adv. Energy Mater.* **2017**, *7* (12), 1602251.
- [9] V. W.-h. Lau, D. Klose, H. Kasap, F. Podjaski, M.-C. Pigne, E. Reisner, G. Jeschke, B. V. Lotsch, *Angew. Chem. Int. Ed.* **2017**, *56*, 510-514.
- [10] H. Kasap, C. A. Caputo, B. C. M. Martindale, R. Godin, V. W.-H. Lau, B. V. Lotsch, J. R. Durrant, E. Reisner, *J. Am. Chem. Soc.* **2016**, *138*, 9183-9192.
- [11] F. Podjaski, J. Kröger, B. V. Lotsch, *Adv. Mater.* **2018**, *30* (9), 1705477.
- [12] J. Kröger, A. Jiménez-Solano, G. Savasci, P. Rovó, I. Moudrakovski, K. Küster, H. Schlöberg, H. A. Vignolo-González, V. Duppel, L. Grunenberg, C. B. Dayan, M. Sitti, F. Podjaski, C. Ochsenfeld, B. V. Lotsch, *Adv. Energy Mater.* **2021**, *11* (6), 2003016.
- [13] L. Liang, L. Shi, F. Wang, *Diamond Relat. Mater.* **2019**, *91*, 230-236.
- [14] L. Svoboda, P. Praus, M. J. Lima, M. J. Sampaio, D. Matýsek, M. Ritz, R. Dvorský, J. L. Faria, C. G. Silva, *Mater. Res. Bull.* **2018**, *100*, 322-332.
- [15] K. L. Corp, C. W. Schlenker, *J. Am. Chem. Soc.* **2017**, *139* (23), 7904-7912.
- [16] S. Yang, Y. Gong, J. Zhang, L. Zhan, L. Ma, Z. Fang, R. Vajtai, X. Wang, P. M. Ajayan, *Adv. Mater.* **2013**, *25* (17), 2452-2456.
- [17] X. Dong, F. Cheng, *J. Mater. Chem. A* **2015**, *3* (47), 23642-23652.
- [18] Y. Shiraishi, Y. Kofuji, S. Kanazawa, H. Sakamoto, S. Ichikawa, S. Tanaka, T. Hirai, *Chem. Commun.* **2014**, *50* (96), 15255-15258.
- [19] Q. Han, B. Wang, J. Gao, Z. Cheng, Y. Zhao, Z. Zhang, L. Qu, *ACS Nano* **2016**, *10* (2), 2745-2751.
- [20] C. Merschjann, S. Tschierlei, T. Tyborski, K. Kailasam, S. Orthmann, D. Hollmann, T. Schedel-Niedrig, A. Thomas, S. Lochbrunner, *Adv. Mater.* **2015**, *27* (48), 7993-7999.
- [21] P. Merkl, F. Mooshammer, P. Steinleitner, A. Girnghuber, K. Q. Lin, P. Nagler, J. Holler, C. Schüller, J. M. Lupton, T. Korn, S. Ovesen, S. Brem, E. Malic, R. Huber, *Nat. Mater.* **2019**, *18* (7), 691-696.
- [22] Z. Xue, F. Liu, J. Jiang, J. Wang, T. Mu, *Green Chem.* **2017**, *19* (21), 5041-5045.
- [23] M. J. Bojdys, N. Severin, J. P. Rabe, A. I. Cooper, A. Thomas, M. Antonietti, *Macromol. Rapid Commun.* **2013**, *34* (10), 850-854.
- [24] Z. Zhou, J. Wang, J. Yu, Y. Shen, Y. Li, A. Liu, S. Liu, Y. Zhang, *J. Am. Chem. Soc.* **2015**, *137* (6), 2179-2182.
- [25] F. Cheng, H. Wang, X. Dong, *Chem. Commun.* **2015**, *51* (33), 7176-7179.
- [26] M. Wu, J.-M. Yan, X.-n. Tang, M. Zhao, Q. Jiang, *ChemSusChem* **2014**, *7* (9), 2654-2658.
- [27] W. Ren, J. Cheng, H. Ou, C. Huang, M.-M. Titirici, X. Wang, *ChemSusChem* **2019**, *12* (14), 3257-3262.
- [28] H. Yu, R. Shi, Y. Zhao, T. Bian, Y. Zhao, C. Zhou, G. I. N. Waterhouse, L.-Z. Wu, C.-H. Tung, T. Zhang, *Adv. Mater.* **2017**, *29* (16), 1605148.
- [29] P. Niu, M. Qiao, Y. Li, L. Huang, T. Zhai, *Nano Energy* **2018**, *44*, 73-81.
- [30] Y. Wang, P. Du, H. Pan, L. Fu, Y. Zhang, J. Chen, Y. Du, N. Tang, G. Liu, *Adv. Mater.* **2019**, *31* (40), 1807540.
- [31] J. Zhang, J. Chen, Y. Wan, H. Liu, W. Chen, G. Wang, R. Wang, *ACS Appl. Mater. Inter.* **2020**, *12* (12), 13805-13812.

- [32] R. Godin, Y. Wang, M. A. Zwijnenburg, J. Tang, J. R. Durrant, *J. Am. Chem. Soc.* **2017**, *139* (14), 5216-5224.
- [33] J. Xue, M. Fujitsuka, T. Majima, *Phys. Chem. Chem. Phys.* **2019**, *21* (5), 2318-2324.
- [34] P. Wu, J. Wang, J. Zhao, L. Guo, F. E. Osterloh, *J. Mater. Chem. A* **2014**, *2* (47), 20338-20344.
- [35] H. Ou, L. Lin, Y. Zheng, P. Yang, Y. Fang, X. Wang, *Adv. Mater.* **2017**, *29* (22), 1700008.
- [36] J. Huang, Y. Cao, H. Wang, H. Yu, F. Peng, H. Zou, Z. Liu, *Chem. Eng. J.* **2019**, *373*, 687-699.
- [37] K. Takanahe, *ACS Catal.* **2017**, *7* (11), 8006-8022.
- [38] O. Simonetti, L. Giraudet, *Polym. Int.* **2019**, *68* (4), 620-636.
- [39] M. Lotya, A. Rakovich, J. F. Donegan, J. N. Coleman, *Nanotechnology* **2013**, *24*, 265703.
- [40] K. S. W. Sing, *Pure Appl. Chem.* **1985**, *57* (4), 603.
- [41] N. Pokhrel, P. K. Vabbina, N. Pala, *Ultrason. Sonochem.* **2016**, *29*, 104-128.
- [42] S. J. Makowski, P. Köstler, W. Schnick, *Chem.–Eur. J.* **2012**, *18* (11), 3248-3257.
- [43] J. Oh, R. J. Yoo, S. Y. Kim, Y. J. Lee, D. W. Kim, S. Park, *Chem.–Eur. J.* **2015**, *21* (16), 6241-6246.
- [44] F. T. Johra, J.-W. Lee, W.-G. Jung, *J. Ind. Eng. Chem.* **2014**, *20* (5), 2883-2887.
- [45] H. Katsumata, F. Higashi, Y. Kobayashi, I. Tateishi, M. Furukawa, S. Kaneco, *Sci. Rep.* **2019**, *9* (1), 14873.
- [46] J. Chen, X. Xu, T. Li, K. Pandiselvi, J. Wang, *Sci. Rep.* **2016**, *6* (1), 37318.
- [47] Z. Zhou, Y. Shen, Y. Li, A. Liu, S. Liu, Y. Zhang, *ACS Nano* **2015**, *9* (12), 12480-12487.
- [48] T. P. Fehlner, *J. Organomet. Chem.* **1977**, *132* (1), C9-C10.
- [49] T. S. Miller, A. B. Jorge, T. M. Suter, A. Sella, F. Corà, P. F. McMillan, *Phys. Chem. Chem. Phys.* **2017**, *19* (24), 15613-15638.
- [50] C.-C. Hu, M.-S. Wang, W.-Z. Hung, *Chem. Eng. Sci.* **2017**, *167*, 1-9.
- [51] B. Choudhury, K. K. Paul, D. Sanyal, A. Hazarika, P. K. Giri, *J. Phys. Chem. C* **2018**, *122* (16), 9209-9219.
- [52] X. Wei, X. Liu, H. Liu, S. Yang, H. Zeng, F. Meng, X. Lei, J. Liu, *Sol. Energy* **2019**, *181*, 161-168.
- [53] X. Wang, L. Chen, S. Y. Chong, M. A. Little, Y. Wu, W.-H. Zhu, R. Clowes, Y. Yan, M. A. Zwijnenburg, R. S. Sprick, A. I. Cooper, *Nat. Chem.* **2018**, *10* (12), 1180-1189.
- [54] Y. Wang, A. Vogel, M. Sachs, R. S. Sprick, L. Wilbraham, S. J. A. Moniz, R. Godin, M. A. Zwijnenburg, J. R. Durrant, A. I. Cooper, J. Tang, *Nat. Energy* **2019**, *4* (9), 746-760.
- [55] Z. Chen, S. Mitchell, E. Vorobyeva, R. K. Leary, R. Hauert, T. Furnival, Q. M. Ramasse, J. M. Thomas, P. A. Midgley, D. Dontsova, M. Antonietti, S. Pogodin, N. López, J. Pérez-Ramírez, *Adv. Funct. Mater.* **2017**, *27* (8), 1605785.
- [56] N.-N. Vu, S. Kaliaguine, T.-O. Do, *ACS Sustain. Chem. Eng.* **2020**, *8* (2), 853-863.
- [57] X. Li, W. Bi, L. Zhang, S. Tao, W. Chu, Q. Zhang, Y. Luo, C. Wu, Y. Xie, *Adv. Mater.* **2016**, *28* (12), 2427-2431.
- [58] W. Xing, W. Tu, M. Ou, S. Wu, S. Yin, H. Wang, G. Chen, R. Xu, *ChemSusChem* **2019**, *12* (9), 2029-2034.
- [59] V. W.-h. Lau, D. Klose, H. Kasap, F. Podjaski, M.-C. Pignié, E. Reisner, G. Jeschke, B. V. Lotsch, *Angew. Chem. Int. Ed.* **2017**, *56* (2), 510-514.
- [60] S. Cao, J. Jiang, B. Zhu, J. Yu, *Phys. Chem. Chem. Phys.* **2016**, *18* (28), 19457-19463.
- [61] G. Zhang, G. Li, T. Heil, S. Zafeirotos, F. Lai, A. Savateev, M. Antonietti, X. Wang, *Angew. Chem. Int. Ed.* **2019**, *58* (11), 3433-3437.
- [62] A. Isacson, A. W. Cummings, L. Colombo, L. Colombo, J. M. Kinaret, S. Roche, *2D Mater.* **2016**, *4* (1), 012002.
- [63] Y. Wang, P. Han, X. Lv, L. Zhang, G. Zheng, *Joule* **2018**, *2* (12), 2551-2582.
- [64] H. F. Haneef, A. M. Zeidell, O. D. Jurchescu, *J. Mater. Chem. C* **2020**, *8* (3), 759-787.
- [65] Y. Zhang, Y. Dai, H. Li, L. Yin, M. R. Hoffmann, *Commun. Mater.* **2020**, *1* (1), 66.
- [66] A. F. van Driel, I. S. Nikolaev, P. Vergeer, P. Lodahl, D. Vanmaekelbergh, W. L. Vos, *Phys. Rev. B* **2007**, *75* (3), 035329.
- [67] A. C. Fogarty, A. C. Jones, P. J. Camp, *Phys. Chem. Chem. Phys.* **2011**, *13* (9), 3819-3830.
- [68] R. Brüninghoff, K. Wenderich, J. P. Korterik, B. T. Mei, G. Mul, A. Huijser, *J. Phys. Chem. C* **2019**, *123* (43), 26653-26661.
- [69] W. Yang, R. Godin, H. Kasap, B. Moss, Y. Dong, S. A. J. Hillman, L. Steier, E. Reisner, J. R. Durrant, *J. Am. Chem. Soc.* **2019**, *141* (28), 11219-11229.

- [70] J. E. Ellis, D. C. Sorescu, S. C. Burkert, D. L. White, A. Star, *ACS Appl. Mater. Interfaces* **2017**, *9* (32), 27142-27151.
- [71] R. Meng, Y. Li, C. Li, K. Gao, S. Yin, L. Wang, *Phys. Chem. Chem. Phys.* **2017**, *19* (36), 24971-24978.
- [72] H. Wang, X. Sun, D. Li, X. Zhang, S. Chen, W. Shao, Y. Tian, Y. Xie, *J. Am. Chem. Soc.* **2017**, *139* (6), 2468-2473.
- [73] C. Adamo, V. Barone, *J. Chem. Phys.* **1999**, *110* (13), 6158-6170.
- [74] M. Ernzerhof, G. E. Scuseria, *J. Chem. Phys.* **1999**, *110* (11), 5029-5036.
- [75] J. P. Perdew, K. Burke, M. Ernzerhof, *Phys. Rev. Lett.* **1996**, *77* (18), 3865-3868.
- [76] S. Grimme, J. Antony, S. Ehrlich, H. Krieg, *J. Chem. Phys.* **2010**, *132* (15), 154104.
- [77] A. Schäfer, C. Huber, R. Ahlrichs, *J. Chem. Phys.* **1994**, *100* (8), 5829-5835.
- [78] K. Eichkorn, F. Weigend, O. Treutler, R. Ahlrichs, *Theor. Chem. Acc.* **1997**, *97* (1), 119-124.
- [79] J. Xue, M. Fujitsuka, T. Majima, *Chem. Commun.* **2020**, *56* (44), 5921-5924.
- [80] V. Sridhar, F. Podjaski, J. Kröger, A. Jiménez-Solano, B.-W. Park, B. V. Lotsch, M. Sitti, *Proc. Natl. Acad. Sci. U.S.A.* **2020**, *117*, (40), 24748-24756.

6. Interfacial engineering of PHI for improved photocatalysis

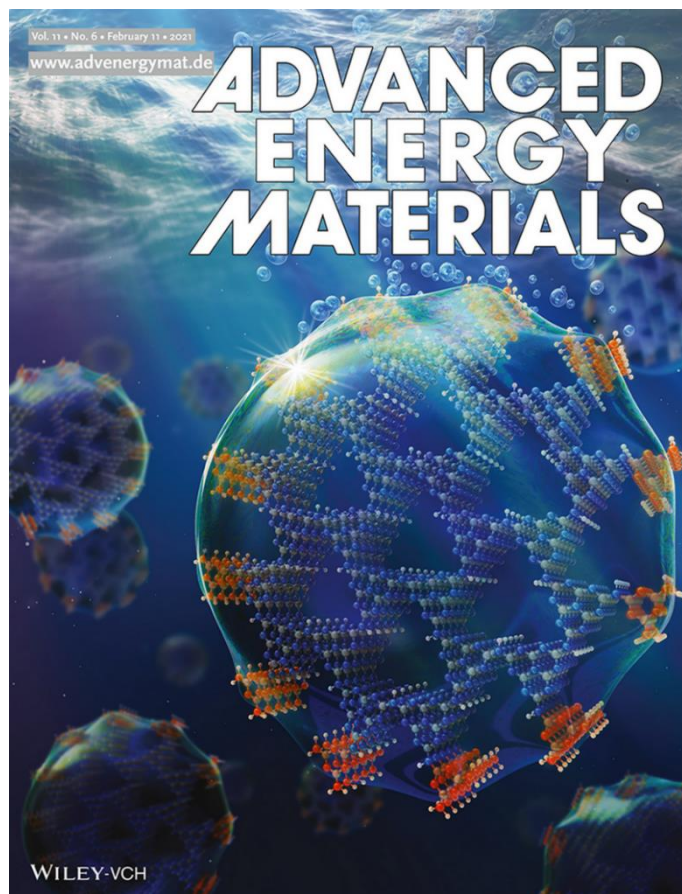
The work in this chapter was published, reproduced and adapted from:

*Interfacial engineering for improved photocatalysis in a charge storing 2D carbon nitride:
Melamine functionalized poly(heptazine imide)*

Julia Kröger, Alberto Jiménez-Solano, Gökçen Savasci, Petra Rovó, Igor Moudrakovski, Kathrin Küster, Hendrik Schlomberg, Hugo A. Vignolo-González, Viola Duppel, Lars Grunenberg, Cem B. Dayan, Metin Sitti, Filip Podjaski, Christian Ochsenfeld and Bettina V. Lotsch

Adv. Energy Mater. **2021**, 11, (6), 2003016. DOI:10.1002/aenm.202003016

Cover: DOI:10.1002/aenm.202170028



Julia Kröger and Filip Podjaski designed the project. Julia Kröger wrote the manuscript with assistance of Filip Podjaski and Bettina V. Lotsch. Julia Kröger conducted the synthesis, with the help of Hendrik Schlomberg. Julia Kröger performed structural characterization, photocatalysis experiments, and evaluated all corresponding data. Alberto Jiménez-Solano performed PL measurements. Gökçen Savasci performed the quantum-chemical calculations, supervised by Christian Ochsenfeld. Petra Rovó and Igor Moudrakovski performed NMR measurements. Kathrin Küster performed XPS and UPS measurements. Hugo A. Vignolo-González performed QY and continuous flow GC experiments. Viola Duppel took TEM and SEM images. Lars Grunenberg performed HPLC-MS analysis. Cem B. Dayan and Filip Podjaski performed contact angle measurements with supervision of Metin Sitti. Filip Podjaski performed the photoelectrochemical experiments. All authors assisted the analysis of their respective experiments. Bettina V. Lotsch supervised the work

This work was highlighted with a back side cover in the journal of Advanced Energy Materials. The cover image was designed by Vera Hiendl, e-conversion.

Supporting information can be found in Chapter 9.3.

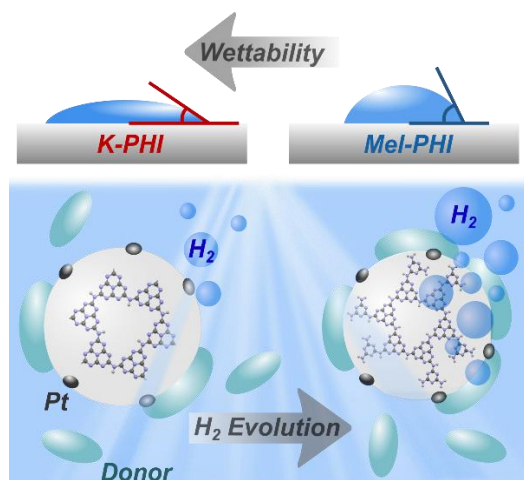


Figure 6.1: Table of content figure for interfacial engineering for improved hydrogen evolution.

Abstract

Carbon nitrides constitute a class of earth-abundant polymeric semiconductors, which have high potential of tunability on a molecular level, despite their high chemical and thermal inertness. Here the first post-synthetic modification of the 2D carbon nitride poly(heptazine imide) (PHI) is reported, which was decorated with terminal melamine (Mel) moieties by a functional group interconversion. The covalent attachment of this group is verified based on a suite of spectroscopic and microscopic techniques supported by quantum-chemical calculations. Using triethanolamine as a sacrificial electron donor, Mel-PHI

outperforms most other carbon nitrides in terms of hydrogen evolution rate ($5570 \mu\text{mol h}^{-1} \text{g}^{-1}$), while maintaining the intrinsic light storing properties of PHI. The origin of the observed superior photocatalytic performance is traced back to a modified surface electronic structure and enhanced interfacial interactions with the amphiphile triethanolamine, which imparts improved colloidal stability to the catalyst particles especially in contrast to methanol used as donor. However, this high activity can be limited by oxidation products of donor reversibly building up at the surface, thus blocking active centers. The findings lay out the importance of surface functionalization to engineer the catalyst-solution interface, an underappreciated tuning parameter in photocatalytic reaction design.

6.1. Introduction

The transformation of intermittent solar energy into storable chemical fuels, but also the direct electrochemical storage of sunlight in a solar battery are cornerstones of a future sustainable energy economy. Since the early days of photocatalysis, initiated by the prototype oxide, TiO_2 ,^[1] the material's landscape has become increasingly rich and diverse, encompassing myriads of inorganic and organic semiconductors that have been adapted for various solar-to-fuel conversion schemes. Among these, carbon nitrides, first reported in 1834,^[2] have evolved into one of the most actively researched classes of materials for photocatalytic water splitting. In 2009, Wang *et al.*^[3] demonstrated that the archetypical carbon nitride, known as Liebig's melon^[4], shows activity for overall photocatalytic water splitting.^[3] As a direct consequence of the high synthesis temperatures, carbon nitrides are invariably formed through triazine or heptazine building units, from which three distinct material systems are obtained: 1D heptazine-based melon, 2D poly(triazine imide) (PTI), and the recently reported 2D poly(heptazine imide) (PHI).^[5-7] Among those materials, PHI has received particular attention as it exhibits an intriguing dual functionality: light absorption and storage of photo-generated electrons within one and the same material. The

controlled release of these charge carriers hence enables “dark photocatalysis”^[8] as well as time-delayed photoredox reactions^[9], reminiscent of the photoreactions in Photosystem I, followed by the Calvin-Benson cycle in nature. Besides, the direct electrical discharge of the photo-reduced state enables novel types of single-component solar batteries.^[10] Structure analysis of PHI has not only evidenced its 2D nature, but also pore filling of the trigonal PHI network by charge compensating hydrated potassium ions (K-PHI), which can be replaced by hydrated protons (H-PHI).^[5]

Owing to the chemical inertness of carbon nitrides, the improvement of their photocatalytic performance by rational design of their optoelectronic and surface properties has been a key challenge ever since their discovery. Photocatalytic activity engineering in 1D melon-type carbon nitrides includes surface area optimization^[11-13], backbone doping^[14-16] or formation of heterojunctions and copolymerization.^[17-20] Besides these methods, rational defect engineering has proven useful for enhanced hydrogen evolution, e.g. by changing the number of terminal sites or by introducing cyanamide, hydroxyl or urea moieties to the backbone.^[14, 21-24] In addition, functional groups can be used to enhance the interaction with sacrificial electron donors and to design donor-acceptor-structures apt to separate strongly bound excitons.^[24, 25] The ability to control the type and number density of functional groups on the carbon nitride backbone is thus instrumental in overcoming the major bottleneck in carbon nitride photocatalysts, which is the intrinsically high charge carrier recombination rate limiting solar-to-fuel conversion.^[26] However, structural analysis of carbon nitrides is often hampered by an inherently low crystallinity of these polymers,^[5] which renders quantitative structural insights challenging. Yet, the rational design of enhanced carbon nitride photocatalysts is contingent on an in-depth understanding of structure-property-activity relationships in these systems, calling for innovative synthetic approaches to access highly crystalline systems, as well as their unambiguous structural characterization.

Here we present melamine-modified PHI (Mel-PHI), a crystalline 2D heptazine-based carbon nitride that is surface-functionalized with triazine moieties to form an extended π -aromatic system with an internal heterojunction architecture imprinted on its backbone. An internal heterojunction of a heptazine-triazine-based 1D copolymer with enhanced charge separation, presumably arising from a donor-acceptor structure, was recently described elsewhere.^[27] In contrast, also to melamine-intercalated PHI,^[28] where melamine is loosely bound to the pore walls of a PHI structure through hydrogen bonding interactions, in Mel-PHI the triazine unit is covalently attached to the PHI particle surface. Intriguingly, we find that Mel-PHI, synthesized by a straightforward ionothermal method, yields one of the most active carbon nitride photocatalysts reported to date in terms of hydrogen evolution activity ($5570 \mu\text{mol h}^{-1} \text{g}^{-1}$), with comparably low applied Pt loading of 1.75 wt%. Through its surface functionalization, Mel-PHI is more hydrophobic than K-PHI, which promotes stronger interactions with the sacrificial donor and surfactant triethanolamine (TEoA), resulting in a substantially increased photocatalytic activity. We also show that the enhanced interaction between TEoA and Mel-PHI reversibly limits the hydrogen evolution rate

over time, since oxidation products formed on the Mel-PHI surface kinetically hinder the diffusion of the donor to the catalyst surface, as evidenced by time-dependent photoluminescence (PL) and continuous flow gas chromatography (GC) analysis. As such, this material showcases how functional group design in general and surface modification in particular can be used to enhance charge separation and photocatalytic activity in carbon nitrides. More generally, our studies reveal that engineering the interaction between sacrificial electron donor and carbon nitride photocatalyst is a crucial, but often neglected factor for efficient charge carrier separation and extraction, as electron extraction for hydrogen evolution is limited by the kinetics of hole quenching through the sacrificial donor.

6.2. Results and discussion

Synthesis and structure analysis

Melamine-functionalized poly(heptazine imide) (Mel-PHI) was synthesized ionothermally as described in the experimental section. Briefly, potassium containing poly(heptazine imide) (K-PHI) was mixed with ammonium chloride and dicyandiamide, the latter being a known precursor of melamine (Figure 6.2a, Scheme S3.1). Ammonium chloride acts as a mineralizer by adjusting the autogenous ammonia pressure during the synthesis, thus enhancing the reversibility of the polycondensation reaction.^[29, 30] During this reaction, the terminal cyanamide moieties at the surface of K-PHI (roughly every 4th to 5th heptazine unit is functionalized with a cyanamide moiety^[5]) react with the molten dicyandiamide to form melamine, resulting in a surface functionalized Mel-PHI as shown in Figure 6.2a. Several reaction conditions using different dicyandiamide and NH₄Cl loadings as well as temperatures were tested in order to elucidate the influence of various synthesis conditions on the formed carbon nitride (CN_x) structure (Figure S3.1-S3.7). Only heating to 250°C in the presence of ammonium chloride results in the formation of 2D Mel-PHI, providing a sufficiently high temperature for the transformation of dicyandiamide to melamine to occur, while still preventing further condensation of melamine (Figure S3.5, S3.6).^[31, 32]

During synthesis probably also excess melamine residing inside the PHI pores is formed as a side phase along with the melamium salt C₆N₁₁H₁₀Cl_x0.5NH₄Cl.^[33, 34] Those phases as well as residual NH₄Cl were removed by thorough washing with boiling water, resulting in a phase-pure material hosting only ammonium and water in the pores. Further details on the side phase formation and analysis can be found in Figure S3.8-S3.13. The assumed stoichiometry of melamine functionalized PHI (C_{6.5}N₉H_{1.75}) is consistent with the assumption that every NCN-functional group in K-PHI^[5] is transformed into a melamine unit. Elemental analysis shows the presence of additional amounts of hydrated ions in the pores, giving rise to an overall composition of (NH₄)₁ K_{0.05}(C_{6.5}N₉H_{1.75})₁ * (H₂O)_{0.7}. Hence, approximately one ammonium ion is present for every heptazine unit, which is comparable to the amount of potassium in K-PHI.^[5]

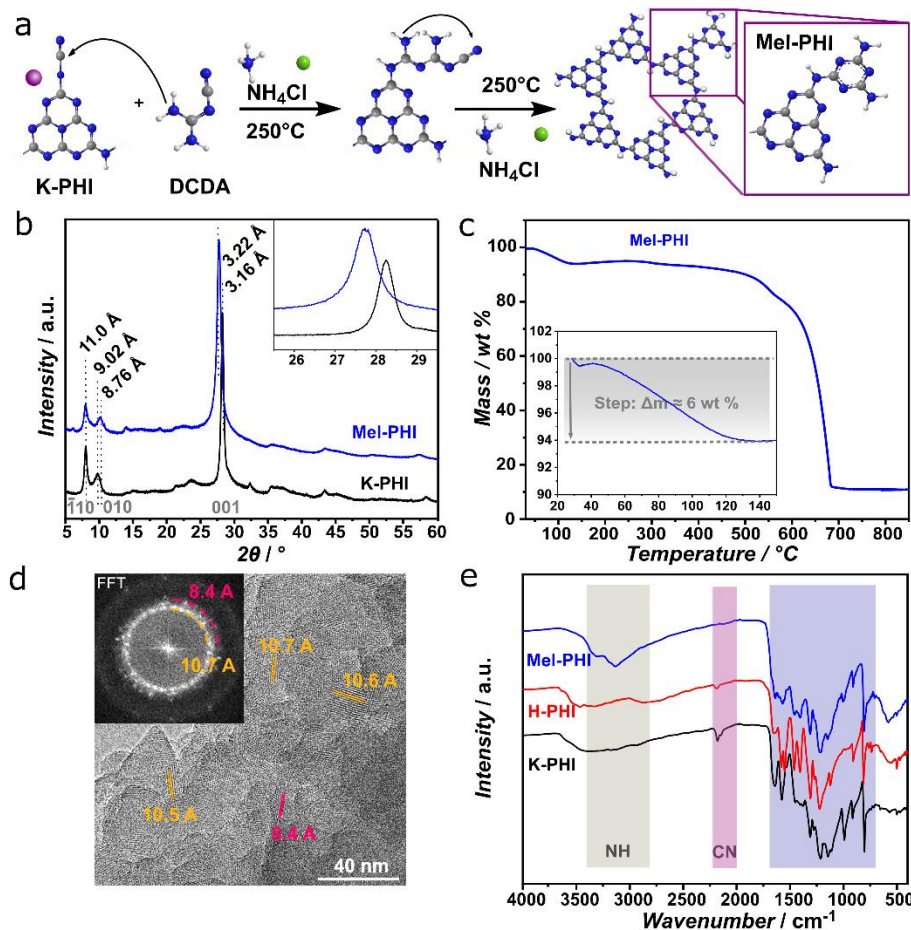


Figure 6.2: Structural analysis of Mel-PHI. a) Schematic depiction of the synthesis of Mel-PHI, formed from NCN'-functionalized K-PHI ground with NH_4Cl and DCDA and heated to 250°C (blue: nitrogen, gray: carbon, white: hydrogen, purple: potassium, green: chlorine). b) PXRD of Mel-PHI and K-PHI and close-up of the stacking peak as inset, measured with $\text{Cu K}\alpha$ irradiation. c) TGA analysis of Mel-PHI. d) TEM images of the 2D layers of Mel-PHI and inset with Fourier transformed TEM image. e) FT-IR of Mel-PHI, H-PHI and K-PHI in comparison. Gray area depicts NH vibrations; purple area shows the CN groups and the blue area depicts the fingerprint area containing heptazine and amine vibrations.

Functionalization of PHI by melamine results in an essentially unchanged polymer backbone compared to K-PHI, as demonstrated by powder X-ray diffraction (PXRD). The patterns of K-PHI and Mel-PHI both feature the same in-plane reflexes ($\bar{1}10$ and 010) at $8.00^\circ 2\theta$ (11.0 \AA) and $10.10^\circ 2\theta$ (8.76 \AA), respectively (Figure 6.2b).^[5, 22] This suggests retention of the arrangement of the heptazine units in the 2D layer in Mel-PHI and K-PHI. Only a shift of the stacking peak (001) centered at $28.25^\circ 2\theta$ (3.16 \AA) in K-PHI to $27.65^\circ 2\theta$ (3.22 \AA) in Mel-PHI is observed, suggesting that the surface and edges of PHI are functionalized with melamine, causing a slight increase in the stacking distance. The formation of PTI can be excluded from PXRD data (Figure S3.14).^[35] In Mel-PHI, the alkali ions are replaced by ammonium ions as shown by elemental analysis (see above) and nuclear magnetic resonance (NMR) (see below). Besides ammonium ions, the pores contain up to 6 wt% water as determined by thermogravimetric analysis (TGA) (Figure 6.2c), whereas for K-PHI a value of 10 wt% was reported.^[5] Transmission electron microscopy (TEM)

imaging of Mel-PHI confirmed the structural model based on PXRD (Figure 6.2d). The fast Fourier transformation (FFT) revealed a characteristic distance of 10.7 Å, corresponding to the ($\bar{1}10$) plane, similar to K-PHI, and 8.4 Å corresponding to the (010) plane.^[5] In scanning electron microscopy (SEM) images a distribution of the agglomerates with particle sizes between 200 nm and 2 μm can be seen (Figure S3.15).

Fourier transform infrared (FT-IR) spectroscopy likewise emphasizes the similarity of K-PHI and Mel-PHI in the fingerprint area, suggesting that also the local structure of the polymeric backbone is largely preserved (Figure 6.2e). For both materials, the signal at 802 cm⁻¹ is characteristic of the heptazine ring out-of-plane bending mode^[36], whereas signals at 1640, 1450 and 1309 cm⁻¹ are caused by stretching vibrations of the heptazine ring (blue area Figure 6.2e).^[37, 38] Differences in the vibrational spectra are observed at higher wavenumbers only, where the NC stretching mode of the cyanamide (NCN) group of the K-PHI network (2210-2120 cm⁻¹) disappears in Mel-PHI. The broad signal between 3400-2800 cm⁻¹, caused by NH, NH₂ or OH stretching vibrations in K-PHI, is more prominent and well-defined in Mel-PHI (gray area in Figure 6.2e). This is likely due to additional NH₂ groups being located at the melamine moiety, which also give rise to bending vibrations between 1700 to 1550 cm⁻¹ in the fingerprint area (Figure S3.14).^[4, 36] In addition, the more distinct NH₂ signals in Mel-PHI either point to a more isolated or locally more ordered structure around the melamine unit, as described in crystalline melon, where the NH or NH₂ bands become narrower with increasing crystallinity.^[39]

To obtain further information on the incorporation of melamine into the PHI backbone and its attachment mode, an in-depth magic-angle-spinning (MAS) solid-state NMR spectroscopy analysis was performed with all assignments being supported by quantum-chemical calculations of NMR chemical shifts on the B97-2^[40]/pcsSeg-2^[41]//PBE0-D3^[42-44]/def2-TZVP^[45, 46] level of theory using the FermiONs++^[47-48] program package. Computationally, we investigated various model systems where melamine was either covalently bound at the surface or located in the PHI pores without a covalent attachment (Figure S3.16-S3.20), and found that the best match between experimental and theoretical chemical shifts is obtained when the triazine unit is covalently attached to the backbone via transformation of the cyanamide groups as described before (Scheme S3.1).^[5]

The structural similarity of the polymer backbone of Mel-PHI and K-PHI was confirmed by ¹H¹³C cross polarization (CP) spectra, where the carbon signals of the heptazine unit at 157 ppm (C1) and 163 ppm (C2) are both present in K-PHI and Mel-PHI (Figure 6.3a). Those two signals show small shoulders in Mel-PHI (at 158 and 164 ppm), pointing to a desymmetrization of the PHI backbone through partial protonation, similarly as observed for H-PHI.^[5] However, the signal at 171.0 ppm, which is related to the carbon atom next to the NCN-groups in K-PHI^[5] as well as the signal at 120.0 ppm (NCN group) disappear in Mel-PHI, indicating that the NCN moiety is transformed during reaction with dicyandiamide. In addition, new signals at 168-169 ppm (C3) hint to the presence of the triazine ring,^[38, 49] whose formation is supported by quantum-chemical

calculations (Figure S3.16-S3.18), thus showing the successful functionalization. Direct excitation ^{13}C MAS NMR was used to estimate the density of melamine groups introduced after functionalization, revealing the modification of every 5th-6th heptazine unit (Figure S3.21). This is in excellent agreement with elemental analysis (Table S3.2) assuming an average crystallite size of ~ 20 nm as estimated by TEM, and decoration of the structure with point defects, similar to K-PHI.^[5]

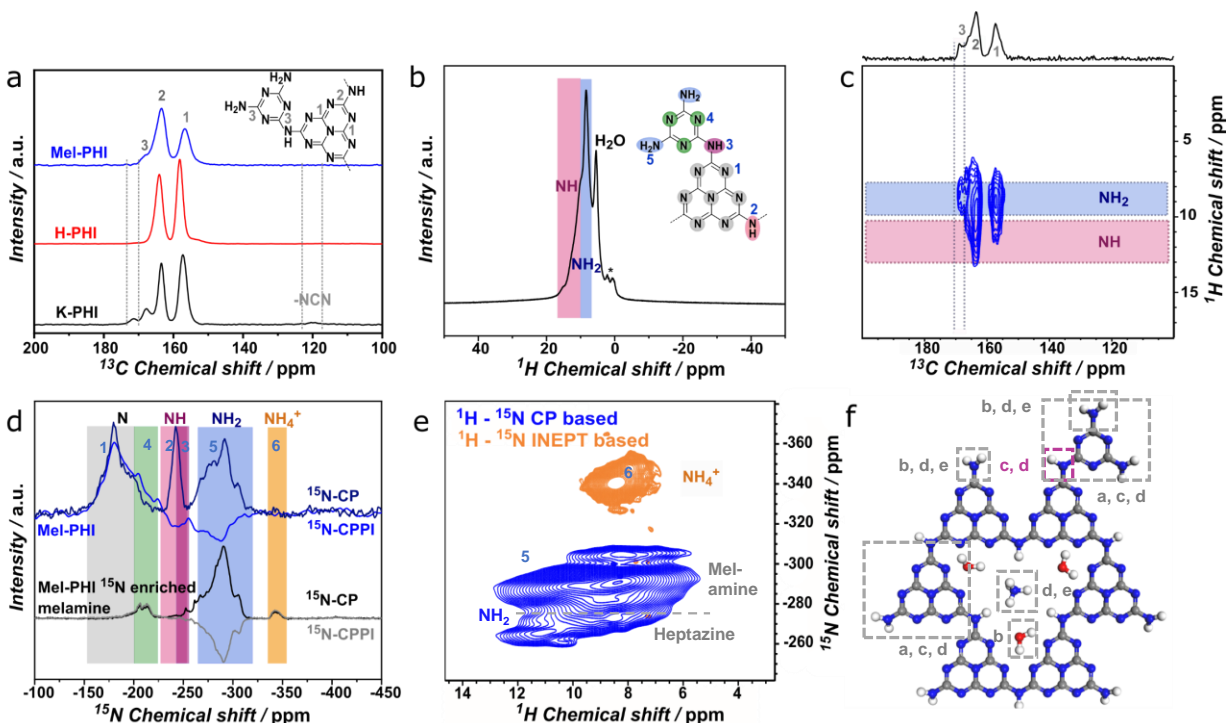


Figure 6.3: Solid-state NMR analysis of Mel-PHI and ^{15}N enriched melamine-containing Mel-PHI. a) Comparison of $\{^1\text{H}\}^{13}\text{C}$ CP spectra of Mel-PHI, K-PHI and H-PHI, confirming the intact PHI backbone. The inset shows the molecular structure with the assignment of carbon atoms. Gray dotted lines depict the shift of the NCN-group and its neighboring carbon atom. b) ^1H NMR of ^{15}N enriched melamine in Mel-PHI at a spinning frequency of 55.5 kHz showing signals of water, as well as NH, NH_2 and NH_4^+ groups (overlapping), asterisk marks some impurities. The inset shows the molecular structure with the assignment by number (N atoms) and color (N-H connectivity). c) ^1H - ^{13}C HETCOR MAS spectrum of the ^{15}N enriched melamine in Mel-PHI with 12.5 kHz spinning frequency and CP contact times of 1 ms. The projection of the ^{13}C axis shows the assigned carbon resonances as displayed in (a). d) $\{^1\text{H}\}^{15}\text{N}$ CP and CPPI experiments of natural abundance and ^{15}N -enriched-melamine-containing Mel-PHI with colored areas showing the bonding situation of nitrogen atoms and protons. e) ^1H - ^{15}N CP-based and ^1H - ^{15}N INEPT-based HSQC spectra of ^{15}N enriched melamine in Mel-PHI, allowing the detection of mobile ammonium ions, rigid melamine and heptazine units. f) Structure of Mel-PHI, which is consistent with NMR experiments. Letters marking the experiments that were used for the respective part of the structure assignment.

In the 1D ^1H -NMR spectrum of Mel-PHI substantial amount of water is visible, (Figure 6.3b) so that 2D experiments revealing heteronuclear couplings can help to disentangle the various interactions between the protons. In the ^1H - ^{13}C heteronuclear correlation (HETCOR) NMR the carbon signal C3 shows a cross peak with protons at around 8-10 ppm, which could be assigned to the interaction of NH_2 protons of melamine with a triazine ring carbon atom (Figure 6.3c, S3.23). Additionally, a small cross peak with protons of NH-groups and C2 gives a first indication of an imide bridge between melamine and the PHI backbone. In the ^{15}N spectrum of Mel-PHI all the

backbone nitrogen signals at -150 to -220 ppm (N1, gray), -245 ppm (N2, pink) and -260 to -280 ppm (N5, blue) are found to be similar to K-PHI (Figure 6.3d, S3.24). However, there are some shifts and intensity differences between the spectra of the two samples, which are a consequence of melamine functionalization.^[32, 38, 49, 50] In particular, the broad peak between -275 and -305 ppm is associated with NH₂ groups of melamine, while the shoulder around -260 ppm belongs to the NH₂ groups of the heptazine backbone, as seen for K-PHI (Figure S3.24). The downfield shift of the heptazine ring nitrogen signal from -185 ppm in K-PHI to -175 ppm in Mel-PHI indicates a slightly increased charge of the backbone, which is balanced by cations in the pores.

The presence of melamine NH₂ groups is further confirmed by ¹⁵N spectra of a selectively ¹⁵N labeled sample, where the incorporation of ¹⁵N was performed after the heptazine backbone was prepared, and hence only the melamine and some exchangeable ammonium nitrogen atoms could lead to ¹⁵N signals (Figure 6.3d). In direct comparison between ¹⁵N CP and CP combined with polarization inversion (CPPI) experiments of the non-enriched Mel-PHI sample, the nitrogen atoms in melamine (-200 ppm to -210 ppm) can be distinguished from signals caused by heptazine rings (Figure 6.3d). In addition, an upfield shifted imide bridge N3 (-247 to -254 ppm; dark pink)^[35] (Figure S3.18, S3.24, S3.25) is visible, similar to an additional NH signal in 2D ¹H-¹⁵N HETCOR NMR and ¹H-¹⁵N 2D CP-based correlation experiments (Figure 6.3e, S3.26). One likely reason for this shift is the formation of a new imide bridge between the heptazine and the triazine unit, which is confirmed by quantum-chemical calculations, where an upfield shift for the NH-bonds between heptazine and triazine in comparison to bridges between heptazine units is predicted (Figure S3.18).

To judge whether the ¹⁵N melamine is indeed covalently attached to the backbone or not, we performed further experiments at 55.55 kHz MAS frequency, namely a ¹⁵N 1D direct excitation and detection spectrum with a recycle delay of 60 s (Figure S3.27), a ¹H-detected ¹H-¹⁵N 2D CP-based correlation experiment, a ¹H-detected ¹H-¹⁵N 2D insensitive nuclei enhanced polarization transfer (INEPT)-transfer-based heteronuclear single quantum coherence (HSQC) experiment (Figure 6.3e), and a series of ¹H and ¹⁵N *R*₁ and *R*_{1ρ} measurements (Figure S3.31). ¹⁵N in the CP-based experiment primarily shows signals of rigid, proton-bound nitrogen atoms, where the INEPT-based experiment shows signals of highly flexible, direct ¹H-¹⁵N bonds. Based on their NMR chemical shifts, the three major signals in the 1D ¹⁵N spectrum can be assigned to a tertiary ring N of melamine at -200 ppm (N4, green), to a NH₂ group of melamine at -285 ppm (N5, blue), and to an ammonium ion (N6, orange) at -345 ppm (Figure S3.27).^[30] As N5 signals appear in the CP experiment but not in the INEPT-based spectrum, while the signal at -345 ppm (N6) shows the opposite behavior, it is likely that melamine is rigid and hence it is incorporated into the backbone covalently, while some ammonium ions with much higher motional freedom are present in the pores (Figure S3.28, S3.31). Melamine located in the pores, connected by hydrogen bonds only, would be mobile enough to be detectable in INEPT-based spectra (Figure S3.29, S3.30). The covalent attachment of the melamine unit is further supported by solid-state ¹H and ¹⁵N

relaxation data (Figure S3.31). The ^{15}N R_1 rates of the signals associated with the melamine (N5) and heptazine units (11 ppm ^1H , -260 ppm ^{15}N) in the CP-based 2D experiments are the same within experimental error (0.003 s^{-1}), while the ^{15}N $R_{1\rho}$ rates are only marginally increased for the NH_2 group of melamine, indicating that the melamine unit has no high amplitude motion on the ps to ns time scale.

When comparing the data to ammonium chloride exchanged K-PHI, it can be further stated that ammonium ions are most likely the counterions to a partially negatively charged polymer network (Table S3.1, Figure S3.32, S3.33). The broad NH_4^+ , ^1H and ^{15}N signals and the appearance of the water signals in the ^1H - ^1H double quantum single quantum (DQ-SQ) 2D spectrum (Figure S3.22) indicate that the hydrated NH_4^+ counterions as well as structured water molecules remain in permanent close contact with the polymer backbone.

X-ray photoelectron spectroscopy (XPS) measurements are consistent with the findings from NMR and elemental analysis (Figure S3.34). Two signals at 398.5 eV and 400.1 eV can be discerned in the N 1s spectrum, which are broadly assigned to the heptazine/triazine ring (C-N=C) and NH_x ($x=1,2$) groups, respectively.^[22, 51] Similar to K-PHI, the C 1s spectrum of Mel-PHI contains three different signals at 288.1 eV, 286.6 eV, and 284.6 eV, which are assigned to N-C=N bonds in the heptazine and triazine rings, C-NH_x groups and adventitious carbon (C-C or C=C moieties), respectively.^[5, 22, 51-53] OH groups observed in the O 1s spectrum at 531.8 eV are consistent with the water contained in the PHI pores as verified by elemental analysis and thermal analysis.^[21, 54]

Optoelectronic and photocatalytic properties

A covalent connection between heptazine and triazine units can have multiple implications on the photocatalytic processes. First, on the electronic level a heterojunction-type structure is formed with heptazine and triazine potentially acting as a donor – acceptor couple, which can assist in charge localization and separation.^[27, 55, 56] Second, surface functionalization with melamine modifies the catalyst – solution interface, which impacts the interaction with the sacrificial electron donor and the solvent, hence affecting both colloidal stability and interfacial charge transfer.

Comparing the position of the valence band (VB) edges of Mel-PHI relative to that of K-PHI in vacuum suggests a change in electronic character, which is dominated by the triazine surface functionalization. Analysis of the VB edges of K-PHI (-5.9 (± 0.1) eV vs Vac.) and Mel-PHI (-5.5 (± 0.1) eV vs Vac.) by ultraviolet photoelectron spectroscopy (UPS) shows that Mel-PHI has a VB edge located 0.4 eV closer to the vacuum level. This results in a higher driving force for photo-excited electrons in the conduction band of Mel-PHI, since the band gap of 2.7 eV remains unchanged as also confirmed by quantum chemical calculations (Figure 6.4a, S3.35-S3.37, Table S3.5). In principle, the higher valence band position of Mel-PHI is consistent with the fact that triazine-based systems typically have more negative conduction and valence band edges compared to heptazine-based ones such as in K-PHI (Figure S3.38).^[57-59] However, whether UPS

probes melamine surface states only or the valence band position of bulk Mel-PHI cannot be resolved unambiguously. Nevertheless, it is plausible to assume that surface functionalization with melamine modulates charge carrier separation and extraction at the surface of PHI.

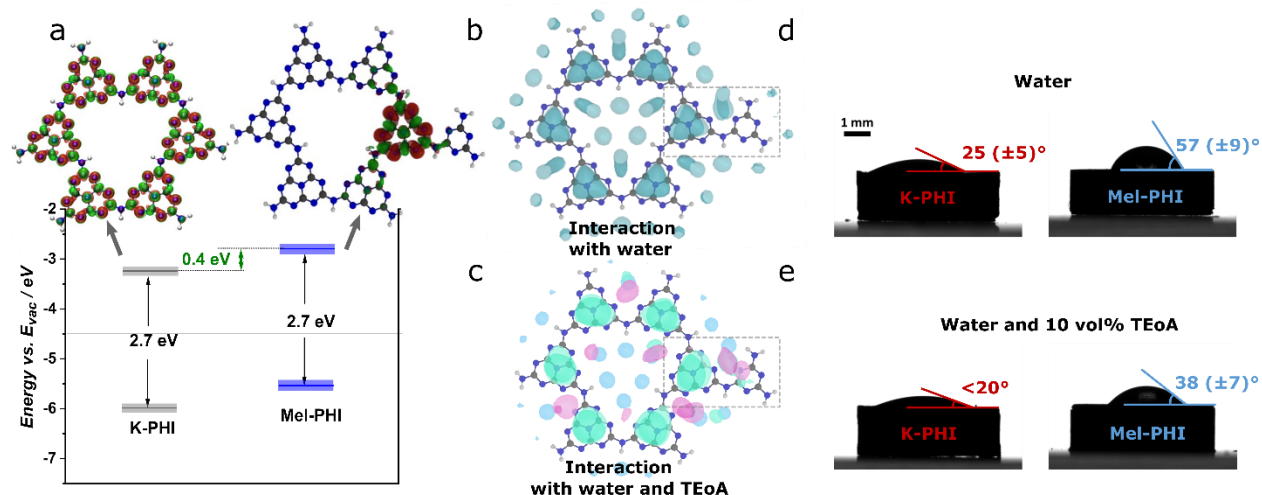


Figure 6.4: Band position determination and quantum-chemical calculations of spin density delocalization and interaction maps with water and TEOA in water: a) UPS valence band measurement and conduction band edge estimation by adding the optical band gap of Mel-PHI and K-PHI; on top calculated non-and melamine functionalized *single pore* poly(heptazine imide) showing difference densities for the exciton delocalization after excitation and a higher amount of exciton localization in the first excited state near the melamine group at the surface in a Mel-PHI model system. b) Interaction of the Mel-PHI model system with water molecules. Blue areas depict the interaction of water molecules with Mel-PHI model system. c) Interaction of Mel-PHI model system with TEOA and water. Blue areas depict the interaction of water with Mel-PHI model system, green areas the N atoms of TEOA and red areas the OH groups, which are interacting strongly with the melamine group in Mel-PHI. d) Contact angle measurement images of K-PHI (left) and Mel-PHI (right) after 30 s of equilibration time. Wetting with water showing the more hydrophobic nature of Mel-PHI. e) Wetting with water containing 10 vol% TEOA, which enhances the wetting on both samples.

To address the question of charge carrier separation, we first studied the potential role of the triazine units attached to PHI as a seed for exciton localization and, ultimately, charge separation, by quantum-chemical calculations. Our selected model system consists of a single pore of six imide bridged heptazine units, with and without the melamine functionalization, as a proxy for the synthesized 2D material Mel-PHI (Figure S3.39, S3.40). Calculations of the localization of the energetically lowest excitonic state directly after excitation show significant differences in the degree of delocalization between the two model systems (Figure 6.4a). When no melamine is bound (single pore PHI model), the exciton is delocalized homogeneously over each heptazine unit with discontinuities at the imide bridges. In contrast, a single pore Mel-PHI, has a strongly localized excitonic state at the heptazine unit right next to melamine. As melamine units are mainly located at the surface of PHI, where the photo-induced redox reactions take place, localization of the charge carrier at the melamine “defect” is expected to assist the exciton separation (Figure S3.41), thereby facilitating the interaction with an electron donor in solution. As hole extraction is a well-known bottleneck in carbon nitrides, ^[22, 60] melamine-functionalization can alleviate this potential loss channel.

Next, we studied the effect of the covalently bound melamine group on the interaction with water and TEOA. The weighted atomic density of water molecules around Mel-PHI reveals that the melamine unit is not surrounded by water molecules as densely as compared to the heptazine units, pointing to a more hydrophobic character of the triazine group (Figure 6.4b, S3.42). On the other hand, the surfactant and donor TEOA interacts well with both melamine and the neighboring heptazine unit primarily through hydrogen bonding. This leads to the formation of a catalyst-solution interface that supports charge transfer from the electron donor to the neighboring exciton, assisting donor oxidation and preventing charge recombination (Figure 6.4c, S3.42).

The less hydrophilic character of Mel-PHI in comparison to K-PHI, caused by the melamine surface functionalization, was also evidenced by contact angle measurements. The deposition of droplets of ultrapure deionized (DI) water on pressed K-PHI and Mel-PHI pellets (Figure 6.4d) results in significantly smaller contact angles and hence, better wetting on K-PHI. The addition of 10 vol% TEOA (Figure 6.4e) further enhances the wetting for both samples due to the decreased surface tension of the surfactant mixture ($\sim 66 \text{ mN m}^{-1}$ vs. 72 mN m^{-1} for DI water).^[61] These findings show that the use of TEOA is beneficial to enhance the interaction with the liquid environment for both materials, amplified in the Mel-PHI case through the weaker interactions with water alone.

To probe the impact of this surface functionalization of PHI on the photocatalytic properties, Mel-PHI was tested for its hydrogen evolution reaction (HER) activity in the presence of Pt as co-catalyst and different electron donors including methanol (MeOH), TEOA and 4-methylbenzyl alcohol (4-MBA) (Figure 6.5a, S3.44). Notably, we observe a striking influence of the sacrificial donor on the maximum HER. Using MeOH (10 vol%) gives rise to a moderate HER activity of $450 \mu\text{mol h}^{-1} \text{g}^{-1}$ at optimized Pt loadings (4 wt%) (Figure S3.43). A more than 10-fold increase ($5600 \mu\text{mol h}^{-1} \text{g}^{-1}$) was observed with TEOA, similar to the apparent quantum yield values, while the optimal Pt amount could be reduced to 1.75 wt% (Table S3.6, Figure S3.43). In contrast, K-PHI exhibits only a 1.2-fold increase (from $1800 \mu\text{mol h}^{-1} \text{g}^{-1}$ (MeOH) to $2200 \mu\text{mol h}^{-1} \text{g}^{-1}$ (TEoA) at optimized 8 wt% Pt loading), whereas the activity of H-PHI is even decreased by 80 % (from $3500 \mu\text{mol h}^{-1} \text{g}^{-1}$ (MeOH) to $725 \mu\text{mol h}^{-1} \text{g}^{-1}$ (TEoA) at optimized 2 wt% Pt loading), i.e. we find a much weaker dependence on the donor than for Mel-PHI. In addition, Mel-PHI outperforms most other reported carbon nitrides in hydrogen evolution when TEOA is present as a donor (Table S3.7).^[62-63]

Besides direct hydrogen evolution during illumination, Mel-PHI was also tested for “dark photocatalysis”, i.e. time delayed hydrogen evolution in the dark after illumination ceased, as reported for K- and H-PHI.^[5, 8] Hydrogen evolution in the dark was tested with TEOA as electron donor by adding Pt nanoparticles to the suspension on demand after the material was illuminated for 2 hours. Sampling the amount of hydrogen after Pt addition shows a significant increase by a factor of 2.6 in the presence of TEOA compared to using MeOH as a donor (30.1 and $11.7 \mu\text{mol g}^{-1}$, respectively) (Figure 6.5b). Even after a time delay of two hours before adding the

co-catalyst in the dark, $18.4 \mu\text{mol g}^{-1}$ (61% of the initial activity without time delay) of hydrogen is evolved with TEOA. It hence appears that not only the efficiency of hydrogen evolution is increased, but also the photo-charging process leading to trapping of electrons on Mel-PHI significantly benefits from the enhanced interaction with TEOA. The decay in the HER rate can be explained by oxygen leaking into the reactor, which acts as an electron scavenger and other charge recombination loss channels. Photoelectrochemical measurements with Mel-PHI nanosheets deposited on FTO showed a transient negative shift to -0.7 V vs Ag/AgCl and a long charge stabilization after 120 s of photo-excitation even in pure water, which can be attributed to a comparably efficient electrode substrate coverage by the more hydrophobic Mel-PHI in comparison to K-PHI as will be shown later (Figure S3.45). In the presence of TEOA, the photopotential reached its saturation value of -1.1 V vs Ag/AgCl almost instantly, which underlines the good charge separation and storage properties of this functionalized PHI.

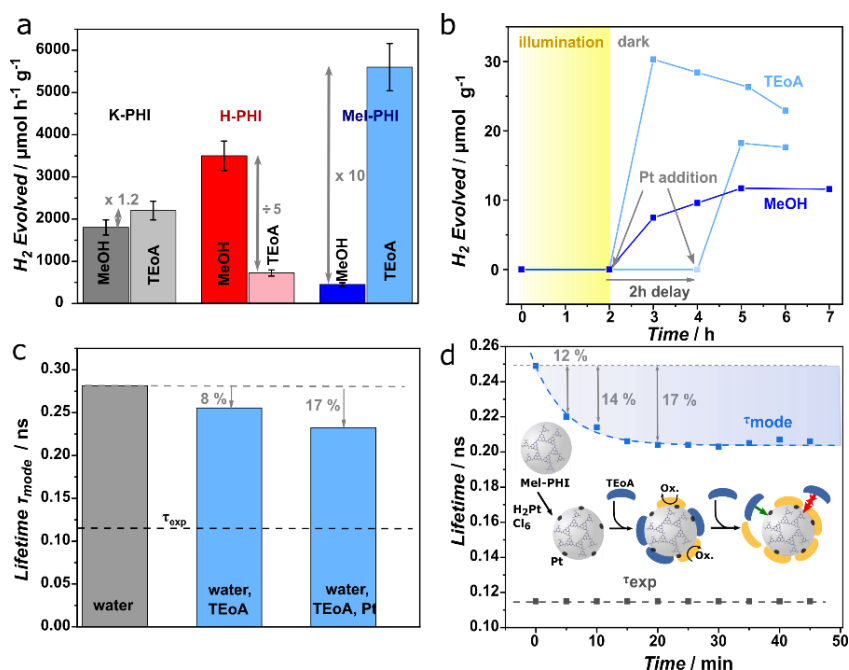


Figure 6.5: Photocatalytic hydrogen evolution and photoluminescence spectroscopy of Mel-PHI. a) Hydrogen evolution of K-PHI, H-PHI and Mel-PHI at optimized Pt loadings with the donors MeOH and TEOA. b) “Dark photocatalysis” with MeOH and TEOA as donor. c) PL lifetimes of Mel-PHI comparing the effect of donor addition as well as the case with donor and deposited Pt after 1 h under photocatalytic conditions. The lifetime was fitted with two different functions represented by τ_{exp} and τ_{mode} . d) PL lifetime evolution of Mel-PHI under photocatalytic conditions, i.e. after TEOA and H_2PtCl_6 addition under continuous illumination (AM 1.5 G, 100 mW cm^{-2}) and the illustration of the surface modification process under photocatalytic conditions.

Next, we took a closer look at the interface between Mel-PHI and the surrounding solution. The Brunauer-Emmett-Teller (BET) surface area of Mel-PHI is only $27.3 \text{ m}^2 \text{ g}^{-1}$ and hence comparable to that of K-PHI and H-PHI (Figure S3.46). We therefore rule out a surface area effect as the main reason for the increased HER rates. However, we observe pronounced agglomeration of suspended Mel-PHI particles during the photocatalysis experiments when methanol or 4-MBA are used as donors. Only in the presence of TEOA, this agglomeration of particles is suppressed, which is

most probably a consequence of the surfactant function of TEOA.^[64-66] This tendency could be confirmed and rationalized by zeta-potential measurements, where Mel-PHI in MeOH showed a close-to-neutral value (-1.6 mV), in contrast to the presence of TEOA (-37.2 mV), which apparently stabilizes the suspended particles. This effect can be explained by the slightly more hydrophobic character of Mel-PHI (Figure S3.47-S3.49, Table S3.8) compared to K-PHI as evidenced by contact angle measurements, and especially by the more efficient hydrogen bonding interactions between the amphiphilic electron donor and the triazine periphery of Mel-PHI, giving rise to an enhanced interaction with TEOA. This is in line with previous observations by Cooper *et al.* for hydrophilic sulfone containing polymer photocatalysts,^[67-69] where wettability was identified as crucial parameter for electron transfer during proton reduction. Our study demonstrates that interfacial effects in general are a bottleneck reaction, i.e. hole extraction, which is also important to enable efficient charge carrier separation and with it, high HER rates.

Long-term measurements, however, reveal a strong decrease in photocatalytic HER rate if TEOA is used as donor (Figure S3.50, S3.51). The apparent shorter stability of the photocatalytic system in the presence of TEOA as an electron donor had been widely observed, but the reason for this behavior has not been resolved yet, to the best of our knowledge.^[21, 62, 70] Degradation of Mel-PHI during photocatalysis could be safely ruled out by PXRD, FT-IR, NMR and XPS analysis after photocatalysis (Figure S3.52-S3.58). It rather appears that the strong adsorption of various TEOA oxidation products^[71, 72] to the catalyst's surface is the reason for the strong decrease in activity, hindering fresh TEOA to interact with PHI (Figure S3.59-S3.61, Scheme S3.2). To verify this hypothesis, constant flow GC measurements were used to disentangle the desired process from the fast parasitic surface blocking (Figure S3.50, Table S3.9). By fitting the exponential decay of the hydrogen evolution rate, an initial hydrogen evolution rate as high as $5566 \pm 287 \mu\text{mol h}^{-1} \text{g}^{-1}$ can be obtained, which is followed by an exponential decay of activity, levelling out at $1343 \pm 71 \mu\text{mol h}^{-1} \text{g}^{-1}$ (-75%) after 5 h. Indeed, washing off the photocatalyst with acetone, which is a good solvent for TEOA and some of its oxidation products, showed a restoration effect (Figure S3.51). In contrast, the addition of fresh donor only or washing with water did not restore the photocatalytic hydrogen rate, since oxidation products of TEOA remain bound to the Mel-PHI surface (Figure S3.54-62, Scheme S3.2).

To better understand the origin of the differences between the photocatalytic properties of Mel-PHI in the presence of different donors, photoluminescence (PL) measurements were performed under different conditions, i.e. in the presence of TEOA or MeOH, and with or without Pt deposited on the materials. In general, all PL emission spectra have a similar shape, ranging from 400 to 800 nm with a maximum intensity at 450 nm (Figure S3.63). The addition of TEOA causes an enhancement of the total PL intensity by 55%, which indicates an enhancement in the recombination rate due to the interaction of Mel-PHI with TEOA, whereas for MeOH, no such effect is observable (Figure S3.63, S3.64). In contrast, K-PHI shows a total PL intensity depletion

independent of the added donor, which is even stronger in the presence of Pt, pointing to different donor interactions in Mel-PHI and K-PHI (Figure S3.63, S3.64).

Next, we studied the materials' PL lifetimes by exciting them at a wavelength of 370 nm and probing at 480 nm. The signal was fitted by a convolution of an exponential decay function with a lifetime τ_{exp} and a Γ -distribution of lifetimes, which has a characteristic value at its maximum, τ_{mode} (Figure S3.65, S3.66).^[73] The first, exponential decay process can be attributed to an internal recombination in the bulk, since it is independent of the environment and fits well with the fastest values obtained for electron decay in transient absorption spectroscopy (TAS) experiments for melon-type CN_x .^[26, 60] The Γ -distribution however describes the surface mediated process, since each decay senses a different local density of states (e.g. by particle size or shape),^[74] and is therefore better suited as a descriptor for photocatalytic effects.

Interestingly, the overall lifetimes (radiative and non-radiative) are reduced after the addition of TEOA, by 8% (Figure 6.5c). This is consistent with previous carbon nitride-based studies^[26, 60, 75, 76] showing that an excessive accumulation of stabilized electrons leads to enhanced recombination of continuously photo-generated electron-hole pairs during illumination in presence of a donor. Here, stored charges do not contribute to the PL measurement in this lifetime regime. This accelerated recombination is revealed more strongly with TEOA than with MeOH due to the enhanced interaction and hence, faster charging kinetics. Consistent with it an overall less pronounced effect is observed in K-PHI (Figure S3.67-S3.69). The further addition of Pt to the TEOA containing system decreases the characteristic lifetime (τ_{mode}) even stronger in comparison to the aqueous system without donor, by 17%, in line with observations in the literature.^[77] Here, a new, non-radiative reaction path for charge carriers is enabled (via Pt). When comparing samples in similar environments, such as Mel-PHI with Pt in TEOA or MeOH, it can be argued that the longer the lifetime of photo-generated charges, the higher the probability that those charges can be used in photocatalysis,^[77-79] as it is the case for the Mel-PHI-Pt system in TEOA. A kinetic PL analysis monitoring the PL lifetime evolution from the beginning of a photocatalytic experiment (i.e. Mel-PHI with TEOA and H_2PtCl_6 added) onwards helps us to shed light on the overall process and hence also the temporally decreasing photocatalytic hydrogen evolution observed with TEOA (Figure 6.5d, S3.50). We observe that the lifetime of Pt containing Mel-PHI continuously and monotonously decreases over time. Within the first 15 min of illumination, i.e. while Pt is photo-deposited, a slow decrease of τ_{mode} can be observed (Figure 6.5d). The decrease of τ_{mode} reaches ~12% and ~14% after 5 and 10 min and then stabilizes at ~17% after 15 min. In principle, this is consistent with the formation and accumulation of oxidation products of TEOA on the Mel-PHI surface as discussed earlier, which can favor charge recombination on the surface. Hence, when studying the interaction with donors, different contributions need to be balanced. While exciton separation and charge extraction must be efficient at the interface, the desorption of the oxidation product must also remain possible to enable not only efficient, but also sustained photocatalytic hydrogen evolution.

6.3. Conclusion

Our work reports the first covalent modification of 2D poly(heptazine imide) and reveals the significant impact of surface functionalization on the optoelectronic properties and colloidal stability of Mel-PHI, with the effect of boosting its photocatalytic performance. The successful functionalization with melamine was evidenced by a kaleidoscope of spectroscopic and microscopic techniques and supported by quantum-chemical calculations. With a well-defined surface modification in place, Mel-PHI presents itself as a powerful model system to study the interplay of various factors and their impact on photocatalytic performance, including intrinsic effects such as exciton localization and polarity, and extrinsic effects such as colloidal stability, wettability, interaction with the sacrificial electron donor, and interfacial charge transfer. As a result of the covalent functionalization, the catalyst—electron—donor interaction and stabilization of the catalysts suspension are enhanced and, hence, hole quenching at the interface becomes more efficient. Consequently, we observe a distinctly different dependence of the photocatalytic activity on the donor in the three PHI-based materials K-, H-, and Mel-PHI. Specifically, the decreased surface polarity in Mel-PHI enhances its colloidal stability and interaction with TEOA significantly, preventing agglomeration and boosting the photocatalytic hydrogen evolution rate ($5570 \mu\text{mol h}^{-1} \text{g}^{-1}$) by a factor of 10 compared to MeOH at Pt-loadings of only 1.75 wt%, thus outperforming most other carbon nitride materials. We also show that the ability of Mel-PHI to trap and store light-induced electrons can benefit from the surface functionalization as well as the use of TEOA as an electron donor, which again testifies towards the important, yet underappreciated role of interfacial interactions for hole quenching on carbon nitrides. While fast hole extraction is key to prevent recombination, care needs to be taken that donor-assisted charge extraction does not become kinetically limiting due to the accumulation of oxidation products at the Mel-PHI surface. Our findings can thus be cast in a modified Sabatier's principle according to which the electron donor should interact maximum efficiently with the photocatalyst, but also the oxidation product should quickly desorb thereafter to allow the influx of new donor molecules to react at the surface. Hence, if sacrificial agents are deployed, the charge separation at catalytic interfaces, which is assisted by an optimal donor interaction, should be considered as one of the key parameters for a targeted design of highly active photocatalytic materials. On a more general level, we anticipate that our findings have implications also for other photocatalytic redox reactions, including dye sensitized systems and solar batteries, where the rate of product formation or charge transfer is limited by extraction of the counter charge, which often is the kinetic bottleneck. In addition, these findings can pave the way for tailored functionalization of carbon nitrides to enhance reaction selectivity.

6.4. Bibliography

- [1] A. Fujishima, K. Honda, *Nature* **1972**, 238 (5358), 37-38.
- [2] J. Liebig, *Annalen der Pharmacie* **1834**, 10 (1), 1-47.
- [3] X. Wang, K. Maeda, A. Thomas, K. Takanabe, G. Xin, J. M. Carlsson, K. Domen, M. Antonietti, *Nat. Mater.* **2009**, 8 (1), 76-80.
- [4] B. V. Lotsch, M. Döblinger, J. Sehnert, L. Seyfarth, J. Senker, O. Oeckler, W. Schnick, *Chem.–Eur. J.* **2007**, 13 (17), 4969-4980.
- [5] H. Schlöberger, J. Kröger, G. Savasci, M. W. Terban, S. Bette, I. Moudrakovski, V. Duppel, F. Podjaski, R. Siegel, J. Senker, R. E. Dinnebier, C. Ochsenfeld, B. V. Lotsch, *Chem. Mater.* **2019**, 31 (18), 7478-7486.
- [6] I. F. Teixeira, E. C. M. Barbosa, S. C. E. Tsang, P. H. C. Camargo, *Chem. Soc. Rev.* **2018**, 47 (20), 7783-7817.
- [7] F. K. Kessler, Y. Zheng, D. Schwarz, C. Merschjann, W. Schnick, X. Wang, M. J. Bojdys, *Nat. Rev. Mater.* **2017**, 2 (6), 17030.
- [8] V. W.-h. Lau, D. Klose, H. Kasap, F. Podjaski, M.-C. Pignié, E. Reisner, G. Jeschke, B. V. Lotsch, *Angew. Chem. Int. Ed.* **2017**, 56 (2), 510-514.
- [9] A. Savateev, B. Kurpil, A. Mishchenko, G. Zhang, M. Antonietti, *Chem. Sci.* **2018**, 9 (14), 3584-3591.
- [10] F. Podjaski, J. Kröger, B. V. Lotsch, *Adv. Mater.* **2018**, 30 (9), 1705477.
- [11] V. W.-h. Lau, M. B. Mesch, V. Duppel, V. Blum, J. Senker, B. V. Lotsch, *J. Am. Chem. Soc.* **2015**, 137 (3), 1064-1072.
- [12] M. Peer, M. Lusardi, K. F. Jensen, *Chem. Mater.* **2017**, 29 (4), 1496-1506.
- [13] K. S. Lakhi, D.-H. Park, K. Al-Bahily, W. Cha, B. Viswanathan, J.-H. Choy, A. Vinu, *Chem. Soc. Rev.* **2017**, 46 (1), 72-101.
- [14] Y. Wang, M. K. Bayazit, S. J. A. Moniz, Q. Ruan, C. C. Lau, N. Martsinovich, J. Tang, *Energ. Environ. Sci.* **2017**, 10 (7), 1643-1651.
- [15] J. Ran, T. Y. Ma, G. Gao, X.-W. Du, S. Z. Qiao, *Energ. Environ. Sci.* **2015**, 8 (12), 3708-3717.
- [16] Z. Chen, T.-T. Fan, X. Yu, Q.-L. Wu, Q.-H. Zhu, L.-Z. Zhang, J.-H. Li, W.-P. Fang, X.-D. Yi, *J. Mater. Chem. A* **2018**, 6 (31), 15310-15319.
- [17] K. Kailasam, A. Fischer, G. Zhang, J. Zhang, M. Schwarze, M. Schröder, X. Wang, R. Schomäcker, A. Thomas, *ChemSusChem* **2015**, 8 (8), 1404-1410.
- [18] C. Bai, J. Bi, J. Wu, Y. Han, X. Zhang, *New J. Chem.* **2018**, 42 (19), 16005-16012.
- [19] M. Luo, Q. Yang, K. Liu, H. Cao, H. Yan, *Chem. Commun.* **2019**, 55 (41), 5829-5832.
- [20] M. Kombo, L.-B. Ma, Y.-N. Liu, X.-X. Fang, N. Ullah, A. H. Odda, A.-W. Xu, *Catal. Sci. Technol.* **2019**, 9 (9), 2196-2202.
- [21] V. W.-h. Lau, V. W.-z. Yu, F. Ehrat, T. Botari, I. Moudrakovski, T. Simon, V. Duppel, E. Medina, J. K. Stolarczyk, J. Feldmann, V. Blum, B. V. Lotsch, *Adv. Energy Mater.* **2017**, 7 (12), 1602251.
- [22] V. W.-h. Lau, I. Moudrakovski, T. Botari, S. Weinberger, M. B. Mesch, V. Duppel, J. Senker, V. Blum, B. V. Lotsch, *Nat. Commun.* **2016**, 7 (1), 12165.
- [23] W. Ren, J. Cheng, H. Ou, C. Huang, M.-M. Titirici, X. Wang, *ChemSusChem* **2019**, 12 (14), 3257-3262.
- [24] Y. Wang, A. Vogel, M. Sachs, R. S. Sprick, L. Wilbraham, S. J. A. Moniz, R. Godin, M. A. Zwijnenburg, J. R. Durrant, A. I. Cooper, J. Tang, *Nat. Energy* **2019**, 4 (9), 746-760.
- [25] T. Banerjee, F. Podjaski, J. Kröger, B. P. Biswal, B. V. Lotsch, *Nat. Rev. Mater.* **2021**, 6, 168-190.
- [26] R. Godin, Y. Wang, M. A. Zwijnenburg, J. Tang, J. R. Durrant, *J. Am. Chem. Soc.* **2017**, 139 (14), 5216-5224.
- [27] G. Zhang, L. Lin, G. Li, Y. Zhang, A. Savateev, S. Zafeirotos, X. Wang, M. Antonietti, *Angew. Chem. Int. Ed.* **2018**, 57 (30), 9372-9376.
- [28] M. Döblinger, B. V. Lotsch, J. Wack, J. Thun, J. Senker, W. Schnick, *Chem. Commun.* **2009**, (12), 1541-1543.
- [29] T. Botari, W. P. Huhn, V. W.-h. Lau, B. V. Lotsch, V. Blum, *Chem. Mater.* **2017**, 29 (10), 4445-4453.
- [30] N. E. Braml, A. Sattler, W. Schnick, *Chem.–Eur. J.* **2012**, 18 (6), 1811-1819.
- [31] C. Fettkenhauer, J. Weber, M. Antonietti, D. Dontsova, *RSC Adv.* **2014**, 4 (77), 40803-40811.
- [32] S. Acharya, S. Martha, P. C. Sahoo, K. Parida, *Inorg. Chem. Front.* **2015**, 2 (9), 807-823.
- [33] B. V. Lotsch, W. Schnick, *Chem.–Eur. J.* **2007**, 13 (17), 4956-4968.

- [34] A. Sattler. Investigations into s-Heptazine-Based Carbon Nitride Precursors. LMU Munich, **2010**.
- [35] E. Wirnhier, M. Döblinger, D. Gunzelmann, J. Senker, B. V. Lotsch, W. Schnick, *Chem.– Eur. J.* **2011**, *17* (11), 3213-3221.
- [36] E. Wirnhier, M. B. Mesch, J. Senker, W. Schnick, *Chem.– Eur. J.* **2013**, *19* (6), 2041-2049.
- [37] T. Saplinova, V. Bakumov, T. Gmeiner, J. Wagler, M. Schwarz, E. Kroke, *Z. Anorg. Allg. Chem.* **2009**, *635* (15), 2480-2487.
- [38] B. Jürgens, E. Irran, J. Senker, P. Kroll, H. Müller, W. Schnick, *J. Am. Chem. Soc.* **2003**, *125* (34), 10288-10300.
- [39] T. S. Miller, A. B. Jorge, T. M. Suter, A. Sella, F. Corà, P. F. McMillan, *Phys. Chem. Chem. Phys.* **2017**, *19* (24), 15613-15638.
- [40] P. J. Wilson, T. J. Bradley, D. J. Tozer, *J. Chem. Phys.* **2001**, *115* (20), 9233-9242.
- [41] F. Jensen, *J. Chem. Theory Comput.* **2015**, *11* (1), 132-138.
- [42] M. Ernzerhof, G. E. Scuseria, *J. Chem. Phys.* **1999**, *110* (11), 5029-5036.
- [43] C. Adamo, V. Barone, *J. Chem. Phys.* **1999**, *110* (13), 6158-6170.
- [44] S. Grimme, J. Antony, S. Ehrlich, H. Krieg, *J. Chem. Phys.* **2010**, *132* (15), 154104.
- [45] A. Schäfer, C. Huber, R. Ahlrichs, *J. Chem. Phys.* **1994**, *100* (8), 5829-5835.
- [46] F. Weigend, R. Ahlrichs, *Phys. Chem. Chem. Phys.* **2005**, *7* (18), 3297-3305.
- [47] J. Kussmann, C. Ochsenfeld, *J. Chem. Theory Comput.* **2015**, *11* (3), 918-922.
- [48] J. Kussmann, C. Ochsenfeld, *J. Chem. Phys.* **2013**, *138* (13), 134114.
- [49] M. B. Mesch, K. Bärwinkel, Y. Krysiak, C. Martineau, F. Taulelle, R. B. Neder, U. Kolb, J. Senker, *Chem.– Eur. J.* **2016**, *22* (47), 16878-16890.
- [50] R. A. El-Ghazawy, A. G. Mahmoud, M. J. Ferreira, C. S. B. Gomes, P. T. Gomes, K. A. Shaffei, A. M. Atta, *J. Polym. Res.* **2014**, *21* (6), 480.
- [51] H. Yu, R. Shi, Y. Zhao, T. Bian, Y. Zhao, C. Zhou, G. I. N. Waterhouse, L.-Z. Wu, C.-H. Tung, T. Zhang, *Adv. Mater.* **2017**, *29* (16), 1605148.
- [52] K. Schwinghammer, M. B. Mesch, V. Duppel, C. Ziegler, J. Senker, B. V. Lotsch, *J. Am. Chem. Soc.* **2014**, *136* (5), 1730-1733.
- [53] S. Yang, Y. Gong, J. Zhang, L. Zhan, L. Ma, Z. Fang, R. Vajtai, X. Wang, P. M. Ajayan, *Adv. Mater.* **2013**, *25* (17), 2452-2456.
- [54] X. Fu, X. Hu, Z. Yan, K. Lei, F. Li, F. Cheng, J. Chen, *Chem. Commun.* **2016**, *52* (8), 1725-1728.
- [55] H. Liu, D. Chen, Z. Wang, H. Jing, R. Zhang, *Appl. Catal., B* **2017**, *203*, 300-313.
- [56] A. Jin, Y. Jia, C. Chen, X. Liu, J. Jiang, X. Chen, F. Zhang, *J. Phys. Chem. C* **2017**, *121* (39), 21497-21509.
- [57] L. Lin, C. Wang, W. Ren, H. Ou, Y. Zhang, X. Wang, *Chem. Sci.* **2017**, *8* (8), 5506-5511.
- [58] J. M. Osorio-Guillén, W. F. Espinosa-García, C. M. Araujo, *J. Chem. Phys.* **2015**, *143* (9), 094705.
- [59] Y. Li, F. Gong, Q. Zhou, X. Feng, J. Fan, Q. Xiang, *Appl. Catal., B* **2020**, *268*, 118381.
- [60] W. Yang, R. Godin, H. Kasap, B. Moss, Y. Dong, S. A. J. Hillman, L. Steier, E. Reisner, J. R. Durrant, *J. Am. Chem. Soc.* **2019**, *141* (28), 11219-11229.
- [61] G. Vázquez, E. Alvarez, R. Rendo, E. Romero, J. M. Navaza, *J. Chem. Eng. Data* **1996**, *41* (4), 806-808.
- [62] Y. Wang, J. Hong, W. Zhang, R. Xu, *Catal. Sci. Technol.* **2013**, *3* (7), 1703-1711.
- [63] M. Liu, P. Xia, L. Zhang, B. Cheng, J. Yu, *ACS Sustain. Chem. Eng.* **2018**, *6* (8), 10472-10480.
- [64] P. Bhattacharyya, S. Paul, A. R. Das, *RSC Adv.* **2013**, *3* (10), 3203-3208.
- [65] M. Khandelwal, S. H. Hur, J. S. Chung, *Chem. Eng. J.* **2019**, *363*, 120-132.
- [66] B. Song, C. Sizemore, L. Li, X. Huang, Z. Lin, K.-s. Moon, C.-P. Wong, *J. Mater. Chem. A* **2015**, *3* (43), 21789-21796.
- [67] T. Banerjee, B. V. Lotsch, *Nat. Chem.* **2018**, *10* (12), 1175-1177.
- [68] D. J. Woods, S. A. J. Hillman, D. Pearce, L. Wilbraham, L. Q. Flagg, W. Duffy, I. McCulloch, J. R. Durrant, A. A. Y. Guilbert, M. A. Zwijnenburg, R. S. Sprick, J. Nelson, A. I. Cooper, *Energ. Environ. Sci.* **2020**, *13* (6), 1843-1855.
- [69] X. Wang, L. Chen, S. Y. Chong, M. A. Little, Y. Wu, W.-H. Zhu, R. Clowes, Y. Yan, M. A. Zwijnenburg, R. S. Sprick, A. I. Cooper, *Nat. Chem.* **2018**, *10* (12), 1180-1189.
- [70] L. Stegbauer, K. Schwinghammer, B. V. Lotsch, *Chem. Sci.* **2014**, *5* (7), 2789-2793.
- [71] B. Kurpil, Y. Markushyna, A. Savateev, *ACS Catal.* **2019**, *9* (2), 1531-1538.
- [72] S. Horikoshi, N. Watanabe, M. Mukae, H. Hidaka, N. Serpone, *New J. Chem.* **2001**, *25* (8), 999-1005.

- [73] A. C. Fogarty, A. C. Jones, P. J. Camp, *Phys. Chem. Chem. Phys.* **2011**, 13 (9), 3819-3830.
- [74] A. Jiménez-Solano, J. F. Galisteo-López, H. Míguez, *Small* **2015**, 11 (23), 2727-2732.
- [75] Z. Chen, Q. Zhang, Y. Luo, *Angew. Chem. Int. Ed.* **2018**, 57 (19), 5320-5324.
- [76] M. Z. Rahman, C. B. Mullins, *Acc. Chem. Res.* **2019**, 52 (1), 248-257.
- [77] S.-W. Cao, X.-F. Liu, Y.-P. Yuan, Z.-Y. Zhang, J. Fang, S. C. J. Loo, J. Barber, T. C. Sum, C. Xue, *Phys. Chem. Chem. Phys.* **2013**, 15 (42), 18363-18366.
- [78] D. Zheng, C. Huang, X. Wang, *Nanoscale* **2015**, 7 (2), 465-470.
- [79] M. V. Dozzi, C. D'Andrea, B. Ohtani, G. Valentini, E. Selli, *J. Phys. Chem. C* **2013**, 117(48), 25586-25595.

7. Conductivity insights and correlation to photocatalytic hydrogen evolution in ionic PHI

The work in this chapter was reproduced and adapted from:

Conductivity mechanism in ionic 2D carbon nitrides: from hydrated ion motion to enhanced photocatalysis

Julia Kröger, Filip Podjaski, Gökçen Savasci, Alberto Jiménez-Solano, Igor Moudrakovski, Maxwell W. Terban, Sebastian Bette, Viola Duppel, Markus Joos, Alessandro Senocrate, Robert Dinnebier, Christian Ochsenfeld and Bettina V. Lotsch

Submitted

Julia Kröger and Filip Podjaski conceived the project. Julia Kröger synthesized the material, performed most of the structural characterization methods, as well as all photocatalysis and electrochemical measurements. Julia Kröger evaluated the experiments and wrote the manuscript with assistance of Filip Podjaski. Gökçen Savasci performed the quantum-chemical calculations, which were supervised by Christian Ochsenfeld. Igor Moudrakovski performed NMR measurements. Alberto Jiménez-Solano performed PL measurements. Maxwell W. Terban and Sebastian Bette performed PDF and XRD measurements, analysis and simulations, with supervision of Robert Dinnebier. Viola Duppel conducted TEM analysis. Filip Podjaski, Alessandro Senocrate and Markus Joos assisted the design and analysis of electrochemical measurements. All authors assisted the analysis of their respective experiments. Filip Podjaski and Bettina V. Lotsch supervised the project.

Supporting information can be found in Chapter 9.4.

Abstract

Carbon nitrides are among the most studied materials for photocatalysis, however, limitations arise from inefficient charge separation and transport within the material. Here, this aspect is

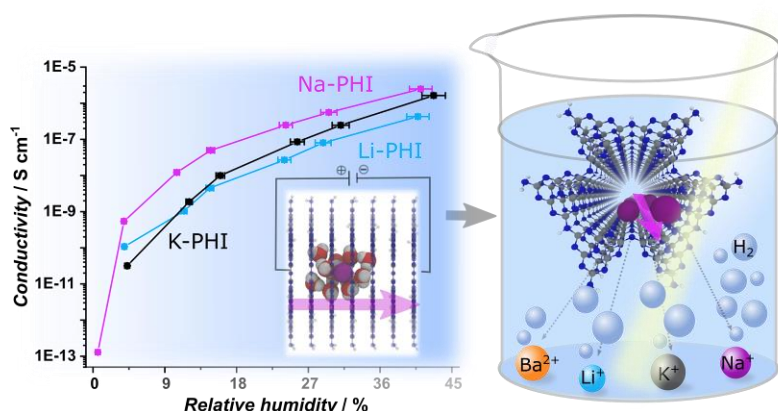


Figure 7.1: Table of content figure for conductivity analysis in poly(heptazine imide) and its influence on photocatalysis.

addressed in the 2D carbon nitride poly(heptazine imide) (PHI) by investigating the influence of various counterions, such as $M = \text{Li}^+$, Na^+ , K^+ , Cs^+ , Ba^{2+} , NH_4^+ and tetramethyl ammonium, on the material's conductivity and photocatalytic activity. These ions in the PHI pores affect the stacking of the 2D layers, which further influences the predominantly ionic conductivity in M -PHI.

Na-containing PHI outperforms the other *M*-PHI in various relative humidity (RH) environments (0-42 %RH) in terms of conductivity, likely due to pore channel geometry and size of the (hydrated) ion. With increasing RH, the ionic conductivity increases by 4-5 orders of magnitude (for Na-PHI up to 10^{-5} S cm^{-1} at 42 %RH). At the same time, the highest photocatalytic hydrogen evolution rate is observed for Na-PHI, which is mirrored by increased photo-generated charge carrier lifetimes, pointing to efficient charge carrier stabilization by mobile ions. These results indicate that ionic conductivity is an important parameter that can influence the photocatalytic activity. Besides, RH-dependent ionic conductivity is of high interest for separators, membranes, or sensors.

Introduction

Our energy-intensive society has an increasing demand for alternative, renewable energy sources due to their natural abundance and increasing environmental pollution by the current predominantly used energy sources.^[1] Consequently, solar-driven energy conversion technologies, including photocatalytic water splitting, are coming to the fore, with an increasing focus on earth-abundant organic materials. Among the wide variety of photocatalysts, carbon nitride polymers are among the most widely studied classes of semiconductor materials due to their affordability and ease of synthesis, chemical and thermal stability, suitably positioned visible light band gap, and high activity. Since the first report in 2009 by Wang *et al.*^[2] on the photocatalytic activity of 1D melon-type carbon nitride for water splitting, the number of reports on modified carbon nitrides with increasing performance has grown tremendously.^[3]

In recent years, a novel carbon nitride called poly(heptazine imide) (PHI) was identified, bearing an intriguing dual functionality of light absorption and simultaneous charge storage.^[4-6] This 2D polymer is built up of heptazine units forming pores, which can be filled with hydrated alkali ions, in contrast to the archetype carbon nitride melon, often simplistically called $\text{g-C}_3\text{N}_4$ in the literature.^[4] PHI's intrinsic energy storing ability have recently enabled hybrid concepts interfacing energy conversion and storage, such as "dark photocatalysis". Akin to natural photosynthesis it temporally decouples the process of light absorption from the catalytic conversion (or fixation) of light-induced charge carriers, which instead is triggered in the dark.^[5] By illuminating the yellow PHI suspension in the presence of an electron donor, a photo-reduced blue state is generated, which is stable for several days in the absence of oxygen.^[4, 5] Then, a co-catalyst like Pt can be added, and solar hydrogen is produced on demand in the absence of light. Photocatalytic propulsion of PHI Janus particles or a direct electric discharge of the photo-reduced, blue state is also possible, enabling solar batteries to be realized from this abundant material.^[6, 7] However, the long-term charge storage process itself can limit the direct photocatalytic activity by enhancing parasitic recombination of the light-induced charge carriers as charge builds up on the system.^[8] An in-depth study of charge storage mechanism is still missing while being of high interest for the targeted design of (photo)electrochemical energy conversion and storage.^[6, 9]

Besides charge storage, charge carrier transport is a crucial parameter, not only in electrical energy storing devices but also in photocatalysis.^[10] The overall photocatalytic performance of a particular system is the sum of various processes that occur at different timescales; from below ps to a few seconds, which in principle can all be limiting, but also individually optimized to obtain more efficient systems.^[11, 12] These processes include light absorption, charge carrier separation, their transport to the solid-liquid interface and to the surface catalytic center or the co-catalyst, where catalytic reactions take place. At the moment, mobility and diffusion of charge carriers in carbon nitrides is not well understood. The pertinent picture is that of predominantly localized charge carriers with low mobility. Insights into charge carrier mobility and diffusion can thus provide valuable information on carrier lifetimes, diffusion lengths, electronic conductivity, activation energies for diffusion, and transfer coefficients.^[11, 13] In addition, it is not clear whether an intrinsic, enhanced ionic or electronic conductivity can be beneficial for lifetimes of photo-generated charges, which would increase the photocatalysis rate.

Carbon nitrides are generally considered polymeric semiconductors that behave like “quasi monomers”^[14] with largely localized charge carriers and low or local intrinsic conductivity. For example, Merschjann *et al.*^[15] characterized the charge transfer (of excitons as dominant charge carriers) in the 1D carbon nitride melon as an interlayer conduction mechanism by transient absorption spectroscopy (TAS). It was observed that the exciton dissociates into a singlet polaron pair, which then diffuses out-of-plane via overlapping molecular orbitals. Such transport is electronically beneficial in contrast to an electron transfer within the polymer chain, due to a high energy barrier caused by imide bridges, which interrupts in-plane conjugation.^[15, 16] Out-of-plane charge hopping was recently also postulated in the 2D carbon nitride poly(triazine imide) (PTI) by TAS and electrochemical measurements. Noda *et al.*^[17] reported an anisotropic charge transport behavior, where the out-of-plane overall conductivity σ (1.0×10^{-4} S cm⁻¹) was reported to be two orders of magnitude greater than the in-plane conductivity (1.5×10^{-6} S cm⁻¹). However, no distinction between the ionic (σ_{ion}) and electronic conductivity (σ_{el}) was reported, while it is likely that ions significantly contribute to the overall conductivity, since lithium ion motion in porous PTI was already reported for PTI-based cathode materials.^[18] Besides, proton transport via a Grotthuss mechanism was suggested for PTI in humid environments.^[19] With increasing humidity the conductivity was found to be enhanced by orders of magnitude,^[20, 21] which can be exploited in devices like field effect transistors^[22] or actuators.^[9, 23]

So far, little information is available on the dominant type of charge carrier transport (ionic σ_{ion} or electronic σ_{el}) for carbon nitrides, or the influence of conductivity on the photocatalytic performance. Since PHI has the unique ability to store long-lived electrons, we have chosen this carbon nitride as a model system to study its conductivity mechanism. Depending on the cation being present in the structural pores, we find that the stacking of the 2D PHI polymer is altered by the effective size of the hydrated cation and its interaction strength with the polymer backbone. This further influences the channel geometry and the ion motion within those channels. Cation

containing PHI (*M*-PHI), a mixed conductor, has an at least two orders of magnitude higher ion conductivity as compared to the electron conductivity. Due to an interplay of optimized geometry, effective ionic radius, and backbone interaction, dry Na-PHI exhibits an order of magnitude better conductivity than K-PHI, followed by $\text{Li}^+ \sim \text{Cs}^+ \sim \text{NH}_4^+ > \text{tetramethyl ammonium (TMA}^+) \gg \text{Ba}^{2+}$ containing PHI materials. This trend remains when increasing the relative humidity (RH) from dry conditions to ambient RH of approximately 42%, where all materials show an increase in conductivity of 4-5 orders of magnitude and are almost fully hydrated. In addition, we find that higher ion conduction correlates with a better stabilization of the photo-generated charges under photocatalytic conditions, which is mediated by the mobile counterions in the pores. Likewise, the highest photocatalytic hydrogen evolution rate is found for materials with highly mobile ions as in Na-PHI. Understanding the coupled electronic-ionic processes described herein thus opens new design pathways for rationally enhancing the photocatalytic activity in ion-containing porous materials with tunable optoelectronic and ionic transport properties.^[10, 24-26]

7.1. Results and discussion

Structural analysis

Potassium containing poly(heptazine imide) (K-PHI) was synthesized by heating the 1D heptazine polymer melon in a KSCN salt melt as described previously.^[27] The resulting ionic 2D polymer hosts potassium ions in its 1D pore channels formed along the *c*-direction.^[4] Stirring K-PHI in a freshly prepared 1M $M\text{Cl}_x$ ($x = 1, 2$; $M = \text{Li, Na, K, Cs, Ba, tetramethyl ammonium (TMA), NH}_4$) aqueous solution multiple times results in facile ion exchange (*M*-PHI),^[28] as evidenced by elemental analysis (Table S4.1, Figure S4.1). The concentration of ions present in the PHI pores is not dependent on the type of alkali ion (Na, K or Li), but is reduced to half when K^+ is exchanged for Ba^{2+} ions, consistent with the requirement of overall charge balance. To investigate possible structural changes after ion exchange, the materials were analyzed by a combination of long-range and local structural and spectroscopic techniques, including powder X-ray diffraction (PXRD), total scattering pair distribution function (PDF) analysis, transmission electron microscopy (TEM), Fourier-transformed infrared (FT-IR), nuclear magnetic resonance (NMR) and UV-visible light (UV-vis) spectroscopy. Analysis of the stacking order of the 2D PHI layers suggests a structure-directing influence of the incorporated cation, as explained below.

For the as-synthesized material K-PHI, two distinct low angle reflections ($\bar{1}10$ and 010 at 8.03° 2θ / 11.0 \AA and 9.97° 2θ / 8.9 \AA) are observed, which are diagnostic of an ordered staggered stacking of the 2D layers (Figure 7.2a).^[4] When the local slipping directions become increasingly disordered, as demonstrated by recursive simulations of the stacking fashion using TOPAS,^[29] the two low-angle reflections become more diffuse (Figure S4.7-S4.9, Table S4.3), until both reflections merge, and an additional reflection ($\bar{1}20$) around 14° 2θ (6.3 \AA) becomes more pronounced (Figure S4.8).^[4] For small but random layer offsets, the apparent long-range order appears hexagonal, as would be the case for an ordered eclipsed stacking relationship, which is

the case for Li-PHI compared to other *M*-PHI materials. Similar behavior is observed in covalent organic frameworks.^[30] The water content has a significant impact on the stacking behavior, to an extent that the three-dimensional coherence is strongly decreased if the amount of water is reduced in the pores.^[4] The structure of Na-PHI is best described as intermediate to those of K-PHI and Li-PHI.

Lithium ions in an aqueous environment are known to form two hydration shells of 4 to 6 and 7 to 10 water molecules, respectively. In contrast, potassium and sodium ions coordinate only one inner hydration shell with 5 to 6 or 6 to 7 water molecules.^[31-33] In agreement with this trend, the water content, which can be removed by heating, detected by thermogravimetric analysis (TGA) for samples under ambient conditions was around 9-10 wt% (1.5-1.7 H₂O per heptazine or 2.0-2.3 H₂O per K⁺) for K-PHI, 12-13 wt% (2.0-2.2 H₂O per heptazine or 2.7-2.9 H₂O per Na⁺) for Na-PHI, and 14-15 wt% (2.3-2.4 H₂O per heptazine or 3.1-3.2 H₂O per Li⁺) for Li-PHI (Figure S4.17). Water retention was measured up to 473-523 K, suggesting that water strongly interacts with the cation or the polymer backbone and indicates that water cannot be removed completely, so that TGA can only detect a minimum amount of water being present (Figure S4.17, S4.48). TEM data of K-PHI, Na-PHI (*vide infra*), and Li-PHI are consistent with the PXRD data, confirming that the 2D backbone remains intact, but the layers adopt different stacking polytypes (Figure 7.2b-d). The diagnostic first two reflections in PXRD are also visible by TEM, with a constant value around 10.2 Å ($\bar{1}10$) for all three samples (being slightly smaller than in PXRD), but with decreasing distances of 8.8(±0.1) Å to 8.3(±0.1) Å (010) on going from K-PHI via Na-PHI to Li-PHI. This TEM observation is in line with signal broadening combined with a slight shift of the maximum of the second reflection to higher angles until merging of the first reflections in PXRD occurs. From these changes, a slightly different pore channel geometry for the different alkali ion containing PHI can be assumed.

Consistent with TEM data, FT-IR (Figure 7.2e, S4.14) and NMR spectroscopy (Figure S4.15) prove that only the stacking is affected by ion exchange, since the structure of the covalent 2D polymer backbone remains unchanged.^[4] The only change observed in direct ¹³C-NMR experiments is a line broadening in Li-PHI compared to K-PHI (Figure S4.15), whereas the peak position and intensities remain the same. The broadening of the signal at 167-168 ppm, corresponding to carbon atoms next to a primary amine group, points to a slightly larger disorder in the Li-PHI structure, which is consistent with ¹⁵N-CP-NMR experiments (Figure S4.15).^[34]

These findings are corroborated by PDF analysis. The polymer backbones of K-PHI, Na-PHI, and Li-PHI are shown to be the same due to similarity in sharp peaks assigned to intralayer atom-pair correlations at short distances up to approx. 5 Å (Figure S4.2-S4.6). Slight differences in the exact shape and relative intensities in the range above ~3 Å can be affected, for instance, by differences in local structuring of the pore content. Significant additional intensity is present in the range of 2.8 to 3.0 Å for the K-PHI sample, which corresponds to K-O and possibly K-N interactions (Figure 7.2g, h, S4.3). The apparent lack of such a correlation for Na-PHI and Li-PHI is explained by the

smaller scattering cross-sections of Na and Li relative to K. The position is expected to shift due to the smaller distance between the water and Na/Li ions as predicted by quantum chemical calculations (Figure S4.3, S4.10, S4.11, S4.50) - approx. 2.75 Å (K-O), 2.42 Å (Na-O), and 2.0 Å (Li-O). In fact, we do observe subtle increases in diffuse intensity that may correspond to the first Na-O and Li-O shells, respectively.

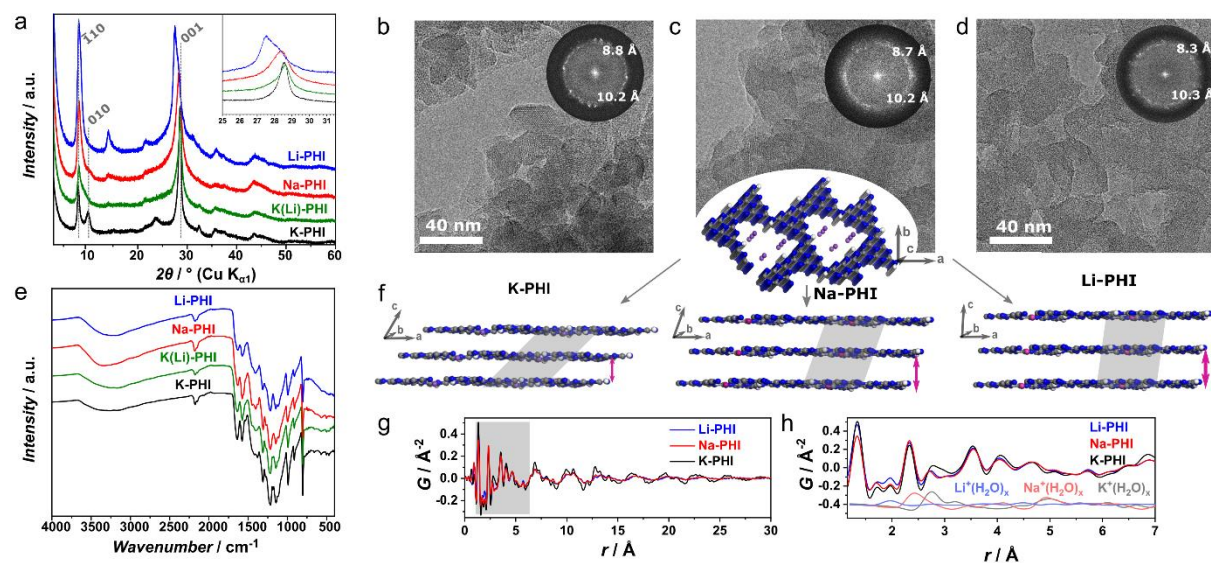


Figure 7.2: Comparison of PHI filled with different alkali ions in the pores. a) PXRD of K-, Na-, Li-, and K(Li)-PHI; b) TEM image of K-PHI and fast Fourier transformed (FFT) image (inset); c) TEM image of Na-PHI and inset showing fast Fourier transform (FFT); d) TEM image of Li-PHI and inset showing fast Fourier transform (FFT); e) FT-IR of K-, Na-, Li-, and K(Li)-PHI; f) Schematic of the idealized difference in stacking order between K-PHI, Na-PHI and Li-PHI and the resulting channels for ion transport (grey shading). g and h) Short- r range of PDFs of Li-, Na- and K-PHI. h) Zoom in the grey area in g). The PDF data for the K-/Na-/Li-water shells are obtained from quantum chemical calculations.

Local structure models, based on that previously determined for highly ordered K-PHI,^[4] were fit to the experimental PDFs to further probe for differences in the local stacking behavior (Figure 7.2g, h, S4.5). We found that while the interlayer distance in the 001 direction increases from K- (3.15 ± 0.01 Å) to Na- (3.17 ± 0.01 Å) to Li-PHI (3.18 ± 0.02 Å), the on-average neighbor layer offset over the first few interlayer distances appears to decrease (from 2.8 in K-PHI to 2.3 in Li-PHI) (Table S4.2). This observation also coincides with an increased disorder for both Na-PHI and Li-PHI indicated by broader interlayer stacking correlations. Taken in the context of the apparent hexagonal symmetry of the Li-PHI diffraction pattern, we can conclude the following: K^+ with their solvation shells drive a larger layer offset, combined with a more unidirectional ordering of the interlayer slipping. This leads to a triclinic lattice, though likely with occasional stacking faults, affecting the pore channel geometry.^[4] For Li-PHI, the differences in ion-solvation-layer interactions produce shorter slipping distances that are more directionally disordered, which leads to long-range averaging to a higher apparent symmetry. Less favorable interlayer interactions then likely result in the increased interlayer distances observed for Li-PHI. Na-PHI displays the predominantly K-PHI-type structure but with increased stacking disorder similar to Li-PHI (Figure 7.2f, S4.6-S4.9, Table S4.2, S4.3).^[4] Similar to K, Na rather tends to form only one hydration

shell,^[32, 35] however, the radius of hydrated sodium ion (3.6 Å) is slightly larger than the one of potassium (3.3 Å), which might cause the observed increase in layer distance.^[36]

The effect of the pore content in the PHI pores, which have a radius of only 3.8 Å,^[4, 6] on the stacking behavior was also tested with even larger ions. Ammonium ions do not affect the structure of PHI compared to K-PHI, most likely a consequence of the similar size of ammonium and potassium ions, both in the presence or absence of water (Table S4.4). In Cs-PHI, however, a disappearance or significant broadening of the stacking and in-plane reflections in PXRD experiments was observed (Figure S4.13). This loss might be due to partial dehydration of the Cs⁺^[37] due to a comparably low hydration energy,^[38] or a predicted enhanced interaction energy of carbon nitrides and Cs ions.^[39] Similar effects might be present in Ba-PHI, where no stacking reflection is visible any more. Yet, due to the much higher hydration energy of Ba²⁺,^[40] the ion is not likely to be de-hydrated and therefore is too large (4.0 Å) to reside in the pore of PHI (Figure S4.13, Table S4.4). The same is true for TMA⁺,^[37] where no ion exchange was observed (Table S4.1). Taking all these findings together, only the stacking behavior and hence the pore channel geometry is affected when exchanging the ions and modifying the water content in the PHI pores. However, only those hydrated ions can be exchanged that fit into the PHI pores, which might hint to a “sweet spot” enabling optimized backbone interactions, pore geometry and transport for a specific hydrated ion size. Especially, when taking into account the calculated minimum spacing for easy sodium ion motion, which was found to be slightly above, the pore diameter of the PHI pore (3.7 Å).^[41]

Conductivity analysis

As described above, the type of ion residing in the structural pores and the water content significantly influences the stacking of 2D PHI layers. To reveal if those changes have a possible impact on ion mobility and photocatalytic behavior, we first studied the overall conductivity of PHI.^[6, 28] The mobility of ions in the PHI pores was probed by different techniques spanning various timescales and diffusion distances: Electrochemical impedance spectroscopy (EIS), galvanostatic polarization measurements, and ⁷Li pulsed field gradient (PFG) NMR were used as long-range sensitive methods,^[42-44] whereas NMR line shape analysis and relaxometry were employed for correlating the macroscopic ion diffusion. Its microscopic origin is probed by temperature and frequency dependence of the diffusion-induced NMR spin-lattice or spin-spin relaxation rates, which are influenced by local dipolar-magnetic or quadrupolar-electric fluctuations.^[42-44]

First, the effect of humidity on the conductivity will be discussed, followed by an analysis including different types of ions in the PHI pores. For accurate humidity-dependent electrochemical measurements, the degree of swelling of PHI under humid conditions has to be known prior. Therefore, we analyzed the role of pore water in *M*-PHI by PXRD analysis at RHs between 1 % and 90 %, which reveals almost no change in the K-PHI structure with the state of hydration

(Figure 7.3a). The stacking reflection is only shifted from $28.27^\circ 2\theta$ (3.16 Å) at 1 %RH to $27.97^\circ 2\theta$ (3.22 Å) at 90 %RH, indicating that water is not intercalated in-between the layers, but rather within the pore channels, hence not causing swelling. Small changes seen by water uptake are reversible, however, a hysteresis in the wetting – drying behavior can be observed, possibly pointing to a strong interaction of water with the polymer backbone. Also by solid state NMR, no changes could be observed in the PHI structure due to drying (Figure S4.23).

To conduct EIS and galvanostatic direct current (DC) measurements the *M*-PHI powder was pressed to a pellet with the PHI particles arranging randomly (with approximately 85 % theoretical density) (Table S4.9). DC and impedance measurements of the various *M*-PHI samples with different applied currents were performed with ion-blocking electrodes since PHI was not stable in a non-blocking configuration (Figure S4.18-S4.22). Ionic and electronic conductivity were distinguished in DC measurements by the initial voltage jump of the steady-state response (Figure 7.3b, S4.24).^[45-48] The DC potential drop over a dried Na-PHI sample is 30 times higher compared to the sample under ambient conditions, i.e., the resistance is increased by a factor of 30 (Figure 7.3b), similar to the behavior of K- and Li-PHI (Figure S4.25, Table S4.6). Additionally, the DC curves for dry samples point to a dominant electric contribution. In contrast, *M*-PHI under ambient conditions at around 30-40 %RH showed a mixed conduction with a dominantly ionic contribution (10^{-7} - 10^{-8} S cm⁻¹) to the overall conductivity and a significantly smaller electronic conductivities by two orders of magnitude (10^{-9} - 10^{-10} S cm⁻¹) (Figure S4.27, S4.28, Table S4.7). The electronic conductivity seems not to be affected by the humidity, whereas the ionic conductivity is significantly increasing with enhanced humidity. Even further enhancement in conductivity (10^{-6} - 10^{-7} S cm⁻¹) can be observed for samples stored in a 75 %RH environment, clearly pointing to a significant contribution of the water content on the ion conduction.

To validate these results, EIS was measured in a frequency range of 10^{-2} - 10^6 Hz. In general, the Nyquist plots of all PHI samples can be described by one semi-circle at higher frequencies, corresponding to bulk transport processes and a constant phase element (or possibly a second semi-circle) at lower frequencies correlated to grain boundary or interface effects (Figure 7.3c, S4.29). The high-frequency response was confirmed as a bulk conduction process by extracting the capacitance (10^{-10} – 10^{-12} F) and dielectric constant (reaching values of 8-12) supported by PHI particle size-dependent impedance measurements as well as a study with variation of the pellet thickness (Figure S4.30-S4.34, Table S4.8), and might also hint to anisotropic conductivity in this 2D materials.^[49] The Nyquist plot of Na-PHI in 2-42 %RH is depicted in Figure 7.3c, showing only one high-frequency semi-circle over the whole humidity range (with a capacitance of 10^{-12} F). The overall conductivity, represented by the semi-circles, is depending on the water content, in accordance to DC measurements. The conductivity, influenced mainly by the ion motion, for (Na-, K-, Li-)PHI is increased by 4-5 orders of magnitude within this humidity range. However, Na-PHI outperforms the other materials by roughly one order of magnitude under all conditions (e.g. Na-PHI: $4.5 (\pm 3.0) \times 10^{-10}$ S cm⁻¹ at 2 %RH and $2.5 (\pm 1.0) \times 10^{-6}$ S cm⁻¹ at 42 %RH) (Figure 7.3d, S4.35).

Notably, with increasing water content, the dielectric constant of *M*-PHI increases from 5-6 under dry to 8-12 under ambient to 15-16 under humid conditions, as calculated from impedance data (Table S4.12). This increase suggests a more efficient dielectric screening of the cations by water molecules in response to an electric field, along with additional motional degrees of freedom with increasing pore water content, resulting in higher ion conductivity.

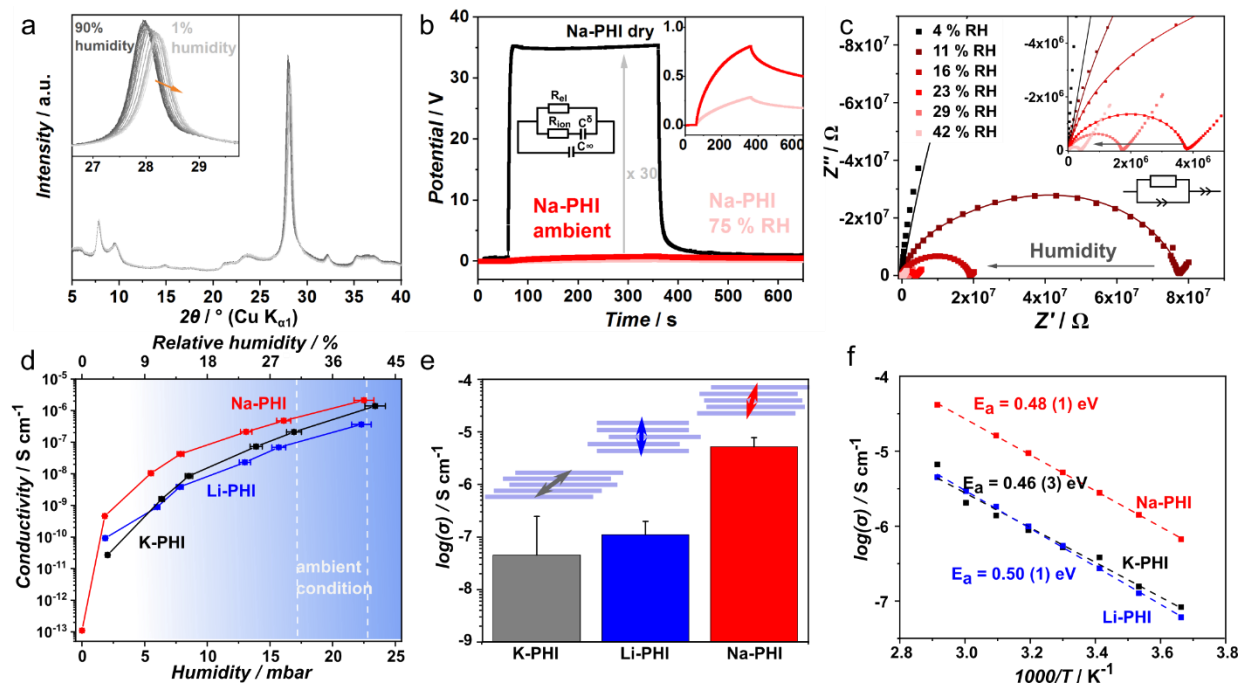


Figure 7.3: Analysis of ion conductivity in *M*-PHI. a) Humidity-dependent PXRD measurements of K-PHI from 1 to 90 %RH in 5 %RH steps and the 1 %RH steps for the last 5%; b) DC polarization experiments of Na-PHI for a dry sample (dried in vacuum oven for 1 day) (black), ambient conditions (around 35 %RH) (red) and 75 %RH (pink) with 2 nA applied; c) Humidity-dependent impedance measurements of Na-PHI from 4 up to 42 %RH mbar at 308 K (Ru sputtered pellet, which did not change the resistance compared to steel electrodes (Table S4.10)). Data of the first semi-circle were fitted with a (RQ) element; d) Overview of humidity-dependent conductivity extracted from impedance spectroscopy of K-, Na- and Li-PHI at 308 K with Ru sputtered contacts; e) Comparison of overall conductivities estimated by impedance measurements of ambient K-, Na-, and Li-PHI with suggested 1D ion conduction along the pore channels; f) Arrhenius plot of K-, Na-, and Li-PHI to determine the activation energy of ion conductivity under ambient conditions.

To investigate the effect of different ions on the conductivity, we looked at the conductivity at ambient conditions (around 30-40 %RH), where 9-15 wt% water is present in PHI, depending on the cation (Figure S4.17). The highest conductivity values of $5.0 (\pm 3.0) \times 10^{-6} \text{ S cm}^{-1}$ were obtained for Na-PHI (Li-PHI: $1.0 (\pm 1.0) \times 10^{-7} \text{ S cm}^{-1}$ and K-PHI: $6.0 (\pm 10.0) \times 10^{-8} \text{ S cm}^{-1}$) (Figure 7.3e with suggested directional conductivity). From these values the diffusion coefficients for the ion motion (D^0) were determined via the Nernst-Einstein equation (Na-PHI: $5.0 (\pm 0.7) \times 10^{-14} \text{ m}^2 \text{ s}^{-1}$, K-PHI and Li-PHI: $5.0 (\pm 0.7) \times 10^{-15} \text{ m}^2 \text{ s}^{-1}$) (Chapter 9.4.5). The fact that similar values for the activation energy of the three PHI materials were obtained ($E_a = 0.46\text{-}0.50 \text{ eV}$) (Figure 7.3f, S4.38) point to similar transport process in the materials and are in the expected range for polymeric systems.^[50-52] Under ambient conditions, the cations in the PHI pores are (almost) fully hydrated, which enables motion of the cations in the pores - in contrast to dry conditions, where the de-hydrated

cation is strongly interacting with the negatively charged PHI backbone and mainly electronic conductivity is measured with high activation energies (up to $E_a = 0.84 (\pm 0.6)$ eV, Figure S4.40).^[53] When increasing the water content, the transport mechanism of the hydrated cations in the PHI pores is similar for all pore fitting *M*-PHI, as the activation energies under ambient conditions are comparable. However, the overall conductivity values are dependent on the type of cation. This clearly points to a mixed contribution of the hydrated ion size, the stacking behavior of the 2D PHI layers, and hence the pore geometry, which is affected by the type of ion. An optimized hydrated cation size and pore geometry might therefore be fulfilled for Na-PHI, enabling a comparable fast ion conduction. This interpretation is further verified when looking at PHI containing Cs^+ , Ba^{2+} , NH_4^+ or TMA^+ ions. The conductivity obtained from EIS decreases from Cs- and NH_4 -PHI with similar hydrated ion radii ($1.0 (\pm 0.5) \times 10^{-7}$ S cm^{-1}) via TMA-PHI with partially remaining K^+ ($8.0 (\pm 9.0) \times 10^{-8}$ S cm^{-1}) to a complete breakdown for Ba-PHI ($1.0 (\pm 0.4) \times 10^{-11}$ S cm^{-1}) (Figure S4.41). As mentioned in the structure section, Ba^{2+} with its hydrated ion radius of 4.0 Å is too big (Table S4.4) to move along the PHI pores, and the energy for dehydration is comparably high, resulting in a low overall conductivity, which might be based on electronic contributions, since the ions are not mobile in this setting. All in all, these findings point to water-assisted ion motion, leading to humidity-enhanced conductivity. Such enhanced hydrated ion motion in the *M*-PHI channels in contrast to the non-hydrated ions is affected by the pore channel geometry and the size of the cation being present.

An important question to address is whether the observed ionic conductivity is partially due to mobile protons, as described for melon-type carbon nitrides.^[21, 54] To this end, the potassium ions were replaced by protons (forming H-PHI), and the conductivity was probed by EIS and DC measurements, which resulted in a two to three orders of magnitude lower overall conductivity (10^{-9} S cm^{-1}) of H-PHI compared to *M*-PHI (Figure S4.41, S4.42), even though the water content is increased in H-PHI (Figure S4.17). For H-PHI a similar electronic conductivity as *M*-PHI (10^{-9} S cm^{-1}) and an ionic conductivity of 10^{-10} S cm^{-1} was observed (Figure S4.27, Table S4.7). This suggests that the protons interact strongly with the PHI backbone and are not very mobile. At the same time, the even stronger conductivity decrease in Ba-PHI vs H-PHI is probably caused by structure disruption, hindering electron transport. We previously found electronic transport in PHI to be best described by a multiple trapping and release (MRT) process.^[12, 55]

Moreover, solid-state NMR spectroscopy was used to gain further insights into the microscopic mechanism of ion diffusion in Li- and Na-PHI. For all conditions both ^7Li and ^{23}Na NMR exhibit one single signal, resulting from hydrated alkali ions in the pores. However, interactions between the backbone and the ions cannot be entirely ruled out, caused by signal broadening (Figure 7.3e, S4.47). ^1H NMR analysis revealed a only broad signal around 4 ppm caused by water in the PHI pores, which could not be removed completely, even after extended sample drying (Figure S4.48), thus precluding NMR analysis.

The activation energy obtained by temperature-dependent ^7Li PFG NMR in Li-PHI ($E_a = 0.56$ (± 0.05) eV) (Figure S4.44) under ambient conditions (around 35 %RH) is comparable to the values received from EIS. However, the determined tracer diffusion coefficients for the lithium ion motion are at the sensitivity limit of NMR, so that those values are just taken as an upper limit for the ionic diffusivity ($D^{\text{tr}} 1.2$ (± 0.1) $\times 10^{-13}$ $\text{m}^2 \text{s}^{-1}$ at 343 K (Table S4.13), corresponding to 1.3 (± 0.2) $\times 10^{-5}$ S cm^{-1}). When increasing the humidity to 75 %RH, we revealed two diffusion processes above 353 K, characterized by substantially different diffusion coefficients on the order of 10^{-12} $\text{m}^2 \text{s}^{-1}$ and 10^{-10} $\text{m}^2 \text{s}^{-1}$ (Figure S4.44). This observation highlights two different transport processes co-existing within the sample at higher humidity and particularly at elevated temperatures. The mechanism behind a faster ion motion at higher temperatures requires further studies. A reason might be an additional lithium motion scheme in confined spaces, textural voids, grain boundaries or at the particle surface due to multilayer water adsorption^[56] in contrast to the ion motion inside the pores, which are more hindered due to interaction of the ion (or its hydration shell) with the backbone, resulting in a small change of the diffusion coefficient with temperature.

The differences between the line width in dry, ambient (approximately 35 %RH), and 75 %RH Li-PHI at room temperature (303 K) in ^7Li NMR line broadening experiments further proves an enhancement of lithium mobility with increasing humidity (FWHM of 2838 Hz at dry samples vs. 1418 Hz under ambient conditions, 1044 Hz in 75 %RH) (Figure 7.4a, S4.47). Such a water-assisted increase in ion conduction has not only been shown for polymers,^[53, 57] but also for layered inorganic systems,^[9] highlighting that 2D carbon nitrides may be intriguing candidates for ion-conducting membranes or separators. However, it must be stated that a considerable contribution of proton motion, especially at high humidity values, could not be fully excluded to contribute to the overall conductivity of *M*-PHI.

Next, variation of static ^7Li and ^{23}Na NMR line shapes under ambient conditions was analyzed at different temperatures, and the onset of motional narrowing was estimated, which occurs when the Li or Na jump rate exceeds the rigid lattice line width, averaging out the local dipolar interaction between the Li or Na spins (Figure 7.4b, c, S4.47-S4.49). The ^7Li signal is broad (full width at half maximum (FWHM) = 6700 Hz) at 193 K and gradually narrows with increasing temperature to a FWHM of 604 Hz (at 373 K), resulting in a jump rate of lithium of $\tau_c^{-1} \approx 6.7$ (± 5.0) $\times 10^3$ s^{-1} at 229 K and an uncorrelated tracer diffusion coefficient (D^{uc}) of 3.4 (± 0.3) $\times 10^{-16}$ $\text{m}^2 \text{s}^{-1}$ (Table S4.14). Extrapolating the conductivity values obtained by EIS, a smaller diffusion coefficient from EIS ($D^\sigma \sim 7 \times 10^{-17}$ $\text{m}^2 \text{s}^{-1}$ at 229 K) is obtained at similar temperatures, pointing to a faster ion motion on the microscopic scale analyzed in the FWHM analysis (on the kHz domain) in comparison to the macroscopic DC measurements. This is in line with a reduced activation energy of 0.37 (± 0.01) eV for the Li diffusion on a shorter time scale (Figure 7.4c) in contrast to 0.50 (± 0.01) eV for longer timescales. Further evidence of hindered lithium diffusion on the long-range due to the hydration shell can be found by humidity-dependent spin-lattice relaxation experiments for Li-PHI, which are sensitive to even shorter time intervals (Figure S4.46). In comparison, Na-PHI shows a slightly

lower onset temperature and a jump rate of $\tau_c^{-1} \approx 7.1 (\pm 6.0) \times 10^3 \text{ s}^{-1}$ at 206 K ($D^{\text{uc}} = 3.7 (\pm 0.4) \times 10^{-16} \text{ m}^2 \text{ s}^{-1}$) (Figure S4.49), as well as a slightly lower activation energy of 0.33 eV for shorter timescale measurements. This highlights a higher sodium mobility in the pores, also at shorter time scales in agreement to EIS results and substantiates the influence of the ion size and pore geometry on the mobility. However, at such low temperatures where the onset of motion narrowing is observed (240 K), water in the PHI pores might be frozen already, which would result in different activation energies and diffusion values, as evidenced by T_1 experiments of ^7Li , ^{23}Na , and ^1H below 240 K (Figure S4.45, S4.46).^[58, 59]

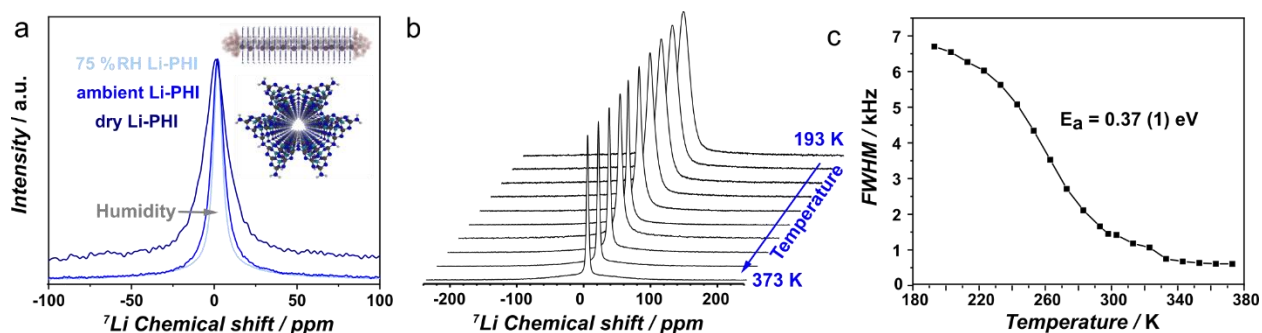


Figure 7.4: Humidity dependent ^7Li NMR measurements of Li-PHI. a) ^7Li NMR static measurements at 303 K of dry, ambient (approximately 35 %RH) and 75 %RH humid sample of Li-PHI. Inset shows the PHI pore filled with water and hydrated ions from the side and an empty staggered stacked pore from the top; b) Variable temperature ^7Li ssNMR spectra of Li-PHI; c) Motional narrowing curve of the static ^7Li -NMR line width (full width of half maximum (FWHM)) plotted against the temperature, with the corresponding activation energy for Li motion.

Quantum-chemical calculations

To obtain further insights into the impact of the type of ion in the pores, the stacking and pore structure on the conductivity, quantum-chemical calculations were performed on a model system of 21 stacked PHI pores (Chapter 9.4.7). For Li-PHI, lithium ions were calculated to have a first hydration shell of 5 water molecules in the PHI pores (Figure S4.53), in accordance with free solvated lithium ions, which have a hydration shell of 4 or 6 water molecules according to literature.^[32] In Na- and K-PHI, the first hydration shell is reduced by one (for Na^+) or two (for K^+) water molecules for ions residing in the PHI pore channel, in contrast to free solvated ions with six (Na^+) or seven (K^+) water molecules, in agreement with previously published work on K-PHI (Figure S4.53).^[4] Energy calculations of the ion-water interaction energy in the PHI pores also reflect this trend of a more reduced hydration shell in PHI pores containing larger alkali ions. Here, potassium ions are found to have a slightly stronger interaction with the PHI pore structure than Li^+ and Na^+ , which might explain the lower conductivity of K-PHI vs. Na-PHI (Figure S4.54-S4.56) due to stronger binding of K^+ . The comparably high hydration energy of Li^+ combined with the interaction energies of water molecules with the PHI backbone might explain the lower conductivity of Li^+ in comparison to Na^+ , resulting in an optimal ion-water-PHI polymer interaction for Na-PHI. Those results are in good agreement with the experimentally observed conductivity values. The theoretical results of two different pore model systems with different deprotonation

pattern of the imide bridges (which however do not include stacking faults) strongly suggest that the charge distribution on the backbone along with the stacking behavior impacts ion diffusion measured in the experiment as well. Hence, an interplay of hydrated ion size, stacking order, and interaction strength of ions with the polymer backbone has to be considered together for their combined impact on cation conductivity.

Correlation between conductivity and photocatalysis

Having established that *M*-PHI materials show predominant ionic conductivity under humid conditions, we now turn to whether a correlation between the observed conductivity and the photocatalytic activities in these materials exists.^[60, 61] One hint on a possible correlation was published recently, showing a more pronounced photoelectric response of K-PHI in the presence of a hole conducting polymer in contrast to bare K-PHI.^[62] Here, we use the series of *M*-PHI as a pertinent model system to study such correlations for the photocatalytic hydrogen evolution rate (HER). In addition, the optical bandgap is similar in all materials (~2.75 eV), besides Cs-, TMA- and NH₄-PHI with a slightly enlarged bandgap of 2.80 eV, probably caused by partial protonation (Figure S4.57).^[4]

PHI is known to form long-lived electrons on the polymer backbone when illuminated in the absence of oxygen and in the presence of an electron donor, which quenches the light-induced holes.^[5, 6] During this process, PHI itself remains stable (Figure S4.60, S4.61, Table S4.17). The charge accumulation on PHI is accompanied by a color change from yellow to blue, which allows for time delayed hydrogen evolution^[5] or other photocatalytic reactions,^[7, 63] as well as solar battery applications, and is most probably the reason for an enhanced photocatalytic activity when compared to melon. To test the impact of ions in the charge stabilization, an aqueous suspension of H-PHI, without the mobile counterions, was illuminated in the presence of an electron donor, but no color change could be observed. However, when adding salts containing Li⁺, Na⁺, K⁺, Cs⁺ or NH₄⁺, which increase the conductivity as discussed above, the suspension turns blue, highlighting the participation of ions in this process (Table S4.16). Those ions have to be mobile and fit into the pore, as demonstrated by the absence of the color change characteristic of photocharging when Ba²⁺ or TMA⁺ salts were added. As such, it appears that mobile alkali ions reorganize upon light excitation to screen the trapped electrons on the PHI backbone (Figure 7.5c). A related process was described for 1D carbon nitride melon, which was shown to act as a light-driven ion pump.^[64] Upon asymmetric illumination, charges are generated at the surface, separated by electrons moving away from the illumination spot, which was ascribed to an n-type conductivity-induced band bending. This generated charge gradient was described as the driving force for the alkali ions in solution to follow the electrons.^[64-66]

In photocatalysis experiments with suspended particles of similar size (500-1000 nm) we hypothesize that the mobile cations in the pores of PHI act to stabilize the trapped electrons through Coulombic interactions, while the pore water assists in dielectric screening and acts as a

vehicle to facilitate movement of the cations through the pores additionally. As outlined above, the ionic conductivity is enhanced in humid environment and is therefore assumed to be the highest in an aqueous environment, approximating 100 %RH, as applicable during photocatalysis in aqueous suspension. Indeed, in line with the conductivity results, we observe the highest photocatalytic HER activity for Na-PHI ($24(\pm 1) \mu\text{mol h}^{-1}$) compared to Li- and K-PHI ($18(\pm 4) \mu\text{mol h}^{-1}$ and $19 (\pm 4) \mu\text{mol h}^{-1}$), under illumination with simulated sunlight and in the presence of 8 wt% Pt loading acting as co-catalyst (Figure 7.5a). When comparing the photocatalytic activity and the conductivity, a similar correlation was identified for *M*-PHI with the other cations studied (Figure S4.58, S4.59), e.g. the lowest photocatalytic activity results for Ba-PHI ($10 (\pm 1) \mu\text{mol h}^{-1}$), which also has the lowest overall conductivity. We rationalize the observed trends in photocatalysis and color change experiments by a more efficient stabilization of the photo-generated charges by ions being mobile in the structure. Nevertheless, it must be stated that an excessive stabilization of charges on the material can also have detrimental effects on the photocatalytic activity, since excessively accumulated, photo-generated charges, cannot be used for the redox reactions anymore and can recombine.^[6] This is resulting in a sweet spot of charge stabilization and photocatalytic efficiency, where the time scales of charge stabilization and photocatalysis are suitably matched.

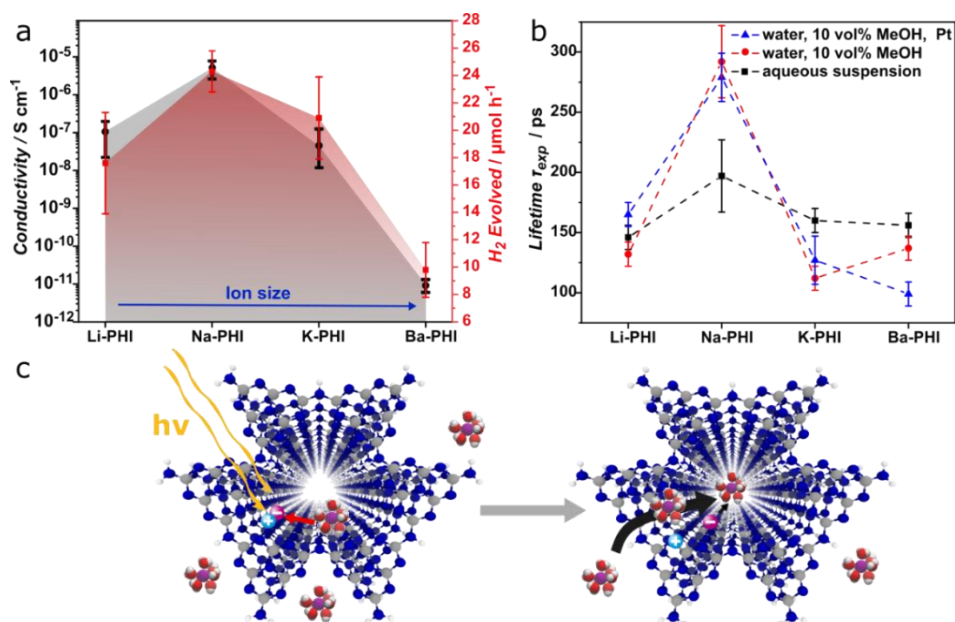


Figure 7.5: Optical characterisation and photocatalytic hydrogen evolution of K-, Na-, Li- and Ba-PHI. a) Hydrogen evolution of *M*-PHI at 100 mW cm^{-1} illumination in the presence of 10 vol% MeOH and 8 wt% Pt loading, and its correlation with the observed conductivity, measured for PHI pellets; b) Lifetimes of *M*-PHI determined by time-dependent PL measurements in aqueous suspensions, aqueous suspensions with 10 vol% MeOH, and after photodeposition of Pt. Lifetime as fitted with two different functions represented by T_{exp} and T_{mode} ; c) Scheme of photo-generated charges in *M*-PHI, which are stabilized by mobile alkali ions.

To further substantiate this behavior in PHI, where mobile alkali ions are already built into the system as opposed to melon, electrochemical measurements in the presence of light and photoluminescence (PL) studies were performed. PL emission and lifetime measurements in

aqueous suspension of PHI (containing, Li^+ , Na^+ , K^+ , Ba^{2+}) in the presence and absence of methanol as well as after Pt deposition were performed systematically to study the effect of each component used for photocatalysis experiments. The PL emission spectra of all alkali ion-bearing PHI materials is similar, with a maximum intensity around 450 nm (Figure S4.62, S4.63). However, the relative PL intensity is not a suitable measure for the photocatalytic performance due to the overall low PL quantum yields observed for PHI.

Time-resolved PL measurements, excited at a wavelength of 370 nm, were fitted by an exponential decay function and a Γ distribution (Figure S4.64)^[67, 68] highlighting at least two different decay processes being present on the probed time scales in the material. The shorter lifetime (τ_{exp}) of ~110 ps up to ~290 ps corresponds to an internal recombination of charge carriers in the bulk of PHI, whereas the longer lifetime (τ_{mode}) of ~200 ps to 840 ps is likely caused by decay processes on the surface (Table S4.18).^[8, 12, 69] When comparing the lifetime corresponding to the bulk properties in different environments, it can be clearly seen that lifetimes of Na-PHI are prolonged by 20-60% in comparison to the other *M*-PHI materials, which corresponds to a lower overall recombination rate in the Na-PHI bulk (Figure 7.5b). This behavior is consistent with the assumption of ion-assisted stabilization of light-induced electrons. Prolonged lifetimes of the photo-induced charge carriers in turn increase the probability of productively using the generated electrons in the photocatalytic HER, which is in line with the highest photocatalytic activity observed for Na-PHI. To estimate the impact of ion motion on possible charge stabilization, a diffusion length ($L = \sqrt{D * \tau}$) of the ions in the pores can be calculated on the time scales extracted from PL with the conductivity diffusion coefficients (D°) determined above for humid pellets (Table S4.15).^[70] Diffusion lengths of 0.10 (for K- and Li-PHI) to 0.35 Å (for Na-PHI) were calculated, which will be significantly higher under aqueous conditions, but presumably with a preserved relative trend (Figure 7.4c). This however means that within the measured timescales, only short range motion is enabled, which is likely sufficient to reach and stabilize an electron residing nearby (polaronic effect),^[65] and hence is most efficient for Na-PHI with the highest ion conductivity. A diffusion distance corresponding to the layer separation (3.2 Å) would require for example roughly 22 ns for Na-PHI, which is too long to be detected by PL, since the radiative decay signal being used as measure for the charge recombination process is shorter lived. Nevertheless, the PL data shows a contribution of ion stabilizing the photo-generated charge already on short time and length scales, which is described to be most important for an efficient charge separation.^[71]

To probe the possible effect of ion-mediated charge stabilization on the photocatalytic activity on the timescale of long-lived electrons, which are observable by the blue state, the build-up of a photopotential and its relaxation in *M*-PHI pellets under ambient conditions during illumination with AM 1.5 G (100 mW cm^{-1}) was studied (Figure S4.65). It can be seen that a negative photovoltage builds up instantaneously on the illumination side in all cases. After illumination, the generated photopotential decays, most slowly for Na-PHI while not reaching the initial potential after 30 s in the dark. This behavior signifies that the photoexcited electrons are stabilized on the

material (negative shift in Fermi energy), probably due to charge trapping assisted by efficient Na^+ migration. For the other *M*-PHI materials, the negative photovoltage decay occurs faster, which points to a less efficient charge stabilization after photoexcitation. This trend, showing clear differences in magnitude and time scale of charge stabilization, is in line with the findings from conductivity and PL lifetime measurements, and suggests a correlation between conductivity, electrostatic screening and charge carrier lifetimes. Since these factors are consistent with trend observed for the photocatalytic HER activity of *M*-PHI, our study points to a correlation between ion conductivity, charge stabilization and photocatalytic efficiency. Although a causal relationship between these factors can neither be proven nor excluded at this stage, we emphasize that enhancing the conductivity of a material may be an important, yet so far largely overlooked design parameter to enhance the photocatalytic activity. If conductivity – ionic or electronic – is limiting photocatalysis, it can cause significant recombination and be detrimental for charge extraction, since in that case only those charge carriers generated and separated close to the solid-liquid interphase remain available for photocatalytic reactions.^[10]

7.2. Conclusion

In this study, the impact of ion mobility in the structural pores of 2D carbon nitride poly(heptazine imide) and its influence on the stabilization of photo-generated charges and hence, the photocatalytic hydrogen evolution was investigated. First, *M*-PHI ($M = \text{K}^+, \text{Li}^+, \text{Cs}^+, \text{NH}_4^+, \text{TMA}^+, \text{Ba}^{2+}$) was structurally analyzed with different counterions being present in the pores. Depending on the pore content and the size of the hydrated cations, the stacking of the 2D layers and thereby the pore geometry is modified while the polymer backbone remains unchanged. The differences between effective channel sizes, hydrodynamic cation radius and ion-backbone interactions for the different *M*-PHI translate into distinctly different ion motion within the PHI pore channels. Ion transport is found to be fastest for Na-PHI, which outperforms the other cation containing PHI materials by minimum one order of magnitude. Irrespective of the cation, the conductivity of the ions increases significantly with the water content, which influences the electrostatic interactions between the ions and the polymer backbone. For Na-PHI, which showed the fastest ion motion under all conditions, the conductivity is increased by 5 to 6 orders of magnitude (from $10^{-9} \text{ S cm}^{-1}$ to $10^{-4} \text{ S cm}^{-1}$) with increasing relative humidity from 2 to around 80 %.

With the documented ability of PHI to stabilize and trap photo-generated electrons over hours, we studied the influence of the mobile ions in *M*-PHI on the charge trapping ability on short time scales and on the photocatalytic hydrogen evolution activity of PHI. A fast cation motion was found to be beneficial for increasing the photo-generated charge carrier lifetimes in PHI on short (ps) and long (s) time scales, which shows a positive correlation with the hydrogen evolution rate, likely caused by the interaction between the photo-generated electron and the mobile hydrated cations in the PHI pores. In agreement with the ionic conductivity values, the longest PL lifetimes were found for Na-PHI, which also exhibits the highest hydrogen evolution rate. For Na-PHI, the

size of the hydrated cation shows an optimal match with the effective PHI channel size, which is determined by finite, but small random layer shifts that enable high mobility of the hydrated Na ions in the pores.

From our findings we conclude that the ionic conductivity is an important, but so far underappreciated design parameter in catalyst design, especially in porous materials or materials where the conductivity can represent a bottleneck for immediate charge carrier stabilization and extraction. And yet, charge stabilization by motion of the mobile counterion in porous organic semiconductors is not only relevant for photocatalysis, but also for the realization of field effect transistors, chemical capacitors or sensors, where a high sensitivity for water and ion content is desirable to tune the material properties and thus, the read-out/output, such as conductivity.

7.3. Bibliography

- [1] B. S. R. o. W. Energy, *Statistical review of world energy*, Vol. 69, BP, **2020**.
- [2] X. Wang, K. Maeda, A. Thomas, K. Takanabe, G. Xin, J. M. Carlsson, K. Domen, M. Antonietti, *Nat. Mater.* **2009**, 8 (1), 76-80.
- [3] R. Malik, V. K. Tomer, *Renew. Sustain. Energy Rev.* **2021**, 135, 110235.
- [4] H. Schlomberg, J. Kröger, G. Savasci, M. W. Terban, S. Bette, I. Moudrakovski, V. Duppel, F. Podjaski, R. Siegel, J. Senker, R. E. Dinnebier, C. Ochsenfeld, B. V. Lotsch, *Chem. Mater.* **2019**, 31 (18), 7478-7486.
- [5] V. W.-h. Lau, D. Klose, H. Kasap, F. Podjaski, M.-C. Pignié, E. Reisner, G. Jeschke, B. V. Lotsch, *Angew. Chem. Int. Ed.* **2017**, 56 (2), 510-514.
- [6] F. Podjaski, J. Kröger, B. V. Lotsch, *Adv. Mater.* **2018**, 30 (9), 1705477.
- [7] V. Sridhar, F. Podjaski, J. Kröger, A. Jiménez-Solano, B.-W. Park, B. V. Lotsch, M. Sitti, *Proc. Natl. Acad. Sci. U. S. A.* **2020**, 117 (40), 24748-24756.
- [8] W. Yang, R. Godin, H. Kasap, B. Moss, Y. Dong, S. A. J. Hillman, L. Steier, E. Reisner, J. R. Durrant, *J. Am. Chem. Soc.* **2019**, 141 (28), 11219-11229.
- [9] V. Augustyn, Y. Gogotsi, *Joule* **2017**, 1 (3), 443-452.
- [10] T. Banerjee, F. Podjaski, J. Kröger, B. P. Biswal, B. V. Lotsch, *Nat. Rev. Mater.* **2021**, 6 (2), 168-190.
- [11] K. Takanabe, *ACS Catal.* **2017**, 7 (11), 8006-8022.
- [12] J. Kröger, A. Jiménez-Solano, G. Savasci, V. W. h. Lau, V. Duppel, I. Moudrakovski, K. Küster, T. Scholz, A. Gouder, M.-L. Schreiber, F. Podjaski, C. Ochsenfeld, B. V. Lotsch, *Adv. Funct. Mater.* **2021**, 31 (28), 2102468.
- [13] X. Li, A. F. Masters, T. Maschmeyer, *ChemCatChem* **2015**, 7 (1), 121-126.
- [14] C. Merschjann, T. Tyborski, S. Orthmann, F. Yang, K. Schwarzburg, M. Lublow, M. C. Lux-Steiner, T. Schedel-Niedrig, *Phys. Rev. B* **2013**, 87 (20), 205204.
- [15] C. Merschjann, S. Tschierlei, T. Tyborski, K. Kailasam, S. Orthmann, D. Hollmann, T. Schedel-Niedrig, A. Thomas, S. Lochbrunner, *Adv. Mater.* **2015**, 27 (48), 7993-7999.
- [16] M. N. Huda, J. A. Turner, *J. Appl. Phys.* **2010**, 107 (12), 123703.
- [17] Y. Noda, C. Merschjann, J. Tarábek, P. Amsalem, N. Koch, M. J. Bojdys, *Angew. Chem. Int. Ed.* **2019**, 58 (28), 9394-9398.
- [18] K. A. See, S. Hug, K. Schwinghammer, M. A. Lumley, Y. Zheng, J. M. Nolt, G. D. Stucky, F. Wudl, B. V. Lotsch, R. Seshadri, *Chem. Mater.* **2015**, 27 (11), 3821-3829.
- [19] Z. Zhang, J. Huang, Q. Yuan, B. Dong, *Nanoscale* **2014**, 6 (15), 9250-9256.
- [20] R. Malik, V. K. Tomer, V. Chaudhary, M. S. Dahiya, A. Sharma, S. P. Nehra, S. Duhan, K. Kailasam, *J. Mater. Chem. A* **2017**, 5 (27), 14134-14143.
- [21] V. K. Tomer, N. Thangaraj, S. Gahlot, K. Kailasam, *Nanoscale* **2016**, 8 (47), 19794-19803.
- [22] S. P. Lee, J. G. Lee, S. Chowdhury, *Sensors* **2008**, 8 (4), 2662-2672.

- [23] H. Arazoe, D. Miyajima, K. Akaike, F. Araoka, E. Sato, T. Hikima, M. Kawamoto, T. Aida, *Nat. Mater.* **2016**, *15* (10), 1084-1089.
- [24] S. Cao, J. Low, J. Yu, M. Jaroniec, *Adv. Mater.* **2015**, *27* (13), 2150-2176.
- [25] L. Ge, F. Zuo, J. Liu, Q. Ma, C. Wang, D. Sun, L. Bartels, P. Feng, *J. Phys. Chem. C* **2012**, *116* (25), 13708-13714.
- [26] S. Gope, S. Malunavar, A. J. Bhattacharyya, *ChemistrySelect* **2018**, *3* (19), 5364-5376.
- [27] V. W.-h. Lau, I. Moudrakovski, T. Botari, S. Weinberger, M. B. Mesch, V. Duppel, J. Senker, V. Blum, B. V. Lotsch, *Nat. Commun.* **2016**, *7* (1), 12165.
- [28] A. Savateev, S. Pronkin, M. G. Willinger, M. Antonietti, D. Dontsova, *Chem.– Asian J.* **2017**, *12* (13), 1517-1522.
- [29] A. Coelho, *J. Appl. Crystallogr.* **2018**, *51* (1), 210-218.
- [30] A. M. Pütz, M. W. Terban, S. Bette, F. Haase, R. E. Dinnebier, B. V. Lotsch, *Chem. Sci.* **2020**, *11* (47), 12647-12654.
- [31] H. Y. Liu, Y. Q. Zhou, F. Y. Zhu, W. Q. Zhang, G. G. Wang, Z. F. Jing, C. H. Fang, *Eur. Phys. J. D* **2020**, *74* (1), 2.
- [32] J. Mähler, I. Persson, *Inorg. Chem.* **2012**, *51* (1), 425-438.
- [33] X. Wang, D. Toroz, S. Kim, S. L. Clegg, G.-S. Park, D. Di Tommaso, *Phys. Chem. Chem. Phys.* **2020**, *22* (28), 16301-16313.
- [34] X. Guo, S. Theissen, J. Claussen, V. Hildebrand, J. Kamphus, M. Wilhelm, B. Luy, G. Guthausen, *Macromol. Chem. Phys.* **2019**, *220* (2), 1800350.
- [35] G. A. Gerencser, *Epithelial Transport Physiology*, Humana Press, **2010**.
- [36] E. R. Nightingale, *J. Phys. Chem.* **1959**, *63* (9), 1381-1387.
- [37] S. Ringe, E. L. Clark, J. Resasco, A. Walton, B. Seger, A. T. Bell, K. Chan, *Energ. Environ. Sci.* **2019**, *12* (10), 3001-3014.
- [38] J. K. W. Chui, T. M. Fyles, *Chem. Soc. Rev.* **2012**, *41* (1), 148-175.
- [39] F. Guo, S. Li, Y. Hou, J. Xu, S. Lin, X. Wang, *Chem. Commun.* **2019**, *55* (75), 11259-11262.
- [40] P. Atkins, J. de Paula, *Atkins' physical chemistry*, Oxford University Press, New York, **2002**.
- [41] Y. Cao, L. Xiao, M. L. Sushko, W. Wang, B. Schwenzler, J. Xiao, Z. Nie, L. V. Saraf, Z. Yang, J. Liu, *Nano Lett.* **2012**, *12* (7), 3783-3787.
- [42] A. Kuhn, S. Dupke, M. Kunze, S. Puravankara, T. Langer, R. Pöttgen, M. Winter, H.-D. Wiemhöfer, H. Eckert, P. Heitjans, *J. Phys. Chem. C* **2014**, *118* (49), 28350-28360.
- [43] V. Epp, Q. Ma, E.-M. Hammer, F. Tietz, M. Wilkening, *Phys. Chem. Chem. Phys.* **2015**, *17* (48), 32115-32121.
- [44] A. Kuhn, V. Duppel, B. V. Lotsch, *Energ. Environ. Sci.* **2013**, *6* (12), 3548-3552.
- [45] A. Senocrate, I. Moudrakovski, G. Y. Kim, T.-Y. Yang, G. Gregori, M. Grätzel, J. Maier, *Angew. Chem. Int. Ed.* **2017**, *56* (27), 7755-7759.
- [46] T.-Y. Yang, G. Gregori, N. Pellet, M. Grätzel, J. Maier, *Angew. Chem. Int. Ed.* **2015**, *54* (27), 7905-7910.
- [47] N. G. Park, M. Grätzel, T. Miyasaka, *Organic-inorganic halide perovskite photovoltaics: From fundamentals to device architectures*, **2016**, 1-366.
- [48] G. Y. Kim, A. Senocrate, T.-Y. Yang, G. Gregori, M. Grätzel, J. Maier, *Nat. Mater.* **2018**, *17* (5), 445-449.
- [49] D. Prutsch, B. Gadermaier, H. Brandstätter, V. Pregartner, B. Stanje, D. Wohlmuth, V. Epp, D. Rettenwander, I. Hanzu, H. M. R. Wilkening, *Chem. Mater.* **2018**, *30* (21), 7575-7586.
- [50] N. S. Schausser, G. E. Sanoja, J. M. Bartels, S. K. Jain, J. G. Hu, S. Han, L. M. Walker, M. E. Helgeson, R. Seshadri, R. A. Segalman, *Chem. Mater.* **2018**, *30* (16), 5759-5769.
- [51] Y. Hu, N. Dunlap, S. Wan, S. Lu, S. Huang, I. Sellinger, M. Ortiz, Y. Jin, S.-h. Lee, W. Zhang, *J. Am. Chem. Soc.* **2019**, *141* (18), 7518-7525.
- [52] D. M. DeLongchamp, P. T. Hammond, *Chem. Mater.* **2003**, *15* (5), 1165-1173.
- [53] M. Wieland, C. Dingler, R. Merkle, J. Maier, S. Ludwigs, *ACS Appl. Mater. Inter.* **2020**, *12* (5), 6742-6751.
- [54] J. Li, Y.-H. Yang, Q. Chen, W.-Q. Zhu, J.-H. Zhang, *J. Mater. Chem. C* **2020**, *8* (12), 4065-4072.
- [55] C. Adler, S. Selim, I. Krivtsov, C. Li, D. Mitoraj, B. Dietzek, J. R. Durrant, R. Beranek, *Adv. Funct. Mater.* **2021**, 2105369.
- [56] H. Park, P. P. M. Schleker, Z. Liu, N. Kowalew, T. Stamm, R. Schlögl, R.-A. Eichel, S. Heumann, J. Granwehr, *J. Phys. Chem. C* **2019**, *123* (41), 25146-25156.

- [57] M. Liu, P. Xia, L. Zhang, B. Cheng, J. Yu, *ACS Sustain. Chem. Eng.* **2018**, 6 (8), 10472-10480.
- [58] S. Nakhal, D. Wiedemann, B. Stanje, O. Dolotko, M. Wilkening, M. Lerch, *J. Solid State Chem.* **2016**, 238, 60-67.
- [59] A. Kuhn, M. Kunze, P. Sreeraj, H. D. Wiemhöfer, V. Thangadurai, M. Wilkening, P. Heitjans, *Solid State Nucl. Magn. Reson.* **2012**, 42, 2-8.
- [60] H. Gao, S. Yan, J. Wang, Y. A. Huang, P. Wang, Z. Li, Z. Zou, *Phys. Chem. Chem. Phys.* **2013**, 15 (41), 18077-18084.
- [61] S. Yang, Y. Gong, J. Zhang, L. Zhan, L. Ma, Z. Fang, R. Vajtai, X. Wang, P. M. Ajayan, *Adv. Mater.* **2013**, 25 (17), 2452-2456.
- [62] A. Savateev, Y. Markushyna, C. M. Schüßlbauer, T. Ullrich, D. M. Guldi, M. Antonietti, *Angew. Chem. Int. Ed.* **2021**, 60 (13), 7436-7443.
- [63] A. Savateev, B. Kurpil, A. Mishchenko, G. Zhang, M. Antonietti, *Chem. Sci.* **2018**, 9 (14), 3584-3591.
- [64] K. Xiao, L. Chen, R. Chen, T. Heil, S. D. C. Lemus, F. Fan, L. Wen, L. Jiang, M. Antonietti, *Nat. Commun.* **2019**, 10 (1), 74.
- [65] F. Podjaski, B. V. Lotsch, *Adv. Energy Mater.* **2021**, 11 (4), 2003049.
- [66] P. Jia, Q. Wen, D. Liu, M. Zhou, X. Jin, L. Ding, H. Dong, D. Lu, L. Jiang, W. Guo, *Small* **2019**, 15 (50), 1905355.
- [67] A. C. Fogarty, A. C. Jones, P. J. Camp, *Phys. Chem. Chem. Phys.* **2011**, 13 (9), 3819-3830.
- [68] J. Kröger, A. Jiménez-Solano, G. Savasci, P. Rovó, I. Moudrakovski, K. Küster, H. Schlomberg, H. A. Vignolo-González, V. Duppel, L. Grunenberg, C. B. Dayan, M. Sitti, F. Podjaski, C. Ochsenfeld, B. V. Lotsch, *Adv. Energy Mater.* **2021**, 11 (6), 2003016.
- [69] R. Godin, Y. Wang, M. A. Zwijnenburg, J. Tang, J. R. Durrant, *J. Am. Chem. Soc.* **2017**, 139 (14), 5216-5224.
- [70] H. Mehrer, *Diffusion in Solids: Fundamentals, Methods, Materials, Diffusion-Controlled Processes*, Springer Berlin Heidelberg, **2007**.
- [71] S. Shoaee, M. Stolterfoht, D. Neher, *Adv. Energy Mater.* **2018**, 8 (28), 1703355.

8. Conclusion and outlook

Carbon nitrides are among the most widely reported and promising organic based semiconductors for photocatalytic transformations and are of particular interest for hydrogen production from water. Despite their comparably high efficiency and robustness, little is known about the intrinsic optoelectronic properties and the underlying structure-property-relationships. This is most probably caused by their poor crystallinity and control of defect activities, resulting in ill-defined structure models and incomplete or vague structure-activity correlations. However, to tailor the complex multistep photocatalytic properties, such insights are a fundamental prerequisite in order to enable the development of a design concept for highly efficient photocatalysts. Hence, rational tailoring of properties could help to establish carbon nitrides and other materials for commercial applications, such as the production of solar fuels.

In this thesis, an in-depth structure-property analysis of the 2D carbon nitride poly(heptazine imide) (PHI) is performed, from which multiple design strategies for carbon nitrides are derived. To achieve this, different steps during the photocatalytic process were analyzed and tuned to study their impact on the optoelectronic and photocatalytic performance. Generally, the photocatalytic process depends on the following four steps: (i) light absorption and charge generation, (ii) exciton or charge separation, (iii) charge transport through the material towards the surface, and finally, (iv) charge transfer to a co-catalyst or the redox active center, where the photocatalytic reaction occurs. To gain a holistic picture of PHI acting as photocatalyst, it is important to analyze those four steps involved in light driven processes in a semiconductor in detail, since all influence the photocatalytic activity. The parameters studied here, affecting these steps, are the 2D backbone structure, the type and magnitude of charge transport properties (i.e. the conductivity), the PHI particle size optimization, as well as post synthetic functionalization affecting interfacial properties. Especially the particle size has tremendous effects on surface functionalities induced by defects, affecting various steps in the photocatalytic process at a time, making the analysis of its influence a complex multidimensional challenge.

As a first step, a new synthesis strategy was designed to obtain a crystalline material, enabling the precise analysis of the chemical structure of PHI. This 2D porous polymer exhibits trigonal symmetry with the pore content being structure directing concerning the stacking order. Due to the stacking of the 2D layers, a more or less ordered 1D pore channel structure results in this material. As a consequence of the potassium salt melt-based synthesis method, hydrated potassium ions are located in these pores (K-PHI), which can be exchanged by different cations (including protons) that fit in the pores and are mobile therein. It was found that besides the structural changes induced by different pore contents, also the degree of crystallinity affects photocatalytic hydrogen evolution rates. The highest rate was measured for the protonated PHI with smaller crystallites, which outperforms K- or H-PHI with bigger crystallites. In addition, photo-generated electrons can be stabilized and “stored” on PHI in the absence of a co-catalyst, which

is enabled by the presence of cations fitting into the PHI pores. This unusual property bridges light absorption and intrinsic battery-like properties in a semiconductor. Since this electron accumulation and storage is very efficient and long-lasting, the material can also be used for “dark photocatalysis”, where the catalytic surface reaction is triggered by the addition of an electrocatalyst, which can be delayed for many hours after illumination. It has been observed that this property is a common denominator for all PHI structures, upon addition of alkali metal ions.

The role of ions in this material hence plays an important role, as was described in this thesis. After the photo-induced charges are generated, they have to be separated to avoid recombination. The electrons, which most probably are only mobile on short range, can be stabilized by mobile cations and hence reduce the recombination rates. Out of this reason fast ion conduction is hypothesized to be beneficial for charge separation and transport in this material. For cation-containing PHI, the conductivity was found to be mainly ionic along the 1D channels. As such, the mobility is influenced by the stacking defects, interaction strength of the cation with the polymer backbone, which always includes some water molecules in its vicinity, and the overall humidity or water content. This water affects the hydration of the cation and hence can shield the cation and influence the interaction with the backbone, resulting in strongly modified and environmentally sensitive ionic conductivity. Those influences were found to be best balanced for hydrated sodium ions that showed the highest mobility in the PHI pores. Sodium not only enables the fastest stabilization of photo-induced charges, but also enhances the ion assisted electron transport in the material, which was shown to be an important tuning parameter and possible bottleneck for the photocatalytic activity.

Unlike the ion mobility, the pure electron transport is found to be based on a multiple trapping and release model (MRT). Here, the electrons are diffusing in a band like transport mechanism in the crystalline areas (probably via inter-layer hopping). At particle interfaces, hopping via the trap states is enabled, caused by terminal functional groups or defects. Hence, for each material, the optimum surface to bulk material ratio should be found and a targeted surface design by functional group attachment should be considered for an efficient charge separation and transport. However, care must be taken, since the amount of surface functional groups, which can also be influenced by the particle size, simultaneously affect several other parameters. They are shown to change the light absorption ability, the suspension stability and the density and depth of trap states, which influence the charge carrier lifetime, charge transport and transfer to Pt as well as its deposition behavior. In principle, an analysis and optimization of each of these parameters individually is needed to obtain the most efficient photocatalyst. This allows to optimize the particle size for the highest photocatalytic efficiency, which is observed when no factor becomes detrimental while positive influences are exposed most strongly. For H-PHI this optimum is found for particles in the range of 180-500 nm, which are ideally partially re-agglomerated.

As an example of targeted surface functionalization and its influence on photocatalysis, the covalent attachment of melamine groups at PHI is demonstrated in this thesis. After developing

a functionalization strategy for the chemically stable PHI, the often neglected bottleneck process in photocatalysis with organic materials, namely the quenching of the hole, could be studied in detail and optimized. Akin to Sabatier's principle, the donor and its oxidation products have to interact well with the catalyst to allow a fast reaction, but not too strong to also allow the desorption of donor oxidation products afterwards. Depending on the interaction strength of electron donor and carbon nitride, the photocatalytic hydrogen evolution can be boosted significantly in melamine functionalized PHI. Due to the decreased wettability by this functionalization, the sacrificial oxidation kinetics with the surfactant and electron donor TEOA is enhanced. Hence, the HER is increased significantly even though the Pt content could be reduced, whereas no such distinct effects are observed on other PHI material. These findings highlight one big advantage of organic-based semiconductors in contrast to inorganic materials, which is their high degree of diversification. The functionalization with melamine groups is a model system, representative for a wide range of different functionalization possibilities that have to be tailored for their respective function, and not only for their direct influence on hydrogen evolution. As such, organic semiconductors are a versatile and promising platform for next generation semiconductors, which can be designed targeted for their respective photocatalytic application on purpose.

The insights gained into the structure-activity relationships of PHI in this thesis, in combination with a new functionalization strategy, offer the opportunity to address other important challenges in the field of photocatalysis, such as tailored donor oxidation to value-added products, CO₂ reduction, or nitrogen fixation. In the following, some of the remaining challenges for hydrogen evolution on carbon nitrides are discussed in more detail, which exist for other light driven reactions in similar way.

First, the light absorption should be enhanced so that a wider range of the solar spectrum can be used. For a commercial application of photocatalysts for hydrogen production, a STH of 10% is targeted, to be cost-competitive to other hydrogen production possibilities. To reach this goal, also the AQY at every wavelength has to be increased. Assuming for example a spectrally stable AQY of 60%, the absorption edge of the semiconductor should be above 600 nm to reach this target.^[1] However, the reduction of the overall band gap inevitably decreases the thermodynamic driving force for the overall process, which complicates the implementation. A possible solution for this will be discussed below. To achieve a decreased band gap in an organic system like carbon nitrides, the π -conjugation can be increased. This can for example be accomplished by copolymerizing an electron-rich and electron-poor material, to build a donor-acceptor system with a preferably strong electron donor and a weak acceptor.^[2-6] Hence, for carbon nitrides, with a comparably large optical band gap of 2.7 eV (450 nm), a covalent attachment, copolymerization, or bulk heterojunction with narrow-band gap polymers might be suitable solutions.^[2] Examples of such attachments are: perylene-based molecules^[7] or sulfone groups^[8], semiconductor polymers with an optical band gap of around 2 eV, including polymeric pyrene and phenyl-based systems,^[9] or co-polymers of thiophene and benzothiadiazole.^[10] The best results in terms of band gap

narrowing and charge transport were reported for planar polymeric or covalent organic framework (COF) materials.^[2, 11-13] Besides, also insights gained from heterojunctions studied for organic photovoltaic systems can be used^[2], where especially the extension of the absorbed solar light is studied in detail.^[4] Such heterojunctions may offer a job-sharing strategy in order to couple light absorption properties of both semiconductors synergistically.

Second, for an abundant and renewable upscaling of photocatalytic hydrogen evolution, another challenge arises from the replacement of the co-catalyst Pt by more abundant and less expensive alternatives.^[14] Several covalently bound or incorporated molecular co-catalysts were successfully reported for hydrogen evolution already, including Zn-phthalocyanine^[15], Co-bipyridine^[16] or Ni-oxime^[17] complexes. Also various non-covalently attached systems such as Ni-bis(diphosphine)^[18], Ni-bis(diphosphine)^[19] and Ni-, Co- or Fe-bis(TEoA) complexes^[20] were described as suitable HER catalysts, where the stability and performance might be further enhanced by covalently attaching them.^[16]

Third, due to the limitations on the OER side, which can hamper also the HER in an overall charge neutral photo-redox process, sacrificial electron donors are commonly used when studying the HER. Although they enable to bypass the limitations on the hole extraction side, their oxidation is often a downhill reaction, effectively consuming energy. Therefore, they should be replaced by organic waste products that are degraded photocatalytically or by molecules being oxidized to higher value chemicals. Examples for such reactions are cycloaddition^[21] reactions, the synthesis of bioactive molecules like NADH,^[22] or degradation of plastics like poly(ethylene terephthalate)^[23], lignocellulose^[18] and medical compounds like 5-sulfosalicylic acid.^[24] To tailor and enhance those reactions the insights gained in donor interaction strength and the hole extraction kinetics via surface functionalization of the carbon nitride describe a key pathway.

Another challenge arises from photocatalytic overall water splitting. One way of addressing this issue is the utilization of Z-scheme devices, where two photoabsorbers are employed. While the thermodynamic STH limit is 30% for a single absorber system, the theoretical maximum of the STH efficiency for a Z-scheme is around 40%.^[2, 25] Since each material has to provide the driving force for one reaction, the HER or OER respectively, materials with more narrow band gaps can be used. An additional benefit is the locally separated hydrogen and oxygen evolution at two different systems, which can be tuned individually. However, the surface and interfacial design is crucial in such devices, especially when redox mediators are used to shuttle the photo-generated charges in order to prevent recombination.^[2] Such redox mediators can be solid or liquid.^[14] Besides, the accumulation of both, hydrogen and oxygen, in one chamber is not desired for security issues and requires additional energy to separate the gases subsequently. Also the presence of both gases will unavoidably lead to back-reactions at the co-catalysts, limiting the STH efficiency, which makes Z-schemes a promising possibility for photocatalytic water splitting. At present, however, the biggest bottleneck is the design of an efficient OER photocatalyst. Some reports about carbon nitrides or covalent triazine frameworks exist, which are capable of

catalyzing this reaction as well.^[26, 27] However, due to the four-electron process of the OER and the harsher reaction conditions, which might lead to photo-corrosion, further research is needed to efficiently drive this process as well.^[2, 28]

Besides normal photocatalytic water splitting or hydrogen evolution the charge storing properties of PHI also enable different applications. They allow to store the solar energy directly and to use it on demand for the production of solar fuels or for electrical energy storage, and not only when the sunlight is present. Due to the materials' organic backbone and synthesis from abundant precursors, the flexible use of cations stabilizing charges in the PHI pores, the materials' stability and non-toxicity, carbon nitrides can further be used for sensors or transistors, as light-driven microswimmers, and for medical applications.^[29-31]

Since carbon nitrides are not soluble, their processing is challenging, which is especially relevant for the measurement of (photo)physical properties in defined (usually thin film) geometries and to enable (photo)electrochemical applications. The wettability and stability in suspension can be engineered by attaching polymers to carbon nitrides to allow homogeneous thin film preparation. In addition, hybrids of polymers and carbon nitrides can enhance the sensitivity of carbon nitride sensors, transistors or energy storing devices.^[31-33] Here, MeI-PHI exhibits additional potential. However, most of the reported hybrid materials so far are based on physical interactions only.^[32] Especially the charge separation and conductivity enhancements due to the addition of conductive polymers, like poly(3,4-ethylenedioxythiophene) poly(styrene) sulfonate,^[34] might become more intense when polymer and carbon nitride are covalently bound to each other.^[32]

The surface property tuning and polymer attachment is also of high interest for drug delivery. Light-driven Janus particles consisting of metal or SiO₂ capped PHI were recently shown to be efficiently propelled by photocatalytic reactions.^[30] The fast propulsion of the Janus particles was found to be based on efficient charge separation in the particle and enhanced photocatalytic activity. Making use of PHI light storing properties, a lasting enhanced propulsion after the illumination could be demonstrated, reaching 30 min after only 30 s of photo-charging time.^[35] In addition, pure PHI microswimmers, without additional capping materials, are enabled with PHI. Such microswimmers are the first to be propelled without additional sacrificial fuels, but in high ionic-strength and biologically relevant media, which was a long-standing bottleneck in the field. Due to textural pores being present in PHI, those particles can be loaded with the anti-cancer drug doxorubicin, which can be released subsequently on purpose by changing the pH-value or illuminating the particle.^[29, 35] Especially for the drug immobilization of the PHI particles, surface functionalization is key, to enhance the interaction with the drug. Depending on the type of interaction or bonding, the drug release can be tailored as well. In addition, the efficiency of the charge separation can be tuned, which might be optimized by particle size variation or exchange of the cation being present in the PHI pores. By those different strategies, various cargo or drug delivery and hence, therapeutic functions can be addressed.

These examples highlight the vast potential of especially PHI-type carbon nitrides for different applications, including photocatalysis, (photo)electrochemical and biomedical needs. Due to the carbon nitrides' high stability, abundant and non-toxic nature, they offer a promising alternative to inorganic systems mostly used in these fields, especially due to their high degree of tunability to design the interfacial properties for the targeted application. In combination with the property of carbon nitrides to store the energy of the sunlight, which allows for overcoming the fluctuating solar energy accessibility even over to the day-night cycle, this material class is highly suitable for supply issues associated with fluctuating renewable energies. Especially for the increasing relevance of hydrogen gas as energy source, photocatalytic water splitting approaches are promising for a clean solar fuel production, since solar light can be used directly, without the intermediate step of electricity production. At the same time, carbon nitrides offer the possibility to degrade plastics and treat waste water while producing hydrogen. The knowledge gained in this thesis from carbon nitrides for light driven processes can be transferred to other organic semiconductors to design highly efficient photoactive materials. This might allow our society to solve a variety of environmental issues. Therefore, carbon nitrides offer a sustainable material solution for the energy infrastructure of the future. Further research advancement and tailored solutions as the ones presented in this thesis might help to speed up the process of the implementation of this technology and the development of future materials.

Bibliography

- [1] T. Hisatomi, K. Takanabe, K. Domen, *Catal. Lett.* **2015**, *145* (1), 95-108.
- [2] J. Kosco, F. Moruzzi, B. Willner, I. McCulloch, *Adv. Energy Mater.* **2020**, *10* (39), 2001935.
- [3] J. Kosco, M. Bidwell, H. Cha, T. Martin, C. T. Howells, M. Sachs, D. H. Anjum, S. Gonzalez Lopez, L. Zou, A. Wadsworth, W. Zhang, L. Zhang, J. Tellam, R. Sougrat, F. Laquai, D. M. DeLongchamp, J. R. Durrant, I. McCulloch, *Nat. Mater.* **2020**, *19* (5), 559-565.
- [4] L. Krückemeier, P. Kaienburg, J. Flohre, K. Bittkau, I. Zonno, B. Krogmeier, T. Kirchartz, *Commun. Phys.* **2018**, *1* (1), 27.
- [5] S. Gélinas, A. Rao, A. Kumar, S. L. Smith, A. W. Chin, J. Clark, T. S. van der Poll, G. C. Bazan, R. H. Friend, *Science* **2014**, *343* (6170), 512-516.
- [6] L. Li, Z. Cai, Q. Wu, W.-Y. Lo, N. Zhang, L. X. Chen, L. Yu, *J. Am. Chem. Soc.* **2016**, *138* (24), 7681-7686.
- [7] X. Wang, J. Meng, X. Yang, A. Hu, Y. Yang, Y. Guo, *ACS Appl. Mater. Inter.* **2019**, *11* (1), 588-602.
- [8] R. S. Sprick, Y. Bai, A. A. Y. Guilbert, M. Zbiri, C. M. Aitchison, L. Wilbraham, Y. Yan, D. J. Woods, M. A. Zwijnenburg, A. I. Cooper, *Chem. Mater.* **2019**, *31* (2), 305-313.
- [9] R. S. Sprick, J.-X. Jiang, B. Bonillo, S. Ren, T. Ratvijitvech, P. Guiglion, M. A. Zwijnenburg, D. J. Adams, A. I. Cooper, *J. Am. Chem. Soc.* **2015**, *137* (9), 3265-3270.
- [10] P. B. Pati, G. Damas, L. Tian, D. L. A. Fernandes, L. Zhang, I. B. Pehlivan, T. Edvinsson, C. M. Araujo, H. Tian, *Energ. Environ. Sci.* **2017**, *10* (6), 1372-1376.
- [11] Z. Wang, X. Yang, T. Yang, Y. Zhao, F. Wang, Y. Chen, J. H. Zeng, C. Yan, F. Huang, J.-X. Jiang, *ACS Catal.* **2018**, *8* (9), 8590-8596.
- [12] V. S. Vyas, F. Haase, L. Stegbauer, G. Savasci, F. Podjaski, C. Ochsenfeld, B. V. Lotsch, *Nat. Commun.* **2015**, *6* (1), 8508.
- [13] X. Wang, L. Chen, S. Y. Chong, M. A. Little, Y. Wu, W.-H. Zhu, R. Clowes, Y. Yan, M. A. Zwijnenburg, R. S. Sprick, A. I. Cooper, *Nat. Chem.* **2018**, *10* (12), 1180-1189.

- [14] S. Chen, T. Takata, K. Domen, *Nat. Rev. Mater.* **2017**, 2 (10), 17050.
- [15] W. Lu, T. Xu, Y. Wang, H. Hu, N. Li, X. Jiang, W. Chen, *Appl. Catal., B* **2016**, 180, 20-28.
- [16] Z. Pan, P. Niu, M. Liu, G. Zhang, Z. Zhu, X. Wang, *ChemSusChem* **2020**, 13 (5), 888-892.
- [17] W. Zhen, X. Yuan, X. Ning, X. Gong, C. Xue, *ACS Appl. Mater. Inter.* **2020**, 12 (1), 868-876.
- [18] H. Kasap, D. S. Achilleos, A. Huang, E. Reisner, *J. Am. Chem. Soc.* **2018**, 140 (37), 11604-11607.
- [19] H. Kasap, C. A. Caputo, B. C. M. Martindale, R. Godin, V. W.-h. Lau, B. V. Lotsch, J. R. Durrant, E. Reisner, *J. Am. Chem. Soc.* **2016**, 138 (29), 9183-9192.
- [20] J. Dong, M. Wang, X. Li, L. Chen, Y. He, L. Sun, *ChemSusChem* **2012**, 5 (11), 2133-2138.
- [21] A. Savateev, S. Pronkin, M. G. Willinger, M. Antonietti, D. Dontsova, *Chem.– Asian J.* **2017**, 12 (13), 1517-1522.
- [22] W. Wu, J. Zhang, W. Fan, Z. Li, L. Wang, X. Li, Y. Wang, R. Wang, J. Zheng, M. Wu, H. Zeng, *ACS Catal.* **2016**, 6 (5), 3365-3371.
- [23] T. Uekert, H. Kasap, E. Reisner, *J. Am. Chem. Soc.* **2019**, 141 (38), 15201-15210.
- [24] H. Lan, L. Li, X. An, F. Liu, C. Chen, H. Liu, J. Qu, *Appl. Catal., B* **2017**, 204, 49-57.
- [25] M. C. Hanna, A. J. Nozik, *J. Appl. Phys.* **2006**, 100 (7), 074510.
- [26] M. Liu, L. Guo, S. Jin, B. Tan, *J. Mater. Chem. A* **2019**, 7 (10), 5153-5172.
- [27] G. Zhang, Z.-A. Lan, L. Lin, S. Lin, X. Wang, *Chem. Sci.* **2016**, 7 (5), 3062-3066.
- [28] C. C. L. McCrory, S. Jung, J. C. Peters, T. F. Jaramillo, *J. Am. Chem. Soc.* **2013**, 135 (45), 16977-16987.
- [29] H. Liu, X. Wang, H. Wang, R. Nie, *J. Mater. Chem. B* **2019**, 7 (36), 5432-5448.
- [30] V. Sridhar, F. Podjaski, J. Kröger, A. Jiménez-Solano, B.-W. Park, B. V. Lotsch, M. Sitti, *Proc. Natl. Acad. Sci. U. S. A.* **2020**, 117 (40), 24748-24756.
- [31] S. P. Lee, J. G. Lee, S. Chowdhury, *Sensors* **2008**, 8 (4), 2662-2672.
- [32] Q. Cao, B. Kumru, M. Antonietti, B. V. K. J. Schmidt, *Mater. Horiz.* **2020**, 7 (3), 762-786.
- [33] Y. Miyajima, M. Shkunov, S. R. P. Silva, *Appl. Phys. Lett.* **2009**, 95 (10), 102102.
- [34] A. Savateev, Y. Markushyna, C. M. Schüßlbauer, T. Ullrich, D. M. Guldi, M. Antonietti, *Angew. Chem. Int. Ed.* **2021**, 60 (13), 7436-7443.
- [35] V. Sridhar, F. Podjaski, Y. Alapan, J. Kröger, L. Grunenberg, V. Kishore, B. V. Lotsch, M. Sitti, arxiv:2013.17026v1.

9. Appendix

9.1. Supporting information of chapter 4 “Structural insights into 2D poly(heptazine imide) (PHI)”

9.1.1. Experimental details

Melon: Dicyandiamide (Sigma-Aldrich 99 %) was ground in a mortar and transferred into an open crucible which was heated in a muffle furnace (10 °C/min, 550 °C, 4 h, slow cooling to ambient temperature). The resulting pale, yellow solid was ground and washed four times with DI water.

Potassium melonate: Melon and potassium thiocyanate (Guessing 99 %) were thoroughly ground in a mortar and transferred into a crucible covered with a lid which was placed in a preheated muffle furnace (550 °C, 4 h, slow cooling to ambient temperature). The resulting bright yellow solid was washed three times with DI water. The volume of the combined transparent filtrate was then reduced by rotary evaporation and potassium melonate penta-hydrate precipitated overnight. Filtration yielded a colorless needle shaped compound which was recrystallized from a mixture of water/acetone.

Crystalline ampoule synthesis of potassium poly(heptazine imide) (K-PHI): Dicyandiamide (97 mg, 1.14 mmol, Sigma-Aldrich > 98%), KSCN (18 mg, 0.19 mmol, Guessing 99 %) and potassium melonate penta-hydrate (79 mg, 0.16 mmol) were ground in a mortar and transferred into a Duran glass ampoule, which was subsequently purged four times with argon and then dried under high-vacuum. The ampoule was then sealed and placed into a tube furnace (6 °C/min, 500 °C, 6 h, 1 °C/min, rt). The bright yellow solid was washed four times with DI water and then dried at 60 °C.

Crystalline ampoule synthesis of protonated poly(heptazine) imide (H-PHI): Finely ground cryst. K-PHI (100 mg) was treated with 100 mL of 2 M HCl and stirred for 15 min. The suspension was filtered and the residue washed four times with DI water to yield H-PHI.

Optimized crucible synthesis of potassium poly(heptazine imide): KSCN was heated overnight at 140 °C in vacuum to remove water. Melon (1.5 g) and potassium thiocyanate (3 g, 30.8 mmol, Carl Roth 99 %) were thoroughly ground in a mortar and transferred into an Al₂O₃ crucible which was placed in a tube furnace. The sample was heated in Ar-flow at 400 °C for 1 h with a heating rate of 30 K/min and to 500 °C for 30 min with the same heating rate. After cooling to room temperature the material was washed with DI water six times by centrifugation. The resulting yellow solid was dried at 60 °C in vacuum overnight.

Optimized crucible synthesis of protonated poly(heptazine imide): K-PHI (0.5 g) was stirred in 1 M HCl (100 mL) overnight at room temperature. The material was washed with DI water six times by centrifugation until the supernatant was neutral. The resulting yellow solid was dried at 60 °C in vacuum overnight.

Photocatalytic experiments: In a typical photocatalytic experiment 14-20 mg (note that rates (μmol/gh) were normalized according to the used amount of catalyst) carbon nitride material, 9 mL DI water, 10 vol% of methanol as sacrificial donor and 10 μL of dihydrogen hexachloroplatinate

which forms the platinum co-catalyst *in-situ* were transferred into a glass reactor with a quartz window. The optimized platinum loading of each sample can be extracted from literature (8 wt% for K-PHI and 2 wt% for H-PHI).^[1, 2] The suspension (20 mL total volume) was stirred and sonicated prior to illumination. Additionally, the headspace was evacuated and backfilled with argon several times. A 300 Xenon arc-lamp (Newport, 300 W) equipped with a 1.5 Global AM filter illuminated the suspension with 100 mW/cm² and from the headspace samples were periodically taken and quantified by gas-chromatography (Thermo Scientific TRACE GC Ultra) equipped with a TCD detector using argon as the carrier gas. The reaction was thermostated at 25 °C during illumination as in previous works.^[1, 2]

Dark photocatalysis experiments: Prior to dark photocatalysis experiments the glass vessels were cleaned with *aqua regia*, to avoid contaminations of platinum of previous runs. 15 mg of optimized H-PHI was suspended in 20 mL 1 M sodium phosphate buffer (containing sodium hydrogen phosphate and sodium dihydrogen phosphate only) at a pH of 7. 4-Methylbenzyl alcohol (4-MBA) (35 mg) was added as a sacrificial donor and the headspace was evacuated and flooded with argon several times. The suspension was illuminated with a 300 Xenon arc-lamp (Newport, 300 W) equipped with an 1.5 Global AM filter illuminated the suspension with an intensity of 100 mW/cm² for 2 h. After illumination 50 µL Pt nanoparticle suspension (1000 ppm aqueous colloidal solution, Aldrich) was injected into the reactor by using a gas tight needle to start the hydrogen evolution reaction. This injection was delayed by 0, 2, 4, and 6 h after illumination had stopped. During the periods of darkness the reaction vessel was wrapped in aluminum foil to avoid stray light.^[3]

9.1.2. Instrumental details

Solid state ^{13}C and ^{15}N magic angle spinning (MAS) NMR experiments (main text Figure 4.3 a, b and d, e) were performed on a Bruker Avance-III 400 MHz instrument at the frequencies of 400, 100.61 and 40.53 MHz, respectively ($B_0 = 9.4$ T). All ^1H and ^{13}C spectra are referenced indirectly with respect to tetramethylsilane (TMS) using adamantane as secondary reference and the ^{14}N and ^{15}N to nitromethane using glycine and/or NH_4Cl as a secondary reference. MAS frequencies were between 6.5-14.0 kHz in a 4 mm ZrO_2 rotor.

The 2D ^{13}C - ^{15}N HETCOR spectra (main text Figure 4.3 g) was recorded on a Bruker Avance III 400 DNP spectrometer equipped with an Ascend 400 DNP magnet system and a low temperature 3.2 mm triple-resonance probe. DNP-enhanced spectra were measured with microwave irradiation. The DNP-enhanced spectrum was recorded at a field of 9.4 T corresponding to frequencies of 400.03 MHz for ^1H , 100.60 MHz for ^{13}C , and 40.54 MHz for ^{15}N , at nominally 110 K and at a spinning rate of 8.0 kHz. For DNP, approximately 25 mg of the sample was mixed with 15 μl of a 15 mM AMUPol in glycerol- d_8 /D $_2$ O/H $_2$ O (60:30:10, v/v/v) solution. This resulted in DNP enhancement of about 70. The HETCOR was performed using a double CP experiment. First, the ^1H magnetization was transferred to ^{13}C after a CP contact time of 8 ms (ramped cross-polarization experiment, where the nutation frequency ν_{nut} on the proton channel was varied linearly by 50%). Second, after a t_1 evolution time, a ramped CP from ^{13}C to ^{15}N (ramp of 70% on ^{15}N) with a contact time of 1 ms was employed to transfer the magnetization to ^{15}N and with simultaneously strong continuous wave ^1H decoupling (105 kHz). Finally, ^1H decoupling was applied using a spinal-64 sequence with a radio-frequency field of 80 kHz during t_1 and t_2 acquisition times.

Additional ^1H one-pulse MAS, ^{13}C CP MAS, ^1H - ^{14}N *D*-HMQC MAS and ^1H - ^1H DQ-SQ MAS experiments were acquired on a Bruker Avance III HD spectrometer operating at a B_0 field of 14.1 T. High-speed MAS ^1H (600.15 MHz) one-pulse spectra were recorded after a 90° pulse of 1.2 μs at a spinning frequency of 62.5 kHz using a Bruker 1.3 mm double-resonance MAS probe. ^{13}C (150.91 MHz) CP experiments were acquired at a spinning rate of 62.5 kHz with a contact time of 3 ms and a ^1H Spinal-64 decoupling of 25 kHz during acquisition. ^1H - ^{14}N *D*-HMQC experiment was performed at a spinning speed of 40.0 kHz using a triple-resonance 1.9 mm probe (^{14}N at 43.35 MHz). The super-cycled symmetry based SR4_1^2 sequence^[4] was used for the ^1H - ^{14}N dipolar recoupling which lasted 200 μs . For the ^1H - ^1H DQ-SQ experiments the sample were spun at 62.5 kHz (1.3 mm rotors). The DQ excitation and reconversion was executed using the R12_2^5 symmetry based recoupling.^[5]

The ^{13}C and ^{15}N direct excitation Figure S1.11 were acquired on a Bruker Avance III HD spectrometer operating at a B_0 field of 9.4 T using a double-resonance 4 mm Bruker MAS probe and rotation frequencies of 12.5 kHz and 10.0 kHz, respectively. The ^{13}C (100.61 MHz) and ^{15}N (40.56 MHz) Bloch-decay experiments were performed using respective 90° pulses of 3.5 and 4.8 μs , and recycle delays of 600 s and 900 s. Acquisition was accompanied by high power proton decoupling using a spinal-64 sequence with a radio-frequency field of 70 kHz.

Laboratory X-ray powder diffraction (PXRD) patterns of H-PHI and K-PHI were collected using a STOE Stadi P diffractometer with $\text{CuK}\alpha 1$ radiation ($\lambda = 1.540598 \text{ \AA}$) equipped with a MYTHEN 1 K detector (Dectris Ltd.) and a curved Ge(111) monochromator.

X-ray total scattering measurements were performed on a separate set of samples using beamline 28-ID-2 (XPD) of the National Synchrotron Light Source II (NSLS-II) at Brookhaven National Laboratory. Powders were loaded into 1 mm ID Kapton capillaries and measured in rapid acquisition PDF mode^[6] with an x-ray energy of 68.01 keV ($\lambda = 0.1823 \text{ \AA}$) using a Perkin-Elmer 2D detector (2048 x 2048 pixels and 200 x 200 μm pixel size) mounted orthogonal to the incident beam path with a sample-to-detector distance of 205.6443 mm for data collected to a high maximum value of momentum transfer Q_{max} (where $Q=4\pi\sin\theta/\lambda$ for elastic scattering) and 1421.219 mm for data with higher Q resolution. Calibration of the detector geometry was carried out using a standard Ni sample.

Additional total scattering measurements were performed at beamline ID31 at the ESRF using an incident energy of 68.54 keV ($\lambda = 0.1809 \text{ \AA}$), sample-to-detector distance of 273.38 mm, DECTRIS Eiger2X 16M single photon counting detector, and calibration using NIST CeO₂ 674b.

Force field minimizations and dynamics were performed using the Amber16 program package.^[7] Periodic boundary conditions and particle mesh Ewald summation (PME) with a cutoff value of 12 \AA were employed. A single potassium ion placed in a solvent box of water was minimized using the conjugate gradient algorithm in 10000 steps. The system was then heated to 300 K in 30 picoseconds and equilibrated subsequently for 30 nanoseconds with time steps of 2 femtoseconds employing the SETTLE algorithm. Molecular dynamics calculations were performed using the NAMD program package.^[8]

Diffuse reflectance UV-Vis spectra were collected on a Cary 5000 spectrometer referenced to PTFE or barium sulfate as reference.

Infrared (IR) spectra were recorded on a JASCO Fourier transform infrared spectrometer equipped with a diamond attenuated total reflectance (ATR) unit and a resolution of 4 cm^{-1} .

Transmission electron microscope: Powders, ground and suspended in butanol, were distributed onto a holey carbon/copper grid and studied with a Philips CM 30 ST microscope (300 kV, LaB₆ cathode). Images were taken with a TVIPS TemCam-F216 CMOS Camera. Simulations of the selected area electron diffraction patterns were obtained with the JEMS software package.^[9]

Thermogravimetric (TG) analyses were performed at using a STA 449 F5-Jupiter (Netzsch) device. The sample was heated up in a corundum crucible in a dynamic argon (50 mL/ min) atmosphere to 300, 350 or 400 $^{\circ}\text{C}$ with a heating rate of 10 K min^{-1} , respectively. An empty corundum crucible was used as a reference. Corrections of instrumental effects and the buoyancy were performed with Al₂O₃ as an inert reference material during a separate measurement.

Combustion analysis for detection of C, H, N, S was performed on a Elementar Analysensysteme GmbH – Vario micro elemental analyzer.

Inductively coupled plasma atomic emission spectroscopy (ICP-AES) data was obtained from a Varian Vista RL CCD simultaneous ICP-ACS device. The sample was dissolved in concentrated HNO₃ in the microwave oven at 150 °C, before injecting into the plasma.

Electron paramagnetic resonance (EPR) spectra were measured on a Bruker EMXnano X-band device operating at an excitation frequency of ~9.6 GHz and 100 mW microwave power.

Water sorption measurements were performed on an Autosorb-iQ surface analyzer with vapor option (Quantachrome Instruments, USA). To initially remove guest molecules the samples were outgassed in vacuum at 200 °C for 12 h. The measurements were performed at 273 K.

The Raman spectra were taken with a Jobin Yvon Typ V 010 labram single grating spectrometer equipped with a double super razor edge filter and a peltier cooled CCD camera. The spectra were recorded in quasi-backscattering geometry using the linearly polarized light of a 632.8 nm He/Ne Laser and a 532.0 nm diode laser, respectively with powers of approx. 1 mW. The beam was focused to a 2-5 μm spot through the 100 x objective of an microscope onto the sample within a glass capillary.

9.1.3. Transmission electron microscopy (TEM)

H-PHI:

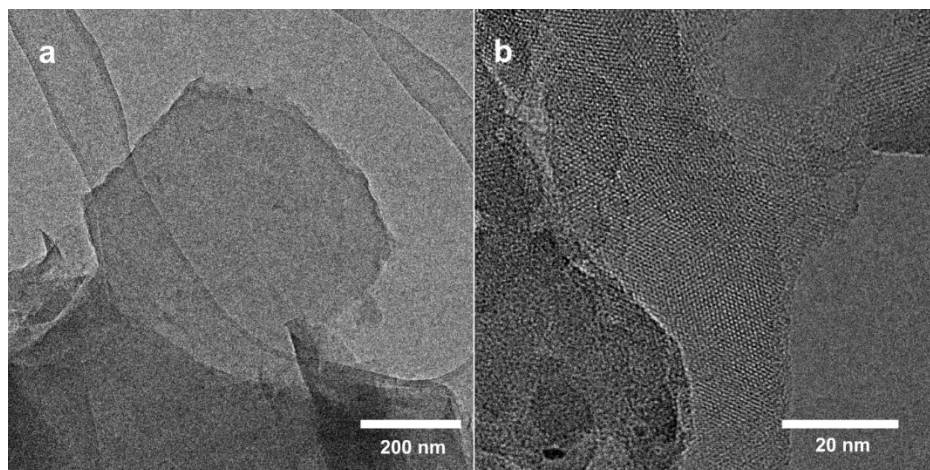


Figure S1.1: a) TEM overview image of H-PHI revealing the sheet-like morphology, b) high-resolution TEM image of the same sample.

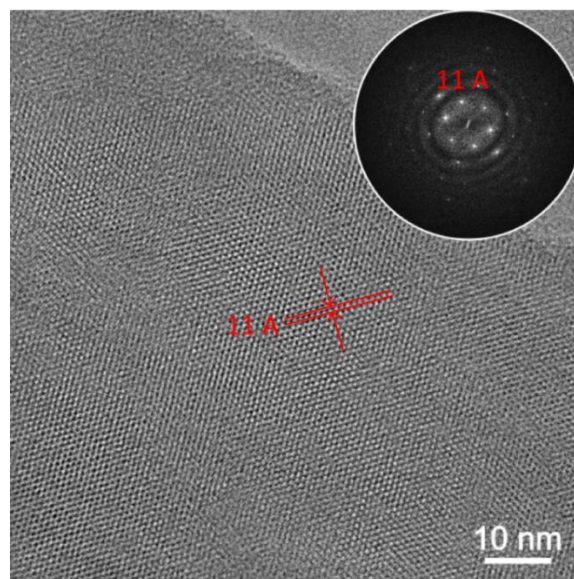


Figure S1.2: HR-TEM image (Average Background Subtraction Filtered) of highly crystalline H-PHI, lattice planes could be determined at 11 Å in accordance with XRD results (picture in the main text is zoomed into the upper right part to enhance visibility of the lattice fringes). A clear hexagonal pattern is observable in the FFT, however weak powder rings indicate the presence of polycrystalline material.

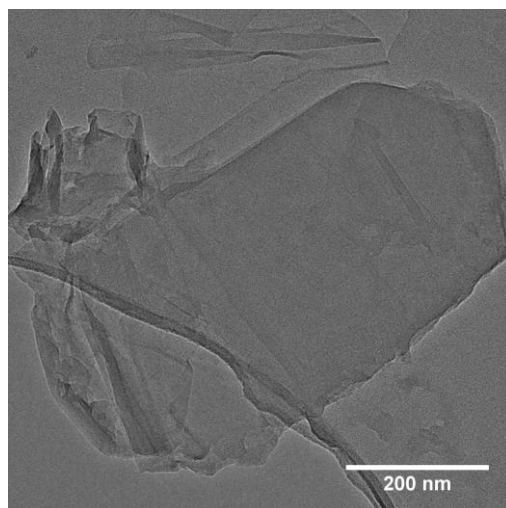
K-PHI:

Figure S1.3: TEM overview image of K-PHI revealing the sheet-like morphology and large lateral extension of the sheets. Large thin flakes exhibit wrinkles.

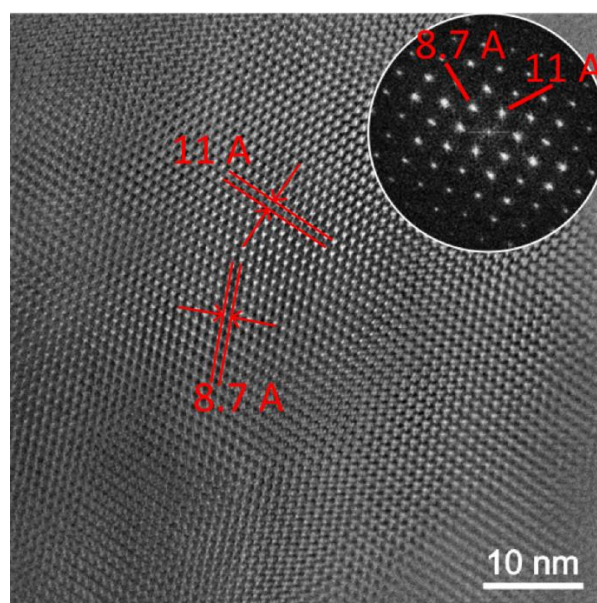


Figure S1.4: HR-TEM image (Average Background Subtraction Filtered) of highly crystalline K-PHI, lattice planes could be determined at 11.1 Å and 8.7 Å in accordance with XRD results (picture in the main text is zoomed into upper right part to enhance visibility of the lattice fringes). The clean FFT in the inset suggests a single crystalline sheet.

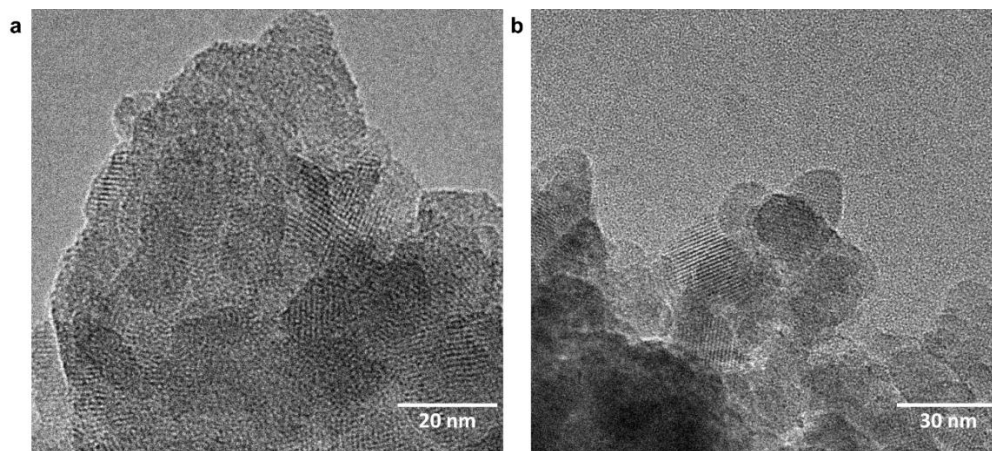


Figure S1.5: In comparison to the crystalline sheets (e.g. in Figure S1.3): two (a and b) TEM micrographs of an optimized K-PHI sample revealing much smaller crystallite sizes in the range of 20-30 nm. Please also see crystallite size estimation in Table S1.1, section 9.1.5. X-ray powder diffraction.

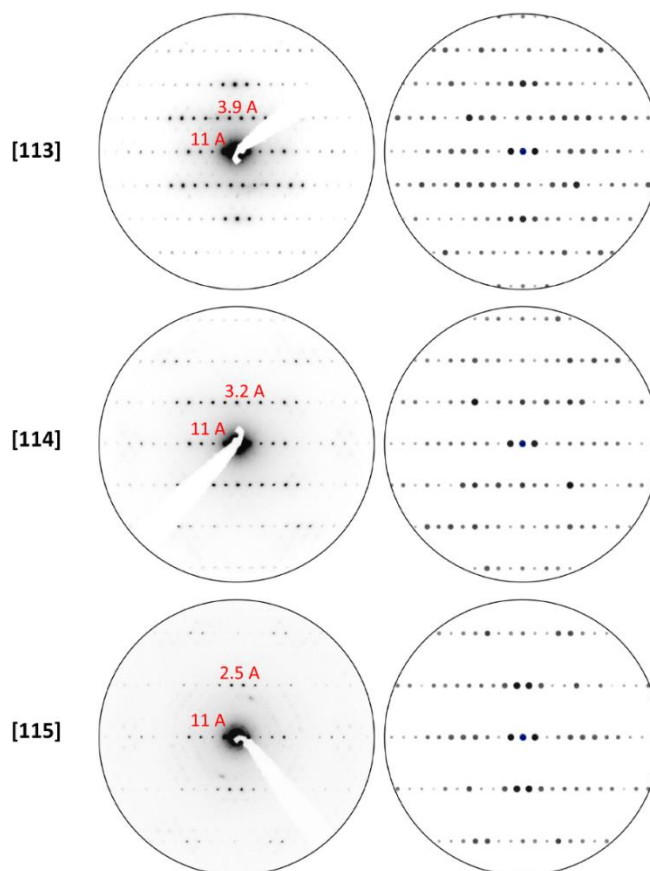


Figure S1.6: a, c, f) Experimental SAED patterns of ampoule-synthesized cryst. K-PHI and b, d, f) ED-simulation from Rietveld refined model for zone axis [113], [114] and [115], respectively. The reasonable agreement for experimental and simulated patterns is rare for carbon nitrides. In some cases it was even possible to obtain the ED of multiple zone axes by tilting of the specimen. Usually carbon nitrides crystallites are prone to electron beam damage and amorphization upon too long exposures in the electron beam.

Tilting series of H-PHI:

Interestingly, the observed hexagonal diffraction pattern for H-PHI (Figure 4.2b, main text) is relatively insensitive to the tilting angle of the specimen for up to $\pm 10^\circ$. This “robustness” is not found in K-PHI where the crystallites need to be correctly aligned to obtain the pattern seen in Figure 4.2f, main text). This effect may be influenced by several factors: Slightly distorted stacking distances in H-PHI can cause the reciprocal lattice points to elongate thus satisfying the Laue condition in a range of orientations of the TEM grid. This points towards a lesser degree of order in the H-PHI crystals. Additionally, buckling of very thin layers can also cause such a behavior as observed for 2D materials such as graphene or MoS₂.^[10, 11]

9.1.4. Fourier-transform infrared spectrum

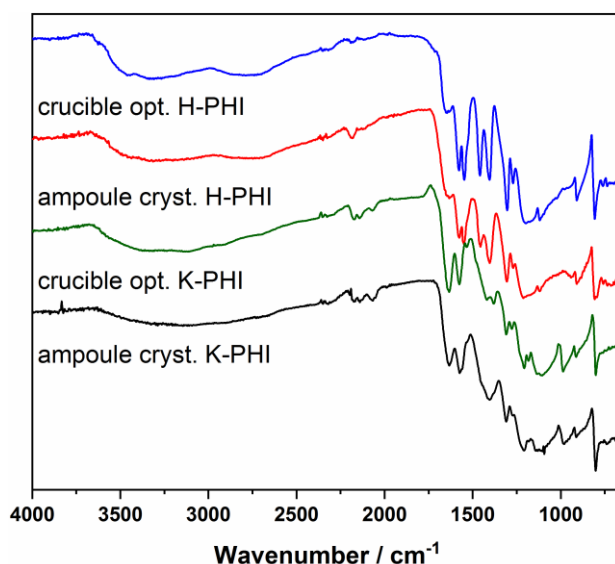


Figure S1.7: FT-IR spectra of K/H-PHI from ampoule synthesis (crystalline) and optimized synthesis in a crucible. In terms of absorption bands the respective ampoule and crucible species do not differ significantly except for slightly higher water content (from elemental analysis) in the open crucible case, which causes higher intensity in the OH and hydrogen bond regime.

9.1.5. X-ray powder diffraction (XRD) and size estimations

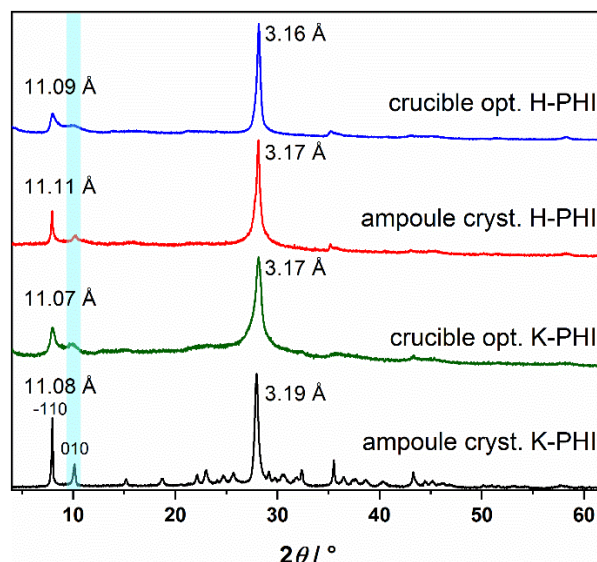


Figure S1.8: PXRD of optimized crucible and ampoule synthesized K-PHI and H-PHI, respectively. Cyan marked area highlights the 010 reflection, which is broadened in the optimized samples and in H-PHI.

Determination of crystallite size from PXRD:

The lateral and vertical sizes of the crystalline and optimized PHI-materials were determined from the powder patterns presented in Figure S1.8 by using the Scherrer-equation^[12]:

$$\tau = \frac{K \cdot \lambda}{\beta \cdot \cos \theta}$$

where τ is the mean size of the ordered domains, K a dimensionless shape factor, λ is the wavelength of the diffractometer, β is the diffraction line broadening and θ is the Bragg angle. The instrumental profile was determined by refining the instrumental function, described by the fundamental parameter^[13, 14] approach using a diffraction pattern of the Si640D NIST standard and subtracted from the diffraction line profile. The lateral crystallite size was determined by a single line fit in a 2θ range of 6.0 to 12.5° of the $\bar{1}10$ reflection using the TOPAS^[15] software. As the $\bar{1}10$ reflection overlaps with the anisotropically broadened 010 reflection a 2nd peak was included into the refinement and independently refined. The background was modeled with Chebychev polynomials of 2nd order. For the estimation of the vertical crystallite size a single line fit of the 001 reflection in a 2θ range of 26.5 to 29.5° was performed.

The estimated crystallite sizes of the crystalline and optimized PHI samples are presented in Table S1.1. Due to the complex background of the diffraction patterns, that is governed by diffuse scattering and due to the overlap with anisotropically broadened reflections, a vastly increased analytical error ($\approx 10\%$) is given, that is far larger than the analytical error which is to be expected for a crystallite size determination using a high resolution laboratory X-ray powder diffractometer ($\approx 1-2\%$). Despite the large analytical error it can be clearly seen that the crucible optimization procedure leads to a significantly smaller lateral crystallite size of both K- and H-PHI (Table S1.1), whereas the vertical crystallite size is almost not affected. Hence, the crucible optimization leads

to a decrease of the extension of the 2-dimensional layers, i.e. lateral crystallite size but the number of layers in a crystallite, i.e. vertical crystallite size remains the same.

Table S1.1: Estimation of the lateral and the vertical crystallite sizes of ampoule crystalline and crucible optimized K- and H-PHI.

Sample	lateral size / nm	vertical size / nm
ampoule cryst. K-PHI	102 ± 10	25 ± 3
crucible opt. K-PHI	19 ± 2	19 ± 2
ampoule cryst. H-PHI	48 ± 5	18 ± 2
crucible opt. H-PHI	17 ± 2	23 ± 2

Effect of crystallite sizes on cyanamide groups and defects:

Depending on the batch, we observe one NCN-group per 2-5 heptazine units as retrieved from quantitative (i.e. direct excitation) ^{13}C -ssNMR spectroscopy. However, this value is slightly higher than can be explained just by terminating cyanamide at the edges of the sheets, given the lateral sizes found via PXRD analysis (Table S1.1). In order to account for the higher NCN content, especially for larger crystallites, defects in the form of missing heptazine building blocks may be present, which in turn increase the NCN terminations within the sheet. Note that in this context a point defect is defined as a missing heptazine unit. Hence, after removal of a heptazine unit, three additional NCN moieties are introduced into the PHI sheet. As the sheets are also terminated with NCN at the perimeter, the sheet size also influences the overall amount of NCN. A theoretical estimation of the level of these defects is made in Figure S1.9 for a 100 nm and 20 nm sheet according to the values in Table S1.1. For each size (100 nm or 20 nm) of the rectangular sheet the following boundary conditions are used for the mathematical function that yields the curves in Figure S1.9:

100 nm K-PHI rectangular sheet:

- 100 nm is the diagonal of the model sheet, the distance from pore to pore is 12.8 Å
- The sheet consists of **~7308 heptazine units** (before introduction of internal point defects)
- The sheet is terminated by **~280 NCN**-groups at edge sites (perimeter)
- Heptazine/NCN group = 26.1

20 nm K-PHI rectangular sheet:

- 20 nm is the diagonal of the model sheet, the distance from pore to pore is 12.8 Å
- The sheet consists of **~420 heptazine units** (before introduction of internal point defects)
- The sheet is terminated by **~74 NCN**-groups at edge sites (perimeter)
- Heptazine/NCN group = 5.7

From the two examples above it is visible that the 20 nm sheet (without any defects) intrinsically contains more NCN-groups per heptazine due to its larger perimeter to diagonal ratio. However, in the real samples the amount of cyanamide was found to be larger in the large crystallites.

Therefore, point defects are introduced into the sheets, as described, above to yield a higher amount of cyanamide and to match the experimental NCN content for the respective sample.

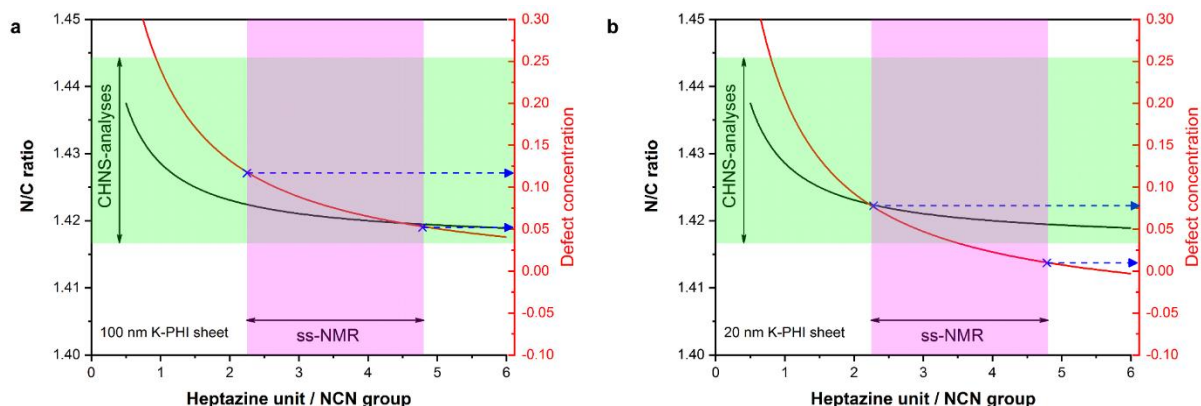


Figure S1.9: Mathematical function of the N/C ratio (black line) and defect concentration (red line) for a 100 nm (left) and 20 nm (right) K-PHI sheet as a function of the heptazine unit/NCN ratio. The defect concentration is the ratio of the heptazine vacancies to the amount of heptazine units in the defectless sheet. The calculation of the defect concentration is taking the terminating NCN-groups at edges into account. The extension of the green and magenta areas presents the batch to batch variation observed for synthesis of K-PHI. The green area represents values obtained from combustion analysis while the magenta area represents the integrated intensities of ^{13}C -ssNMR measurements (heptazine/cyanamide intensity) in different batches. The dashed blue lines show the minimal and maximal defect concentration based on the experimentally found range of heptazine/NCN group, respectively.

In Figure S1.9 a, the resulting defect concentration and the N/C ratio is theoretically calculated as a function of the ratio of heptazine units per NCN-group for a 100 nm K-PHI sheet. The starting values for the calculations are the sheets without any defects as given in the boundary conditions above. As more and more heptazine units are replaced by NCN-groups, the defect concentration is increased and also the N/C ratio is affected (going from right to left on the abscissa). The green area represents the experimentally observed distribution of the N/C ratio which is a relatively large span due to batch to batch variations and the uncertainty of the method. The magenta area represents the values for the heptazine/NCN-group ratio obtained from the integrated intensities of the direct ^{13}C -ssNMR spectroscopy. According to the 100 nm model, for a ratio on the abscissa of one NCN-group in roughly every 2nd to 5th heptazine units, the concentration of point defects would have to range from 5-12%. This would mean that in a 100 nm sheet every 8th to 20th heptazine unit is missing and replaced by three internal NCN-groups.

The N/C ratio for these x-values would range from 1.420-1.422, which correlates quite well with the measured N/C ratio of 1.416 for the batch whose data is presented in Figure S1.8. Note that the N/C ratio should be taken with a grain of salt as there is significant variance in the combustion analyses even for the same batch, which does not allow for an exact determination of the experimental N/C ratio.

For the crucible optimized K-PHI sample (compare Table S1.1) the lateral sheet size is approx. 20 nm (Figure S1.9b) and therefore the defect concentration (i.e. missing heptazine units) ranges from 1-9% for the same range of x-values (approx. 2 to 5). This shows that in order to yield the same experimental heptazine/NCN group ratio smaller crystallites have less point defects. This is related to the fact that the heptazine/edge NCN-terminations ratio (compare to the boundary conditions) is higher for those sheets. Although having less point defects, these crystallites are

very small and therefore yield a significant broadening in the PXRD pattern. The N/C ratio for this span ranges from 1.422-1.419 accordingly, while the experimental value for this batch amounts to 1.422.

Overall, the above estimations, implying a higher amount of point defects in the sheets for the larger sheets, yield a possible explanation for why a higher amount of NCN-groups in the crystalline samples is observed in NMR spectroscopy. The higher nitrogen content for the crystalline ampoule material could, however, also originate from amorphous pore material, which is blocked and cannot be removed during the washing procedure. Another explanation can be the different synthetic approach for the large crystallite samples. For the large crystalline sheets, we have used potassium melonate as a starting material, which intrinsically has NCN-moieties attached, while in the case of the 20 nm sheets, polymeric melon was used as a starting, which bears no NCN-moieties.

9.1.6. Electron paramagnetic resonance (EPR)

The g-factors of the paramagnetic compounds were determined with the following formula on a X-band device.

$$g = \frac{h \nu_{MW}}{\mu_B B_{res}}$$

where g is the g-factor, h the Planck constant, ν_{MW} the microwave frequency, μ_B the Bohr magneton and B_{res} the magnetic field at resonance.

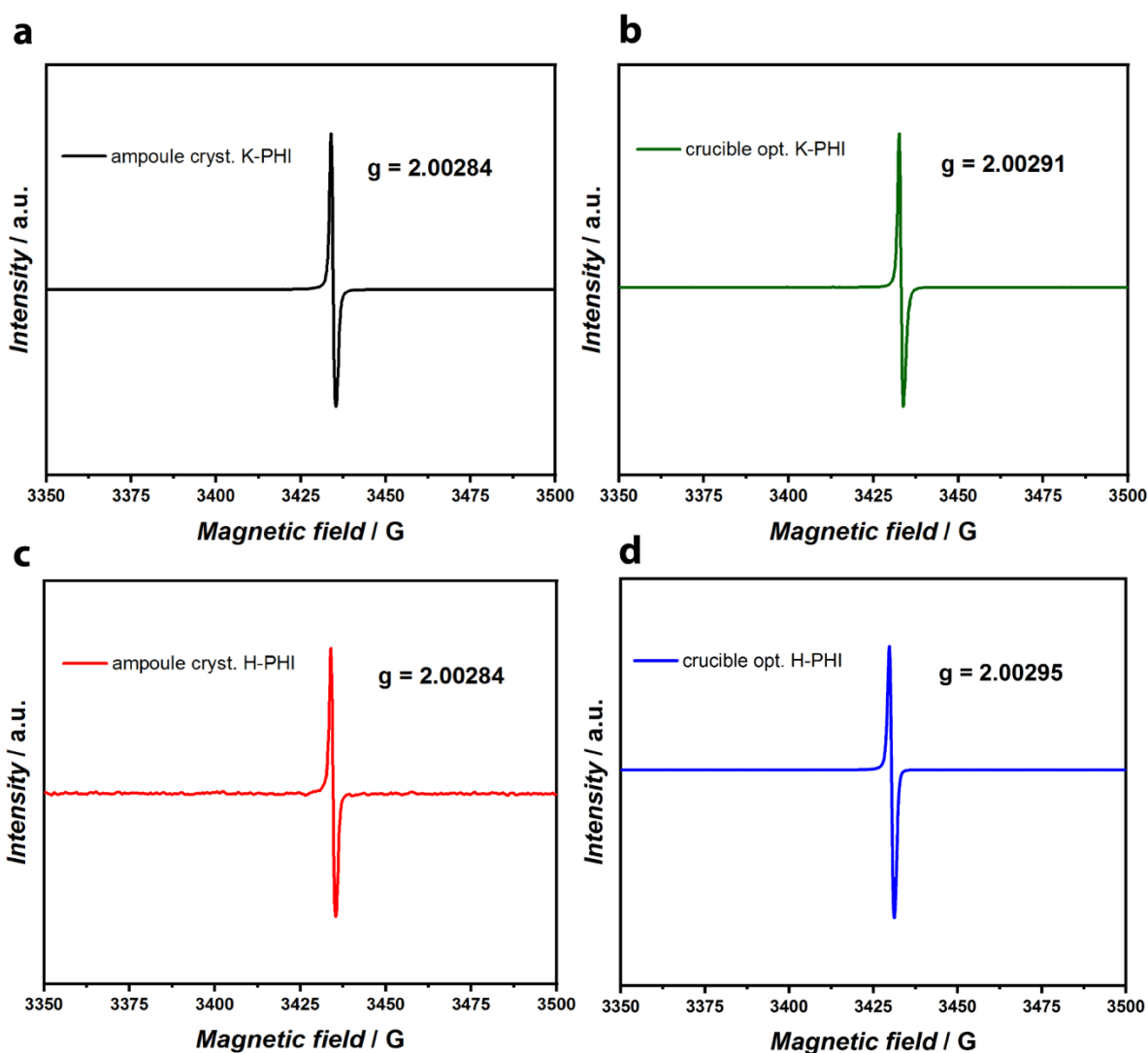


Figure S1.10: Electron paramagnetic resonance (EPR) spectra of a) crystalline (ampoule) and b) optimized (crucible) K-PHI and c) crystalline (ampoule) and d) optimized (crucible) of H-PHI. g-factors values are very similar to the free electron with ca. 2.0028. The samples have been prepared with 4-MBA as an electron donor and flushed with argon. The samples were irradiated with a Xe-lamp (AM 1.5 G filter) prior to the measurement.

9.1.7. Solid-state nuclear magnetic resonance (ssNMR)

^{13}C and ^{15}N spectra:

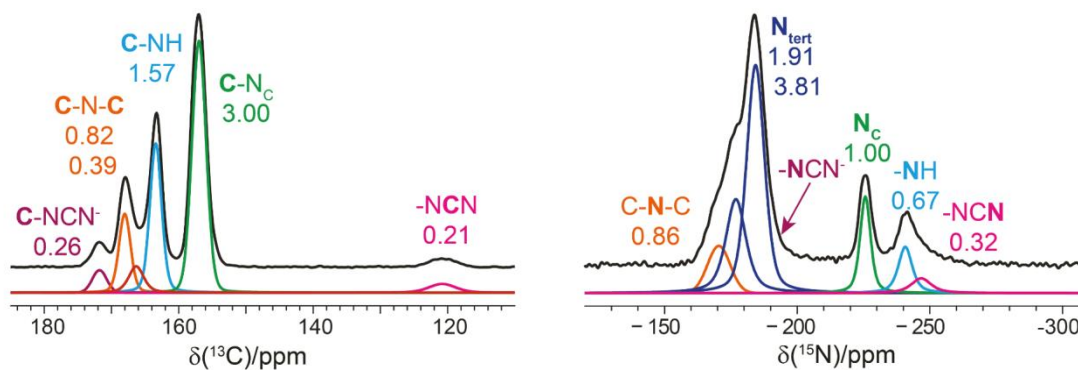


Figure S1.11: One-pulse ^{13}C (left) and ^{15}N (right) ssNMR spectra of K-PHI along with their deconvolution. Area for each individual peak is given next to the peaks.

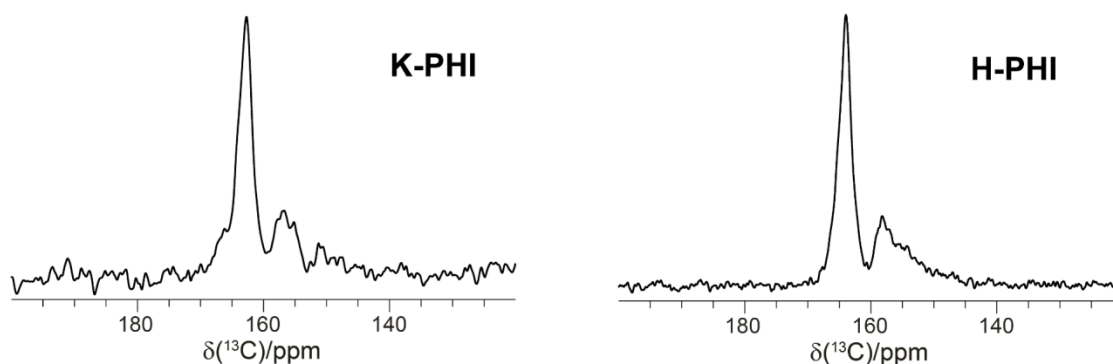


Figure S1.12: ^{13}C CP MAS spectra of K-PHI (left) and H-PHI (right) acquired at a MAS of 62.5 kHz.

^1H -ssNMR spectra at high spinning frequencies of 62.5 kHz:

Unexpectedly, the range of proton shifts is rather large for only water and the bridging NH-group in the structure. However, this variety may be explained by water/NH-, water/heptazine-, water/water- and water/potassium- interactions within K-PHI and H-PHI. The more acidic character of H-PHI with leads further downfield shifted signals (12.3 ppm in H-PHI), thus an even broader distribution.

Drying the samples at 120 °C in vacuum for two days leads to changes in the peak intensities. On the one hand the loss of water causes the “naked” proton shift (7.0 ppm for K-PHI and 7.3 ppm for H-PHI) of the imide bridge to emerge more strongly. DFT calculations show that the pore water is responsible for a broader distribution of this signal due to the described interactions named above (compare Figure S1.19 and Figure S1.20). In the calculated case the imide proton shifts from 7.8 ppm without water to 11.0 ppm with an attached water molecule. On the other hand not all water is removed by the drying step, also indicated by more than one step in the TG-

experiments (compare Figure S1.26) related to less strongly and strongly bound water, where the latter species are only removed at higher temperatures or in ultra-high vacuum.

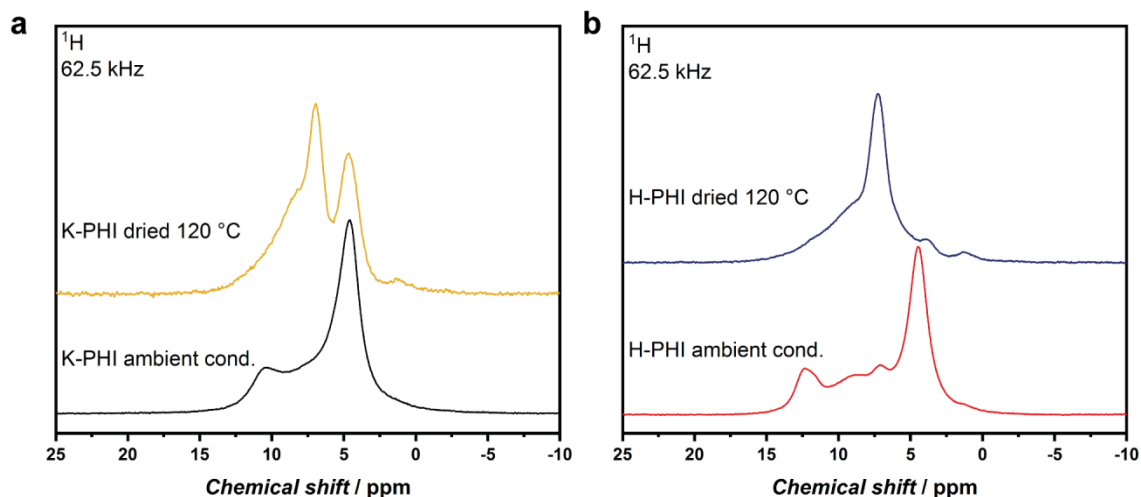


Figure S1.13: ^1H ssNMR spectra of a) ampoule cryst. K-PHI dried in vacuum at 120 °C for two days, and at ambient conditions, b) corresponding spectra for H-PHI. Loss of water detectable by reduced intensity of the water peak at 5 ppm and changed intensities/positions for the NH-group upon drying, likely caused by water/network interactions and a loss thereof in dried state.

In summary, proton ssNMR first of all shows that chemically different water species are present within the pores of the poly(heptazine imide) backbone. The water interaction causes a broad distribution of ^1H -signals (at least five for H-PHI). Additionally, (partial) removal of water has a major effect as it changes the position of signals due to a loss of interaction while at the same time the amount of protons in the sample is reduced therefore increasing the difficulty of assignment. Nevertheless, ^1H - ^{14}N -HMQC SR-4 experiments for the wet (Figure 4.3g, main text) and the dried H-PHI (Figure S1.17) sample show that there is predominantly a correlation between a network nitrogen atom and the proton at 12.3 ppm, while the dry sample shows a major contribution from a network nitrogen atom with the proton at 7.3 ppm.

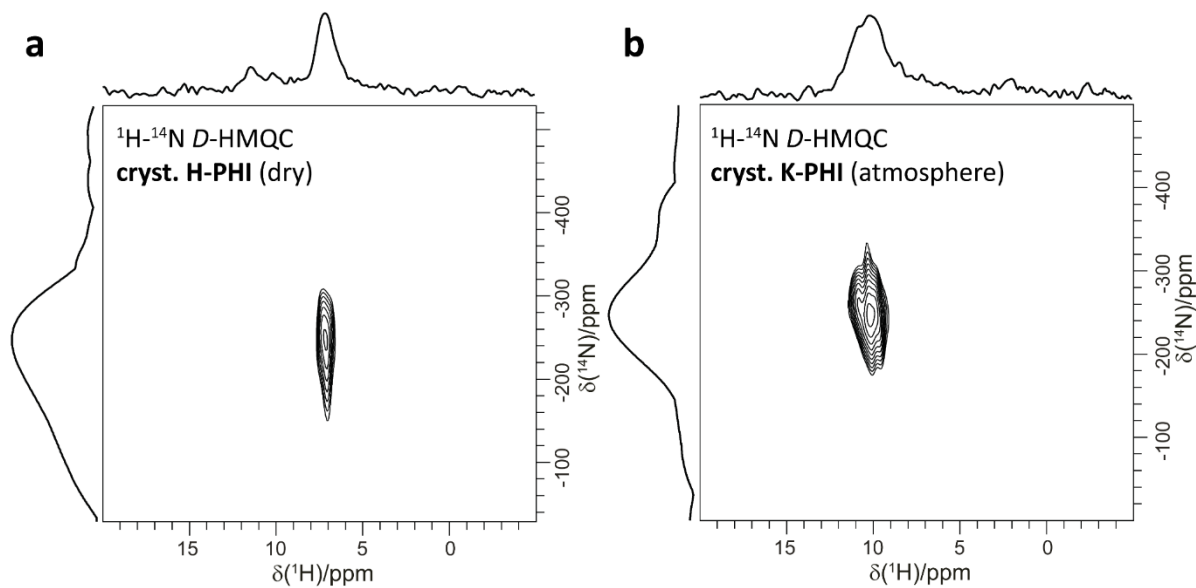


Figure S1.14: a) ^1H - ^{14}N D-HMQC MAS spectrum of H-PHI dried at 120 °C and vacuum (10^{-2} mbar) as a comparison to the spectrum in Figure 4.3 h at ambient conditions. It is well visible that compared to Figure 4.2 h in the main text, the correlation signal is shifted upfield when dried. b) ^1H - ^{14}N D-HMQC MAS spectra of K-PHI under ambient conditions.

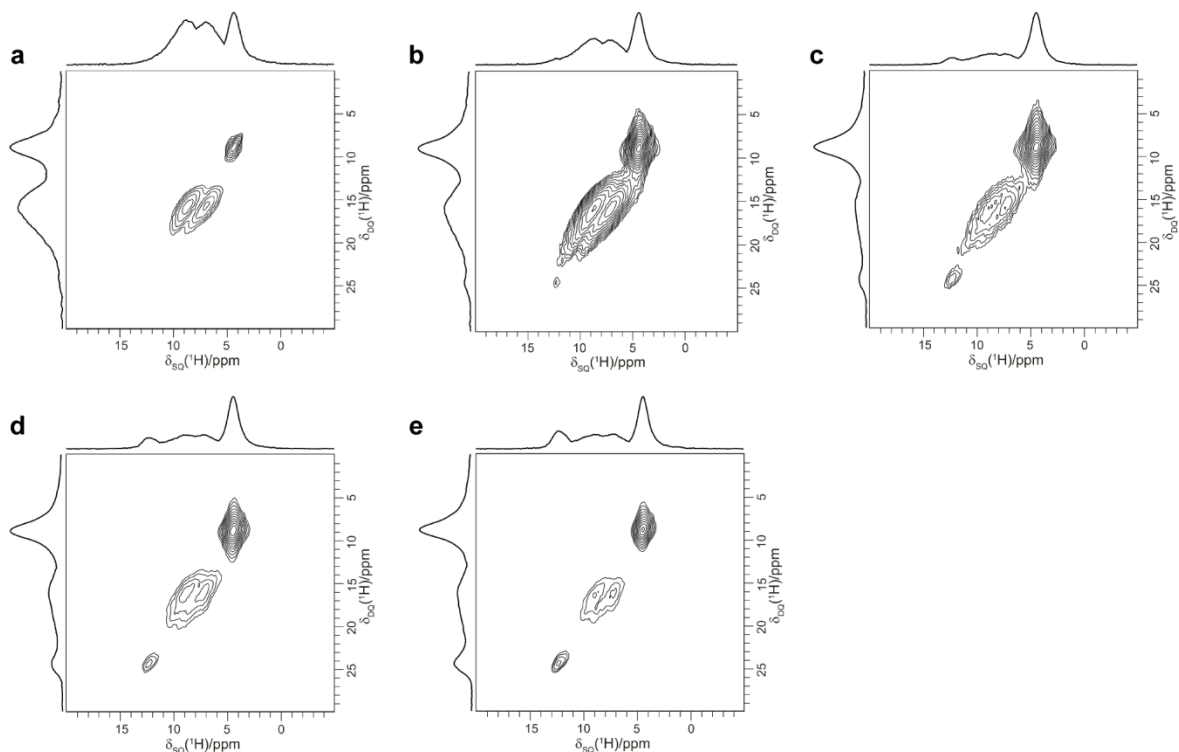


Figure S1.15: ^1H - ^1H DQ-SQ MAS spectra of H-PHI with increasing recoupling times of a) 32 μs , b) 64 μs , c) 96 μs , d) 128 μs and e) 160 μs . Increasing recoupling times correspond to greater distances between coupling protons.

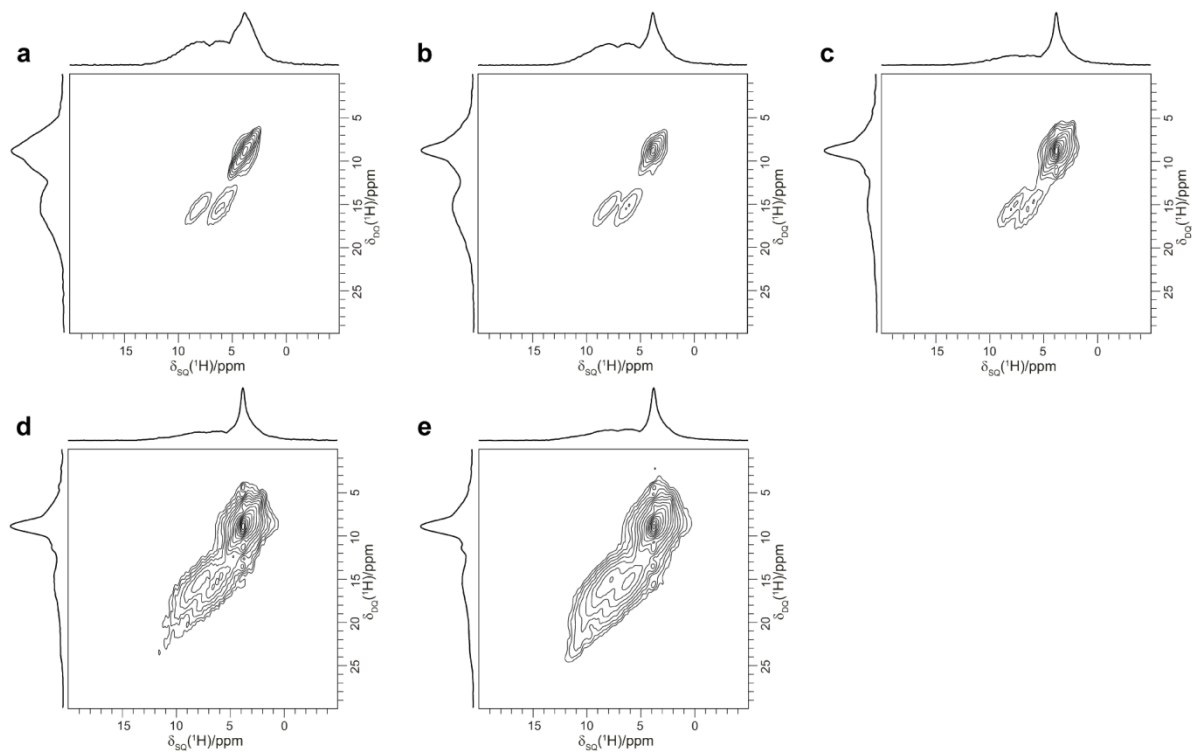


Figure S1.16: ^1H - ^1H DQ-SQ MAS spectra of K-PHI with increasing recoupling times of a) 32 μs , b) 64 μs , c) 96 μs , d) 128 μs and e) 160 μs . Increasing recoupling times correspond to greater distances between coupling protons.

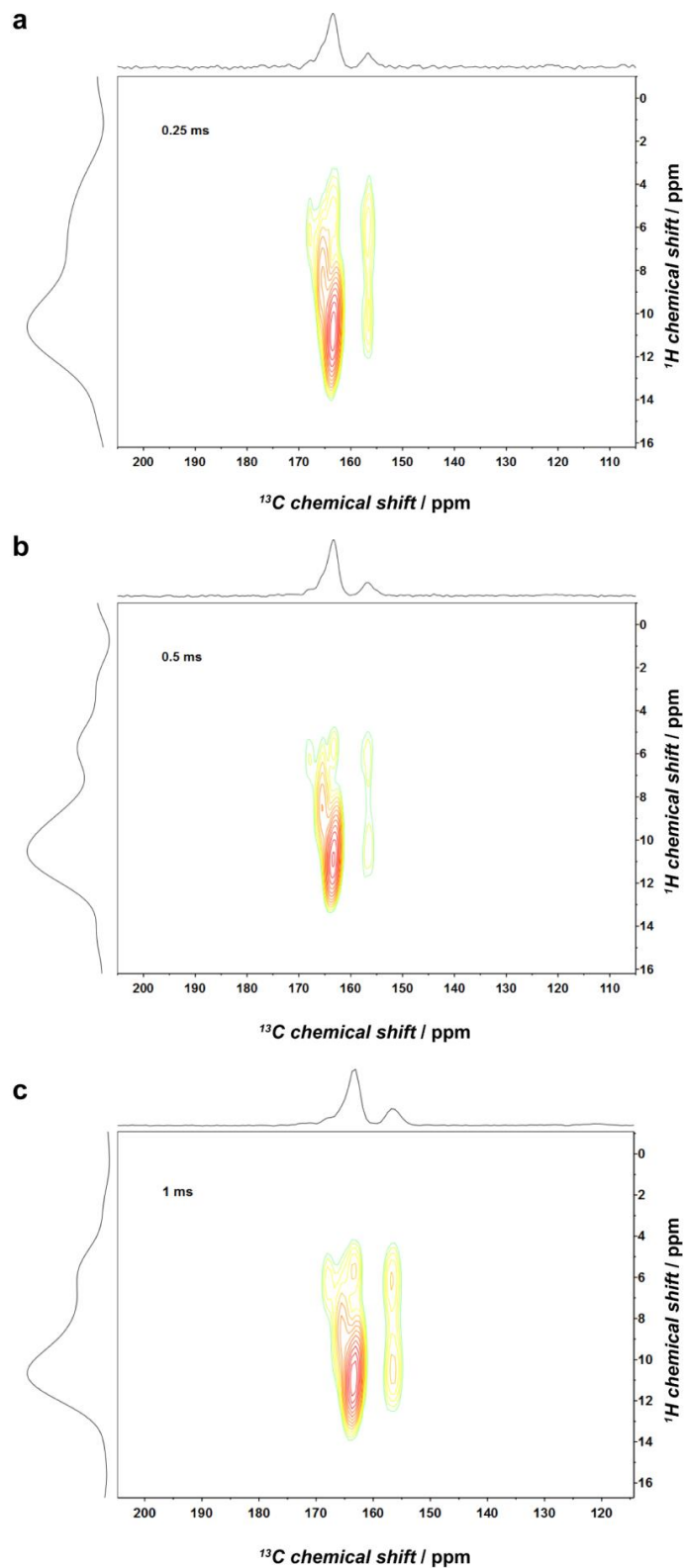


Figure S1.17: Solid state ^{13}C - ^1H MAS HETCOR NMR spectrum of K-PHI partially enriched via the use of $\text{KS}^{13}\text{C}^{15}\text{N}$ as starting material. a) 0.25 ms b) 0.5 ms and c) 1 ms contact time.

9.1.8. Quantum-chemical calculations

Methodology:

Structures for all investigated geometries were optimized at the PBE0-D3/def2-TZVP^[16-19] level of theory. Monosolvated model systems were optimized by optimizing the PHI pore fragment and a single water molecule in separate calculations, optimizing the monosolvated PHI pore fragment complex afterwards with constraints on the PHI pore fragment.

NMR chemical shifts were obtained on B97-2/pcsSeg-2^[20, 21] level of theory using previously obtained geometries.

Geometry optimizations were performed using the Turbomole^[22] program package in version 7.0.2, NMR chemical shifts were calculated using the FermiONS++^[23, 24] program package.

H-PHI

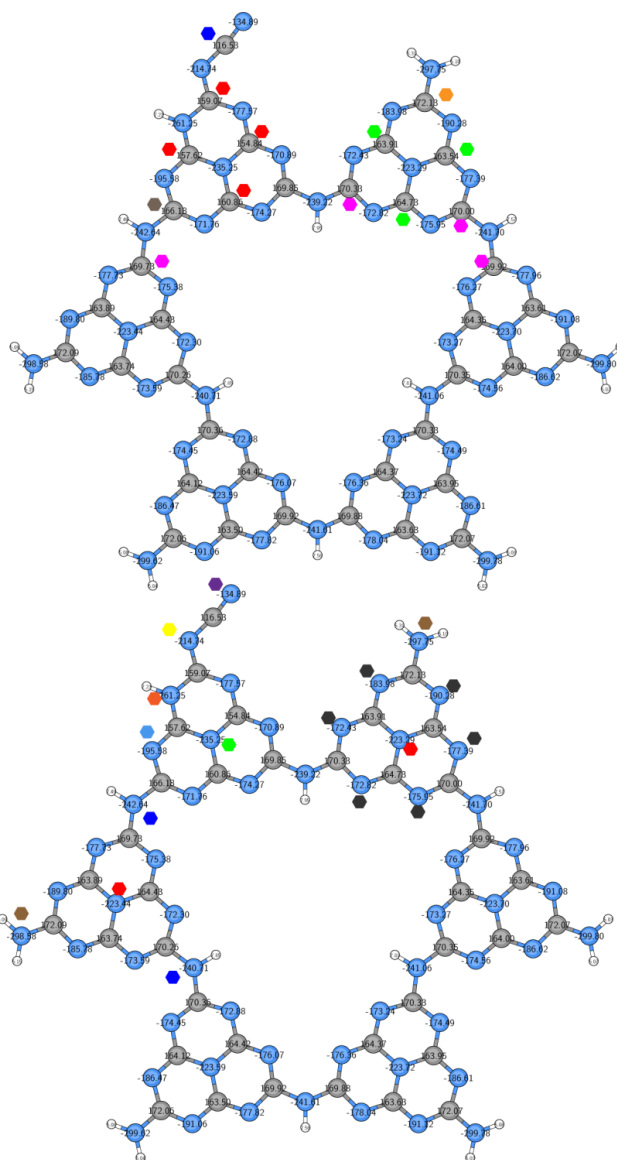
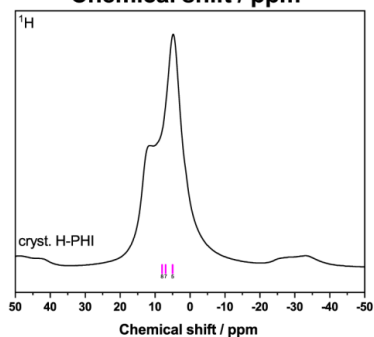
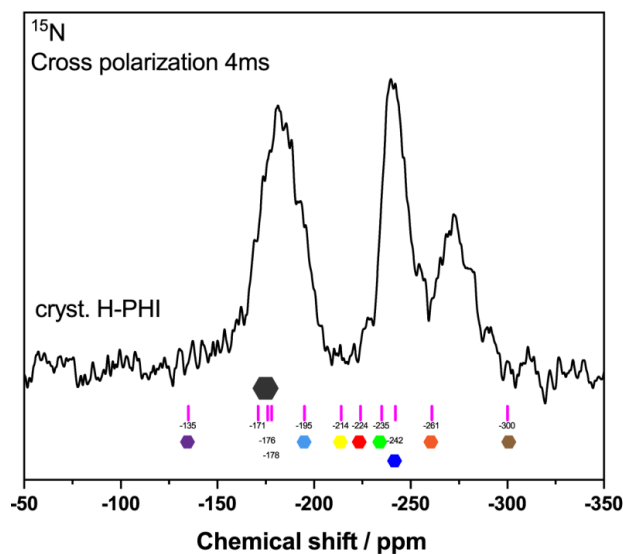
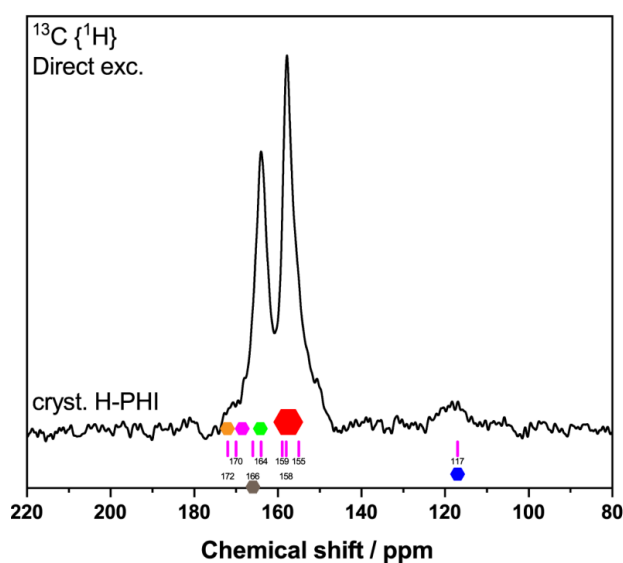


Figure S1.18: ^{13}C - (direct exc.), ^{15}N - (CP) and ^1H - ssNMR spectra of protonated poly(heptazine imide) (H-PHI) and calculated NMR chemical shifts for a single protonated (neutral) heptazine pore, obtained on B97-2/pcsSeg-2//PBE0-D3/def2-TZVP level of theory. Protonation is located adjacent to the cyanamide group at the heptazine ring. This configuration fits the experimental results best. For better visualization, groups of atoms are marked with symbols in the corresponding pictures.

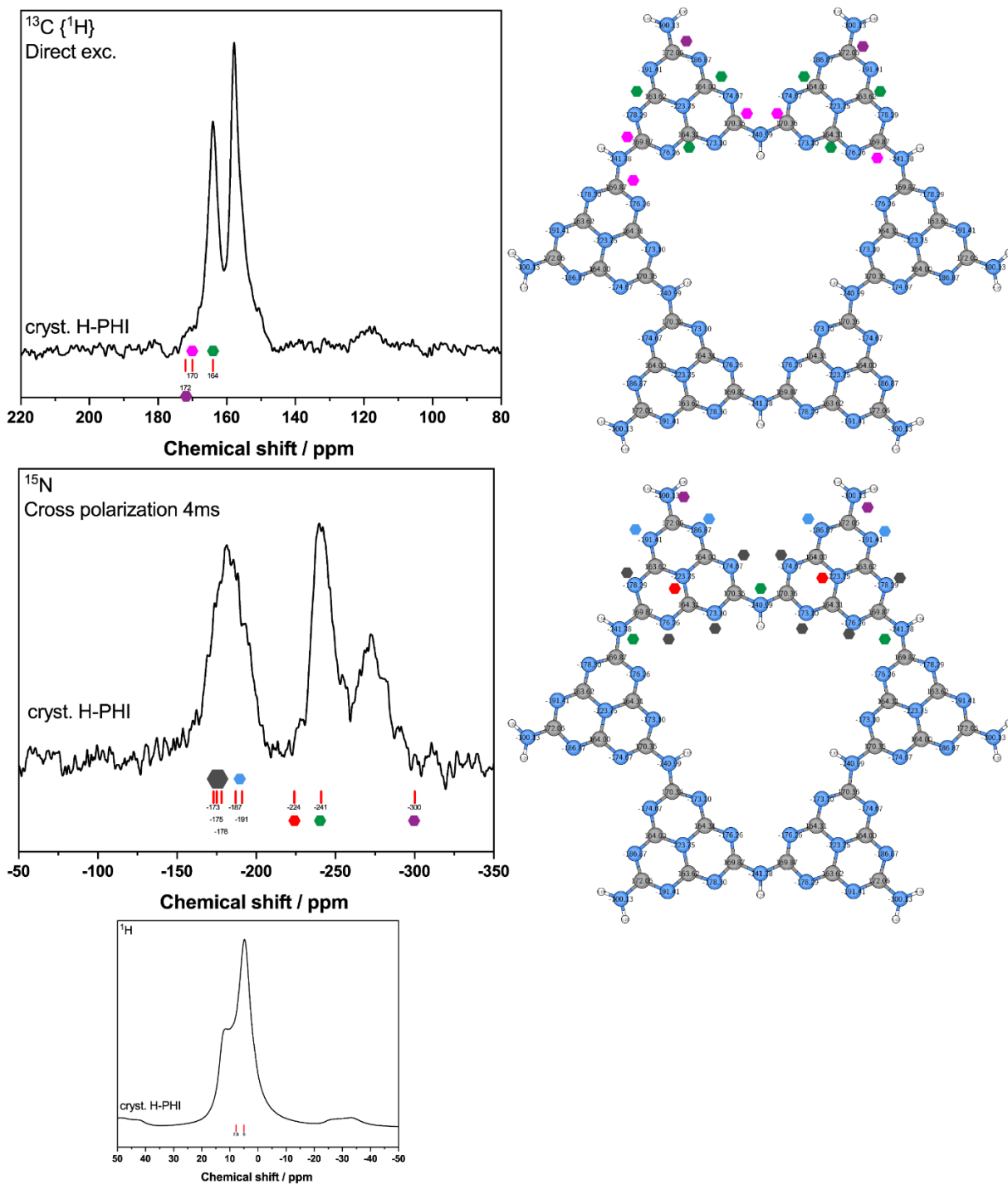


Figure S1.19: ^{13}C - (direct exc.), ^{15}N - (CP) and ^1H - ssNMR spectra of protonated poly(heptazine imide) (H-PHI) and calculated NMR chemical shifts for a single protonated (neutral) heptazine pore, obtained on B97-2/pcsSeg-2//PBE0-D3/def2-TZVP level of theory. Protonation is located at the bridging nitrogen atom. For better visualization, groups of atoms are marked with symbols in the corresponding pictures.

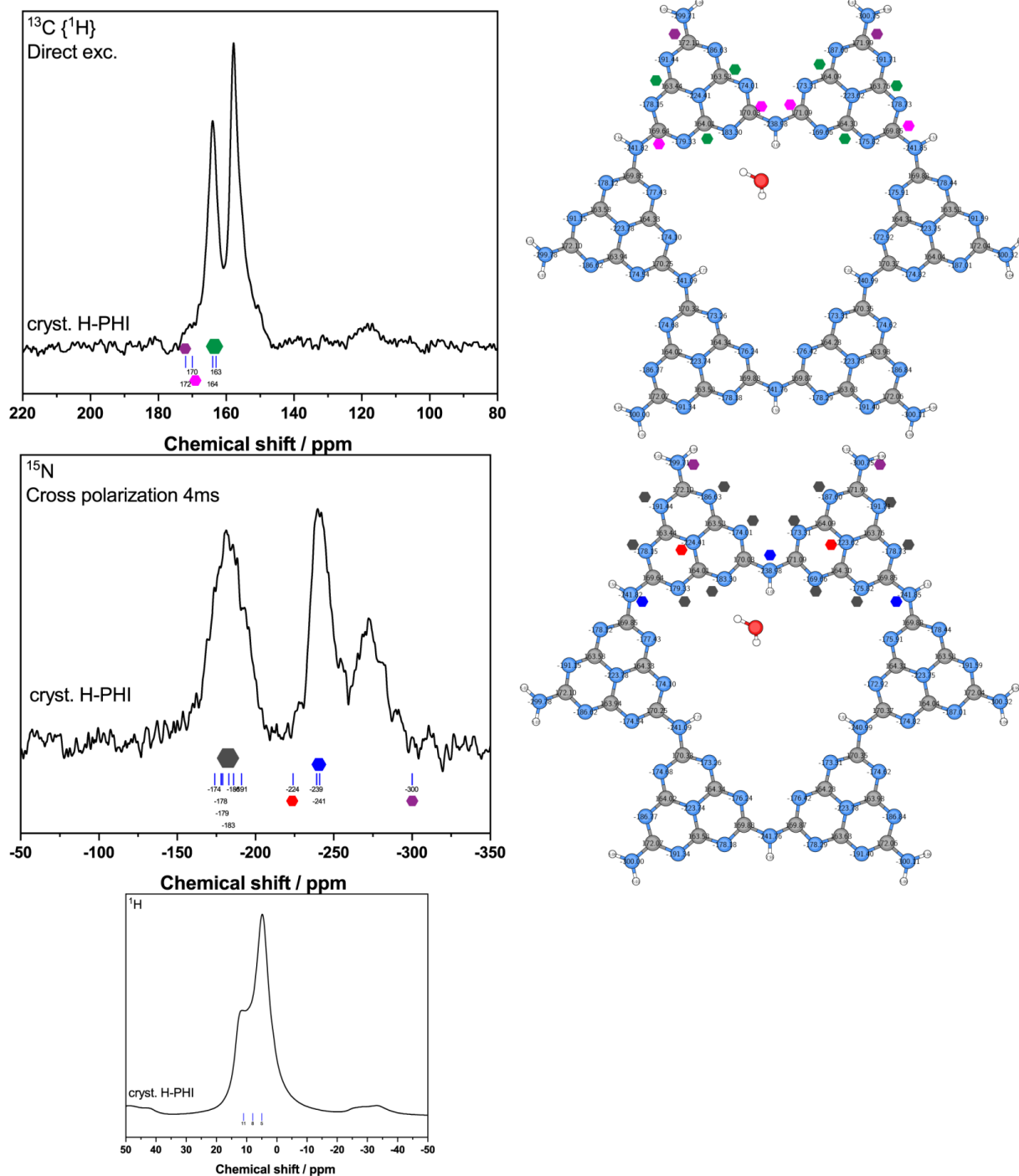


Figure S1.20: ^{13}C - (direct exc.), ^{15}N - (CP) and ^1H - ssNMR spectra of protonated poly(heptazine imide) (H-PHI) and calculated NMR chemical shifts for a single protonated (neutral) heptazine pore, obtained on B97-2/pcsSeg-2//PBE0-D3/def2-TZVP level of theory. Protonation is located at the bridging nitrogen atom. Additionally, this simulation shows the influence of a water molecule within the pore on the chemical shifts. Especially the proton spectrum is simulated far better than without the influence of water. This is also in line with elemental analysis which shows a varying water content depending on synthesis conditions. For better visualization, groups of atoms are marked with symbols in the corresponding pictures.

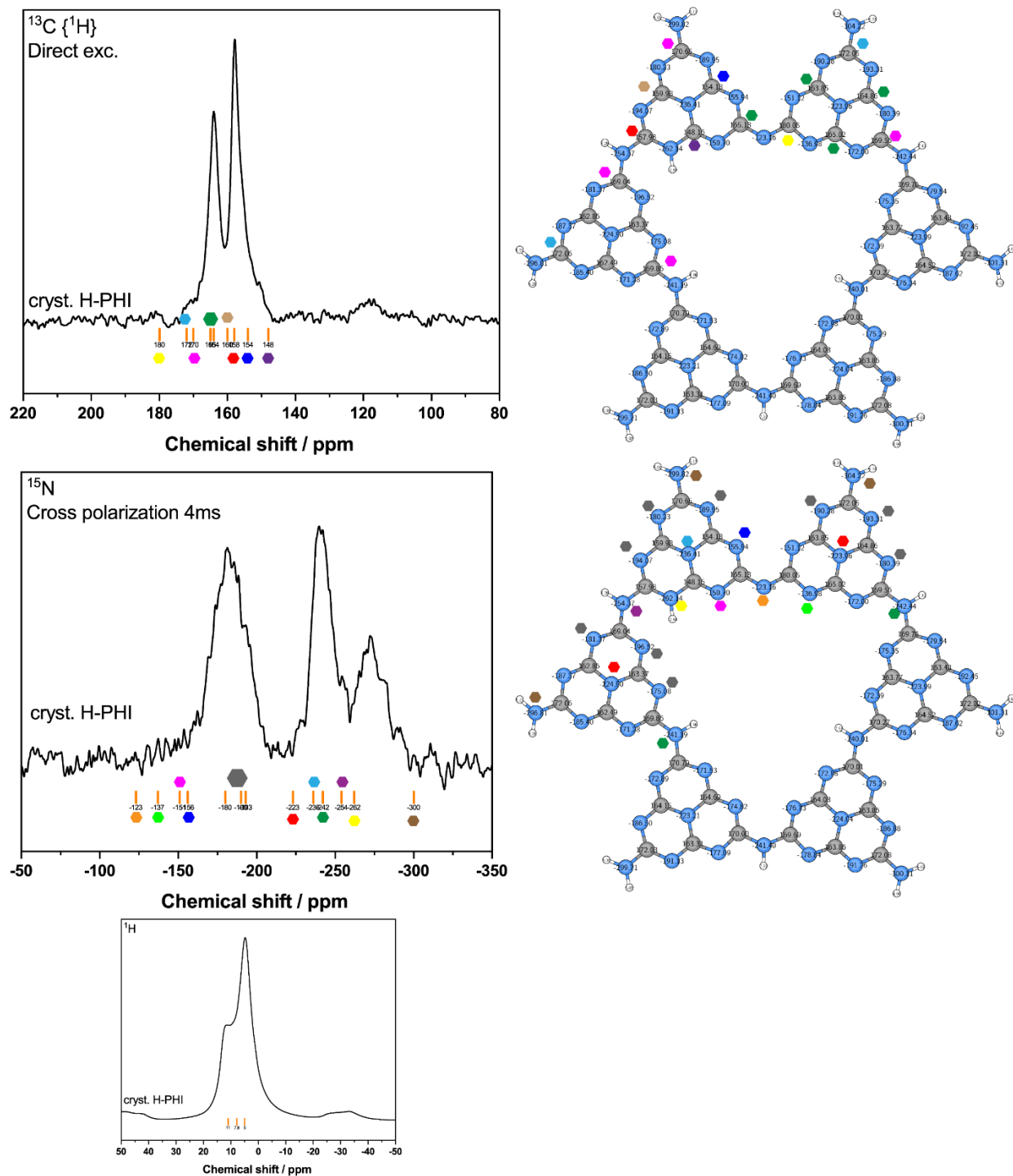


Figure S1.21: ^{13}C - (direct exc.), ^{15}N -CP and ^1H - ssNMR spectra of protonated poly(heptazine imide) (H-PHI) and calculated NMR chemical shifts for a single protonated (neutral) heptazine pore, obtained on B97-2/pcsSeg-2//PBE0-D3/def2-TZVP level of theory. The proton is located at the heptazine ring farthest away from the bridging nitrogen atom. For better visualization, groups of atoms are marked with symbols in the corresponding pictures.

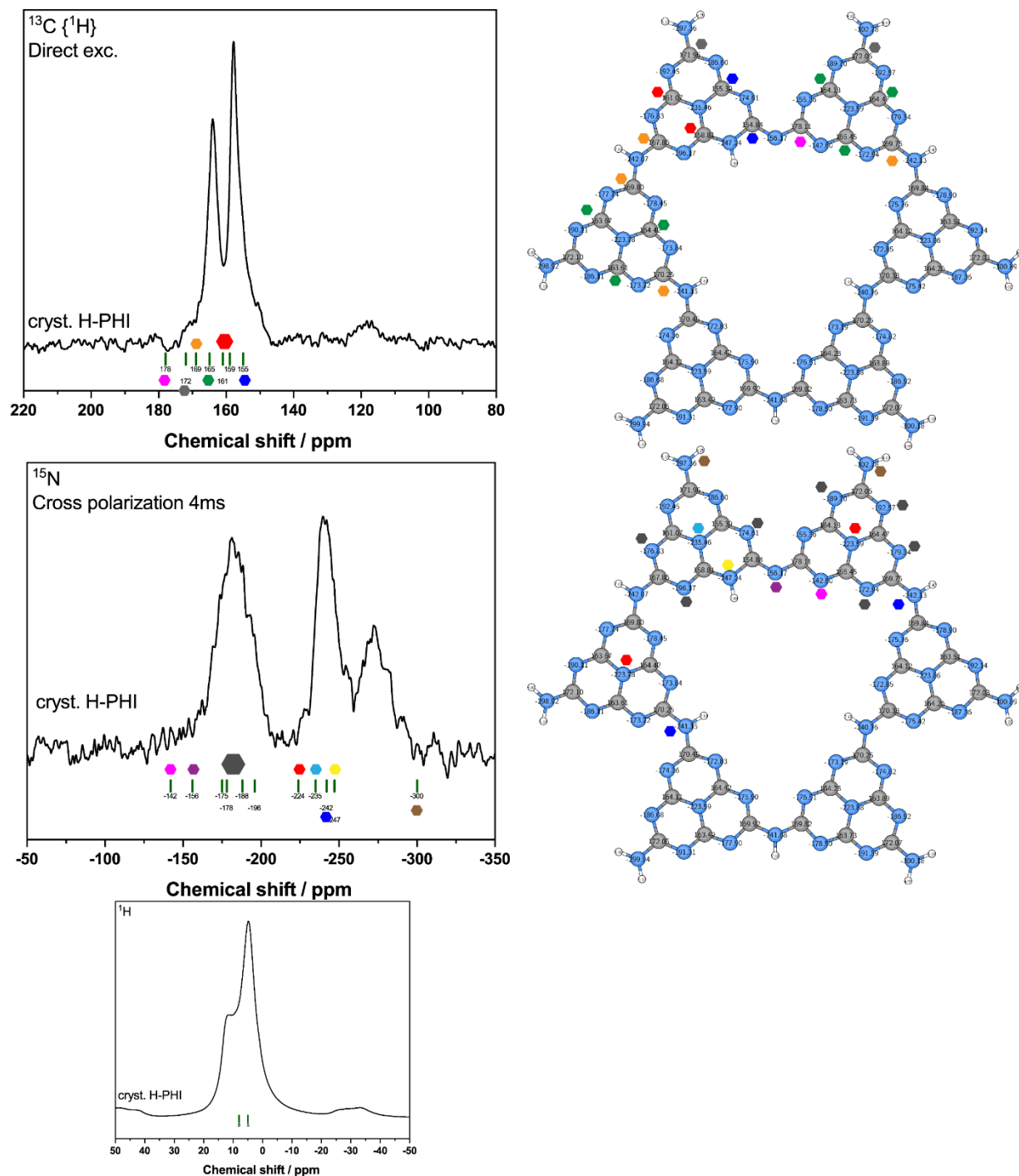


Figure S1.22: ^{13}C - (direct exc.), ^{15}N - (CP) and ^1H - ssNMR spectra of protonated poly(heptazine imide) (H-PHI) and calculated NMR chemical shifts for a single protonated (neutral) heptazine pore, obtained on B97-2/pcsSeg-2//PBE0-D3/def2-TZVP level of theory. The proton is located at the heptazine ring next to the bridging nitrogen atom. For better visualization, groups of atoms are marked with symbols in the corresponding pictures.

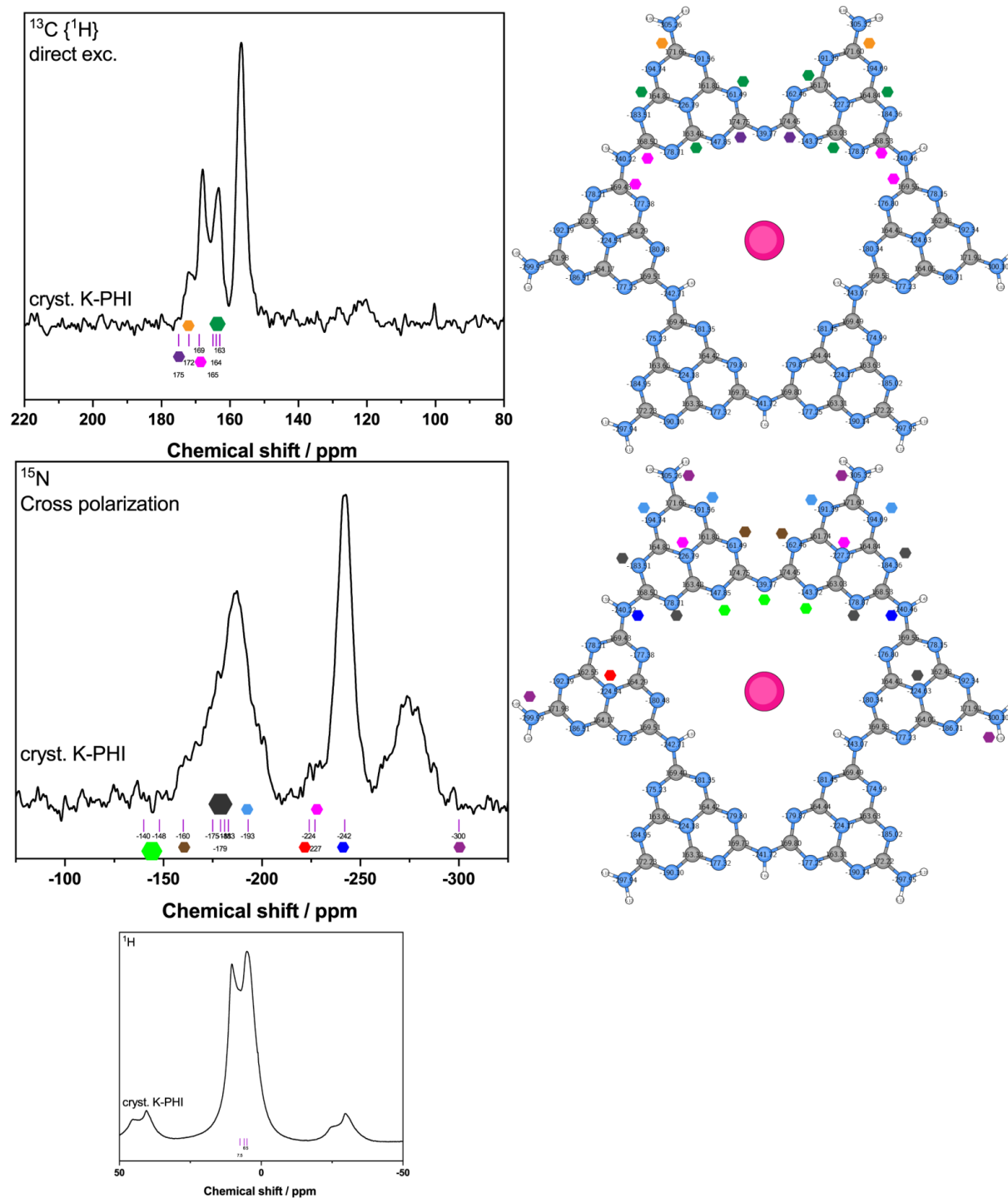


Figure S1.24: ^{13}C - (direct exc.), ^{15}N -CP and ^1H - ssNMR spectra of potassium poly(heptazine imide) (K-PHI) and calculated NMR chemical shifts for a single a pore containing a potassium ion, obtained on B97-2/pcsSeg-2//PBEO-D3/def2-TZVP level of theory. The potassium ion is allocated centrally in the pore. This configuration is not very likely, because the distance to nitrogen atoms of the heptazines for a reasonable interaction is too far. For better visualization, groups of atoms are marked with symbols in the corresponding pictures.

Solvation shell model for potassium:

A solvated potassium ion model was constructed by running a molecular dynamics simulation with a single potassium ion in a solvated water box. The observed solvation shell (Figure S1.25, left) shows 7 water molecules within the closest proximity and is line with experimentally available data.^[25]

Potassium to oxygen distances were then extracted from the trajectory to compare with experimental PDFs for K-PHI (main text, Figure 4.4c), confirming the occurrence of a water-K⁺ coordination within the pores of K-PHI.

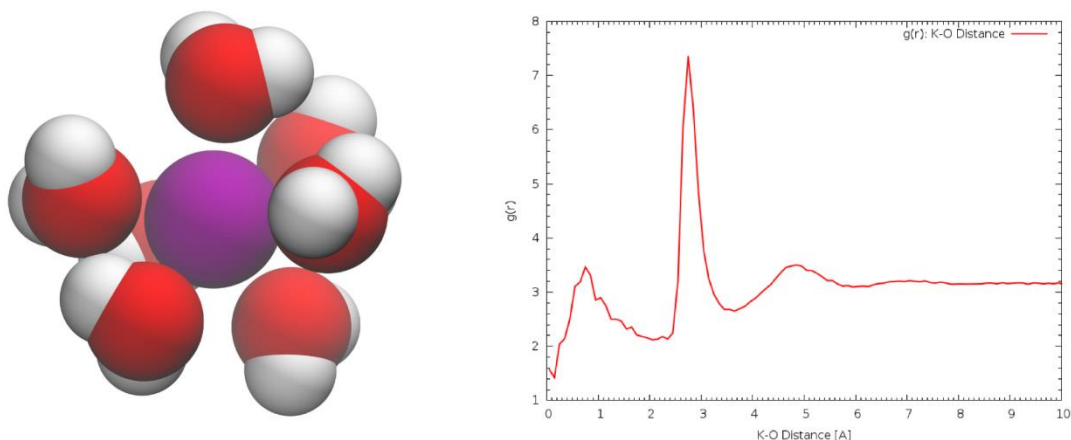


Figure S1.25: Exemplary geometry for a potassium ion (purple) coordinated by 7 water molecules as extracted from a molecular dynamics trajectory (left) and the corresponding pair distribution function (right). The intense peak in the PDF at 2.7-3.3 Å represents typical, most observed K-O distances.

9.1.9. XRD and PDF experiments combined with structure modeling

TGA-XRD experiments:

Thermogravimetric (TG) analyses were performed using a STA 449 F5-Jupiter (Netzsch) device. The sample was heated up in a corundum crucible in a dynamic argon (50 mL min^{-1}) atmosphere to 300, 350 or 400 °C with a heating rate of 10 K min^{-1} respectively. An empty corundum crucible was used as a reference. Corrections of instrumental effects and the buoyancy were performed with Al_2O_3 as an inert reference material during a separate measurement.

TGA in combination with *ex situ* PXRD was carried out to investigate the thermal behavior of H-PHI, in particular the release of water molecules located in the pores of the poly(heptazine imide) network. The sample was heated up with a heating rate of 10 °C min^{-1} in an argon gas flow to 300, 350 and 400 °C. Directly after the respective temperature was reached the sample was removed from the oven and the powder was filled in a capillary that was immediately sealed afterwards. In Figure S1.26 the TG-curve is depicted. The temperatures where the heating was stopped for PXRD analysis (Figure S1.27) are indicated by red, filled circles.

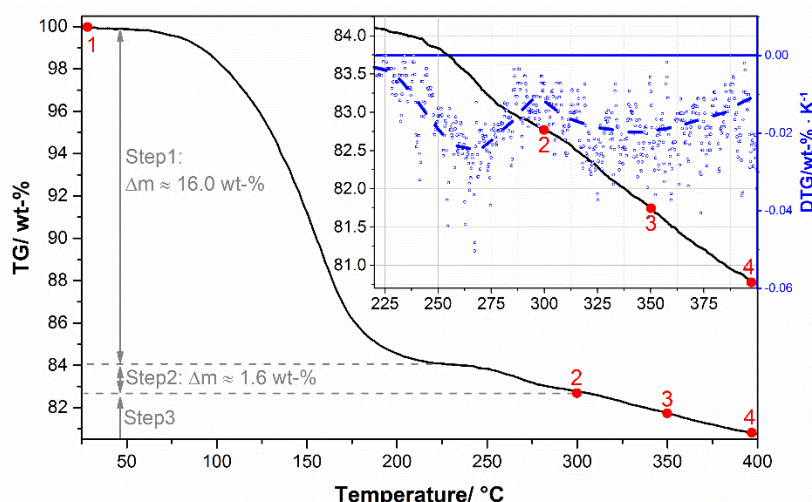


Figure S1.26: Measured TG-curve of the H-PHI material. In the inset the second and third mass-loss step, as well as the 1st derivative of the TG-curve (blue circles and blue, dashed trend line) are presented. Temperatures at which *ex situ* PXRD analyses were performed (Figure S1.27) are indicated by red circles and red numbers.

Three distinct mass loss steps can be observed in the TG graph (Figure S1.26, black line), which are attributed to the release of pore-water-molecules. The first water release step starts at ca. 75 °C and at 225 °C a small plateau indicates completion of this step, with a total mass loss of 16 wt%. During the first step water, which is most likely not or only loosely bound to the poly(heptazine imide) network is released. The second and third mass loss step vastly overlap and can only be distinguished by inspecting the first derivative of the TG-curve (Figure S1.26, inset, blue circles and line). During the second step approx. 1.6 wt% of the sample mass is released. In the *ex situ* PXRD pattern (Figure S1.27, orange pattern) the $\bar{1}10$ and the 010 reflections indicating 2-dimensional intra-layer ordering are still apparent. Therefore, the second decomposition step cannot be attributed to hydrolysis of the poly(heptazine imide) network, but to the release of more tightly bound pore water. In the diffraction pattern the 001 basal reflection is located almost at the same position.

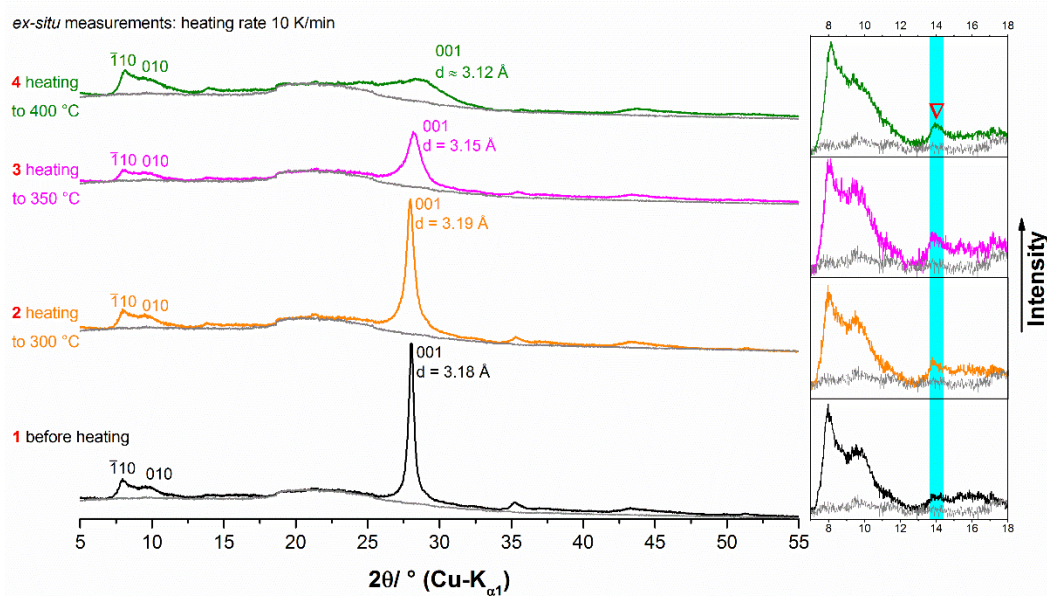


Figure S1.27: *Ex-situ* PXRD analysis of the residue of H-PHI before and after heating up in the TGA-device to different temperatures. In order to illustrate the instrumental background effects, an empty capillary of the same batch was measured applying the same conditions (grey patterns). The low angle region of the PXRD pattern is presented in the inset. The expected position of the diffraction line, indicating eclipsed stacking is highlighted with cyan background.

The third mass loss step was investigated by *ex situ* PXRD at 350 °C, which corresponds to the peak of the mass release and at 400 °C at which the decomposition step is almost completed. In the diffraction patterns (Figure S1.27, magenta and green patterns) the $\bar{1}10$ and the 010 are slightly broadened but still clearly apparent. This indicates 2-dimensional coherence of the material, i.e. the poly(heptazine imide) layers are not completely depolymerized by hydrolysis. Therefore, the third mass loss step can be attributed mainly to the release of strongly bound pore water molecules. The 001 reflection is shifted towards smaller d-values, as the complete removal of pore water molecules leads to a shortening of the interlayer distances. The symmetrical, vast broadening of this reflection indicates a loss of three dimensional coherence in the crystal lattice, i.e. before heating H-PHI large stacks of poly(heptazine imide) layers were apparent and by removal of pore water the layers get partially exfoliated. Thus, only small stacks of a few nm (\approx 3-9 layers) remain. In addition, in the diffraction patterns at around 14 ° 2θ (Figure S1.27, inset, cyan background) a Bragg peak (red triangle) arises from the diffuse scattering present in this region of the pattern. This peak indicates small domains (\approx 3-9 layers) of eclipsed stacked layers (see Implications on the 3-dimensional structure of the poly(heptazine imide) framework from X-ray powder diffraction data) after complete removal of pore-water, which is in accordance with the observations from SAED (see Figure 4.2 in the main text, and Transmission electron microscopy (TEM)).

Structure modeling based on PXRD

Indexing/Rietveld refinement:

PXRD reflections were indexed to a triclinic cell. The cell metric was verified by Pawley refinement, which resulted in a pseudo-hexagonal cell with lattice parameters $a = b = 12.78 \text{ \AA}$, $c = 4.31 \text{ \AA}$, $\alpha = \beta = 109.63^\circ$, and $\gamma = 120^\circ$, $R_{wp} = 3.87\%$, Figure S1.28. Anisotropic peak broadening was accounted for by using a modification for cylindrical domain morphology^[26] oriented along the c -axis. Additional broadening was described using a Lorentzian-type microstrain parameter, with additional corrections for the instrumental profile. A second Pawley phase of equally spaced reflections was used for the background. This cell was also suitable for describing the remaining diffraction features in the H-PHI pattern as well, Figure S1.29. In this case, strain broadening was described using a hexagonal-type Stephens' model.^[27]

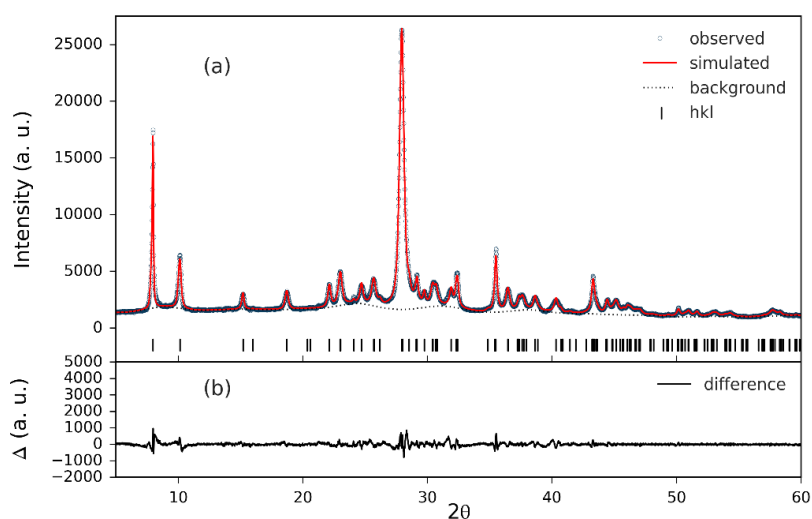


Figure S1.28: a) Resulting fit from Pawley refinement to the K-PHI dataset measured with $\text{CuK}\alpha_1$ radiation. The reflection positions and background function are also plotted. b) The difference curve is plotted for reference.

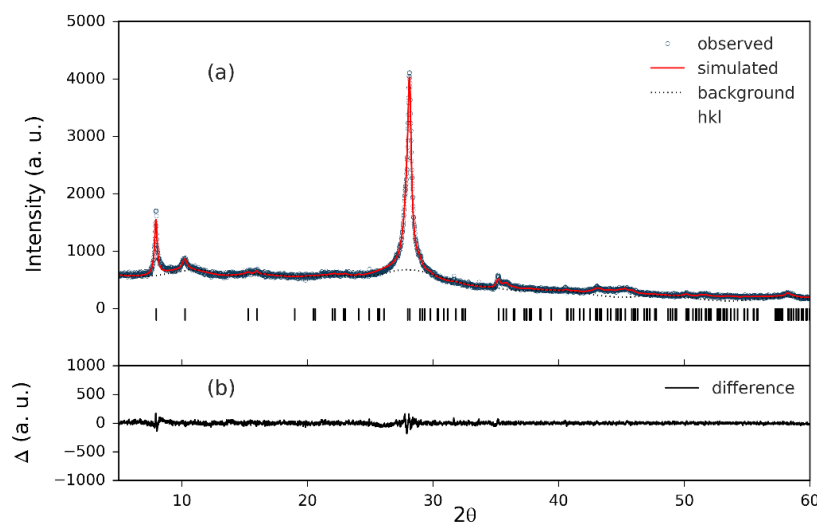


Figure S1.29: a) Resulting fit from Pawley refinement to the H-PHI dataset measured with $\text{CuK}\alpha_1$ radiation. The reflection positions and background function are also plotted. b) The difference curve is plotted for reference.

A structure model for Rietveld refinement was based upon the previously solved structure of poly(triazine imide) reimagined for polymerized heptazine imide sheets.^[28] The cell indexing indicates a single layer per cell, which given the non-90° α/β , must stack in a staggered fashion. A planar heptazine dimer was defined as a rigid body and oriented in the x-y plane, forming large triangular pores with two heptazine units on each side, and an interlayer distance of approximately 3.2 Å.

To obtain reasonable intensities, it was necessary to include atoms to account for the pore content. In all refinements for K-PHI, a single K atom was included in the pore with site position refined. Modeling of the additional species was attempted using different methods. First, the additional electron density in the pore was described using a pseudo-atom, i.e. a single atom with refined scattering contribution, and ADPs refined either isotropically or anisotropically, Figure S1.30a). This approximation was not sufficient for achieving a satisfactory fit. The second method involved sequentially adding oxygen atoms to represent water molecules, which were freely refined within the pore, Figure S1.30b). The final result used 7 oxygen atoms. 1 K and 7 O atoms corresponds roughly to 7 wt% K and 20 wt% water which is consistent with estimates from elemental analysis. Bond distance constraints, determined from DFT relaxations, were defined to maintain reasonable distances between O-O, K-O and O-C/N pairs. The fit, $R_{wp} = 8.61\%$, indicates that this is a plausible crystallographic model, Figure S1.31. Pawley and Rietveld refinements were performed using TOPAS v6.^[29]

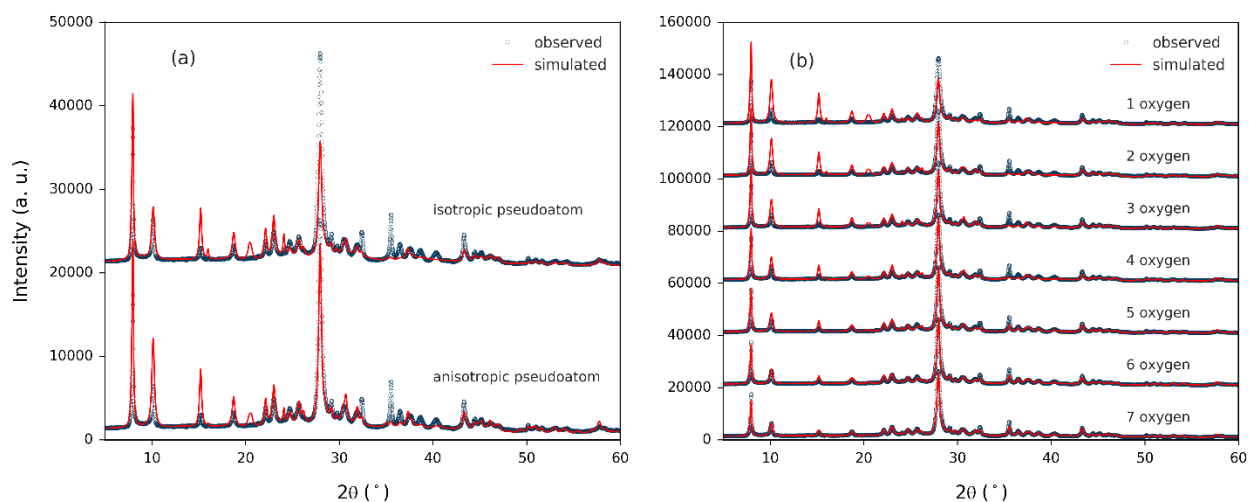


Figure S1.30: a) Rietveld refinement results from simulation of pore content by potassium and a single pseudo-atom of arbitrary electron number with site positions and ADPs refined. b) Rietveld refinement results from simulation of pore content by potassium and various number of oxygen atoms with site positions refined and ADPs fixed.

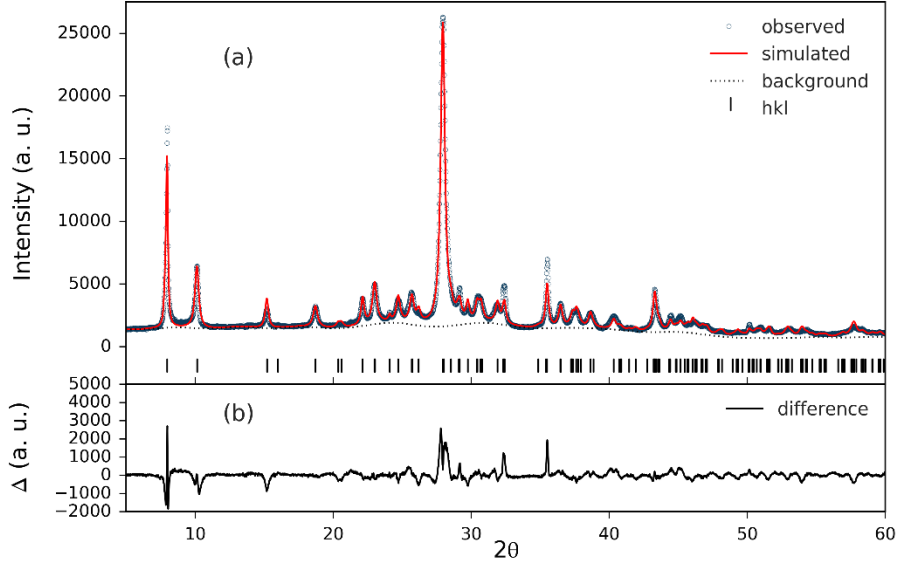


Figure S1.31: a) Final Rietveld refinement to the K-PHI dataset measured with $\text{CuK}\alpha_1$ radiation. The reflection positions and background function are also plotted. b) The difference curve is plotted for reference.

Pair distribution function (PDF) analysis

Data processing:

The raw 2D data from BNL and ESRF were corrected for polarization effects, masked, and azimuthally integrated into 1D powder diffraction intensities using FIT2D^[30] and pyFAI^[31] respectively. Further correction, normalization, and Fourier transformation of the data to the PDF, $G(r)$, was performed using PDFgetX3^[32], within xPDFsuite.^[33]

The total scattering structure function $S(Q)$ is obtained from the coherent scattering intensities $I_c(Q)$, after removal of the self-scattering, by,

$$S(Q) = \frac{I_c(Q) - \langle f_i(Q)^2 \rangle + \langle f_i(Q) \rangle^2}{\langle f_i(Q) \rangle^2}. \quad (1)$$

Q is the magnitude of the scattering momentum transfer ($Q = 4\pi \sin \theta / \lambda$ for elastic scattering, where λ is the wavelength, and 2θ is the scattering angle). $f_i(Q)$ is the atomic form factor for atom i , and averaging denoted by $\langle \dots \rangle$ is performed stoichiometrically over all atom species in the sample. The experimental PDF, $G(r)$, is obtained via truncated Fourier transformation of the reduced total structure function $F(Q) = Q[S(Q) - 1]$, by

$$G(r) = \frac{2}{\pi} \int_{Q_{min}}^{Q_{max}} F(Q) \sin(Qr) dQ \quad (2)$$

$$= 4\pi r [\rho(r) - \rho_0 \gamma_0], \quad (3)$$

where ρ_0 is the average atomic number density and $\rho(r)$ is the local atomic pair density, which is the average density of neighboring atoms at a distance r from an atom at the origin. γ_0 is the characteristic function of the diffracting domains which equals 1 for bulk crystals, but has an r -

dependence for nano-sized domains.³⁰ The maximum ranges of diffraction data used in the Fourier transform for the different measurements were $Q_{max} = 25.0 \text{ \AA}^{-1}$ and 8.5 \AA^{-1} .

Data comparison:

The reduced total scattering data and resulting pair distribution functions are shown in Figure S1.32 and Figure S1.33, for both the high Q_{max} /low Q_{res} and the high Q_{res} /low Q_{max} measurements at BNL. The former measurement gives high real space resolution, allowing for resolving distinct nearest neighbor atom-pair correlations from within the heptazine units. The latter measurement results in much lower real space resolution, and therefore specific intramolecular characteristics cannot be discerned. However, the higher reciprocal-space resolution of the measurement allows the real space structure information to be observed over longer distances, thus allowing for comparison of density modulations between the stacked layers to be compared between samples. It is clear that despite the loss of orientational coherence between stacked layers in the H-PHI sample, there is still a robust packing relationship between the layers, which is maintained at least up to 20-30 nm or more.

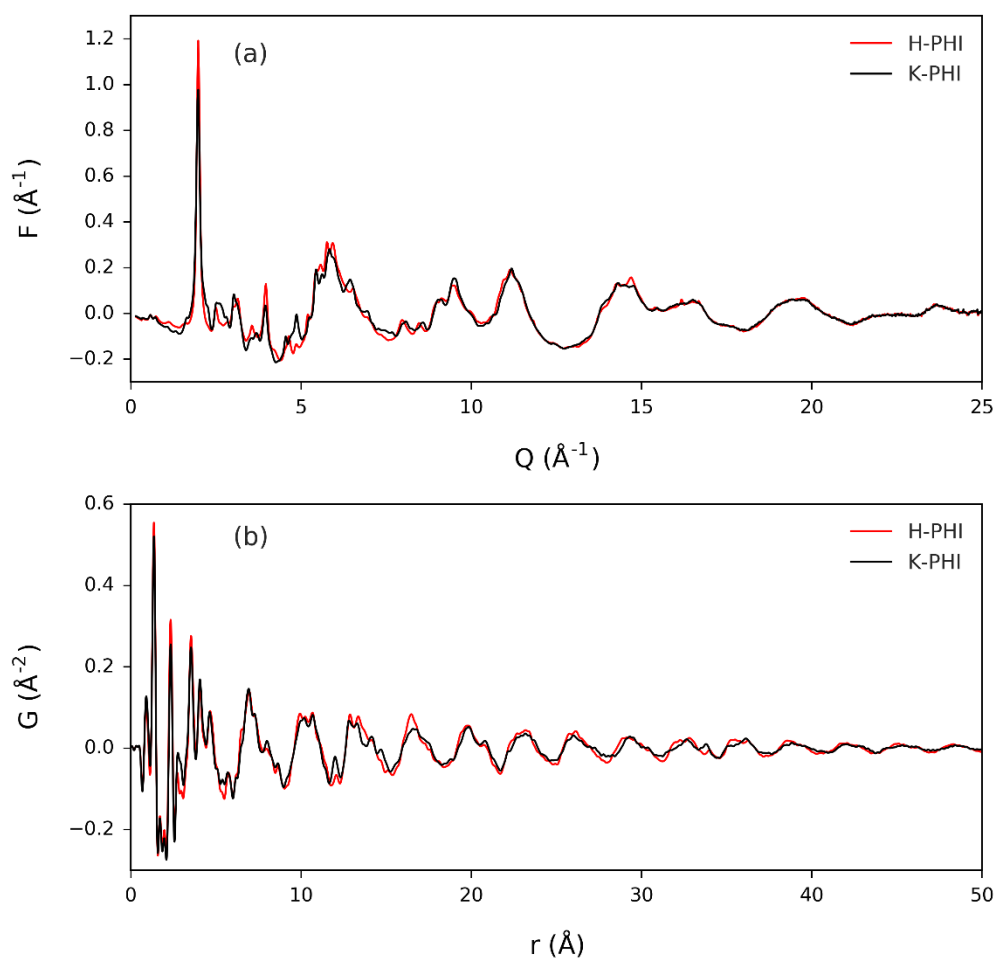


Figure S1.32: a) Reduced total scattering data for H-PHI and K-PHI measured with short detector distance (high Q_{max} /low Q_{res} setup, $Q_{max} = 25.0 \text{ \AA}^{-1}$), b) Resulting PDFs compared up to 50 \AA .

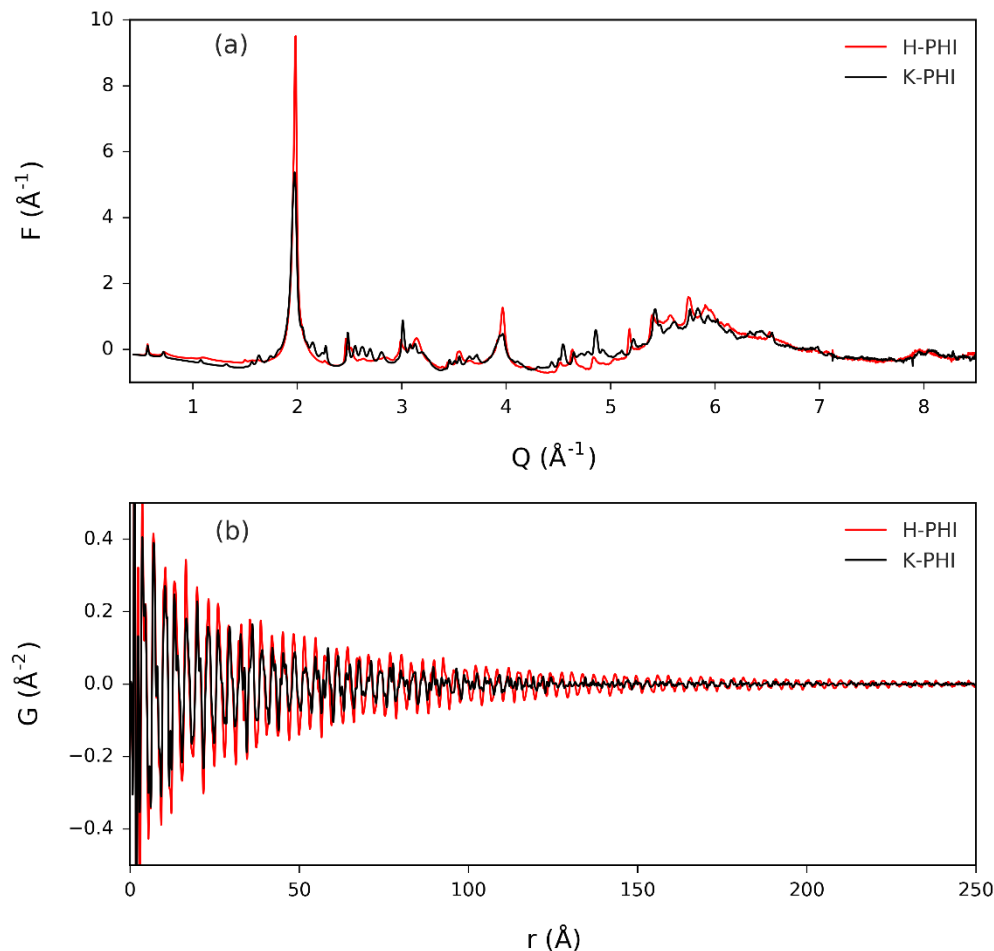


Figure S1.33: a) Reduced total scattering data for H-PHI and K-PHI measured with far detector distance (high Q_{res} /low Q_{max} setup, $Q_{max} = 8.5 \text{ \AA}^{-1}$) b) Resulting PDFs compared up to 250 \AA .

Data modeling – single molecule, single layer, crystal structure:

Simulation of the PDF for a single layer was performed using Diffpy-CMI.^[34] Further PDF refinements, and co-refinement of XRD/PDF data were carried out using TOPAS v6.^[29] The PDF was calculated from a crystallographic model by,

$$G(r) = \frac{1}{rN} \sum_i \sum_{j \neq i} \left[\frac{f_i f_j}{\langle f \rangle^2} \delta(r - r_{ij}) \right] - 4\pi r \rho_0, \quad (4)$$

$$R_w = \sqrt{\frac{\sum_{i=1}^n [G_{obs}(r_i) - G_{calc}(r_i, P)]^2}{\sum_{i=1}^n G_{obs}(r_i)^2}}. \quad (6)$$

For XRD/PDF corefinement, R_w was minimized for both datasets simultaneously, fitted to the same structure. In this case, different weightings of the XRD and PDF were attempted, and a

suitable result was found using a weighting of 100:1 PDF:XRD to account for the relative order of magnitudes of the peak intensities in each dataset. The XRD/PDF corefinement of synchrotron measured K-PHI sample is shown in Figure S1.34, showing that the model can be consistently refined in both reciprocal and real space. Slightly improved fits to the PDF data were obtained by single dataset refinement for both K-PHI and H-PHI, shown in Figure S1.35.

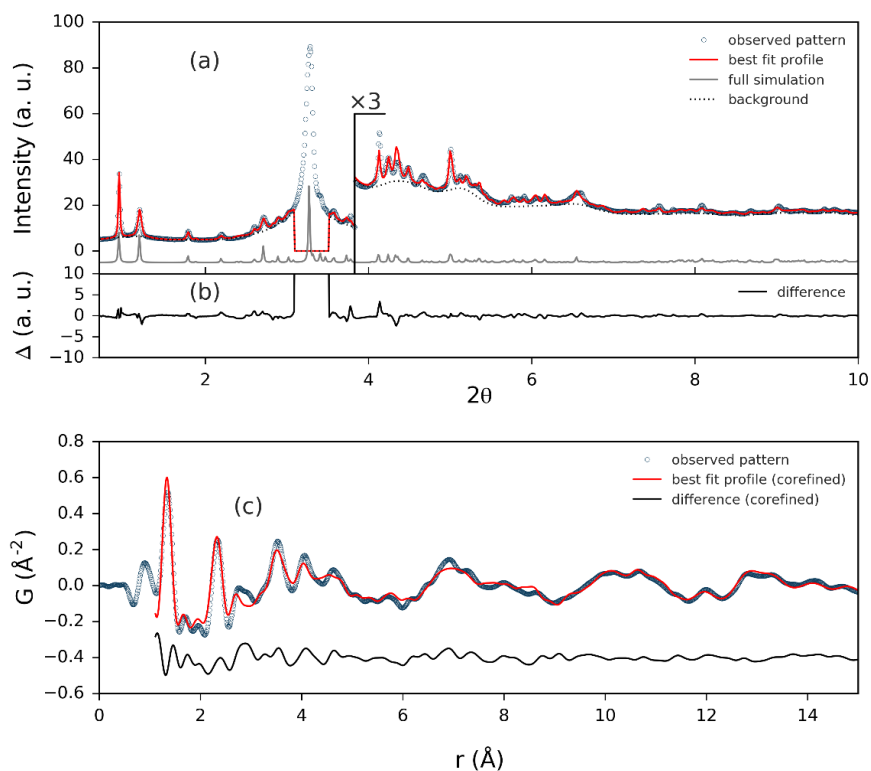


Figure S1.34: Corefinement of K-PHI model to synchrotron XRD and PDF measurements. (a) Fit to the high Q resolution XRD dataset. The (001) peak was excluded due to an over-biasing effect on the refinement result. (b) The residual is shown for reference. (c) The resulting fit to the real space PDF from 1-15 \AA .

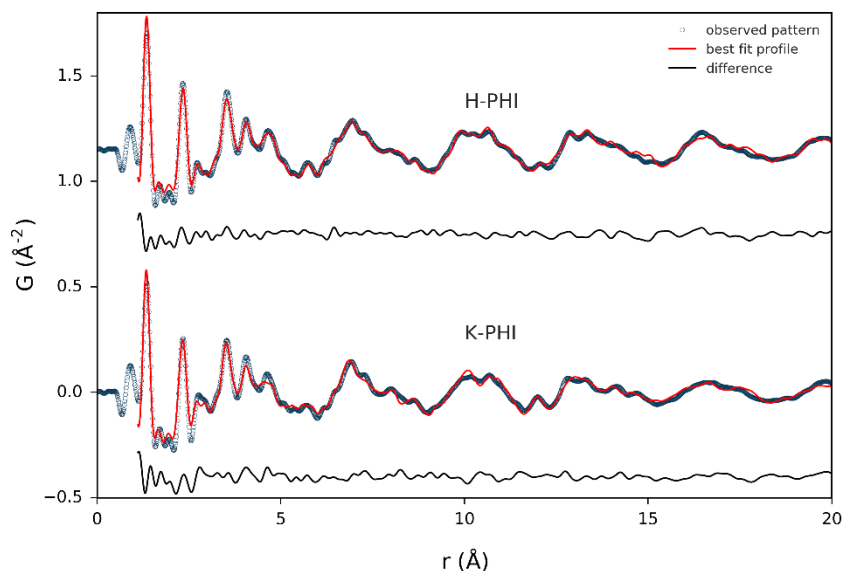


Figure S1.35: PDF-only refinements to the H-PHI and K-PHI measurements. K-PHI contained 7 O and 1 K atom in the pore. For H-PHI, the K atom was replaced by an eighth O atom. The model gives a suitable result in both cases.

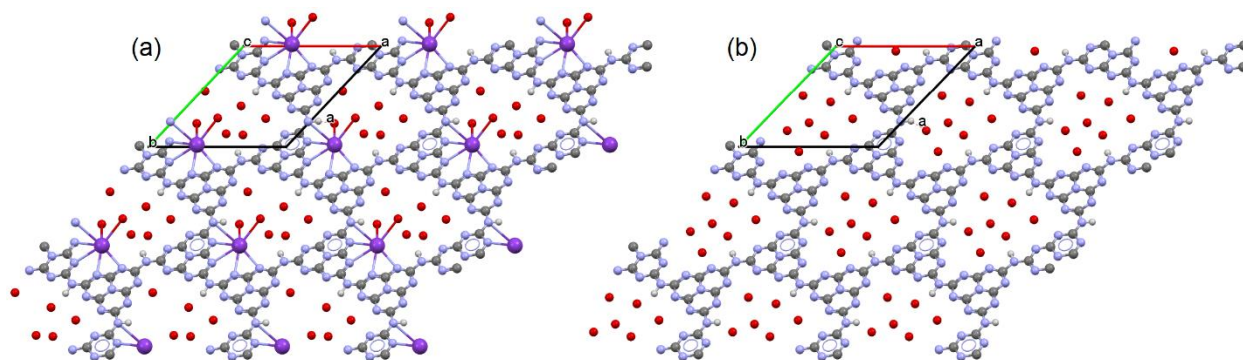


Figure S1.36: Structures resulting from PDF-only refinements to the a) K-PHI and b) H-PHI measurements, both refined using the staggered stacking relationship determined from Rietveld refinement to K-PHI lab diffraction data.

Table S1.2: PDF-only refinements to the H-PHI and K-PHI measurements. K-PHI contained 7 O and 1 K atom in the pore. For H-PHI, the K atom was replaced by an eighth O atom. The model gives a suitable result in both cases.

	Pawley		Rietveld		PDF*	
	K-PHI	H-PHI	K-PHI	K-PHI	H-PHI	
wavelength	1.5406	1.5406	1.5406	0.1823	0.1823	
refinement range	3.0-60.0 °	3.0-60.0 °	3.0-60.0 °	1.1-20.0 Å	1.1-20.0 Å	
a=b	12.78	12.78	12.78	12.80	12.92	
c	4.31	4.33	4.31	4.33	4.33	
$\alpha=\beta$	109.63	109.96	109.63	109.76	109.60	
γ	120.0	120.0	120.0	120.0	120.0	
R_{wp}	0.0387	0.0434	0.0861	0.2254	0.1901	

*Separate samples prepared for PDF measurements.

Short range order:

By comparing PDF datasets measured for various K-PHI and H-PHI samples measured at BNL and ESRF, as well as melem (with no ion content), we were able to observe an increase in the weighting of atom-pair correlations from approximately 2.5-3.2 Å with increasing ion concentration. These distances are found to correspond to the K-O coordination shell, as determined from DFT calculations, giving direct evidence that water coordination (either partial or full) of the K ions occurs within the pores. This distance range also corresponds to the distances expected for coordination of N atoms in K-azine complexes^[35], meaning that there could be some contribution due to the off-centering of the K atoms within the pore.

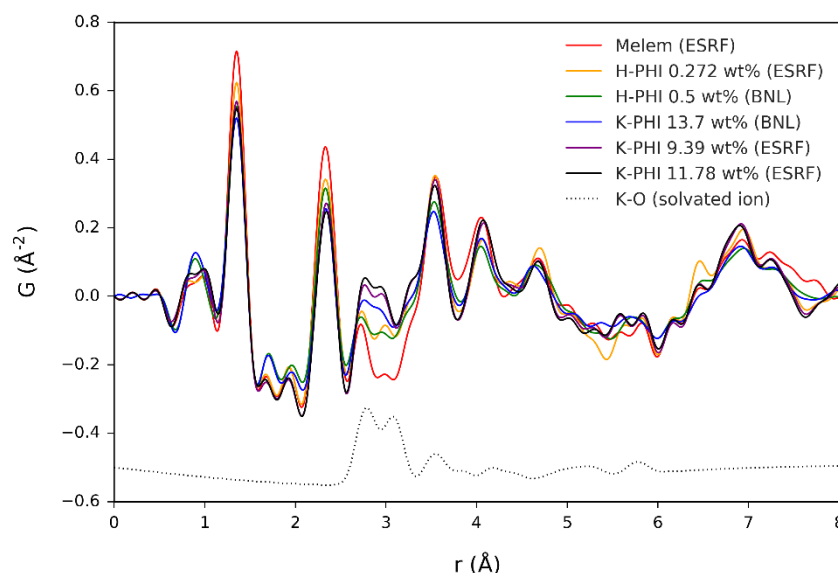


Figure S1.37: Short range ordering of heptazine and pore contents as shown by the PDFs for H-PHI, K-PHI, and melem samples measured at either BNL or ESRF.

Implications on the 3-dimensional structure of the poly(heptazine imide) framework from X-ray powder diffraction data:

Information on the 3-dimensional structure of the poly(heptazine imide) framework can be extracted from the X-ray powder diffraction (PXRD) patterns, as these represent an averaged analysis of the bulk material. In contrast to ideal conventional crystalline material, the presence of different kinds of defects is expected in the PHI materials, such as: intralayer defects caused by incomplete polymerization, disorder of the pore material and planar defects occurring as stacking faults. Only the latter kind of faulting governs the structural coherence perpendicular to the poly(heptazine imide) planes. Hence the 3-dimensional structure of the poly(heptazine imide) framework can only be understood completely when these defects are taken into account. Therefore, systematic series of simulations of the diffraction patterns of the faulted poly(heptazine imide) using distinct faulting scenarios were performed and compared to the measured data in order to obtain qualitative information on the kinds and degree of faulting that is present in the material. Due to the presence of different kind of defects, as mentioned above, no attempt was made to fit the measured diffraction patterns with any faulting model.

Comparison of the powder patterns of K-PHI and H-PHI:

A comparison of the diffraction patterns of K-PHI and H-PHI is presented in Figure S1.38. In total H-PHI (black pattern) seems to exhibit less reflections than the potassium phase (blue pattern). The main reflections ($\bar{1}10$, 010, 001) in the hydrogen compound are situated at identical positions as in the pattern of K-PHI, which indicates that basic structural motifs such as the constitution of the poly(heptazine imide) layers are identical. The smaller number of reflection may indicate a higher symmetry of the structure of H-PHI but a close inspection of the diffraction pattern (Figure S1.38, inset) reveals that there are many, but vastly broadened reflection apparent that almost merge with the background. Hence, there is much diffuse scattering in the diffraction pattern of H-PHI. The background itself and the basis of the $\bar{1}10$, 010 reflections exhibit a characteristic triangular shape, which is indicative for planar defects in the crystal structure.^[36] Therefore, the lower number of reflections present in the diffraction pattern of H-PHI rather indicate a higher degree of disorder in the structure than a higher symmetry.

Diffuse scattering can also originate from the disorder of the solvent molecules present in the pores of the poly(heptazine imide) framework. In order to rule out the scattering contribution of the pore particles, diffraction patterns (Figure S1.39) of fully ordered H-PHI were simulated using the structural model derived from the PDF-analysis (see Structure modeling based on and Pair distribution function (PDF) analysis) with (black pattern) and without (blue pattern) the pore water related oxygen sites. Excluding the pore particles does not decrease the number of peaks in the diffraction pattern and therefore does not artificially increase the symmetry of the lattice. However, it affects the peak intensities in relation to the 001 basal reflection. In consequence systematic simulations of the diffractive effects of planar defects in the stacking of the poly(heptazine imide) framework without including the pore-water can be used to demonstrate which reflections are broadened due to the different faulting scenarios which are discussed in the next sections. But as the reflection intensities are affected by the pore particles, the simulations can only be used for a qualitative description of the 3-dimensional structure of the poly(heptazine imide) framework.

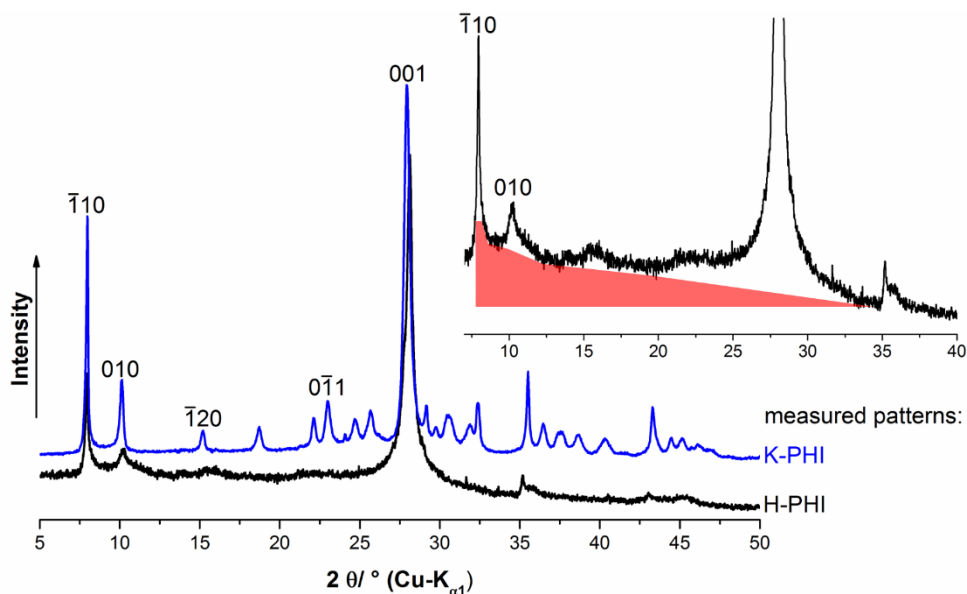


Figure S1.38: Comparison of the measured powder patterns of K-PHI and H-PHI including selected reflection indices. Peak broadening appearing in a triangular shape that merges with the background in the pattern of H-PHI is highlighted by red color (inset).

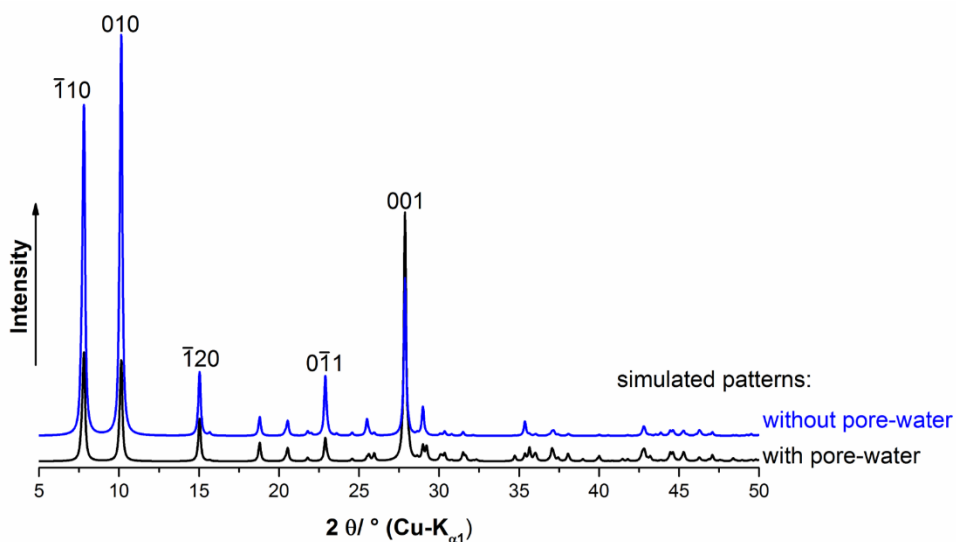


Figure S1.39: Simulated diffraction patterns of H-PHI including and excluding pore water.

Possible arrangements of the poly(heptazine imide) layers:

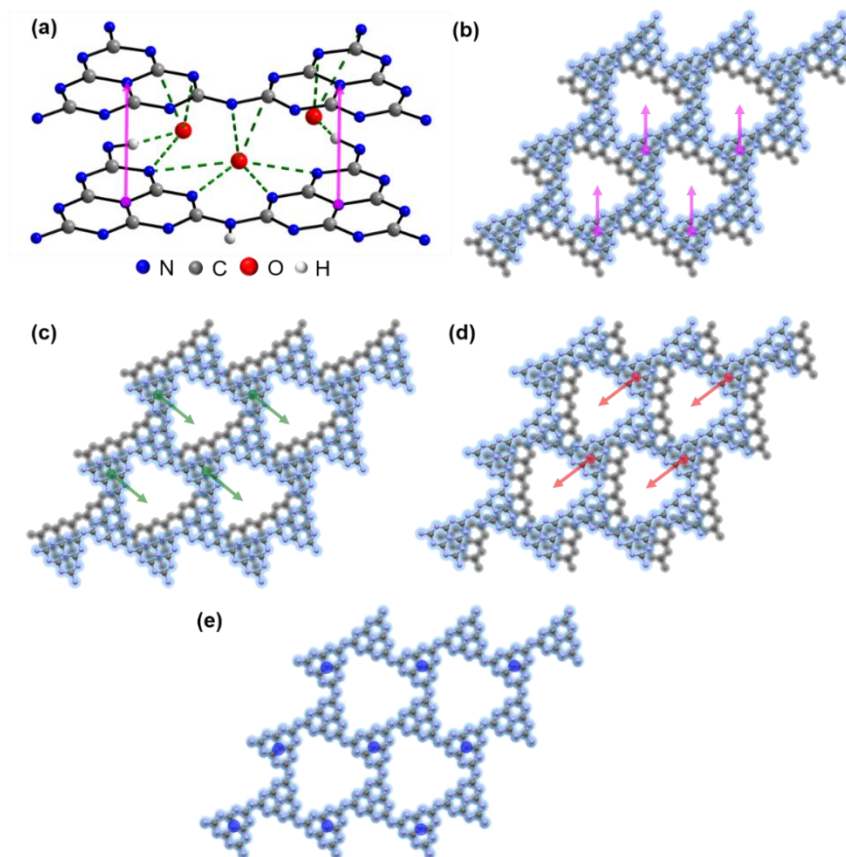


Figure S1.40: a) Interlayer interactions in the structural model of H-PHI mediated by water molecules (presented as oxygen atoms), possible attractive interactions between poly(heptazine imide) related nitrogen and hydrogen sites and pore water are indicated by green, dashed bonds, the stacking vector describing the layer-to-layer arrangement is represented by the magenta arrows. b-e) Top view on possible layer to layer arrangements in the structure of H-PHI, molecules in the pore are omitted, the preceding layer is presented in grey and stacking vectors as colored arrows, b) stacking order on the proposed structured model of H-PHI = pore I stacking, c, d) alternative stacking order directed by one of the neighboring pores = pore II stacking, e) completely eclipsed stacking.

Possible layer arrangements, i.e. stacking orders, in the poly(heptazine imide) material can be derived from the idealized structure model of H-PHI obtained by the PDF-analysis (see Structure modeling based on and Pair distribution function (PDF) analysis). Short N-H \cdots O (1.7 Å to 1.9 Å) and N \cdots O (2.8 Å to 3.7 Å) distances, as well the NMR- and TG- analyses (see NMR section of main Text, Solid-state nuclear magnetic resonance (ssNMR) and XRD and PDF experiments) indicate possible attractive interactions in terms of potential hydrogen bonds or dipole-dipole interactions between the poly(heptazine imide) backbone and the water molecules in the pores (Figure S1.40a, green, dashed bonds). These interactions occur both *within* a layer and *in-between* neighboring layers. Hence, the position of a layer is shifted towards the pore of the preceding layer (Figure S1.40b). Due to the 3-fold symmetry of the heptazine SBU and the disorder of the pore water, the layer can be shifted towards each of the three neighboring pores (Figure S1.40b, c, d). In addition, a completely eclipsed stacking of the poly(heptazine imide)

layers (Figure S1.40e) will be considered, as this stacking leads to a higher lattice symmetry and therefore to fewer peaks in the diffraction pattern.

Simulations of the diffractive effects of planar defects in the poly(heptazine imide) framework:

For the simulations of the diffractive effects of planar defects in the poly(heptazine imide) lattice a supercell approach implemented into the TOPAS software^[37] was used. Therefore, the unit cell of H-PHI had to be transformed into a pseudo-trigonal metric (Table S1.3). The stacking sequence of the poly(heptazine imide) layers was described by *stacking vectors*. In the idealized, faultless model of the H-PHI phase the stacking vector is represented by the orientation of the crystallographic *c*-axis. For the simulations of the diffraction patterns of stacking faulted H-PHI four possible stacking-types were considered (Figure S1.40b-e) with each of them represented by an individual stacking vector that also had to be transformed into the pseudo-trigonal metric. In each simulation the diffraction patterns of 100 randomly created supercells each of them containing 200 poly(heptazine imide) layers using an array of up to four stacking vectors were calculated and averaged, which results in comparable simulation as obtained by the recursive *DIFFaX* routine.^[38] The random creation of the stacking sequences was directed by *transition probabilities* that were systematically varied during one series of simulations (see below). In each series of the simulations a different set of transition probabilities, i.e. a different *transitions probability matrix* and different arrays of stacking vectors were used in order to represent different faulting scenarios.

Table S1.3: Overview on the lattice parameters and the stacking vectors of the determined cell of H-PHI and of the transformed unit cell used for the simulations of the diffractive effects of planar defects using a supercell approach.

original cell		transformed cell	
Space group	$P\bar{1}$	Space group	$P1$
$V/\text{\AA}^3$	460	$V/\text{\AA}^3$	$n \cdot 460$
$a/\text{\AA}$	12.963	$a'/\text{\AA}$	12.963
$b/\text{\AA}$	12.963	$b'/\text{\AA}$	12.963
$c/\text{\AA}$	4.319	$c'/\text{\AA}$	$n \cdot 3.1981$
$\alpha/^\circ$	109.28	$\alpha'/^\circ$	90
$\beta/^\circ$	109.28	$\beta'/^\circ$	90
$\gamma/^\circ$	≈ 120	$\gamma'/^\circ$	≈ 120
\mathbf{S}	$\begin{pmatrix} 0 \\ 0 \\ 1 \end{pmatrix}$	\mathbf{S}	$\in \left\{ \begin{pmatrix} -0.22 \\ -0.22 \\ 1 \end{pmatrix}, \begin{pmatrix} 0.22 \\ 0 \\ 1 \end{pmatrix}, \begin{pmatrix} 0 \\ 0.22 \\ 1 \end{pmatrix}, \begin{pmatrix} 0 \\ 0 \\ 1 \end{pmatrix} \right\}$

n is the number of poly(heptazine imide) layers of the supercells

Faulting Scenario I:

In the first faulting scenario, the diffractive effects of random transitions among pore directed stacking using only one pore (Figure S1.40b) and eclipsed stacking were simulated. For the transition from pore I directed stacking to eclipsed stacking the transition probability parameter P_x was defined, which was also used for the probability of transitions within the eclipsed stacking (Figure S1.41). As the columns of the transition probability matrix (Table S1.4) have to sum up to 1, all other layer-to-layer transitions are associated with a transition probability of $1-P_x$.

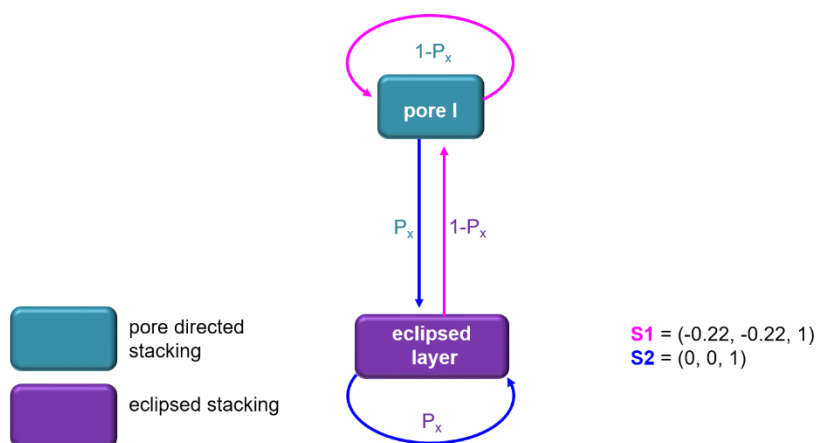


Figure S1.41: Schematic illustration of the microstructural model used for the faulting scenario I, the transition probability matrix is given in Table S1.4.

Table S1.4: Transition probability matrix including the stacking vectors of faulting scenario II (Figure S1.41).

from ↓ / to →	pore I	eclipsed layer
pore I	$1-P_x$, $S1$	P_x , $S2$
eclipsed layer	$1-P_x$, $S1$	P_x , $S2$

In the simulation series the transition parameter P_x was gradually increased from 0 to 1 in order to simulate the transition from the pure, ordered pore directed stacking to eclipsed stacking (Figure S1.42). An initial increase of the fault probability leads to a vast broadening of most reflections in the diffraction patterns. This is most pronounced for the 010 reflection, which is broadened but also shifted towards lower diffraction angles. At $P_x \approx 0.3$, this reflection begins to merge with the $\bar{1}10$ reflection which results in an overall triangular peak shape. Beginning at $P_x > 0.5$ new reflections appear and sharpen with increasing P_x , as a more and more ordered, eclipsed stacking is simulated. The reflections attributed to an ordered, eclipsed stacking (Figure S1.42, grey background) are not apparent in the measured pattern (blue pattern). In addition, in the measured pattern the 010 reflection is still present, not shifted and not broadened to a high degree. As none of the simulated patterns is qualitatively good in agreement with the measured pattern, faulting scenario I does not represent the microstructure of the H-PHI sample.

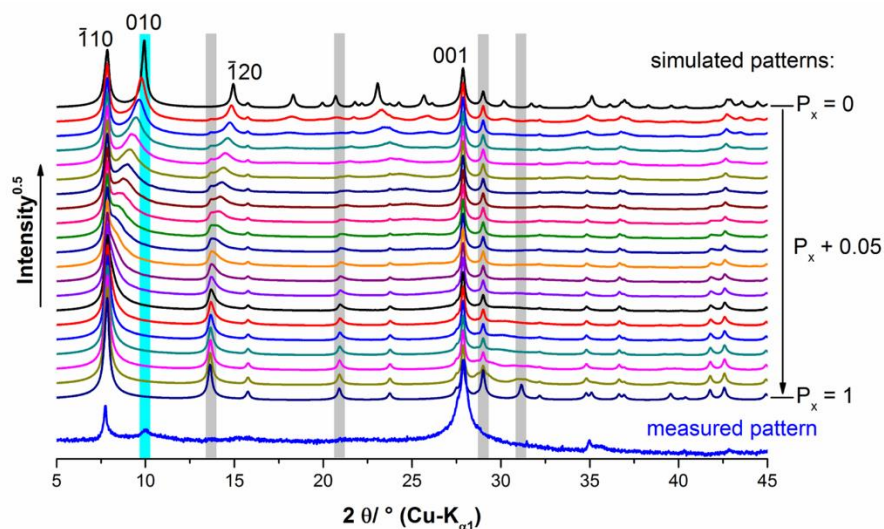


Figure S1.42: Comparison of a series of simulated powder patterns of stacking faulted H-PHI using faulting scenario I (Figure S1.41, Table S1.4) in which the probability for eclipsed stacking, P_x , was gradually increased with the measured pattern. Reflections that are apparent in pure eclipsed stacking ($P_x = 1.0$) but not in the measured pattern are highlighted with grey background color, reflections that are apparent in the measured pattern but not in the simulated are highlighted with cyan background color.

Faulting Scenario II

In another faulting scenario transitions among the three different kinds of pore directed stacking (Figure S1.40b-d) were simulated (Figure S1.43). The 3x3 transition probability matrix (Table S1.5) was constraint by using one parameter, P_y , which describes the probability that there is a change in the direction of the stacking order.

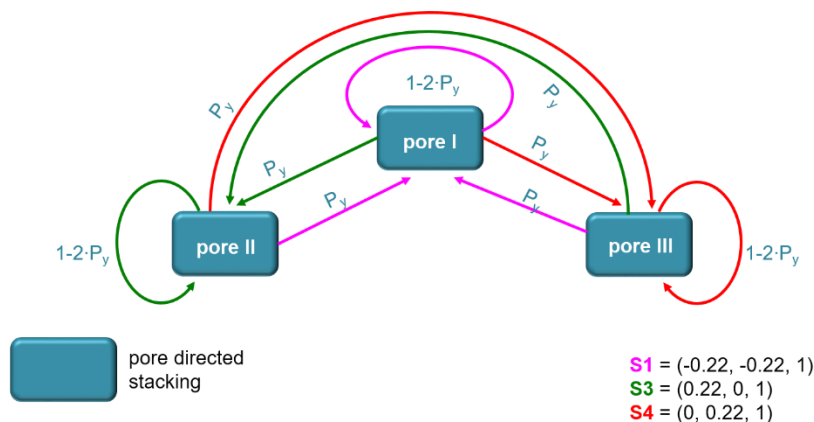


Figure S1.43: Schematic illustration of the microstructural model used for the faulting scenario II, the transition probability matrix is given in Table S1.5.

Table S1.5: Transition probability matrix including the stacking vectors of faulting scenario II (Figure S1.43).

from↓/ to→	pore I	pore II	pore III
pore I	1-2·P _y , S1	P _y , S3	P _y , S4
pore II	P _y , S1	1-2·P _y , S3	P _y , S4
pore III	P _y , S1	P _y , S3	1-2·P _y , S4

In the simulation series the parameter P_y was gradually increased from 0.00 representing a complete ordered pore directed stacking to 0.33, which describes a complete random pore directed stacking (Figure S1.44). An increased probability of a change in the stacking direction leads to broadening of almost all reflections present in the pattern of H-PHI except for the $\bar{1}10$ and the 001 reflection. The peak broadening is most pronounced for the 010 reflection. Nevertheless, it shows only a slight shift towards lower diffraction angles, it merges due to vast broadening with the $\bar{1}10$ reflections, which appears as a triangular peak shape at the basis. The simulated diffraction pattern of a complete random pore directed stacking ($P_y = 0.33$) exhibit strong similarities with the measured pattern (Figure S1.44, blue pattern). A complete random pore directed stacking, however, leads to the disappearance of the 010 reflection, which is still present in the measured pattern (blue background). This indicates that the faulting scenario has to be extended by an additional element.

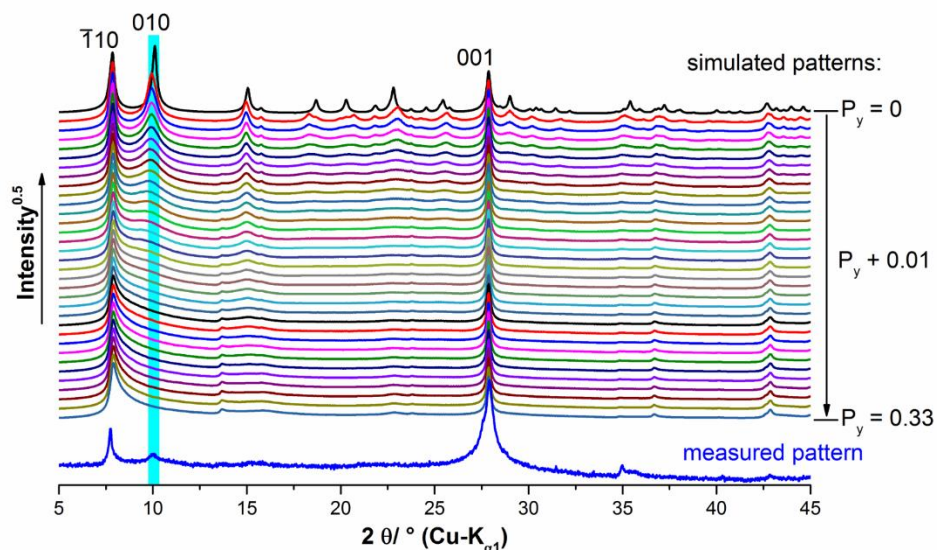


Figure S1.44: Comparison of a series of simulated powder patterns of stacking faulted H-PHI using faulting scenario II (Figure S1.43, Table S1.5) in which the probability for a change in the direction of pore directed stacking, P_y , was gradually increased with the measured pattern. Reflections that are apparent in the measured pattern but not in the simulated for complete random pore directed stacking ($P_y = 0.33$) are highlighted with cyan background color.

Faulting Scenario III

In faulting scenario III, faulting scenario II was extended by adding the eclipsed layer stacking (Figure S1.45). The transition probability matrix (Table S1.6) was constraint by keeping the probability of a change in the direction of pore directed stacking constant at $\frac{1}{3}$, which represents a complete random pore directed stacking. Within this stacking order eclipsed stacked layers were included as defects. Both the number of eclipsed stacked defects and the extension of the eclipsed stacked section were described by the parameter P_x (Figure S1.45, Table S1.6) that was gradually increased during the simulations.

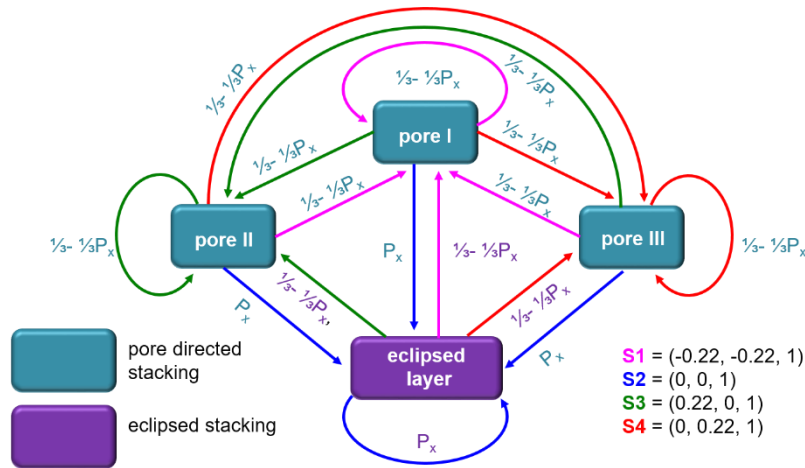


Figure S1.45: Schematic illustration of the microstructural model used for the faulting scenario III, the transition probability matrix is given in Table S1.6.

Table S1.6: Transition probability matrix including the stacking vectors of faulting scenario III (Figure S1.45).

from↓/ to→	pore I	pore II	pore III	eclipsed layer
pore I	$\frac{1}{3}-\frac{1}{3}P_x$, S1	$\frac{1}{3}-\frac{1}{3}P_x$, S3	$\frac{1}{3}-\frac{1}{3}P_x$, S4	P_x , S2
pore II	$\frac{1}{3}-\frac{1}{3}P_x$, S1	$\frac{1}{3}-\frac{1}{3}P_x$, S3	$\frac{1}{3}-\frac{1}{3}P_x$, S4	P_x , S2
pore III	$\frac{1}{3}-\frac{1}{3}P_x$, S1	$\frac{1}{3}-\frac{1}{3}P_x$, S3	$\frac{1}{3}-\frac{1}{3}P_x$, S4	P_x , S2
eclipsed layer	$\frac{1}{3}-\frac{1}{3}P_x$, S1	$\frac{1}{3}-\frac{1}{3}P_x$, S3	$\frac{1}{3}-\frac{1}{3}P_x$, S4	P_x , S2

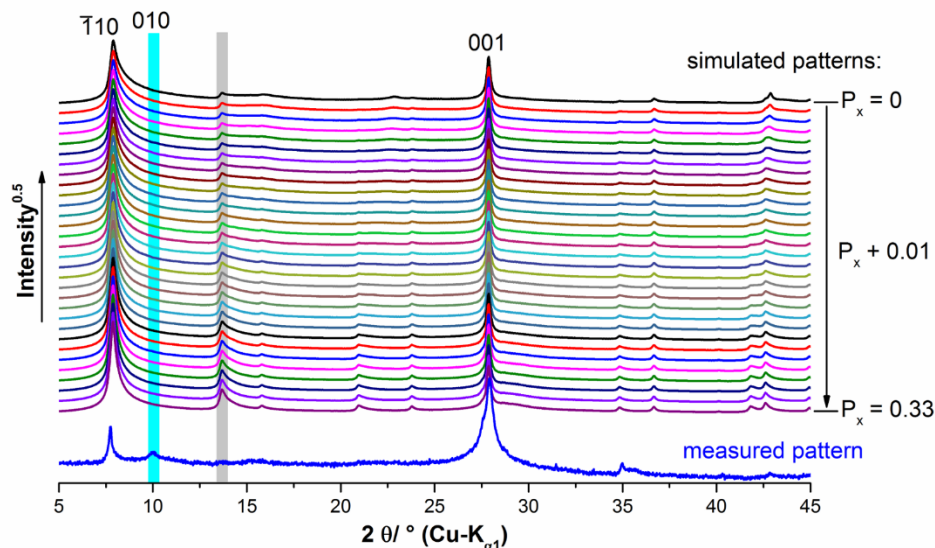


Figure S1.46: Comparison of a series of simulated powder patterns of stacking faulted H-PHI using faulting scenario III (Figure S1.45, Table S1.6) in which the probability of eclipsed stacking, P_x , in a complete random pore directed stacking was gradually increased with the measured pattern. Reflections that appear during increasing the number and extension of eclipsed stacked layers (P_x) but are not in the measured pattern are highlighted with grey background, reflections that are apparent in the measured pattern, but not in the simulation, are highlighted with cyan background color.

The increase of the number and the extension of eclipsed stacked defects in a complete random pore directed stacking in H-PHI leads to the appearance of additional reflections. These reflections, however, are not present in the measured pattern, which is most striking at around $14^\circ 2\theta$ (Figure S1.46, grey background). This faulting scenario also does not explain the appearance of the residue of the 010 reflection in the simulated pattern (cyan background). Hence, extending the microstructural model of a complete random pore directed stacking by eclipsed stacking does not lead to a satisfying explanation for the observed diffractive effects.

Faulting Scenario IV

In faulting scenario IV only transitions among pore directed stacking were used to simulate a crystallographic intergrowth of a complete random pore directed stacked domain ($P_y = \frac{1}{3}$) with an ordered pore directed stacked domain (Figure S1.47). A probability parameter P_{dom} was defined that describes the *number* of ordered domains intergrown with a random domain directed stacking. After the transition from random pore directed stacking to an ordered domain, the stacking will continue in the same pore direction (Figure S1.47, thick arrows). The parameter P_{ext} describes the probability for a transition from an ordered pore directed stacking to a randomly oriented pore directed stacking and therefore the *extension* of the ordered domain. The transition probability matrix is given in Table S1.7.

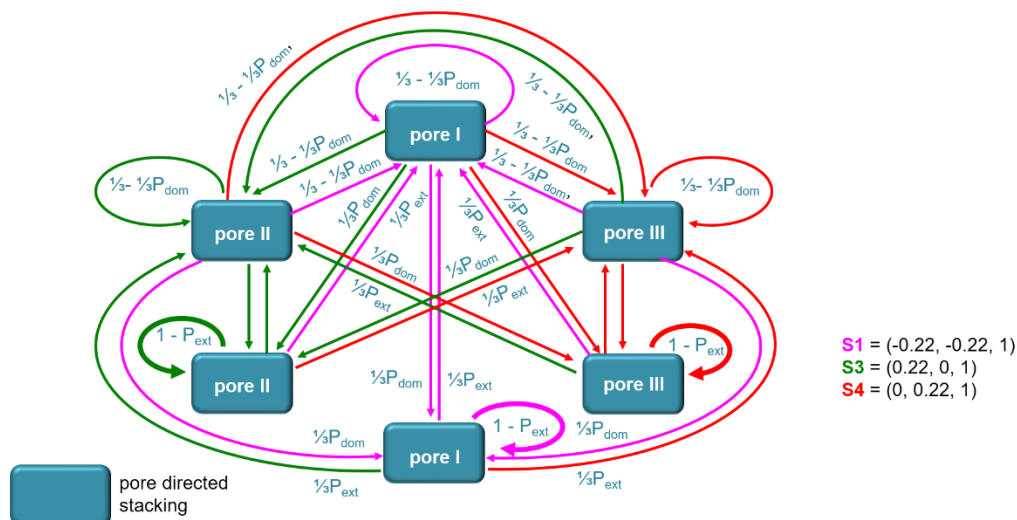


Figure S1.47: Schematic illustration of the microstructural model used for the faulting scenario IV, the transition probability matrix is given in Table S1.7.

Table S1.7: Transition probability matrix including the stacking vectors of faulting scenario IV (Figure S1.47).

from ↓ / to →		random stacking			ordered domains		
		pore I	pore II	pore III	pore I	pore II	pore III
random stacking	pore I	$\frac{1}{3} \cdot \frac{1}{3} \cdot P_{\text{dom}}$, S1	$\frac{1}{3} \cdot \frac{1}{3} \cdot P_{\text{dom}}$, S3	$\frac{1}{3} \cdot \frac{1}{3} \cdot P_{\text{dom}}$, S4	$\frac{1}{3} \cdot P_{\text{dom}}$, S1	$\frac{1}{3} \cdot P_{\text{dom}}$, S3	$\frac{1}{3} \cdot P_{\text{dom}}$, S4
	pore II	$\frac{1}{3} \cdot \frac{1}{3} \cdot P_{\text{dom}}$, S1	$\frac{1}{3} \cdot \frac{1}{3} \cdot P_{\text{dom}}$, S3	$\frac{1}{3} \cdot \frac{1}{3} \cdot P_{\text{dom}}$, S4	$\frac{1}{3} \cdot P_{\text{dom}}$, S1	$\frac{1}{3} \cdot P_{\text{dom}}$, S3	$\frac{1}{3} \cdot P_{\text{dom}}$, S4
	pore III	$\frac{1}{3} \cdot \frac{1}{3} \cdot P_{\text{dom}}$, S1	$\frac{1}{3} \cdot \frac{1}{3} \cdot P_{\text{dom}}$, S3	$\frac{1}{3} \cdot \frac{1}{3} \cdot P_{\text{dom}}$, S4	$\frac{1}{3} \cdot P_{\text{dom}}$, S1	$\frac{1}{3} \cdot P_{\text{dom}}$, S3	$\frac{1}{3} \cdot P_{\text{dom}}$, S4
ordered domains	pore I	$\frac{1}{3} \cdot P_{\text{ext}}$, S1	$\frac{1}{3} \cdot P_{\text{ext}}$, S3	$\frac{1}{3} \cdot P_{\text{ext}}$, S4	$1 - P_{\text{ext}}$, S1	-	-
	pore II	$\frac{1}{3} \cdot P_{\text{ext}}$, S1	$\frac{1}{3} \cdot P_{\text{ext}}$, S3	$\frac{1}{3} \cdot P_{\text{ext}}$, S4	-	$1 - P_{\text{ext}}$, S3	-
	pore III	$\frac{1}{3} \cdot P_{\text{ext}}$, S1	$\frac{1}{3} \cdot P_{\text{ext}}$, S3	$\frac{1}{3} \cdot P_{\text{ext}}$, S4	-	-	$1 - P_{\text{ext}}$, S4

In the series of simulation presented in Figure S1.48 the probability for a backshift from an ordered to a random pore directed stacking was kept constant at $P_{\text{ext}} = 3\%$, which means that the ordered domain was kept at a high extension, i.e. after 22 layers $\equiv 7$ nm of ordered stacking there is a probability of $> 50\%$ for a backshift to random pore directed stacking. The number of domains represented by the parameter P_{dom} was gradually increased. An increase of the number of ordered domains ($P_{\text{dom}} > 0.03$) leads to the appearance of the 010 reflection in the simulated patterns (Figure S1.48, cyan background). Additional reflections become visible only after a further increase of the number of ordered domains ($P_{\text{dom}} > 0.10$). Hence, it can be concluded that faulting scenario IV (Figure S1.48) is a suitable, qualitative approximation of the microstructure of the H-PHI phase.

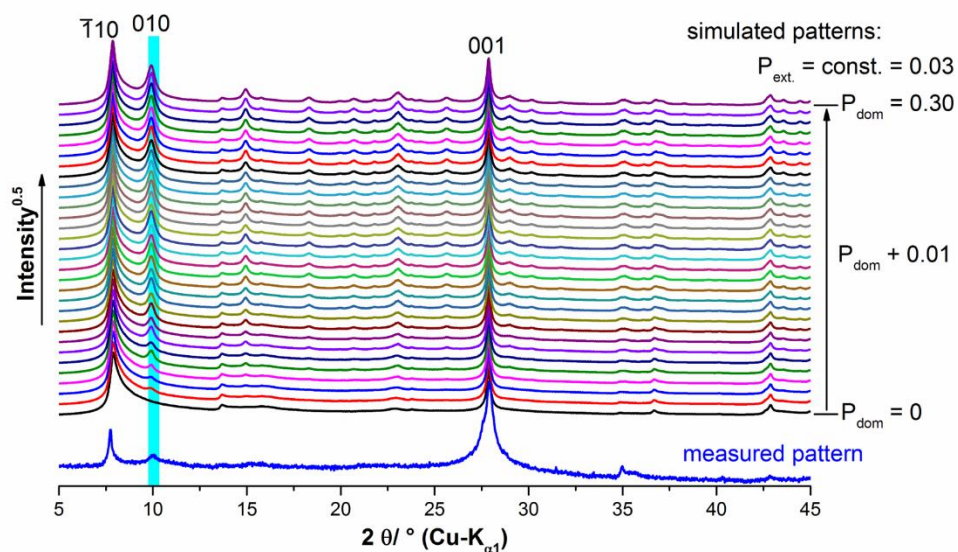


Figure S1.48: Comparison of a series of simulated powder patterns of stacking faulted H-PHI using faulting scenario IV (Figure S1.47, Table S1.7) in which the probability of the occurrence of an ordered domain, P_{dom} , in a complete random pore directed stacking was gradually increased while the extension of the ordered domain was kept constant ($P_{\text{ext.}} = 0.03$) with the measured pattern. The position of the 010 reflection is highlighted by cyan background.

Final evaluation

The absence of eclipsed stacking related reflections at (13.6, 15.8, 21.0, 23.8, 29.0, 31.2) °2θ in the measured patterns clearly indicated that there are no coherently scattering domains of eclipsed stacked poly(heptazine imide) layers in the H-PHI material. The presence of a few, isolated eclipsed stacked defects in the material, however, cannot be excluded. Systematic simulations indicated that the microstructure of H-PHI is mainly governed by pore directed stacking. Due to the intrinsic trigonal symmetry of the heptazine SBU, this type of stacking exhibits three fundamental directions. The vast broadening of the reflections indicated a non-coherent stacking, i.e. the stacking order is a complete random distribution of these three fundamental stacking directions. A remnant of the 010 reflection also points to the fact that few domains of ordered pore directed stacking are still apparent in the microstructure of the material (Figure S1.49). As the scattering effect of the pore material, which modulates the peak intensities in relation to the intensity of 001 basal reflection, could not be included into the simulation series, quantitative information on the amount and extensions of the ordered stacked domains in the material, cannot be extracted.

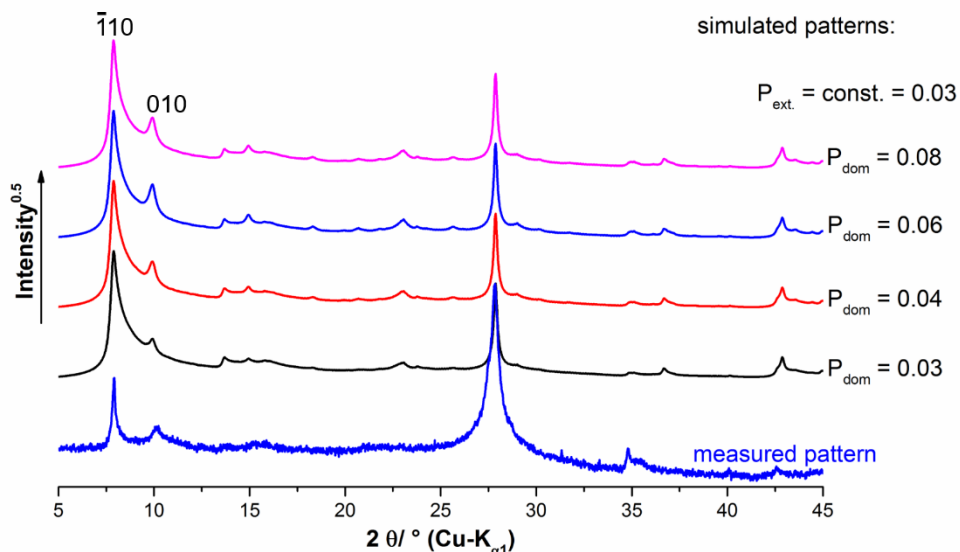


Figure S1.49: Comparison of selected simulated diffraction patterns of faulting scenario IV (Table S1.7, Figure S1.47) with the measured pattern of H-PHI.

Synopsis: The 3-dimensional structure of the poly(heptazine imide) framework

The 3-dimensional structure of the poly(heptazine imide) framework, i.e. the arrangement of poly(heptazine imide) layers is governed by the ions and molecules (e.g. K⁺ and H₂O) situated in the pores. By interactions between the pore particles and the poly(heptazine imide) backbone a stacking order in which the layers are arranged in a slightly staggered fashion, i.e. a layer is shifted towards the pore of the preceding layer, is more favorable than a complete eclipsed stacking. Due to the trigonal symmetry of the heptazine SBU, there are three symmetry equivalent pores per heptazine unit. In H-PHI the pores are exclusively filled with water molecules. According to the small spacial extension of water molecule and due to the interlayer spacing of ≈ 3.2 Å, water only mediates the interactions between two adjacent layers. In consequence there is no long-range order of the layer orientation in the structure of H-PHI. Hence, transitions among all three possible pore directed stackings occur in a complete random fashion. In contrast the powder pattern of K-PHI indicates a long-range order in *c*-direction. Due to the positive charge and the large ionic radius of potassium a partial hydration sphere is formed with the water molecule in the pores. Therefore, potassium directs the stacking order of at least three adjacent layers directly and by the arrangement of pore water molecules by forming the partial hydration sphere even more layers indirectly. The ordered domains that are present in the microstructure of H-PHI can be attributed to residual potassium (as indicated by elemental analysis showing 0.5 w% potassium for H-PHI) that was not completely exchanged during the conversion from K-PHI to H-PHI.

9.1.10. Protonation with different acids/concentrations

Figure S1.50 - Figure S1.52 show that neither the type of acid, e.g. HCl, H₃PO₄, H₂SO₄ or HClO₄, nor the molarity of the acid is relevant for the transformation from K-PHI to H-PHI. Higher acid concentration most likely just result in a faster hydrolysis of attached functional groups. Also none of the anions could be found in the corresponding H-PHI. Thus the formed salt from the acid/base reaction is washed out from the pores upon washing with water. This is not the case for the related poly(triazine imide) structure where “LiCl” is present within the pore.^[28] As expected, all differently treated H-PHI samples performed similarly well in photocatalytic experiments. Additionally, we tried to extract the potassium ions by stirring the polymer in a crown-18-ether known to complex alkali ions. However, we could not detect any change in the structure after washing why we conclude that either the pores are not accessible to the cryptand or the potassium ions are bound to the network quite strongly.

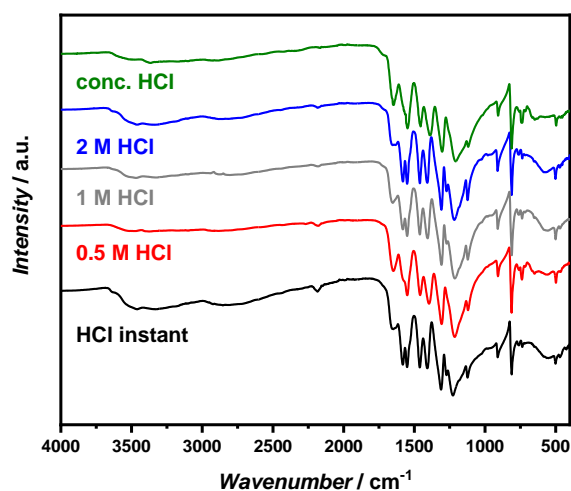


Figure S1.50: IR spectra of K-PHI treated with different concentrations of hydrochloric acid. HCl instant was treated for only 5 min. while the rest was treated overnight. The major difference is the complete removal of the NCN-vibration at ca. 2170 cm⁻¹ with higher concentrations.

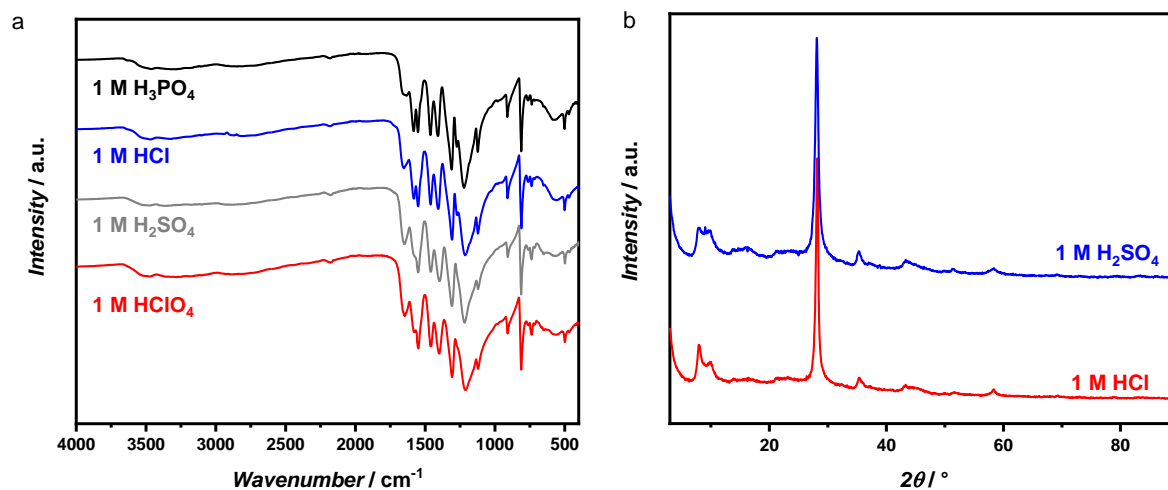


Figure S1.51: a) IR spectra and b) powder XRD of K-PHI treated with HCl and H_2SO_4 . We conclude that there is no significant influence of the acid that is used. Asterisk marks an artifact of the diffractometer.

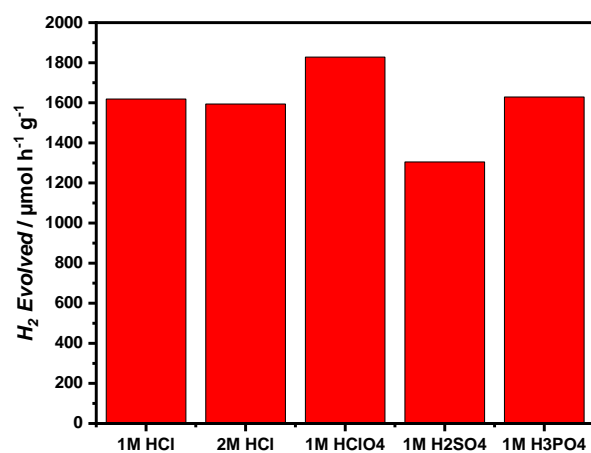


Figure S1.52: Photocatalytic performance of K-PHI treated with various acids. The catalytic performance is neither dependent on the concentration of the acid nor their type.

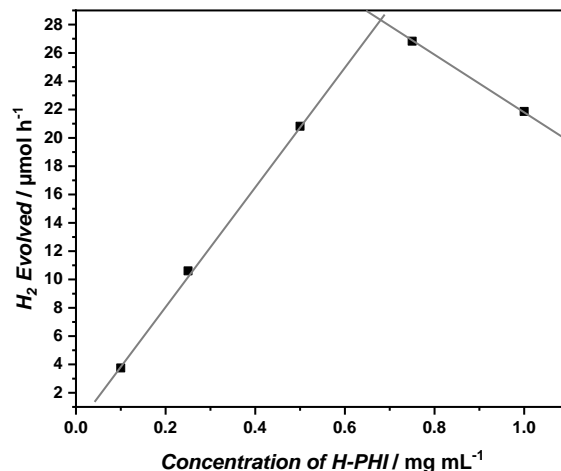


Figure S1.53: Photocatalytic activity with respect to the H-PHI concentration in the suspension. According to this a concentration of approx. 0.7 mg/mL is suitable for optimal performance. The catalytic reaction was performed with Pt as co-catalyst (2 wt%) and methanol as sacrificial donor.

9.1.11. Base treated H-PHI

H-PHI may be treated with a base to revert it back to its anionic form and the corresponding alkali metal cation. The transformation from optimized K-PHI to H-PHI by stirring in diluted aqueous HCl and back to K-PHI by stirring in aqueous KOH is presented in Figure S1.54. Although partial hydrolysis and hence degradation of the backbone and the functional NCN-groups may be expected, the main characteristic peaks in the analyses are retained. However, due to a likely loss of functional groups during the initial treatment with acids, the activity of the pristine K-PHI for H₂-Evolution is not totally recovered. Additionally, the increased tail in the diffuse reflectance spectrum (Figure S1.54e) gives rise to the assumption of increased degradation of the photocatalyst, e.g. due to hydrolysis.

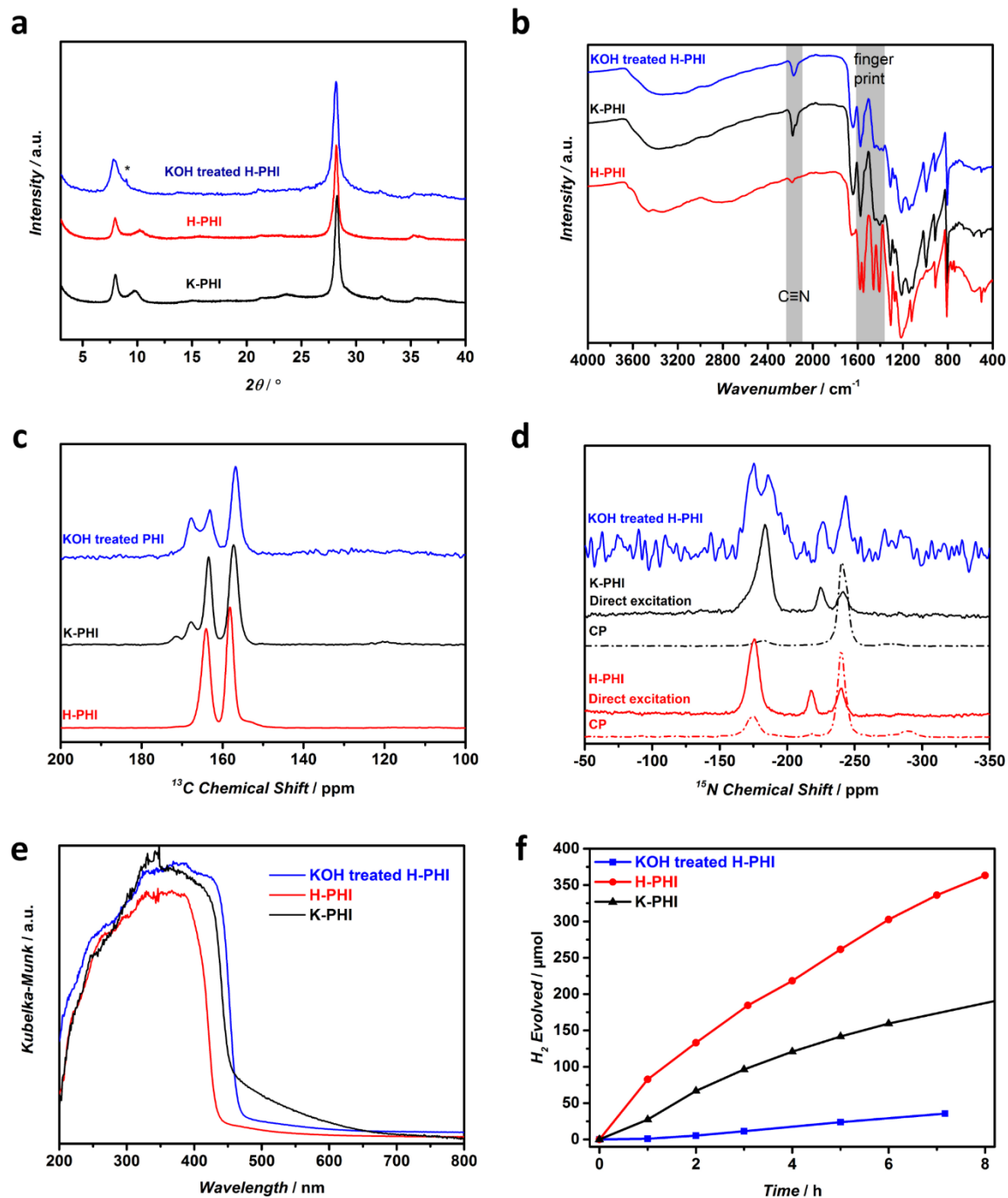


Figure S1.54: a) PXRD patterns, b) FT-IR spectra, c) ^{13}C cross-polarization (CP) MAS ssNMR spectra, d) ^{15}N MAS ssNMR (direct and CP) e) diffuse reflectance spectra and f) photocatalytic performance of pristine optimized K-PHI, the acid treated H-PHI and the back-converted KOH treated H-PHI.

9.1.12. Elemental analysis

Table S1.8: Composition of crystalline K-PHI and optimized K-PHI determined by combustion analysis and ion coupled plasma (ICP) analysis. The values were averaged over several batches. Water was indirectly determined as the residual mass.

	Ampoule crystalline K-PHI		Crucible optimized K-PHI	
	wt%	mol%	wt%	mol%
C	27.6	34.9	26.2	32.6
N	46.3	50.1	43.6	46.5
K	13.7	5.3	9.0	3.4
S	2.0	0.9	0.4	0.2
H	(1.7)	-	(2.2)	-
H₂O^{a)}	10.4	8.7	20.8	17.3
Total	100.0		100.0	100.0
N/C	1.438	$C_7N_{10}K_1S_{0.18}$	1.426	$C_7N_{10}K_{0.7}S_{0.04}$

^{a)} All weight percent were added and the rest along with the hydrogen content was defined as water. This way the hydrogen content is not reliable and therefore not included in the chemical formula.

Table S1.9: Composition of crystalline H-PHI and optimized H-PHI determined by combustion analysis and ion coupled plasma (ICP) analysis. The values were averaged over several batches. Water was indirectly determined as the residual mass.

	Ampoule crystalline H-PHI		Crucible optimized H-PHI	
	wt%	mol%	wt%	mol%
C	29.0	33.9	28.7	33.6
N	49.7	49.8	48.0	48.2
K	0.5	0.2	0.2	0.1
S	0.4	0.2	0	0
H	(3.0)	-	(3.1)	-
H₂O^{a)}	20.4	15.9	23.1	18.1
Total	100.0		100.0	
N/C	1.469	$C_7N_{10.2}K_{0.04}S_{0.04}$	1.434	$C_7N_{10.2}K_{0.02}$

^{a)} All weight percent were added and the rest along with the hydrogen content was defined as water. This way the hydrogen content is not reliable and therefore not included in the chemical formula.

As washing the substance with THF did not significantly impact the sulfur content, it is either covalently bound (doping in the backbone) or inaccessible in pores. However, when washed with diluted acids such as HCl a loss of sulfur is observed which may be explained by a delamination and successive removal of intraporous molecules/ions.

9.1.13. Water sorption

Water sorption isotherms were measured on an Autosorb-iQ surface analyzer with vapor option (Quantachrome Instruments, USA). To initially remove guest molecules the samples were outgassed in vacuum at 200 °C for 12 h. The measurements were performed at 273 K. The overall uptake of water is 340 ccm/g for optimized K-PHI, 417 ccm/g for optimized H-PHI, 169 ccm/g for crystalline K-PHI and 196 ccm/g for crystalline H-PHI. The desorption of water is reversible. However, at low pressures the initial amount is not reached and complete desorption of strongly bound water likely requires higher temperatures for these materials. This is expected since the ssNMR results also indicate a rather strong binding situation between water and the carbon nitride network. In the case of optimized H-PHI and K-PHI a significant uptake of water can be observed. The maximum adsorbed amount is somewhat larger in the case of H-PHI, which is in line with the other experimental data, since elemental analyses also show that more water is present in H-PHI. The lower adsorption volume for crystalline samples is expected due to the larger crystallites and therefore less accessible surface area and also follows the data from elemental analysis.

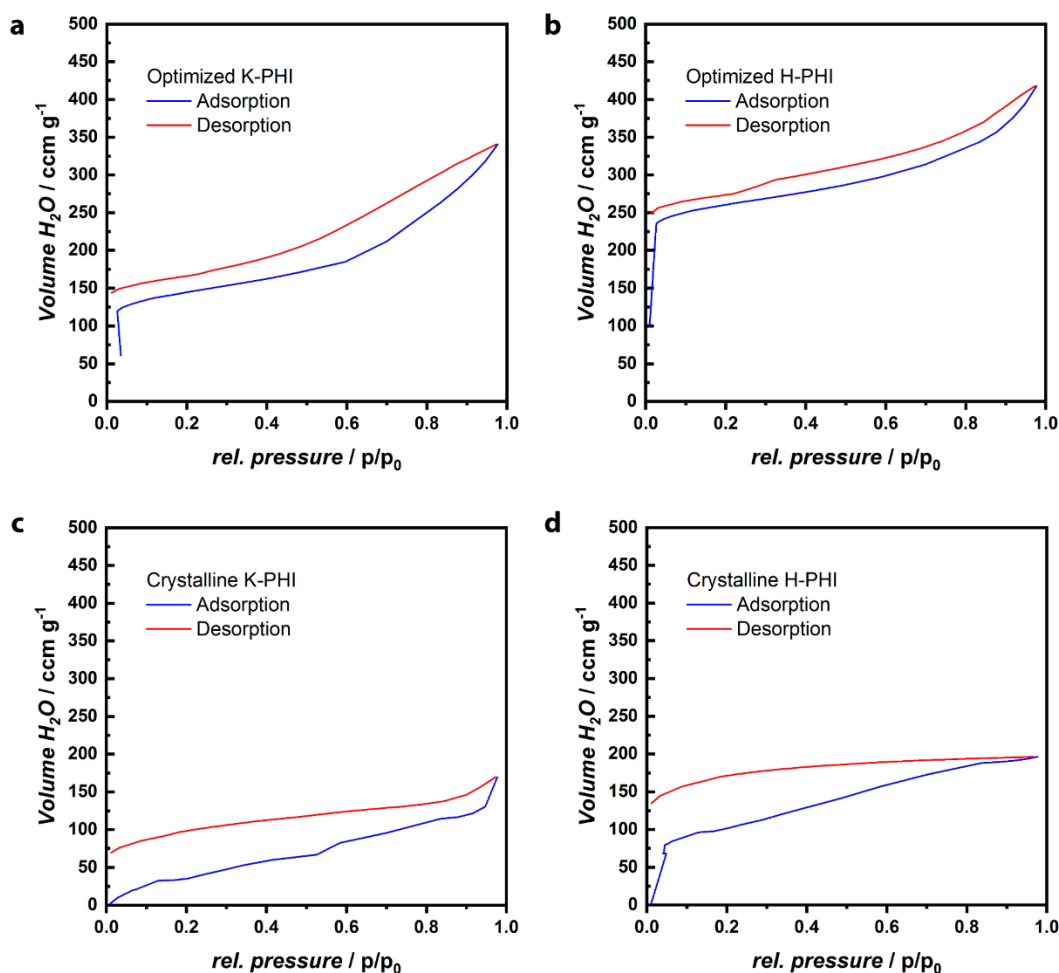


Figure S1.55: Water sorption isotherms at 273 K for a) optimized K-PHI, b) optimized H-PHI, c) crystalline K-PHI and d) crystalline H-PHI.

9.1.14. Raman spectroscopy

The Raman spectra were recorded with an excitation wavelength of 532 nm and 632 nm. In general, K-PHI and H-PHI both show a strong luminescence background for both measured excitation wavelengths (Figure S1.56). Some of the main signals are still distinguishable from the background, which are within the expected range for triazine or heptazine-based systems.^[39-40] No significant differences of those signals were observed for H-PHI and K-PHI. The weaker intensities in crystalline samples are likely to arise from looser packing in the capillary and therefore less substance in the focus of the laser.

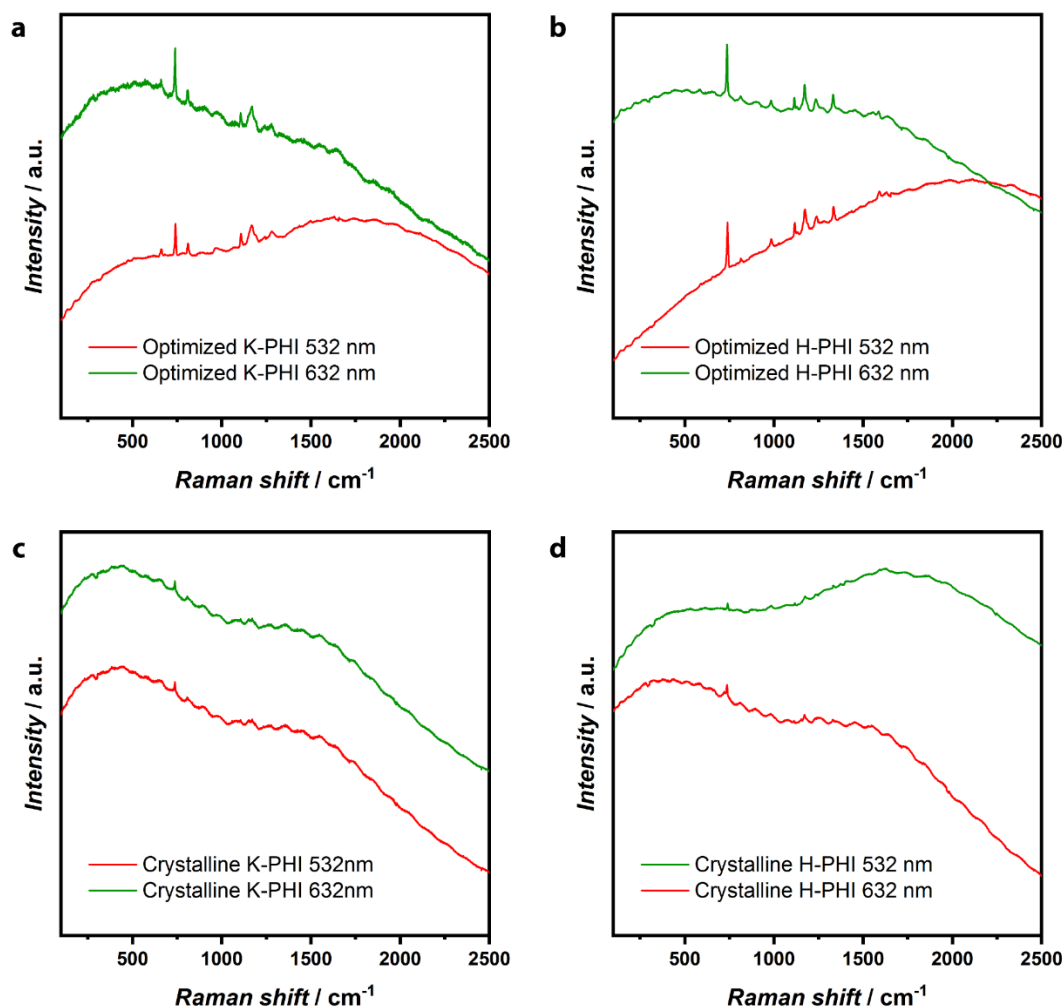


Figure S1.56: Raman spectra of a) optimized K-PHI, b) optimized H-PHI, c) crystalline K-PHI and d) crystalline H-PHI recorded with a 532 nm and 632 nm laser, respectively. The signals are overlapped by a strong fluorescence for both wavelengths.

9.1.15. Bibliography

- [1] V. W.-h. Lau, I. Moudrakovski, T. Botari, S. Weinberger, M. B. Mesch, V. Duppel, J. Senker, V. Blum, B. V. Lotsch, *Nat. Commun.* **2016**, 7(1), 12165.
- [2] V. W.-h. Lau, V. W.-z. Yu, F. Ehrat, T. Botari, I. Moudrakovski, T. Simon, V. Duppel, E. Medina, J. K. Stolarczyk, J. Feldmann, V. Blum, B. V. Lotsch, *Adv. Energy Mater.* **2017**, 7(12), 1602251.
- [3] V. W.-h. Lau, D. Klose, H. Kasap, F. Podjaski, M.-C. Pignié, E. Reisner, G. Jeschke, B. V. Lotsch, *Angew. Chem. Int. Ed.* **2017**, 56(2), 510-514.
- [4] A. Brinkmann, A. P. M. Kentgens, *J. Am. Chem. Soc.* **2006**, 128(46), 14758-14759.
- [5] M. H. Levitt, Symmetry-Based Pulse Sequences in Magic-Angle Spinning Solid-State NMR. In *eMagRes*, **2007**.
- [6] P. J. Chupas, X. Qiu, J. C. Hanson, P. L. Lee, C. P. Grey, S. J. L. Billinge, *J. Appl. Crystallogr.* **2003**, 36(6), 1342-1347.
- [7] D. Case, R. Betz, D. S. Cerutti, T. Cheatham, T. Darden, R. Duke, T. J. Giese, H. Gohlke, A. Götz, N. Homeyer, S. Izadi, P. Janowski, J. Kaus, A. Kovalenko, T.-S. Lee, S. LeGrand, P. Li, C. Lin, T. Luchko, P. Kollman, *Amber 16, University of California, San Francisco.* **2016**.
- [8] J. C. Phillips, R. Braun, W. Wang, J. Gumbart, E. Tajkhorshid, E. Villa, C. Chipot, R. D. Skeel, L. Kalé, K. Schulten, *J. Comput. Chem.* **2005**, 26(16), 1781-1802.
- [9] P. A. Stadelmann, *Ultramicroscopy* **1987**, 21(2), 131-145.
- [10] J. Brivio, D. T. L. Alexander, A. Kis, *Nano Lett.* **2011**, 11(12), 5148-5153.
- [11] J. C. Meyer, A. K. Geim, M. I. Katsnelson, K. S. Novoselov, T. J. Booth, S. Roth, *Nature* **2007**, 446(7131), 60-63.
- [12] A. L. Patterson, *Phys. Rev.* **1939**, 56(10), 978-982.
- [13] R. W. Cheary, A. A. Coelho, J. P. Cline, *J. Res. Natl. Inst. Stand. Technol.* **2004**, 109(1), 1-25.
- [14] R. W. Cheary, A. Coelho, *J. Appl. Crystallogr.* **1992**, 25(2), 109-121.
- [15] A. Coelho, *J. Appl. Crystallogr.* **2018**, 51(1), 210-218.
- [16] C. Adamo, V. Barone, *J. Chem. Phys.* **1999**, 110(13), 6158-6170.
- [17] M. Ernzerhof, G. E. Scuseria, *J. Chem. Phys.* **1999**, 110(11), 5029-5036.
- [18] S. Grimme, J. Antony, S. Ehrlich, H. Krieg, *J. Chem. Phys.* **2010**, 132(15), 154104.
- [19] A. Schäfer, C. Huber, R. Ahlrichs, *J. Chem. Phys.* **1994**, 100(8), 5829-5835.
- [20] P. J. Wilson, T. J. Bradley, D. J. Tozer, *J. Chem. Phys.* **2001**, 115(20), 9233-9242.
- [21] F. Jensen, *J. Chem. Theory Comput.* **2015**, 11(1), 132-138.
- [22] R. Ahlrichs, M. Bär, M. Häser, H. Horn, C. Kölmel, *Chem. Phys. Lett.* **1989**, 162(3), 165-169.
- [23] J. Kussmann, C. Ochsenfeld, *J. Chem. Phys.* **2013**, 138(13), 134114.
- [24] L. D. M. Peters, J. Kussmann, C. Ochsenfeld, *J. Chem. Theory Comput.* **2017**, 13(11), 5479-5485.
- [25] J. Mähler, I. Persson, *Inorg. Chem.* **2012**, 51(1), 425-438.
- [26] D. Ectors, F. Goetz-Neunhoffer, J. Neubauer, *J. Appl. Crystallogr.* **2015**, 48(1), 189-194.
- [27] P. Stephens, *J. Appl. Crystallogr.* **1999**, 32(2), 281-289.
- [28] E. Wirnhier, M. Döblinger, D. Gunzelmann, J. Senker, B. V. Lotsch, W. Schnick, *Chem.–Eur. J.* **2011**, 17(11), 3213-3221.
- [29] A. Coelho, *J. Appl. Crystallogr.* **2018**, 51(1), 112-123.
- [30] A. P. Hammersley, S. O. Svensson, M. Hanfland, A. N. Fitch, D. Hausermann, *High Press. Res.* **1996**, 14(4-6), 235-248.
- [31] G. Ashiotis, A. Deschildre, Z. Nawaz, J. P. Wright, D. Karkoulis, F. E. Picca, J. Kieffer, *J. Appl. Crystallogr.* **2015**, 48(2), 510-519.
- [32] P. Juhas, T. Davis, C. L. Farrow, S. J. L. Billinge, *J. Appl. Crystallogr.* **2013**, 46(2), 560-566.
- [33] X. Yang, P. Juhas, C. L. Farrow, S. J. L. Billinge, *xPDFsuite: An end-to-end software solution for high throughput pair distribution function transformation, visualization and analysis.* **2014**.
- [34] P. Juhas, C. L. Farrow, X. Yang, K. R. Knox, S. J. L. Billinge, *Acta Crystallogr. A* **2015**, 71(6), 562-568.
- [35] R. Amunugama, M. T. Rodgers, *Int. J. Mass spectrom.* **2000**, 195-196, 439-457.
- [36] B. E. Warren, *Phys. Rev.* **1941**, 59(9), 693-698.
- [37] A. A. Coelho, J. S. O. Evans, J. W. Lewis, *J. Appl. Crystallogr.* **2016**, 49(5), 1740-1749.
- [38] M. M. J. Treacy, J. M. Newsam, M. W. Deem, *Proc. R. Soc. A* **1991**, 433(1889), 499-520.

- [39] T. S. Miller, A. B. Jorge, T. M. Suter, A. Sella, F. Corà, P. F. McMillan, *Phys. Chem. Chem. Phys.* **2017**, *19* (24), 15613-15638.
- [40] C. Fan, J. Miao, G. Xu, J. Liu, J. Lv, Y. Wu, *RSC Adv.* **2017**, *7* (59), 37185-37193.

9.2. Supporting information of chapter 5 “Morphology control in PHI: impact on optoelectronic properties and photocatalysis”

9.2.1. Instrumental details

A Philips CM30 ST (300 kV, LaB₆ cathode) was used for transmission electron microscopy (TEM). The samples were suspended in n-butanol and drop-cast onto a lacey carbon film (Plano). Electron diffraction patterns were simulated from the crystal information reported in a previous paper of our group.^[1]

Scanning electron microscopy (SEM) was performed on a Zeiss Merlin electron microscope. The samples were drop-cast onto a Si substrate after cleaning with acetone and isopropanol.

Diffusive light scattering (DLS) and zeta-potentials were measured with a Malvern Zetasizer Nano ZS. DLS measurements were performed at concentration of 0.25 mg mL⁻¹ for the suspensions. The amount of big particles >3000 nm was not quantifiable due to an upper limit of measurable particles sizes by the DLS instrument. For zeta-potential measurements the carbon nitride sample was suspended at concentration of 10 µg mL⁻¹ in aqueous solutions of various pH adjusted by HCl or NaOH, with the ionic strength maintained at 10 mM using NaCl.

AFM was performed with an Asylum Research (Oxford Instruments) MFP-3D AFM in tapping mode with an Olympus cantilever with a resonance frequency of ≈300 kHz. The colloidal sample was drop-cast onto a Si/SiO₂ substrate that had been cleaned with acetone and isopropanol.

Powder X-ray diffraction (PXRD) patterns were collected at room temperature on a laboratory powder diffractometer in Debye-Scherrer geometry (Stadi P-Diffraktometer (Stoe), Cu-K_{α1} radiation from primary Ge(111)-Johann-type monochromator, triple array of Mythen 1 K detectors (Dectris)). The samples were sealed in 0.5 mm diameter borosilicate glass capillaries.

The lateral and vertical sizes of PHI-materials were determined from the powder patterns by using the Scherrer-equation^[2]

$$\tau = \frac{K \cdot \lambda}{\beta \cdot \cos \theta}$$

with τ as the mean size of the ordered domains, K as a dimensionless shape factor, λ as the wavelength of the diffractometer, β as the diffraction line broadening, and θ as the Bragg angle. The instrumental profile was determined by refining the instrumental function, described by the fundamental parameter approach^[3, 4] using a diffraction pattern of the Si640d NIST standard and fixed for crystallite size analysis. The lateral crystallite size was determined by a single line fit in the 2θ range of 6.5–8.7° of the $\bar{1}10$ reflection using the Jana2006 software.^[5] As the $\bar{1}10$ reflection overlaps with the anisotropically broadened 010 reflection, a 2nd peak was included into the refinement and refined independently. The background was modeled with Chebychev polynomials of 2nd order. For the estimation of the vertical crystallite size, a single line fit of the 001 reflection in a 2θ range of 26.5–29.5° was performed. The complex background of the diffraction patterns, that is governed by diffuse scattering, and the overlap with anisotropically broadened reflections causes an increased analytical error (≈ 10 %), that is far larger than the analytical error, which is to be expected for a crystallite size determination using a high resolution laboratory X-ray powder diffractometer (≈ 1–2 %).

Fourier transformed infrared (FT-IR) spectra were performed with a PerkinElmer UATR TWO spectrometer equipped with a diamond crystal.

Diffuse reflectance UV and visible light (UV-Vis) spectra were collected on a Cary 5000 spectrometer (referenced to PTFE or barium sulfate) and the spectra in percentage reflectance were converted using the Kubelka Munk function. These data are plotted in a Tauc plot, with the assumption of a direct optical band gap, to estimate the optical band gap.

C, H, N elemental analyses were performed with a UNICUBE (Elementar Analysensysteme GmbH). Other elements were quantified with a Vista Pro Simultaneous ICP-OES Spectrometer combined with axially plasma system as excitation source and echelle polychromator with CCD detector (Varian Darmstadt). Calibrations were carried out by standard addition and the data were analyzed by the ICP-Expert software. Samples were digested in concentrated HNO₃ at 185 °C for 25 min in a microwave (Discover SP-D, CEM GmbH).

Sorption measurements were acquired on a Quantachrome Autosorb iQ gas sorption analyzer using argon as the sorbent at 87.45 K. To activate and outgas the samples, they were left in vacuum (10⁻⁷ mbar) overnight at 150 °C. The surface area was calculated from the adsorption isotherm by using the Brunauer–Emmett–Teller (BET) theory.

For X-ray photoelectron spectroscopy (XPS), the powder samples were pressed into an indium foil. The spectra were collected on an Axis Ultra (Kratos Analytical, Manchester) X-ray photoelectron spectrometer equipped with a monochromatized Al K_α X-ray source and charge neutralization. The spectra were processed with the software CasaXPS 2.3.16 and referenced with the adventitious carbon 1s peak at 284.80 eV.^[6,7] For the Pt 4f_{7/2} and Pt 4f_{5/2} the area ratio was constrained to 4:3 and the binding energy separation to 3.33 eV.^[8] The comparison of binding energies was performed with the NIST Standard Reference Database 20 (Version 4.1) unless otherwise specified. For quantification the spectra were corrected by the transmission function and the relative transmission functions given by the instrument manufacturer were used.

Solid-state ¹H, ¹³C and ¹⁵N nuclear magnetic resonance (NMR) experiments were performed on a Bruker Avance-III 400 MHz instrument at frequencies of 400, 100.61 and 40.53 MHz, respectively (B₀ = 9.4 T). Chemical shifts for ¹H and ¹³C are referenced to tetramethylsilane (TMS, δ(¹H, ¹³C) = 0.0 ppm), while ¹⁵N is referenced to nitromethane (δ = 0.0 ppm). Magic Angle Spinning (MAS) with spinning rates ranging between 10 and 12.5 kHz was used in all experiments on solids. ¹³C and ¹⁵N spectra with cross-polarization (CP) were recorded with a ramped polarization mixing and SPINAL-64 proton decoupling (¹H RF field of 50 kHz).^[9,10]

Photoluminescence (PL) spectra were collected on a double monochromator spectrofluorometer (Edinburgh FLS980) at an excitation wavelength of λ = 370 nm. Prior to every measurement the suspension (0.25 mg mL⁻¹) was degassed with a constant flow of Ar. Different conditions of each samples were measured starting with 0.25 mg mL⁻¹ aqueous suspension, methanol was added as a sacrificial donor and an optimized amount of hexachloroplatinum acid used for photo-depositing Pt before measurements, similar to photocatalysis experiments. Time-dependent lifetime measurements were performed with a 5 nm spectral window, which was centered at λ = 480 nm. The decay signal was fitted with a combination of a δ function and a Γ function, as it was described in a previous paper of our group^[11]:

$$I(t) = \int_0^{\infty} p(k)e^{-kt} dk = \frac{A_{\Gamma\text{mean}}}{(1 + \beta t)^{\alpha+1}} + A_{\text{exp}}e^{-kt}$$

where the first term corresponds to the Γ -distribution, defined by the α and β parameters, and the second one describes an exponential decay. In this manner, $A_{\Gamma\text{mean}}$ and A_{exp} show the relative weight of each contributions. To prevent agglomeration or sedimentation, the suspensions were stirred during the measurement.

9.2.2. Experimental details

Material synthesis: K-PHI and H-PHI were prepared as reported previously.^[1, 12, 13] Melamine (5.0 g; Carl Roth > 99%) was heated at 550 °C for 12 h at 5 °C min⁻¹ ramp rate under argon to yield melon as a yellow solid (2.0–2.4 g), which was ground to a fine powder before further processing. K-PHI was prepared by heating a finely ground mixture of melon (1.5 g) and KSCN (3.0 g, dried at 150 °C in vacuum; Carl Roth 99%) under argon at 400 °C for 1 h, then 500 °C for 30 min, both under maximum ramp rate. The resulting yellow solid was dispersed in water, centrifuged to isolate the product, and then repeatedly washed with water to remove all trace of KSCN. After drying at 60 °C in a vacuum oven, K-PHI was isolated as a yellow solid (1.0–1.3 g). H-PHI was prepared by stirring K-PHI (1.0 g) in HCl (100 mL, 1 M) overnight. The off-white solid was isolated by centrifugation, washed repeatedly with water until the supernatant was neutralized, then dried at 60 °C in a vacuum oven to afford H-PHI as an off-white solid (700–900 mg).

Sonication procedure: Colloidal solution of H-PHI (P4) was prepared by subjecting an aqueous suspension of H-PHI at concentration of 10 mg mL⁻¹ to ultrasonication for 24 h. The resulting dispersion was then centrifuged at RCF 500 to precipitate out the aggregates and the supernatant was collected as the colloidal solution. For solid state characterization and determination of the colloid concentration, a known volume of the solution was taken and dried on a weighed petri dish on a hot plate at no more than 60 °C overnight.

For the ultrasonication treatment, a Sonorex (Bandelin) Super RX1028 H with a nominal power of 300 W was used. To prevent heating during sonication, and hence reduce possible damage of the material, the ultrasonication bath was cooled with ice, which was refilled in constant time intervals. In addition, roughly every 30 min the reaction vessel was shaken to re-suspend sediment particles and prevent re-agglomeration.

The particle size separation for H-PHI and K-PHI was performed by sonicating 300 mg of the powder in 100 mL deionized water for 2 h while frequently shaking of the suspension, similar to literature.^[14, 15] To prevent heating the sonication bath was cooled with an ice bath. To separate the particles according to their size, three centrifugation steps were used. The precipitate of the first step at 353 RCF for 25 min gained P1 particles. The supernatant was further centrifuged at 795 RCF for 40 min to obtain smaller precipitated particles (P2) and the smallest particles (P3) were obtained by centrifugation of the supernatant again at 35329 RCF for 90 min (Table S2.1).

Table S2.1: Sample name and corresponding synthesis conditions.

Sample name	Synthesis conditions
K/H-PHI pristine	No sonication
K/H-PHI P1	2 h sonication Particle separation: Precipitate of centrifuging at 353 RCF
K/H-PHI P1 re-agglomerated	K/H-PHI P1 dried in vacuum
K/H-PHI P2	2 h sonication Particle separation: Precipitate of centrifuging at 795 RCF after P1 is removed
K/H-PHI P3	2 h sonication Particle separation: Precipitate of centrifuging at 35329 RCF after P2 is removed
H-PHI P4	24 h sonication Particle separation: Supernatant of centrifugation at 500 RCF

Photocatalytic hydrogen evolution: Photocatalytic experiments were performed in a double-walled glass reactor, where the outer compartment is circulated with thermostated water (25 °C), as previously described.^[12, 13] The reactor was top-irradiated through a quartz window with a xenon lamp (Newport, 300 W) equipped with a water filter and a full spectrum mirror (2000 nm > λ > 200 nm). An air mass (AM) 1.5 G filter was used unless specified different and the light intensity was 100 mW cm⁻². The catalyst powder (5, 10 or 20 mg) was suspended in a solution of water (4.5 mL, 9 mL or 19 mL), methanol (0.5 mL, 1 mL or 2 mL) and dihydrogen hexachloroplatinic (8 wt% aqueous solution, Aldrich, optimized volume as previously reported^[12-13]), which forms the platinum co-catalyst from its in-situ reduction. Colloidal suspension of PHI were diluted with water to reach an equal concentration as in the experiments with powder samples. The total volume of the diluted suspension was 18, 9 or 4.5 mL, where 2, 1 or 0.5 mL methanol respectively (10 vol%) and an optimized amount of dihydrogen hexachloroplatinic were added. The headspace was subjected to several cycles of evacuation and argon backfill prior to the experiment. The headspace of the reactor was periodically sampled and hydrogen was quantified by gas chromatography (Thermo Scientific TRACE GC Ultra) equipped with a TCD detector using argon as the carrier gas.

Electrochemical characterization: The pellets (diameter of 5 or 6 mm) for impedance measurements were pressed in a uniaxial press with 1.5-2 bar of the respective powder.

The impedance spectra were recorded in a frequency range of 1×10^6 - 1×10^{-1} Hz with a Metrohm (Autolab PGSTAT302N) single potentiostat. As measurement cell, a Swagelok cell with steel electrodes was used. Galvanostatic DC polarization experiments were performed with a Keithley 2604B Source Meter by applying 2 nA current to the pressed pellets in a Swagelok cell.

9.2.3. Quantum-chemical calculations

The optimization of atom positions and lattices of all periodic structures was performed on RI-PBE-D3/def2-TZVP^[16-19] level of theory using an acceleration scheme based on the resolution of the identity (RI) technique and the continuous fast multipole method (CFMM^[20-22]) implemented^[23, 24] in Turbomole version V7.3.^[25, 26]

Structures of the molecular compounds were optimized on PBE0-D3/def2-TZVP^[17, 18, 27, 28] and RI-PBE-D3/def2-TZVP^[16-19] level of theory. To ensure all minima to be true minima on the potential energy hypersurface subsequent frequency calculations were performed on the same level of theory.

The same level of theory was used for spin densities, starting from the optimized ground state geometry with a subsequent single-point calculation. An additional electron was added to yield a radical-anionic state as a model for the reduced state and an additional hole to yield a radical cationic state as a model for the oxidized state. Differences of total energies were used to calculate Electron Affinities and Ionization Potentials accordingly.

NMR chemical shifts were calculated on B97-2/pcS-2^[29, 30] level of theory using the FermiONS++^[31, 32] program package. NMR chemical shifts were calculated as differences of calculated NMR chemical shielding with respect to Nitromethane and Tetramethylsilane computed on the same level of theory.

Optical band gaps were calculated as lowest singlet excitation energies on TD-PBE0/def2-TZVP//RI-PBE-D3/def2-TZVP level of theory.

Single Point energies on XTB^[33-35] level of theory were performed with the XTB program package in Version 6.2 RC2 (SAW190805).

9.2.4. Particle size and morphology analysis

Scanning electron microscopy (SEM)

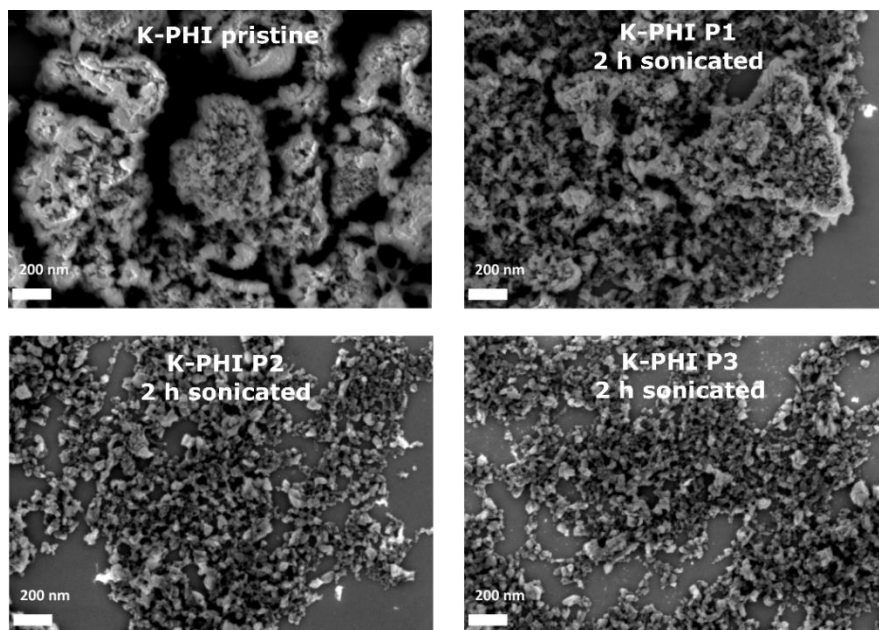


Figure S2.1: SEM images of K-PHI pristine, P1, P2 and P3 (from top left to bottom right).

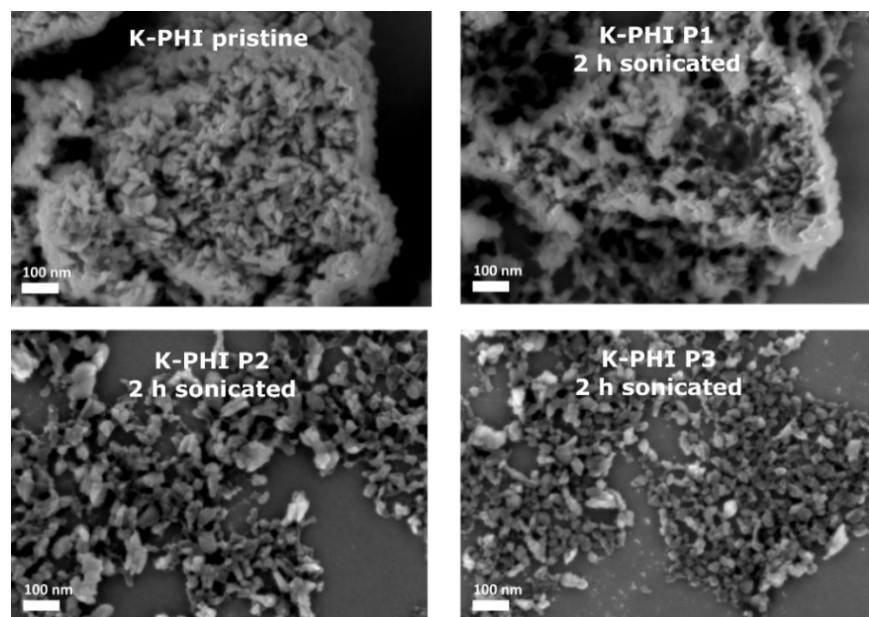


Figure S2.2: SEM images of K-PHI pristine, P1, P2 and P3 with higher resolution (from top left to bottom right).

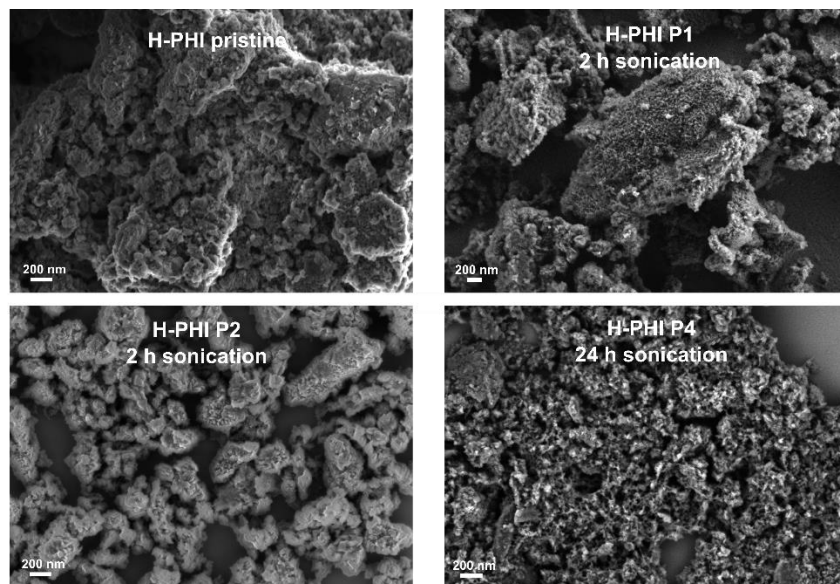


Figure S2.3: SEM images of H-PHI pristine, P1, P2 and P4 (from top left to bottom right).

Transmission electron microscopy (TEM)

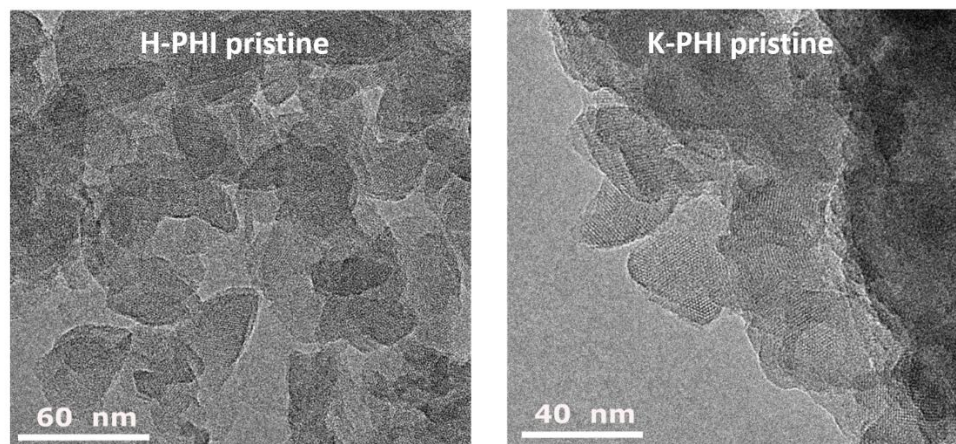


Figure S2.4: TEM images of pristine H-PHI (left) and K-PHI (right).

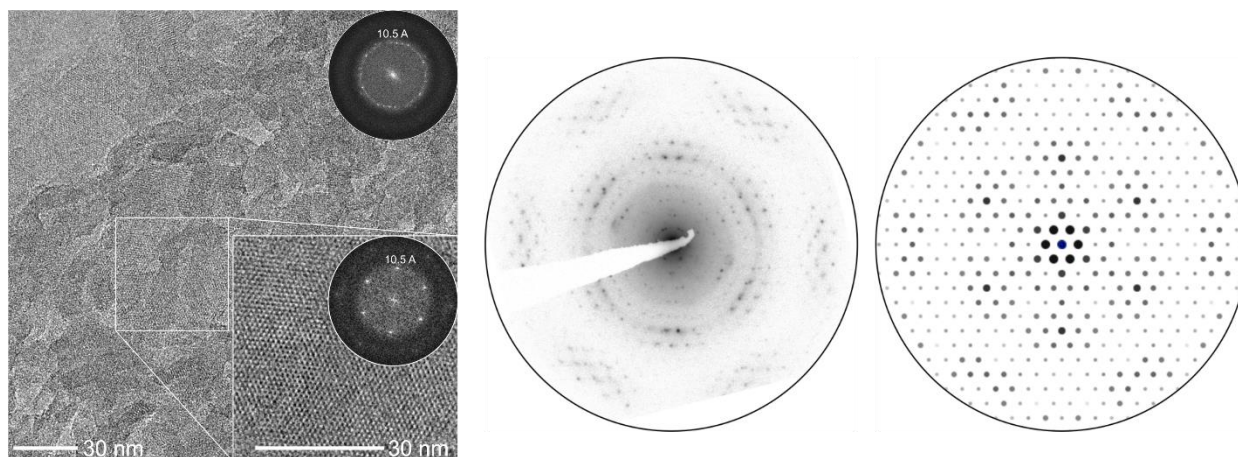


Figure S2.5: TEM of H-PHI P4 after 24 h sonication (left) and electron diffraction image measured (middle) and simulated (right) based on the structure of H-PHI described in a previous publication. Inset on the left shows the Fast Fourier Transformed (FFT) image.^[1]

Atomic force microscopy (AFM)

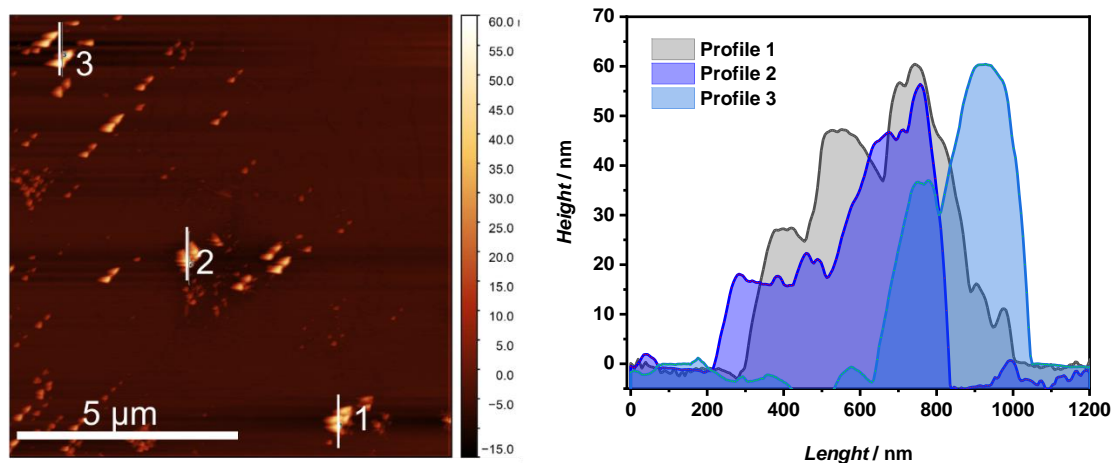


Figure S2.6: AFM images of H-PHI P4 and height profile of bigger particles after 24 h sonication. Measurements were performed with a double tip, which might lead to slight bigger measured particle sizes.

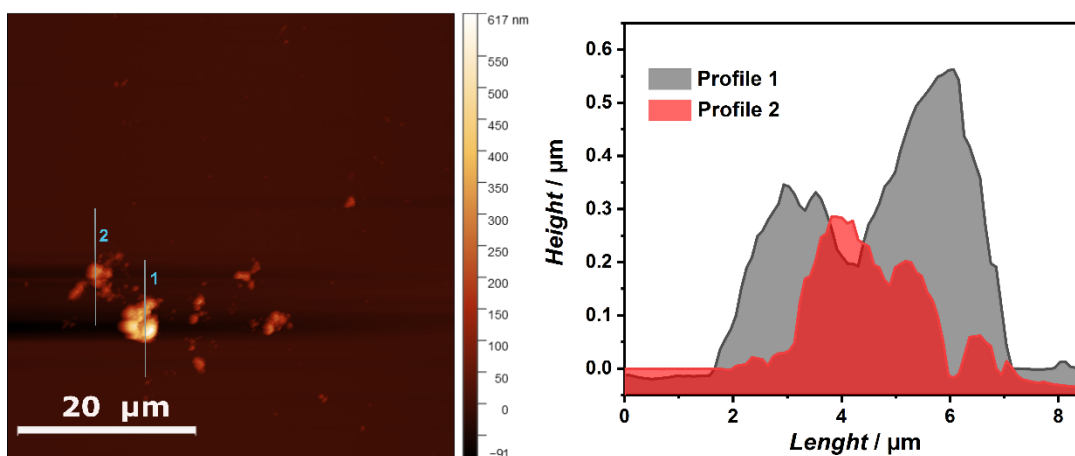


Figure S2.7: AFM image of pristine H-PHI and height profile of the particles.

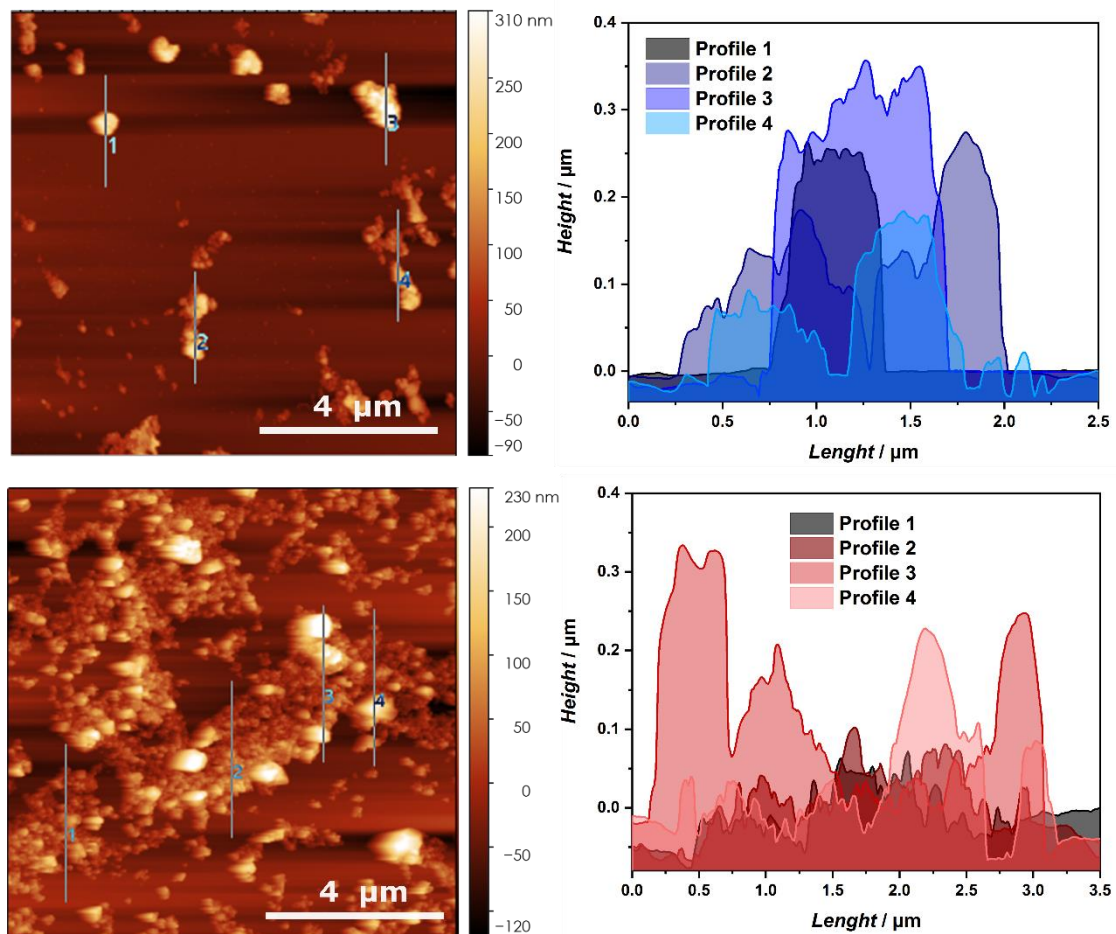


Figure S2.8: AFM images (left) of K-PHI P2 (top) and P3 (bottom) and their height profiles (right). Smaller particles cannot be resolved from background, so that only bigger particles are measured here as an upper limit for particle sizes in P3.

Zeta-potential

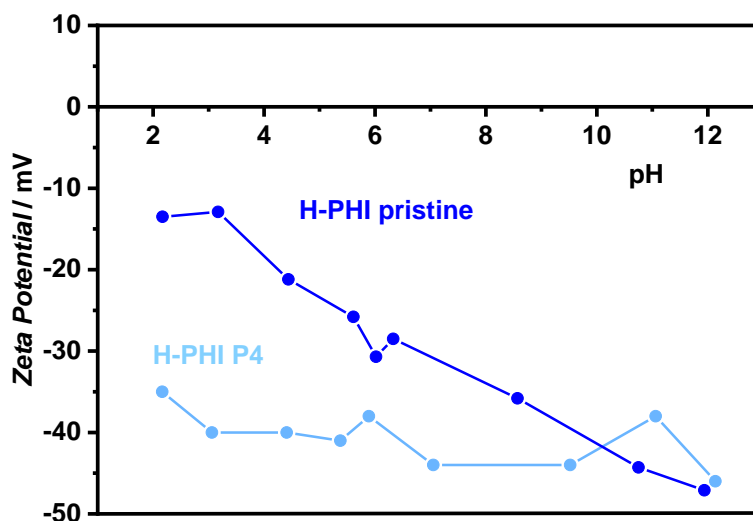


Figure S2.9: Zeta-potential at different pH values for H-PHI pristine and P4.

Table S2.2: Zeta-potential of two different batches of H-PHI pristine and P4 as well as K-PHI pristine, P1, P2 and P3 at pH=6,3.

Sample	Zeta-potential [mV]
H-PHI pristine 1	-28.3 (± 2.0)
H-PHI P4 1	-37.5 (± 3.0)
H-PHI pristine 2	-17.3 (± 2.1)
H-PHI P4 2	-22.9 (± 2.0)
K-PHI pristine	-33.8 (± 1.0)
K-PHI P1	-32.9 (± 1.2)
K-PHI P2	-35.1 (± 1.0)
K-PHI P3	-35.1 (± 1.0)

The zeta-potential measurements clearly show, that with decreasing particle size the suspension stability is increasing for H-PHI. In Table S2.2, the zeta-potentials of two different batches of H-PHI pristine with their respective P4 particles are compared. For H-PHI P4 1 the average particle size was decreased down to 75 nm, whereas in H-PHI P4 2 the average particle size was around 120 nm, which might be a reason for the different values. However, it has to be stated, that there is a batch to batch variance of the pristine H-PHI particles already, which has to be taken into account. For K-PHI also an increase in suspension stability with decreasing particle sizes can be observed.

Diffuse light scattering (DLS)

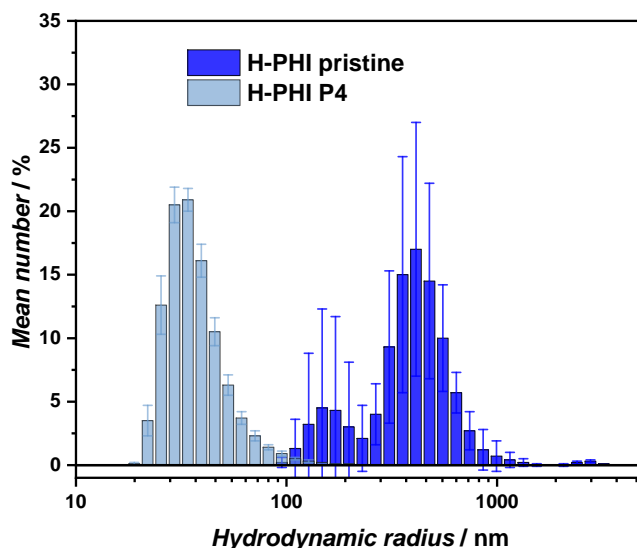


Figure S2.10: DLS measurement of H-PHI pristine and P4 depicting the hydrodynamic radius (particle size is twice the radius).

Table S2.3: Average particle sizes estimated by DLS measurement and polydispersity index (PDI) of some H-PHI samples from different batches. Although all H-PHI P4 batches were synthesized analogous slightly different average particle sizes were obtained, which allows a detailed particle size dependent study in a wide particle size range.

Sample	Average particle size [nm]	PDI
H-PHI pristine 1	810	0.55
H-PHI pristine 2	1300	0.81
H-PHI P4 1	70	0.36
H-PHI P4 2	79	0.27
H-PHI P4 3	147	0.40
H-PHI P4 4	160	0.48
H-PHI P4 5	165	0.42
H-PHI P4 6	178	0.41

Table S2.4: Average particle size measured by DLS, SEM, AFM, TEM analysis and estimated from PXRD via the Scherrer equation (in-plane \times vertical expansion).

Sample	Particle size according to DLS [nm]	Particle size according to SEM [nm]	Particle size according to AFM [nm]	Crystallite size according to PXRD [nm]	Crystallite size according to TEM [nm]
K-PHI pristine	200-3000	30-1500	-	18 (\pm 1) \times 17 (\pm 1)	25-40
K/H-PHI P1	300-1500	20-900	-	17 (\pm 1) \times 17 (\pm 1) 16 (\pm 3) \times 27 (\pm 1)	-
K/H-PHI P1 re-aggregated	250-1500	20-750	-	17 (\pm 1) \times 17 (\pm 1)	-
K/H-PHI P2	100-400	18-200	60-500	16 (\pm 1) \times 15 (\pm 3)	-
K/H-PHI P3	40-100	10-200	40-300	14 (\pm 2) \times 13 (\pm 3)	-
H-PHI pristine	600-3000	60-2500	200-3000	14 (\pm 1) \times 26 (\pm 1)	20-45
H-PHI P4	20-200	20-350	25-250	13 (\pm 1) \times 22 (\pm 1)	10-45

Although all batches were synthesized in an analogous way, for each extracted fraction (P1, P2, P3 or P4) slightly different average particle sizes were obtained, which are caused by batch to batch variations. Therefore, for every fraction a particle size range is given, which was obtained from analyzing different batches (by DLS and SEM) of each fraction. Nevertheless, this variation in average particles sizes for the different fractions, allows a detailed particle size dependent study in a wide particle size range. In the following for each batch the average particle size is given, which was obtained, from several measurements (mostly DLS) of the same sample.

BET analysis

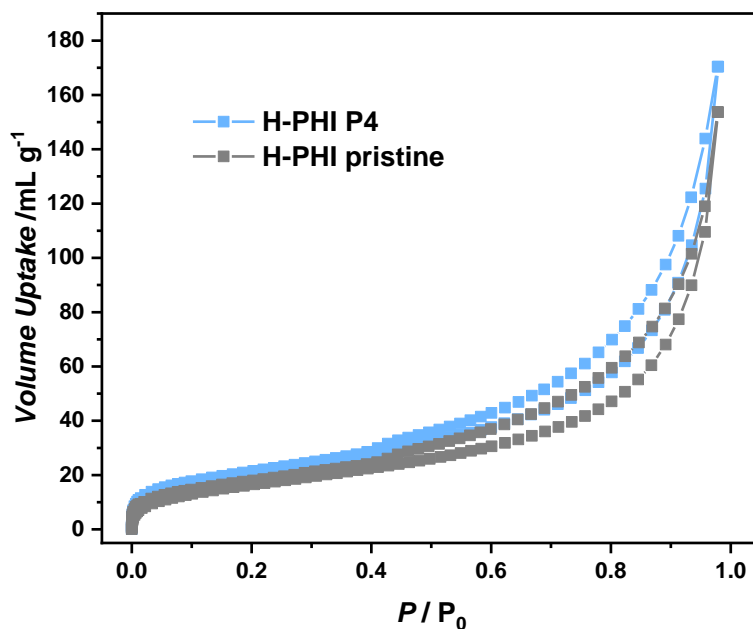


Figure S2.11: Isotherm of H-PHI pristine and P4 H-PHI. The fitting is use to extract BET surface area.

Table S2.5: BET surface area by DFT analysis of H-PHI pristine and P4.

Sample	BET by DFT analysis [cm ³ g ⁻¹]
H-PHI pristine	60
H-PHI P4	70

9.2.5. Structural analysis

Powder XRD

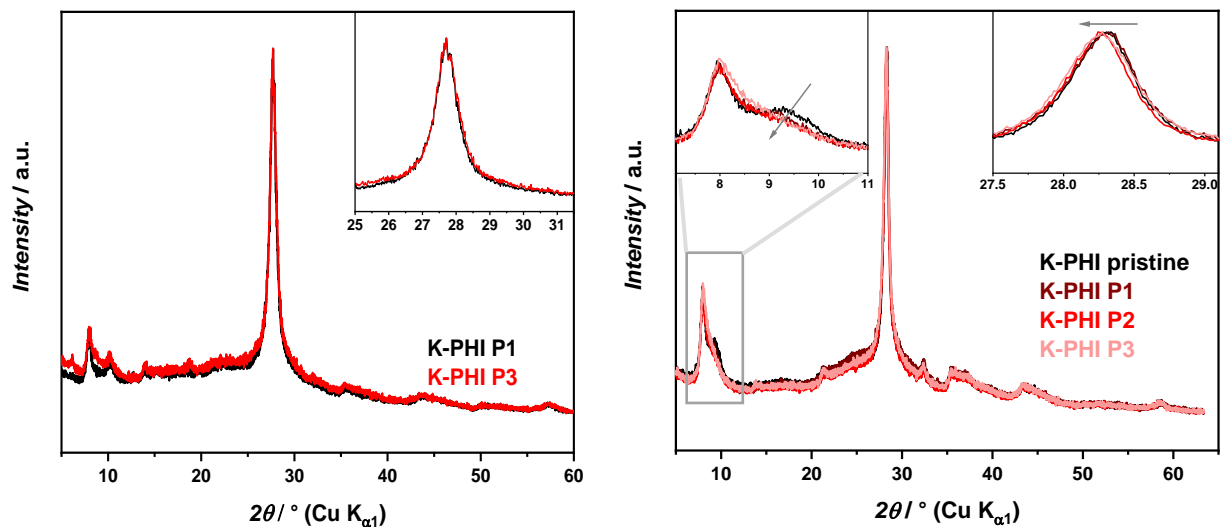


Figure S2.12: PXRD of K-PHI P1 and P3 particles, showing slightly more diffuse background in P3 and broader peaks, pointing to more disorder (left). PXRD of K-PHI pristine, P1, P2 and P3 showing a stepwise increasing peak width and a shift of the stacking peak to lower 2θ values (right, see grey arrow in the insets).

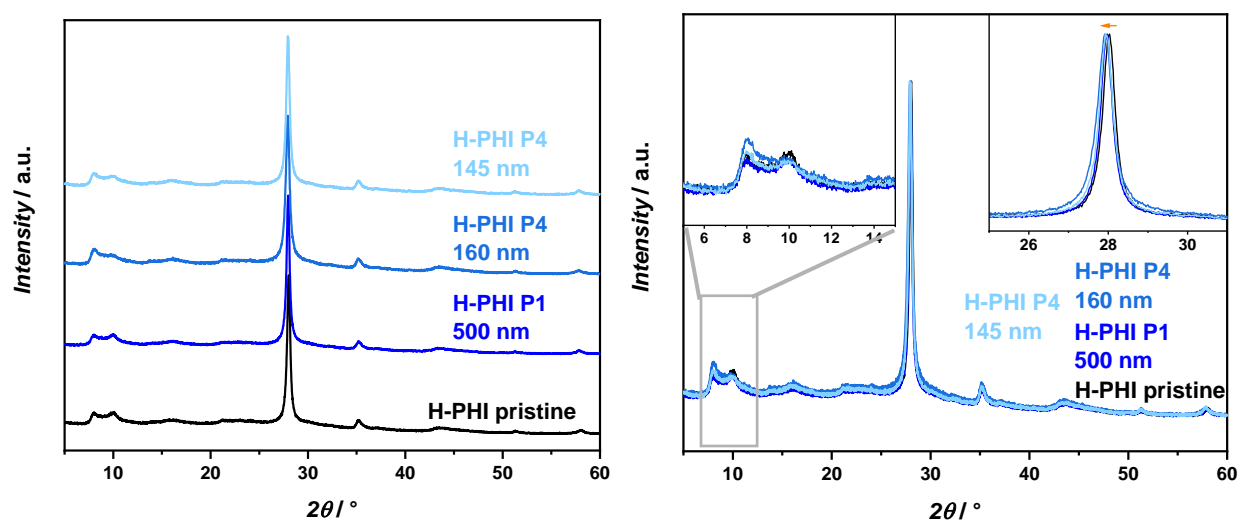


Figure S2.13: PXRD of H-PHI pristine, P1 and P4 with particle size of 160 nm and 145 nm.

FT-IR measurements

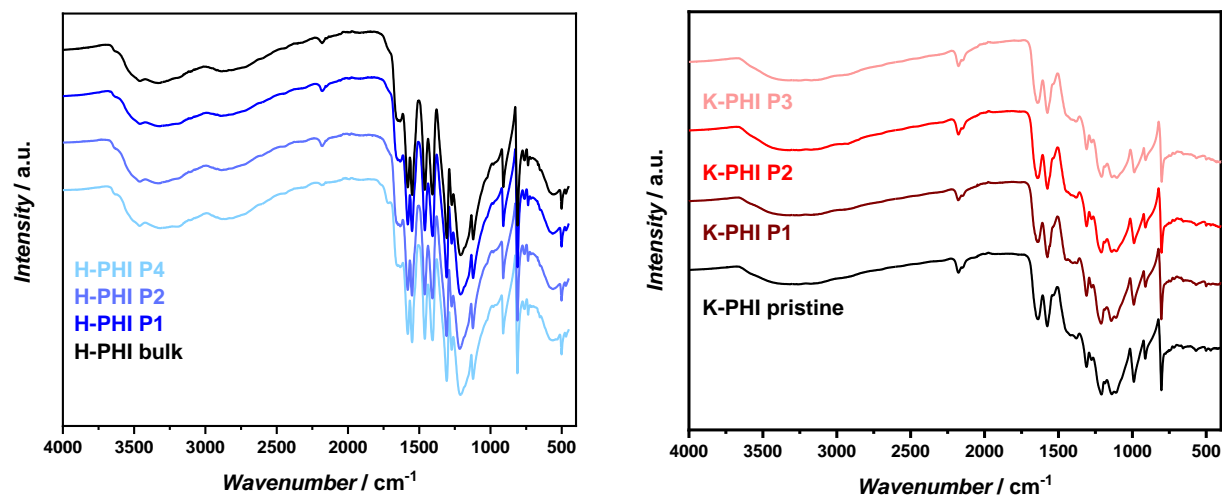
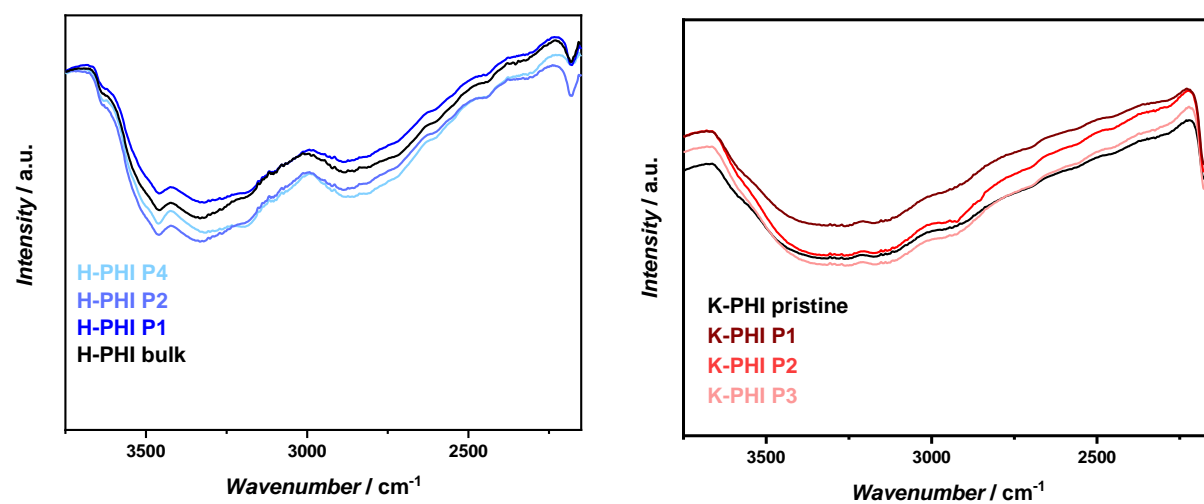


Figure S2.14: FT-IR spectra of H-PHI pristine, P1, P2 and P4 (left) and K-PHI pristine and P1-P3 (right).

Figure S2.15: FT-IR spectra of H-PHI pristine, P1, P2 and P4 (left) and K-PHI pristine, P1-P3 (right) normalized to signal at 810 cm^{-1} , to extract the relative amount of overlaying NH and OH vibrations.Table S2.6: Comparison of the area of the NH/OH- ($\sim 3670\text{-}2220 \text{ cm}^{-1}$) and $\text{C}\equiv\text{N}$ - ($\sim 2220\text{-}2110 \text{ cm}^{-1}$) bands in FT-IR for K-PHI.

Sample	Area between $3669\text{-}2223 \text{ cm}^{-1}$	Area between $2217\text{-}2107 \text{ cm}^{-1}$
K-PHI pristine	1.00	1.00
K-PHI P1	1.06	0.77
K-PHI P2	1.23	1.06
K-PHI P3	1.23	1.11

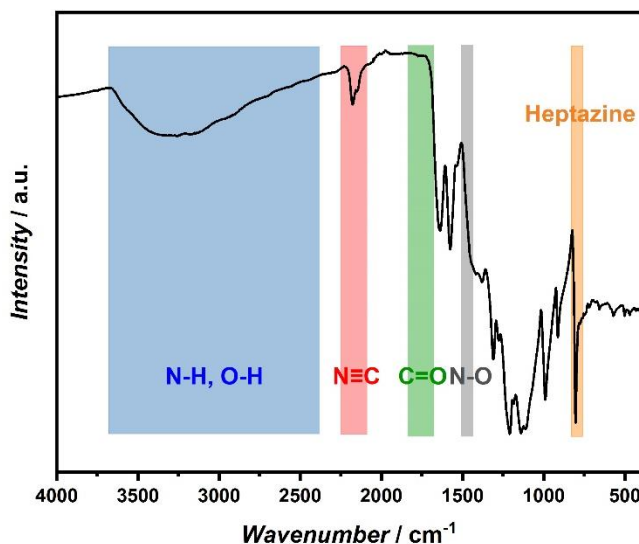


Figure S2.16: FT-IR of K-PHI with highlighted areas of vibrations analyzed in the following. The heptazine vibration is used to normalize the spectra. Based on literature the NH and OH vibration might be distinguishable, where OH vibrations in carbon nitriles are rather located at 3450 cm^{-1} , whereas NH vibrations can be found at 3100 cm^{-1} .^[36] However, since the distinction is difficult here, NH and OH vibrations are discussed together.

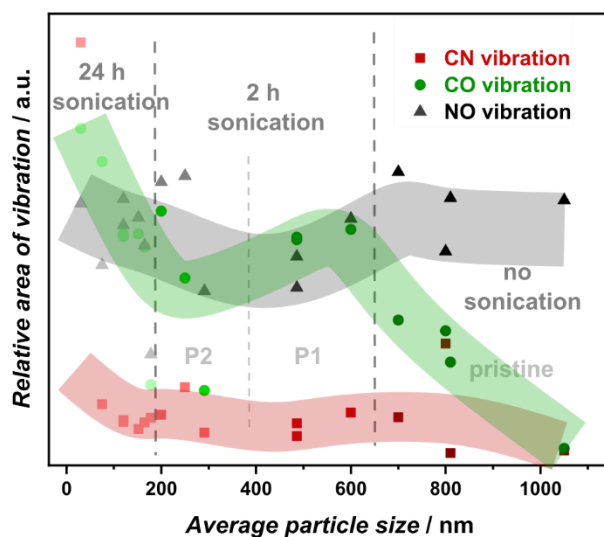


Figure S2.17: Correlation of particle size and sonication duration of H-PHI with the relative amount of C≡N, CO and NO vibrations observed in FT-IR.

Table S2.7: Average amount of functional groups normalized to the pristine material depending on the particle size for H-PHI (pristine, P1, P2 and P4) estimated by FT-IR.

Particles	NH/OH vibration	N≡C vibration	CO vibration	NO vibration
H-PHI pristine	1.00	1.00	1.00	1.00
H-PHI P1	1.20 (± 0.01)	2.07 (± 0.30)	1.75 (± 0.10)	1.02 (± 0.02)
H-PHI P2	1.27 (± 0.03)	2.70 (± 0.37)	2.06 (± 0.18)	0.98 (± 0.07)
H-PHI P4	1.47 (± 0.11)	1.42 (± 0.19)	2.27 (± 0.16)	0.91 (± 0.07)

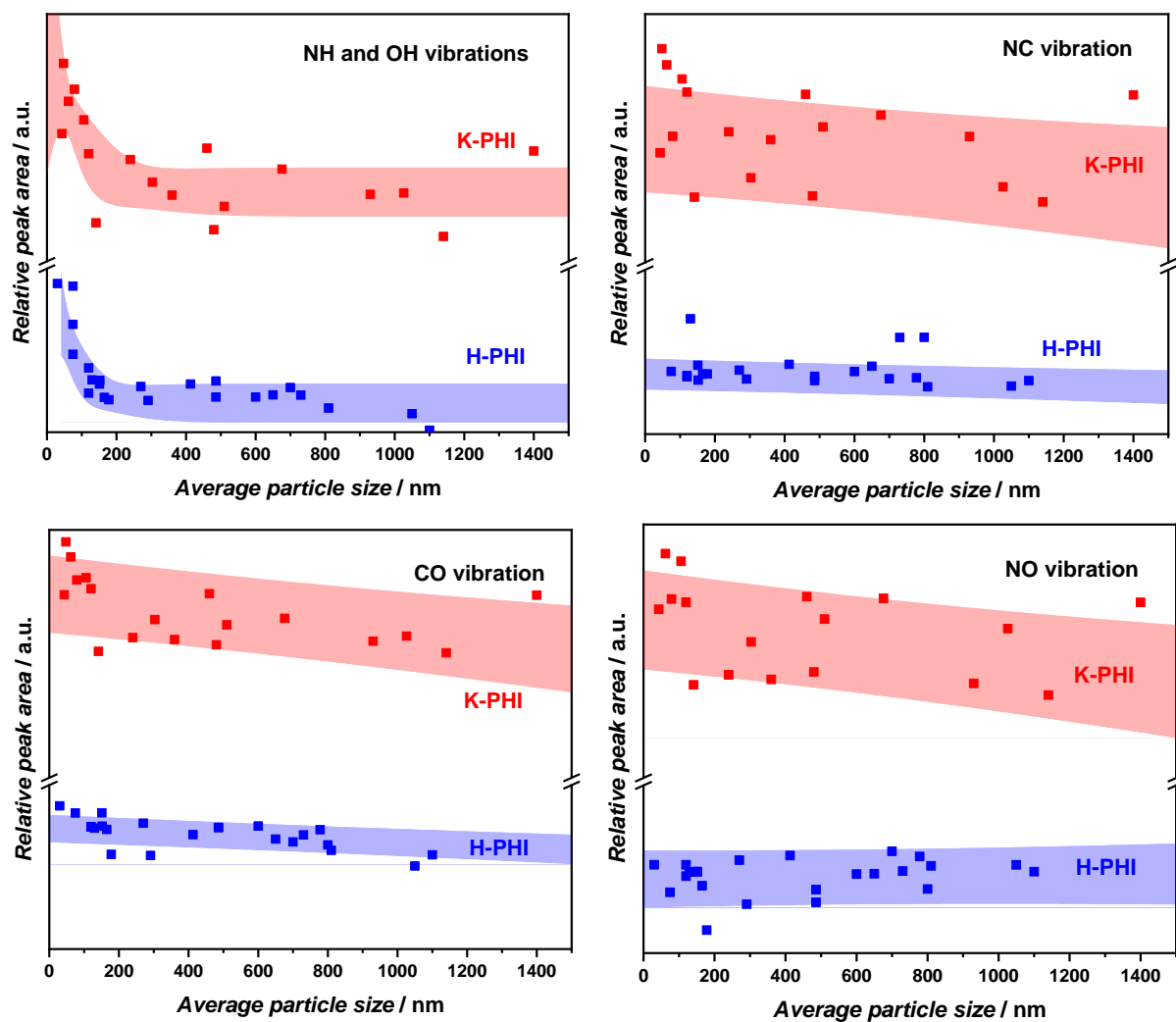


Figure S2.18: Relative peak area of NH/OH, NC, CO and NO vibrations of K-PHI and H-PHI as a function of particle size. FT-IR spectra were normalized to heptazine out-of-plane vibration at 805-811 cm^{-1} . Red and blue shaded areas illustrate the trend depending on the particle size to guide the eye.

Elemental analysis

Table S2.8: Elemental analysis in weight percentage of H-PHI P1, P2 and P4 compared to its pristine counterpart. Different batches were measured, to also include the batch to batch variance.

	C [wt%]	N [wt%]	Residual weight [wt%]	C:N molar ratio
H-PHI pristine (batch 1)	28.9 (± 0.3)	48.2 (± 0.2)	19.6	0.698 (± 0.007)
H-PHI P4 (batch 1)	28.3 (± 0.1)	47.1 (± 0.5)	21.8	0.701 (± 0.005)
H-PHI pristine (batch 2)	28.1 (± 0.2)	46.7 (± 0.3)	25.2	0.601 (± 0.008)
H-PHI P4 (batch 2)	27.3 (± 0.1)	46.0 (± 0.1)	26.7	0.594 (± 0.003)
H-PHI pristine (batch 3)	28.8 (± 0.1)	47.5 (± 0.1)	23.7	0.607 (± 0.003)
H-PHI P1 (batch 3)	28.7 (± 0.1)	47.3 (± 0.2)	24.0	0.606 (± 0.005)
H-PHI P2 (batch 3)	28.6 (± 0.2)	46.4 (± 0.2)	25.0	0.616 (± 0.007)

XPS analysis

Table S2.9: Comparison of relative areas of XPS signals of H-PHI pristine and smaller particles after 2 h and 24 h sonication. The number in () describes the error of the values given in %. The signal intensities were determined by relative sensitivity factors and detector function. Numbers in green denote the % change relative to the pristine material.

XPS Signal	Corresponding binding conditions	H-PHI P4 (24 h sonication) ~79 nm	H-PHI P2 (2 h sonication) 350-400 nm	H-PHI pristine 1000-1500 nm
C 1s 1 (284.8 eV)	C-C	488.9 (8.57) -62%	559.4 (4.5) -52%	1174.6 (8.8)
C 1s 2 (286.4 eV)	C-O(H) / C-N(H) _x	252.4 (4.43) -51%	402.1 (3.2) -22%	515.7 (3.8)
C 1s 3 (288.4 eV)	N-C=N	3375.2 (59.2) 4.3%	3117.6 (24.9) -3.7%	3236.9 (24.1)
C 1s 4 (288.9 eV)	C=O	1117.7 (19.6) 7.1%	1131.2 (9.1) 8.4%	1043.6 (7.8)
Ratio C-O(H)/N-C=N		0.075	0.129	0.159
Ratio C=O/N-C=N		0.331	0.363	0.322
N 1s 1 (398.9 eV)	C-N=C	3614.6 (50.7) 2.7%	3531.0 (50.2) 0.3%	3519.5 (26.2)
N 1s 2 (400.6 eV)	NH _x / N-C ₃	2544.0 (35.7) 14%	2372.7 (33.8) 6.7%	2224.2 (16.6)
N 1s 3 (404.2 eV)	NO	198.1 (2.8) 21%	176.6 (2.5) 8.1%	163.3 (1.2)
N 1s 4 (406.0 eV)	π-π* excitation	275.2 (3.9) 49%	188.4 (2.7) 2.2%	184.4 (1.4)
Ratio NH _x /C-N=C		0.704	0.672	0.632
Ratio NO/ C-N=C		0.055	0.050	0.046
O 1s 1 (531.7 eV)	OH	306.4 (4.3) -36%	302.4 (4.3) -37%	479.2 (3.6)
O 1s 2 (533.6 eV)	NO / O-C=O	192.5 (2.7) 44%	127.1 (1.81) -4.6%	133.2 (1.0)
O 1s 3 (536.1 eV)	N(H)-C=O / O ₂	-	47.0 (0.67) -45%	85.0 (0.63)
Pt 4f 1 (71.2 eV)	Pt ⁰	32.0 (0.56) -56%	57.8 (0.82) -20%	72.4 (0.54)
Pt 4f 2 (73.0 eV)	Pt ²⁺	43.7 (0.77) -65%	116.8 (0.93) -5.2%	123.2 (0.92)
Ratio Pt ²⁺ /Pt ⁰		1.37	1.46	1.70
Ratio Pt/N		0.012	0.029	0.033

In most of the XPS spectra also a residual indium signals from the support material are visible. Contaminations of the indium surface by carbon or/and oxygen bearing groups could possibly contribute to the signals attributed to PHI, so that their contribution was estimated by XPS measurements on bare indium. From this measurements, we find that the substrate induced signals of carbon and oxygen bearing groups are in the range of 45 at% (carbon) and 24 at% (oxygen), with 30 at% indium signal. A significant substrate contribution to the PHI C 1s signals can be excluded, since the In signal intensity in the PHI samples reaches maximally 1.4 at% of

the total material amount. However, for O 1s signals, where the intensity in the PHI on In measurement is low, a partial contribution of InO_x and $\text{In}(\text{OH})_x$ cannot be ruled out. Based on the In signal in the PHI sample and assuming a constant proportion of the substrate induced oxygen peaks, their relative contribution was estimated to be at maximum 25% of the overall O 1s signal.

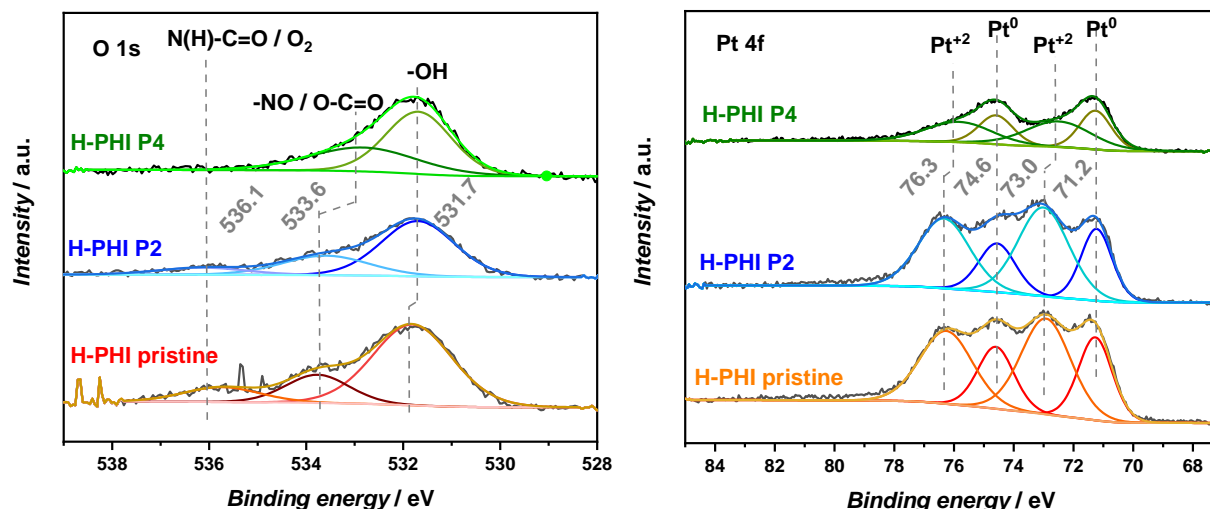


Figure S2.57: XPS analysis of pristine H-PHI (particle size 1500-1000 nm) and H-PHI particles after 2 h (P2, particle size 400-350 nm) and 24 h sonication (P4, particle size around 79 nm) O 1s und Pt 4f spectrum.

The N 1s XPS spectra show two major signals at 398.9 and 400.6 eV, which can be assigned to C-N=C (grey area) and overlapping NH_x (blue are) and N-C₃, respectively (Figure 5.3f).^[12, 13, 37-39] The smaller the particle size, the bigger the area of the signals of NH_x and N-C₃ (increases 14 %), whereas the C-N=C amount is not changed. Since no evidence of changes in the N-C₃ concentration could be found, this enhancement is probably mainly caused by increasing amounts of NH_x .

The formation of nitrogen vacancies due to sonication can be excluded. By elemental analysis an increase in C/N ratio should be observed, when nitrogen vacancies are formed.^[40, 41] This trend might be observed for samples with longer sonication treatment (pristine: C/N = 0.601 (± 0.008); P4: C/N = 0.594 (± 0.003)), however those changes are within the measurement error (Table S2.8). The XPS analysis can also be used for vacancy formation analysis, where the ratio of C-N=C / N-C₃ would be decreasing when vacancies are formed.^[40, 41] Since the N-C₃ and the NH_x signal cannot be deconvoluted easily, the exact estimation of vacancies is not possible. By just taking the ratio of C-N=C/N-C₃ and NH_x signal, it appears that a low amount of nitrogen vacancy formation is possible, for smaller particles below 200 nm. The C-N=C / N-C₃ and NH_x ratio of 1.58 in the pristine material is reduced to 1.43 in the 24 h sonicated sample, which might hint to a small vacancy formation during sonication, resulting from increasing amounts of terminal groups. However, since no clear trend in elemental analysis or FT-IR is visible and the deconvolution of the N-C₃ and NH_x signal is not possible here, it can be assumed that the nitrogen vacancy formation is not significant.

Besides, two additional, small signals in the N 1s XPS spectra at 404.1 and 405.9 eV can be caused by N-O groups^[42-45] and π -excitation or charging,^[37, 46, 47] respectively (Figure 5.3f). In comparison to the O 1s spectra, the signal at a binding energy of 533.6 eV can be attributed to N-O bonding, chemisorbed water^[48] or O-C=O^[49, 50]. A third small signal in O 1s at 536.1 eV can

be assigned to adsorbed oxygen or C=O bonding in urea [42, 43, 51, 52], which is in good agreement with C 1s and N 1s spectra, where also C=O or N-O groups were observed.

Pt analysis

In addition, different Pt loading can be observed by XPS for H-PHI pristine, P2 and P4. In literature, the ratio of Pt:N is used to describe the coverage of the carbon nitride surface with Pt after photocatalysis. For the pristine material, a value of 0.033 was measured (Table S2.8). However, when comparing this result to elemental analysis, assuming a loading of 2 wt% Pt and 46 wt% N atoms, which results in an atom ratio of 0.01 Pt/ 3.29 N, a ratio of 0.003 is obtained. This is in line with literature reported values, for a similar material, estimated by elemental analysis with a ratio of 0.0012. [13] From this it can be clearly seen that XPS is a surface sensitive method. [53] Due to the inhomogeneous surface coverage of H-PHI pristine material with Pt clusters (Figure S2.37-S2.40), the amount of detected Pt by XPS depends on the measured spot. Therefore, elemental analysis is preferred to determine the overall Pt deposition in different materials, rather than XPS.

Different ratios of Pt²⁺/Pt⁰ can be seen in XPS for pristine, P2 and P4 particles. It was described in literature that a higher amount of Pt²⁺ can be found when more functional groups are present (as a result of nitrogen vacancies), since those are stabilizing the Pt²⁺ oxidation state. [54] Furthermore, it was described that Pt⁰ and Pt²⁺ are important in the hydrogen evolution reaction, since both are responsible for different reactions. Pt⁰ acts as electron trap centers and catalyzes the hydrogen formation, whereas Pt²⁺ prevents the back-oxidation of the formed hydrogen. [55] However, it was also reported that the Pt²⁺/Pt⁰ ratio changes during the first 4-6 h of illumination. [56] Although. Each sample was illuminated for the same time, a different amount of Pt²⁺ and Pt⁰ in our case here can also just arise from different reactivity, as it was seen in photocatalytic hydrogen evolution. As a result, the comparison of the amount of different oxidation states of Pt is difficult, especially since defect concentration as well as efficiency of charge transfer influences the Pt²⁺/Pt⁰ ratio. It was described that the shape and size as well as the amount of Pt and Pt clusters affects the hydrogen evolution rate more significantly than their oxidation state. [56, 57]

NMR measurements and quantum-chemical calculations

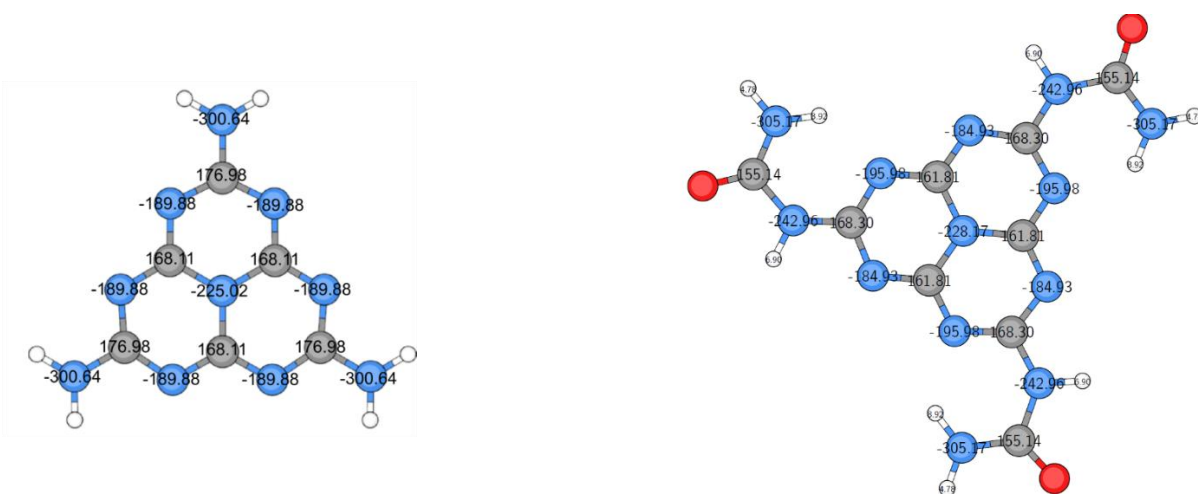


Figure S2.20: Calculated NMR chemical shifts of melem and urea functionalized melem, obtained on B97-2/pcsSeg-2//PBE0-D3/def2-TZVP level of theory (blue: N-atoms, grey: C-atoms, red: O-atoms, white: H-atoms).

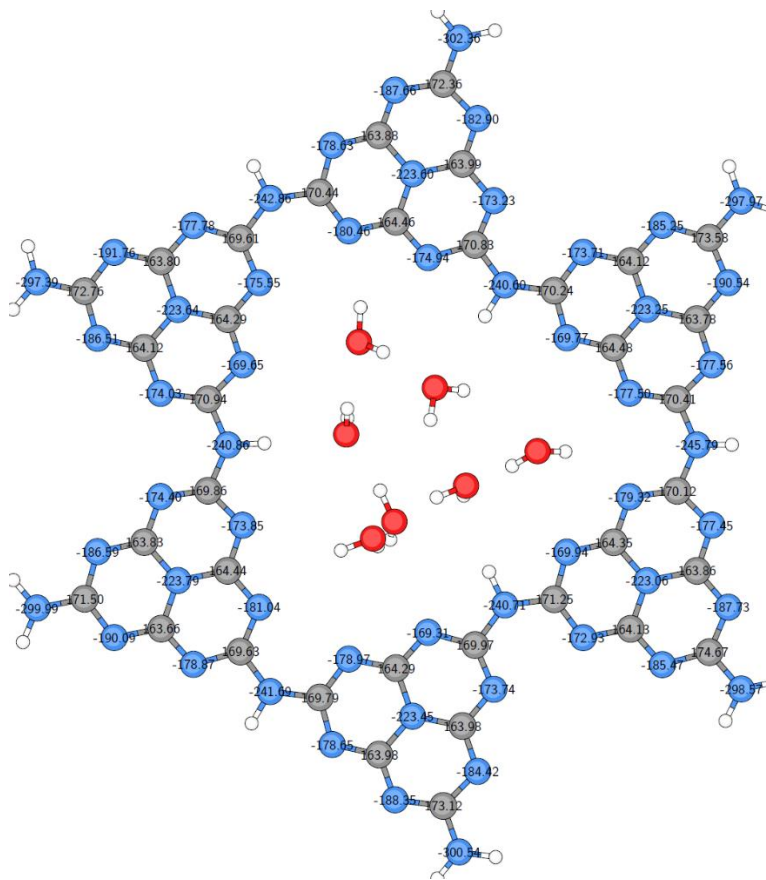


Figure S2.21: Calculated NMR chemical shifts of a single PHI pore filled with 7 water molecules, obtained on B97-2/pcsSeg-2//PBE0-D3/def2-TZVP level of theory.

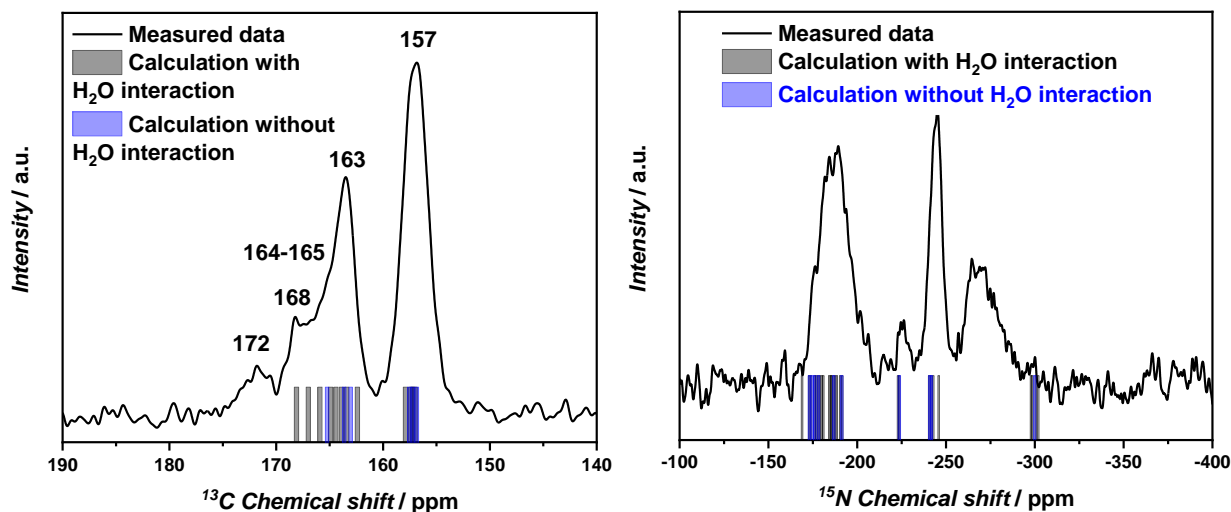


Figure S2.22: Comparison of measured direct ^{13}C (left) and $^{15}\text{N} \{^1\text{H}\}$ CP (right) NMR data with calculated NMR shifts, assuming a model without water in the pores (blue)^[1] or with 7 water molecules in one PHI pore (black).

NMR could not be used to verify the findings of NO and C=O groups, since the ^{13}C NMR signal of a COOH and urea group is expected at around 180 ppm and to be of relatively low intensity.^[58] Similar to the detection limit of low concentrations of C=O in PHI, the N-O signal (expected around -20 ppm)^[59] in ^{15}N NMR cannot be detected.

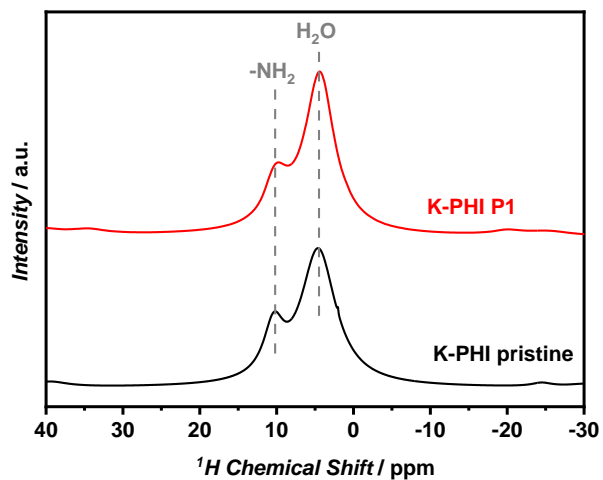


Figure S2.23: ^1H NMR of K-PHI pristine and P1.

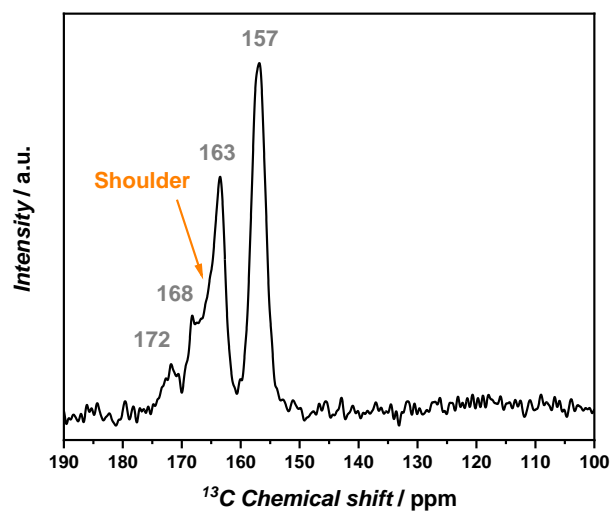


Figure S2.24: Direct ^{13}C NMR of K-PHI P1. The “shoulder” depicts an additional signal, which is not as pronounced in the pristine material. This shoulder might be caused by a relative increased amount of functional groups at the heptazine units.

9.2.6. Photocatalysis and optical characterization

UV-Vis spectroscopy

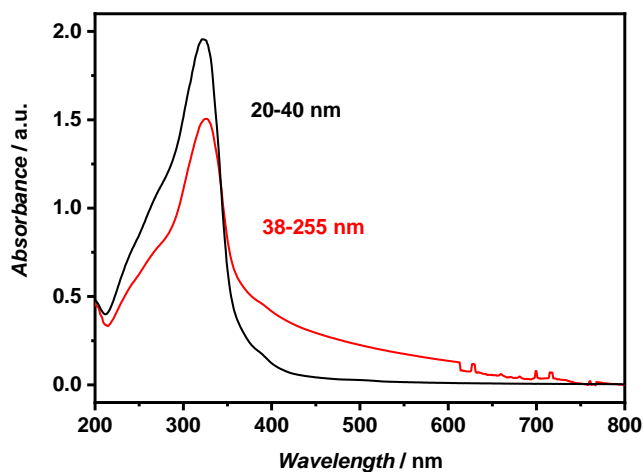


Figure S2.25: UV-Vis spectrum of H-PHI P4 (average particle size of 20-40 nm) and P4 (average particle size of 38-255 nm) in aqueous suspension.

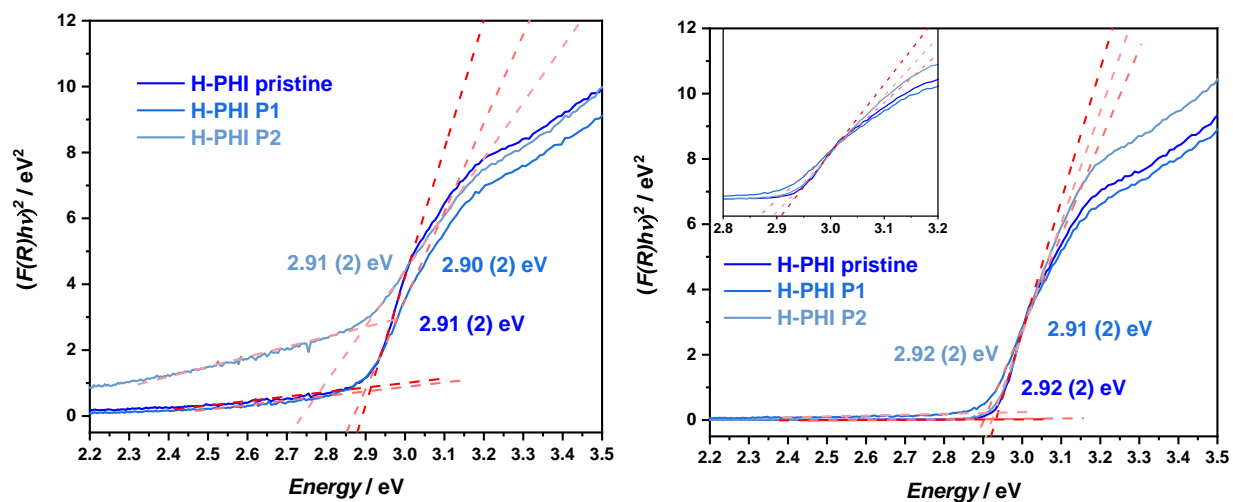


Figure S2.26: Tauc plot of H-PHI pristine, P1 and P2 in aqueous suspension (left) and in presence of 10 vol% methanol with photo-deposited Pt (right). The errors of the band gaps are given as an error of the fit function here.

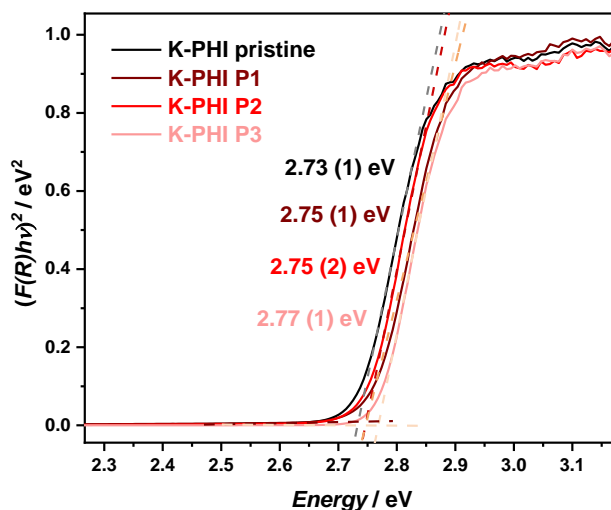


Figure S2.27: Tauc plot of K-PHI pristine, P1, P2 and P3 of the solid powder.

Table S2.10: Optical band gap of K-PHI pristine, P1, P2 and P3 and H-PHI pristine, P1, P2, P4 and P4 re-agglomerated (re-ag.) in aqueous suspensions (susp.), in presence of methanol or methanol and photo-deposited Pt.

Compound	Band gap in aqueous susp. [eV]	Band gap in aqueous susp. with methanol [eV]	Band gap in aqueous susp. with methanol, Pt [eV]
K-PHI pristine	2.79	2.79	2.85
K-PHI P1	2.82	2.82	2.89
K-PHI P2	2.90	2.90	2.90
K-PHI P3	2.88	2.88	2.90
H-PHI pristine	2.92	2.92	2.91
H-PHI P1	2.91	-	2.90
H-PHI P2	2.92	-	2.91
H-PHI P4	2.95	2.95	2.94
H-PHI P4 re-ag.	2.95	2.96	2.95

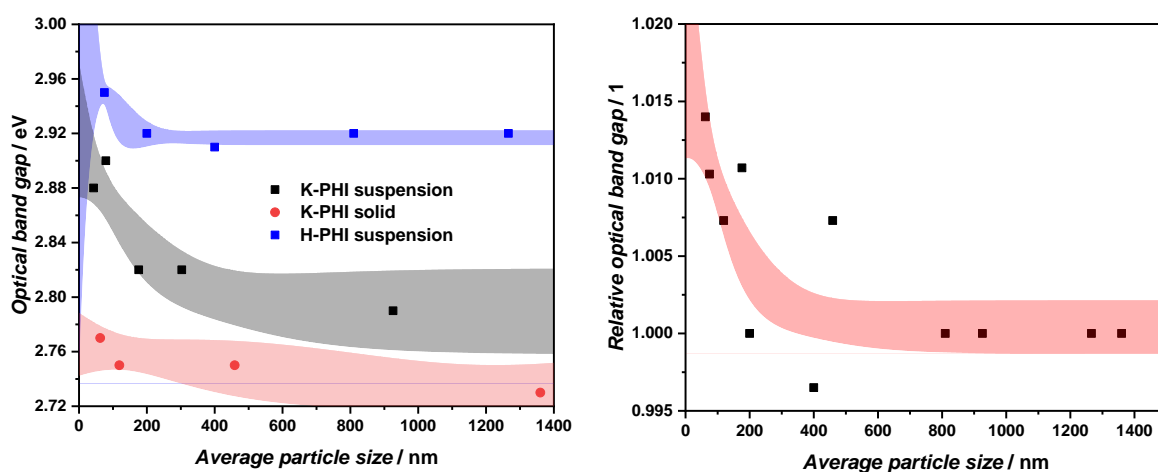


Figure S2.28: Optical band gap obtained from Tauc plots of K-PHI and H-PHI in suspension and as solid depending on particle size (left). Relative change of the optical band gap of K-PHI and H-PHI (obtained from solid and suspension measurements and normalized to the pristine material) depending on the particle size (right). Colored lines were included to guide the eye.

Photocatalysis

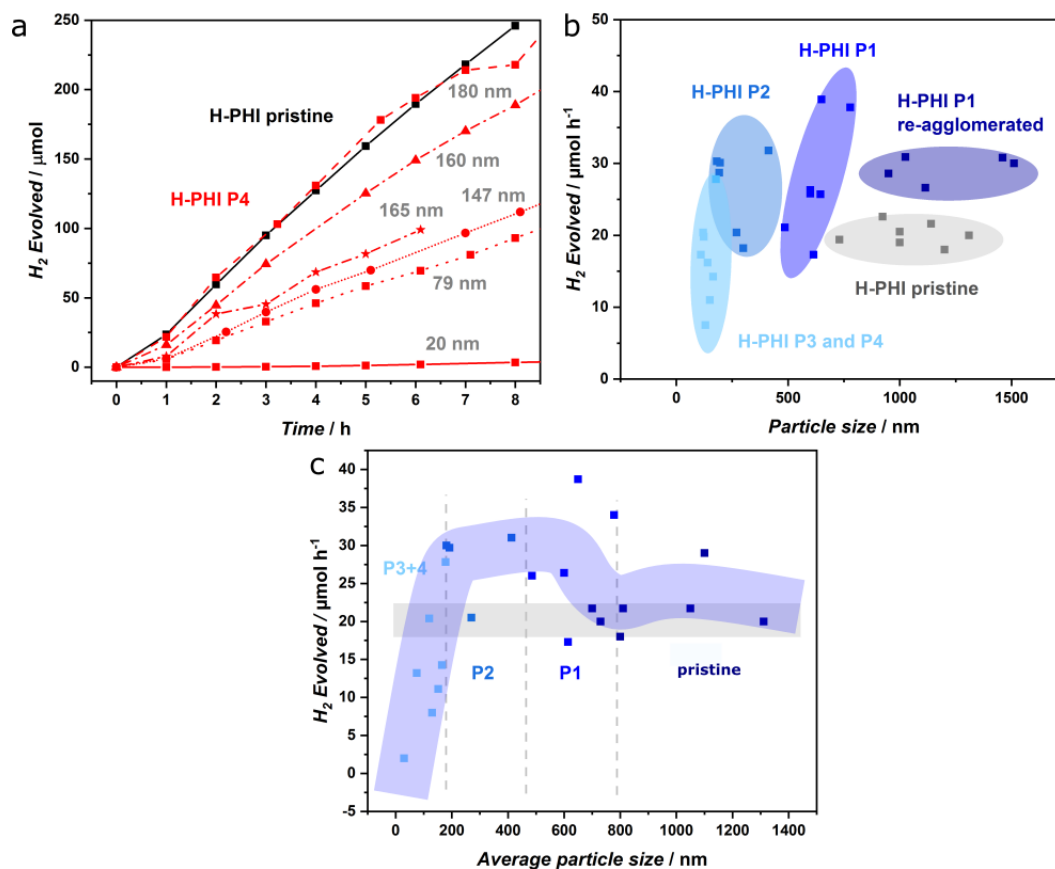


Figure S2.29: a) Photocatalytic hydrogen evolution of H-PHI pristine and P4, with different particle sizes. b) and c) Dependence of photocatalytic hydrogen evolution on particle size. Besides the average particle size the width of the distribution of the particle size is also important, which might be the reason for scattering of the data points. The blue line in c) is included to guide the eye. The grey line depicts the average activity of the pristine material.

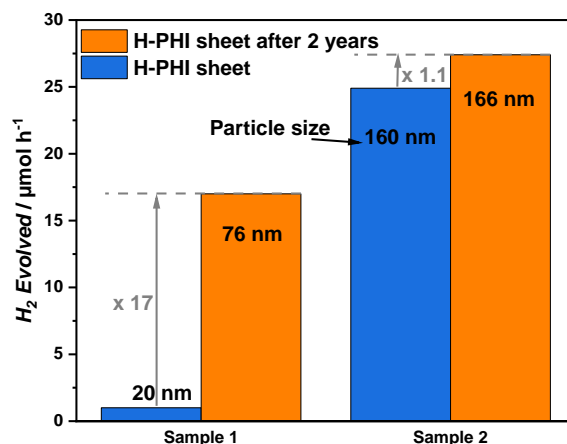


Figure S2.30: Photocatalytic hydrogen evolution of suspensions of H-PHI P4 freshly prepared (blue) and H-PHI P4 after 2 years of storage (orange). After 2 years the particles agglomerate partially, which then enhances the photocatalytic activity. This points to a certain particle size, which is ideal for efficient charge separation.

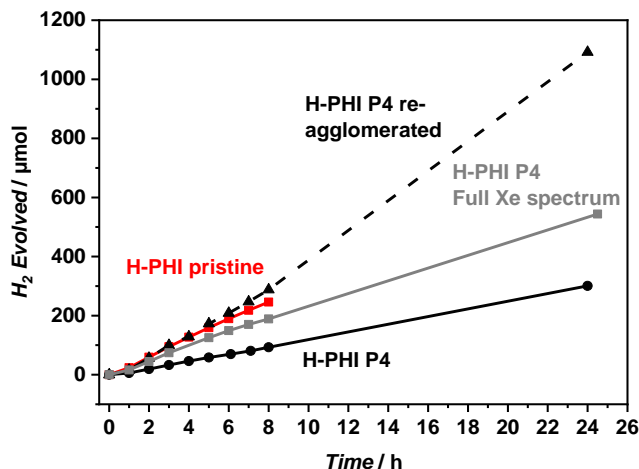


Figure S2.31: Photocatalytic hydrogen evolution of H-PHI pristine, P4 and P4 re-agglomerated with visible light illumination (> 420 nm) and H-PHI P4 full spectrum illumination of a Xe 300 W lamp (100 mW cm^{-2}).

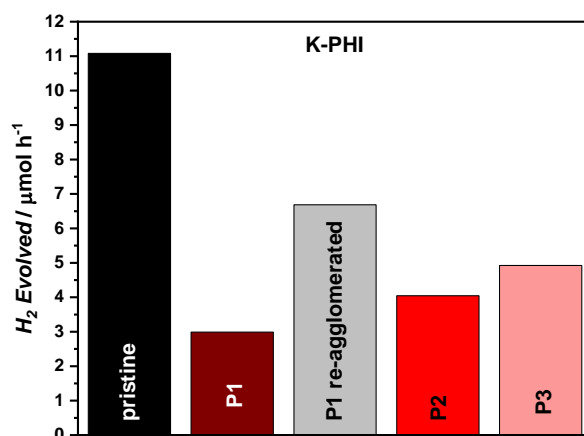


Figure S2.32: Photocatalytic hydrogen evolution of K-PHI depending on particle size (pristine, P1, P1 re-agglomerated, P2 and P3) with Pt (8 wt%) and MeOH (10 vol%) as donor, however K-PHI is transformed to H-PHI during photocatalysis experiments.

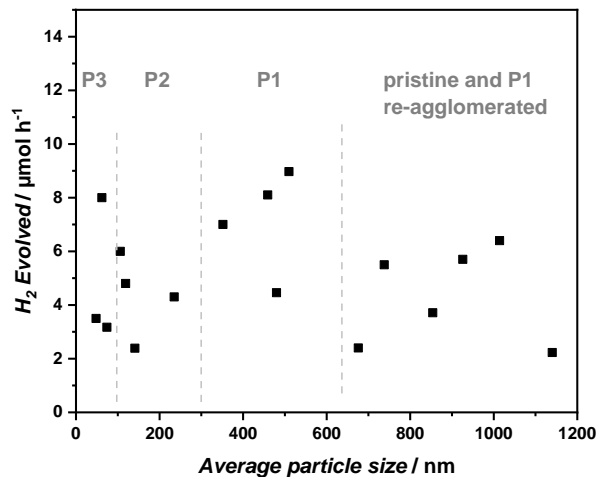


Figure S2.33: Dependence of photocatalytic hydrogen evolution of K-PHI on particle size. Smaller particles tend to protonate faster than bigger particles and form H-PHI (see below in PL part). For this reason, the particle size dependent analysis was only performed with H-PHI in the following and no clear trend was observed for K-PHI.

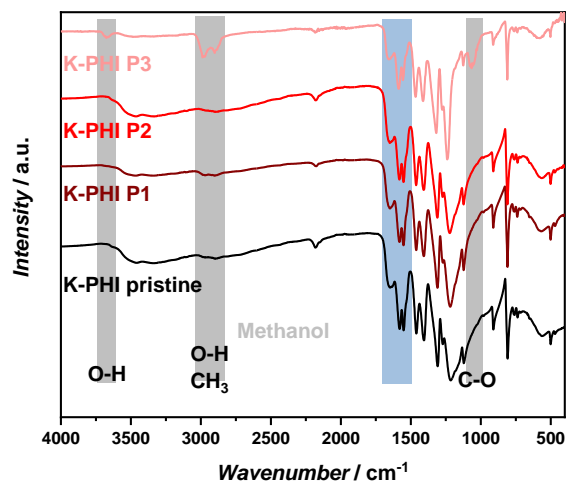


Figure S2.34: FT-IR of dried K-PHI pristine, P1-P3 after photocatalytic hydrogen evolution in presence of Pt and MeOH as donor. Grey areas depict vibrations of remaining methanol and blue the changes due to protonation of the K-PHI backbone.

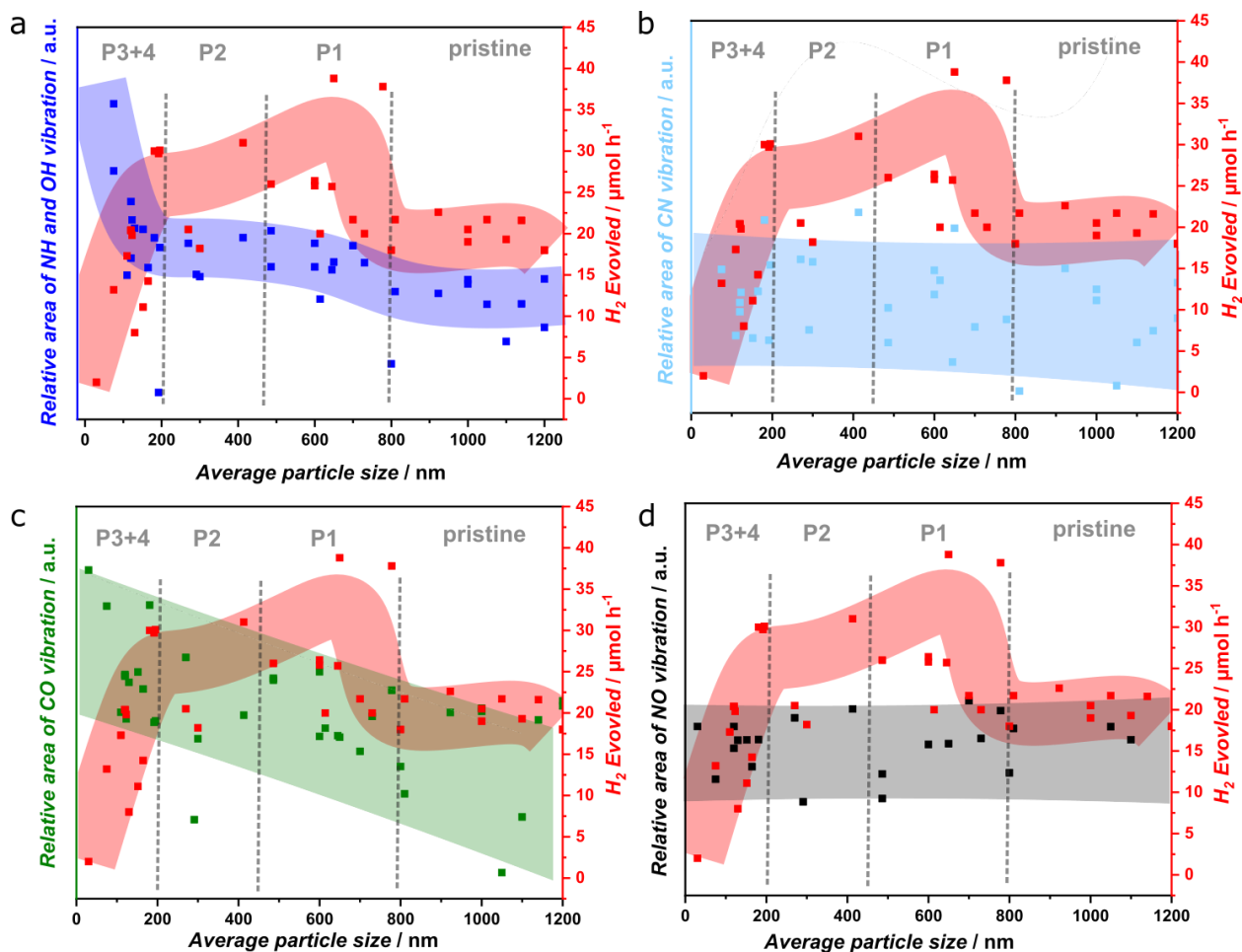


Figure S2.35: Comparison of photocatalytic hydrogen evolution and amount of defects (a) HN/OH, b) C≡N, c) CO, d) NO) with particle size of H-PHI. The defect amount was estimated by FT-IR by normalizing the defect vibrations to the heptazine vibration at 805- 811 cm^{-1} . No clear correlation could be observed for the amount of C≡N or NO vibration modes with respect to the particle size.

9.2.7. Analysis of PHI after photocatalysis

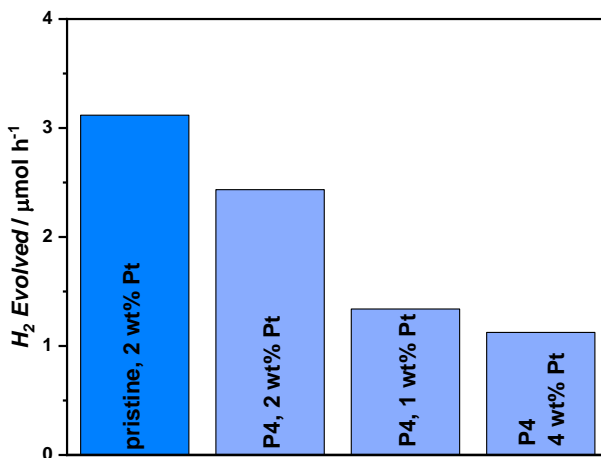


Figure S2.36: Photocatalytic hydrogen evolution of H-PHI pristine and P4. For H-PHI P4 the HER rate is depicted for different Pt amounts used for photo-deposition from H_2PtCl_6 .

Table S2.11: Amount of Pt photo-deposited after photocatalysis experiments with H-PHI measured with elemental analysis. For photocatalysis experiments 2 wt% Pt (photo-deposition of H_2PtCl_6) and 10 vol% methanol were used. No clear trend can be observed besides a Pt amount increase for particles sizes at around 200 nm.

Average particle size [nm]	Pt amount deposited [wt%]
1270	1.37 (± 0.01)
890	1.43 (± 0.01)
650	0.93 (± 0.01)
250	2.01 (± 0.01)
200	2.10 (± 0.11)
165	0.99 (± 0.01)
160	1.06 (± 0.01)
79	1.38 (± 0.01)

Appendix

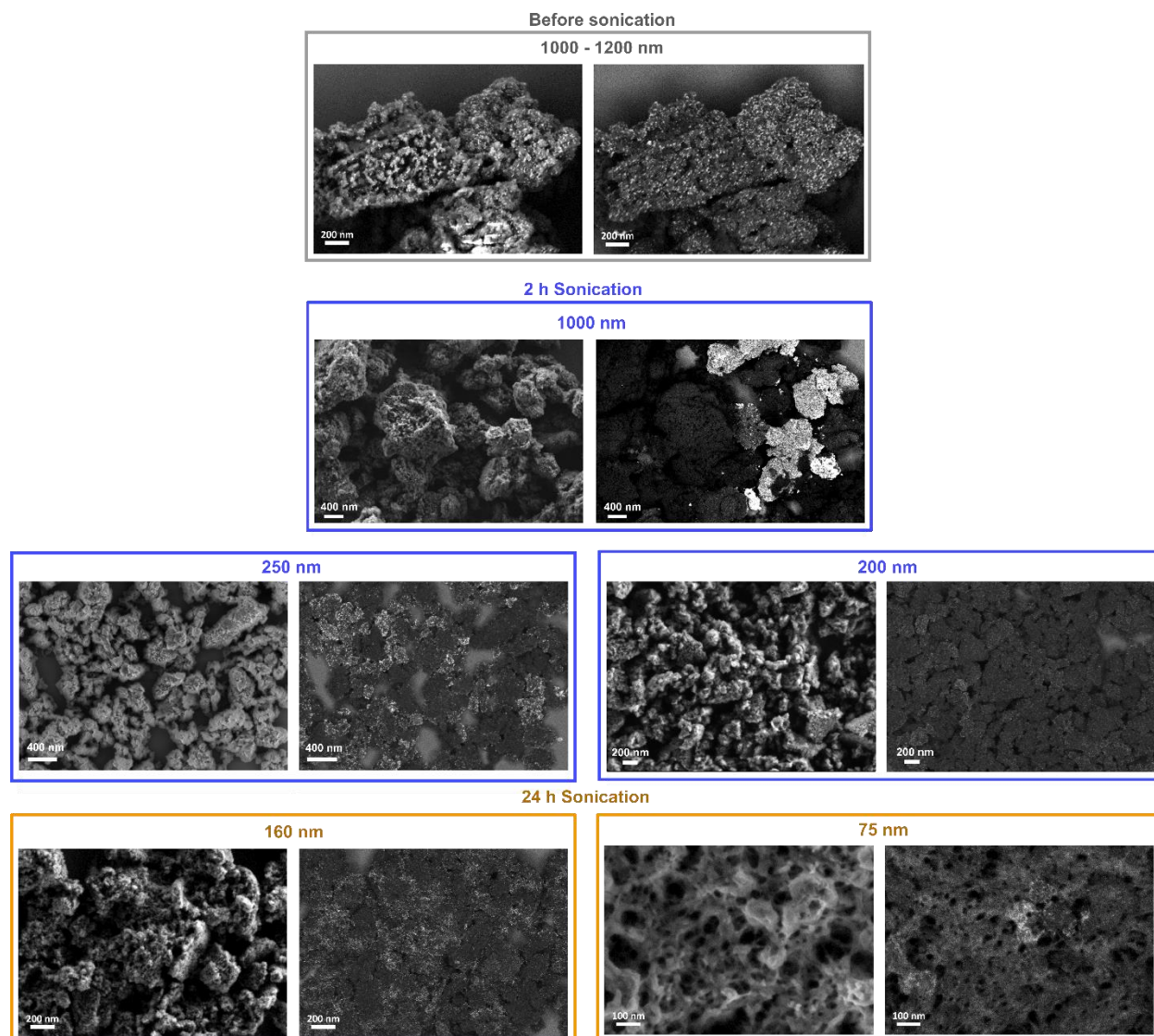


Figure S2.37: SEM images of H-PHI particles after photocatalysis for H-PHI pristine (grey), 2 h (blue) and 24 h (yellow) sonicated. Left side of each box depicts normal SEM images on the right side back-scattered images are shown, for better imaging of Pt deposition (bright spots).

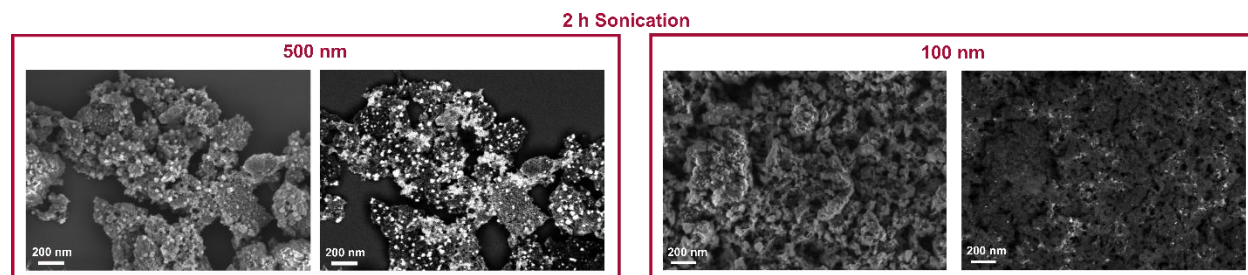


Figure S2.38: SEM images of K-PHI particles after photocatalysis. Left side depicts the secondary electron SEM images on the right side back scattered images are shown for better imaging of Pt deposition (bright spots).

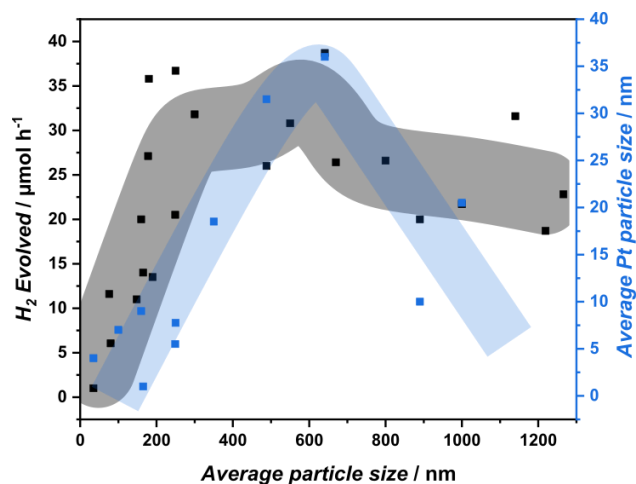


Figure S2.39: Correlation of particle size of H-PHI with average photo-deposited Pt particle size (estimated from SEM images) and hydrogen evolution rate.

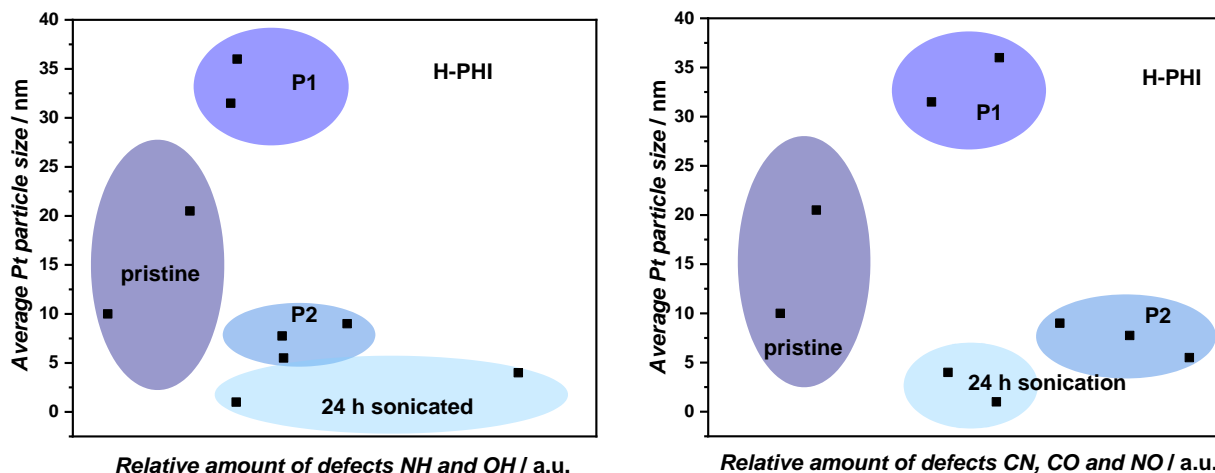


Figure S2.40: Average Pt particle size (estimated from SEM images) after photocatalysis on H-PHI depending on defect amount of NH, OH, C≡N, CO and NO.

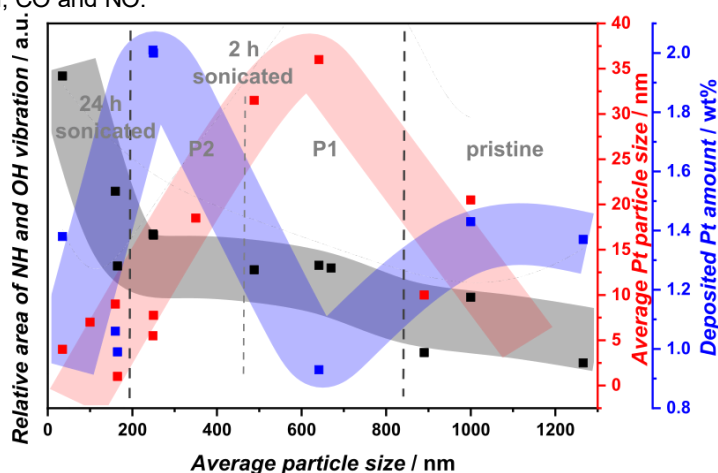


Figure S2.41: Correlation of particle size of H-PHI with average photo-deposited Pt particle sizes (estimated from SEM images), photo-deposited Pt amount after photocatalysis (analyzed with elemental analysis) and NH/OH vibration intensity in FT-IR (normalized to the heptazine vibration at $805\text{-}811\text{ cm}^{-1}$). The photocatalytic experiments were performed with 2 wt% H_2PtCl_6 acid and 10 vol% methanol.

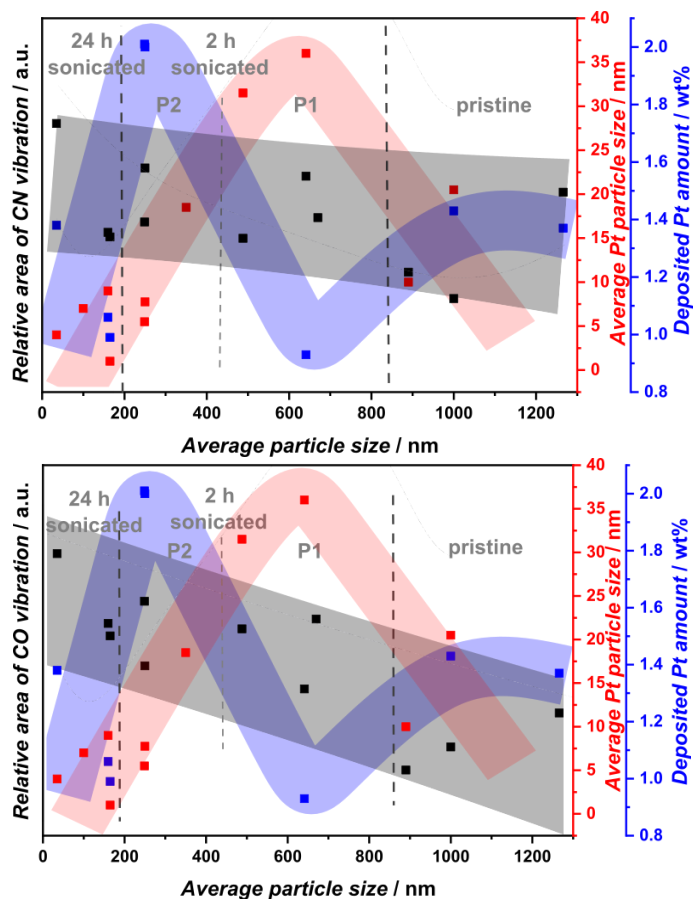


Figure S2.42: Correlation of particle size of H-PHI with average photo-deposited Pt particle size (estimated from SEM images), photo-deposited Pt amount after photocatalysis (analyzed with elemental analysis) and C≡N and CO vibration intensity in FT-IR (normalized to the heptazine vibration at 805-811 cm^{-1}). The photocatalytic experiments were performed with 2 wt% H_2PtCl_6 acid and 10 vol% methanol.

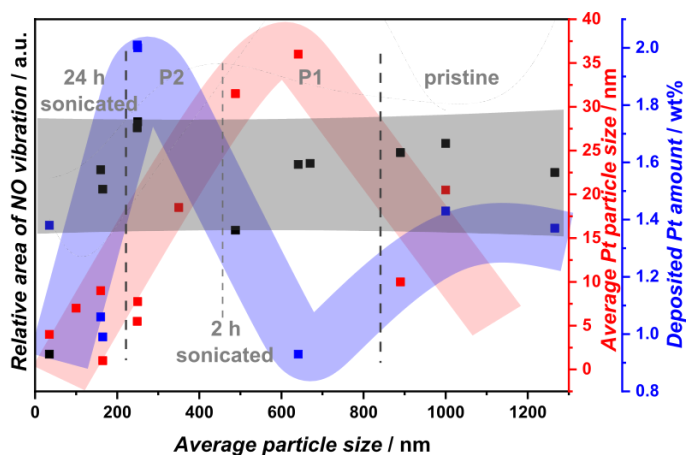


Figure S2.43: Correlation of particle size of H-PHI with average photo-deposited Pt particle size (estimated from SEM images), photo-deposited Pt amount after photocatalysis (analyzed with elemental analysis) and NO vibration intensity in FT-IR (normalized to the heptazine vibration at 805-811 cm^{-1}). The photocatalytic experiments were performed with 2 wt% H_2PtCl_6 acid and 10 vol% methanol.

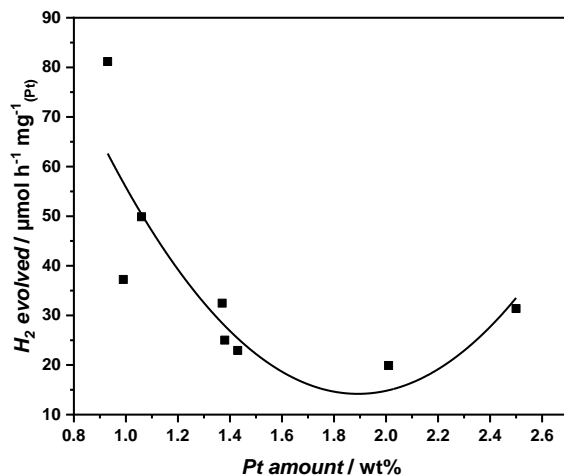


Figure S2.44: Correlation of deposited Pt amount with photocatalytic hydrogen evolution of H-PHI.

9.2.8. PL analysis

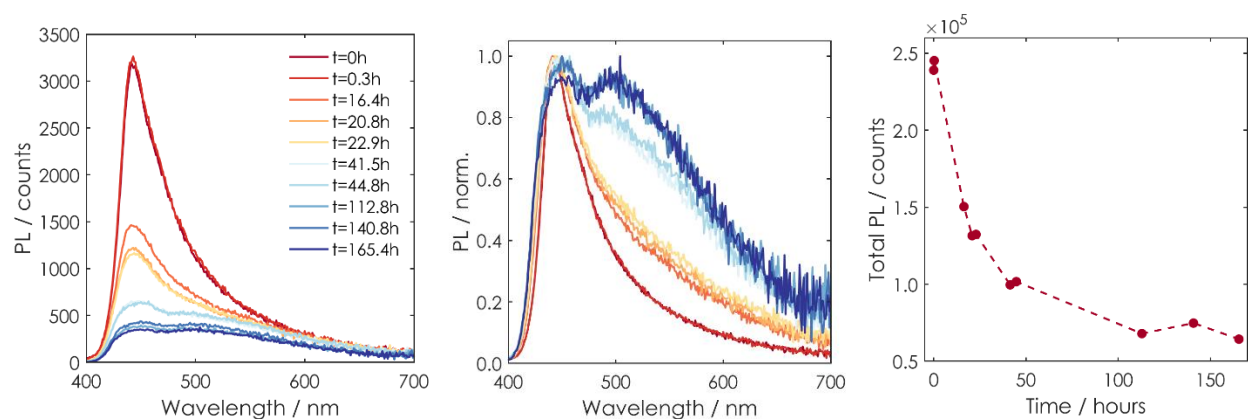


Figure S2.45: PL emission spectra of K-PHI in aqueous suspension. The transformation of K-PHI to H-PHI can be seen over time, by a reduction of the overall PL count as well as the increasing contribution of an additional emission peak around 510 nm. For K-PHI mainly on emission peak (centered at 450 nm) is observed.

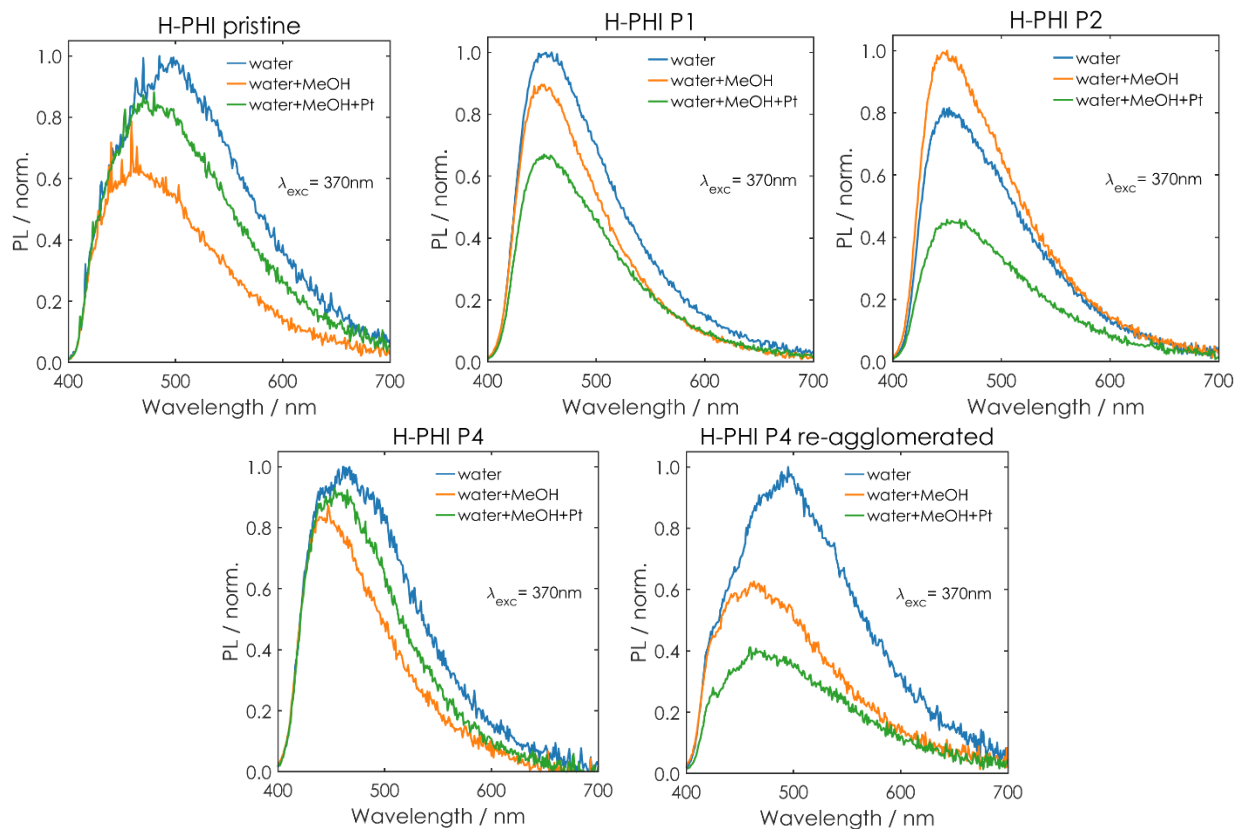


Figure S2.46: PL emission spectra of H-PHI pristine, P1, P2, P4 and P4 re-agglomerated in aqueous suspension, aqueous suspension with methanol and aqueous suspension with methanol and Pt.

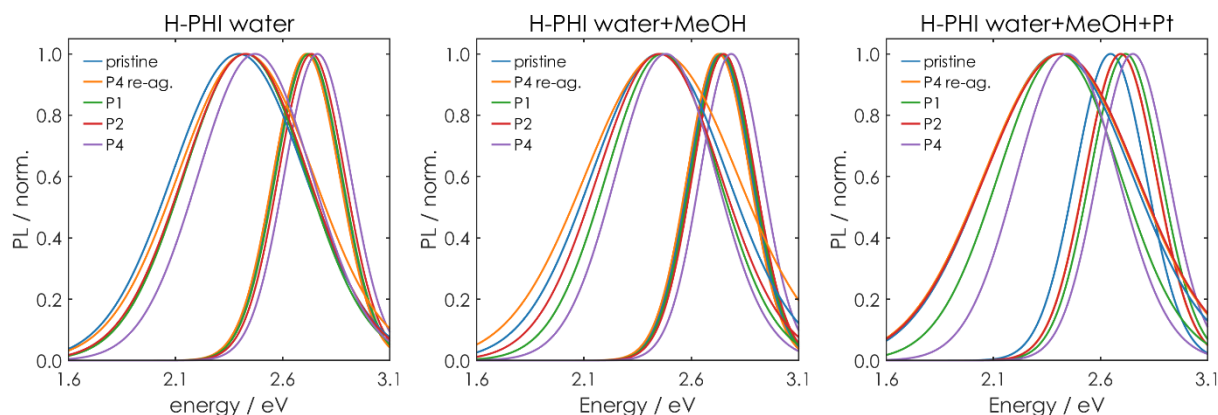


Figure S2.47: Comparison of PL contributions (convoluted of two Gauss functions) of H-PHI pristine, P4, P4 re-agglomerated, P1 and P2 in aqueous suspension, aqueous suspension with methanol and aqueous suspension with methanol and Pt.

From the spectral analysis of PL contributions, it is not possible to extract the relative contribution of traps, since these give rise to both radiative and non-radiative decays (such as charge transfer). When methanol as a hole quencher and the co-catalyst Pt were present during the PL measurement, an expected quenching of photoluminescence intensity up to 50% was observed in all the measured samples (Figure S2.46-S2.49). These results are consistent with literature about Pt deposition on melon-type carbon nitride^[60], where the presence of an electron donor and

acceptor can cause efficient exciton dissociation and charge transfer at the expense of radiative decay.

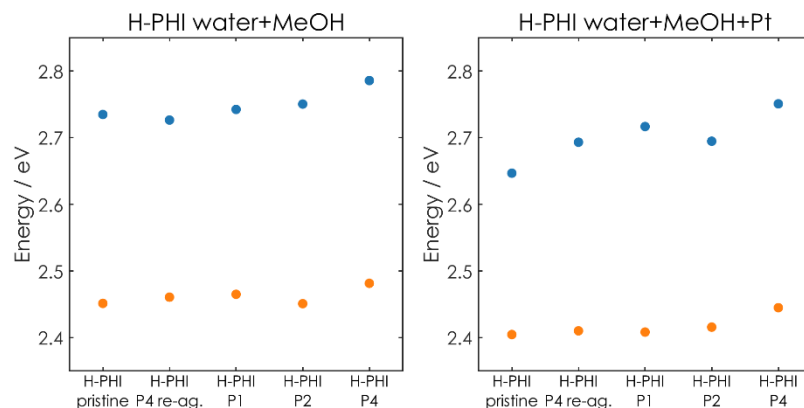


Figure S2.48: PL contributions for different H-PHI materials, plotted with their main energy in presence of MeOH (left) and MeOH and Pt (right). Blue signs depict the center of the Gauss function corresponding to the PL deconvolution at higher energies and orange signs depict the center of the Gauss function corresponding to the PL deconvolution at lower energy.

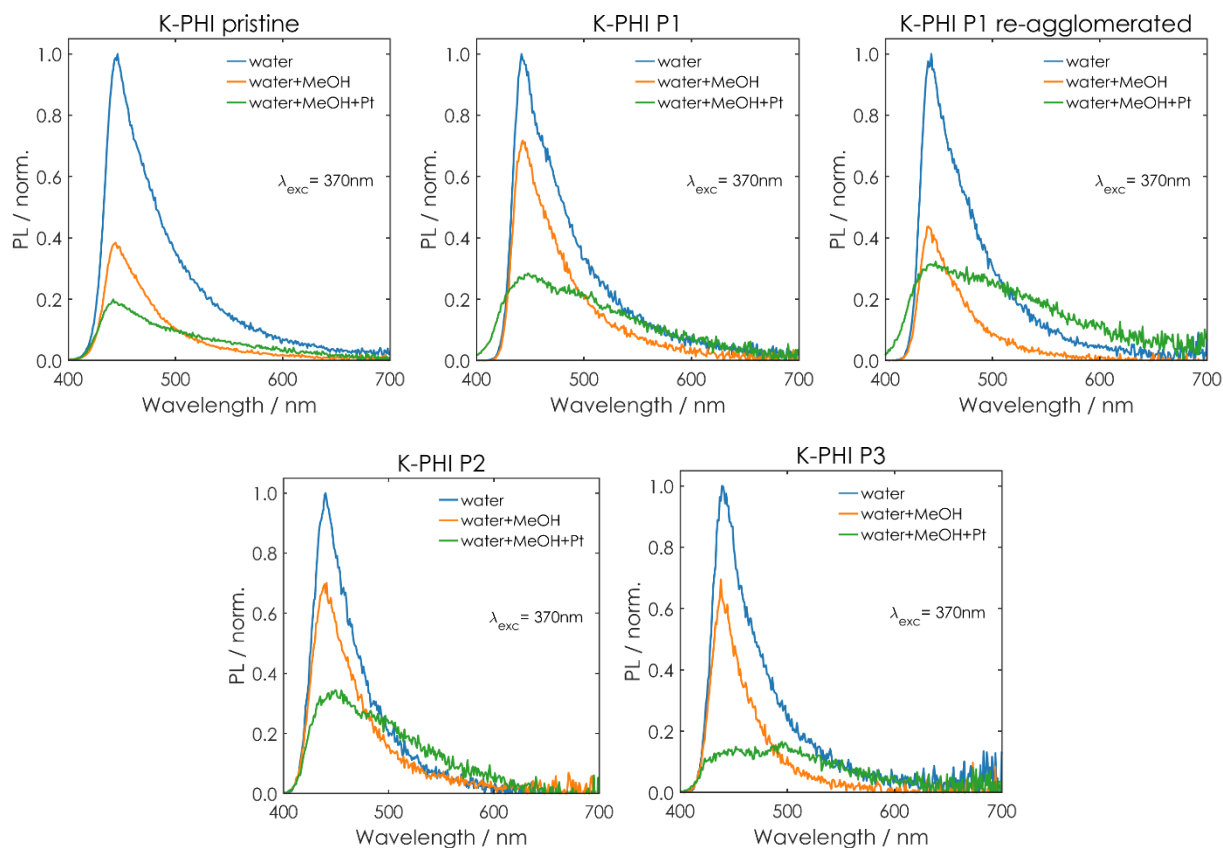


Figure S2.49: PL emission spectra of K-PHI pristine, P1, P1 re-agglomerated, P2 and P3 in aqueous suspension, aqueous suspension with methanol and aqueous suspension methanol and Pt.

Appendix

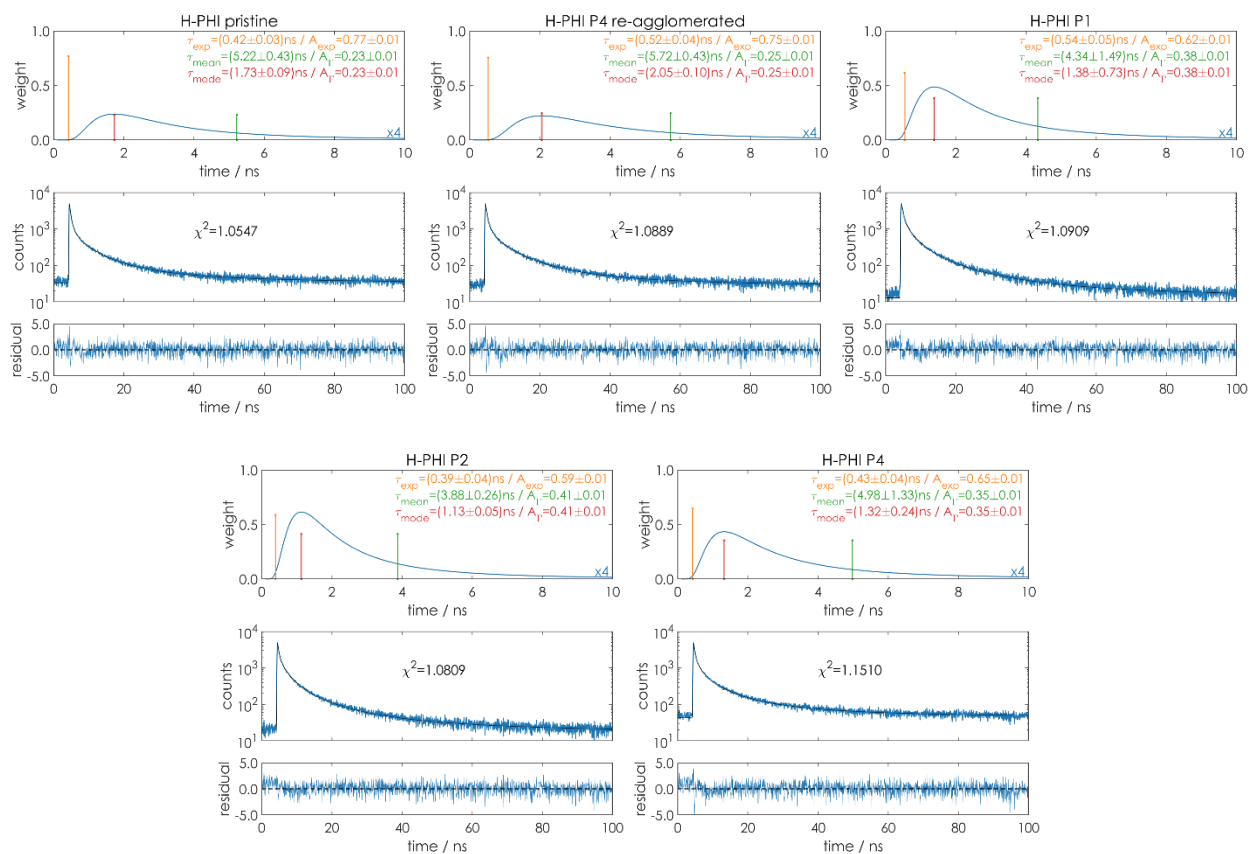


Figure S2.50: Time-resolved PL analysis of H-PHI in aqueous suspension for pristine, P1, P2, P4 and P4 re-agglomerated.

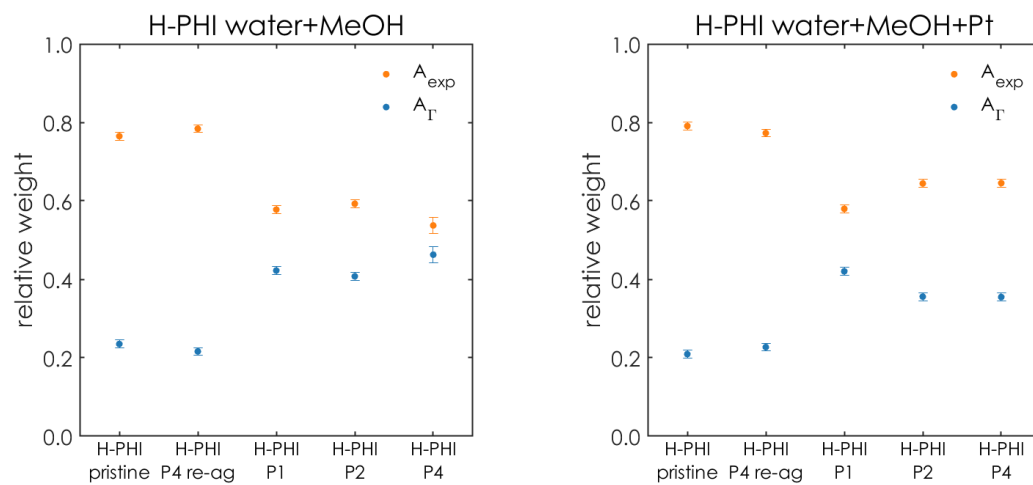


Figure S2.51: Relative contribution of the exponential and Γ function in the fit for time-resolved PL analysis of H-PHI in presence of MeOH (left) and MeOH and Pt (right). The particle sizes of are: pristine H-PHI (810 nm), P4 re-ag. H-PHI (300 nm), P1 H-PHI (500 nm), P2 H-PHI (230 nm) and P4 H-PHI (around 75 nm).

Appendix

Table S2.12: Fitted lifetimes (τ_{exp} and τ_{mode}) and their weighing factors (A) for time-dependent PL measurements of H-PHI with different particle sizes (pristine, P1, P2, P4 and P4 re-agglomerated (re-ag.)) and environments (white: aqueous suspension; light grey: water with 10 vol% MeOH; dark grey: water, MeOH and Pt).

Sample	τ_{exp} [ns]	A_{exp}	τ_{mode} [ns]	τ_{mean} [ns]	A_{Γ}	Average size [nm]
H-PHI pristine	0.42 (\pm 0.03)	0.77 (\pm 0.01)	1.73 (\pm 0.09)	5.22 (\pm 0.43)	0.23 (\pm 0.01)	810
H-PHI P1	0.54 (\pm 0.05)	0.62 (\pm 0.01)	1.38 (\pm 0.73)	4.34 (\pm 1.49)	0.38 (\pm 0.01)	500
H-PHI P4	0.52 (\pm 0.04)	0.75 (\pm 0.01)	2.05 (\pm 0.10)	5.73 (\pm 0.43)	0.25 (\pm 0.01)	300
H-PHI P2	0.39 (\pm 0.04)	0.59 (\pm 0.01)	1.13 (\pm 0.05)	3.88 (\pm 0.26)	0.41 (\pm 0.01)	230
H-PHI P4	0.43 (\pm 0.04)	0.65 (\pm 0.01)	1.32 (\pm 0.24)	4.98 (\pm 1.33)	0.35 (\pm 0.01)	75
H-PHI pristine	0.35 (\pm 0.02)	0.76 (\pm 0.01)	0.92 (\pm 0.05)	4.67 (\pm 0.52)	0.24 (\pm 0.01)	810
H-PHI P1	0.47 (\pm 0.04)	0.58 (\pm 0.01)	1.13 (\pm 0.84)	4.05 (\pm 1.81)	0.42 (\pm 0.01)	500
H-PHI P4	0.49 (\pm 0.03)	0.78 (\pm 0.01)	1.91 (\pm 1.02)	5.85 (\pm 1.48)	0.22 (\pm 0.01)	300
H-PHI P2	0.40 (\pm 0.04)	0.59 (\pm 0.01)	1.08 (\pm 0.19)	3.90 (\pm 0.78)	0.41 (\pm 0.01)	230
H-PHI P4	0.31 (\pm 0.04)	0.54 (\pm 0.02)	0.68 (\pm 0.03)	3.72 (\pm 0.34)	0.46 (\pm 0.02)	75
H-PHI pristine	0.49 (\pm 0.03)	0.79 (\pm 0.01)	1.63 (\pm 0.09)	4.76 (\pm 0.42)	0.21 (\pm 0.01)	810
H-PHI P1	0.46 (\pm 0.05)	0.58 (\pm 0.01)	1.05 (\pm 0.05)	3.63 (\pm 0.25)	0.42 (\pm 0.01)	500
H-PHI P4	0.42 (\pm 0.03)	0.77 (\pm 0.01)	1.41 (\pm 0.08)	3.92 (\pm 0.33)	0.23 (\pm 0.01)	300
H-PHI P2	0.42 (\pm 0.03)	0.64 (\pm 0.01)	0.93 (\pm 0.04)	3.41 (\pm 0.27)	0.36 (\pm 0.01)	230
H-PHI P4	0.40 (\pm 0.04)	0.65 (\pm 0.01)	1.07 (\pm 0.05)	4.27 (\pm 0.34)	0.35 (\pm 0.01)	75

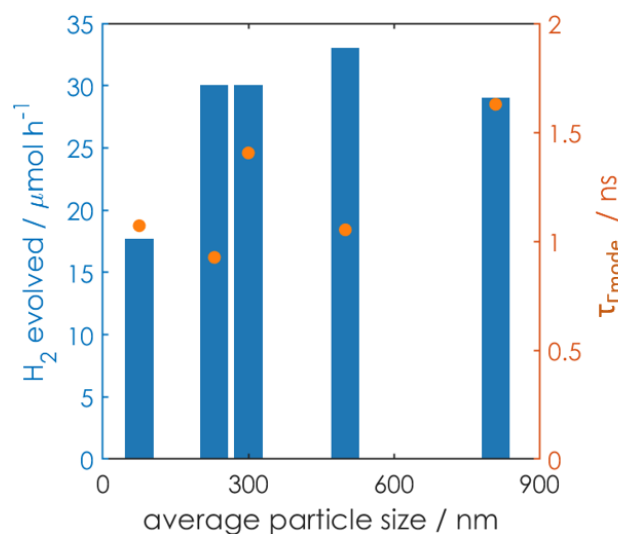


Figure S2.52: Lifetime attributed to the Γ -function (measured in presence of methanol and photo-deposited Pt) of H-PHI in comparison to photocatalytic hydrogen evolution activity depending on particle size.

9.2.9. Electrochemical measurements

The electrochemical impedance spectroscopy as well as electrochemical polarization experiments were performed with pressed pellets in between of two steel electrodes. Out of this reason, only re-agglomerated particles could be analyzed. The charge transfer abilities of H-PHI pristine, P1, P2 and P4 were studied by impedance spectroscopy, to analyze the effect of different particle sizes and an increasing amount of functional groups on the electronic and ionic conductivity behavior within the material. With decreasing particle size, the amount of grain boundaries is increasing. Since the conductivity is slightly increasing with decreasing particle size, the conductivity might be based on grain boundary transport. Due to the shape of response in the electrochemical polarization experiments a rather electron based conductivity can be assumed and ionic motions can be neglected.^[61, 62] In combination with the particle size dependent conductivity measurements this points to an enhanced electron transfer between re-agglomerated particles (grain sizes), if more functional groups are present at the interface (e.g. in P4).

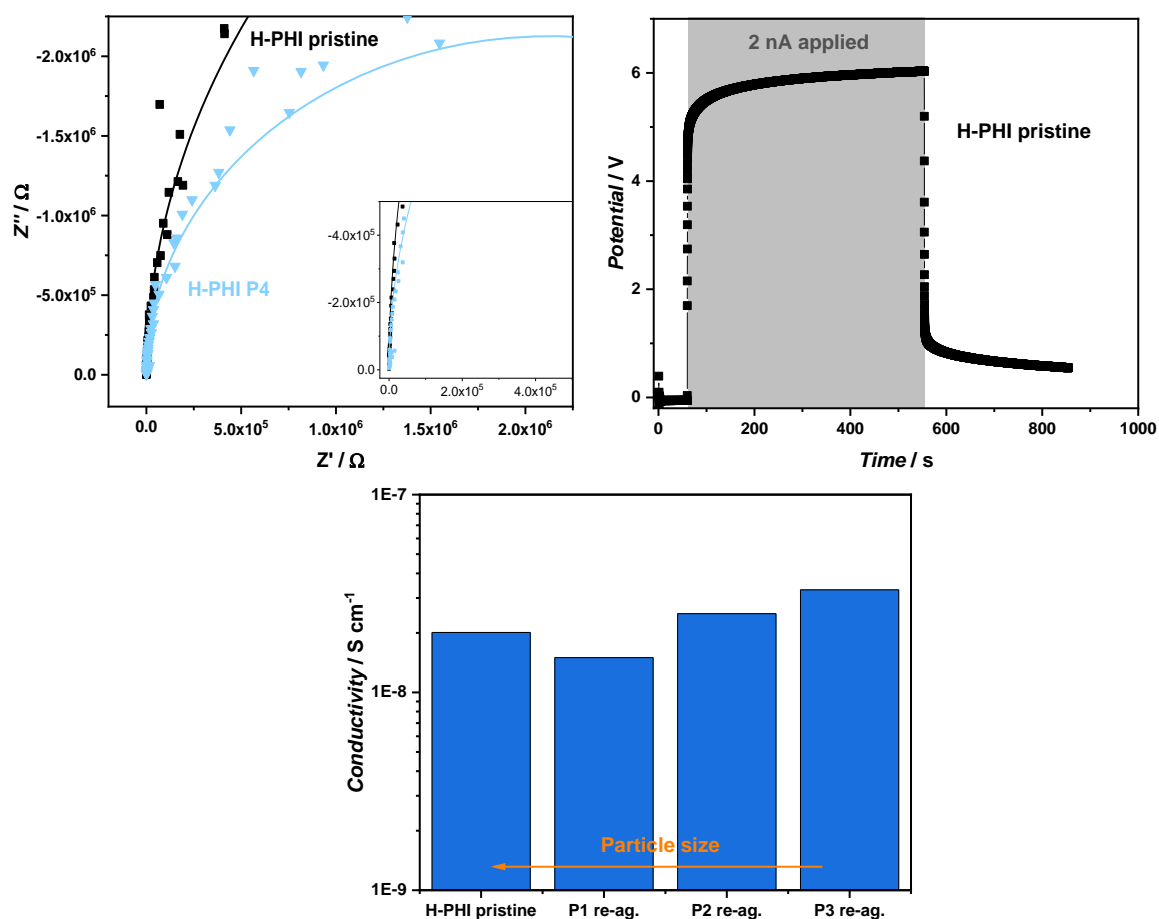


Figure S2.53: Electrochemical characterization of H-PHI pellets (pristine, P1-P3 re-agglomerated (re-ag.)) between two steel electrodes by impedance spectroscopy (top left) and DC polarization experiments with the grey area depicting the 2 nA applied current (top right). To fit the impedance spectroscopy data a resistance in series with a constant phase element and a resistance in parallel was used. From DC measurements, a mainly electron driven charge transport can be assumed. Bottom: Conductivity depending on particle size.

9.2.10. Quantum-chemical calculations

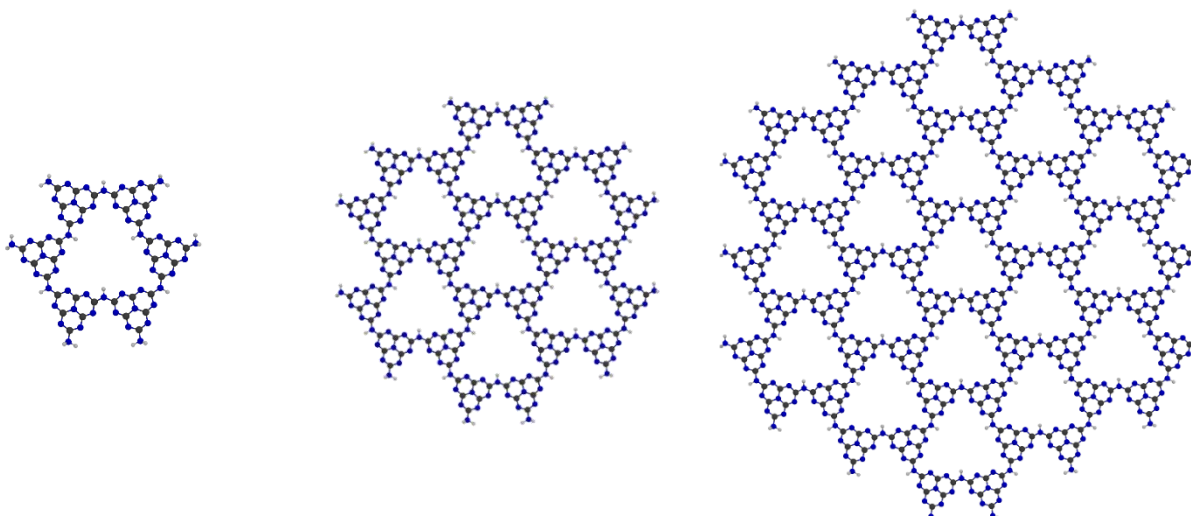


Figure S2.54: Designed PHI model systems with 1, 7 and 19 pores. Structures were obtained as cut-outs from a 2D periodic optimization of H-PHI.

In general, orbital contributions are rather localized on heptazine units, with negligible contribution of the NH bridge, between two heptazine units.

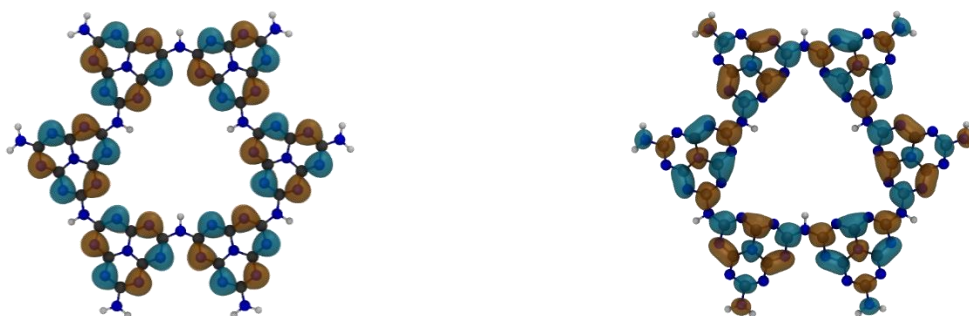


Figure S2.55: HOMO (left) and LUMO (right) of the 1 pore model system, obtained on RI-PBE/def2-SVP//RI-PBE-D3/def2-TZVP level of theory.

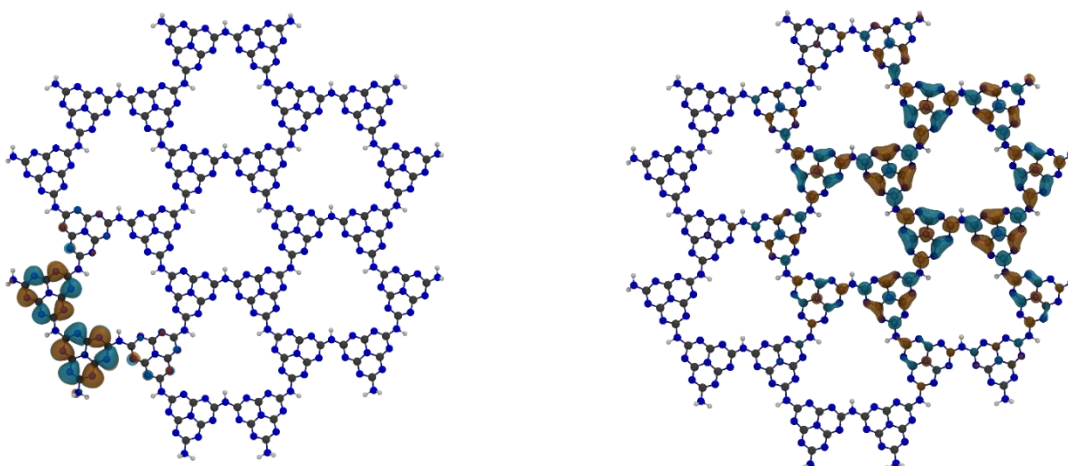


Figure S2.56: HOMO (left) and LUMO (right) of the 7 pore model system, obtained on RI-PBE/def2-SVP//RI-PBE-D3/def2-TZVP level of theory.

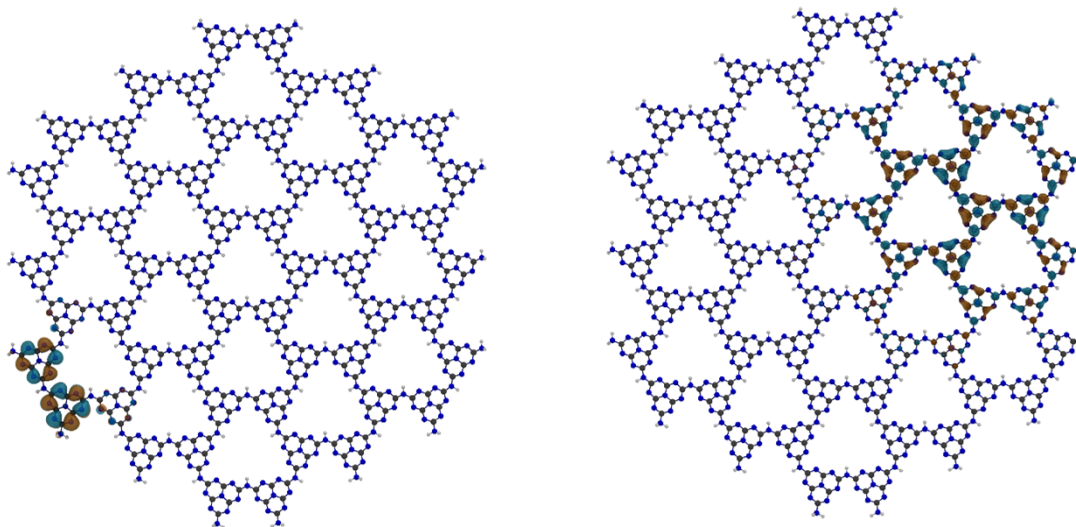


Figure S2.57: HOMO (left) and LUMO (right) of the 19 pore model system, obtained on RI-PBE/def2-SVP//RI-PBE-D3/def2-TZVP level of theory.

Table S2.13: HOMO and LUMO energies of the model systems of PHI with 1, 7 and 19 pores obtained on RI-PBE/def2-SVP//RI-PBE-D3/def2-TZVP level of theory.

Model system	HOMO energy [eV]	LUMO energy [eV]
1 pore	-5.65	-3.06
7 pores	-5.77	-3.71
19 pores	-5.74	-3.80

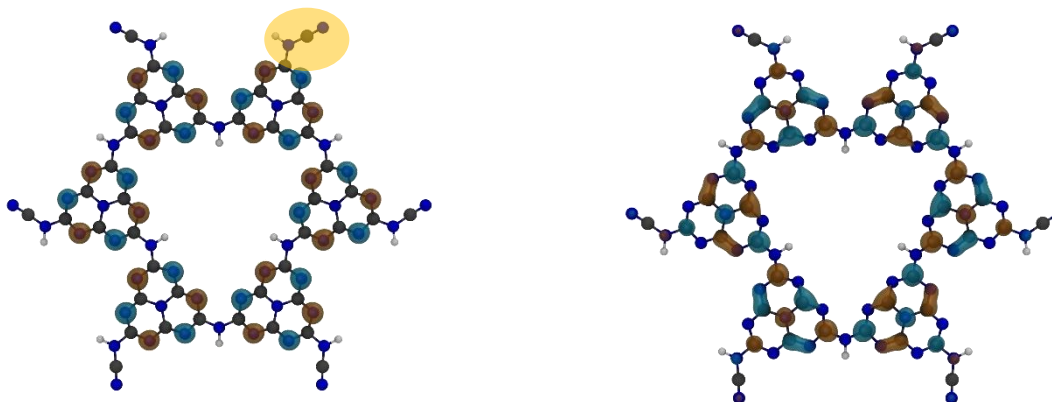


Figure S2.58: HOMO (left) and LUMO (right) of the 1 pore model system with 6 NHC≡N termination groups, obtained on PBE-D3/def2-TZVP//PBE-D3/def2-TZVP level of theory. The functional group is highlighted in orange.

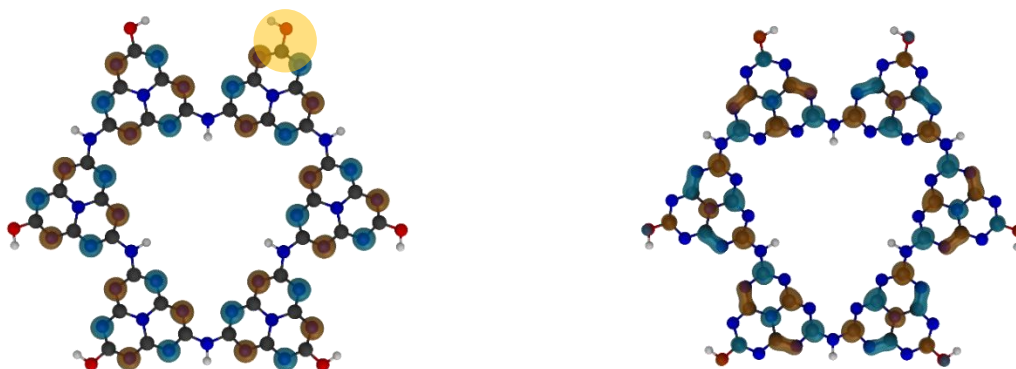


Figure S2.59: HOMO (left) and LUMO (right) of the 1pore model system with 6 OH termination groups, obtained on PBE-D3/def2-TZVP//PBE-D3/def2-TZVP level of theory. The functional group is highlighted in orange.

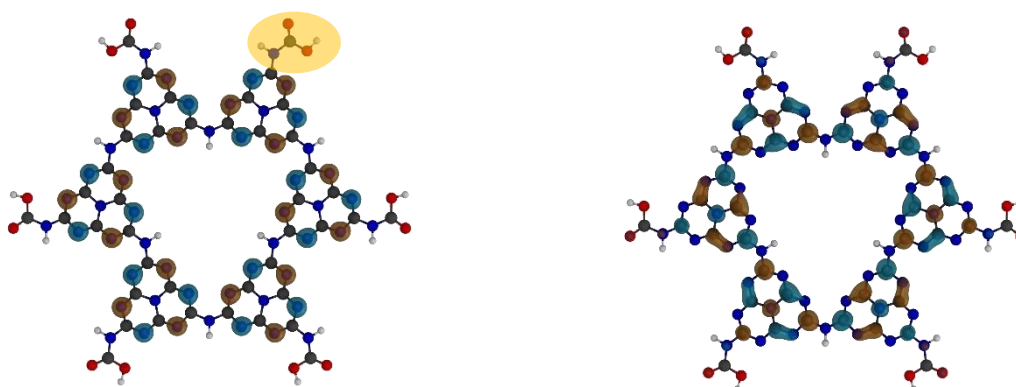


Figure S2.60: HOMO (left) and LUMO (right) of the 1 pore model system with 6 NHCOOH termination groups, obtained on PBE-D3/def2-TZVP//PBE-D3/def2-TZVP level of theory. The functional group is highlighted in orange.

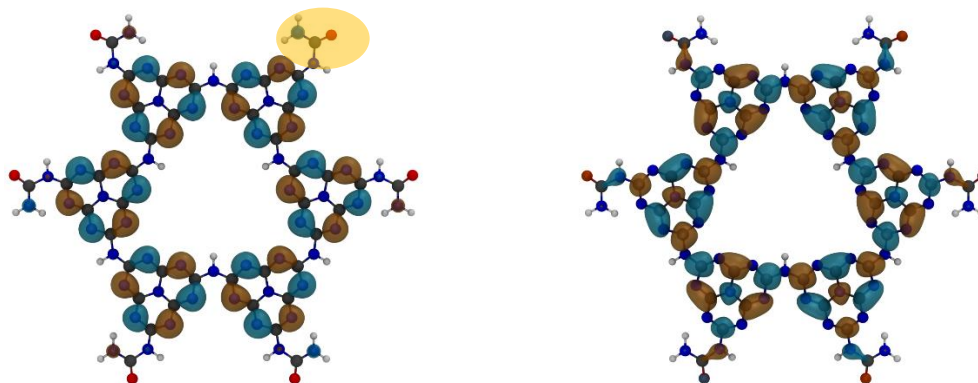


Figure S2.61: HOMO (left) and LUMO (right) of the 1 pore model system with 6 NHCONH₂ termination groups, obtained on PBE-D3/def2-TZVP//PBE-D3/def2-TZVP level of theory. The functional group is highlighted in orange.

Table S2.14: Optical and fundamental band gaps and HOMO and LUMO energies, obtained on RI-PBE-D3/def2-TZVP//PBE-D3/def2-TZVP level of theory using the 1 pore model system with different functionalization.

Functionalization	Optical band gap [eV]	Band gap [eV]	HOMO energy [eV]	LUMO energy [eV]
NH ₂	4.35	2.63	-5.81	-3.18
OH	4.30	2.58	-6.40	-3.82
NHCOOH	4.25	2.55	-6.36	-3.81
NHCONH ₂	4.31	2.59	-6.52	-3.93
NHC≡N	4.27	2.57	-6.76	-4.19

Calculations on XTB level of theory using the 1 pore model for OH edge defects revealed large absolute errors in comparison to PBE/def2-TZVP level of theory (see Methods for details). Referencing these calculations on edge defect models relative to calculations without any edge defects, the methodological errors are reduced significantly. Calculations on larger model systems as the 7 and 19 pore model system were carried out on XTB level of theory only.

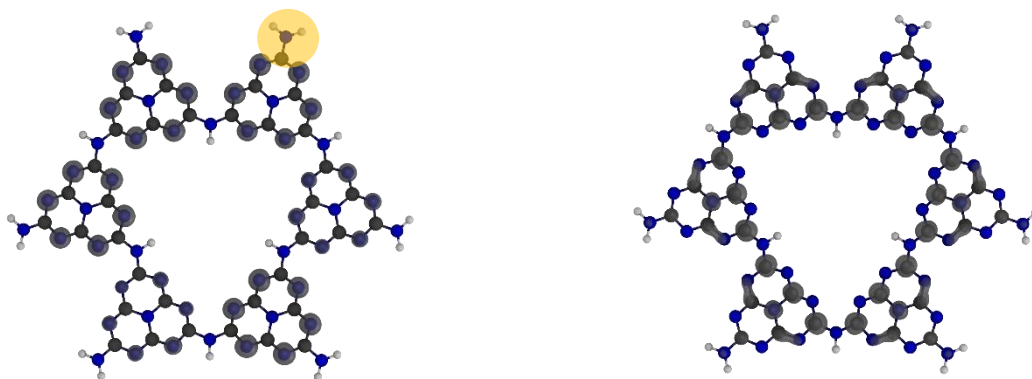


Figure S2.62: Spin density of the radical cation (left) and radical anion (right) of the 1 pore model system with NH₂ functionalization, obtained on PBE-D3/def2-TZVP//PBE-D3/def2-TZVP level of theory. The functional group is highlighted in orange.

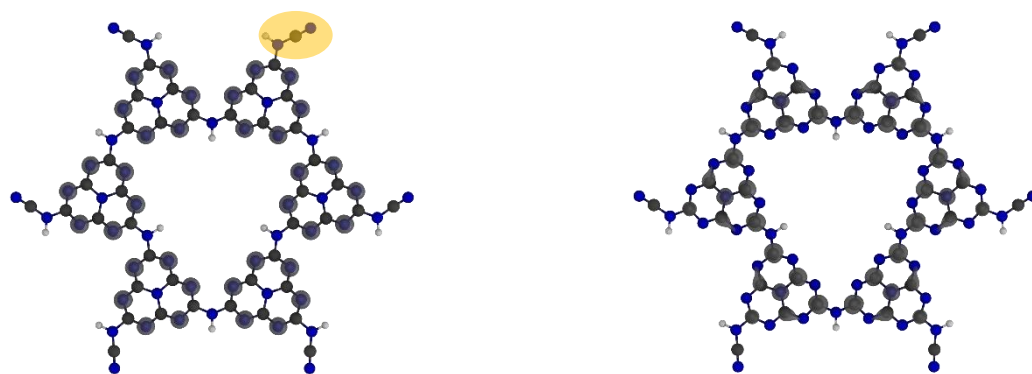


Figure S2.63: Spin density of the radical cation (left) and radical anion (right) of the 1 pore model system with NHC≡N functionalization, obtained on PBE-D3/def2-TZVP//PBE-D3/def2-TZVP level of theory. The functional group is highlighted in orange.

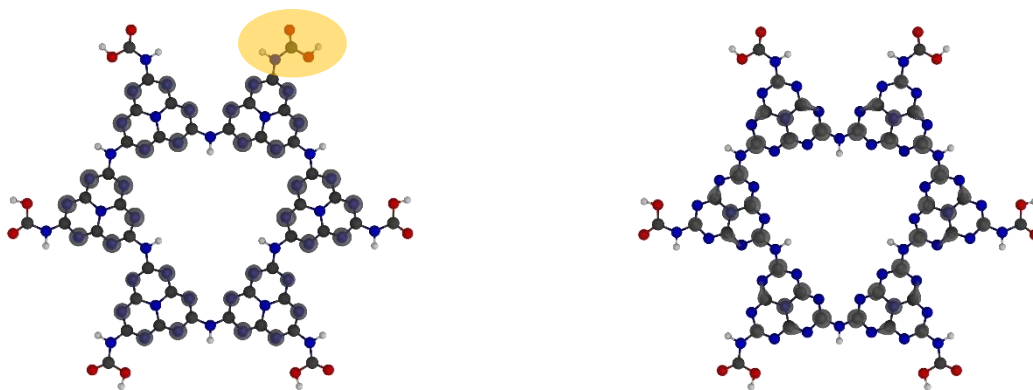


Figure S2.64: Spin density of the radical cation (left) and radical anion (right) of the 1 pore model system with NHCOOH functionalization, obtained on PBE-D3/def2-TZVP//PBE-D3/def2-TZVP level of theory. The functional group is highlighted in orange.

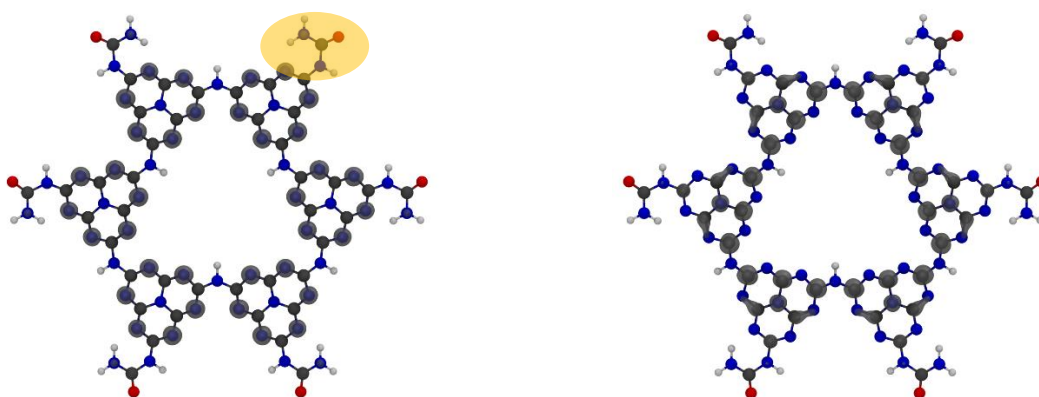


Figure S2.65: Spin density of the radical cation (left) and radical anion (right) of the 1 pore model system with NHCONH₂ functionalization, obtained on PBE-D3/def2-TZVP//PBE-D3/def2-TZVP level of theory. The functional group is highlighted in orange.

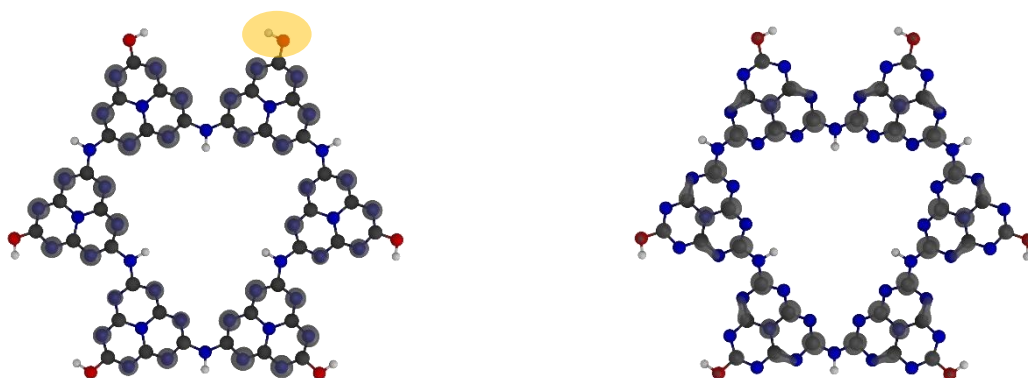


Figure S2.66: Spin density of the radical cation (left) and radical anion (right) of the 1 pore model system with OH functionalization, obtained on PBE-D3/def2-TZVP//PBE-D3/def2-TZVP level of theory. The functional group is highlighted in orange.

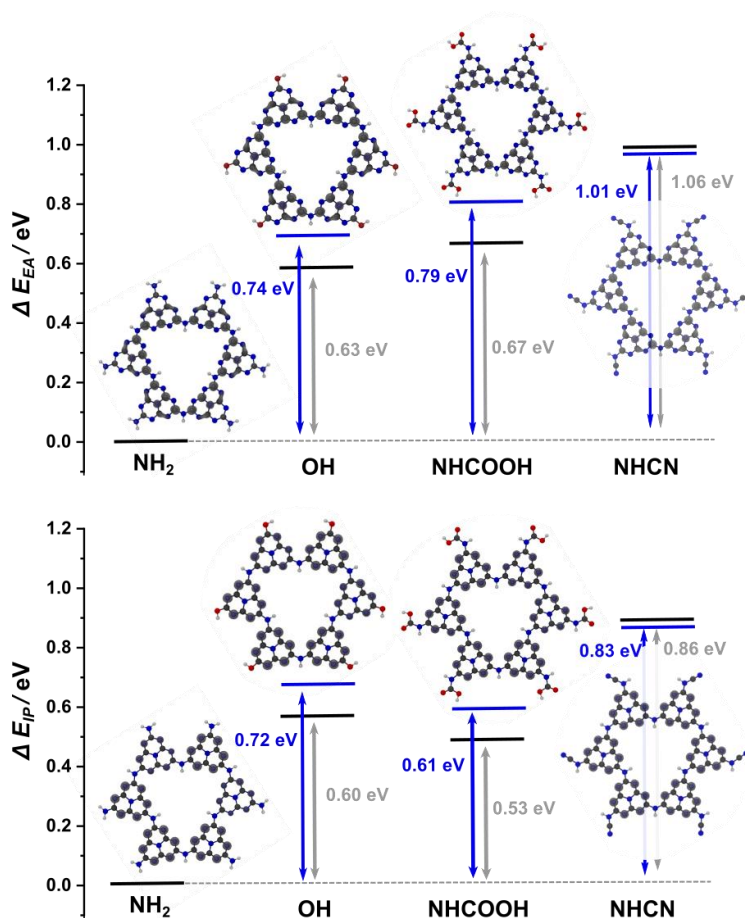


Figure S2.67: Comparison of XTB (blue) and PBE-D3/def2-TZVP (grey) electron affinities (E_{EA}) and ionization potentials (E_{IP}) of different surface functionalization on the 1 pore model system, relative to NH₂ functional groups.

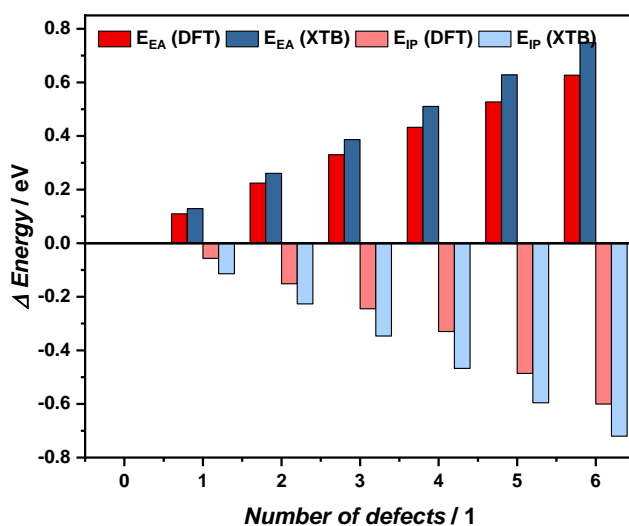


Figure S2.68: Comparison of ionization potential (E_{IP}) and electron affinity (E_{EA}) for the 1 pore model system, obtained on PBE-D3/def2-TZVP and XTB level of theory. 1 pore model with NH₂ terminations, stepwise substitution of NH₂ groups with OH groups, relative to the fully OH terminated system.

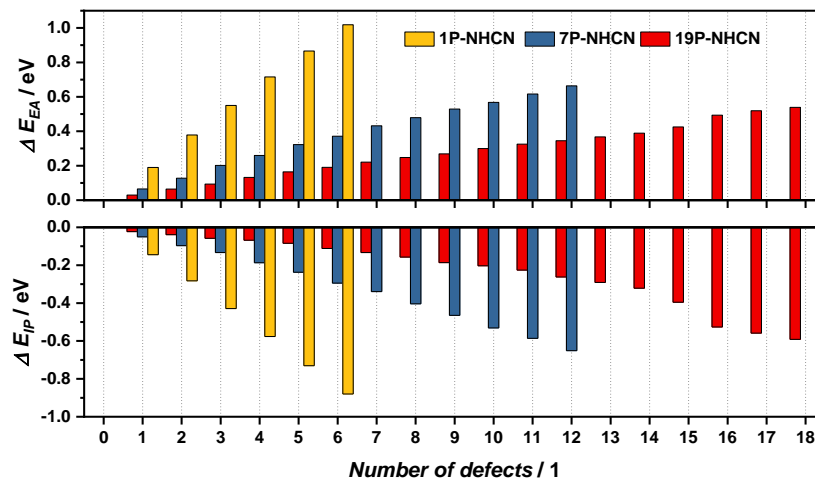


Figure S2.69: Comparison of electron affinity (E_{EA}) and ionization potential (E_{IP}) normalized on the system with NH_2 termination groups. Stepwise substitution of NH_2 functional groups by $\text{NHC}\equiv\text{N}$ on the 1 pore model (yellow), 7 pore model (blue) and 19 pore model (red). Calculations were performed on XTB level of theory.

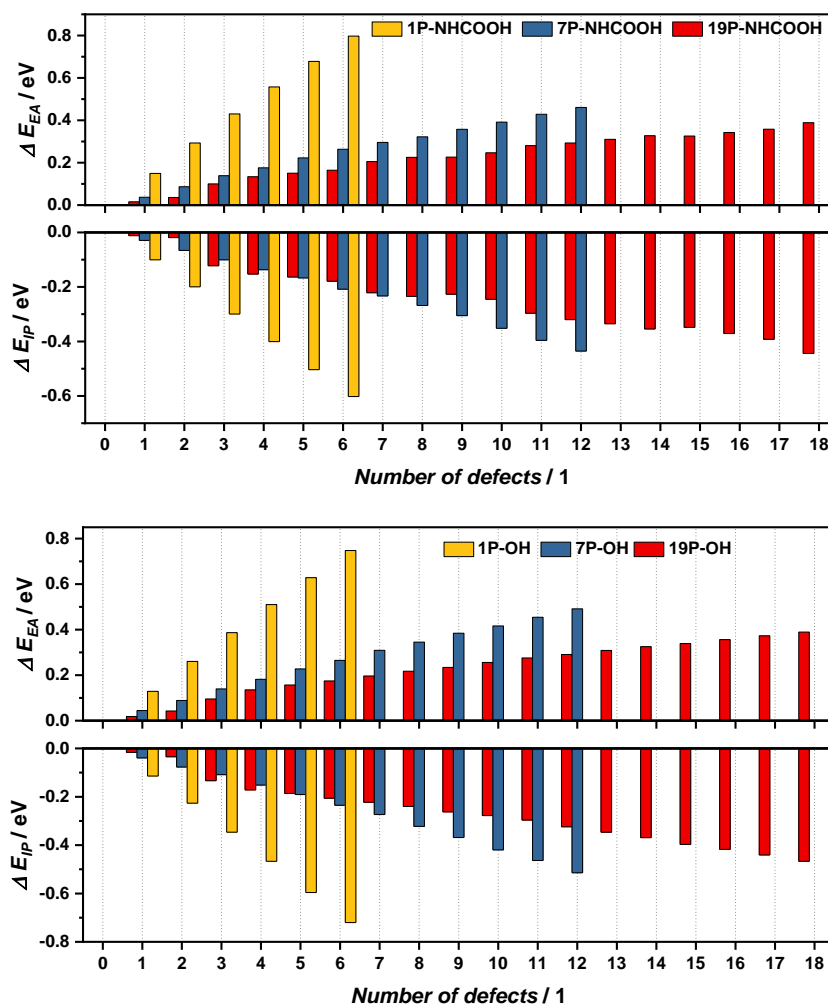


Figure S2.70: Comparison of electron affinity (E_{EA}) and ionization potential (E_{IP}) normalized on the system with NH_2 termination groups. Stepwise substitution of NH_2 functional groups by NHCOOH (top) or OH (bottom) on the 1 pore model (yellow), 7 pore model (blue) and 19 pore model (red). Calculations were performed on XTB level of theory.

9.2.11. Bibliography

- [1] H. Schlomberg, J. Kröger, G. Savasci, M. W. Terban, S. Bette, I. Moudrakovski, V. Duppel, F. Podjaski, R. Siegel, J. Senker, R. E. Dinnebier, C. Ochsenfeld, B. V. Lotsch, *Chem. Mater.* **2019**, *31* (18), 7478-7486.
- [2] A. L. Patterson, *Phys. Rev.* **1939**, *56* (10), 978-982.
- [3] R. W. Cheary, A. A. Coelho, J. P. Cline, *J. Res. Natl. Inst. Stand. Technol.* **2004**, *109* (1), 1-25.
- [4] R. W. Cheary, A. Coelho, *J. Appl. Cryst.* **1992**, *25* (2), 109-121.
- [5] P. Václav, D. Michal, P. Lukáš, *Z. Kristallogr.* **2014**, *229* (5), 345-352.
- [6] P. Swift, *Surf. Interface Anal.* **1982**, *4* (2), 47-51.
- [7] T. L. Barr, S. Seal, *J. Vac. Sci. Technol.* **1995**, *13* (3), 1239-1246.
- [8] J. F. Moulder, J. Chastain, *Handbook of X-ray Photoelectron Spectroscopy: A Reference Book of Standard Spectra for Identification and Interpretation of XPS Data*, Physical Electronics Division, Perkin-Elmer Corporation, **1992**.
- [9] E. O. Stejskal, J. D. Memory, *High Resolution NMR in the Solid State*, Oxford University Press, Oxford, **1994**, 189.
- [10] K. J. D. MacKenzie, M. E. Smith, *Multinuclear Solid-State Nuclear Magnetic Resonance of Inorganic Materials*, Elsevier Science, **2002**.
- [11] J. Kröger, A. Jiménez-Solano, G. Savasci, P. Rovó, I. Moudrakovski, K. Küster, H. Schlomberg, H. A. Vignolo-González, V. Duppel, L. Grunenber, C. B. Dayan, M. Sitti, F. Podjaski, C. Ochsenfeld, B. V. Lotsch, *Adv. Energy Mater.* **2021**, *11* (6), 2003016.
- [12] V. W.-h. Lau, I. Moudrakovski, T. Botari, S. Weinberger, M. B. Mesch, V. Duppel, J. Senker, V. Blum, B. V. Lotsch, *Nat. Commun.* **2016**, *7* (1), 12165.
- [13] V. W.-h. Lau, V. W.-z. Yu, F. Ehrat, T. Botari, I. Moudrakovski, T. Simon, V. Duppel, E. Medina, J. K. Stolarczyk, J. Feldmann, V. Blum, B. V. Lotsch, *Adv. Energy Mater.* **2017**, *7* (12), 1602251.
- [14] F. Podjaski, J. Kröger, B. V. Lotsch, *Adv. Mater.* **2018**, *30* (9), 1705477.
- [15] K. Schwinghammer, M. B. Mesch, V. Duppel, C. Ziegler, J. Senker, B. V. Lotsch, *J. Am. Chem. Soc.* **2014**, *136* (5), 1730-1733.
- [16] J. P. Perdew, K. Burke, M. Ernzerhof, *Phys. Rev. Lett.* **1996**, *77* (18), 3865-3868.
- [17] S. Grimme, J. Antony, S. Ehrlich, H. Krieg, *J. Chem. Phys.* **2010**, *132* (15), 154104.
- [18] A. Schäfer, C. Huber, R. Ahlrichs, *J. Chem. Phys.* **1994**, *100* (8), 5829-5835.
- [19] K. Eichkorn, F. Weigend, O. Treutler, R. Ahlrichs, *Theor. Chem. Acc.* **1997**, *97* (1), 119-124.
- [20] A. M. Burow, M. Sierka, F. Mohamed, *J. Chem. Phys.* **2009**, *131* (21), 214101.
- [21] L. Grajciar, *J. Comput. Chem.* **2015**, *36* (20), 1521-1535.
- [22] A. M. Burow, M. Sierka, *J. Chem. Theory Comput.* **2011**, *7* (10), 3097-3104.
- [23] R. Łazarski, A. M. Burow, L. Grajciar, M. Sierka, *J. Comput. Chem.* **2016**, *37* (28), 2518-2526.
- [24] R. Łazarski, A. M. Burow, M. Sierka, *J. Chem. Theory Comput.* **2015**, *11* (7), 3029-3041.
- [25] V. W.-h. Lau, D. Klose, H. Kasap, F. Podjaski, M.-C. Pignié, E. Reisner, G. Jeschke, B. V. Lotsch, *Angew. Chem. Int. Ed.* **2017**, *56* (2), 510-514.
- [26] R. Ahlrichs, M. Bär, M. Häser, H. Horn, C. Kölmel, *Chem. Phys. Lett.* **1989**, *162* (3), 165-169.
- [27] C. Adamo, V. Barone, *J. Chem. Phys.* **1999**, *110* (13), 6158-6170.
- [28] M. Ernzerhof, G. E. Scuseria, *J. Chem. Phys.* **1999**, *110* (11), 5029-5036.
- [29] P. J. Wilson, T. J. Bradley, D. J. Tozer, *J. Chem. Phys.* **2001**, *115* (20), 9233-9242.
- [30] F. Jensen, *J. Chem. Theory Comput.* **2008**, *4* (5), 719-727.
- [31] J. Kussmann, C. Ochsenfeld, *J. Chem. Phys.* **2013**, *138* (13), 134114.
- [32] J. Kussmann, C. Ochsenfeld, *J. Chem. Theory Comput.* **2015**, *11* (3), 918-922.
- [33] C. Bannwarth, E. Caldeweyher, S. Ehlert, A. Hansen, P. Pracht, J. Seibert, S. Spicher, S. Grimme, *WIREs Comput. Mol. Sci.* **2021**, *11* (2), e1493.
- [34] C. Bannwarth, S. Ehlert, S. Grimme, *J. Chem. Theory Comput.* **2019**, *15* (3), 1652-1671.
- [35] S. Grimme, C. Bannwarth, P. Shushkov, *J. Chem. Theory Comput.* **2017**, *13* (5), 1989-2009.
- [36] Y.-Y. Li, B.-X. Zhou, H.-W. Zhang, S.-F. Ma, W.-Q. Huang, W. Peng, W. Hu, G.-F. Huang, *Nanoscale* **2019**, *11* (14), 6876-6885.
- [37] H. Katsumata, F. Higashi, Y. Kobayashi, I. Tateishi, M. Furukawa, S. Kaneco, *Sci. Rep.* **2019**, *9* (1), 14873.
- [38] J. Chen, X. Xu, T. Li, K. Pandiselvi, J. Wang, *Sci. Rep.* **2016**, *6* (1), 37318.
- [39] Z. Zhou, Y. Shen, Y. Li, A. Liu, S. Liu, Y. Zhang, *ACS Nano* **2015**, *9* (12), 12480-12487.

- [40] X. Liu, B. Jing, G. Lun, Y. Wang, X. Wang, C. Fang, Z. Ao, C. Li, *Chem. Commun.* **2020**, 56 (21), 3179-3182.
- [41] C. Lv, Y. Qian, C. Yan, Y. Ding, Y. Liu, G. Chen, G. Yu, *Angew. Chem. Int. Ed.* **2018**, 57 (32), 10246-10250.
- [42] Z. Lin, G. H. Waller, Y. Liu, M. Liu, C.-p. Wong, *Nano Energy* **2013**, 2 (2), 241-248.
- [43] X. Fu, X. Hu, Z. Yan, K. Lei, F. Li, F. Cheng, J. Chen, *Chem. Commun.* **2016**, 52 (8), 1725-1728.
- [44] S. Thaweesak, S. Wang, M. Lyu, M. Xiao, P. Peerakiatkhajohn, L. Wang, *Dalton T.* **2017**, 46 (32), 10714-10720.
- [45] P. G. Gassman, A. Ghosh, J. Almlöf, *J. Am. Chem. Soc.* **1992**, 114 (25), 9990-10000.
- [46] F. Dong, L. Wu, Y. Sun, M. Fu, Z. Wu, S. C. Lee, *J. Mater. Chem.* **2011**, 21 (39), 15171-15174.
- [47] J. Yu, K. Wang, W. Xiao, B. Cheng, *Phys. Chem. Chem. Phys.* **2014**, 16 (23), 11492-11501.
- [48] B. Zhu, P. Xia, Y. Li, W. Ho, J. Yu, *Appl. Surf. Sci.* **2017**, 391, 175-183.
- [49] G. Beamson, D. Briggs, *J. Chem. Educ.* **1993**, 70 (1), A25.
- [50] D. T. Clark, H. R. Thomas, *J. Polym. Sci.* **1978**, 16 (4), 791-820.
- [51] T. P. Fehlner, *J. Organomet. Chem.* **1977**, 132 (1), C9-C10.
- [52] H. Kiuchi, H. Niwa, M. Kobayashi, Y. Harada, M. Oshima, M. Chokai, Y. Nabae, S. Kuroki, M.-a. Kakimoto, T. Ikeda, K. Terakura, S. Miyata, *Electrochim. Acta* **2012**, 82, 291-295.
- [53] F.-F. Wang, S. Shao, C.-L. Liu, C.-L. Xu, R.-Z. Yang, W.-S. Dong, *Chem. Eng. J.* **2015**, 264, 336-343.
- [54] W. Xing, W. Tu, M. Ou, S. Wu, S. Yin, H. Wang, G. Chen, R. Xu, *ChemSusChem* **2019**, 12 (9), 2029-2034.
- [55] X. Zhou, Y. Li, Y. Xing, J. Li, X. Jiang, *Dalton T.* **2019**, 48 (40), 15068-15073.
- [56] F. Fina, H. Ménard, J. T. S. Irvine, *Phys. Chem. Chem. Phys.* **2015**, 17 (21), 13929-13936.
- [57] S. Cao, J. Jiang, B. Zhu, J. Yu, *Phys. Chem. Chem. Phys.* **2016**, 18 (28), 19457-19463.
- [58] P. Xia, M. Antonietti, B. Zhu, T. Heil, J. Yu, S. Cao, *Adv. Funct. Mater.* **2019**, 29 (15), 1900093.
- [59] A. A. Dippold, T. M. Klapötke, M. Oswald, *Dalton Trans.* **2013**, 42 (31), 11136-11145.
- [60] M. A. Khan, P. Maity, M. Al-Oufi, I. K. Al-Howaish, H. Idriss, *J. Phys. Chem. C* **2018**, 122 (29), 16779-16787.
- [61] A. Senocrate, T.-Y. Yang, G. Gregori, G. Y. Kim, M. Grätzel, J. Maier, *Solid State Ion.* **2018**, 321, 69-74.
- [62] G. Y. Kim, A. Senocrate, T.-Y. Yang, G. Gregori, M. Grätzel, J. Maier, *Nat. Mater.* **2018**, 17 (5), 445-449.

9.3. Supporting information of chapter 6 “Interfacial engineering of PHI for improved photocatalysis”

9.3.1. Experimental Section

Experimental procedure

All used chemicals are reagent grade purity. The carbon nitrides melon and K-PHI were synthesized according to literature.^[1, 2] In summary, melamine (5.0 g, Carl Roth, $\geq 99\%$) was heated in a covered quartz glass boat to 550°C for 12 h with a heating rate of 5°C min⁻¹ in a tube furnace under argon. A yellow product (yield of 2.0-2.8 g) was obtained after cooling to room temperature, which was ground in a ceramic mortar and pestle for analysis and further reactions. For the synthesis of K-PHI in a KSCN salt melt, melon (1.5 g) was thoroughly ground in a ceramic mortar and pestle together with dry KSCN (3.0 g, Carl Roth, $\geq 98.5\%$) that was stored in vacuum (~ 1 mbar) at 140°C overnight. An aluminum oxide boat is filled with the mixture for stepwise heating in a tube furnace under argon to 400°C for 1 h, then 500°C for 30 min at maximal heating rate. After cooling to ambient temperature, KSCN was removed by washing the product repeatedly with deionized water. This product was dried at 60°C in vacuum overnight to yield 1.2-1.6 g of the yellow solid. Mel-PHI was prepared by thoroughly mixing K-PHI (0.5 g), dicyandiamide (DCDA, 0.2 g; Acros organics, $\geq 99.5\%$) and NH₄Cl (0.5 g, Carl Roth, $\geq 99.5\%$) in a ceramic mortar and pestle. The mixture was then heated in a covered aluminum oxide boat under argon to 250°C for 4 h in a tube furnace with a heating rate of 5°C min⁻¹. The product was washed several times with deionized water by centrifugation after it was cooled down to ambient temperature. A yellow product (0.45 g) was obtained after drying in vacuum at 60°C overnight.

Other control samples were prepared to verify if changes of K-PHI occur due to heating. For this purpose K-PHI (0.25 g) was ground in a ceramic mortar and pestle together with DCDA (50 mg or 100 mg) and with or without NH₄Cl (0.25 g). The mixture was filled in a covered aluminum oxide boat and heated in a muffle furnace to 215°C, 250°C, 300°C or 400°C for 4 h with a heating rate of 5°C min⁻¹. After cooling to ambient temperature the above described procedure was repeated again. The sample was washed several times and dried in vacuum at 60°C overnight. A yellow solid was obtained (0.18-0.27 g). Results are discussed in Chapter 4 (Supporting Information).

¹⁵N enriched Mel-PHI was synthesized from ¹⁵N enriched DCDA and ¹⁵N enriched NH₄Cl analogous to the previous described procedure. For this purpose ¹⁵N enriched DCDA was prepared by ion exchange reactions according to a literature known procedure.^[3] In short, an aqueous solution (2 M) of ¹⁵N ammonium chloride was given on an ion exchange resin (Merck, ion exchanger I, H⁺ form) until the eluate reach a pH value of 4-5. The resin was washed with DI water until no Cl⁻ were washed out anymore, which was confirmed with AgNO₃. Afterwards, a 0.5 M Na[N(CN)₂] solution was added to the resin and the eluate was stored over night at room temperature, to evaporate the water. The colorless needle shaped product was used for further synthesis.

¹⁵N enriched ammonium exchange in K-PHI was synthesized by suspending K-PHI (55 mg) in ¹⁵NH₄Cl (150mg) in 1 mL of deionized water. The suspension was sonicated for 1 min and

afterwards stirred for 2 h at room temperature. The suspension was subsequently filtered and replaced by a fresh solution of 150 mg $^{15}\text{NH}_4\text{Cl}$ in 1 mL H_2O twice. Finally, the suspension was filtered and washed three times with ca. 30 mL of water to remove any excess ammonium chloride. After the washing, the filtrate was tested negatively for ammonium or chloride. The light yellow powder was dried.

Instrumental setup

X-ray diffraction patterns were collected using a STOE Stadi P diffractometer ($\text{Cu K}\alpha_1$) in a Debye-Scherrer configuration. FT-IR spectra were performed with a PerkinElmer UATR TWO spectrometer equipped with a diamond crystal.

Diffuse reflectance UV-vis (DR UV-vis) spectra were collected on a Cary 5000 spectrometer (referenced to PTFE or barium sulfate). The diffuse reflectance spectra were converted using the Kubelka Munk function, which is used as a measure of absorbance. The optical band gap was extracted from the Tauc plot, assuming a direct band gap.

Two different NMR machines were used for the measurements. Solid-state ^1H , ^{13}C and ^{15}N nuclear magnetic resonance (NMR) experiments with low frequencies of up to 12.5 kHz were done on a Bruker Avance-III 400 MHz instrument at frequencies of 400.0, 100.61 and 40.53 MHz, respectively. Chemical shifts for ^1H and ^{13}C are referenced indirectly to tetramethylsilane (TMS, $\delta (^1\text{H}, ^{13}\text{C}) = 0.0$ ppm). ^{13}C magic-angle-spinning (MAS) NMR was referenced to adamantane as a secondary reference, while ^{15}N is referenced to nitromethane ($\delta = 0.0$ ppm) and glycine as a secondary reference. Low MAS frequency experiments were performed on a Bruker BL4 double resonance MAS probe in 4 mm OD ZrO_2 spinners. For MAS, rotational frequencies between 8 and 12.5 kHz were used. ^1H spectra were acquired with a simple Bloch Decay experiment (i.e., pulse-acquisition), with a $\pi/2$ pulse of 4.5 μs , and an acquisition delay of 5 s, sufficient for a complete spin-lattice relaxation. The majority of ^{13}C and ^{15}N spectra were acquired using ramped Cross Polarization (CP) accompanied by a composite proton decoupling with the proton RF power of 50 kHz.^[4, 5] Direct excitation quantitative ^{13}C MAS spectra were obtained at the spinning rate of 12.5 kHz, 90° pulse of 3.8 μs , and a recycle delay of 600 s, which was found to be sufficient for a complete recovery of magnetisation. Similar to the CP experiments, the acquisition was accompanied by a composite proton decoupling. Spin-lattice T_1 relaxation times were measured using saturation-recovery method with direct excitation for ^1H , and inversion-recovery method under CP conditions for ^{13}C . Numbers of protons connected to nitrogen atoms were assessed using ^{15}N Cross Polarization Phase Inversion experiment (CPPI),^[6] performed at the spinning rate of 8.0 kHz, cross-polarization time of 2 ms, in a range of dephasing times of 10-500 μs . ^1H - ^{13}C and ^1H - ^{15}N 2D heteronuclear correlation CP MAS spectra were acquired using a Frequency Switched Lee-Goldburg Heteronuclear Correlation^[7, 8] (FSLG HETCOR) experiment. ^1H - ^{13}C FSLG HETCOR spectra were collected at spinning speed of 12.5 kHz and contact time of 250-1000 μs with a total of 48-80 increments in f1-dimension and 512 scans per increment acquired with relaxation delay of 1.5 s. ^1H - ^{15}N - FSLG HETCOR experiments were performed at 12.0 kHz spinning speed, contact times of 500-1000 μs with a total of 80 increments in f1-dimension with 80 scans per increment acquired with relaxation delay of 3 s.

Fast MAS solid-state NMR experiments of the ^{15}N -labeled sample were performed using a Bruker Neo NMR spectrometer operating at a ^1H Larmor frequency of 700.4 MHz using a 1.3 mm triple-resonance MAS probe. The spinning frequency was set to 55.55 kHz, and the temperature was regulated to -5°C , which corresponds to a $\sim 25^\circ\text{C}$ nominal temperature within the rotor. 90° hard pulse length for ^1H and ^{15}N were 1.6 μs and 3.35 μs , respectively. Direct excitation-and-detection ^{15}N measurement was performed with a recycle delay of 60 s without ^1H decoupling and adding up 4096 transients. All 2D experiments with fast MAS frequencies were recorded in a ^1H -detected fashion with a recycle delay of 3 s. In the cross-polarization-based 2D ^1H - ^{15}N experiments, double-quantum CP steps were applied for the magnetization transfer between ^1H and ^{15}N using a 12 kHz 75% tangential shape on ^1H and a 43 kHz rectangular shape on ^{15}N . In the ^1H - ^{15}N refocused insensitive nuclei enhancement by polarization transfer (INEPT), a 2.7 ms delay was used to transfer the magnetization via one-bond ^1H - ^{15}N scalar coupling. During the proton evolution of each experiment, a 10 kHz waltz-16 decoupling was applied on the ^{15}N channel, and a 14 kHz XiX ^1H decoupling was used during the ^{15}N indirect evolution. Direct (^1H) and indirect (^{15}N) acquisition time was 20 and 4.5 ms, respectively. Relaxation experiments were performed in a pseudo-3D fashion using the following delay times: 1, 10, 25, 40 s for the ^{15}N R_1 experiments; 5, 20, 40, 60, 80 ms for the ^{15}N $R_{1\rho}$ experiments; and 5, 8, 12, 15, 20 ms for both the CP-based and refocused-INEPT-based ^1H $R_{1\rho}$ experiments. The on-resonance spin-lock field-strength was 10 kHz for the ^{15}N and 5 kHz for the ^1H $R_{1\rho}$ measurements. The spectra were processed with Topspin 4. For the relaxation analysis, subsequent data manipulation, fitting and error propagation were performed with in-house written Mathematica scripts. Peak intensity uncertainties were propagated to the fitted errors by Monte Carlo analysis with 100 iterations. Relaxation rates were obtained by fitting an exponential decay function in the form of $I = I_0 \exp(-R t)$, where R is R_1 or $R_{1\rho}$.

The ^1H - ^1H NOESY experiment was recorded with a mixing time of 120 ms, 32 scans and 3.6 ms indirect acquisition time recorded in a rotor-synchronized fashion. ^1H - ^1H double-quantum single-quantum (DQSQ) correlation experiment was recorded with the $R_{14}4^2$ symmetry sequence with a simple 180 pulse as a base element. The excitation and the reconversion periods were both four rotor periods (72 μs), and the indirect incrementation time was two times the rotor period. Double-quantum coherence was selected using a four-step phase cycling. The acquisition was done with the State-TPPI scheme.

Sorption measurements were performed on a Quantachrome Autosorb iQ gas sorption analyzer using argon as the sorbent at 87.45 K or nitrogen at 77.35 K. Samples were left in vacuum (10^{-7} mbar) overnight at 150°C to outgas. Brunauer–Emmett–Teller (BET) theory was used to calculate the surface from the adsorption isotherms of the samples.

CHN elemental analyses were performed with a UNICUBE (Elementar Analysensysteme GmbH). The quantification of other elements was done with a Vista Pro Simultaneous ICP-OES Spectrometer combined with axial plasma system as excitation source and echelle polychromator with CCD detector (Varian Darmstadt). The calibration of the ICP-OES Spectrometer was carried out by the addition of standards. Samples were digested in concentrated HNO_3 at 185°C for 25min in a Discover SP-D (CEM GmbH). Data were analyzed by the ICP-Expert software.

For X-ray photoelectron spectroscopy (XPS), the powder samples were fixed on an indium foil and the spectra were collected on an Axis Ultra (Kratos Analytical, Manchester) X-ray photoelectron spectrometer with charge neutralization and a monochromatized Al K α X-ray source. The software CasaXPS 2.3.16 was used to process the spectra, which were referenced with the adventitious carbon 1s peak at 284.80 eV.^[9, 10] The comparison of binding energies was performed with the NIST Standard Reference Database 20 (Version 4.1) unless otherwise specified.

Transmission electron microscopy (TEM) was performed with a Philips CM30 ST (300 kV, LaB6 cathode). The samples were suspended in n-butanol and drop-cast onto a lacey carbon film (Plano). Scanning electron microscopy (SEM) was performed on a Zeiss Merlin electron microscope.

Thermogravimetric analysis (TGA) was performed with a NETZSCH STA 449 F5 Jupiter with a heating rate of 1K/min and an Ar gas flow of 50 ml/min.

The photoluminescence (PL) emission spectra as well as the lifetime of the samples were measured with a double monochromator spectrofluorometer (Edinburgh FLS980). Both steady state and time-resolved photoluminescence spectroscopy were measured at the excitation wavelength $\lambda = 370$ nm. For decay experiments, PL was collected over a 5 nm spectral window centered at $\lambda = 480$ nm. For the fitting of the time-resolved PL, a combination of an exponential function and a Γ function was employed to describe the decay.^[11] Suspensions with concentrations of 0.25 mg mL⁻¹ in water or aqueous methanol (MeOH) or triethanolamine (TEoA) solution (10 vol%) were used for measurements. The suspension was stirred during the measurement to prevent agglomeration and sedimentation.

Zeta-potentials were measured on a Malvern Zetasizer Nano ZS. A suspension of carbon nitride (0.1 mg mL⁻¹) in 10 mM NaCl solution was prepared. Different pH values were adjusted by adding HCl or NaOH. The suspension was sonicated for 10 min before loading in a folded capillary cell (Malvern) for measurement. pH measurements were performed with a Mettler Toledo seven compact pH meter.

Ultraviolet Photoemission Spectroscopy (UPS) measurements were carried out in a UHV system on a PHOIBOS 150 analyzer with a monochromatized HeI lab source (21.2 eV). For UPS measurements the sample was drop-coated from an aqueous suspension on a substrate (Au film on Si) leaving parts of the Au substrate uncovered, which was used as reference. The photoelectrons were collected along the surface normal and with an acceptance angle of $\approx 12^\circ$. For work function measurements the secondary electron cut-off and the Fermi level were determined by applying a bias of -10 V to the sample. The intersection of the linear fitted line of the spectrum with the x-axis ($y=0$) was used to extract the cut-off energy. Work functions of PHI were extracted from the difference of the kinetic energy of the electrons (21.2 eV) and the cut-off energy and Fermi edge energy of PHI on Au. To analyze the valence band edge the background spectrum of Au was subtracted from the UPS spectrum of PHI at Au, to only see the effect of PHI. For this purpose both spectra (Au and PHI on Au) were normalized to the Au signal at 6.05 eV. Since the Au sample measured here had already water adsorbed, this is automatically subtracted with the Au spectrum from PHI measurements.

The static contact angle measurements were performed on a Krüss Drop Shape Analyzer goniometer (DSA 100S). After pressing 6 mm pellets of K-PHI and Mel-PHI (2 bar) approximately 2 μL of liquid (DI water or DI water with 10 vol% TEOA) was deposited on the sample with a flat end needle (Sterican, 0.40 x 25 mm, Blunt Gauge 27) connected syringe. Contact angle measurements were recorded for 40 s, whereas a settled, stable value was reached after \sim 30 s. All measurements were performed at room temperature (\sim 23 $^{\circ}\text{C}$).

High pressure liquid chromatography with mass spectrometry (HPLC-MS) was performed on an Agilent 1290 Infinity II LC system connected to an Agilent InfinityLab LC/MSD XT single quadrupole mass spectrometer. A multimode ESI-APCI ionization source was used for ionization and mass spectra were recorded between 100 and 600 m/z (positive, step size 0.2 Da). Chromatographic separation was achieved on an Agilent Zorbax SB-CN column (2.1x50 mm, 1.8 μL) at 40 $^{\circ}\text{C}$ with mixture of acetonitrile:water, both containing 0.1% formic acid, as solvent (temporal gradient acetonitrile:water 20:80 (0 min) \rightarrow 50:50 (2.00 min) \rightarrow 5:95 (2.01 min) until 2.50 min. Or: acetonitrile:water 20:80 (0 min) \rightarrow 80:20 (4.50 min) \rightarrow 5:95 at 4.51 min until 5.00 min) and a total solvent flow of 0.5 mL min^{-1} . An aliquot (100 μL) of the sample was diluted with acetonitrile:water 80:20 (1 mL) and filtered through a syringe filter (0.2 μm , PTFE) before injecting an appropriate volume (0.2-3 μL) into the HPLC-MS.

Quantum-chemical calculation

Atom positions and lattices of all periodic structures were optimized on RI-PBE-D3/def2-TZVP^[12-15] level of theory using an acceleration scheme based on the resolution of the identity (RI) technique and the continuous fast multipole method (CFMM^[16-18]) implemented^[19, 20] in Turbomole version V7.3.^[21, 22]

The CFMM uses multipole moments of maximum order 20, together with a well-separateness value of 3 and a basis function extent threshold of $10\text{E-}9$ a.u. Grid 7 was used for the numerical integration of the exchange-correlation term. The norm of the gradient was converged to $10\text{E-}4$ a.u. and the total energy to $10\text{E-}8$ Hartree within the structure optimization using the gamma point approximation.

Structures for all investigated molecular compounds were optimized on PBE0-D3/def2-TZVP^[13, 14, 23, 24] level of theory (Turbomole). Subsequent frequency calculations were performed on the same level of theory to ensure all minima to be true minima on the potential energy hypersurface.

Spin Densities were obtained on the same level of theory, using the optimized ground state geometry with a subsequent single-point calculation with an additional electron to yield a radical-anionic state as a model for the reduced state and an additional hole to yield a radical cationic state as a model for the oxidized state.

Excitonic States as Difference Densities were obtained on TD-PBE0/def2-TZVP level of theory using the lowest excited singlet state. Red isosurfaces depict regions with lower electron density in the excited state whereas green isosurfaces represent higher electron density in the excited state, both in comparison to the electron density of the ground state.

NMR chemical shifts were obtained on B97-2/pcSseg-2^[25, 26] level of theory using the FermiONs++^[27, 28] program package.

Parameters for molecular dynamics simulations for the PHI pore were prepared using antechamber.^[29] Force field minimizations and dynamics were performed using the NAMD^[30, 31] program package and GAFF^[32] parameters. Periodic boundary conditions and particle mesh Ewald summation (PME) with a cutoff value of 12 Å were employed.

The modeled PHI pore was minimized using the conjugate gradient algorithm in 10000 steps by constraining the coordinates for the pore excluding the hydrogen atoms that were allowed to relax along with the present solvent molecules. The system was then heated to 300 K in 30 picoseconds and equilibrated subsequently for 30 nanoseconds with time steps of 2 femtoseconds employing the SETTLE algorithm. The appendix for the model PHI pore calculations can be found in Figure S3.70-S3.74.

Photocatalysis procedure

Unless stated otherwise, the photocatalytic experiments were performed in a glass reactor with a quartz glass window for illumination, as previously described.^[1, 33] The reactor is thermostated to 25°C by a circulated water jacket around the reactor. When platinum free reactions were used for dark photocatalysis, the glass reactor was cleaned with aqua regia before photocatalytic experiments. A xenon lamp (Newport, 300 W) equipped with a water filter, a full spectrum mirror (2000 nm > λ > 200 nm), followed by an Air Mass (AM) 1.5 G filter was used for top-illumination of the reactor under 1 sun conditions (100 mW cm⁻²), if not otherwise stated. For a standard photocatalytic experiment, the carbon nitride powder (14 mg) was suspended in a solution of water (18 mL), methanol (MeOH) or triethanolamine (TEoA) (2 mL) and dihydrogen hexachloroplatinate (4.0 or 1.75 wt% aqueous solution, Aldrich). The headspace of the reactor was evacuated and argon backfilled several times to avoid influence of oxygen or nitrogen. During illumination the suspension was stirred. The platinum co-catalyst is formed via *in-situ* photo-reduction from hexachloroplatinate. To measure the hydrogen evolution during illumination, the headspace of the reactor was periodically sampled and the amount of evolved gases was quantified by gas chromatography (Thermo Scientific TRACE GC Ultra). This gas chromatograph is equipped with a TCD detector using argon as the carrier gas. The spent photocatalyst was recovered by washing with water and centrifugation for 3 times of the used suspension. After drying in vacuum at 60°C overnight, the obtained solid was ground for further analysis.

The platinum loading and donor optimization experiments were performed in a smaller reaction vessel (septum-capped glass vials). To this end, MeI-PHI (7 mg), water (9 mL), electron donor (1 mL) and a variable amount of dihydrogen hexachloroplatinate solution were prepared. The vessel was purged with Ar for 10 min prior to every experiment to avoid oxygen contamination. During illumination with a xenon lamp for 3 h the suspension was stirred. Hydrogen evolution rates in the headspace were quantified by gas chromatography, as described before. The trends of hydrogen evolution rate being observed in the small test vials were identical to the bigger photo reactor used for photocatalytic experiments shown in the manuscript.

The continuous flow GC measurements were performed with He (6.0) as carrier gas using a Shimadzu GCMSBID QP-2020, equipped with an oven containing a duplicated circuit with MS-5a sieve columns with a Barrier Discharge Ionization detector (BID) and a mass spectrometer (MS).

The setup and the measurement method was similar to that described in a previously published work.^[34] The gas phase was analyzed every 15 min at the beginning and later every 30 min.

Photoelectrochemistry was performed in a closed glass reactor equipped with a quartz window for side illumination as referenced earlier.^[35] 1 sun illumination (AM 1.5 G) was provided by a SCIENCETECH LightLine A4 solar simulator. An Ag/AgCl reference electrode with saturated KCl (+0.197 V vs. NHE) was used and a Pt plate acted as counter electrode. Mel-PHI nanoparticles were deposited on transparent fluorine doped tin oxide (FTO) by drop casting as reported previously.^[35] To remove dissolved oxygen, the electrolyte was purged with >99% pure Ar prior to the respective measurement through a porous glass frit for at least 30 min. The electrochemical measurements were recorded and analyzed using an IVIUM CompactStat potentiostat and the IviuSoft software.

The bulk Apparent Quantum Yield (AQY) of each material was calculated as the total number of (monoatomic) hydrogen production ($2R_{H_2}$) divided by the number of incident photon flux, for either AM 1.5 G or band pass filter spectral distributions.^[34] An analogous setup as in the photocatalysis experiment was used, with top illumination. A total volume of with 10 ml was used with a suspension of similar density as in the photocatalysis experiments (7 mg for Mel-PHI and 10 mg for K-PHI). The illumination was provided with a xenon lamp (300 W) and a band pass filter of 400 nm (± 20 nm) (1.4 mW cm^{-2}). The incident power was measured with a thermal power sensor (Thorlabs C-series). The simplified equations for said monochromatic source are^[36]:

$$AQY(\%) = 100 \times \left(2 \times R_{H_2} / \phi \right)$$

$$\phi = 3600 \times I \times A \times \left(\lambda / h \times c \right) / N_a$$

Where:

- R_{H_2} : Maximum HER rate / mol h⁻¹
- ϕ : Incident photon rate in / mol h⁻¹
- h, c, N_a : Planck's Constant, speed of light, and Avogadro's number in SI units
- λ : LED wavelength (4.0×10^{-7} / m)
- I : Measured light intensity (0.0014 / W cm⁻²)
- A : Illumination area (6.4 / cm²)

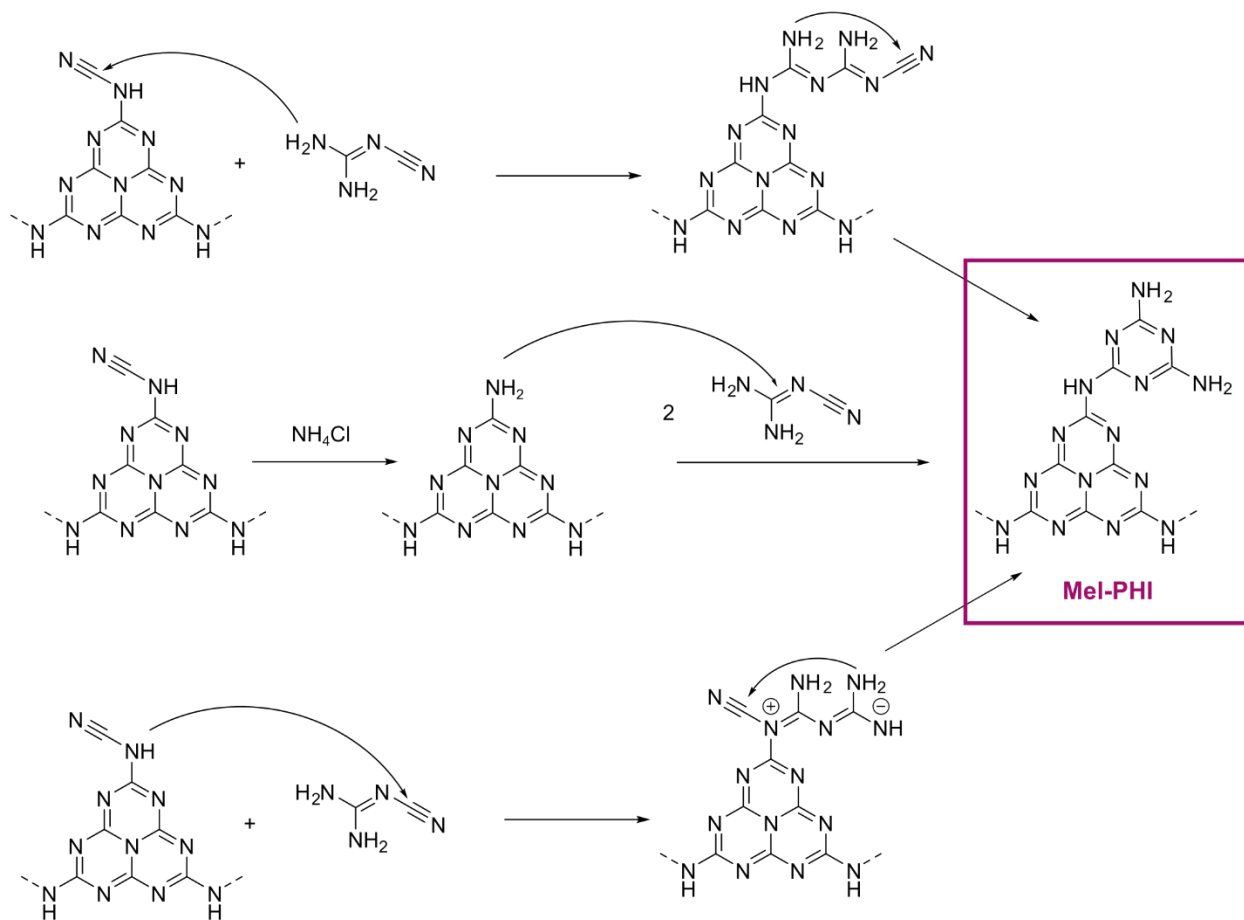
As R_{H_2} is a function of time that has activation and deactivation trends for each material, the asymptotic maximum H₂ rate was considered for the AQY calculation. The standard deviation of the AQY value was around 5%.

When taking the whole solar spectrum into account and not just one wavelength, the overall light-to-chemical conversion (STH) can be calculated, neglecting the donor reaction^[37]:

$$STH = \frac{R_{H_2} \times \Delta G}{P_{sun} \times A}$$

With R_{H_2} being the rate of hydrogen evolution, ΔG the Gibbs free energy of hydrogen formation (237 kJ mol^{-1}), P_{sun} the energy flux at AM 1.5 G condition (100 mW cm^{-2}) and A the illuminated area.

9.3.2. Proposed mechanism of Mel-PHI formation



Scheme S3.1: Suggested mechanism of Mel-PHI formation.

The suggested mechanism is analogous to intermediate steps in published mechanism for graphitic carbon nitride formation. [1, 38]

9.3.3. Alternative synthesis conditions

Synthesis at 215 °C and 250 °C with different amounts of DCDA and ammonium chloride

Ammonium chloride is reported in literature to be an efficient exfoliation agent^[39, 40] or to introduce defects in the carbon nitride backbone at synthesis temperature of 550 °C.^[41] This temperature is higher than the boiling point of ammonium chloride (520 °C)^[42], so that the gas formation and evaporation is causing the exfoliation or defects in the carbon nitride.

For this reason, different lower synthesis temperatures (215 °C, 250 °C, 300 °C and 400 °C) were screened for melamine functionalizing PHI. The first synthesis temperature was chosen at 215 °C, since this is slightly above the melting point of dicyandiamide (DCDA) around 210 °C.^[43] The condensation of dicyandiamide to melamine is taking place around 230-240 °C.^[44, 45] To analyze if NH₄Cl is also necessary for the transformation of NCN-groups to melamine, the synthesis was performed with and without the salt being present. Ammonium chloride sublimates with decomposition starting already at 283 °C and is followed by a second step at 326 °C.^[46] This is within the sublimation and condensation range of melamine from 297 to 390 °C.^[47] At 335 °C the dimerization of melamine to melam (di-melamine adduct) is happening, which is forming melem (heptazine monomer) by further heating to 390 °C.^[38, 44] Hence, an increase of synthesis temperature to 250 °C and 300 °C was used to track possible changes in product formation, and control experiments were carried out at 400 °C.

In summary, the sample synthesized without ammonium chloride does not show any changes compared to the previous K-PHI in PXRD and IR analysis (Figure S3.1, S3.3). Only a slightly larger stacking distance can be seen in the PXRD of 27.75° 2θ (3.21 Å), which was described in a previous paper of our group^[2], due to the interaction with water, which partially evaporates during heating and expands the layer distance. Some additional reflections in addition to PHI can be detected, which are caused by melamine formed *in situ* as a side phase that is not completely removed from the sample.

Ammonium chloride might act as mineralizer/activator in the functionalization of PHI with melamine. So in case of the ammonium chloride containing synthesis, changes in structure in the PXRD are observable at 250 °C with 20 wt% DCDA (Figure S3.1), since DCDA is completely melted at this temperature, forming a liquid reaction medium. The stacking peak is shifted to slightly lower 2θ values, which is a hint for successful functionalization. At low 2θ values an additional peak at 27.2° is pointing to unbound melamine intercalated into the PHI network, similar to a previously published paper.^[48] This is a formed side phase, which can be removed by washing with boiling water as described later. As shown in Figure S3.1 the simulated XRD pattern fits quite well to the additional peaks in the PXRD pattern. Only some intensities do not fit well, since the simulated XRD pattern is based on electron diffraction data and some disorder in the crystal structure can be assumed, similar to K-PHI^[2], but especially because not every pore may be filled by a melamine molecule. Looking at the IR measurements changes can be seen already at 215°C (Figure S3.3). The N≡C vibration at 2100 cm⁻¹ disappears (red area in Figure S3.3), pointing toward a reaction of the NCN-group with ammonium chloride, since no effect was observed in presence of DCDA only. Ammonia was reported to cause C-N bond cleavage in carbon nitrides in presence of water and under pressure.^[49] It might be that this process is partially taking place

during the heating of K-PHI with NH_4Cl as well, since water could not be fully removed from the sample. In presence of ammonia de-polymerization of carbon nitriles is theoretically possible.^[50] In addition some reports in literature show a reduction of $\text{N}\equiv\text{C}$ signals due to post-synthetic annealing as well, even in the absence of additional ammonium chloride.^[51] This hints to a comparable weak bond between PHI and NCN, which is likely to be cleaved in presence of ammonium chloride. In the fingerprint region (blue area, in the range of $1000\text{-}1700\text{ cm}^{-1}$), some changes in signal intensity for 215 and 250 °C synthesis temperature are also observable, which point to the formation of melamine, which is either bound covalently to PHI or located within the pores.

To conclude, ammonium chloride assists melamine formation and temperatures above 215 °C are needed to complete the reaction and attach melamine covalently at the PHI backbone. The higher the DCDA amount, the higher the yield of the reaction, even though some melamine is formed as a side phase, which can be washed out afterwards. Heating solely K-PHI to 250 °C does not cause structural changes besides peak broadening in the PXRD, which means K-PHI is stable and does not show a phase transition during heating besides partial amorphization or exfoliation (Figure S3.2). This increase in the layer distance and disorder might be caused by water evaporation due to heating.^[2] Since some structural changes could be observed, the optical properties of the materials were analyzed as well by UV-vis spectroscopy. No relevant changes in the absorption behavior of the materials can be detected (Figure S3.4).

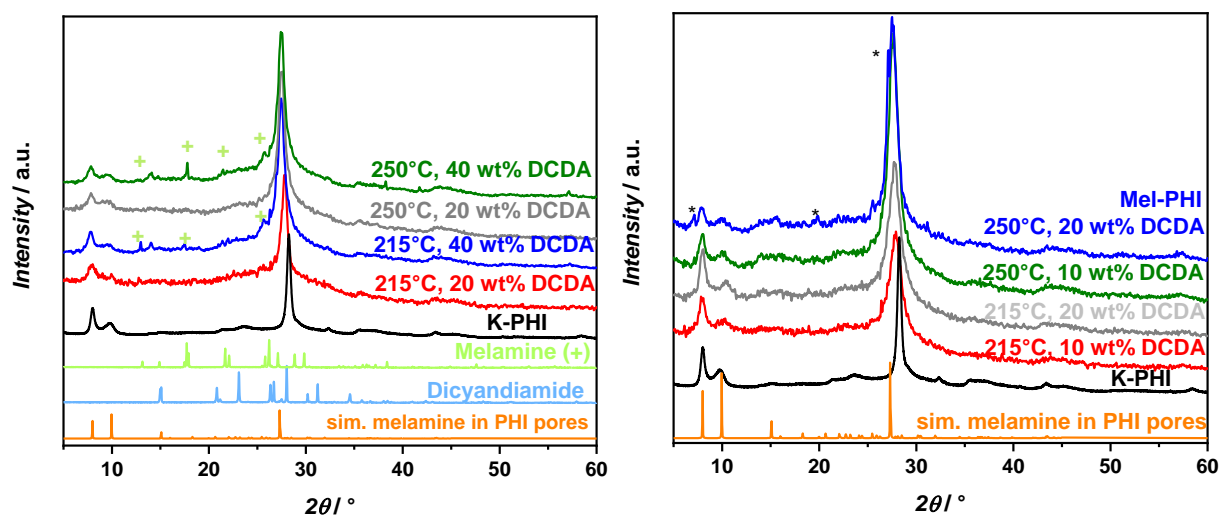


Figure S3.1: PXRD pattern of products of various synthesis conditions. K-PHI heated up to 215 °C and 250 °C with 20/40 wt% DCDA (left) or 10/20 wt% DCDA in presence of ammonium chloride (right). The + marks the side phase of pure melamine and the star the side phase of melamine in the pores of PHI.

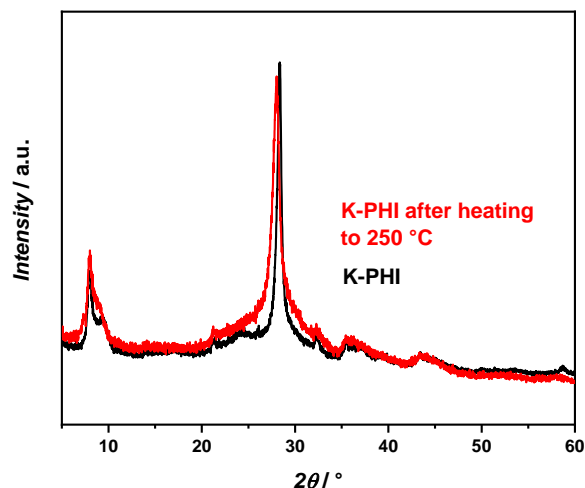


Figure S3.2: PXRD pattern of K-PHI before and after heating to 250 °C for 4 h. No significant changes could be observed, besides peak broadening, which is likely due to partially exfoliation driven by evaporating water.

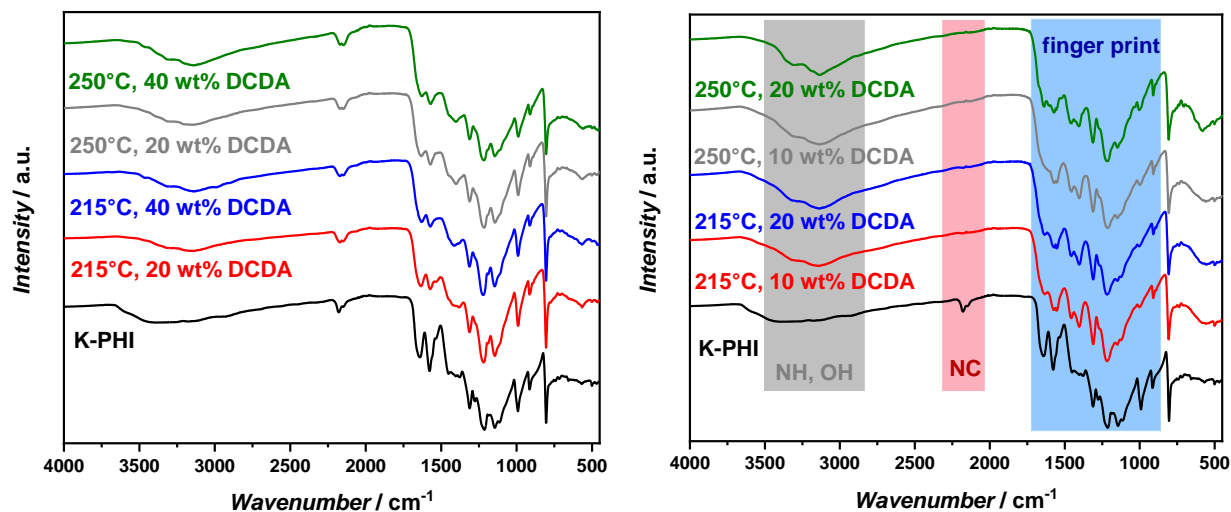


Figure S3.3: FT-IR spectra of products of various synthesis conditions. K-PHI heated up to 215 °C and 250 °C with 20/40 wt% DCDA (left) or 10/20 wt% DCDA in the presence of ammonium chloride (right).

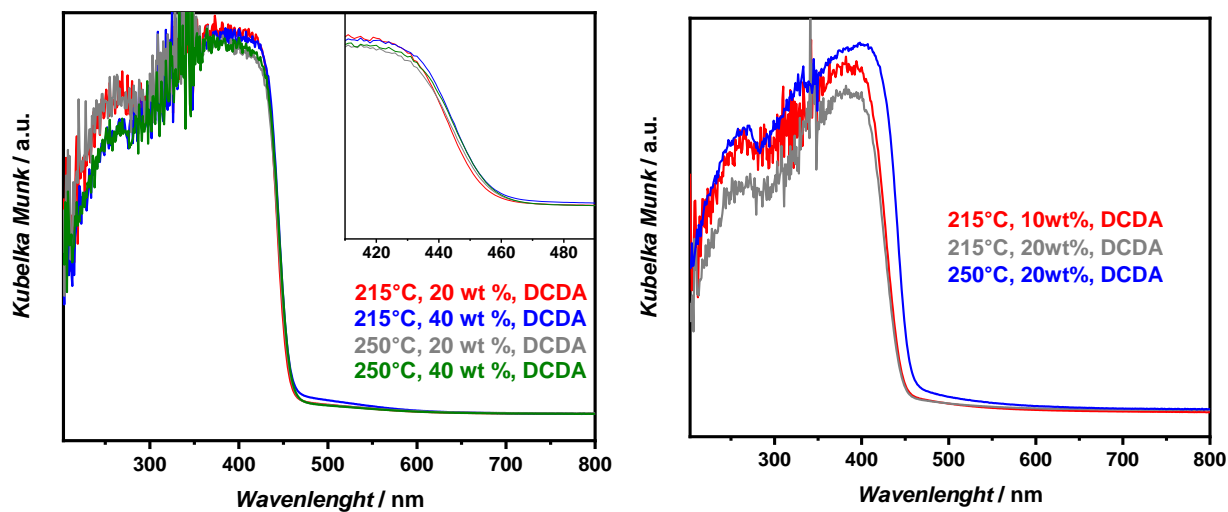


Figure S3.4: UV-vis spectra of products of various synthesis conditions for Mel-PHI. K-PHI heated up to 215 °C and 250 °C with 20/40 wt% DCDA (left) or 10/20 wt% DCDA in the presence of ammonium chloride (right).

Synthesis at 300 °C and 400 °C with different amounts of DCDA and ammonium chloride

Higher synthesis temperatures of 300 and 400 °C were also tested for the Mel-PHI synthesis. At 300 °C melamine is condensing to form melam and ammonium chloride is decomposing and partially sublimating. At 400 °C also the formation of melem is enabled. The intensity of in-plane peaks in PXRD was reduced after heating the starting materials to higher temperatures with and without ammonium chloride, which might affect in-plane crystallinity (Figure S3.5).^[52-54] In all cases, the stacking peak around 27° 2 θ is shifted to smaller angles and is broadened compared to K-PHI for the 300 and 400 °C samples. Hence, not only the in-plane but also the stacking order is reduced similar to 215 and 250 °C samples. In accordance to literature for longer heating an even stronger broadening of the stacking peak, a reduction of stacking distance and, especially in presence of ammonium chloride, a higher amount of amorphitization are expected.^[41]

When ammonium chloride is also present in the synthesis at 300 °C, the formation of a side phase can be observed with 10 and 20 wt% DCDA, which might be melam.^[55] After the heat treatment at 400 °C an additional peak around 14° 2 θ appears in the products synthesized with and without ammonium chloride, indicating an eclipsed stacking shift of the 2D PHI layers. This shift was already described in a previous paper and is correlated with the release of pore-water causing different interactions between the layers.^[2]

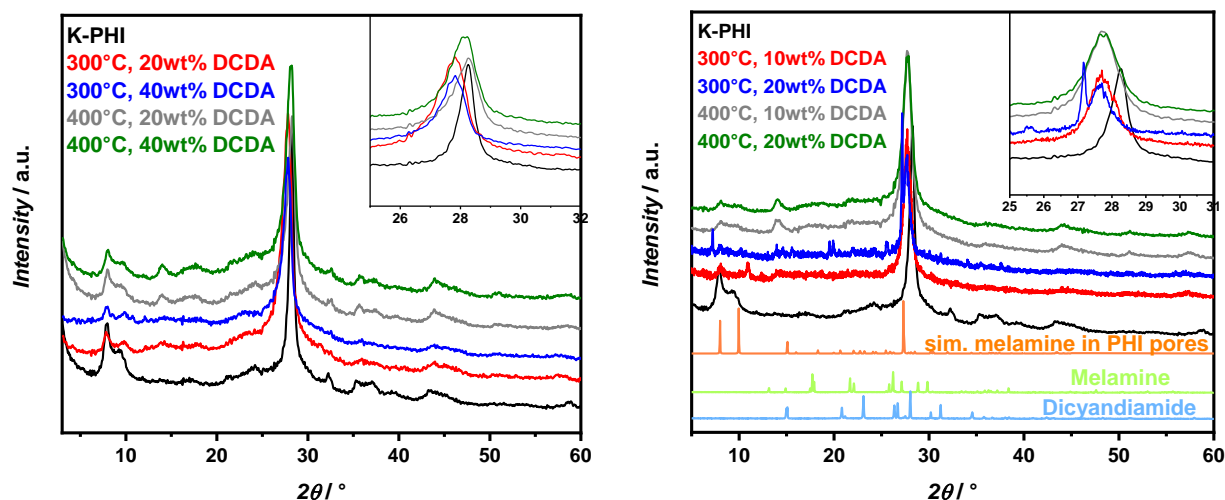


Figure S3.5: PXRD pattern of products of various synthesis conditions. K-PHI heated up to 300 °C and 400 °C with 20/40 wt% DCDA (left) or 10/20 wt% DCDA in the presence of ammonium chloride (right).

IR analysis of samples treated without ammonium chloride showed no difference in the structure, in agreement with the PXRD results (Figure S3.6). In presence of the salt, compounds heated to 400 °C indicate some minor changes in the finger print region and slightly reduced N≡C vibrations in comparison to K-PHI. 300 °C samples obtained sharper vibrations between 3500-3000 cm⁻¹ indicating more distinct NH₂ groups, as it would be the case for a melam side phase. No significant N≡C vibration at 2100 cm⁻¹ is visible for 300 °C, 10 wt% DCDA. Nevertheless, when increasing the DCDA amount the vibration at 2100 cm⁻¹ rises again, which can point to decomposition products of melamine or the heptazine rings. In combination with some additional changes in the finger print region, it can be assumed that NCN-group start forming again, possibly due to decomposition of the melamine functionalization or the condensation to melem.

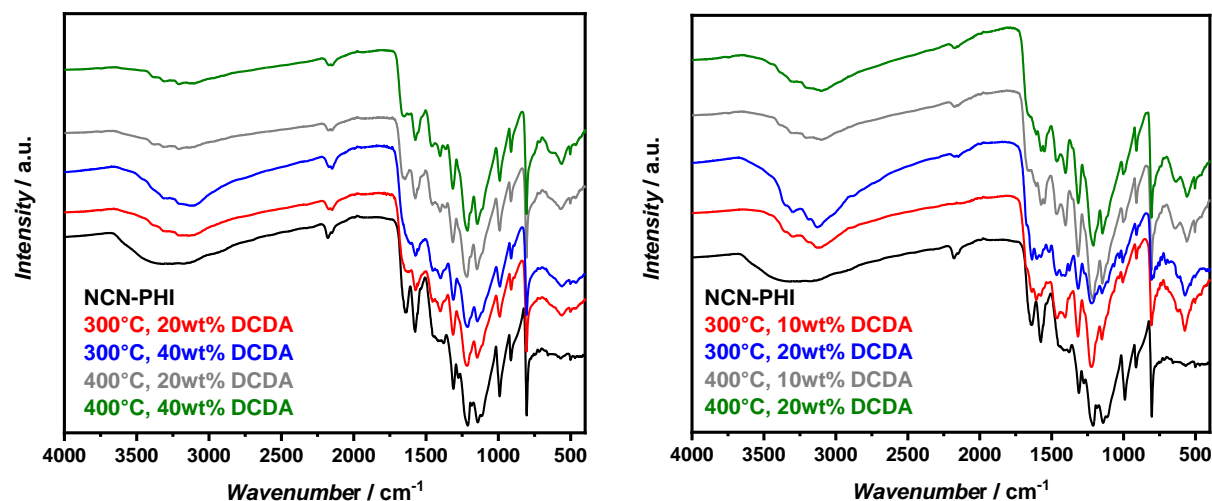


Figure S3.6: FT-IR spectra of products of various synthesis conditions. K-PHI heated up to 300 °C and 400 °C with 20/40 wt% DCDA (left) or 10/20 wt% DCDA in the presence of ammonium chloride (right).

UV-vis analysis of the different samples reveals no significant change in the absorption edges. Only the samples at 300 °C with ammonium chloride during synthesis have a slightly smaller absorption edge (at 453 nm instead of 460 nm) and therefore a slightly larger optical band gap.

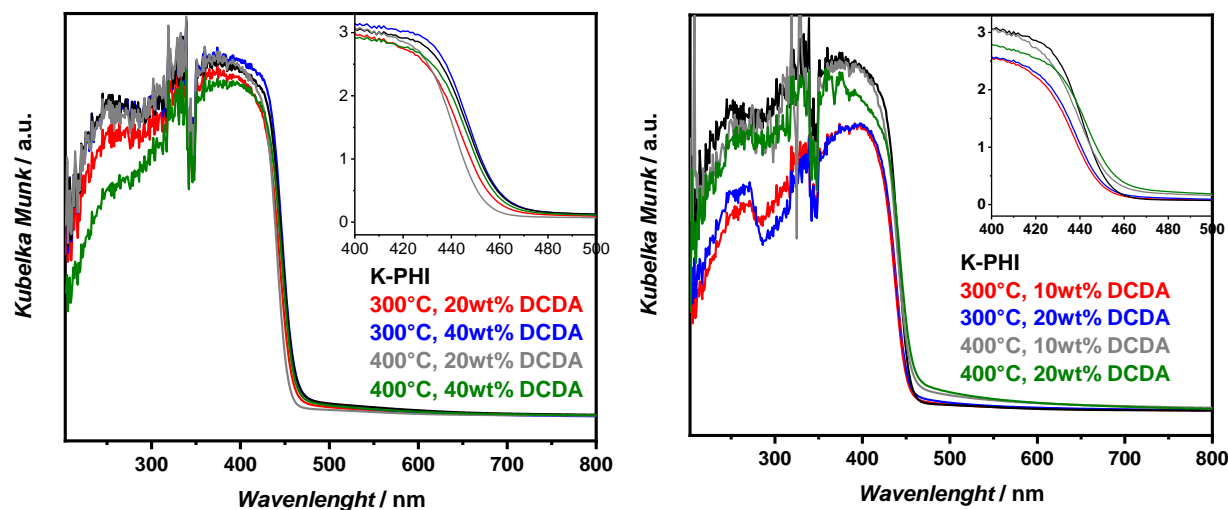


Figure S3.7: UV-vis spectra of products of various synthesis conditions. K-PHI heated up to 300 °C and 400 °C with 20/40 wt% DCDA (left) or 10/20 wt% DCDA in the presence of ammonium chloride (right).

9.3.4. Side phase analysis

Directly after synthesis a side phase was detectable in Mel-PHI. This side phase was visible in SEM (Figure S3.9), PXRD and TEM data, with comparably sharp reflections in contrast to PHI. The significant TEM reflexes were located at 12.4, 7.12 and 6.07 Å, pointing to a melamine adduct $C_6N_{11}H_{10}Cl \cdot 0.5NH_4Cl$ (Figure S3.8).^[54, 56] This triclinic structure consist of single-protonated melamium ions ($C_6N_{11}H_{10}^+$) and chloride as counterion, where the melamium ions are interacting via four hydrogen bonds. The simulated selected area diffraction (SAED) pattern of the [100] zone axis of this structure is in good agreement with the measured data, confirming the presence of the side phase. Similar reflections were found in PXRD (Figure S3.10) (marked by blue areas). In addition a second side phase can be observed, which is melamine in the pores of the PHI network.^[48] The stacking peak of the not washed Mel-PHI phase has a shoulder at $27.2^\circ 2\theta$, which is most probably caused by not covalently bound melamine in the pores. In FT-IR spectroscopy no significant changes between the washed and non-washed phase can be found. Nevertheless, the unbound melamine within the pores and the melamium adduct phase could also be detected by ^{15}N CP MAS NMR, which is depicted in Figure S3.10. The colored areas highlight the peaks, which are caused due to the two side phases. These side phases could be washed away with boiling water, so that only covalently bound melamine remained.

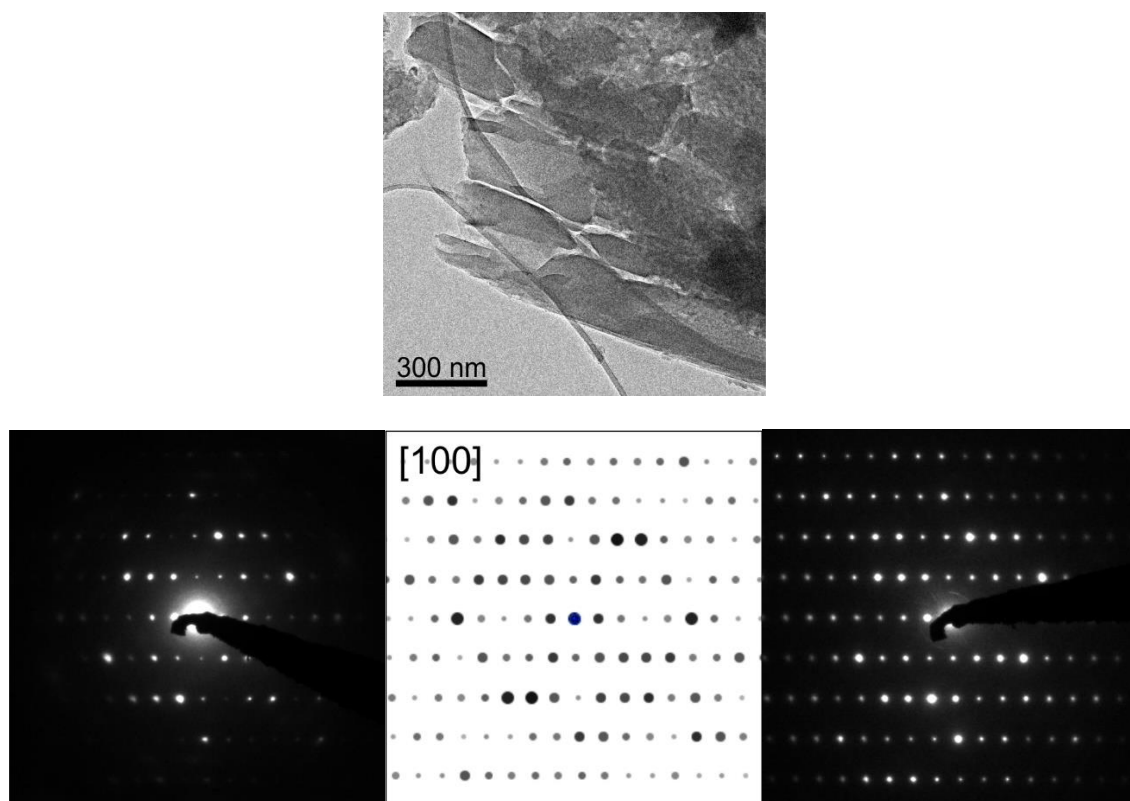


Figure S3.8: TEM image of the crystalline side phase in Mel-PHI, which is $C_6N_{11}H_{10}Cl \cdot 0.5NH_4Cl$ (top). SAED images and simulated SAED pattern of the [100] zone axis of $C_6N_{11}H_{10}Cl \cdot 0.5NH_4Cl$ (bottom).

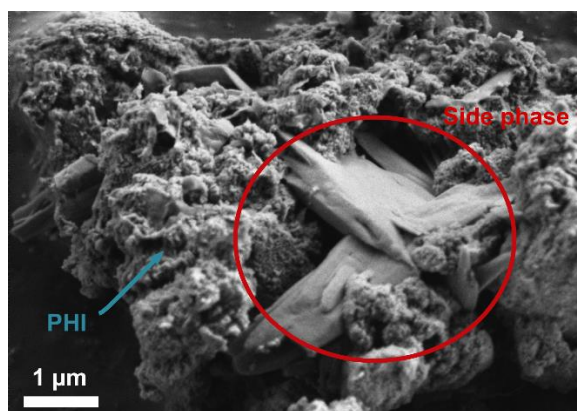


Figure S3.9: SEM image of Mel-PHI (marked with blue arrow) with side phase (red circle) (smooth surface particles).

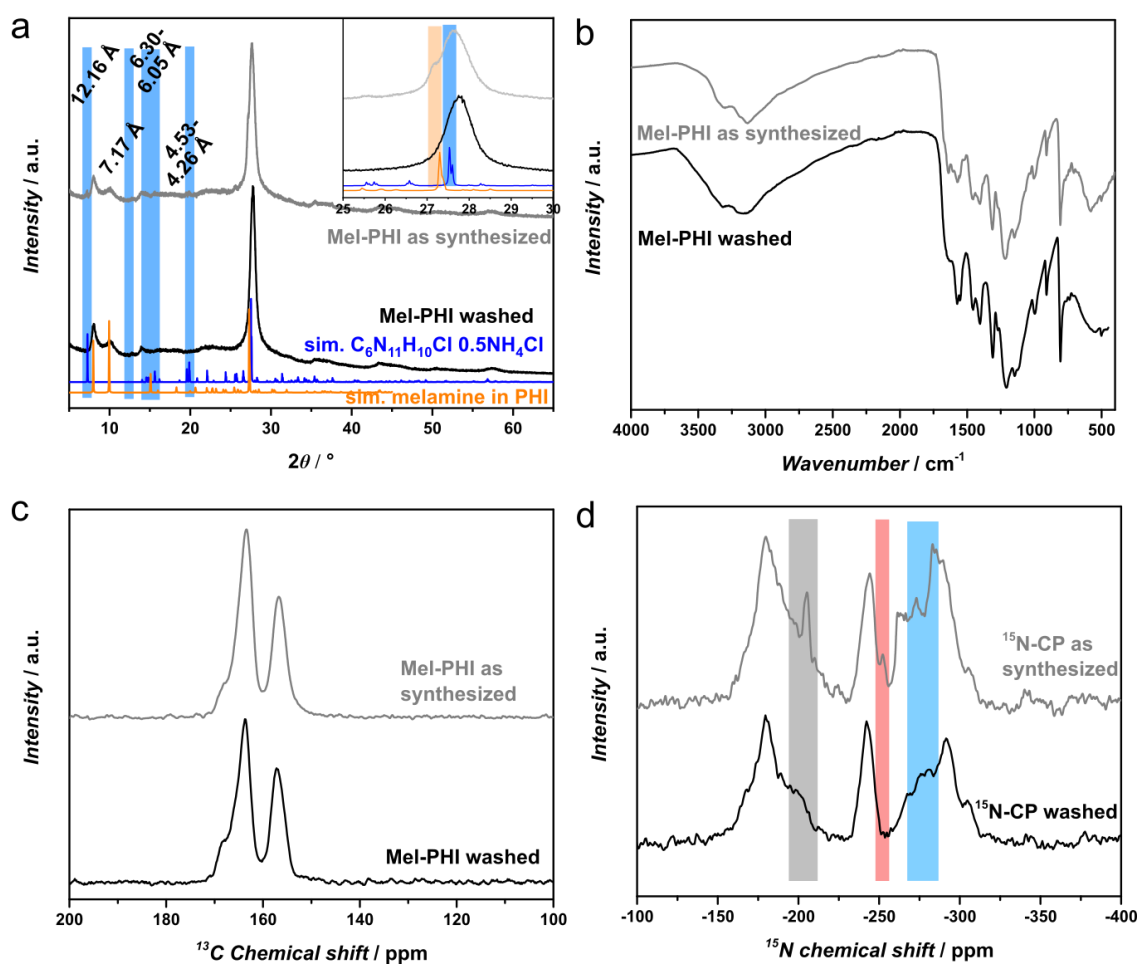


Figure S3.10: Analysis of Mel-PHI side phase. a) PXRD of Mel-PHI as synthesized and washed. Blue areas highlighting the differences; b) FT-IR of Mel-PHI as-synthesized and washed; c) $\{^1\text{H}\}^{13}\text{C}$ -CP ssNMR of Mel-PHI as-synthesized and washed; d) $\{^1\text{H}\}^{15}\text{N}$ -CP ssNMR of Mel-PHI as-synthesized and washed. Grey (N-C), red (N-H) and blue (NH_2) areas highlighting the differences.

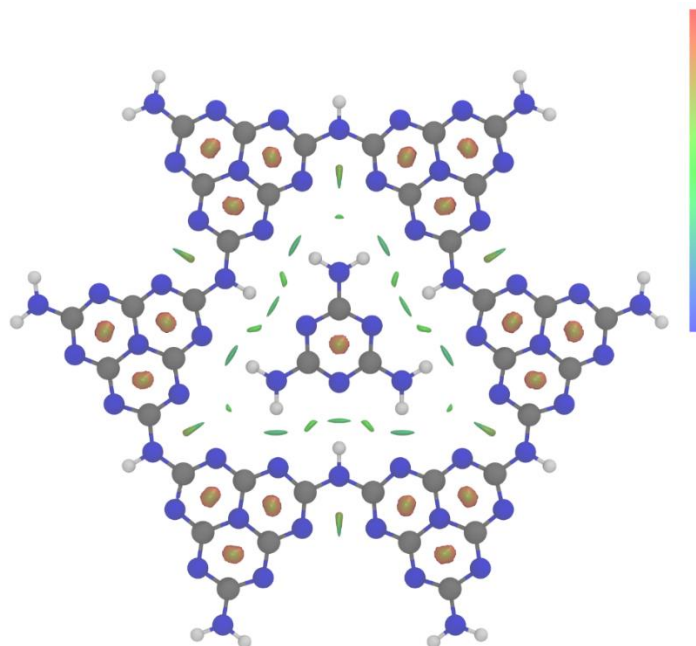


Figure S3.11: Calculated non-covalent interaction plots using the embedded Mel-PHI pore model. Interactions between the PHI pore and the embedded melamine unit are visualized as isosurfaces, color coded to the type of interaction: Strong and attractive interactions (blue), weak dispersive interactions (green), strong and repulsive interactions (red).

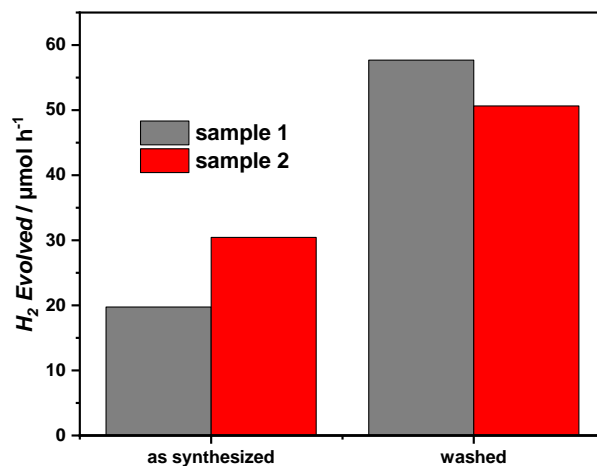


Figure S3.12: Photocatalytic hydrogen evolution of Mel-PHI in the presence of TEoA and with optimized Pt loading of the as-synthesized sample and the washed Mel-PHI of two different batches (sample 1 and 2).

The non-bound melamine and/or the melamium adduct phase is assumed to have some adverse effects on photocatalytic hydrogen evolution behavior. One reason for this might be that the unbound melamine in the pores acts as quenching agent for light absorption, defect side or recombination center.^[57, 58] In the following, the compounds of the washing solution are analyzed further.

Analysis of residue of washing solution

To separate the side phase, Mel-PHI is washed with boiling water. The washing solution was dried and analyzed further by IR and PXRD (Figure S3.13). It can be seen that a mixture of different compounds is washed out, like KCl, NH_4Cl , melamine and other CN_x materials. From IR it can also be observed that most probably small particles of Mel-PHI are present as well.

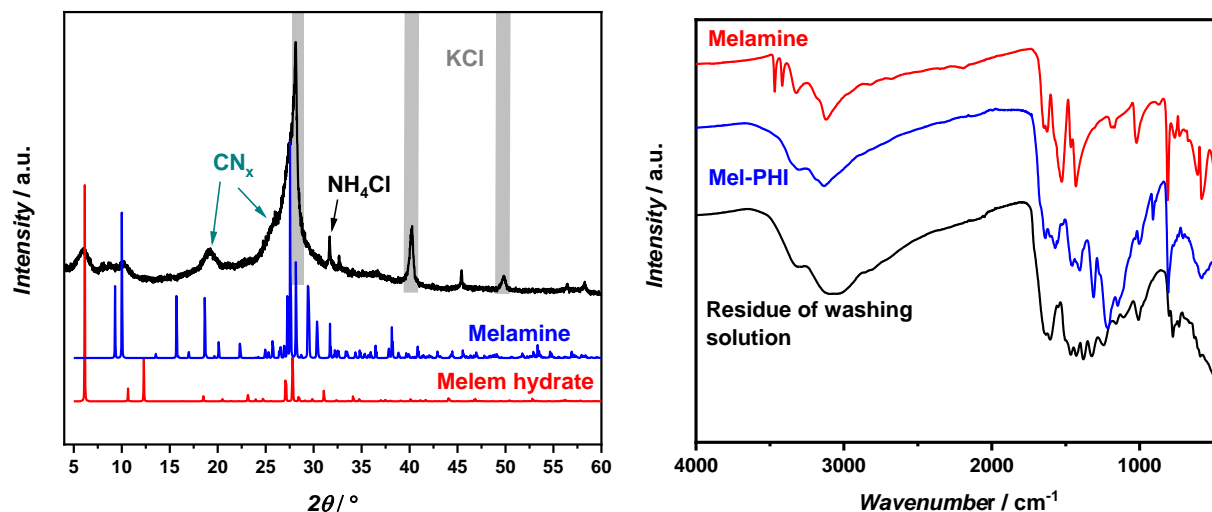


Figure S3.13: Analysis of the residue of washing solution of Mel-PHI: PXRD of the residue with calculated XRD pattern of melamine and melem hydrate (left); FT-IR of residue in comparison to melamine and Mel-PHI (right)

9.3.5. Composition and structural analysis

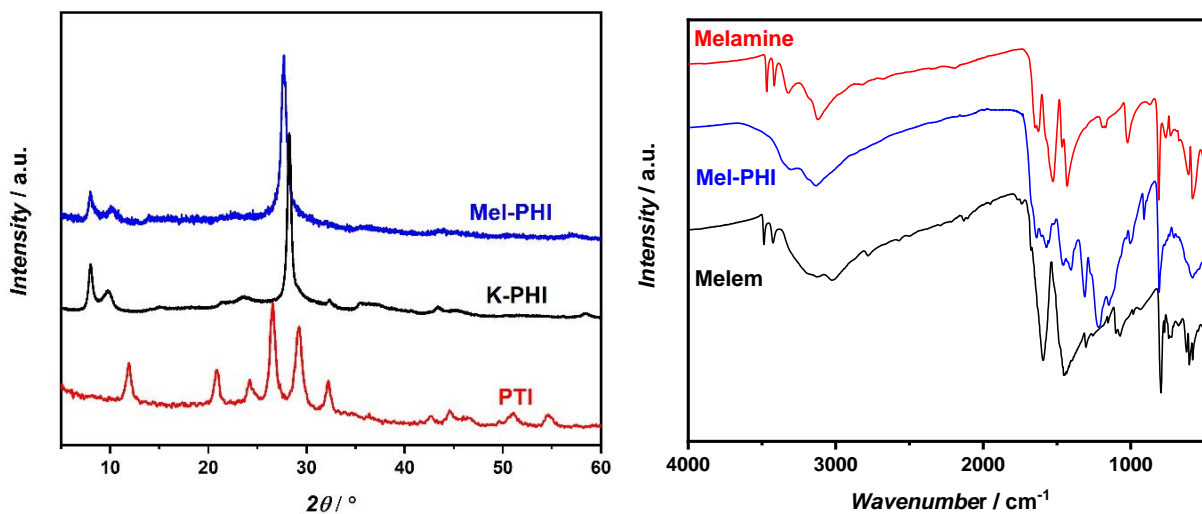


Figure S3.14: PXRD data of Mel-PHI, K-PHI and poly(triazine imide) (PTI) in comparison (left) and FT-IR measurements of melamine, melem and Mel-PHI (right).

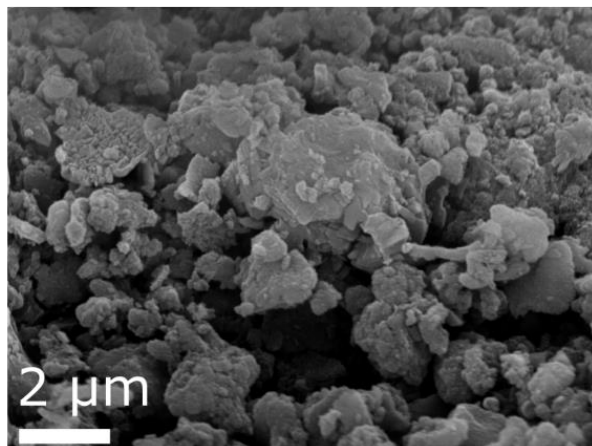


Figure S3.15: SEM image of Mel-PHI.

NMR analysis

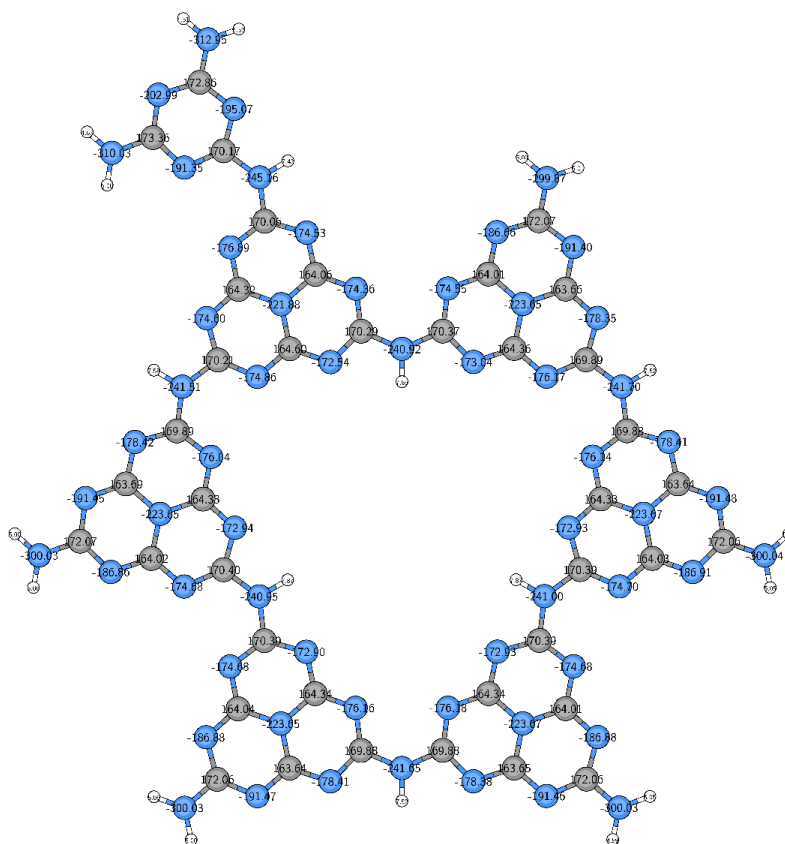


Figure S3.16: Calculated NMR chemical shifts of the Mel-PHI pore model, obtained on PBE0-D3/def2-TZVP//B97-2/pcsSeg-2 level of theory.

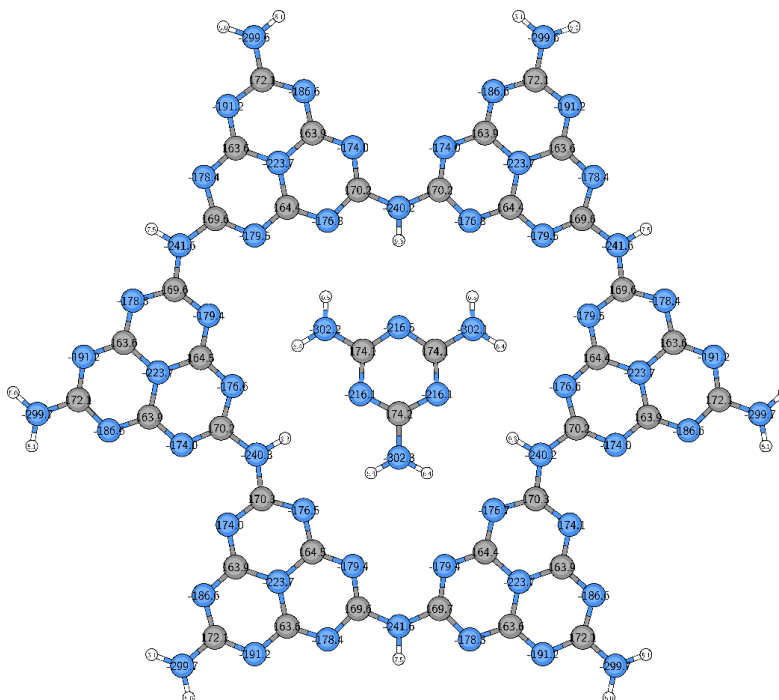


Figure S3.17: Calculated NMR Chemical shifts of the embedded Mel-PHI pore model, obtained on PBE0-D3/def2-TZVP//B97-2/pcsSeg-2 level of theory.

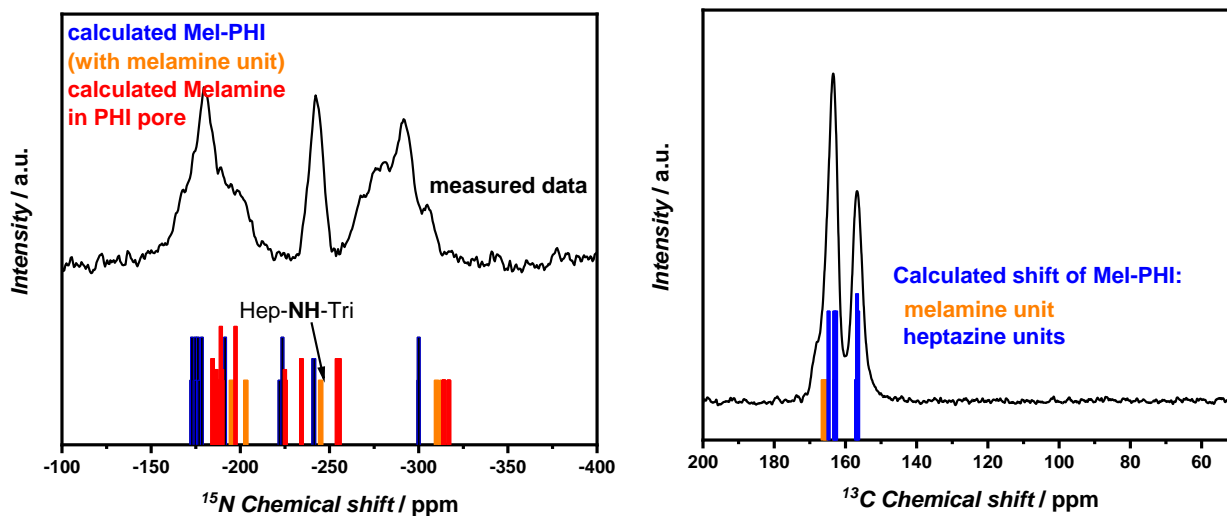


Figure S3.18: $\{^1\text{H}\}^{15}\text{N}$ and ^{13}C CP MAS NMR spectra of Mel-PHI measured (black lines) and calculated positions on B97-2/pcsSeg-2 level of theory (red). ^{13}C MAS NMR shifted by 7 ppm from calculated values to fit the experiment.

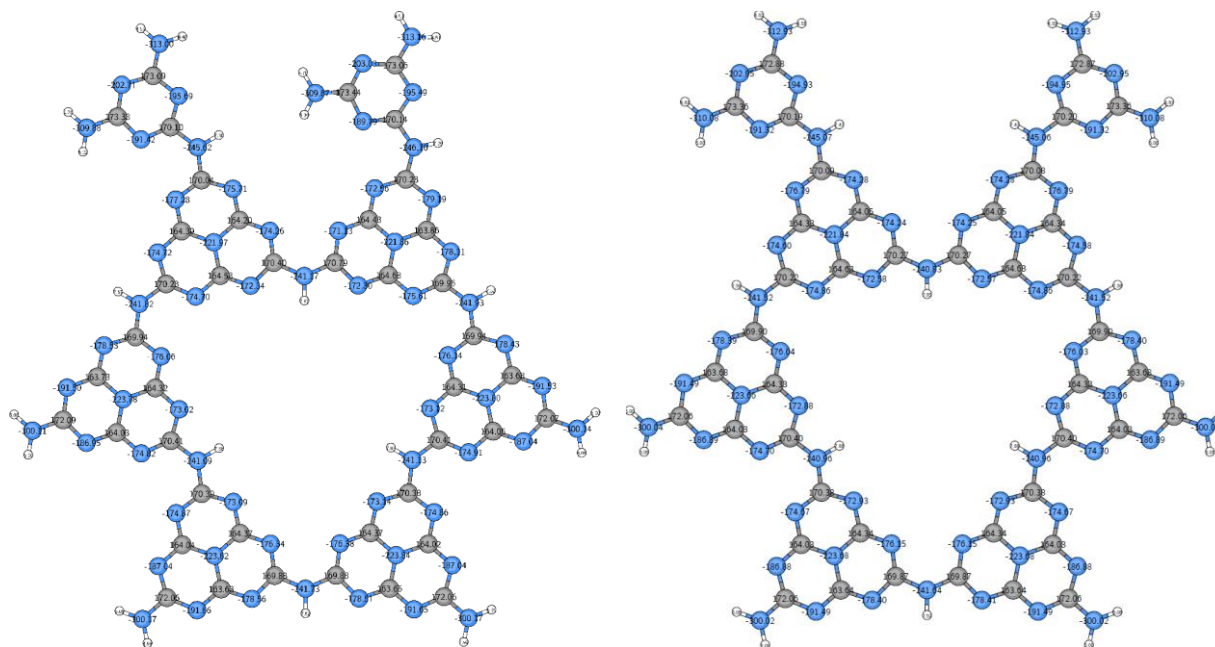


Figure S3.19: Calculated NMR Chemical shifts of the embedded syn-2-Mel-PHI (left) and anti-2-Mel-PHI (right) pore model, obtained on PBE0-D3/def2-TZVP//B97-2/pcsSeg-2 level of theory.

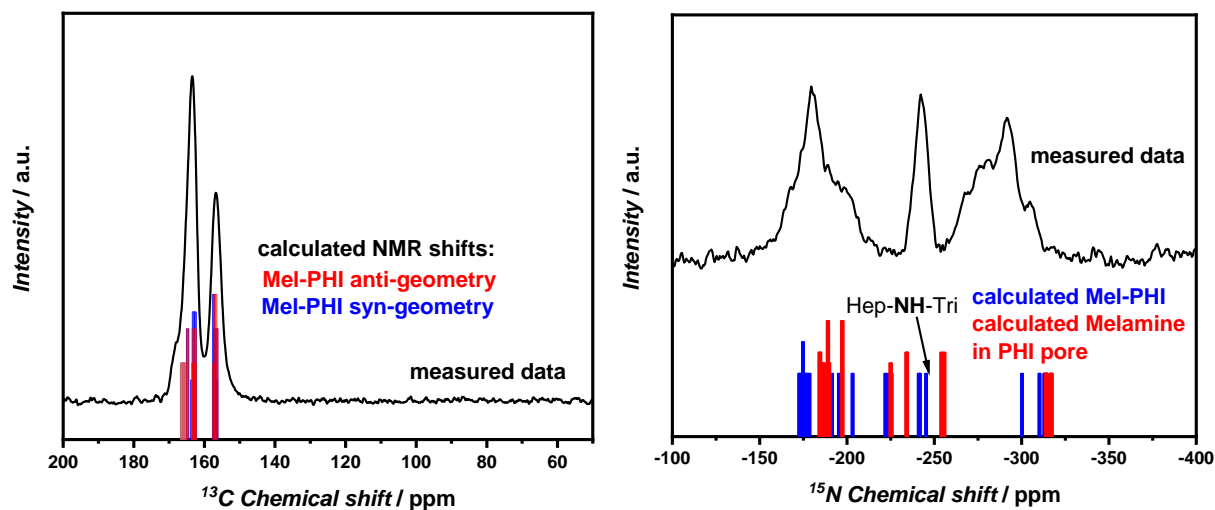


Figure S3.20: $\{^1\text{H}\}^{13}\text{C}$ and ^{15}N CP MAS NMR spectra of Mel-PHI measured (black lines) and calculated positions on B97-2/pcsSeg-2 level of theory (red). ^{13}C MAS NMR shifted by 7 ppm from calculated values to ease the comparison to the experiment.

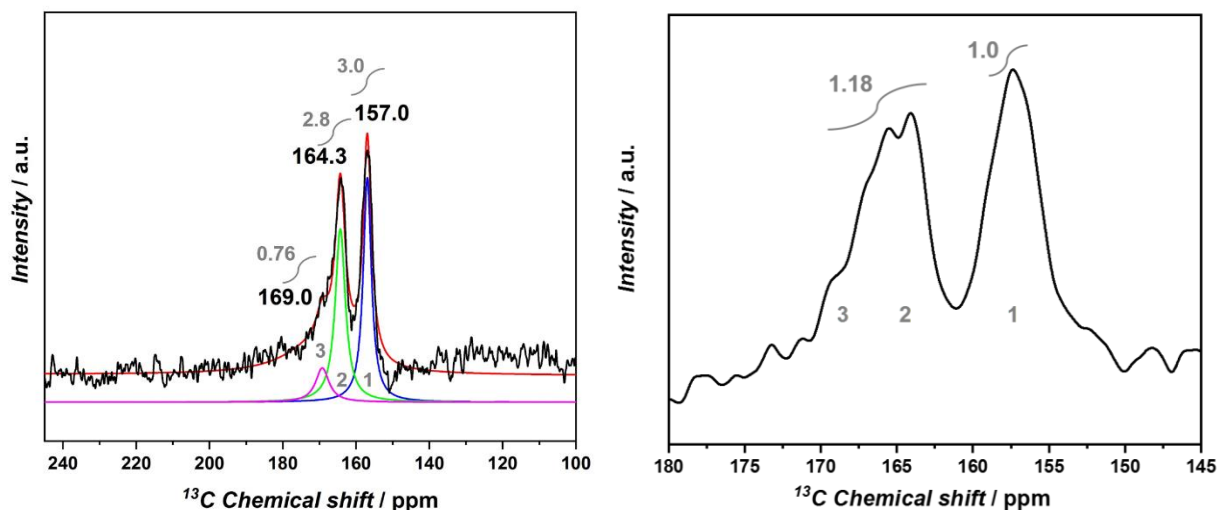


Figure S3.21: ^{13}C direct MAS NMR spectra of Mel-PHI with different peak contributions with a recycle delay of 4 s (left) and 25 s (right).

To estimate the triazine:heptazine ratio, direct ^{13}C excitation and detection was used with a recycle delay of 4 s (Figure S3.21 left) and 25 s (Figure S3.21 right). The signal intensity ratio between the peak at 157 ppm and the ones between 169 and 164 ppm is 1:1.18. The former peak belongs only to the heptazine unit, with no corresponding carbon in melamine, while the latter peaks belong to both triazine and heptazine. If there were only heptazine present then the expected peak intensity ratio would be 1:1. The surplus of 0.18 could be associated with the triazine signals, so that there is for every 2 heptazine carbon atoms 0.18 melamine carbon atoms, i.e. for every six heptazine units (36 carbons) there is one melamine unit (3 carbons). This result is also in accordance with the results of the elemental analysis (Table S3.1). It can be estimated to be in the range of every 5-6 heptazine unit being functionalized with melamine.

^1H - ^1H NOESY experiments (Figure S3.22) are used to track the interactions of protons in space with longer distances of around 5-10 Å.^[59] Cross peaks can be observed for all the different protons, which might be a hint to a homogenous sample. In addition, peaks for water (orange area), NH (red area) or NH_2 (blue area) interactions are visible. The strongest interaction can be seen between water and NH bonds (or NH_4^+), which can be explained by water being present in the pores, allowing strong interactions with the NH bridges via hydrogen bonds. Also in the ^1H - ^1H DQSQ spectrum the appearance of the H_2O signal clearly indicates that there are water molecules in the pores. Additionally, there are crosspeaks between the NH, NH_2 groups and NH_4^+ indicating that the ammonium ions are in close contact with the imide bridges of the pores.

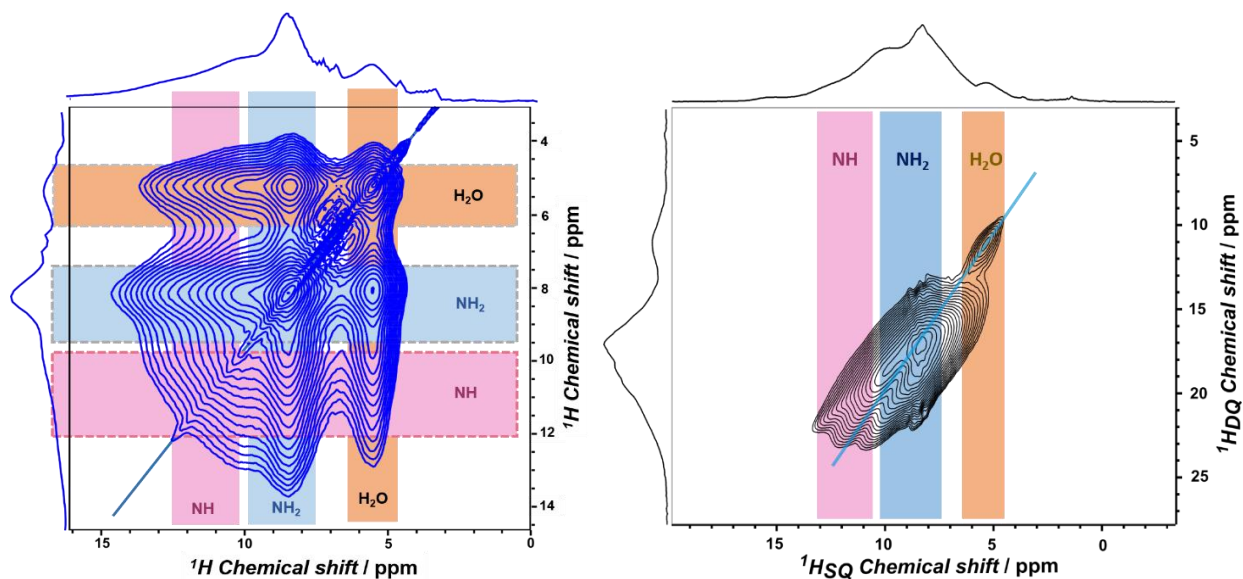


Figure S3.22: ^1H - ^1H NOESY spectrum of ^{15}N enriched melamine in Mel-PHI with 55 kHz spinning frequency and a mixing time of 120 ms (left). ^1H - ^1H DQSQ spectrum of ^{15}N enriched melamine in Mel-PHI with 55 kHz spinning frequency.

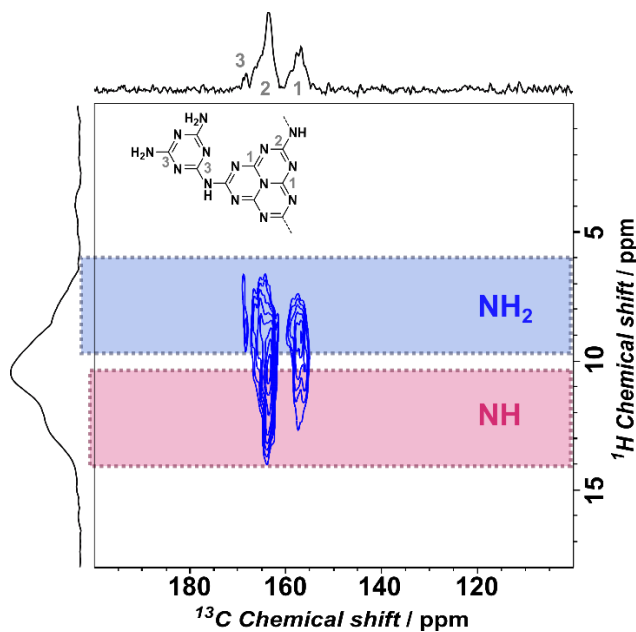


Figure S3.23: ^1H - ^{13}C HETCOR MAS NMR of ^{15}N enriched melamine in Mel-PHI with 12.5 kHz spinning velocity and contact times of 500 μs . In comparison to longer contact times of 1 ms, like in Figure 6.3c, no changes are observed, besides a broader ^1H signal.

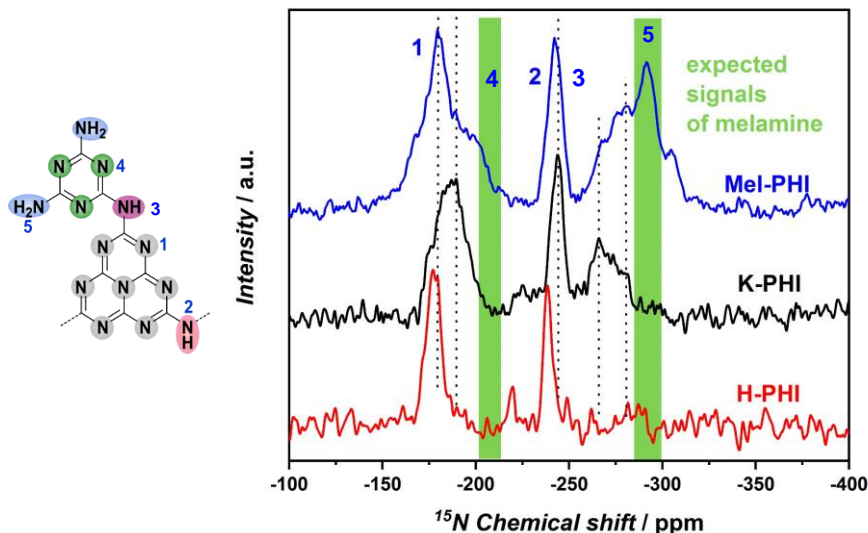


Figure S3.24: $\{^1\text{H}\}^{15}\text{N}$ CP MAS NMR spectra of Mel-PHI (blue), K-PHI (black), and H-PHI (red). The green areas show the expected ^{15}N signal for melamine. The region from -265 ppm to -300 ppm is overrepresented, since in a CP measurement the NH_2 appear more pronounced. Black dotted lines show the shift of the peak maxima.

NMR measurements of ^{15}N enriched melamine in Mel-PHI

Due to the high amount of contributions to the NH and NH_2 signals in ^{15}N experiments, a deconvolution method by fitting single contributions was used to analyze the signal behaviors in ^{15}N CPPI experiments individually (Figure S3.25). It has to be stated though that the fitting is not ideal and that certain values for single peaks should not be understood in absolute terms. ^{15}N CPPI NMR also can be used to observe the time dependence of the polarization inversion dynamics of the nitrogen atoms (Figure 6.3d).^[60, 61] The signals at -207.4, -214.1 and -343.6 ppm do not change in intensity during the experiment, which can be attributed to tertiary or quaternary nitrogen atoms caused by the triazine ring and ammonium ions (green area).^[1, 33, 62] The signals between -305.5 and -275.8 ppm follow a two-step decay process. The crossover points of the decays over the inversion time are around -0.4, close to the theoretical value of $-1/3$ of NH_2 (blue area). The signals at -265.2 and -254.5 ppm also decay with a two steps process, having a crossover point of approximately -0.1, which is close to the theoretical value 0 for NH -groups (red area).^[1, 33, 62]

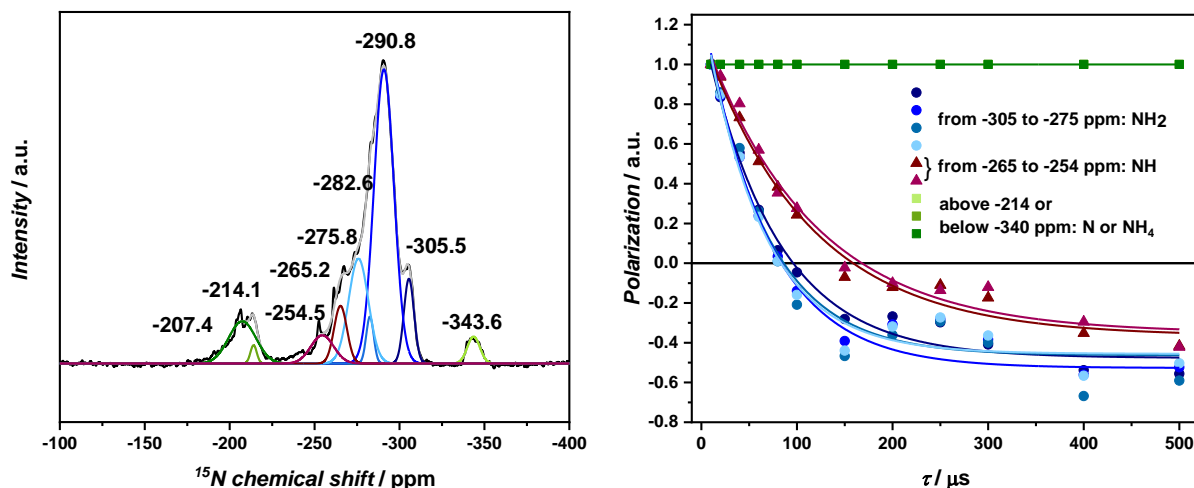


Figure S3.25: ^{15}N CPPI NMR of ^{15}N enriched melamine in Mel-PHI with resolution of different signals overlapping each other for further analysis of time dependent polarization experiments (left) and ^{15}N CPPI of Mel-PHI with time dependent polarization of different signals contributing to ^{15}N CPPI.

Furthermore, the interaction of protons and nitrogen was analyzed by 2D ^1H - ^{15}N HETCOR NMR and ^1H - ^{15}N HSQC vs NHN. In Figure S3.26, a comparison between non-enriched and ^{15}N -enriched Mel-PHI (at the melamine and NH_4^+ only) in a 2D nitrogen-proton NMR is shown. In principle, the same signals can be observed, which are caused by NH (from -230 ppm to -260 ppm) and NH_2 (from -260 ppm to -320 ppm) moieties. Besides, the spectrum of the enriched sample shows a small signal of NH_4^+ around -350 ppm for ^{15}N , which might be located in the pores to balance the charges of the negatively charge PHI network.^[63]

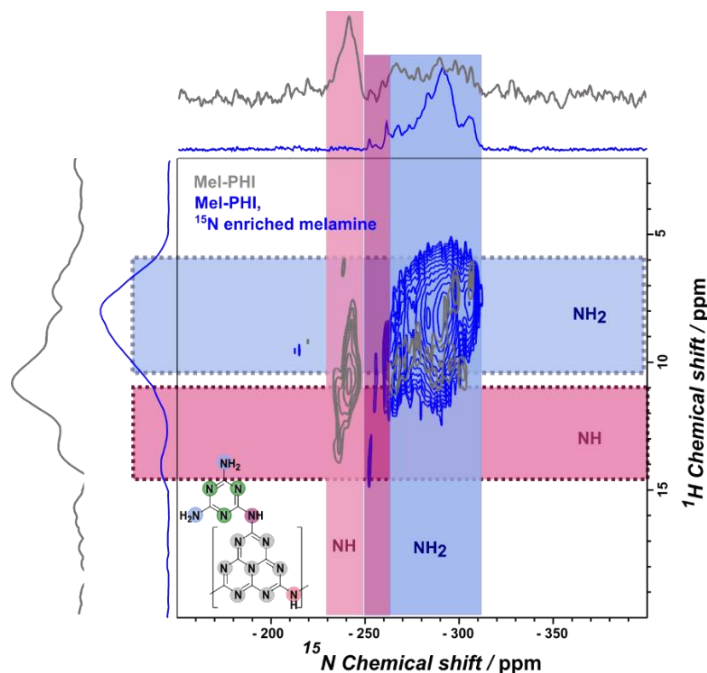


Figure S3.26: ^1H - ^{15}N HETCOR MAS NMR of Mel-PHI (grey) and ^{15}N enriched melamine in Mel-PHI (blue) with 12 kHz spinning frequency and a CP contact time of 500 μs .

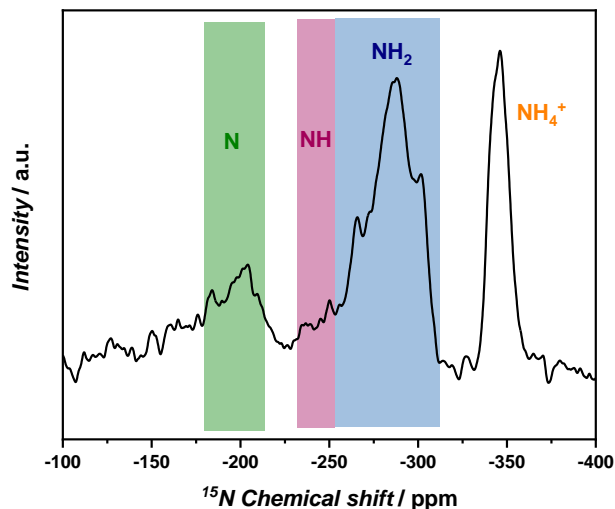


Figure S3.27: ^{15}N direct MAS NMR of ^{15}N enriched melamine in Mel-PHI with 55.5 kHz spinning frequency measured with a recycle delay of 60 s.

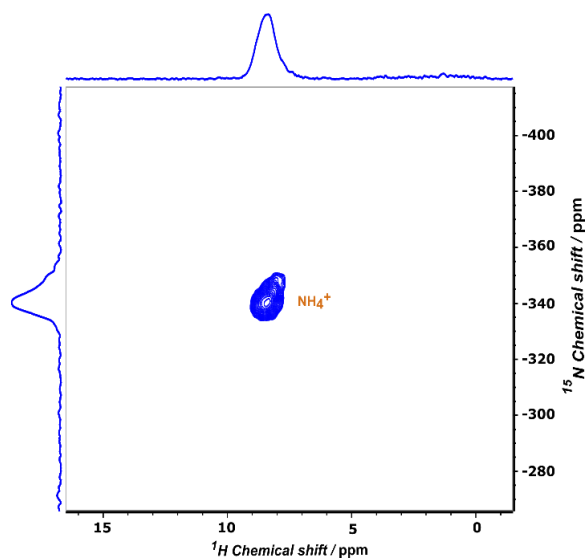


Figure S3.28: ^1H - ^{15}N HSQC MAS NMR of ^{15}N enriched melamine in Mel-PHI with 55.5 kHz spinning. Only mobile NH_4^+ can be observed in this spectra and none of the rigid heptazine or triazine units, confirming the covalently bond triazine unit at the carbon nitride backbone.

In ^1H - ^{15}N HSQC spectrum (Figure S3.28) only signals of direct N-H bonds show up, which are part of an extremely mobile moiety, for example if they belong to a quickly rotating ammonium ion. The ^1H and ^{15}N shifts support the idea that the observed peak in the HSQC spectrum belongs to the NH_4^+ ion, however, the relatively broad ^1H (850 Hz) and ^{15}N (650 Hz) linewidths suggest semi-permanent interactions with the backbone (freely moving ammonium ions would lead to solution-state-like sharp signals).

Computational studies suggest the melamine molecule would require 15 to 18 kJ mol^{-1} for a motion within the range of 2 Å along the pores (Figure S3.29, S3.30), which translates to an average dwell time of maximal 151 ps. Such dynamic behavior would lead to motional averaging of dipolar interactions and hence the signals would disappear in the CP-based spectrum, and appear in the INEPT-based spectrum, which however is not the case.

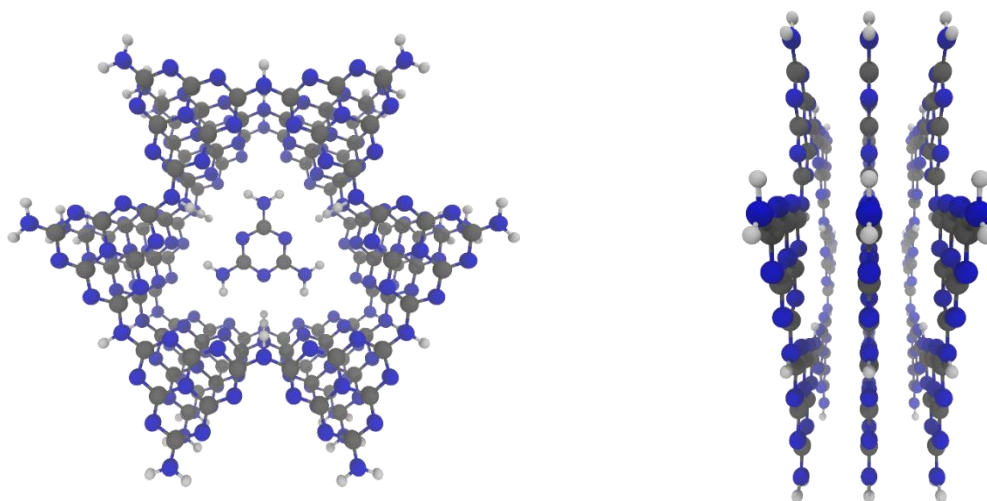


Figure S3.29: Structural model for the melamine in a PHI pore model system, obtained by inserting the optimized H-PHI pore model into a pore canal of three π -stacked optimized H-PHI pore models (view from top (left) and from the side (right)).

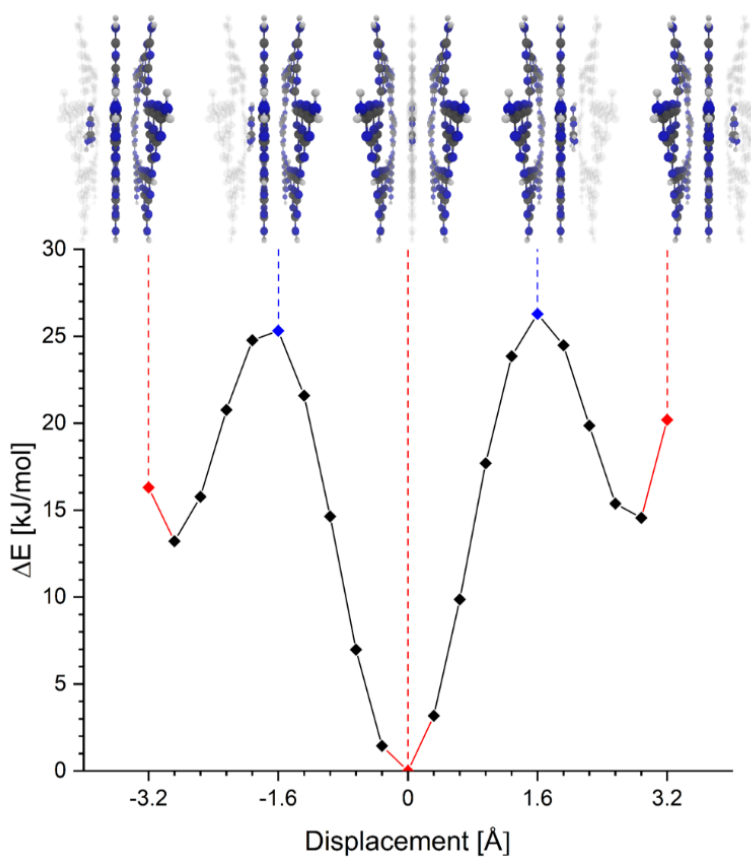


Figure S3.30: Total energy profile for the displacement scan of the inserted melamine unit, obtained on PBE0-D3/def2-TZVP level of theory with structures for the movement of the inserted melamine unit inside the PHI pore canal. Displacement along the z-axis is designated below.

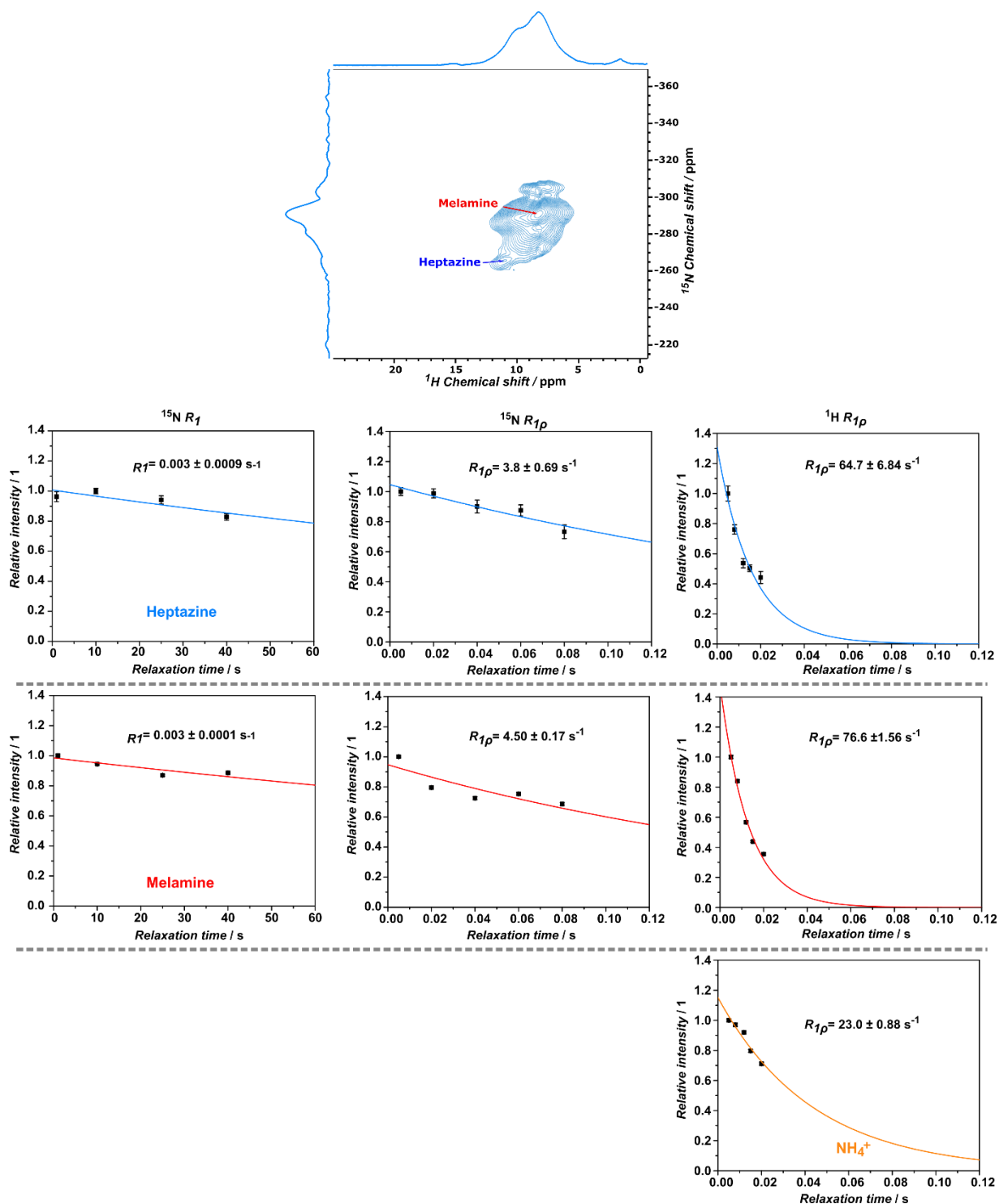


Figure S3.31: ^1H and ^{15}N , R_1 , and $R_{1\rho}$ intensity decays obtained at 55.5 kHz spinning speed in proton-detected 2D experiments. Solid lines are mono-exponential fits, the fitted relaxation rate constants are listed in the figure. Relaxation data for heptazine and melamine were obtained in CP-based 2D experiments (see spectrum above), and for NH_4^+ in INEPT-based HSQC (see Fig S28). The “heptazine” labeled peak is describing the NH bridge between heptazine and triazine units.

A slightly higher amplitude of motion on the μs time scale is observed for the heptazine and melamine labeled signals compared to the ps-ns time scale. This effect could be a consequence of overall higher flexibilities at the edges of the flakes. The ammonium ion on the other hand seems to be less mobile on the μs time scale (apparent from the 3-4 times lower relaxation ^1H $R_{1\rho}$ rates measured in INEPT-based experiments)

Analysis of ammonium exchanged K-PHI

Since ammonium ions were found in the pores of Mel-PHI, K-PHI was used for a cation exchange for ammonium, to study the effect of ammonium ions on the structure. The potassium located in K-PHI pores was replaced by ^{15}N enriched ammonium chloride and NMR studies were done for comparison. The absence of chlorine and potassium in an EDX analysis suggests that the exchange of the alkali ion with the ammonium ion has been successfully achieved (Table S3.1).

Table S3.1: Elemental analysis of NH_4 -PHI.

Element	Composition [at%]
C	56.9
N	41.9
Na	0.33
S	0.26
Cl	0.30
K	0.27

Three distinct signals were observed for the ammonium exchanged K-PHI network in ^1H NMR (Figure S3.32). The peak at 4.9 ppm may be attributed to water inside the pores while the strong peak at 7.2 ppm corresponds to the protons of the ammonium ion. The signal at 10.9 ppm arises from NH-groups that connect the heptazine units of the network. In the ^{13}C NMR spectrum of NH_4 -PHI no significant changes can be observed in comparison to pristine K-PHI, besides signal broadening. Especially the signal at 164 ppm, from carbon atoms located next to an imide bridge, is broadened and reduced in intensity. One reason for this might be a more inhomogeneous chemical environment for those groups, due to stronger and weaker interactions with water or ammonium ions.

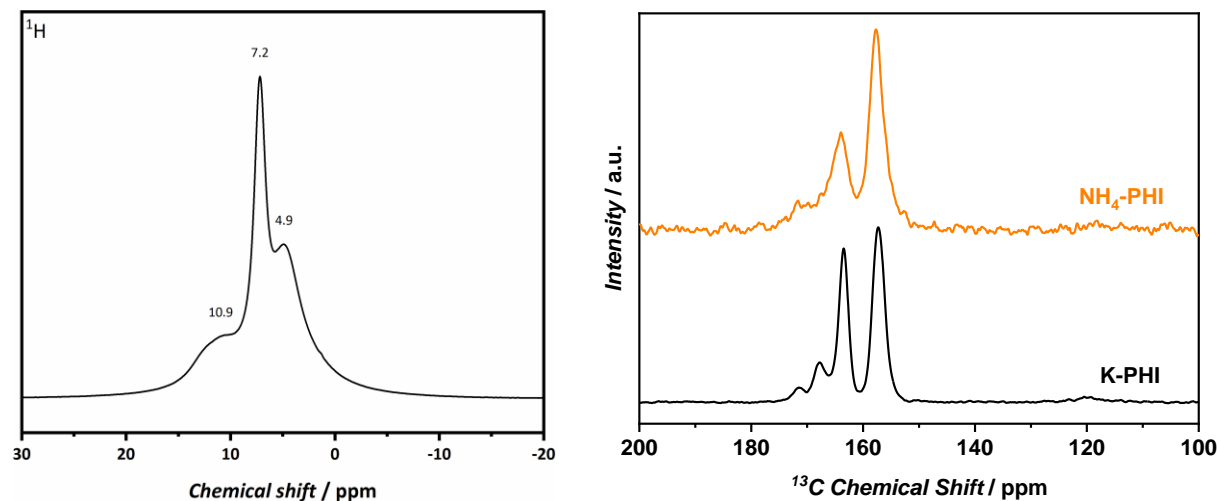


Figure S3.32: MAS NMR analysis of $\text{NH}_4\text{-PHI}$: ^1H NMR of ^{15}N enriched ammonium in $\text{NH}_4\text{-PHI}$ at a spinning rate of 12.5 kHz (left); ^{13}C MAS NMR of post-synthetic NH_4^+ exchanged K-PHI in comparison to K-PHI at a spinning rate of 12.5 kHz (right).

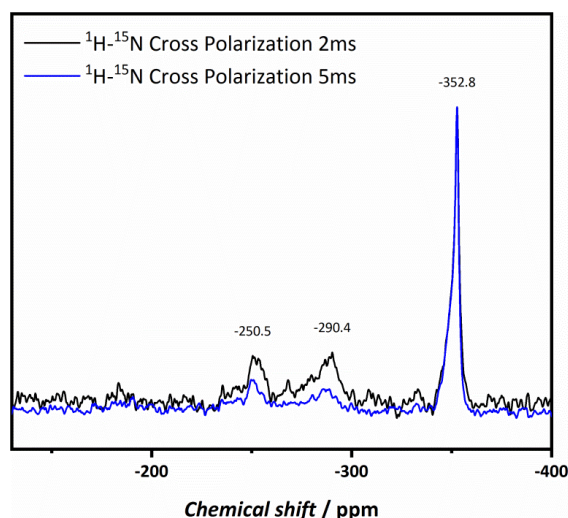


Figure S3.33: $\{^1\text{H}\}^{15}\text{N}$ CP MAS NMR of post-synthetic $^{15}\text{NH}_4$ exchanged K-PHI with a spinning rate of 10 kHz and 2 and 5 ms contact times.

Three signals at -250.5, -290.4 and -352.8 ppm are visible in the $^1\text{H}\text{-}^{15}\text{N}$ CP MAS NMR (Figure S3.33). These correspond to NH and NH_2 groups as well as NH_4^+ , respectively. The NH signal might be caused by an imide bridge or protonation of a nitrogen atom in the heptazine ring.^[2] The peak at -352.8 ppm is clearly related to the ammonium ion since ammonium chloride or ammonium nitrate have a similar chemical shift.^[64] Residual NH_2 -groups, which terminate the polymeric heptazine backbone, give rise to the signal at -290.4 ppm. Bridging NH-groups account for the signal at -250.5 ppm. The slightly high-field shifted signal (-250 ppm in comparison to -240 ppm in K-PHI) of the NH-bridge in $\text{NH}_4\text{-PHI}$ may be explained by the interaction of ammonium ion and the NH bridges by hydrogen bonds.^[2] The signals at -250.5 ppm and -290.4 ppm decrease with increasing contact time, since the magnetization of the protons is transferred to further distant nitrogen nuclei. As potassium was exchanged by isotopically labelled ammonium chloride, this effect does not greatly affect the signal at -352.8 ppm because it is nearly 100% ^{15}N anyway.

From these results we can conclude that ammonium ions are likely to be located in the pores of Mel-PHI.

Elemental analysis

Table S3.2: Elemental analysis of Mel-PHI (pristine and spent after photocatalysis).

	C	N	H	K	Cl	Pt
Pristine wt%	30.16 (± 0.12)	54.30 (± 0.11)	2.52 (± 0.02)	0.809	-	-
Pristine mol%	2.51 (± 0.01)	3.88 (± 0.01)	2.52 (± 0.02)	0.020	-	-
Spent wt% with TEOA as donor	30.26 (± 0.04)	54.28 (± 0.03)	2.96 (± 0.03)	-	-	0.642 (± 0.001)
Spent mol%	2.52 (± 0.01)	3.88 (± 0.01)	2.96 (± 0.03)	-	-	0.003
Spent wt% with MeOH as donor	30.32 (± 0.12)	52.95 (± 0.16)	3.04 (± 0.02)	0.359	-	2.43
Spent mol%	2.52 (± 0.01)	3.78 (± 0.01)	3.04 (± 0.02)	0.008	-	0.012

In some samples, higher amounts of chloride were found, especially before washing with hot water. The maximum measured amount of chloride was 5.5 wt%. After washing with water no chloride was detected anymore.

The expected composition of Mel-PH is based on the assumption that in K-PHI only every 5-6 heptazine unit is functionalized with an NCN-group and each of them is reacted to a melamine group. The exact amount of melamine in Mel-PHI is difficult to extract, since the NMR shifts of heptazine and triazine are overlapping significantly. Nevertheless, a rough estimation of the amount of functionalization could be given by direct ^{13}C MAS NMR, were the amount of functionalization of every 5th-6th heptazine unit could be confirmed. For the elemental analysis a functionalization of every 6th heptazine unit was used.

C/N ratio: 0.65

Mel-PHI expected composition: $\text{C}_{13}\text{N}_{18}\text{H}_{3.7}$

Measured composition: $\text{C}_{13}\text{N}_{20}\text{H}_{13}\text{K}_{0.1}$

As shown by NMR analysis (Figure S3.27), ammonium ions are located in the pores, which can explain the mismatch in the nitrogen amount resulting in:

Composition: $\text{C}_{13}\text{N}_{18}\text{H}_{3.7} (\text{NH}_4)_2, \text{K}_{0.1} * \text{H}_2\text{O}$

XPS analysis

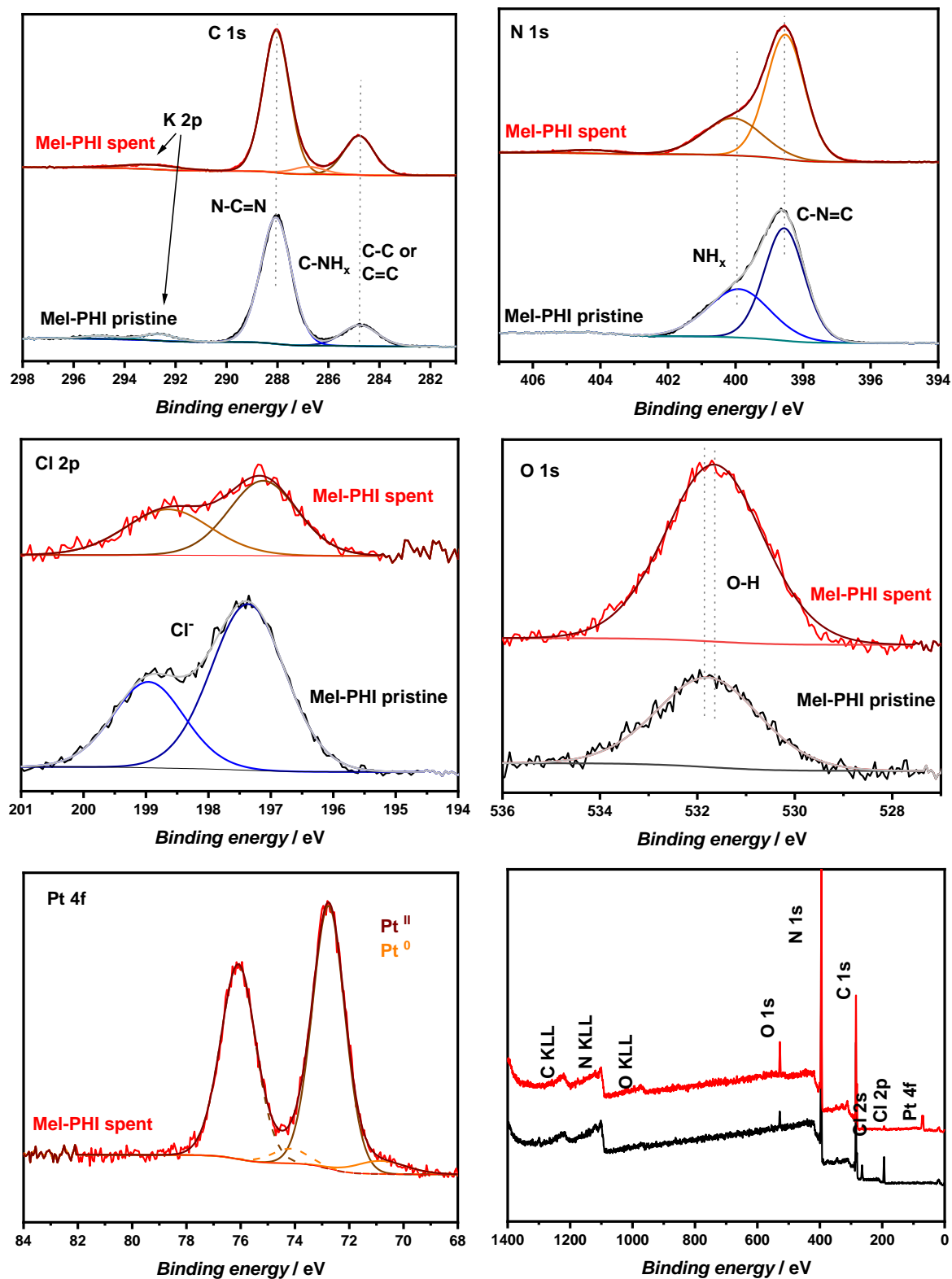


Figure S3.34: XPS of pristine Mel-PHI powder (black curve) and spent Mel-PHI powder (red curve) after photocatalysis with MeOH as donor and optimized Pt loading.

Before washing Mel-PHI with boiling water small amounts of Cl (199.0 eV and 197.4 eV) are assigned to residual Cl⁻ ions, which are not bound to the organic backbone. This side phase is resulting from traces of NH₄Cl in the sample^[65-67] (5% according to elemental analysis). As seen by elemental analysis NH₄Cl and not covalently bound melamine were successfully washed away with boiling water.

The chloride signal is lower in intensity for the spent sample and slightly shifted to lower binding energies (from 199.0 eV and 197.4 eV to 198.6 and 197.1 eV) after photocatalysis experiments. The shift to lower binding energies indicates an addition of valence charge on chloride, which might be caused by a slightly changed environment of the ion, e.g. hydration shells.

9.3.6. Optical band gap analysis

UV-vis analysis

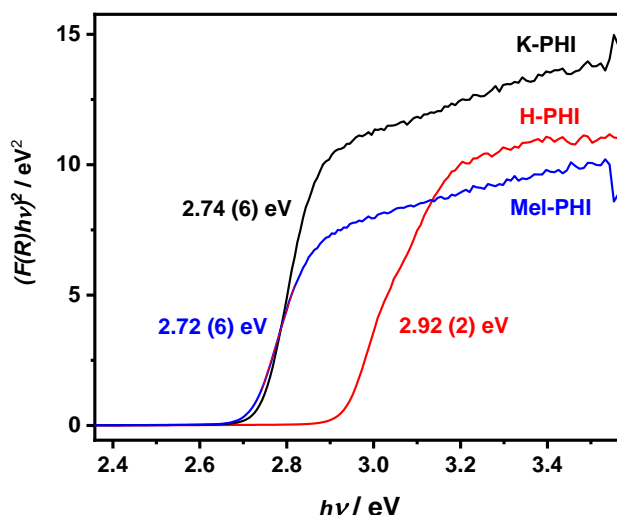


Figure S3.35: Tauc plot of K-PHI, H-PHI and Mel-PHI in comparison, assuming a direct optical band gap.

UPS data analysis

The standard value of the work function for Au of 5.2 eV^[68, 69] could not be reproduced for our Au covered substrate, which is most probably caused by water, which is adsorbed on the Au surface. A slightly reduced work function of 4.8-5.0 eV was obtained in our measurements. To take this into account, the UPS data were analyzed in comparison to each other. The effect of water on the work function was calculated to be the difference between the optimal Au value and the measured value. The band position is given as the mean value of the minimum and maximum deviation of the fitting and measurements at different positions at the sample, resulting in an error of maximum ± 0.1 eV (Figure S3.36c). The VB position with respect to the Vacuum level was then obtained by adding to the work function the onset of the valence band value from fitting, assuming Fermi-level equilibration between PHI and Au (onset in Figure S3.36c).^[70-72] The gold reference values of the work function were set to the same value of 5.0 eV for both measurements to compare Mel-PHI data with K-PHI data.

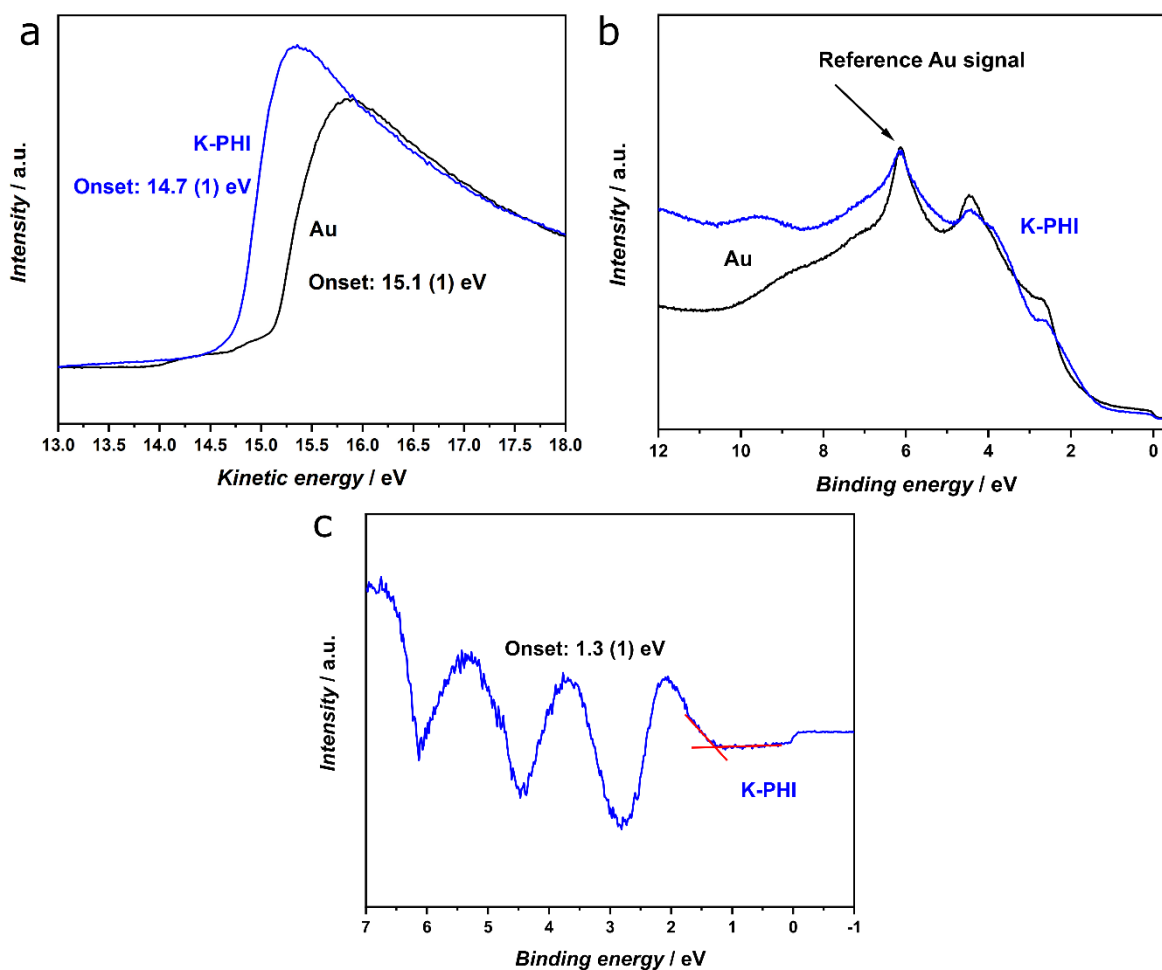


Figure S3.36: UPS data of Au and K-PHI on Au substrate with a) applied potential for work function estimation; b) UPS data normalized to Au signal at 6.09 eV; c) differential UPS data of K-PHI after subtracting the Au substrate signal to fit the onset value, which describes the potential difference between valence band edge and Fermi level. An onset-potential range is given to include fitting errors.

Table S3.3: Work functions of K-PHI on Au.

Material	Work function [eV vs Vac.]
Au	5.0 (± 0.05)
K-PHI on Au	4.6 (± 0.1)

Band positions VB: -5.9 (± 0.1) eV vs Vac.

CB: -3.2 (± 0.1) eV vs Vac.

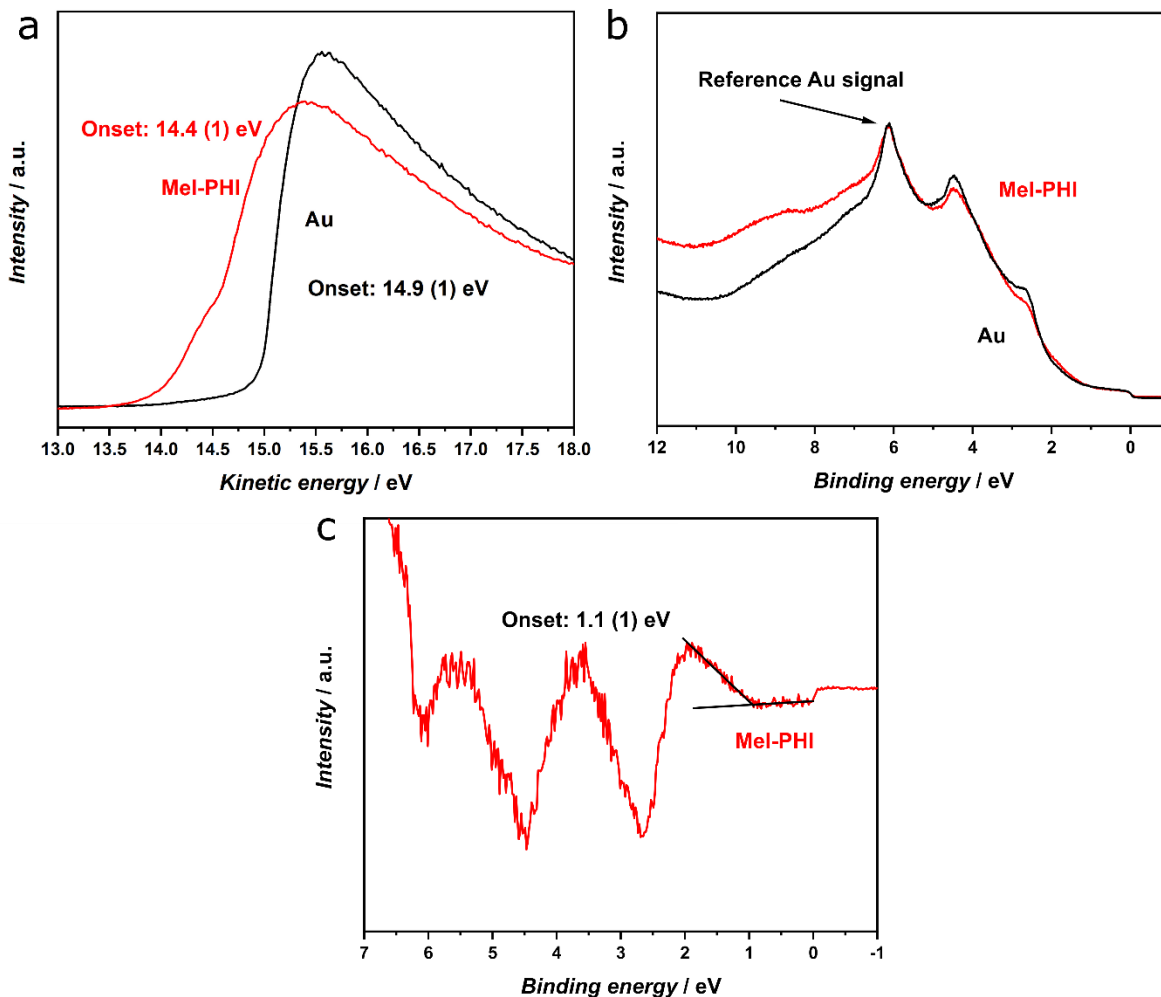


Figure S3.37: UPS of Mel-PHI on Au and pure Au a) with applied potential for work function estimation; b) normalized to the signal of Au at 6.09 eV; c) differential UPS data of Mel-PHI, where the signals of the Au substrate were subtracted to fit the onset values. An onset-potential range is given to include fitting errors.

Table S3.4: Work functions of Mel-PHI on Au.

Material	Work function [eV vs Vac.]
Au	4.8 (± 0.05)
Mel-PHI at Au	4.2 (± 0.1)

Band positions VB: -5.5 (± 0.1) eV vs Vac.

CB: -2.8 (± 0.1) eV vs Vac.

From UPS analysis and the band gap obtained from UV-vis measurements (band gap 2.7 eV for both materials), the band edges of K-PHI (VB: -5.9 (± 0.1) eV vs Vac. and CB: -3.2 (± 0.1) eV vs Vac.) and Mel-PHI (VB: -5.5 (± 0.1) eV vs Vac. and CB: -2.8 (± 0.1) eV vs Vac.) could be extracted. To estimate if the formation of a donor-acceptor function between heptazine and triazine would

be possible in principle, those band edges need to be compared to triazine-based systems, known in literature. When comparing the absorption edges from melamine (5.3 eV) with melem (4.2 eV), the latter heptazine-based molecules have a slightly smaller optical band gap than the triazine-based material melamine.^[73] As an estimation of the oxidation potential of melamine its redox-potential is reported to be more negative than 2.3 V vs NHE.^[57] The trend continues for polymerized samples where poly(triazine imide) (PTI) has an absorption edge of 3.3 -2.8 eV^[73, 74] (depending on the LiCl content) ^[75, 76], which is higher in energy than that of melon (2.7 eV)^[73] and approaching to PHI (2.75 eV).^[1, 2, 33] The band edges reported for PTI (measured and calculated) vary in the range between -0.7 V and -1.5 V vs NHE for the LUMO and +1.7 V to +2.1 V vs NHE for the HOMO.^[76-81] All of these values for the band edges of triazine-based systems are systematically more negative than the band edges of K-PHI reported in literature (CB at -0.5 V vs NHE and VB at 2.22 V vs NHE).^[82] At the interface of PTI and K-PHI, the photo-generated electrons would therefore experience a driving force (and be transferred) from PTI to K-PHI, whereas the holes would travel in the opposite direction (Figure S3.38). In the molecularly combined system Mel-PHI, the band edges measured by UPS (a surface sensitive method) are overall more negative by 0.4 eV than in K-PHI, which might as well be caused by the presence of triazine units with molecular orbitals at more negative potentials. In principle, the monomer heptazine-based melem has more negative band edges than oligomers or polymers buildup of this monomer.^[83] Since Mel-PHI does not contain a polymeric triazine-based system connected to the PHI backbone, it can be expected that the potentials of one melamine unit are even more negative than the values reported for PTI, thus rendering the potential difference between the heptazine and triazine system even stronger and hence, could enabling a donor-acceptor function at their interface i.e. on the surface of the polymeric sheets.

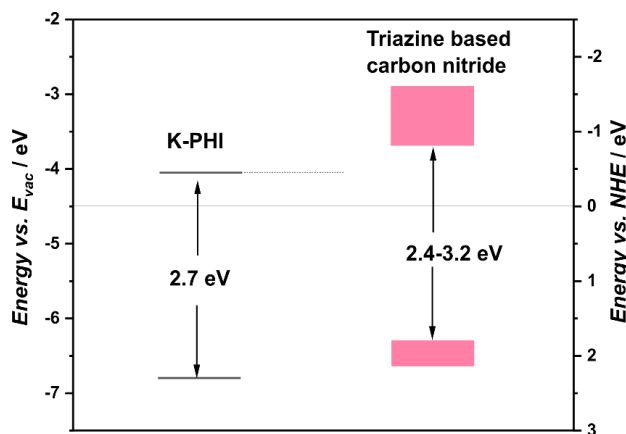


Figure S3.38: Band gap and band edges of K-PHI and triazine-based systems. K-PHI values referenced to NHE were taken from literature.^[82] For triazine-based carbon nitride the values were taken from literature.^[76-81] The shaded areas depict the error bars of the band edges.

Calculations of HOMO and LUMO and solvent interaction

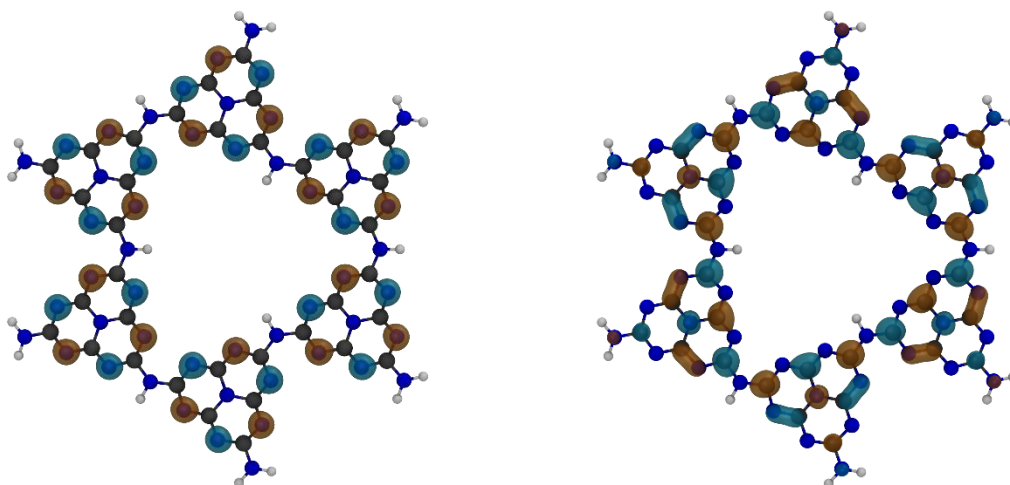


Figure S3.39: HOMO and LUMO for the H-PHI model system, obtained on PBE0-D3/def2-TZVP level of theory. Orange and turquoise depict different orbital phases, which are not considered in the analysis, since only the orbital contribution in total is of interest.

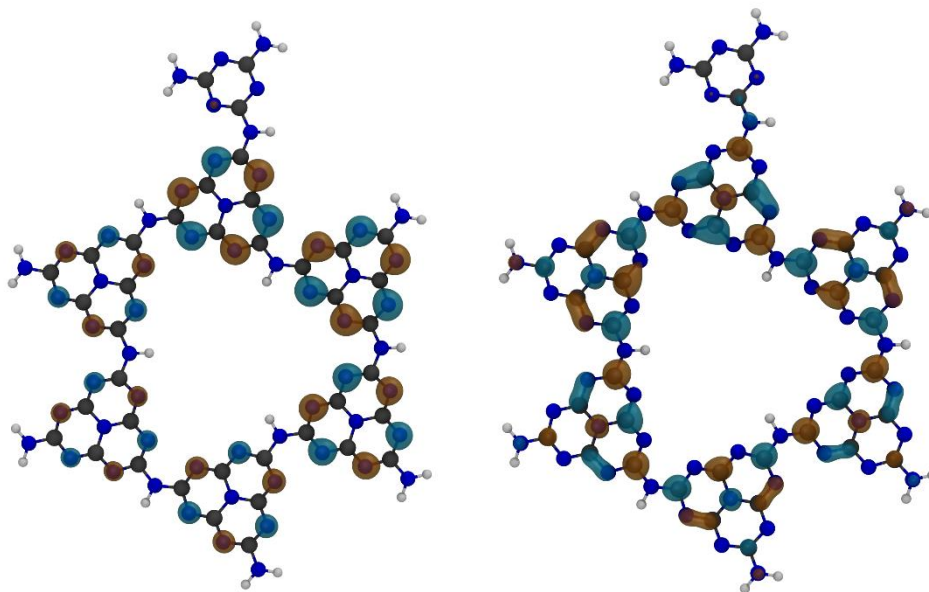


Figure S3.40: HOMO and LUMO for the Mel-PHI model system, obtained on PBE0-D3/def2-TZVP level of theory.

The characters of the highest occupied molecular orbital (HOMO) and the lowest unoccupied molecular orbital (LUMO) can be calculated based on DFT methods. The HOMO is mainly comprised by 2p and sp^2 nitrogen atoms of the triazine and heptazine ring, similar to calculations for melem oligomers in literature.^[1, 84] The LUMO on the other side is dominated by sp^2 orbitals from carbon and nitrogen atoms.^[84-86] Since not only the HOMO and the LUMO orbital are contributing to the light absorption, higher LUMO and lower HOMO orbitals are involved, it might hint to overlapping states.^[87, 88]

Table S3.5: Energies of molecular orbitals for the H-PHI and Mel-PHI pore models, obtained on PBE0-D3/def2-TZVP level of theory. * orbitals are degenerated.

Orbital	Energy in PHI pore model [eV]	Energy in Mel-PHI pore model [eV]
LUMO+2	-2.221	-2.220
LUMO+1	-2.221	-2.245
LUMO	-2.397	-2.413
HOMO	-6.824	-6.816
HOMO-1	-6.854*	-6.846
HOMO-2	-6.854*	-6.853
HOMO-3	-6.919*	-6.911
HOMO-4	-6.919*	-6.917
HOMO-5	-6.952	-6.948

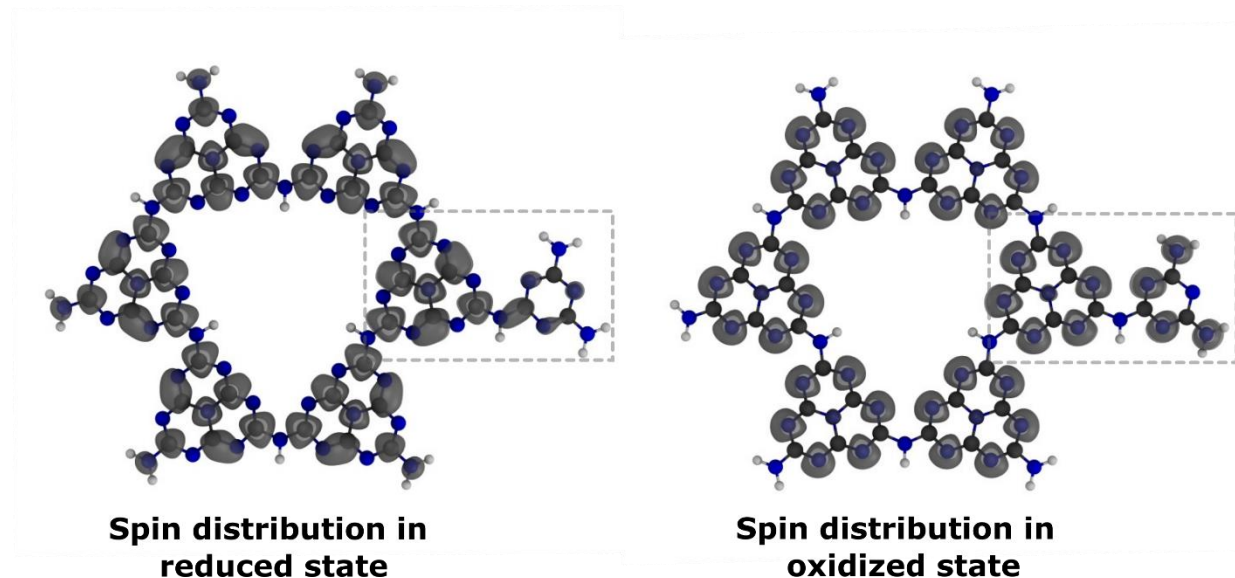


Figure S3.41: Spin density distribution in a reduced (radical anion) and oxidized (radical cation) Mel-PHI model system.

In addition, the spin density distribution in the reduced (radical anion) and oxidized state (radical cation) of single pore Mel-PHI was calculated (Figure S3.41). The reduced state shows a homogeneous delocalization of the electron over the heptazine rings. From this finding, a fast charge separation upon electron accumulation could result for a single pore Mel-PHI, as the hole of the exciton is quenched near the surface and the electron is equally distributed towards the PHI ring afterwards. The same calculation for the oxidized state was performed, showing that holes would be localized also at the melamine unit, which could be beneficial for donor oxidation.

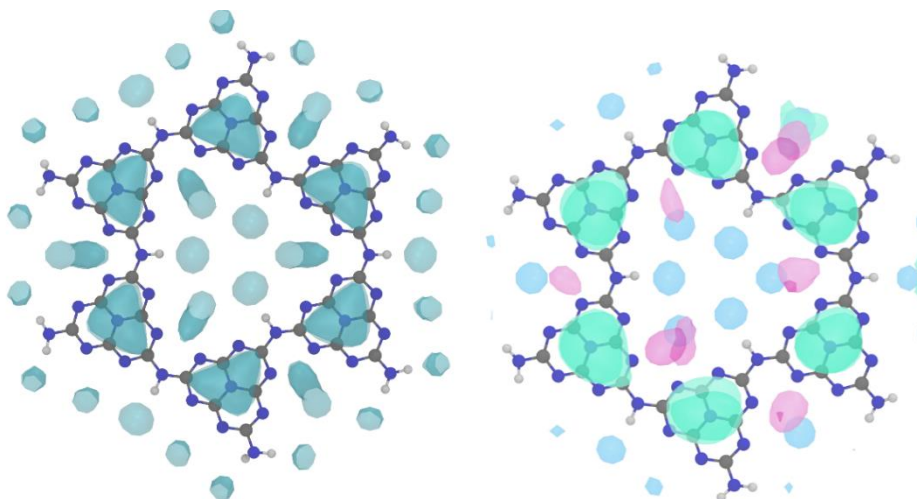


Figure S3.42: Quantum-chemical based calculation of a *single pore* PHI interacting with water (blue) (left) and TEoA, whereas green areas depict N atoms in TEoA and pink the OH groups; blue is the water interaction (right).

9.3.7. Photocatalysis

Hydrogen evolution in presence of different electron donors

To investigate the effect of the strength of the donor, i.e. the thermodynamic driving force for donor oxidation during photocatalysis was compared. The donor strength describes the reductive power of a donor, whereas the driving force is described by the studied material and is lower in Mel-PHI in comparison to K-PHI. A comparably negative redox-potential results in a high driving force for hole quenching.^[89] The hydrogen evolution rate might actually be dependent on the redox-potential,^[90] since MeOH has a comparable small driving force for hole quenching (-0.25 V vs NHE) in comparison to EDTA (-0.4 V vs NHE) or TEoA (-1.1 V vs NHE)^[89], which are both more active. The highest HER rates are obtained with TEoA.

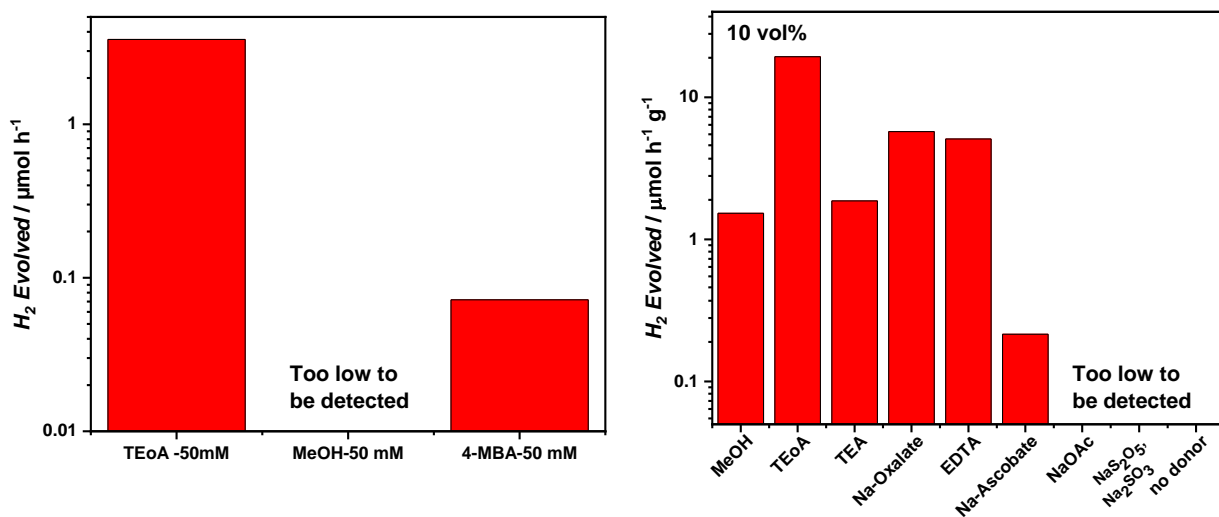


Figure S3.43: Photocatalytic activity of Mel-PHI (7 mg) in comparison for different donors TEoA, MeOH and 4-MBA at low concentrations of 50 μM (left); dependence of photocatalytic hydrogen evolution on various donors with higher donor concentration (10 vol%) (right). The detection limit of the GC is around 0.01 $\mu\text{mol H}_2$.

Table S3.6: Apparent quantum yield (AQY) in photocatalytic hydrogen evolution at 400 nm (± 20 nm) illumination (1.4 mW cm^{-2}) for Mel-PHI (7 mg; 0.7 mg ml^{-1}) in presence of TEoA and MeOH at optimized Pt loading and K-PHI (10 mg, 1 mg ml^{-1}) in presence of MeOH and optimized Pt loading. Solar-to-hydrogen (STH) conversion at AM 1.5 G condition (100 mW cm^{-2}), neglecting the donor reaction, at optimized Pt loading.

Sample	AQY [%]	STH [%]
K-PHI in MeOH	9.0	0.19
Mel-PHI in MeOH	1.7	0.05
Mel-PHI in TEoA	17.8	0.59

Pt loading optimization

The Pt amount that was photo-deposited *in situ* during photocatalysis was found to be dependent on the donor, which results in a decrease of required Pt when TEoA is used compared to MeOH. Two identical suspensions (10 mg Mel-PHI, 9 mL water, 1 mL donor (MeOH or TEoA) and $14 \mu\text{L H}_2\text{PtCl}_6$ (8 wt%)) were prepared for photocatalysis to analyze the amount of Pt being actually deposited by ICP after 4 hours of illumination. After photocatalysis the material was washed three times with water to make sure only the Pt on the surface of the carbon nitride is analyzed. In the presence of methanol 2.43 wt% of Pt from the initially introduced 8 wt% are detected afterwards on the material, whereas for TEoA only 0.64 wt% were measured. Due to this strong dependence on the donor, the amount of Pt, which needs to be added to the suspension, was optimized for both TEoA and MeOH in terms of maximum hydrogen evolution rate, resulting in a reduced initial added Pt amount of 1.75 wt% for TEoA in comparison to methanol (4 wt%) (Figure S3.44).

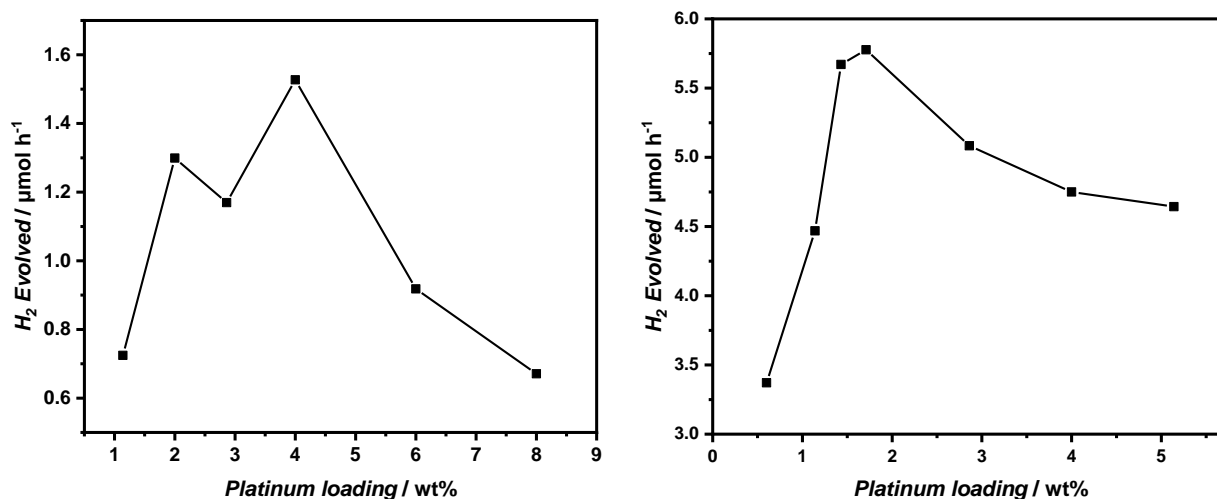


Figure S3.44: Optimization of initial Pt loading with MeOH as donor (left) and TEoA (right).

Appendix

Table S3.7: Comparison of hydrogen evolution rates of different carbon nitride materials, reported in literature.

Sample	Hydrogen evolution [mmol g ⁻¹ h ⁻¹]	Conditions	Reference
Optimized atomic, vacancy containing A-V-g-C ₃ N ₄	3.7	10vol% TEOA λ > 420 nm 1wt% Pt	[91]
Mesoporous g-C ₃ N ₄	3.1	20vol% TEOA λ > 400 nm -	[92]
Barbituic acid functionalized g-C ₃ N ₄	0.3	10vol% TEOA λ > 420 nm 3wt% Pt	[93]
g-C ₃ N ₄ p-n homojunction	4.0	10vol% TEOA λ > 400 nm 3wt% Pt	[94]
Phenyl function- alized g-C ₃ N ₄	10.7	10vol% TEOA λ > 420 nm 3wt% Pt	[95]
PTI nanosheets	3.2	10vol% TEOA λ > 420 nm 8wt% Pt	[96]
K-PHI	0.6	10vol% MeOH λ > 420 nm 8wt% Pt	[2]
Our work	5.6	10vol% TEOA λ > 420 nm 1.75wt% Pt	

Photoelectrochemistry

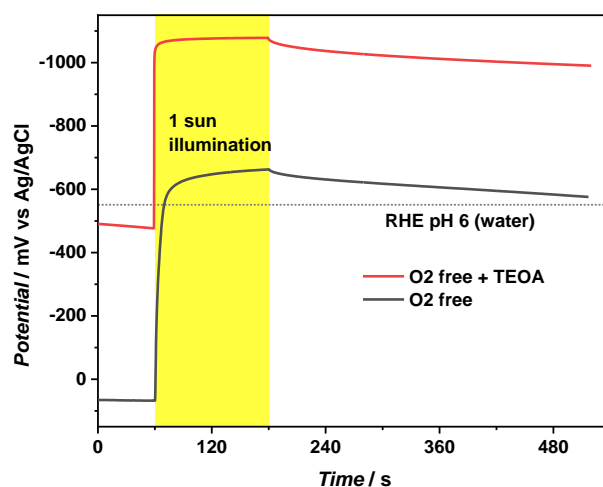


Figure S3.45: Open circuit potential (OCP) measurement of Mel-PHI sheets deposited on FTO before, during and after illumination (1 sun) in O_2 -free conditions. In pure water illumination yields a transient negative OCP shift (-660 mV vs Ag/AgCl) indicating charge accumulation within 120 s of illumination and subsequent storage (grey line). After addition of 10 vol% TEOA and 30 min of Ar purging to remove dissolved O_2 , the OCP shift occurs instantly and at more negative potentials (-1080 mV vs Ag/AgCl, red line), with a similar stability. The more negative starting value (~ -500 mV vs Ag/AgCl) was probably induced by absorption of stray light during the 30 min purging process.

BET analysis, zeta-potentials and DLS measurements

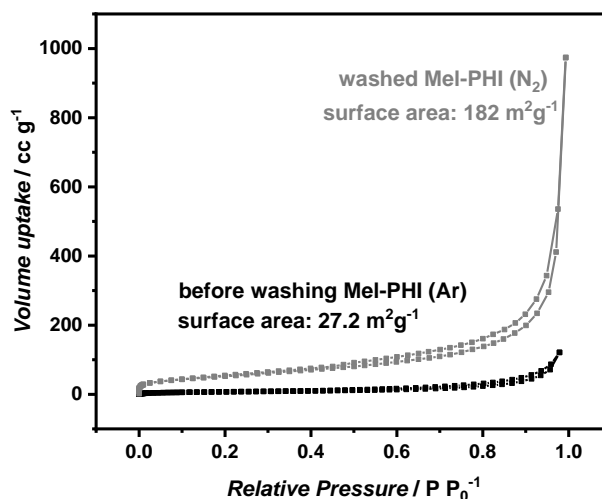


Figure S3.46: BET surface area measurements of Mel-PHI by Ar sorption (before washing) and N_2 sorption (after washing) showing a change of BET area from 27.2 to 182 $m^2 g^{-1}$. Since in carbon nitride material polar heterogeneous surfaces might be present it is preferable to use Ar as a detection gas over nitrogen. Ar does not have a quadrupole moment, so that more reliable data are obtained with this gas. Out of this reason the Ar values are used for comparison to previous literature, especially since the materials there were also measured with Ar.^[97]

The BET area of H-PHI was measured to be 56 $m^2 g^{-1}$ with Ar sorption and for K-PHI a value of 55 $m^2 g^{-1}$ was reported.^[1]

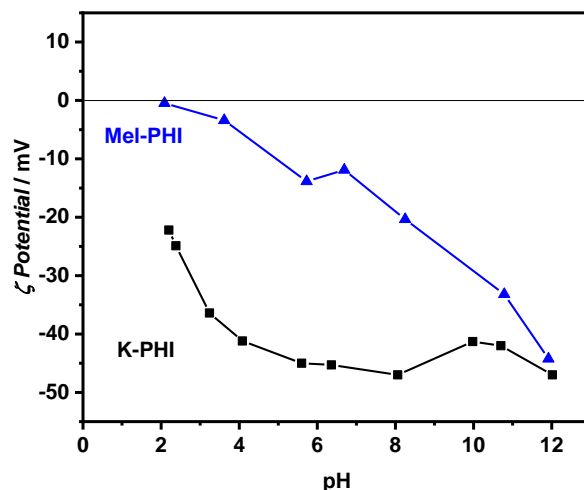


Figure S3.47: Zeta-potentials of Mel-PHI and K-PHI as a function of the pH. The pH values were adjusted with HCl in acidic and KOH in basic conditions.

Since a strong influence of the donor on the hydrogen evolution was detected, the effect of stabilization of PHI suspension was studied by Zeta-potential (Table S3.8). Mel-PHI was analyzed in aqueous suspension without and with the donors MeOH and TEoA. In case of methanol being present, the modulus of the zeta-potential is decreasing, pointing directly to a less stable suspension. The zeta-potential value of -37.2 mV with TEoA confirms the surfactant function of this donor preventing agglomeration.^[98-100]

Table S3.8: Zeta-potential of Mel-PHI in water, in water with 10 vol% MeOH or TEoA.

Material	Zeta-potential [mV]
Mel-PHI in water	-12.0
Mel-PHI + 10vol% MeOH	-1.6
Mel-PHI + 10vol% TEoA	-37.2



Figure S3.48: Images of suspensions, which were allowed to stand for 2 h with MeOH (left) and TEoA (right). After these 2 hours, sedimentation of particles in the MeOH containing sample can be observed, which is the reason for measuring smaller particles sizes within the suspension.

One reason for the strong donor dependence for hydrogen evolution reaction of Mel-PHI might be the different pH values caused by different donors (Figure S3.49). In the photocatalysis

experiment with MeOH and 4-MBA as donor acidic pH values around 4 were measured. Addition of TEoA as a donor results in a pH of 10.4, whereas TEA should have an even more basic value. Dependent on the pH, different mechanisms for hydrogen evolution are enabled on Pt.^[101, 102] However, the overpotential of a Pt catalyst increases with increasing pH (i.e. acidic, proton-coupled HER is more facile), hence, the pH shift can be excluded as reason with respect to modifications of the surface catalytic mechanism. This was also confirmed by changing the pH of a photocatalytic suspension containing MeOH to 10.4 and TEoA containing suspension to a pH of 2.5 (Figure S3.49). Here, no enhanced hydrogen evolution was observed with MeOH or TEoA at these pH values, but a maximum hydrogen evolution rate of Mel-PHI in the presence of TEoA was observed for a pH around 10. Strong acidic (pH = 2) or basic conditions (pH = 13) lead to reduction of hydrogen evolution rate by a factor of 4. It hence appears most likely that the surfactant function of TEoA at different pH values is dominating interaction strength of TEoA with Mel-PHI, rather than a purely pH mediated influence.

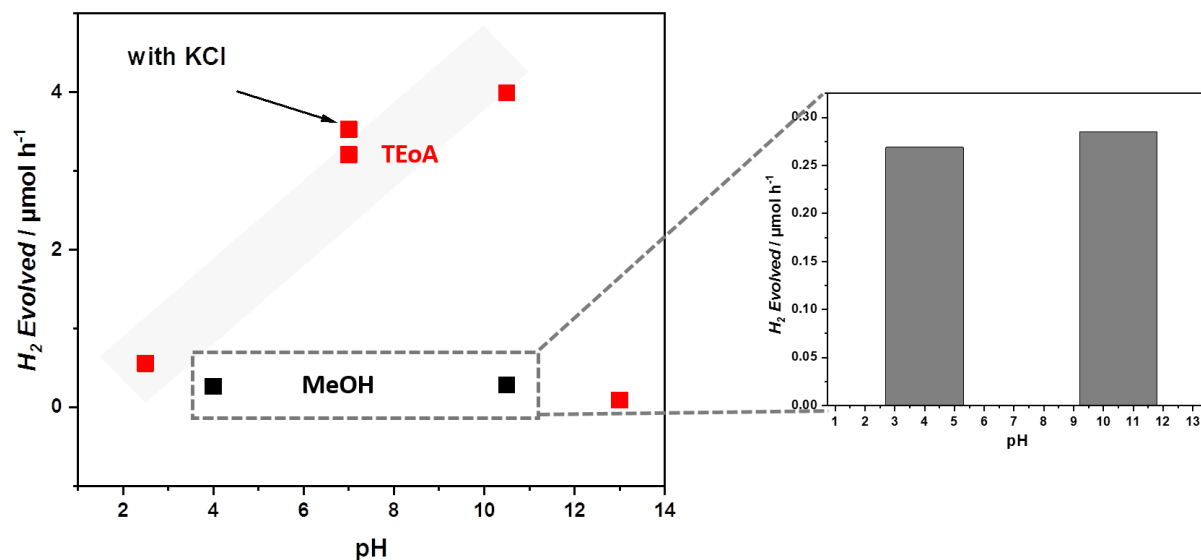


Figure S3.49: pH dependent photocatalysis of Mel-PHI in the presence of TEoA and MeOH as donor and optimized Pt loading of 1.75 wt% (for TEoA) or 4 wt% (for MeOH). pH values were adjusted with HCl in acidic and KOH in basic conditions.

Kinetic analysis of hydrogen evolution

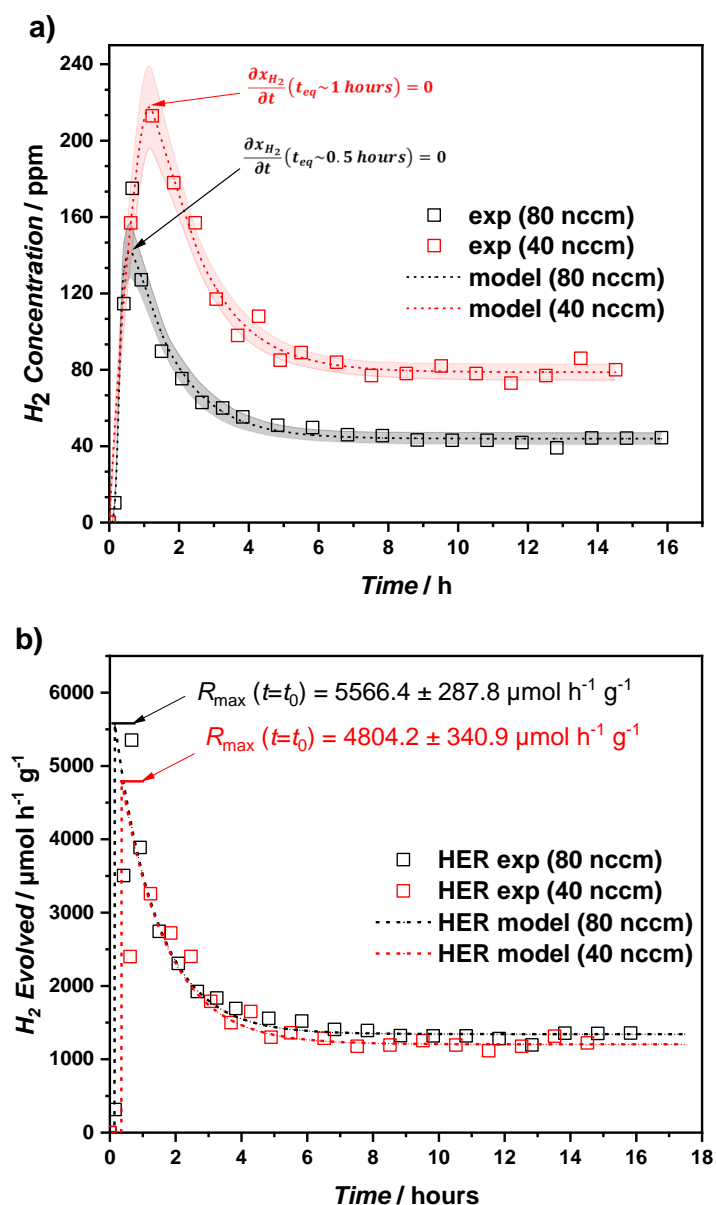


Figure S3.50: Dynamic hydrogen evolution of Mel-PHI in the presence of TEoA and optimized Pt amount (1.75 wt%); a) raw hydrogen headspace concentration measured at reactor outlet versus modeled response based on photocatalytic HER rate (nonlinear fitting), for two different flow conditions (80 and 40 nccm) (dashed lines are model predictions with 95% confidence band in colored area). Illustration of characteristic time t_{eq} is presented in inset equation, which is the estimated time when reactor response is in steady state and reactor hydrogen elution equals HER rates; b) experimental HER rates using (a) and a hydrogen molar balance in steady state. The red curve shows gas phase analysis every 30 min at the beginning, which cannot resolve hydrogen evolution rate at the beginning very precisely.

The measurement of the HER rate in a continuous flow experiment requires an equilibration if the gases produced (i.e. after Pt deposition) and the gases flowing through the headspace are not in steady state. Without the dynamic hydrogen evolution measurements, the initial activity cannot be resolved by regular means of batch analysis every 15 min.^[34] The transient state balance in the flow experiment can also be modeled to access the times before the reactor is equilibrated (t_{eq}), and fit the measured HER curve (Figure S3.50a). At the lower flow condition of 40 nccm, the estimated t_{eq} is 1 hour (red curve), while in the case of the 80 nccm experiment t_{eq} is found to be 0.5 hours (black curve), which is consistent with the criteria for equilibration presented in our previous publication.^[34] The equilibration time t_{eq} can be extracted approximately when the time derivative of hydrogen concentration in the reactor is zero. This t_{eq} represents the cut-off time when the experimentally measured hydrogen evolved represents the HER kinetics trends (Figure S3.50b), without the influence of reactor equilibration time, since after this time the response of the reactor to the dynamic changes in HER rates is immediate. The decay of the hydrogen evolution rate curve (Figure S3.50b) is then fitted in the entire time domain by an exponential function and mathematically disentangling transient times, using the following equation: For $t < t_0$, $R_{H_2} = 0$, for $t > t_0$,

$$R_{H_2} = R_{\infty} \left(1 + \beta e^{\left(\frac{t-t_0}{t_d} \right)} \right)$$

Where R_{H_2} is the hydrogen evolution rate in $\mu\text{mol h}^{-1} \text{g}^{-1}$, R_{∞} is the asymptotic hydrogen evolution rate at the end in $\mu\text{mol h}^{-1} \text{g}^{-1}$, β is a fitted dimensionless parameter describing the theoretical initial hydrogen evolution rate on top of R_{∞} , t is the actual time, t_0 is the induction time after light is turned on, and t_d is a characteristic parameter describing the kinetics of the exponential decay of HER. The parameter t_0 englobes all physical events that happen when the sample starts being irradiated at time $t=0$ and that is faster than the instrumental response. Among other reasons, t_0 can be assumed as the time needed for Pt to deposit. The fitting parameters can be extracted from Table S3.9, which were estimated with a combination of Matlab *nlinefit* and *ode15* libraries. The standard error of nonlinear regression S (in percentage) for the fits is 5.4% for the red curve and 7.4% for the black curve, which shows the model goodness of fit. The maximum hydrogen evolution rate R_{max} from both experiments is extracted at the initial point where the exponential starts at t_0 , with an average value of $5185 \pm 287 \mu\text{mol h}^{-1} \text{g}^{-1}$ (from the red and the black measurement curve in Figure S3.50a). The average asymptotic value R_{∞} is $1273 \pm 44 \mu\text{mol h}^{-1} \text{g}^{-1}$. It has to be noted that the absolute value of R_{max} is strongly dependent on the additional density of points at the beginning and the faster equilibration time when using a higher flow condition (black curve), therefore, a larger systematic error can result from the data acquisition compared to R_{∞} . Additionally, it is clear that the exponential decay approximation does not entirely capture the HER rates at early times, because the maximum of the black curve largely escapes the 95% confidence band, and because the standard error of regression S including additional information at early times is worse, which is underestimated by our approximation. It must be noticed that this coarse grain model has no physical explanation and it was assumed because it is the kinetic approximation that involves less parameters to represent the observed dynamic trends. As an alternative to theoretically estimated R_{max} , the afore said maximum HER rate measured experimentally (maximum point of black curve), can also be interpreted as a rough estimation for R_{max} , since this point was measured around the time t_{eq} when the reactor is in steady state with a value of $5353 \pm 160 \mu\text{mol h}^{-1} \text{g}^{-1}$.

Table S3.9: Fitting parameters and results for the decay analysis of the hydrogen evolution rate.

Fit parameter	First run (red curve)	Second run (black curve)
t_d	1.39 ± 0.29 [h]	1.28 ± 0.26 [h]
R_∞	1204.5 ± 53 [$\mu\text{mol h}^{-1} \text{g}^{-1}$]	1343.0 ± 71 [$\mu\text{mol h}^{-1} \text{g}^{-1}$]
t_0	0.36 ± 0.08 [h]	0.15 ± 0.01 [h]
$R_{\text{max}} (t=t_0)$	4804 ± 340 [$\mu\text{mol h}^{-1} \text{g}^{-1}$]	5566 ± 287 [$\mu\text{mol h}^{-1} \text{g}^{-1}$]
S	5.4 %	7.4 %

Reversibility of the hydrogen evolution activity

Given the chemical stability of the material as evidenced by PXRD, NMR, XPS and IR analysis, we hence conclude that Mel-PHI is deactivated by the interaction of oxidized TEOA products sticking to the surface. Therefore, the activity is decreasing, since the hydrogen evolution gets kinetically limited, due to limited donor diffusion to the surface of Mel-PHI. The initial hydrogen evolution rate shows how efficient this photocatalyst can maximally be for hydrogen evolution. In further studies, this knowledge can be used for the target design of catalysts, also to prevent the fast activity decrease.

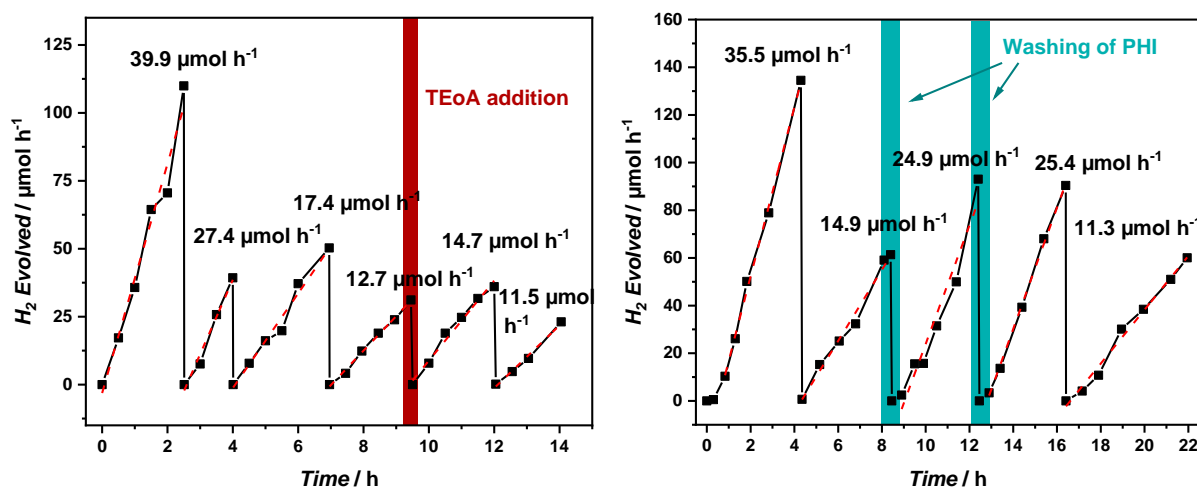


Figure S3.51: Photocatalytic hydrogen evolution of Mel-PHI with TEOA and optimized Pt loading measured in a batch reactor without Ar-flow. 14 h continuous measurement of hydrogen evolution with headspace replacement after 1.5-2.5 h (left) and 4 h (right) (when the amount of evolved hydrogen is set back to zero). TEOA addition (red area) after the 4th cycle showed no significant change in HER (left). Continuous hydrogen evolution measurement within 22 h, where green areas depict photocatalyst washing in between the cycles. The washing was done with water and acetone by centrifugation (right).

9.3.8. Mel-PHI analysis after photocatalysis

In the following, the pristine Mel-PHI powder is compared to the spent material. Spent Mel-PHI means the washed Mel-PHI powder with deposited Pt after the photocatalytic reaction in the presence of a donor and optimized Pt amount. The material was washed three times with water and separated from the solution by centrifugation. After drying the sample in vacuum overnight the material was analyzed by PXRD, IR, XPS (see above), NMR and UV-vis.

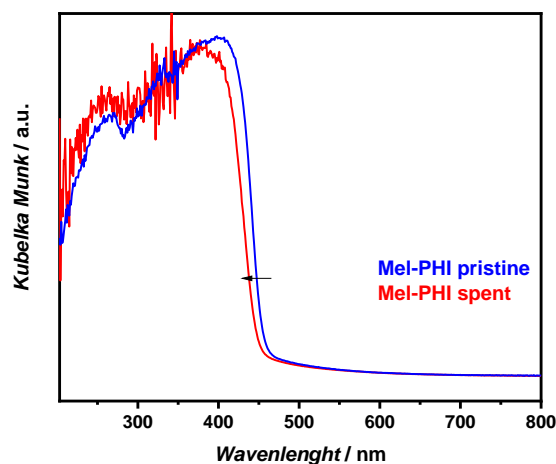


Figure S3.52: UV-vis spectra of pristine Mel-PHI powder (blue curve) and spent Mel-PHI powder (red curve) after photocatalysis with MeOH as donor and optimized Pt loading. The small shift in the absorption edge might be caused by protonation, as seen in previous paper of our group on PHI materials.^[2]

Comparison of Mel-PHI after photocatalysis in the presence of MeOH or TEOA

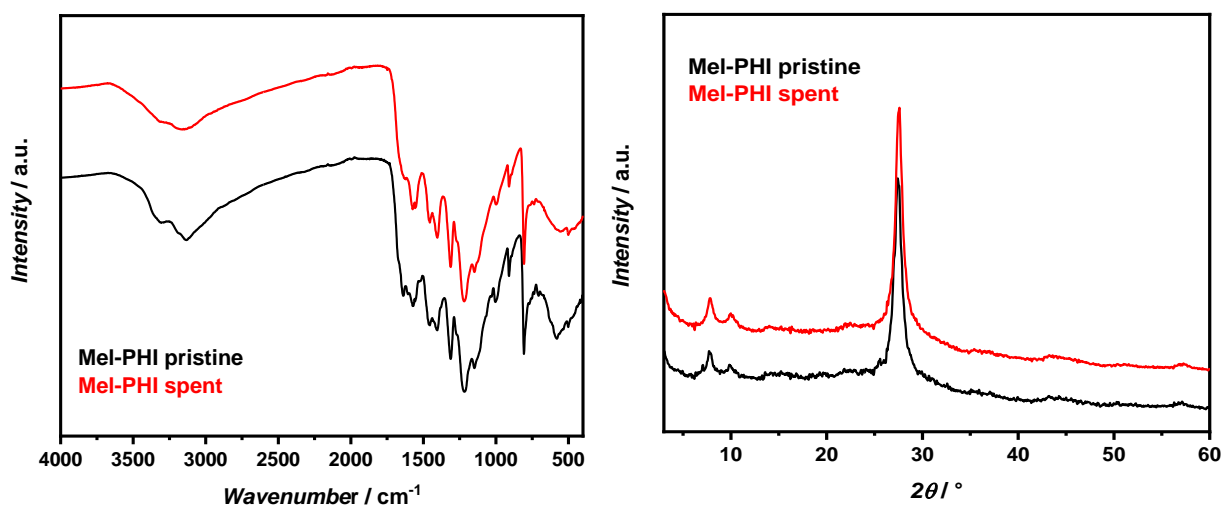


Figure S3.53: FT-IR and PXRD of pristine Mel-PHI powder (black curve) and spent Mel-PHI powder (red curve) after photocatalysis with MeOH as donor and optimized Pt loading.

To determine the strength of interaction of different donors with Mel-PHI during photocatalysis the spent material was analyzed by IR. When MeOH was used as donor during photocatalysis no

changes in the spent and the pristine materials could be observed (Figure S3.53), however, the use of TEOA leads to signals of the donor (grey area) even in the water-washed spent Mel-PHI, pointing to a strong interaction of TEOA or its oxidation products with Mel-PHI (Figure S3.54, S3.56). The TEOA and other residual interaction products can only be removed by washing with acetone (Figure S3.55). Further analysis of Mel-PHI spent with TEOA as donor during photocatalysis by NMR confirmed the presence of TEOA or oxidation products of TEOA in this material when only washed with water, as can be seen by a signal in ^1H -ssNMR around 3 ppm, caused by protons in TEOA or oxidation products (Figure S3.54).

Most probably not the pristine TEOA but rather some decomposition or oxidation products of TEOA are still present in the solution. It was shown in a previous report, that after 90 min of illumination of TEOA without catalysts a huge variety of different products can be formed, which cannot be distinguished anymore.^[103] Most of the possible products contain CH_2 or CH_3 groups, which can explain the signals in IR and ^1H NMR, but for detection in ^{13}C and ^{15}N NMR there might be too many different compounds, which are all below the detection limit, so that no distinct new signals can be observed after photocatalysis.

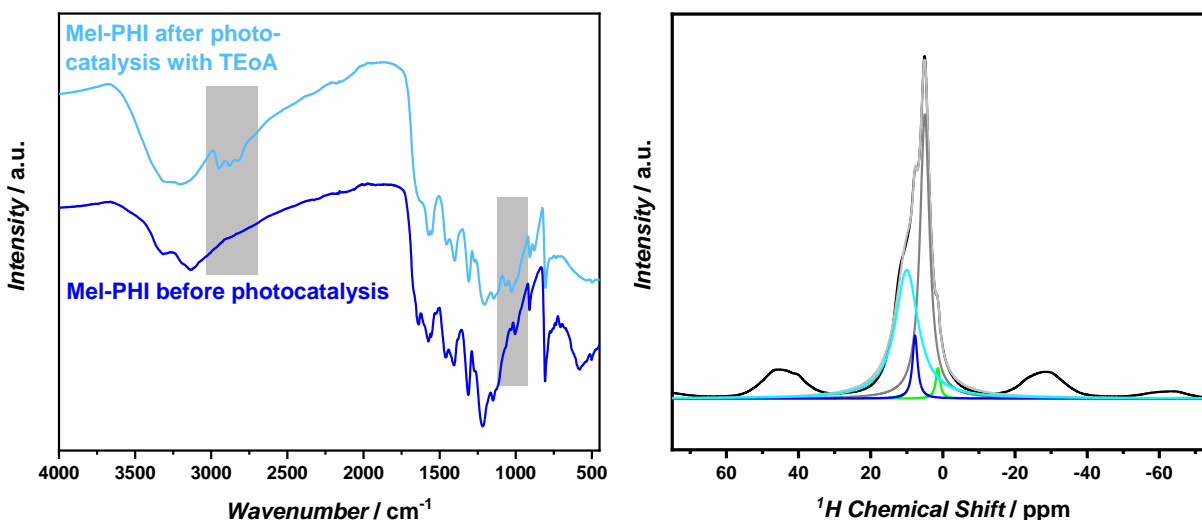


Figure S3.54: FT-IR of Mel-PHI powder before and after photocatalysis with TEOA as donor and optimized Pt loading. The sample was only washed with water. Grey areas highlighting the changes caused by TEOA interacting with Mel-PHI. Signals of TEOA (grey area) are still present even after washing with water (left). ^1H NMR of spent Mel-PHI after photocatalysis with TEOA as donor and optimized Pt loading, with additional signals around 3 ppm (green line), probably caused by protons from TEOA or its oxidation products, which is still attached to Mel-PHI (right).

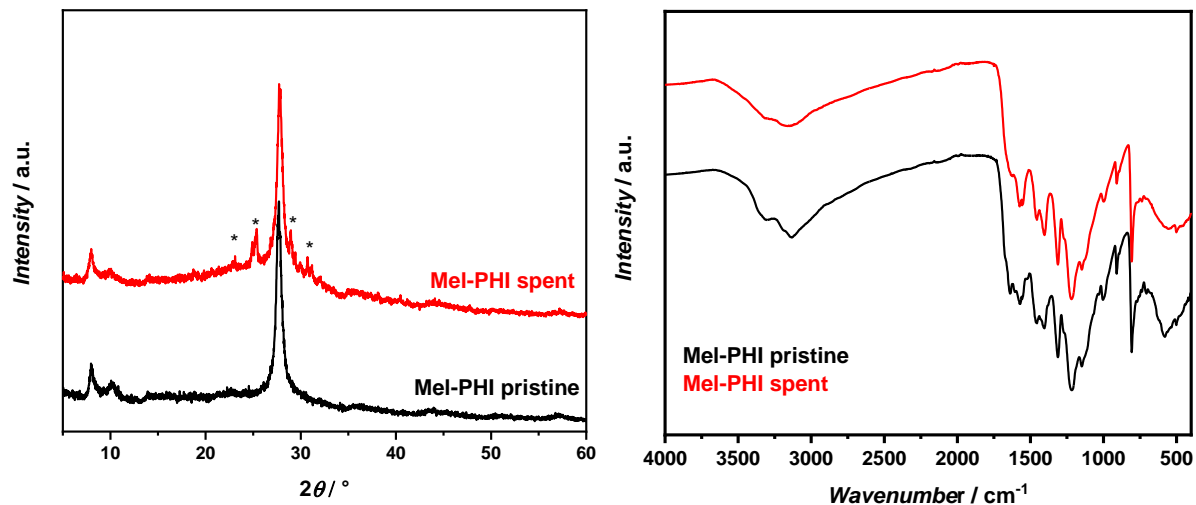


Figure S3.55: PXR (left) and FT-IR (right) of Mel-PHI powder before and after dark photocatalysis with TEoA as donor and washing with acetone after photocatalysis. Stars in the PXR mark remaining phosphate buffer, which was not fully removed by acetone washing. In FT-IR no remaining TEoA can be observed.

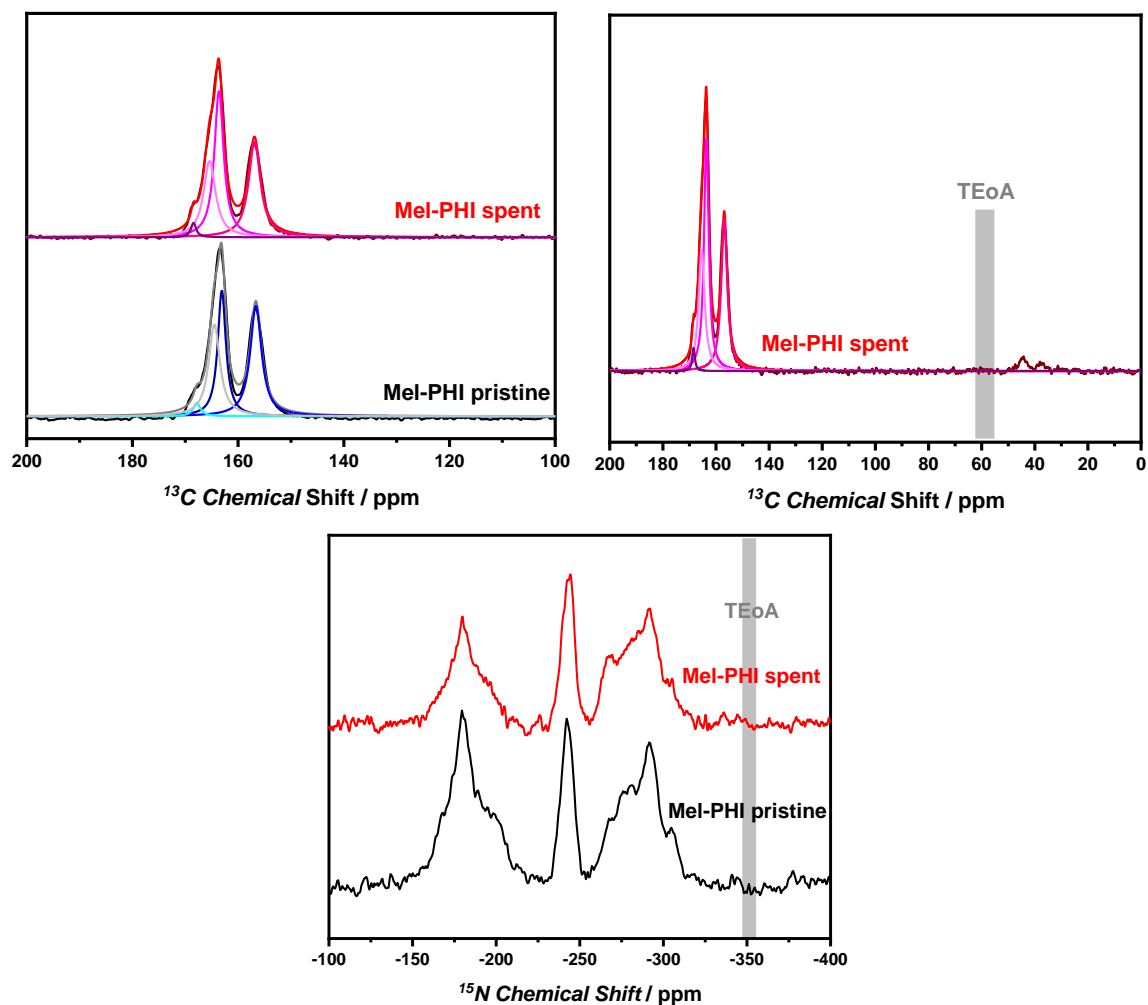


Figure S3.56: ^{13}C and ^{15}N -CP MAS NMR of pristine Mel-PHI powder (black curve) and spent Mel-PHI powder (red curve) after photocatalysis with TEoA as donor and optimized Pt loading and only washed with water. Grey areas depicting signals of TEoA.^[104]

Likewise, no significant changes of the pristine and the spent Mel-PHI were observed in ^{13}C and ^{15}N -CP MAS NMR (Figure S3.56) as well as ^1H - ^{13}C HETCOR (Figure S3.57). The ^{13}C -CP MAS NMR was fitted with four different contributions of carbon atoms, which were described earlier. The position and width of the single contributions did not change before and after photocatalysis. In ^1H - ^{15}N HETCOR (Figure S3.58) small changes in the NH_2 region can be observed, which point to a slightly higher amount of NH_2 groups after photocatalysis compared to the pristine state. This might originate from protonation during hydrogen evolution experiments. In general, the NMR measurements indicate a stable polymer backbone, which is not affected by the photocatalysis experiments.

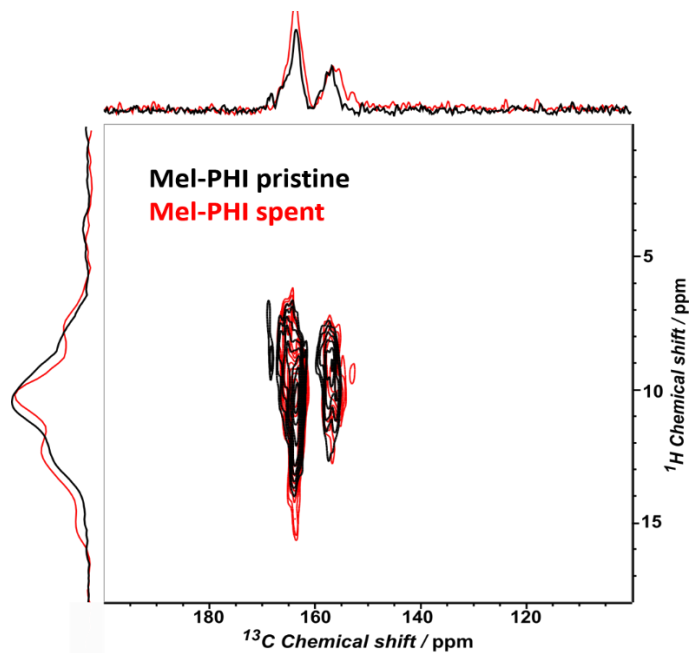


Figure S3.57: ^1H - ^{13}C HETCOR MAS NMR of spent Mel-PHI after photocatalysis with TEOA at optimized Pt loading with spinning frequency of 12 kHz. Contact times were 400 μs for the spent and 500 μs for the pristine Mel-PHI.

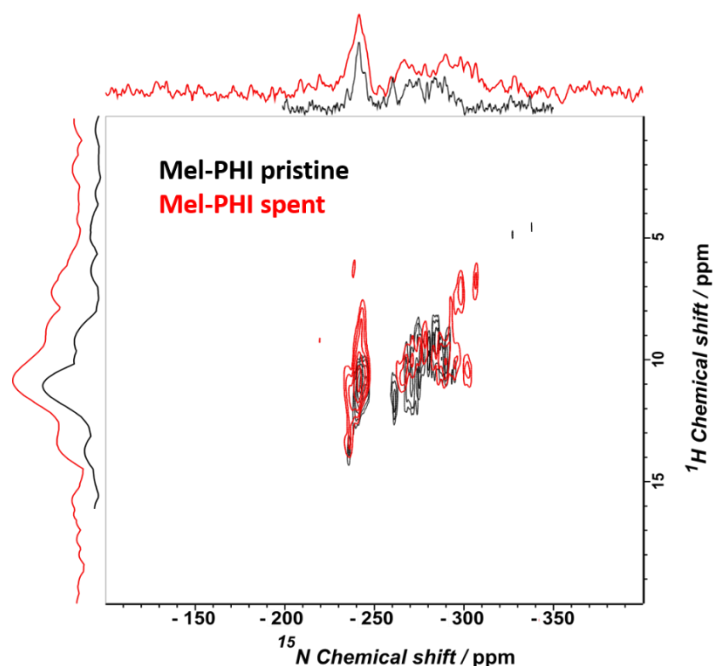
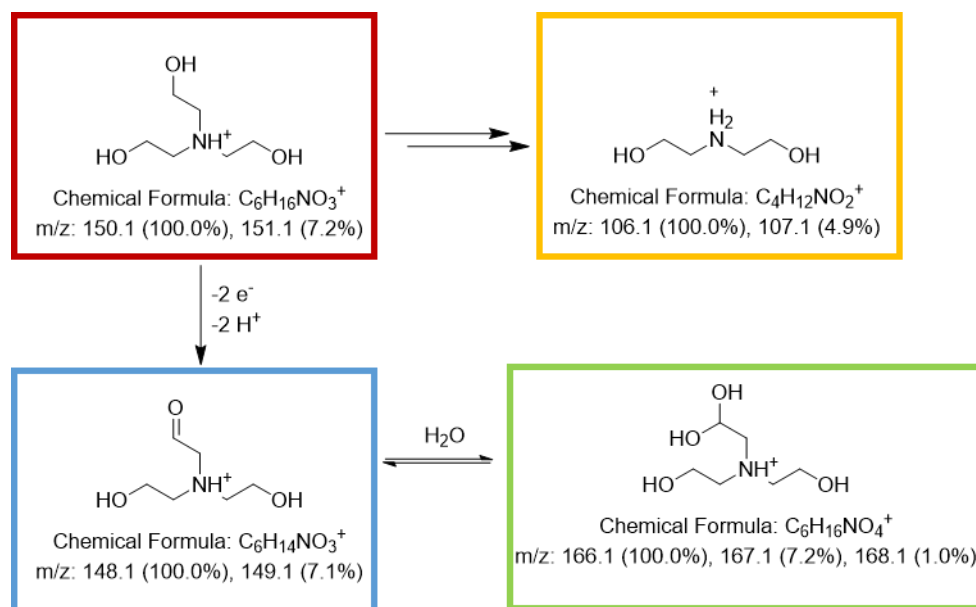


Figure S3.58: ^1H - ^{15}N HETCOR MAS NMR of spent Mel-PHI after photocatalysis with TEOA as donor and optimized Pt loading in comparison to pristine Mel-PHI at spinning frequencies of 12 kHz. Contact times were 500 μs for both measurement.

High pressure liquid chromatography with mass spectrometry (HPLC-MS) was used to analyze the oxidation products in the aqueous solution and in the washing solution (acetone) after photocatalysis. In summary, the oxidation products forming during photocatalytic hydrogen evolution with Mel-PHI and triethanolamine as donor are mainly an aldehyde (blue) and its corresponding diol (green), as well as diethanolamine (orange) (Scheme S2). Those products can be found in both, the aqueous solution and the acetone washing solution after photocatalysis, in similar relation (Figure S3.59-S3.61). However, it cannot be excluded that also further oxidation or decomposition products are present as well, similar to the once described in literature.^[103]



Scheme S3.2: Possible degradation products of triethanolamine, according to literature^[103, 105], which have been detected by mass spectrometry.

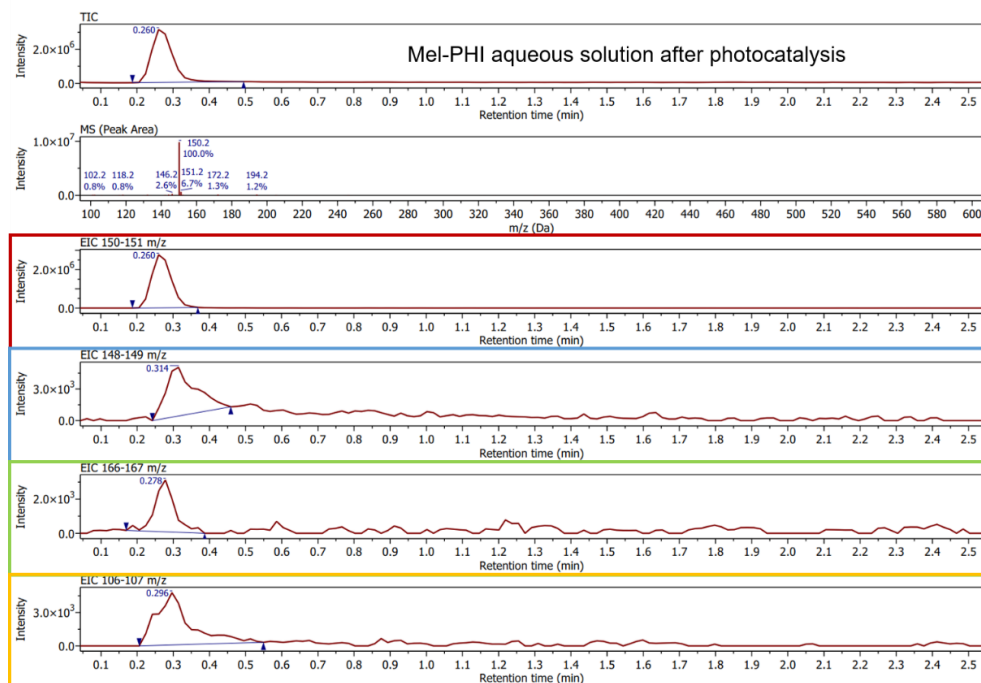


Figure S3.59: HPLC-MS analysis of an aqueous solution after photocatalysis with Mel-PHI. Total ion current (TIC) is shown on top, below the corresponding MS is depicted, followed by the extracted ion currents (EIC) of triethanolamine (red), and oxidation its products: aldehyde (blue), diol (green) and diethanolamine (orange).

Appendix

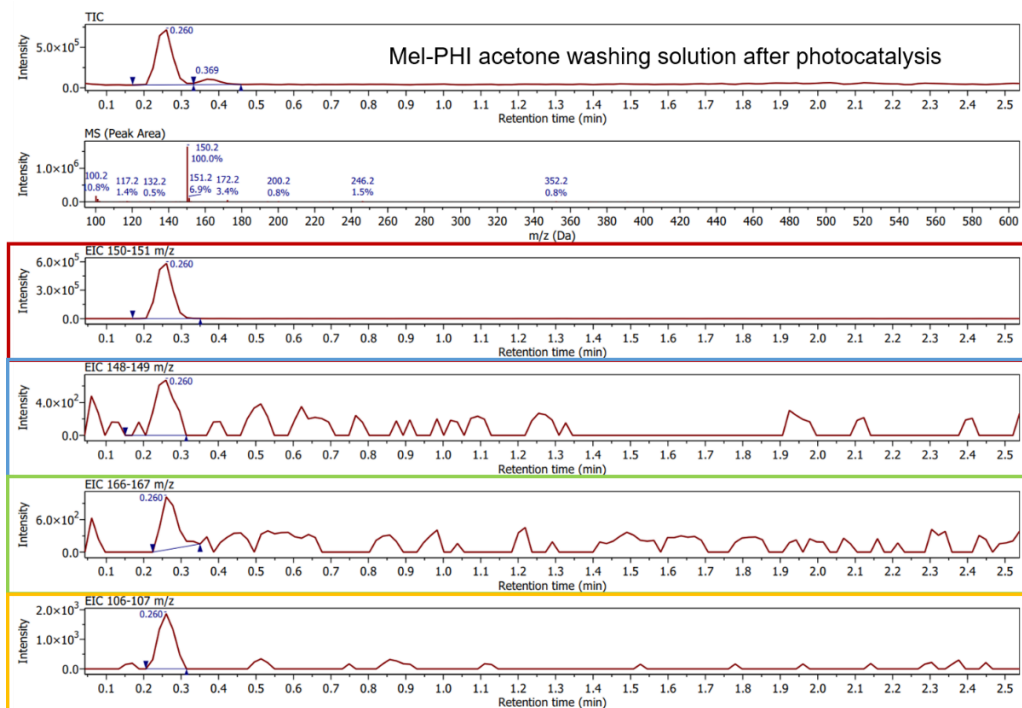


Figure S3.60: HPLC-MS analysis of an acetone washing solution after photocatalysis with Mel-PHI. Total ion current (TIC) is shown on top, below the corresponding MS is depicted, followed by the extracted ion currents (EIC) of triethanolamine (red), and oxidation its products: aldehyde (blue), diol (green) and diethanolamine (orange).

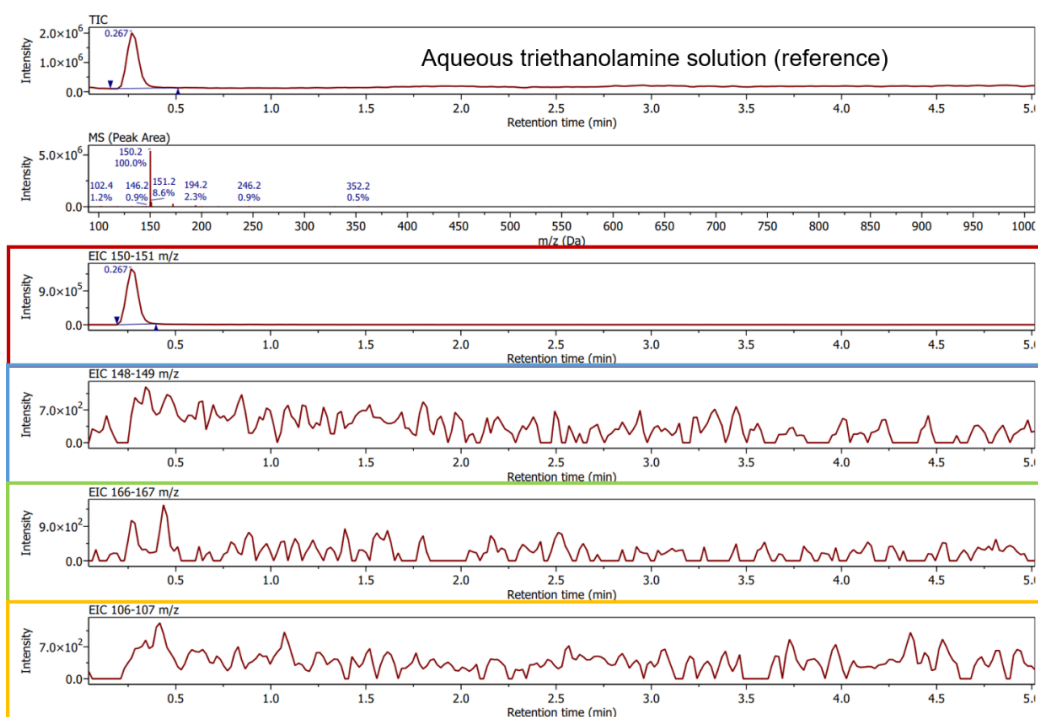


Figure S3.61: HPLC-MS analysis of the aqueous solution of triethanolamine. Total ion current (TIC) is shown on top, below the corresponding MS is depicted, followed by the extracted ion currents (EIC) of triethanolamine (red). The other traces show, the absence of oxidation its products: aldehyde (blue), diol (green) and diethanolamine (orange).

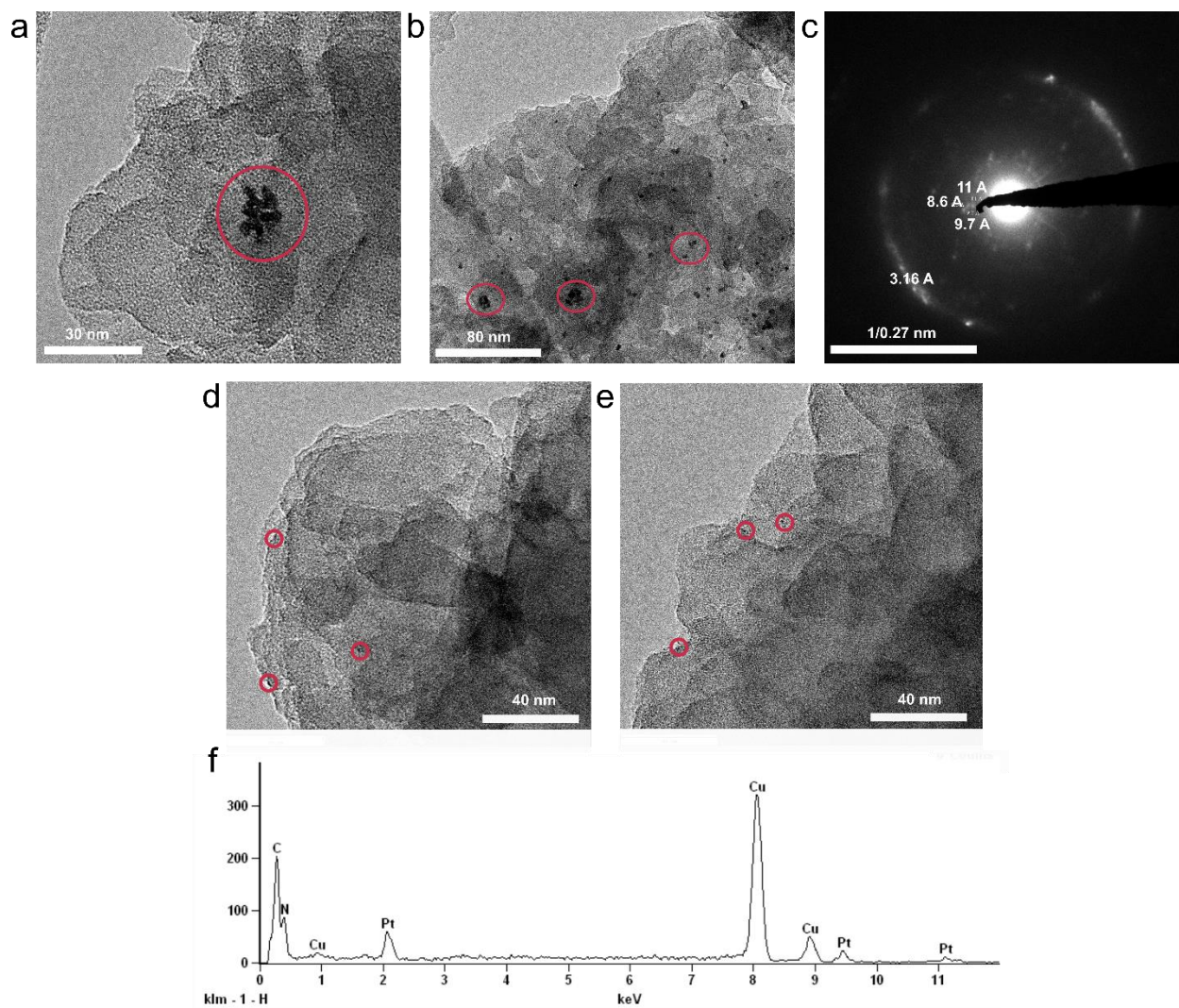


Figure S3.62: TEM images of Mel-PHI spent. Image of Mel-PHI after photocatalysis with TEOA (a-c) and MeOH (d-f) as donor and optimized Pt loading and different magnifications. Black areas depict (agglomerated) Pt nanoparticles photo-deposited at the PHI surface (0.9-5 nm for TEOA and 0.1-1 nm for MeOH), which are highlighted by red circles; c) SAED pattern of Mel-PHI after photocatalysis with TEOA; f) At the bottom, the elemental spectrum of Mel-PHI after photocatalysis with MeOH as donor is depicted, evidencing the presence of Pt.

9.3.9. PL analysis

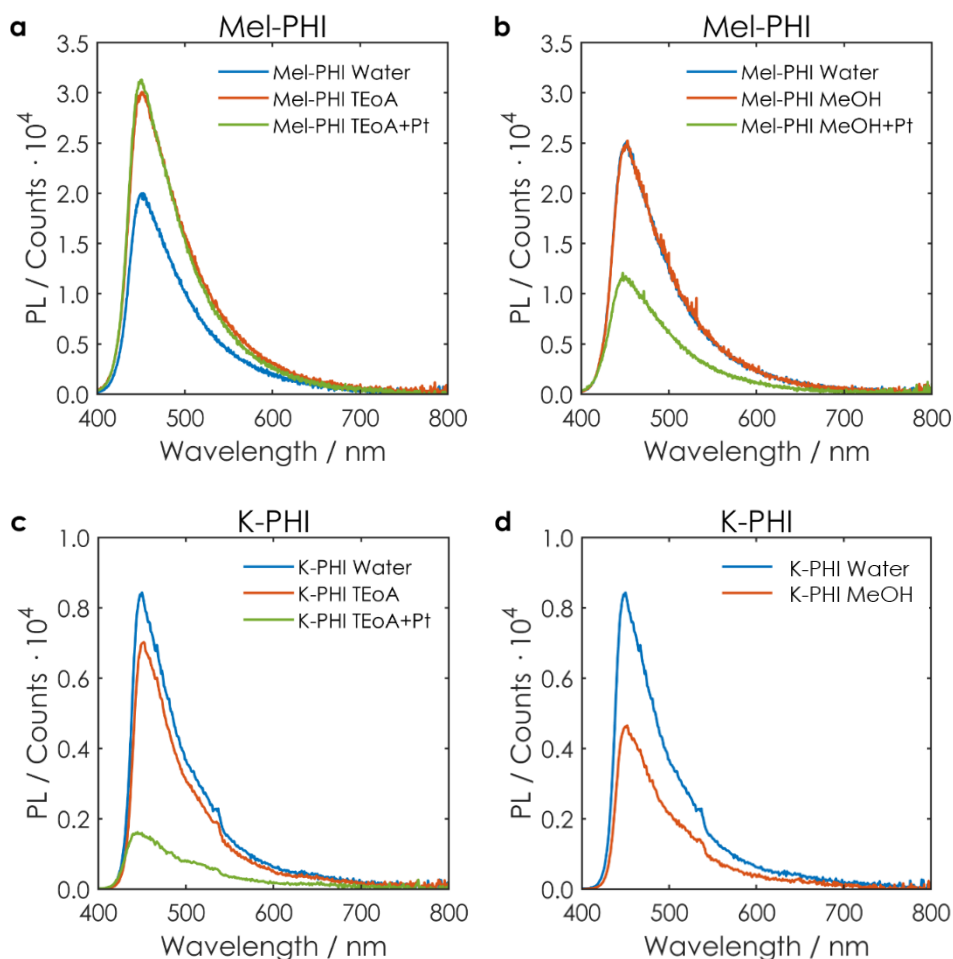


Figure S3.63: PL signal of Mel-PHI (a,b) and K-PHI (c,d) in the presence of water (blue), water and donor (red), or water, donor and Pt (green). As donor TEOA (a,c) and MeOH (b,d) were used. Pt was photo-deposited by 1 h illumination ($AM\ 1.5\ G$, $100\ mW\ cm^{-2}$) and the measurement was performed afterwards.

In general, the PL emission spectra have a similar shape, ranging from 400 to 800 nm with a maximum intensity at 450 nm (Figure S3.63).

$$TPLI = \int_{400}^{800} PL(\lambda) d\lambda$$

The total PL intensity (TPLI) of Mel-PHI with MeOH or TEOA as donor and with photo-deposited Pt shows almost no further modification in case of TEOA and Pt, whereas the TPLI is decreased by 50% in the presence of MeOH and Pt (Figure S3.64). This decay behavior with Pt might be caused by a different size of Pt particles (as seen by TEM and SEM images, Figure S3.62) at the Mel-PHI surface when MeOH or TEOA were used as donor. In contrast, K-PHI shows a TPLI depletion independent of the added donor, which is even stronger in presence of Pt (Figure S3.64).

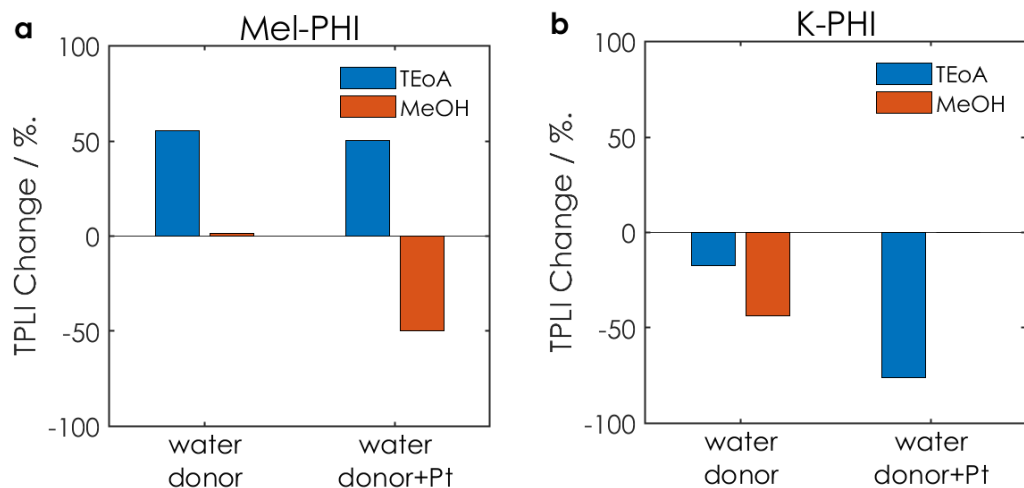


Figure S3.64: Total PL intensity (TPLI) change of Mel-PHI (a) and K-PHI (b) with TEOA (blue) and MeOH (red) with and without photo-deposited Pt containing suspension in comparison to aqueous suspension.

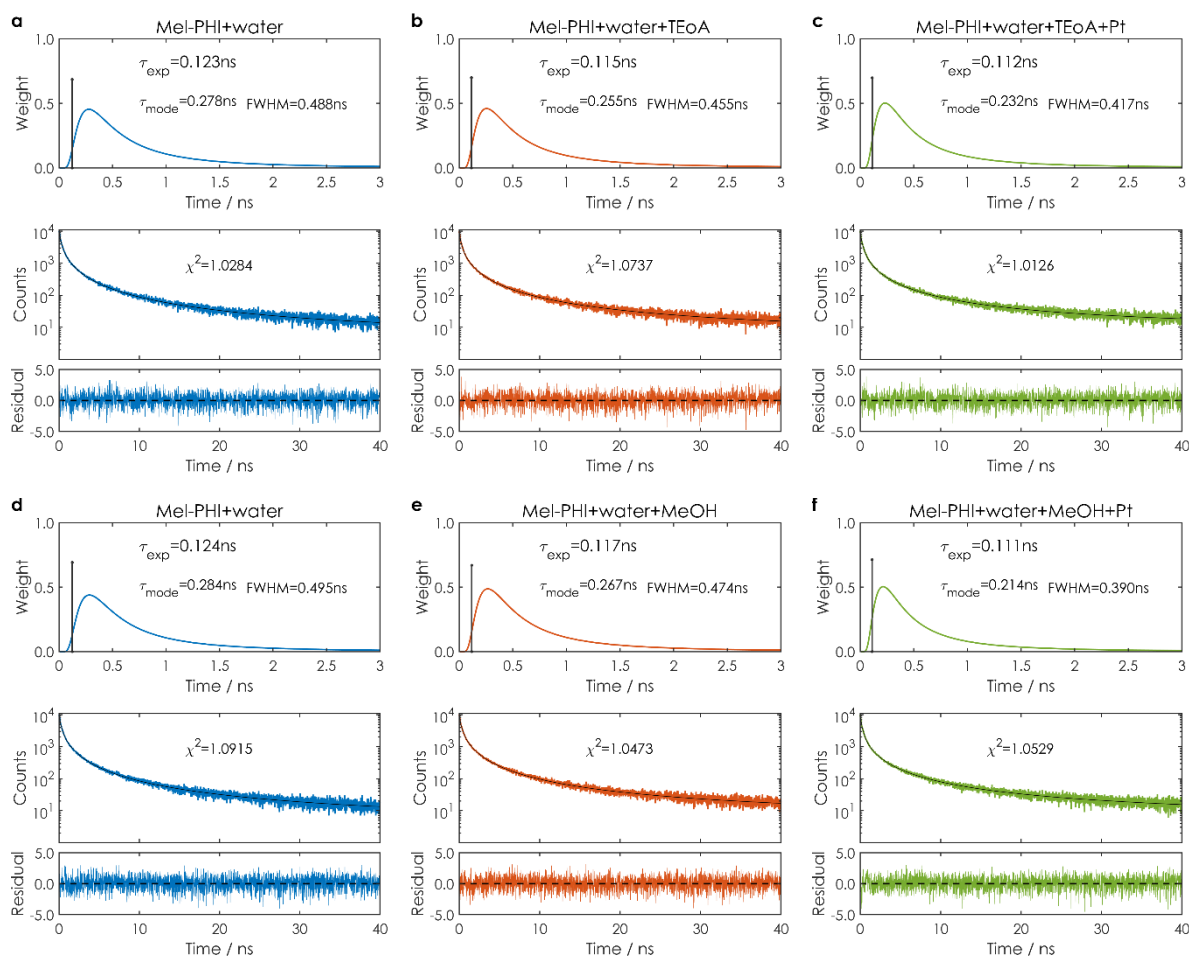


Figure S3.65: PL lifetime measurements and fittings of Mel-PHI in the presence of water (a,d), water and donor (b,e), or water, donor and Pt (c,f). Top panels correspond to TEOA (a-c) and bottom panel to MeOH (d-f) as donor. Lifetime were extracted by fitting the signal decay with a convolution of two different functions, a mono exponential and a Γ distribution^[11], denoted by τ_{exp} and τ_{mode} , respectively. Pt was photo-deposited by 1 h illumination (AM 1.5 G, 100 mW cm^{-2}).

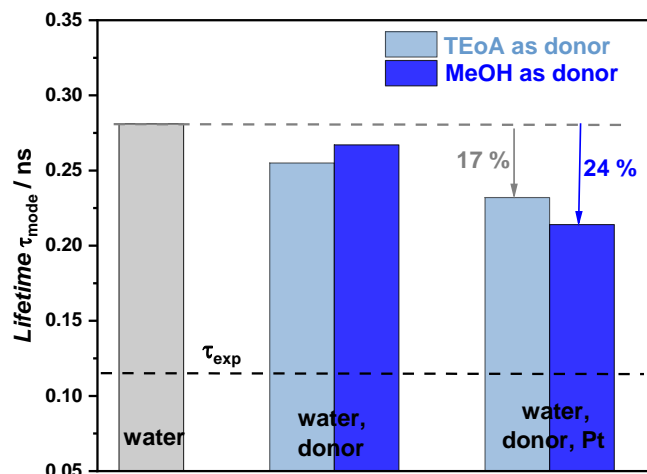


Figure S3.66: PL lifetimes of Mel-PHI comparing the effect of donor (TEoA and MeOH) as well as the case with donor and deposited Pt after 1 h under photocatalytic conditions. The lifetime was fitted with two different functions represented by τ_{exp} and τ_{mode} .

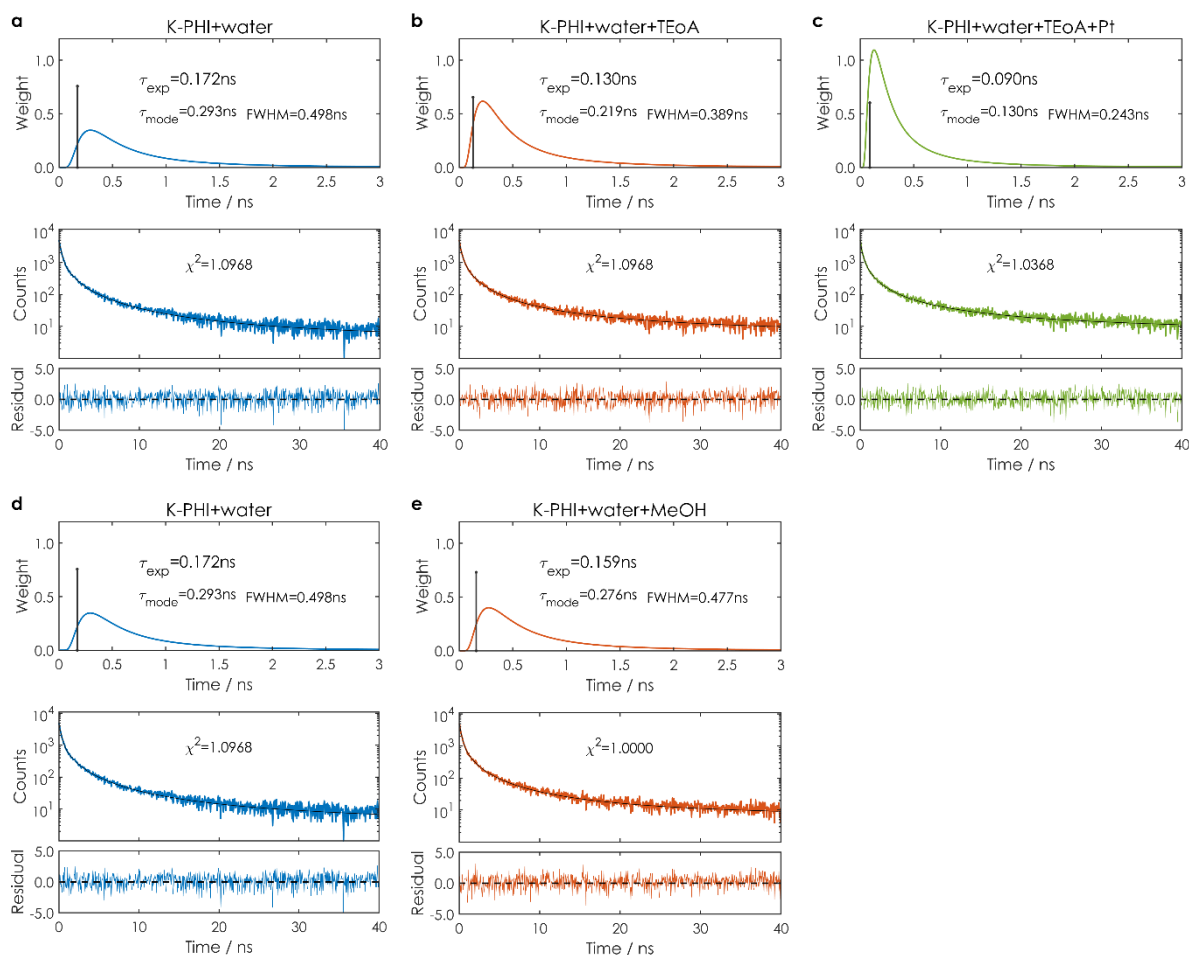


Figure S3.67: PL lifetime measurements and fittings of K-PHI in the presence of water (a,d), water and donor (b,e), or water, donor and Pt (c). Top panels correspond to TEOA (a-c) and bottom panel to MeOH (d-e) as donor. Lifetime were extracted by fitting the signal decay with a convolution of two different functions, a mono exponential and a Γ distribution^[11], denoted by τ_{exp} and τ_{mode} , respectively. Pt was photo-deposited by 1 h illumination (AM 1.5 G, 100 mW cm^{-2}).

In K-PHI (Figure S3.67) a higher decrease in τ_{mode} was observed in comparison to Mel-PHI with the use of TEoA (Figure S3.68), indicating a faster or more efficient back reaction of the electron on K-PHI with the oxidized TEoA or faster charge recombination in K-PHI general. For K-PHI, not only a decrease in τ_{mode} is observed, τ_{exp} shows also a more significant drop (compared to Mel-PHI) indicating a higher recombination rate in the bulk, which would partly explain the lower photocatalytic activity.

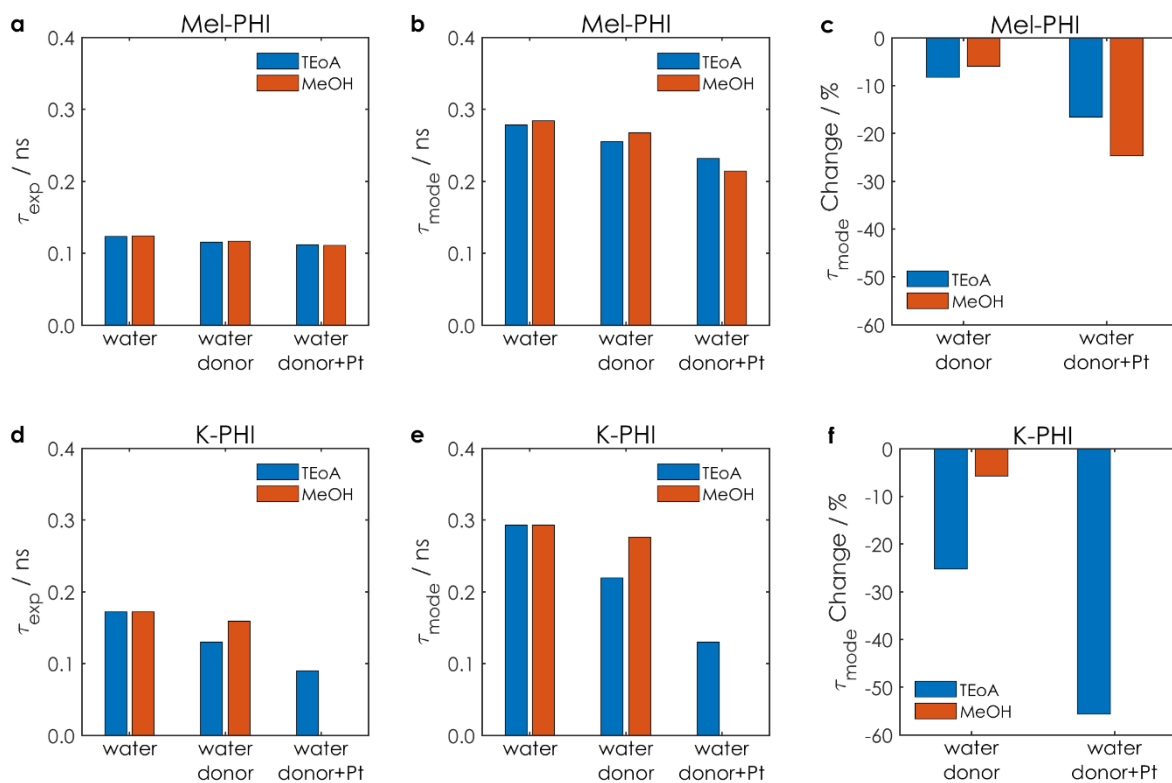


Figure S3.68: PL lifetimes of Mel-PHI (a-b) and K-PHI (d-e) comparing the effect of donor addition as well as the case with donor and deposited Pt after 1 h under photocatalytic conditions. The lifetime is fitted with two different functions represented by τ_{exp} and τ_{mode} . The relative change of τ_{mode} against the donor free suspensions is shown in (c) and (f) for Mel-PHI and K-PHI, respectively.

The PL studies can explain that HER rates decrease via a fast recombination mechanism induced by the species attached to the surface, on top of the reduced, fresh donor accessibility. The TPLI evolution of the Mel-PHI+Pt and K-PHI+Pt as a function of TEoA donor concentration (Figure S3.69) suggests a stronger Mel-PHI+Pt interaction with the donor (necessary for the deposition process) than in the K-PHI+Pt case. The Pt was pre-deposited by photo-deposition of H_2PtCl_6 under illumination for 1 h (AM 1.5 G, 100 mW cm^{-2}). After the illumination the sample was washed three times with water to remove everything that is not strongly interacting with the PHI surface. For PL measurements the powder was re-dispersed in water and the first PL spectra was recorded in the absence of any additional donor. Stepwise, the donor concentration was increased to study the effect of donor on K-PHI and Mel-PHI decorated with Pt.

Summarizing the findings of the PL measurements, we can conclude that they enable a qualitative way to understand the interaction of the active materials with their environment and also the

photocatalytic processes and their temporal evolution (via *in situ* steady-state and decay dynamics measurements).

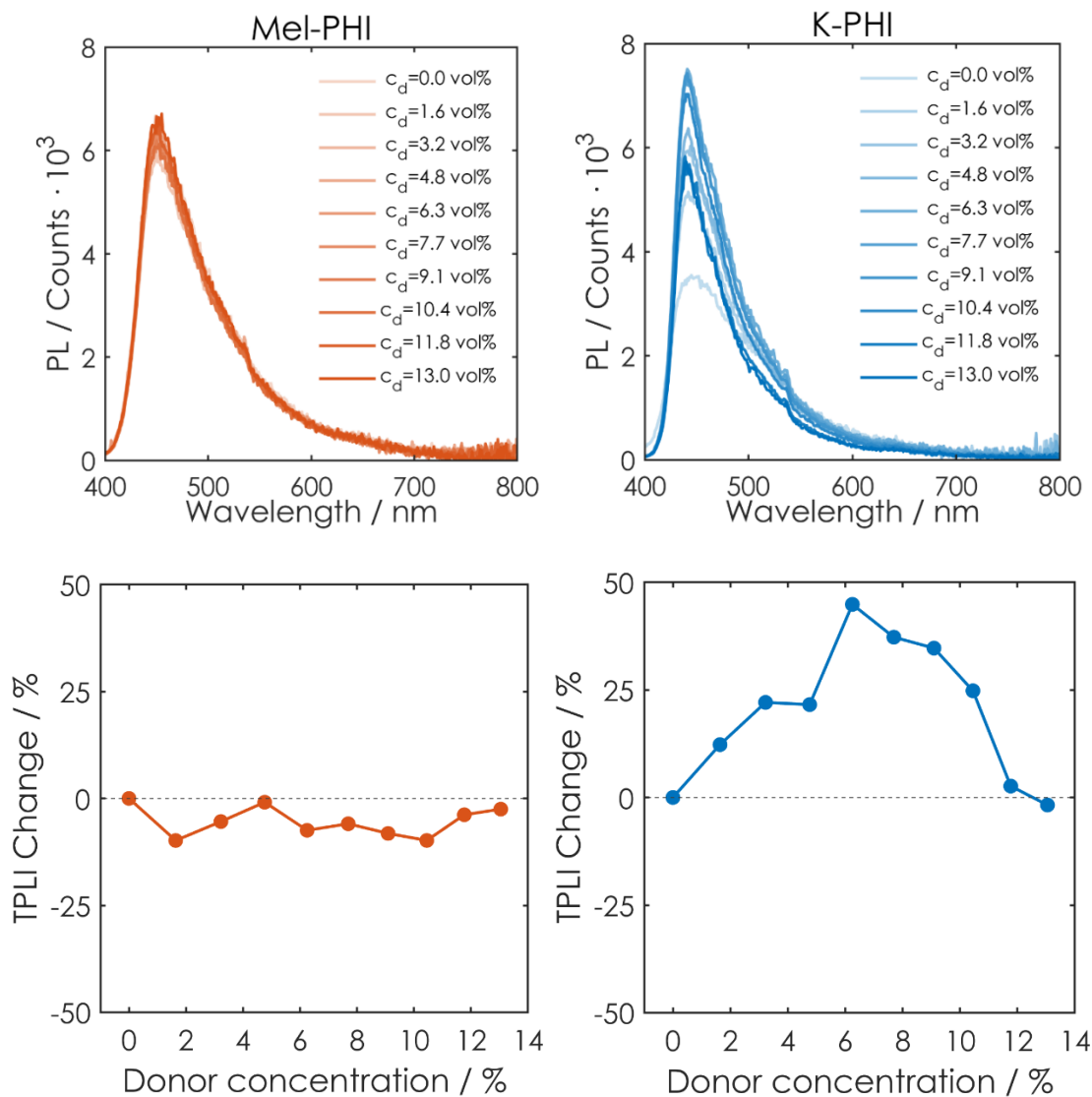


Figure S3.69: PL spectra (top) and total PL intensity (TPLI) change, taking the spent donor free sample as reference, (bottom) in dependence of different TEoA concentrations for Mel-PHI (left-hand panels) and K-PHI (right-hand panels). Prior to measurements, the suspension were degassed. Pt was photo-deposited by 1 h illumination (AM 1.5 G, 100 mW cm⁻²) and the sample was washed with water prior to these measurements.

9.3.10. Appendix quantum-chemical calculations

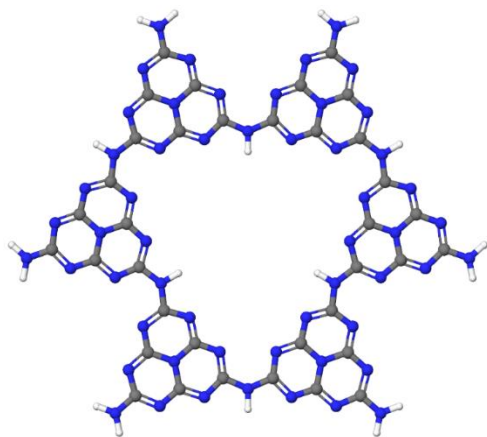


Figure S3.70: Optimized geometry for the PHI model system, obtained on PBE0-D3/def2-TZVP level of theory.

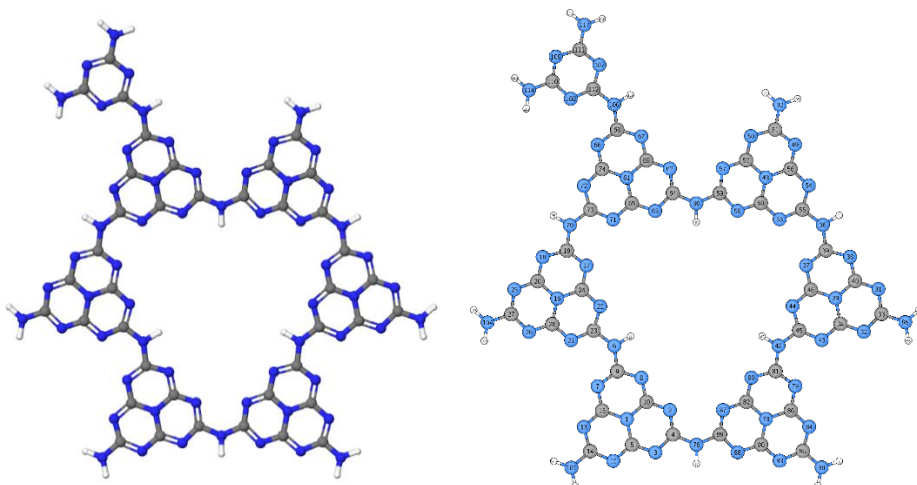


Figure S3.71: Optimized geometry for the Mel-PHI model system, obtained on PBE0-D3/def2-TZVP level of theory (left). Atom labels for the Mel-PHI model system (right).

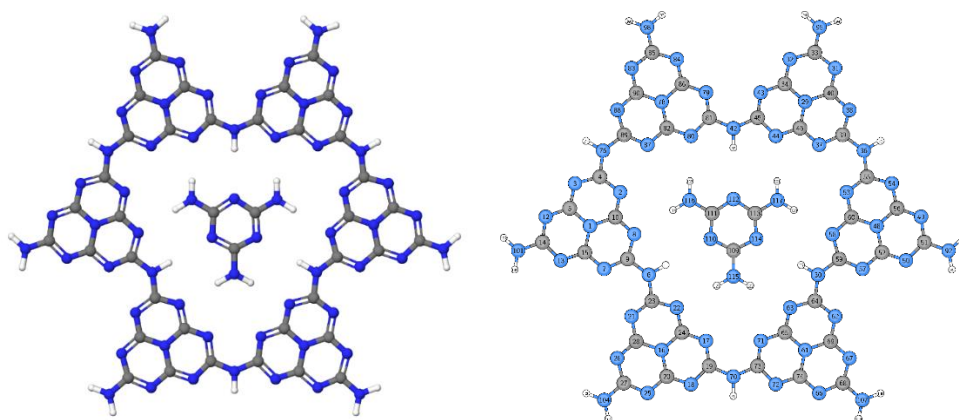


Figure S3.72: Optimized geometry for the embedded Mel-PHI model system, obtained on PBE0-D3/def2-TZVP level of theory (left). Atom labels for the embedded Mel-PHI model system (right).

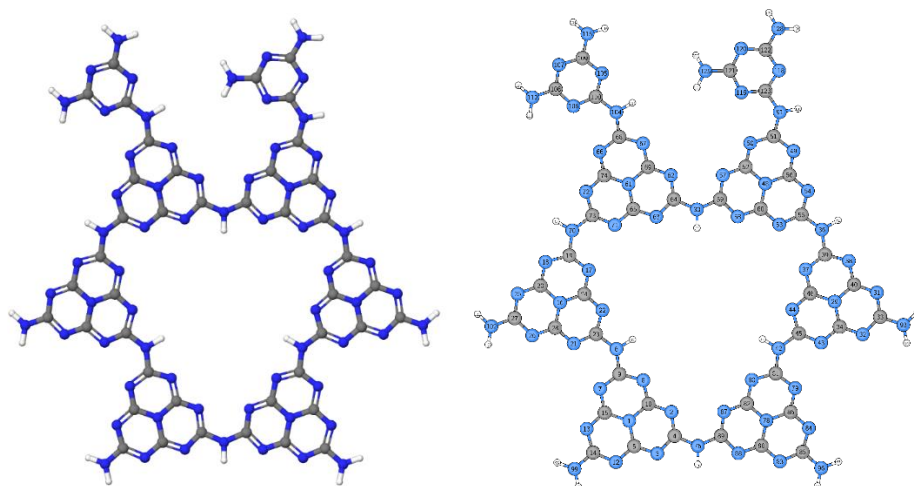


Figure S3.73: Optimized geometry for the 2-Mel-syn-PHI model system, obtained on PBE0-D3/def2-TZVP level of theory (left). Atom labels for the 2-Mel-syn-PHI model system (right).

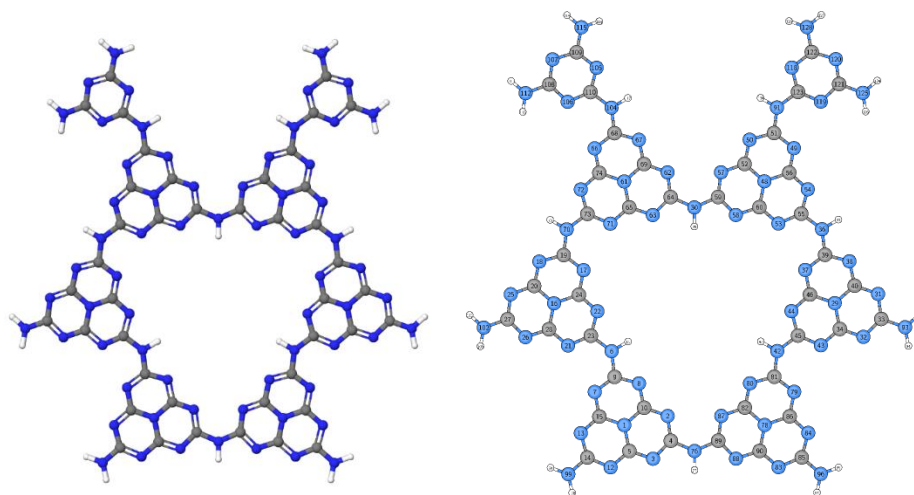


Figure S3.74: Optimized geometry for the 2-Mel-anti-PHI model system, obtained on PBE0-D3/def2-TZVP level of theory (left). Atom labels for the 2-Mel-anti-PHI model system (right).

9.3.11. Bibliography

- [1] V. W.-h. Lau, I. Moudrakovski, T. Botari, S. Weinberger, M. B. Mesch, V. Duppel, J. Senker, V. Blum, B. V. Lotsch, *Nat. Commun.* **2016**, *7* (1), 12165.
- [2] H. Schlomberg, J. Kröger, G. Savasci, M. W. Terban, S. Bette, I. Moudrakovski, V. Duppel, F. Podjaski, R. Siegel, J. Senker, R. E. Dinnebier, C. Ochsenfeld, B. V. Lotsch, *Chem. Mater.* **2019**, *31* (18), 7478-7486.
- [3] B. V. Lotsch, J. Senker, W. Schnick, *Inorg. Chem.* **2004**, *43* (3), 895-904.
- [4] E. O. Stejskal, J. D. Memory, *High Resolution NMR in the Solid State*, Oxford University Press, Oxford, **1994**, 189.
- [5] K. J. D. MacKenzie, M. E. Smith, *Multinuclear Solid-State Nuclear Magnetic Resonance of Inorganic Materials*, Elsevier Science, **2002**.
- [6] R. Sangill, N. Rastrupandersen, H. Bildsoe, H. J. Jakobsen, N. C. Nielsen, *J. Magn. Reson., Ser A* **1994**, *107* (1), 67-78.
- [7] D. P. Burum, A. Bielecki, *J. Magn. Reson.* **1991**, *94* (3), 645-652.
- [8] D. C. Apperley, R. K. Harris, P. Hodgkinson, *Solid-State NMR: Basic Principles and Practice*, Momentum Press, **2012**.
- [9] P. Swift, *Surf. Interface Anal.* **1982**, *4* (2), 47-51.
- [10] T. L. Barr, S. Seal, *J. Vac. Sci. Technol.* **1995**, *13* (3), 1239-1246.
- [11] A. C. Fogarty, A. C. Jones, P. J. Camp, *Phys. Chem. Chem. Phys.* **2011**, *13* (9), 3819-3830.
- [12] J. P. Perdew, K. Burke, M. Ernzerhof, *Phys. Rev. Lett.* **1996**, *77* (18), 3865-3868.
- [13] S. Grimme, J. Antony, S. Ehrlich, H. Krieg, *J. Chem. Phys.* **2010**, *132* (15), 154104.
- [14] A. Schäfer, C. Huber, R. Ahlrichs, *J. Chem. Phys.* **1994**, *100* (8), 5829-5835.
- [15] K. Eichkorn, F. Weigend, O. Treutler, R. Ahlrichs, *Theor. Chem. Acc.* **1997**, *97* (1), 119-124.
- [16] A. M. Burow, M. Sierka, F. Mohamed, *J. Chem. Phys.* **2009**, *131* (21), 214101.
- [17] L. Grajciar, *J. Comput. Chem.* **2015**, *36* (20), 1521-1535.
- [18] A. M. Burow, M. Sierka, *J. Chem. Theory Comput.* **2011**, *7* (10), 3097-3104.
- [19] R. Łazarski, A. M. Burow, M. Sierka, *J. Chem. Theory Comput.* **2015**, *11* (7), 3029-3041.
- [20] R. Łazarski, A. M. Burow, L. Grajciar, M. Sierka, *J. Comput. Chem.* **2016**, *37* (28), 2518-2526.
- [21] TURBOMOLE V7.3 2018, a development of University of Karlsruhe and Forschungszentrum Karlsruhe GmbH, 1989-2007, TURBOMOLE GmbH, since 2007; available from <http://www.turbomole.com>.
- [22] R. Ahlrichs, M. Bär, M. Häser, H. Horn, C. Kölmel, *Chem. Phys. Lett.* **1989**, *162* (3), 165-169.
- [23] C. Adamo, V. Barone, *J. Chem. Phys.* **1999**, *110* (13), 6158-6170.
- [24] M. Ernzerhof, G. E. Scuseria, *J. Chem. Phys.* **1999**, *110* (11), 5029-5036.
- [25] P. J. Wilson, T. J. Bradley, D. J. Tozer, *J. Chem. Phys.* **2001**, *115* (20), 9233-9242.
- [26] F. Jensen, *J. Chem. Theory Comput.* **2008**, *4* (5), 719-727.
- [27] J. Kussmann, C. Ochsenfeld, *J. Chem. Theory Comput.* **2015**, *11* (3), 918-922.
- [28] J. Kussmann, C. Ochsenfeld, *J. Chem. Phys.* **2013**, *138* (13), 134114.
- [29] J. Wang, W. Wang, P. A. Kollman, D. A. Case, *J. Mol. Graphics Modell.* **2006**, *25* (2), 247-260.
- [30] J. C. Phillips, R. Braun, W. Wang, J. Gumbart, E. Tajkhorshid, E. Villa, C. Chipot, R. D. Skeel, L. Kalé, K. Schulten, *J. Comput. Chem.* **2005**, *26* (16), 1781-1802.
- [31] <http://www.ks.uiuc.edu/Research/namd/> (accessed August 2020).
- [32] J. Wang, R. M. Wolf, J. W. Caldwell, P. A. Kollman, D. A. Case, *J. Comput. Chem.* **2005**, *26* (1), 114-114.
- [33] V. W.-h. Lau, V. W.-z. Yu, F. Ehrat, T. Botari, I. Moudrakovski, T. Simon, V. Duppel, E. Medina, J. K. Stolarczyk, J. Feldmann, V. Blum, B. V. Lotsch, *Adv. Energy Mater.* **2017**, *7* (12), 1602251.
- [34] B. P. Biswal, H. A. Vignolo-González, T. Banerjee, L. Grunenberg, G. Savasci, K. Gottschling, J. Nuss, C. Ochsenfeld, B. V. Lotsch, *J. Am. Chem. Soc.* **2019**, *141* (28), 11082-11092.
- [35] F. Podjaski, J. Kröger, B. V. Lotsch, *Adv. Mater.* **2018**, *30* (9), 1705477.
- [36] M. Qureshi, K. Takanabe, *Chem. Mater.* **2017**, *29* (1), 158-167.
- [37] H. A. Vignolo-González, S. Laha, A. Jiménez-Solano, T. Oshima, V. Duppel, P. Schützendübe, B. V. Lotsch, *Matter* **2020**, *3* (2), 464-486.
- [38] A. Schwarzer, T. Saplinova, E. Kroke, *Coord. Chem. Rev.* **2013**, *257* (13), 2032-2062.

- [39] H. Xu, J. Yan, X. She, L. Xu, J. Xia, Y. Xu, Y. Song, L. Huang, H. Li, *Nanoscale* **2014**, 6 (3), 1406-1415.
- [40] X. Lu, K. Xu, P. Chen, K. Jia, S. Liu, C. Wu, *J. Mater. Chem. A* **2014**, 2 (44), 18924-18928.
- [41] M. Liu, P. Xia, L. Zhang, B. Cheng, J. Yu, *ACS Sustain. Chem. Eng.* **2018**, 6 (8), 10472-10480.
- [42] B. D. Craig, D. S. Anderson, A. International, *Handbook of Corrosion Data*, ASM International, **1994**.
- [43] N. Zhang, J. Chen, H. Zhao, W. Shen, X. Zhang, Y. Ren, *J. Chem. Thermodynamics* **2015**, 89, 233-239.
- [44] C. Fettkenhauer, J. Weber, M. Antonietti, D. Dontsova, *RSC Adv.* **2014**, 4 (77), 40803-40811.
- [45] Y. Zhang, T. Mori, J. Ye, *Sci. Adv. Mater.* **2012**, 4 (2), 282-291.
- [46] Q. Guo, Y. Zhang, H.-S. Zhang, Y. Liu, Y.-J. Zhao, J. Qiu, G. Dong, *Adv. Funct. Mater.* **2017**, 27 (42), 1703711.
- [47] S. C. Yan, Z. S. Li, Z. G. Zou, *Langmuir* **2009**, 25 (17), 10397-10401.
- [48] M. Döblinger, B. V. Lotsch, J. Wack, J. Thun, J. Senker, W. Schnick, *Chem. Commun.* **2009**, (12), 1541-1543.
- [49] N.-N. Vu, S. Kaliaguine, T.-O. Do, *ACS Sustain. Chem. Eng.* **2020**, 8 (2), 853-863.
- [50] E. A. Wirnhier, *Solvothetical and Ionothermal Approaches to Carbon Nitride Chemistry*, LMU Munich, **2013**.
- [51] D. Zheng, C. Huang, X. Wang, *Nanoscale* **2015**, 7 (2), 465-470.
- [52] A. Savateev, Z. P. Chen, D. Dontsova, *RSC Adv.* **2016**, 6 (4), 2910-2913.
- [53] T. Botari, W. P. Huhn, V. W.-h. Lau, B. V. Lotsch, V. Blum, *Chem. Mater.* **2017**, 29 (10), 4445-4453.
- [54] N. E. Braml, A. Sattler, W. Schnick, *Chem.– Eur. J.* **2012**, 18 (6), 1811-1819.
- [55] E. Wirnhier, M. B. Mesch, J. Senker, W. Schnick, *Chem.– Eur. J.* **2013**, 19 (6), 2041-2049.
- [56] A. Sattler, *Investigations into s-Heptazine-Based Carbon Nitride Precursors*, LMU Munich, **2010**.
- [57] V. Maurino, M. Minella, F. Sordello, C. Minero, *Appl. Catal., A* **2016**, 521, 57-67.
- [58] A. Bianco Prevot, V. Maurino, D. Fabbri, A. M. Braun, M. C. Gonzalez, *Catal. Today* **2020**, 340, 286-293.
- [59] E. Wirnhier, M. Döblinger, D. Gunzelmann, J. Senker, B. V. Lotsch, W. Schnick, *Chem.– Eur. J.* **2011**, 17 (11), 3213-3221.
- [60] B. Jürgens, E. Irran, J. Senker, P. Kroll, H. Müller, W. Schnick, *J. Am. Chem. Soc.* **2003**, 125 (34), 10288-10300.
- [61] B. V. Lotsch, W. Schnick, *Chem. Mater.* **2006**, 18 (7), 1891-1900.
- [62] B. V. Lotsch, M. Döblinger, J. Sehnert, L. Seyfarth, J. Senker, O. Oeckler, W. Schnick, *Chem.– Eur. J.* **2007**, 13 (17), 4969-4980.
- [63] P. Bertani, J. Raya, B. Bechinger, *Solid State Nucl. Magn. Reson.* **2014**, 61-62, 15-18.
- [64] A. Williams, G. Martin, D. Rovnyak, *Modern NMR Approaches to the Structure Elucidation of Natural Products: Volume 2: Data Acquisition and Applications to Compound Classes*, Royal Society of Chemistry, **2016**.
- [65] C. Liu, Y. Zhang, F. Dong, A. H. Reshak, L. Ye, N. Pinna, C. Zeng, T. Zhang, H. Huang, *Appl. Catal., B* **2017**, 203, 465-474.
- [66] W. He, Y. Wang, C. Fan, Y. Wang, X. Zhang, J. Liu, R. Li, *RSC Adv.* **2019**, 9 (25), 14286-14295.
- [67] K. Baba, G. Bengasi, D. El Assad, P. Grysan, E. Lentzen, K. Heinze, G. Frache, N. D. Boscher, *Eur. J. Org. Chem.* **2019**, 2019 (13), 2368-2375.
- [68] J. C. Rivière, *Appl. Phys. Lett.* **1966**, 8 (7), 172-172.
- [69] W. M. Haynes, *CRC Handbook of Chemistry and Physics, 93rd Edition*, Taylor & Francis, **2012**.
- [70] D. I. Son, H. H. Kim, D. K. Hwang, S. Kwon, W. K. Choi, *J. Mater. Chem. C* **2014**, 2 (3), 510-514.
- [71] Y. Yang, J. Chen, Z. Mao, N. An, D. Wang, B. D. Fahlman, *RSC Adv.* **2017**, 7 (4), 2333-2341.
- [72] H. Zhang, J. Lin, Z. Li, T. Li, X. Jia, X.-L. Wu, S. Hu, H. Lin, J. Chen, J. Zhu, *Catal. Sci. Technol.* **2019**, 9 (2), 502-508.
- [73] F. K. Kessler, Y. Zheng, D. Schwarz, C. Merschjann, W. Schnick, X. Wang, M. J. Bojdys, *Nat. Rev. Mater.* **2017**, 2 (6), 17030.
- [74] Y. Ham, K. Maeda, D. Cha, K. Takanabe, K. Domen, *Chem.– Asian J.* **2013**, 8 (1), 218-224.
- [75] E. J. McDermott, E. Wirnhier, W. Schnick, K. S. Viridi, C. Scheu, Y. Kauffmann, W. D. Kaplan, E. Z. Kurmaev, A. Moewes, *J. Phys. Chem. C* **2013**, 117 (17), 8806-8812.
- [76] L. Lin, C. Wang, W. Ren, H. Ou, Y. Zhang, X. Wang, *Chem. Sci.* **2017**, 8 (8), 5506-5511.

- [77] A. Jin, Y. Jia, C. Chen, X. Liu, J. Jiang, X. Chen, F. Zhang, *J. Phys. Chem. C* **2017**, 121 (39), 21497-21509.
- [78] H. Liu, D. Chen, Z. Wang, H. Jing, R. Zhang, *Appl. Catal., B* **2017**, 203, 300-313.
- [79] J. M. Osorio-Guillén, W. F. Espinosa-García, C. M. Araujo, *J. Chem. Phys.* **2015**, 143 (9), 094705.
- [80] Y. Li, F. Gong, Q. Zhou, X. Feng, J. Fan, Q. Xiang, *Appl. Catal., B* **2020**, 268, 118381.
- [81] Y. Zhao, Y. Lin, G. Wang, Z. Jiang, R. Zhang, C. Zhu, *Appl. Surf. Sci.* **2019**, 463, 809-819.
- [82] A. Savateev, B. Kurpil, A. Mishchenko, G. Zhang, M. Antonietti, *Chem. Sci.* **2018**, 9 (14), 3584-3591.
- [83] P. Guiglion, C. Butchosa, M. A. Zwijnenburg, *Macromol. Chem. Phys.* **2016**, 217 (3), 344-353.
- [84] D. B. Nimbalkar, M. Stas, S.-S. Hou, S.-C. Ke, J.-J. Wu, *ACS Appl. Mater. Inter.* **2019**, 11 (21), 19087-19095.
- [85] K. Akaike, K. Aoyama, S. Dekubo, A. Onishi, K. Kanai, *Chem. Mater.* **2018**, 30 (7), 2341-2352.
- [86] Y. Chen, B. Wang, S. Lin, Y. Zhang, X. Wang, *J. Phys. Chem. C* **2014**, 118 (51), 29981-29989.
- [87] X. Chen, L. Liu, P. Y. Yu, S. S. Mao, *Science* **2011**, 331 (6018), 746-750.
- [88] Y. Wang, P. Du, H. Pan, L. Fu, Y. Zhang, J. Chen, Y. Du, N. Tang, G. Liu, *Adv. Mater.* **2019**, 31 (40), 1807540.
- [89] M. J. Berr, P. Wagner, S. Fischbach, A. Vaneski, J. Schneider, A. S. Sussha, A. L. Rogach, F. Jäckel, J. Feldmann, *Appl. Phys. Lett.* **2012**, 100 (22), 223903.
- [90] M. Sachs, R. S. Sprick, D. Pearce, S. A. J. Hillman, A. Monti, A. A. Y. Guilbert, N. J. Brownbill, S. Dimitrov, X. Shi, F. Blanc, M. A. Zwijnenburg, J. Nelson, J. R. Durrant, A. I. Cooper, *Nat. Commun.* **2018**, 9 (1), 4968.
- [91] J. Zhang, J. Chen, Y. Wan, H. Liu, W. Chen, G. Wang, R. Wang, *ACS Appl. Mater. Inter.* **2020**, 12 (12), 13805-13812.
- [92] D. Ruan, S. Kim, M. Fujitsuka, T. Majima, *Appl. Catal., B* **2018**, 238, 638-646.
- [93] J. Zhang, X. Chen, K. Takanae, K. Maeda, K. Domen, J. D. Epping, X. Fu, M. Antonietti, X. Wang, *Angew. Chem. Int. Ed.* **2010**, 49 (2), 441-444.
- [94] G. Liu, G. Zhao, W. Zhou, Y. Liu, H. Pang, H. Zhang, D. Hao, X. Meng, P. Li, T. Kako, J. Ye, *Adv. Funct. Mater.* **2016**, 26 (37), 6822-6829.
- [95] G. Zhang, X. Wang, *J. Catal.* **2013**, 307, 246-253.
- [96] K. Schwinghammer, M. B. Mesch, V. Duppel, C. Ziegler, J. Senker, B. V. Lotsch, *J. Am. Chem. Soc.* **2014**, 136 (5), 1730-1733.
- [97] F. Ambroz, T. J. Macdonald, V. Martis, I. P. Parkin, *Small Methods* **2018**, 2 (11), 1800173.
- [98] P. Bhattacharyya, S. Paul, A. R. Das, *RSC Adv.* **2013**, 3 (10), 3203-3208.
- [99] M. Khandelwal, S. H. Hur, J. S. Chung, *Chem. Eng. J.* **2019**, 363, 120-132.
- [100] B. Song, C. Sizemore, L. Li, X. Huang, Z. Lin, K.-s. Moon, C.-P. Wong, *J. Mater. Chem. A* **2015**, 3 (43), 21789-21796.
- [101] W. Jones, D. J. Martin, A. Caravaca, A. M. Beale, M. Bowker, T. Maschmeyer, G. Hartley, A. Masters, *Appl. Catal., B* **2019**, 240, 373-379.
- [102] M. T. Yasuda, T., S. Hirata, T. Shiragami, T. Matsumoto, *Catalysts* **2014**, 4 (2), 162-173.
- [103] S. Horikoshi, N. Watanabe, M. Mukae, H. Hidaka, N. Serpone, *New J. Chem.* **2001**, 25 (8), 999-1005.
- [104] S. N. Adamovich, G. A. Kuznetsova, I. A. Ushakov, R. G. Mirskov, A. N. Mirskova, *Russ. Chem. Bull.* **2016**, 65 (3), 826-827.
- [105] B. Kurpil, Y. Markushyna, A. Savateev, *ACS Catal.* **2019**, 9 (2), 1531-1538.

9.4. Supporting information of chapter 7 “Conductivity insights and correlation to photocatalytic hydrogen evolution in ionic PHI”

9.4.1. Experimental procedure

Synthesis of K-PHI

If not state differently, all used chemicals are reagent grade purity. Carbon nitride synthesis was performed according to literature.^[1, 2] Briefly, Melamine (5 g) was filled in a covered quartz glass boat and heated in a tube furnace under argon to 550°C for 12 h. the heating rate was 5°C min⁻¹. After cooling to ambient temperature a yellow powder (Melon) was obtained (yield 2.0-2.8 g) that was thoroughly ground for analysis. Melon (1.5 g) and water free KSCN (3 g) were ground in a ceramic mortar and pestle to synthesize K-PHI. KSCN was stored over night at 140°C in vacuum before using it in synthesis. The mixture was filled in an aluminum oxide boat for stepwise heating in a tube furnace in an argon stream. The sample was heated to 400°C for 1 hour following 500°C for 30 min at maximum heating rate. Once cooled down the sample was washed six times with deionized water by centrifugation (2000 rpm in a SIGMA 3-30k centrifuge) to remove KSCN. The yellow product was dried in vacuum at 60°C overnight, yielding 1.2-1.6 g.

Ion exchange of PHI

Ion exchange of potassium containing carbon nitride was done by adding K-PHI (0.2 mg) in an 1M MCl_x solution (20 mL; M= Li, Na, K, Cs, Ba, NH₄, TMA; x=1, 2). By adding dropwise MOH_x the pH value was adjusted to 9-10, similar to a procedure described in a previous paper of our group.^[3] The suspension was stirred over night at room temperature and washed several times (centrifugation for 10 minutes, 38950 RCF). This procedure of stirring in salt solution and washing was repeated two more times. The yellow product (yield 0.15-0.21 g) was obtained after drying the sample in vacuum at 60°C overnight.

To synthesize K(Li)-PHI the resulting Li-PHI powder was further used to do an analogous ion exchange of lithium to K-ions. Therefor the procedure described above was used.

Na-K-PHI was prepared by adding K-PHI to a slightly alkaline (from NaOH) 1M NaCl solution for 5 minutes and separated the solid from the solution by centrifugation afterwards. The product was washed three times with deionized water and dried in in vacuum at 60°C overnight.

The protonated version, H-PHI, was synthesized by stirring K-PHI (0.5 mg) in 1M HCl (100 mL) overnight at room temperature.^[2] The product was washed several times with water (centrifugation, 2000 rpm) and dried in vacuum at 60°C. 0.45-0.38 g of a white powder was yielded.

Particle size reduction of K-PHI

To gain smaller particles or nanosheets of K-PHI, 300 mg of the powder was sonicated in deionized water (100 mL) with a cooling ice bath surrounding for 2h, according to literature.^[3] To separate the bulk material from sheets two centrifugation steps were used. From the first one at 353 RCF for 25 min the P1 sheets are obtained from the precipitate. The smaller P2 particles are

received from the precipitate after centrifugation at 795 RCF for 40 min. For further used the precipitant was dried in vacuum at 60° over night.

Sample preparation for impedance measurements

The pellets for impedance measurements were pressed in an uniaxial press with 1.5-2 bar of the respective powder. Different diameters of pellets (5, 6 or 8 mm) were used to test the conductivity behavior of PHI. If not stated differently, the diameter of the pellets was 5 mm. The pellets were not stable at the edges and it could not be prevented that some small parted from the edges break apart, during setting up the measurement cells. For enhance the contact between electrode and sample, carbon foil was used or Ru was sputtered on the cold pressed samples. The used contact material is stated in every experiment again.

To distinguish between protonic and ionic conductivity, the pellets were also pressed with water, acidic or basic solutions. Before pressing a pellet one drop of liquid (deionized water, 1M KCl, 1M KCl with different amounts of HCl or KOH) was added.

Li-PHI was also tested in a non-blocking configuration in the glove box. Dry Li-PHI powder was pressed in the glove box (pellet diameter 5 mm) and put in between two Li-foils (Li|Li-PHI|Li). This configuration was used to measure AC and DC polarization measurements.

9.4.2. Instrumental setup

Material characterization

Powder X-ray diffraction (PXRD) was measured on a STOE Stadi P diffractometer (Cu K α 1) in a Debye-Scherrer configuration. PXRD measurements under atmospheres with controlled relative humidity were performed using a Bruker D8 advanced diffractometer in Bragg-Brentano geometry equipped with a copper cathode, a Ge111 Johann-type monochromator and with a Lynx-Eye detector. The diffractometer was also equipped with a CHC plus cryo and humidity chamber (Anton Paar). The atmosphere was created with a MHG-32 Modular Humidity generator. The relative humidity was varied from 1 % to 95 % at 25 °C. For the measurements a 2theta-range from 5-50° and a scan time of 1 h and a delay time of 10 minutes to achieve equilibration was applied.

Total scattering measurements were carried out using beamline P21.1 at PETRA III of the Deutsches Elektronen-Synchrotron (DESY). The rapid acquisition PDF method (RAPDF)^[4] was used with a large-area 2D PerkinElmer detector (2048×2048 pixels, 200×200 μm^2 each) and sample-to-detector distance of 350.38 mm. The incident energy of the x-rays was 101.7 keV ($\lambda = 0.1219 \text{ \AA}$). Samples were loaded into 0.5 mm inner diameter glass capillaries. An empty glass capillary was measured as background and subtracted, and a Ni standard was measured at room temperature for calibration of the setup. Calibration, polarization correction, and azimuthal integration to 1D diffraction patterns were performed using the software pyFAI^[5] with automasking from xpdtools.^[6] Additional total scattering measurements were performed using a Stoe Stadi-P diffractometer with Ag K α 1 radiation ($\lambda = 0.55941 \text{ \AA}$), a Ge(111) Johann monochromator, and a DECTRIS Mythen 1K detector in Debye-Scherrer geometry. Measurements were performed in three increments: 0.405-125.13°, 40.50-125.13°, and 81.0-125.13° with a 0.405° step size, doubling the counting time per step in the third range, and averaging the ranges together to

improve the statistics at higher angles. Data were directly corrected for the 2θ offset of the instrument and polarization effects.

Further correction and normalization of the 1D diffraction intensities were carried out to obtain the total scattering structure function, $F(Q)$, which was Fourier transformed to obtain the PDF, $G(r)$ using PDFgetX3 within xPDFsuite.^[7-10] The maximum value used in the Fourier transform of the total scattering data was 21.0 \AA^{-1} for the synchrotron data and 12.5 \AA^{-1} with a Lorch modification function^[11] for the Ag- $K\alpha_1$ laboratory data. Refinements to the PDF data were performed using TOPAS v6,^[12, 13] as discussed in a previous paper.^[2]

Pawley refinements were also performed using TOPAS v6 using a pseudo-hexagonal cell with $P1$ symmetry ($a=b$, $\alpha=\beta$, $\gamma=120^\circ$). To maximize consistency between refinements, the a cell parameter was fixed from the value determined from K-PHI for Na-PHI and Li-PHI. The peak shape was described using Gaussian and Lorentzian broadening convolutions for domain size and strain. Additionally, spherical harmonics of second order were applied to the peak widths to allow for anisotropic peak broadening as observed in the patterns. Background was described with 1st order Chebychev polynomials and a One_on_X correction for low angle scattering. The Lorentz-polarization factor was set to 27.3 for Ge(111) monochromator and Cu- $K\alpha_1$ radiation.

Transmission electron microscopy (TEM) was performed with a Philips CM30 ST (300 kV, LaB₆ cathode). In n-butanol suspended samples were drop-cast onto a lacey carbon film (Plano).

Scanning electron microscopy (SEM) was performed on a Zeiss Merlin electron microscope.

Fourier-transform infrared spectroscopy (FT-IR) was recorded on a PerkinElmer UATR TWO spectrometer equipped with a diamond crystal.

Solid state NMR measurements were performed on a Bruker Avance-III 400 MHz instrument (magnetic field of 9.4 T) at the ^1H , ^{13}C , ^{15}N , ^7Li and ^{23}Na Larmor frequencies of 400, 100.61, 40.53, 155.51 and 105.8 MHz, respectively. Magic Angle Spinning (MAS) experiments were performed on a Bruker BL4 double resonance MAS probe at spinning rates between 8 and 12.5 kHz. Cross polarization (CP) ^{13}C and ^{15}N experiments spectra were acquired using ramped contact pulses and accompanied by a composite proton decoupling with the proton RF power of 50 kHz.^[14, 15] Direct excitation quantitative ^{13}C MAS spectra were recorded at spinning rates of 12.5 kHz, 90° pulse of $3.8 \mu\text{s}$ and a recycle delay of 600 s, which allowed a complete recovery of magnetisation. The acquisition was accompanied by a composite proton decoupling, similar to the CP experiments. Spin-lattice T_1 relaxation times were measured using saturation-recovery method with direct excitation of studied nuclei.^[14] Relaxation time in the rotating frame $T_{1\rho}$ was measured by varying the duration of spin-locking pulse applied along the magnetization vector at 30-50 kHz RF power.^[14]

^1H , ^7Li and ^{23}Na variable temperature stationary spectra were obtained on a Bruker static double resonance static probe with a horizontal solenoid coil using Bloch decay experiment with central transition selective 90° -degree pulses (for both nuclei the non-selective liquid 90° -degree pulses were scaled by a factor of $1/(I + 1/2) = 1/2$ to ensure that they were central-transition selective^[15]). The temperature in the probes was regulated with a Bruker BVT3000 temperature controller. Actual temperature inside the spinner was calibrated on ^{207}Pb signal of powdered $\text{Pb}(\text{NO}_3)_2$.^[16]

Chemical shifts were referenced externally relative to TMS (^1H and ^{13}C , $\delta_{iso} = 0.0$ ppm), neat nitromethane (^{15}N , $\delta_{iso} = 0.0$ ppm) using glycine as a secondary reference (^{15}N , $\delta_{iso} = -0.0$ ppm), 0.1M NaCl (^{23}Na , $\delta_{iso} = 0.0$ ppm) and 1M LiCl (^7Li , $\delta_{iso} = 0.0$ ppm).^[17]

^7Li NMR spectra and Pulse Field Gradient (PFG) NMR measurements were performed on a Bruker Avance-III 400 MHz instrument equipped with a diff60 single gradient diffusion probe. The probe allows for pulse field gradients g of up to 30 T/m and variable temperature measurements up to +150 C. The diffusion measurements were accomplished using a Stimulated Echo pulse sequence.^[18] The echo attenuation curves $S(g,d,D)$ were processed using the Stejskal-Tanner equation^[19], $S(g,d,D)=\exp(-g^2d^2g^2D(D-d/3))$, where $g=1.398\times 10^8$ Hz/T is the ^7Li gyromagnetic ratio, g is the strength of the pulse field gradient of duration d , D is the effective diffusion coefficient, and D is the time interval between the field gradients that defines the diffusion time scale.

Inductively Coupled Plasma optical emission spectroscopy (ICP-OES) was used for the quantification of elements. The measurements were performed with a Vista Pro Simultaneous ICP-OES Spectrometer combined with axially plasma system as excitation source and echelle polychromator with CCD detector (Varian Darmstadt). ICP-OES Spectrometer was calibrated by standard addition. For analysis the samples were digested in concentrated HNO_3 at 150 °C for 14 h in a Teflon-lined autoclave. Resulting data were analyzed by the ICP-*Expert* software.

Diffusive light scattering was measured on a Malvern Zetasizer Nano ZS in aqueous suspension of PHI (0.25 mg mL⁻¹).

Thermogravimetric analysis (TGA-MS) was performed on a NETZSCH STA 449 F5 Jupiter with an inert gas flow (Ar) of 50 ml/min and a heating rate of 3K/min.

Electrochemical characterization

The impedance spectra were recorded in a frequency range of 1×10^6 - 1×10^{-1} / 1×10^{-2} Hz with a Novocontrol alpha analyzer (high resolution dielectric analyzer) as well as a Metrohm single / multichannel potentiostat. As measurement cell, a Swagelok cell with steel electrodes was used, as well as a self-made impedance cell with steel electrodes and Teflon surrounding for the pellet to avoid static charging of the air next to pellet. The results of both measurements cells were compared to decouple the measurement from specific cell parameter. In both cases, similar results were obtained. The analysis of the impedance spectra were performed with the commercial software Relaxis.

Galvanostatic DC polarization measurements were performed with a Keithley 2604B Source Meter by applying 2, 5 or 10 nA current to the pressed pellets in a Swagelok cell. For higher time resolution in DC polarization, a Metrohm single PGSTAT302N/ multichannel potentiostat with an additional module for high speed measurements was used.

Humidity dependent measurements

For humidity dependent measurements, pre-ried K-PHI (several days in vacuum at 60°C and storing in the glovebox afterwards) was pressed in the glove box (diameter 6 mm). The pellet was sputtered with Ru (99.95 %, Lesker, DC sputtering with Emitech K575X, 100 mA current, 4 min sputter time under Ar) on both sides and contacted with Pt electrodes in a quartz sample holder. The humidity or partial pressure of water was set with a single-walled glass container (humidifier) which was immersed in a thermostat (F 25, Julabo) to regulate its temperature. The humidifier contained water through which dry argon was flushed connected with the measurement cell. The humidified argon was mixed with dry argon close to the measurement cell. Dry and wet Ar gas were set in the range 0-50 and 20-50 sccm respectively, and the thermostat temperature was varied between 5 and 20 °C (0-23.3 mbar). The measurements were done isothermally at 35 °C (rel. humidity 5.2-41.6 %), and the sample temperature was constantly monitored with a dedicated thermocouple next to the pellet. The exhaust gas humidity after the measurement cell was checked with a humidity (Rototronic Messgeräte GmbH) and dew point (EE355-PA1, E+E Elektronik GmbH) sensor. Gas flows were adjusted with flow controllers (FC-7700C, Aera) and the complete set-up as well as measurement cell were leaked checked (helium leak detector, UL 200 dry, Oerlikon Leybold Vacuum). The kinetics of reaching the equilibrium at every humidity step were followed by impedance measurements again. Every hour one impedance spectrum was measured until now further changes were observed, to ensure the pellet has been fully equilibrated with the environment. For Li-PHI also the hysteresis behavior to moisten and drying the pellet stepwise was studied. After reaching the humidity of 23.3 mbar the moisture was reduced to 13.9 and 6.7 mbar again.

For NMR and some impedance as well as DC measurements the sample tube filled with the powder or the pressed pellets were stored in a 75 %RH environment in a closed vessel with 90 g NaCl in 250 mL DI water reservoir for several days to allow the material to equilibrate with environment. Afterwards, the sample tube for NMR measurements was sealed with a glass tube, so that no head space was left. The pressed pellets were measured immediately after removing from the vessel.

Optical characterization and photocatalytic hydrogen evolution

The optical bandgap was measured with a diffusion reflectance UV-Vis (DR UV-Vis) spectrometer (Cary 5000) that was referenced to PTFE or barium sulfate. The measured reflectance spectra are converted using the Kubelka-Munk function. This data are plotted in a Tauc plot, assuming a direct optical band gap, to extract the optical bandgap.

The photoluminescence (PL) spectra as well as the lifetime of the samples were recorded on a double monochromator spectrofluorometer (Edinburgh FLS980) at an excitation wavelength of $\lambda = 370$ nm. For decay experiments, PL was collected over a 5 nm spectral window centered at $\lambda = 480$ nm. The time-resolved PL were fitted with a combination of a δ function and a Γ function, like it was described in a previous paper of our group.^[20, 21] Suspensions with concentrations of 0.25 mg mL⁻¹ in water were used for measurements. To prevent agglomeration and sedimentation, the suspensions were stirred during the measurement.

Photocatalytic hydrogen evolution experiments were conducted in a double-walled glass reactor with a quartz glass window on top, allowing top illumination, as described in literature.^[1, 22, 23] The space between the double-walls was used to thermostate the photocatalytic reaction to 25°C by circulating water. For illumination a xenon lamp (Newport, 300W) was used, which is equipped with a water filter and a full spectrum mirror (2000 nm > λ > 200 nm). Additionally, an air mass (AM) 1.5 G filter was used, to simulate the solar spectrum. For the photocatalytic hydrogen reaction an aqueous suspension (9 mL) of PHI (10mg) in addition to 1 mL methanol as electron donor as well as 20 μ L hexachloroplatinate (8 wt% aqueous solution) were used. The headspace of the reactor was evacuated and backfilled with Argon six times prior to hydrogen evolution experiments. During illumination the suspension is stirred and the co-catalyst Pt is photo-deposited *in-situ* on the carbon nitride material. The headspace is sampled periodically and analyzed by gas chromatography (Thermo Scientific TRACE GC Ultra). The detector in this GC is a thermal conduction detector using Ar as a carrier gas.

Molecular-Mechanics and Quantum-Chemical Calculations

Atom positions and lattices of a 2D periodic PHI structure were optimized on RI-PBE-D3/def2-TZVP^[24-29] level of theory using an acceleration scheme based on the resolution of the identity (RI) technique and the continuous fast multipole method (CFMM)^[30-32] implemented^[33, 34] in Turbomole version V7.3.^[35, 36] The CFMM uses multipole moments of maximum order 20, together with a well-separatedness value of 3 and a basis function extent threshold of 10E-9 a.u. Grid 7 was used for the numerical integration of the exchange-correlation term. The norm of the gradient was converged to 10E-4 a.u. and the total energy to 10E-8 Hartree within the structure optimization using the gamma point approximation.

Using the optimized, 2D periodic PHI structure, a single PHI pore was cut out, deprotonating a single imide bridge by removing the hydrogen atom at the imide bridge of the PHI backbone (Figure S4.50 left). Parameters for molecular dynamics simulations for this single anionic PHI pore were prepared using antechamber.^[37] Force field minimizations and dynamics were performed using the NAMD^[38, 39] program package and GAFF^[40] parameters. Periodic boundary conditions and particle mesh Ewald summation (PME) with a cutoff value of 12 Å were employed.

Using the single anionic PHI pore, a PHI pore canal was modeled by stacking 12 single pores as a defect-free eclipsed stacking with a layer distance of 3.2 Å. Two different deprotonation patterns were modeled: Pore model 1 uses all deprotonated imide bridges located on top of each other, whereas pore model 2 uses deprotonated imide bridges alternating through the layers in a random fashion (Figure S4.51). Each pore model was solvated in a box of TIP3P water with 10 Å padding in *a/b* direction (across the 2D layer) and 15 Å padding in *c* direction (across the pore canal). Corresponding ions were placed in the center of each pore with a distance of 5 Å between ions. This pre-fills the pore with ions and neutralizes the anionic backbone charges. Each PHI pore canal was then minimized using the conjugate gradient algorithm in 10000 steps by constraining the coordinates for the pore excluding the hydrogen atoms that were allowed to relax along with the present ions and solvent molecules. The system was then heated to 300 K in 30 ps and equilibrated subsequently for 30 ns with time steps of 2 fs employing the SETTLE algorithm.

The last frame of the 30 ns simulation was selected from the MM/MD trajectories, from which molecular clusters were cut for each of the ions located in the PHI pore canal with 6.4 Å padding including water and anionic PHI backbone pores, in order to calculate interaction energies next. While we do not statistically average over the many possible configurations, we expect a first impression of the trends. Interaction energies between ion and water (IAE_IW), ion and the PHI pore (IAW_IP), and the water shell around the ions and the PHI backbone (IAE_WP) were calculated on PBE0-D3/Def2-TZVP^[24-27] level of theory performed using the FermiONs++ program package,^[41, 42] without basis set superposition corrections in order to gain a first estimate.

9.4.3. Structural analysis of PHI with different counterions

The ion exchange of K-PHI by different cations can be observed by a small remaining potassium content in PHI and a high amount of the new cation replacing potassium in the same molar ratio (Table S4.1). Only tetramethylammonium (TMA) could not replace potassium within the pores since the ionic radius of this molecule is too big to fit into the PHI pores (“Number” inner diameter). The amount of Cs was not detectable directly by elemental analysis, but the measured decreased potassium amount of only 0.22 wt% suggested an almost complete replacement by Cs.

For an ion exchange the replacement step is repeated three times. To study also what is happening after short time interaction with the exchange solution K-Na-PHI is synthesized. For this compound K-PHI was only stirred for 2 min in a NaCl solution and afterwards washed with water. The remaining potassium was 1.13 wt%, whereas already 2.18 wt% sodium could be found in the PHI material, showing that the ion exchange is quite a fast process.

Table S4.1: Element analysis of ion exchange in PHI.

K [wt%]	Li [wt%]	Na [wt%]	Ba [wt%]	Sample	Composition
9.76	-	-	-	K-PHI	C ₇ N ₁₀ K _{0.75}
0.36	1.63	-	-	Li-PHI	C ₇ N ₁₀ Li _{0.75} K _{0.03}
0.66	-	4.96	-	Na-PHI	C ₇ N ₁₀ Na _{0.68} K _{0.05}
0.09	-	-	16.98	Ba-PHI	C ₇ N ₁₀ Ba _{0.38}
5.77	-	-	-	K(afterLi)-PHI	C ₇ N ₁₀ K _{0.44}
0.22	-	-	-	Cs-PHI	
0.07	-	-	-	NH ₄ -PHI	
4.68	-	-	-	TMA-PHI	
0.25	-	-	-	H-PHI	
1.13	-	2.18	-	K-Na-PHI	C ₇ N ₁₀ Na _{0.30} K _{0.09}

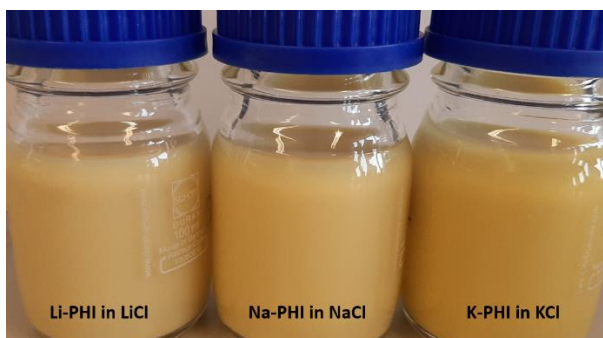


Figure S4.1: Suspensions of Li-PHI in LiCl, Na-PHI in NaCl and K-PHI in KCl, showing a color gradient from lighter yellow for Li-PHI to darker yellow (K-PHI).

Structure of Li-PHI

For Li-PHI the PXRD pattern looks different than K-PHI. In comparison to the known structure of K-PHI^[2] with stacking faults, it appears similar to that theoretically expected for a pattern from a perfectly eclipsed stacking of PHI sheets. However, the intensities trailing to higher- Q and triangular-shaped peaks suggest interlayer stacking disorder, and thus most likely that the on-average hexagonal nature of the lattice, it not representative of the local orientations between neighboring layers.

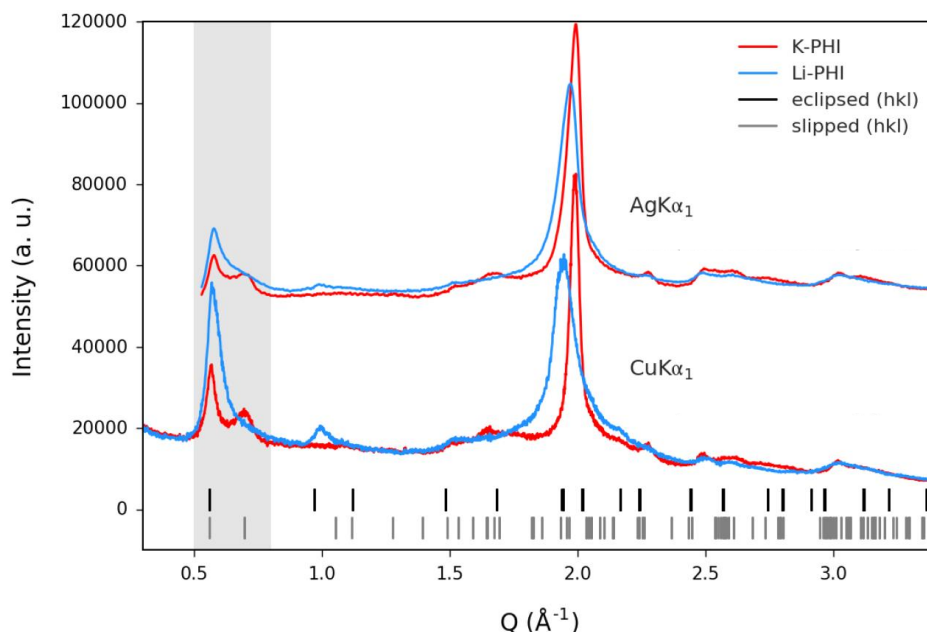


Figure S4.2: Comparison of two different sets of K-PHI and Li-PHI samples, measured by $\text{AgK}\alpha_1$ and $\text{CuK}\alpha_1$ radiation respectively. The $\text{AgK}\alpha_1$ sample patterns have been shifted to account for differences in 2θ offset. The expected hkl reflection positions for unit cells with slipped (gray ticks) and eclipsed (black ticks) packing are also shown for reference.

Both sets of samples in FigureS4.2 show similar trends. The interlayer packing distance is longer in the Li-PHI sample than for the K-PHI sample (i.e. large reflection shifter to lower Q values). Also, the K-PHI sample shows two distinct low angle reflections, indicating slipped packing, while Li-PHI shows a feature that more closely resembles a single peak (see highlighted region). In the $\text{Ag-K}\alpha_1$ measurement of Li-PHI, a shoulder at the second reflection position points to increasing presence of slipped packing. In the $\text{Cu-K}\alpha_1$ sample set, the first peak appears more like a single

peak, however there is still some trailing diffuse intensity on the high- Q side. This may indicate that in both cases, Li-PHI has a more eclipsed-like packing on average, but locally with interlayer positional disorder or slipped-like stacking faults.

PDF analysis and stacking fault simulation

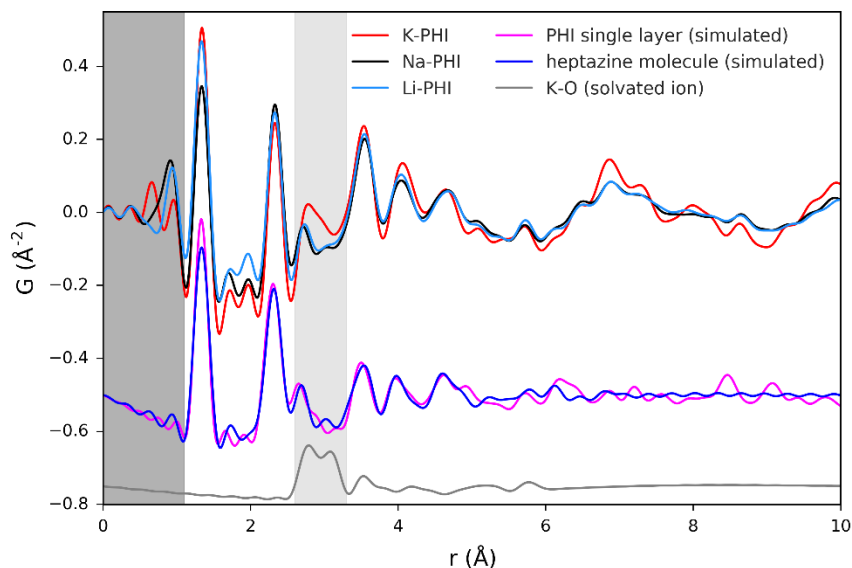


Figure S4.3: Short- r range of PDFs obtained from synchrotron total scattering data. PDFs calculated from a single heptazine molecule (blue), single PHI layer (magenta), and from K-water coordination shell (gray, from previous paper^[2]) are shown for reference.

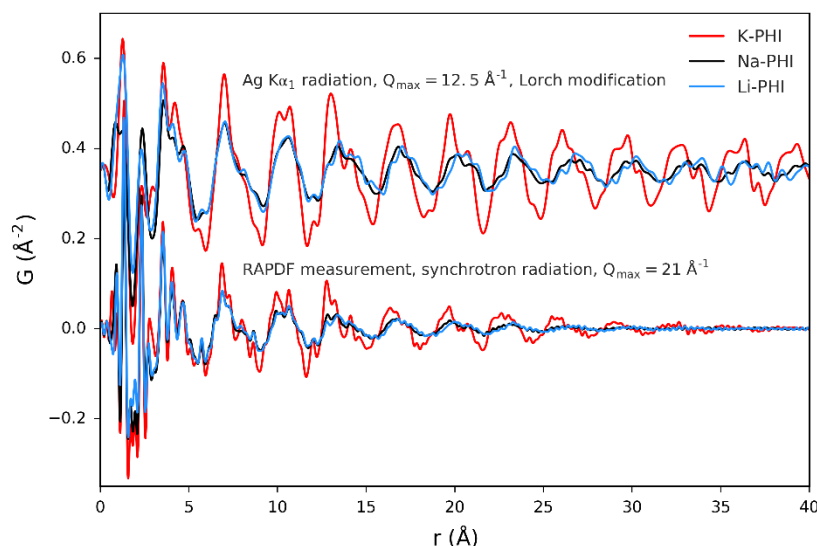


Figure S4.4: Long- r range of PDFs plotted up to 40 Å or about 13 layers. Over the first few interlayer distances, the shape and relative amplitudes of the PDFs are similar, with some subtle differences. In particular, some more distinct lineshapes become a bit broader for the Li- and Na-PHI sample. At longer distances, the longer interlayer packing distance in Li-PHI becomes more apparent by the extension of the broad interlayer peaks to slightly higher distances.

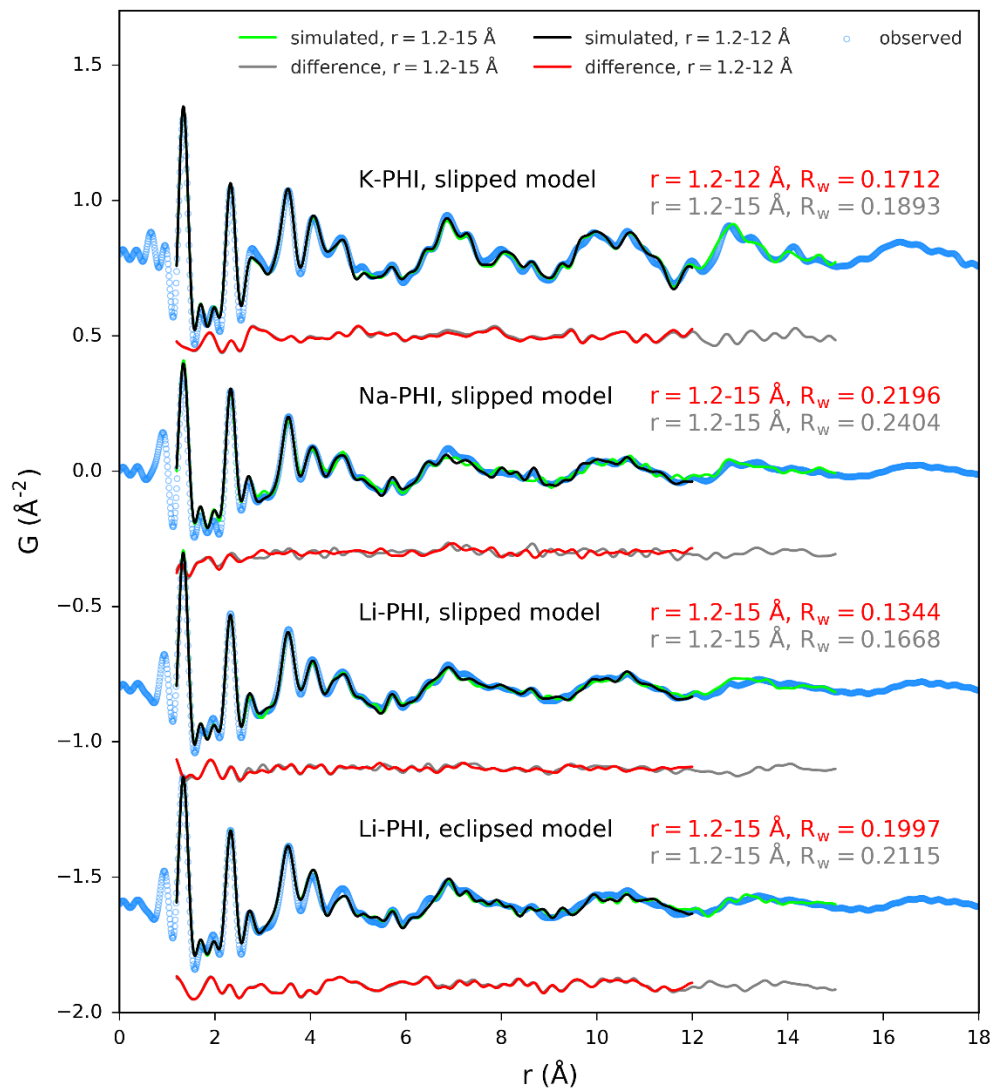


Figure S4.5: Refinements of slipped models derived from the model determined in the previous paper^[2]. The agreement of the slipped model to both K-PHI and Li-PHI is very good, despite our expectation that the Li-PHI sample is more eclipsed-like on average. The fit for Na-PHI is still good, but slightly poorer than the other two which may be indicative of different distributional properties, or possibly other local structure factors such as defects, etc. The eclipsed model (with $\alpha=\beta=90^\circ$) performs poorly compared to the slipped model for Li-PHI. We also fitted the eclipsed model to Na-PHI (not shown) and this also performed worse than the slipped model (eclipsed model $R_w = 0.2534$ over $1.2-12 \text{ \AA}$). Overall, this indicates that the local structures of both Na- and Li-PHI are also dominated by slightly offset orientations of neighboring layers, more similar to the K-PHI sample, but less ordered.

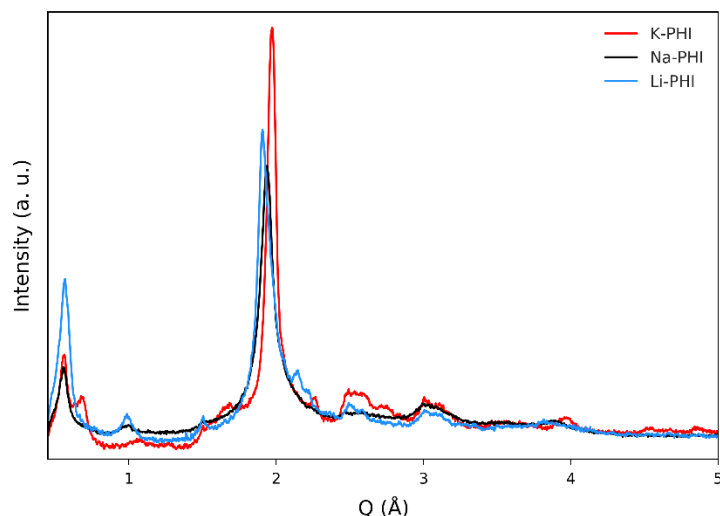


Figure S4.6: Comparison of the background subtracted intensities obtained of PDF analysis for K-, Na-, and Li-PHI, as measured with Ag-K α 1 radiation. The instrument profile has a lower resolution than e.g. the datasets presented as measured from Cu-K α 1 radiation.

On-average interlayer distance and local stacking offsets were determined from local structure model refinement to the PDF data. Refinements were performed with two slightly different parameterizations of the atomic displacement parameters and correlated motion, each over ranges of 1.2–12 and 1.2–15 Å, and the values and standard deviation were determined from the four results to account for some bias by the fitting model and refinement range (Table S4.2). While the distance and offset are correlated, though not completely (~70, 50, and 60% for K-, Na-, and Li-PHI respectively), the refinements were stable and consistent, and the interlayer distances agree well with that estimated from the interlayer Bragg reflections via Pawley refinement, which should be dominated by the stacking distance and less affected by offsets.

Table S4.2: Stacking distances and layer offset of Li-, Na- and K-PHI estimated from PDF refinement.

Sample	Stacking distance (001) [Å] PDF/Pawley refinement	Layer offset in [110] direction [Å]
Li-PHI	3.18(\pm 0.02) / 3.20	2.3(\pm 0.2)
Na-PHI	3.17(\pm 0.01) / 3.17	2.6(\pm 0.1)
K-PHI	3.15(\pm 0.01) / 3.15	2.8(\pm 0.1)

To further study the stacking features in Li-PHI simulations for stacking faults were used. For simulating the diffractive effects of planar defects in the poly(heptazine imide) lattice, a supercell approach implemented in the TOPAS software^[12] was used. The unit cell of the PHI compounds was transformed into a pseudo-trigonal metric as described in previous works.^[2] Due to additional disorder of the water molecules situated within the pores of the PHI materials, we omitted the water related oxygen atoms in the simulations and focused on only the effects of the PHI framework. The stacking sequence of the layers was described by *stacking vectors*. The stacking vectors can be derived directly from the layer constitution. There are six likely stacking vectors that could be expected to lead to a maximization of the favorable interlayer π - π interactions:

$$S1 = \begin{pmatrix} 0.0245 \\ 0.1193 \\ 1 \end{pmatrix} \quad S2 = \begin{pmatrix} 0.0948 \\ -0.0245 \\ 1 \end{pmatrix} \quad S3 = \begin{pmatrix} -0.1193 \\ -0.0948 \\ 1 \end{pmatrix}$$

$$S4 = \begin{pmatrix} -0.0245 \\ -0.1193 \\ 1 \end{pmatrix} \quad S5 = \begin{pmatrix} -0.0948 \\ 0.0245 \\ 1 \end{pmatrix} \quad S6 = \begin{pmatrix} 0.1193 \\ 0.0948 \\ 1 \end{pmatrix}$$

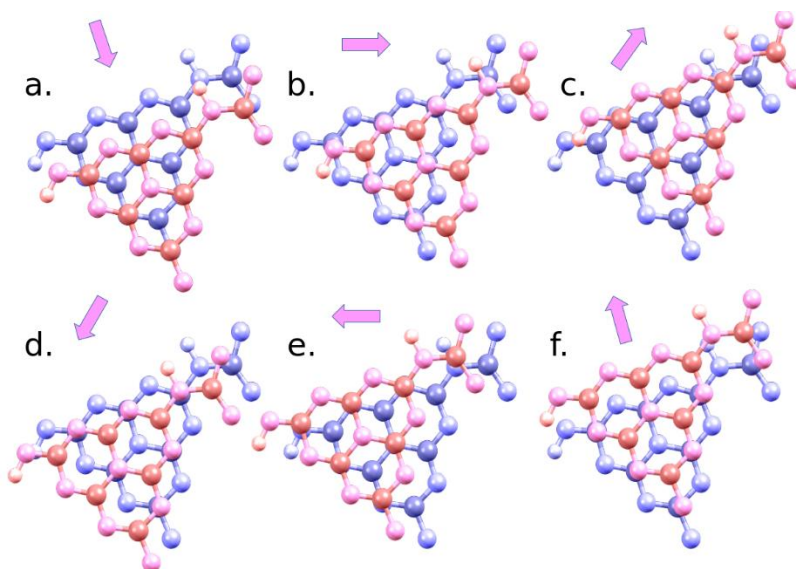


Figure S4.7: Translations associated with the six different shift vectors.

These stacking vectors bring carbon and nitrogen atoms of neighboring layers in direct opposition and therefore lead to staggered stacking order (Figure S4.7). In order to simulate the transition from an eclipsed to a staggered stacking by a gradual layer offset, we introduced an additional parameter, Poff, which modifies the x- and y- components of the stacking vectors, S_i , leading to modified vectors, S_j .

$$S_j = \begin{pmatrix} \text{Poff} \cdot S_{i_x} \\ \text{Poff} \cdot S_{i_y} \\ 1 \end{pmatrix}$$

As the staggered stacking occurs completely undirected in the PHI compounds², the transition probabilities among the six different staggered stacking orders (Table S4.3, stag1-stag6) was fixed to 1/6. In the systematic simulations 100 stacks of 200 layers each were created and averaged. The parameter Poff was increased from 0.00 to 2.00 in 0.05 steps, in order to simulate the gradual transition from eclipsed (Poff = 0.00) to an undirected staggered layer stacking (Poff \geq 1.00).

Table S4.3: Transition probability matrix applied for the systematic simulations of the XRPD patterns of stacking faulted PHI-compounds, including transition probability (first line) and stacking vectors (second line, eq. 1). Stag1-stag6 represent 6 different staggered stacking orders (see above).

from↓/to→	stag1	stag2	stag3	stag4	stag5	stag6
stag1	1/6, S1 · Poff	1/6, S2 · Poff	1/6, S3 · Poff	1/6, S4 · Poff	1/6, S5 · Poff	1/6, S6 · Poff
stag2	1/6, S1 · Poff	1/6, S2 · Poff	1/6, S3 · Poff	1/6, S4 · Poff	1/6, S5 · Poff	1/6, S6 · Poff
stag3	1/6, S1 · Poff	1/6, S2 · Poff	1/6, S3 · Poff	1/6, S4 · Poff	1/6, S5 · Poff	1/6, S6 · Poff
stag4	1/6, S1 · Poff	1/6, S2 · Poff	1/6, S3 · Poff	1/6, S4 · Poff	1/6, S5 · Poff	1/6, S6 · Poff
stag5	1/6, S1 · Poff	1/6, S2 · Poff	1/6, S3 · Poff	1/6, S4 · Poff	1/6, S5 · Poff	1/6, S6 · Poff
stag6	1/6, S1 · Poff	1/6, S2 · Poff	1/6, S3 · Poff	1/6, S4 · Poff	1/6, S5 · Poff	1/6, S6 · Poff

The resulting diffraction patterns, simulated from Poff=0.0 (green) to Poff=2.0 (magenta) are compared to the diffraction pattern of Li-PHI in Figure S4.8. As the offset is increased, we can see that many peaks present lose intensity where there is no or negligible intensity in the measured pattern (highlighted in grey). In some cases, peaks disappear completely at sufficient translation, e.g. the peak at approximately 2.75 \AA^{-1} . Another feature of the increasing offset value, is that $(hk0)$ peaks such as the first two peaks: 100 and -120, become more diffuse with trailing intensities on the higher angle side of the peaks. This feature is also experimentally observed in the slightly triangular, or Warren, peak shape that is characteristic of materials with 2D defects. A comparison of the first few peaks shown in Figure S4.9 to better highlight the change in peak position and shape. Overall, we cannot fully neglect the effects of the pore content on the measured diffraction patterns, however this primarily tends to only modulate the low angle peak intensities and possibly contribute to additional anisotropic broadening of features, as with finite crystallite size. It does not tend to produce new Bragg peaks since the pore content is atomically non-periodic. Our previous structural investigation of K-PHI found an order slip-stacking driven by K-water interactions, while H-PHI was found to be randomly slipped with some ordered domains. Here, it is likely that the small size of the Li ions also has a less drastic effect on directing the layer stacking, and they are more likely to tend toward a random slipping. Thus, the apparent preference for local slipped interaction, and more 'eclipsed'-looking diffraction pattern seem to be plausibly resolved by the possibility for small random local offsets, which manifest over the long-range as an approximately eclipsed crystallographic structure.

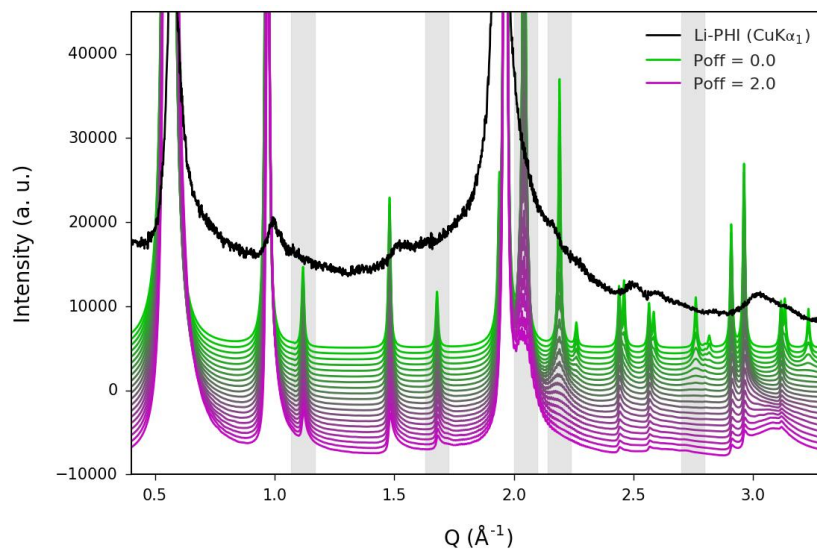


Figure S4.8: Comparison of simulated diffraction patterns with increasing random layer offset to the experimental pattern of Li-PHI.

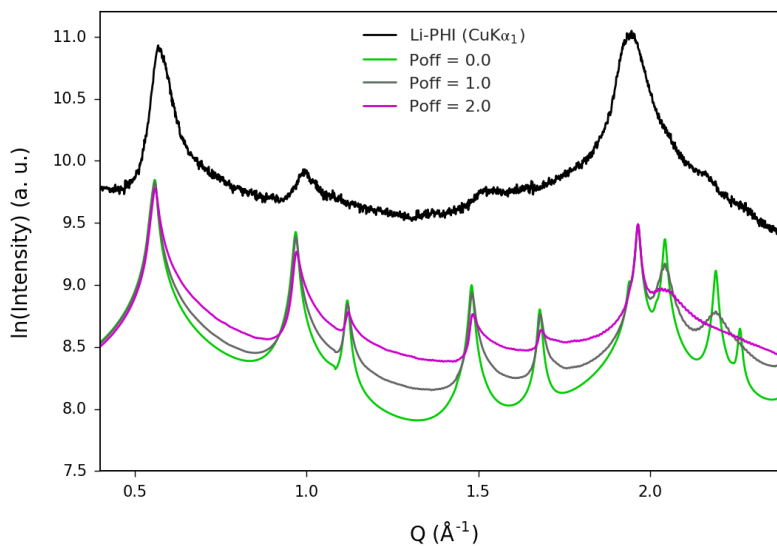


Figure S4.9: Comparison of selected simulated diffraction patterns with increasing random layer offset to the experimental pattern of Li-PHI. Plotted as the natural log of the diffracted intensities, it is easier to see the increase in diffuse intensities trailing on the high angle side of the Bragg peaks due to the random 2D disorder.

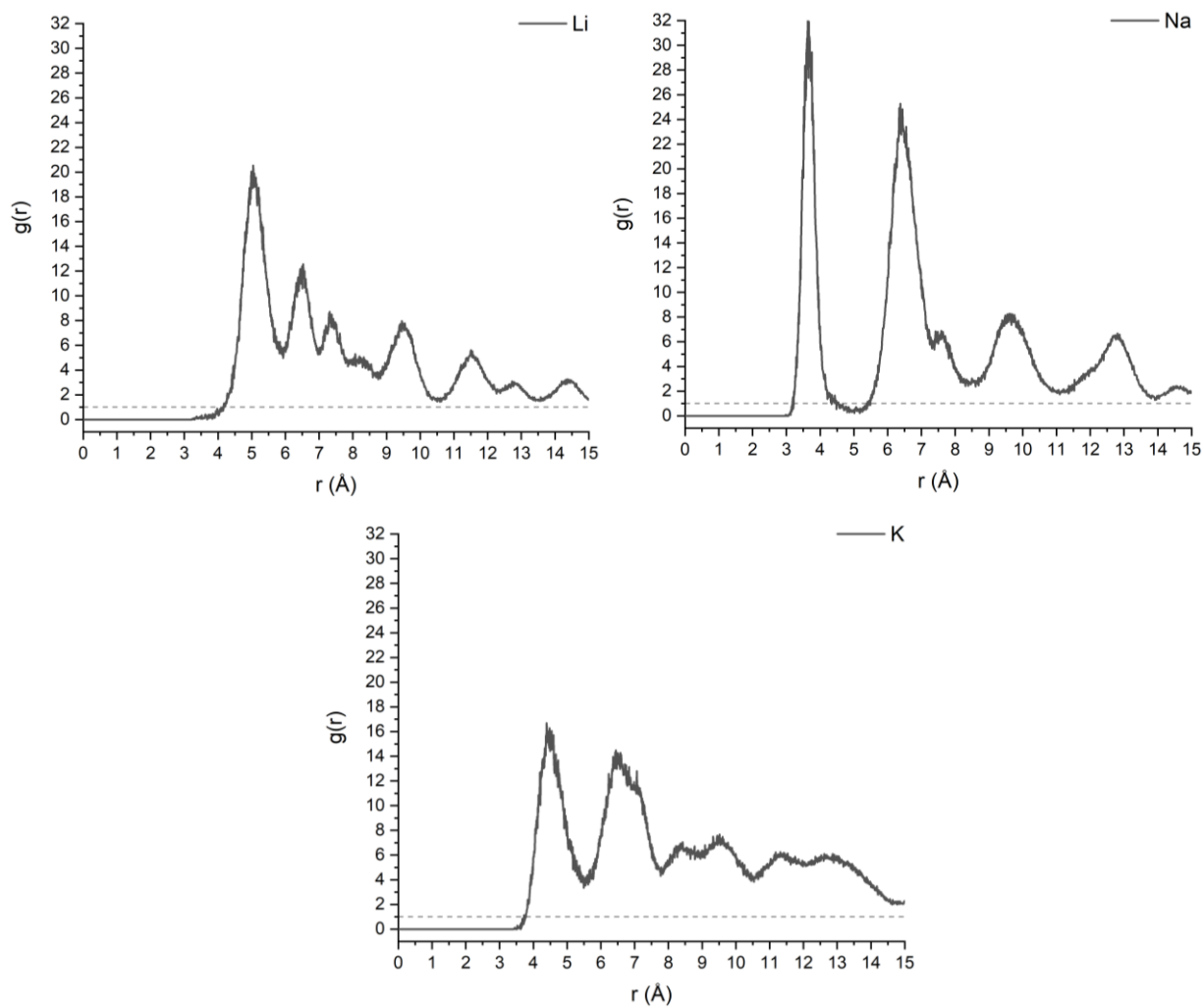


Figure S4.10: Quantum chemical calculations of the PDF data for ion-ion distance in Li-, Na- and K-PHI in an eclipsed model system of PHI.

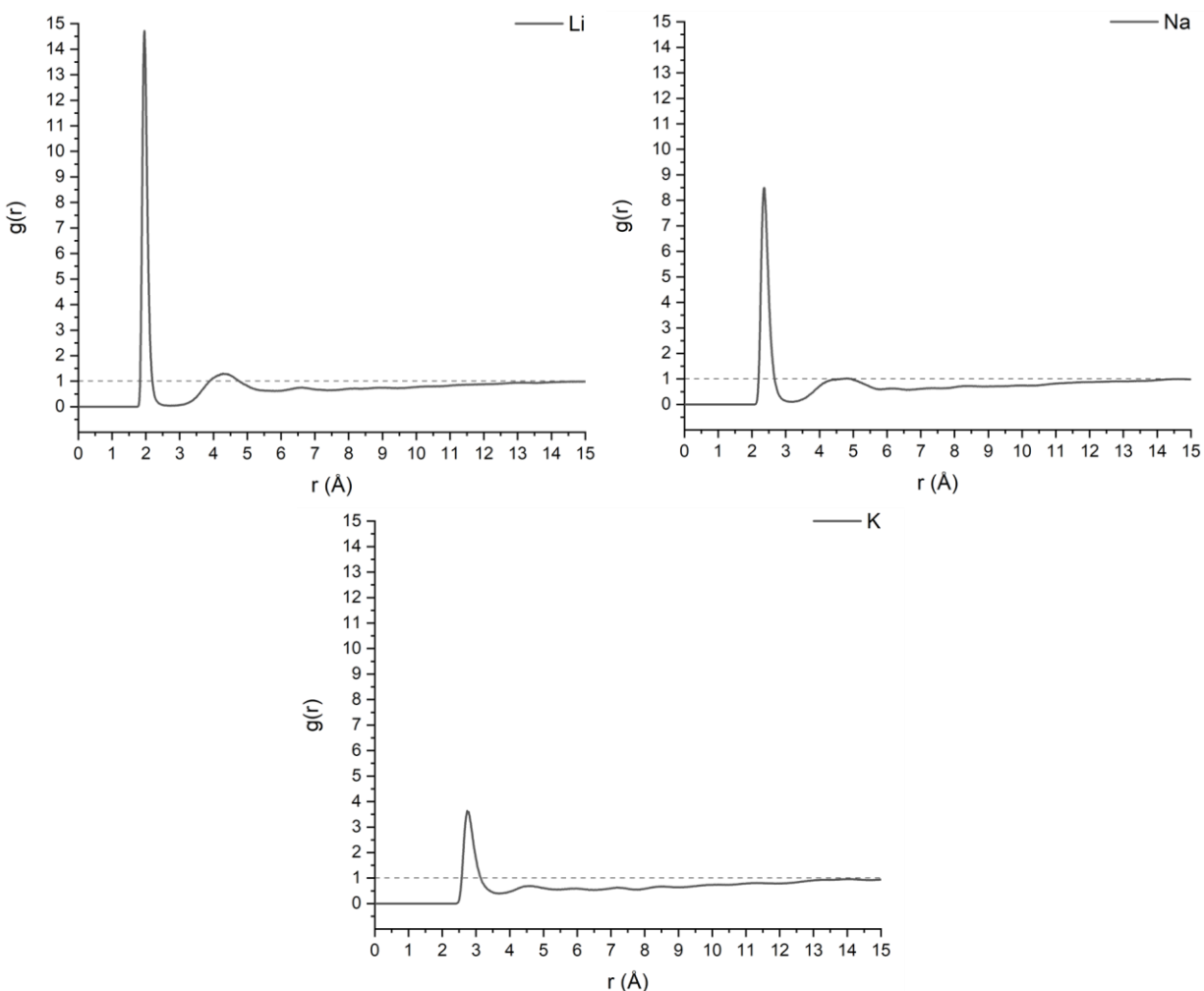


Figure S4.11: Quantum chemical calculations of the PDF data for the water-metal distance in Li-, Na- and K-PHI in an eclipsed model system of PHI.

PXRD data of the ion exchanged samples are depicted in Figure S4.12 and S4.13. Only two defined and distinct stacking varieties can be found as well as random combinations of those two possibilities. The structure of K-PHI can be described by a slipped stacking, whereas Li-PHI shows mainly eclipsed stacking. All the other cation containing PHI structures are mixtures of these two extremes. No structural change of the PHI backbone was observed after ion exchange, as can be seen by FT-IR (Figure S4.14). Only in the case of NH_4 -PHI a slight change in FT-IR spectrum around 1700 cm^{-1} (grey area) points partially toward protonation of PHI (H-PHI).

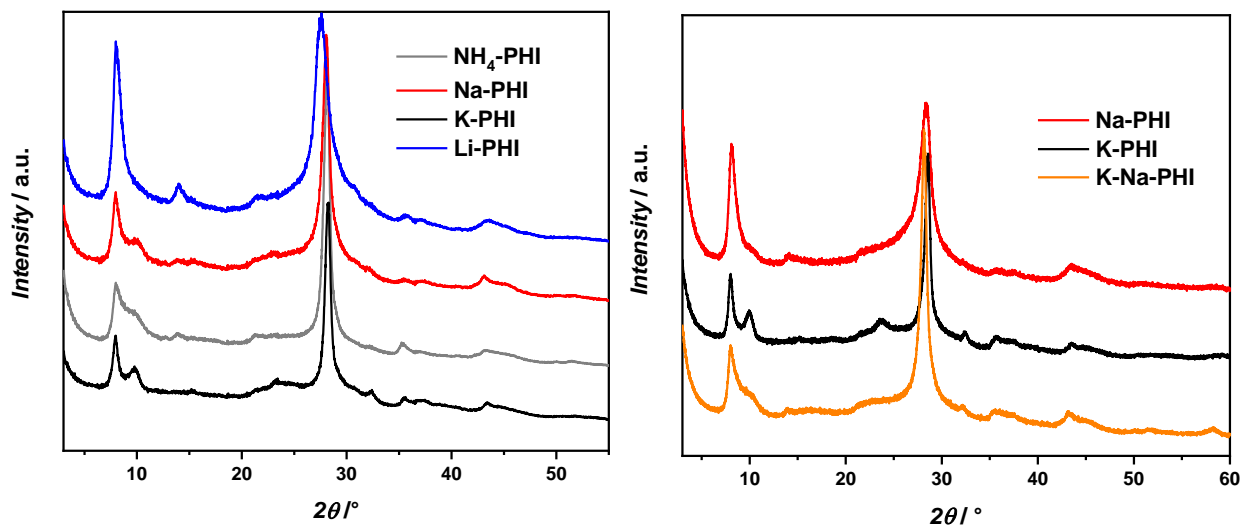
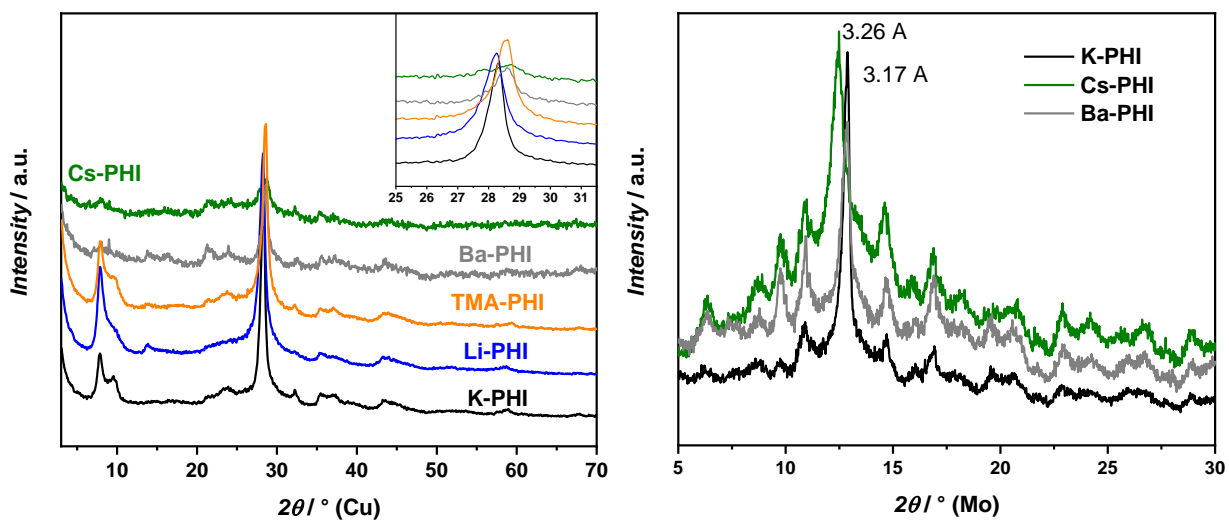
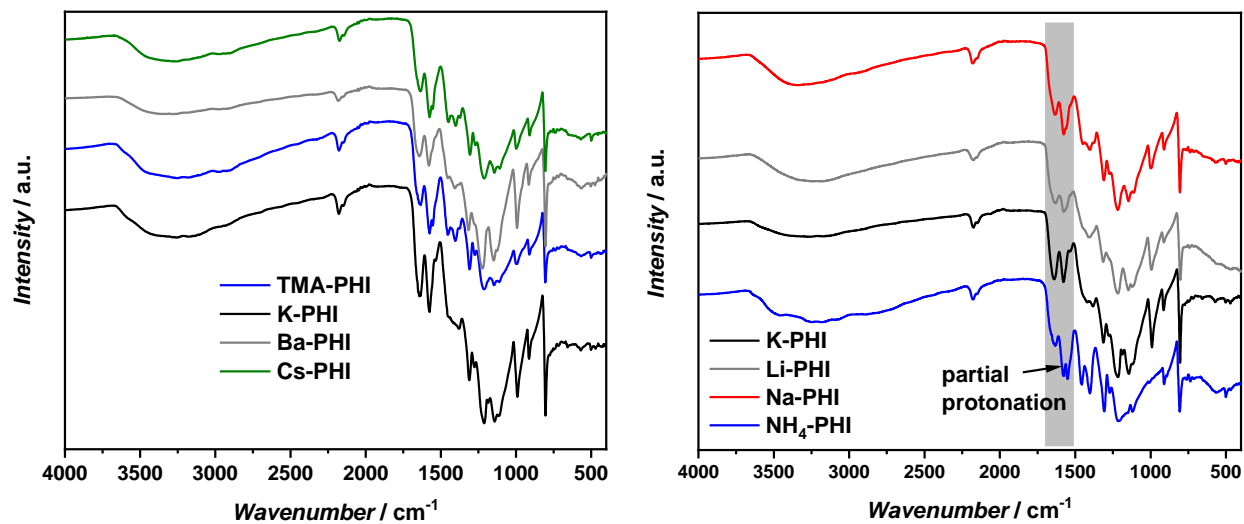
Figure S4.12: PXRD of cation containing PHI structures (NH₄-, Na-, K-, and Li-PHI (left) and Na-, K-, K-Na-PHI (right)).

Figure S4.13: PXRD of different cation containing PHI structures; Cs-, Ba-, TMA-, Li-, and K-PHI.

Figure S4.14: FT-IR of different cation containing PHI structures Cs-, Ba-, TMA-, Li-, Na-, NH₄- and K-PHI.

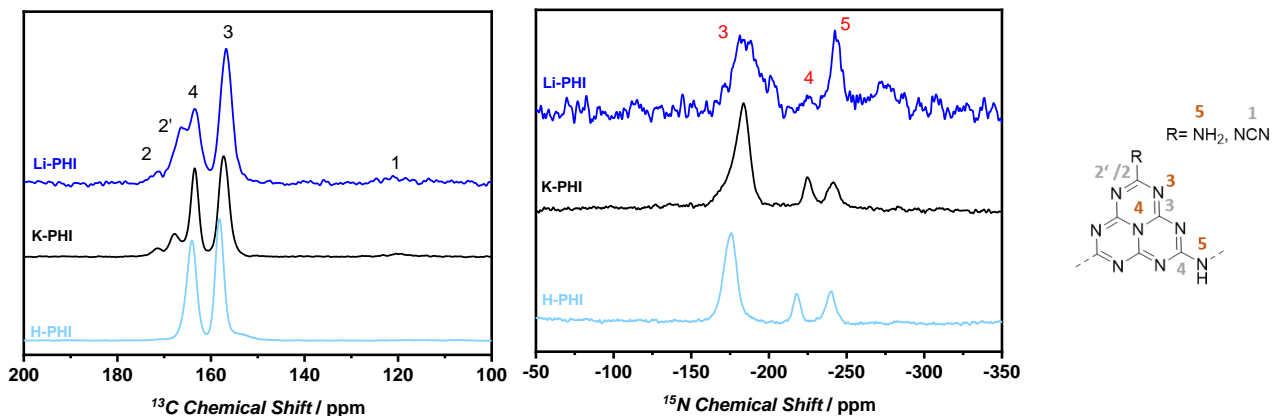


Figure S4.15: ss NMR of Li-, K- and H-PHI; ^{13}C direct NMR (left) and ^1H - ^{15}N CP NMR (right) with signal assignment to C or N atoms.

Table S4.4: Ion radii, hydrated ion radius, Stokes radius, hydrodynamic radii as well as hydration energy of different ions.

Ion	Radius [pm]	Hydrated ion radius [pm] ^[43]	Experimentally obtained interfacial cation radius [pm] ^[44]	Stokes radius [pm] ^[43]	Hydration energy [kJ mol ⁻¹] ^[45,46]
Li ⁺	59 ^[45]	382	580	238	-521
Na ⁺	102 ^[45]	358	520	184	-406
K ⁺	138 ^[45]	331	410	125	-322
Cs ⁺	167 ^[45]	329	350	119	-277
Ba ²⁺	136 ^[45]	404	-	290	-1361
NH ₄ ⁺	147 ^[47]	331	-	125	-304
TMA ⁺	280 ^[48]	367	780	205	-160 ^[48] -204 ^[49]

The type of hydration shell of various alkali ions was reported by J Mähler and I. Persson in 2012.^[50] According to their results lithium ions tend to coordinate 4 or 6 water molecule, sodium ions 5 or 6 and potassium prefers to coordinate 6 or 7 water molecules, which is in good agreement with the result we obtained by quantum-chemical calculations (see Chapter 9.4.7). Cs ions coordinates 8 water molecules^[50] and Ba ions 8.3 water molecules^[51] in the first coordination sphere.

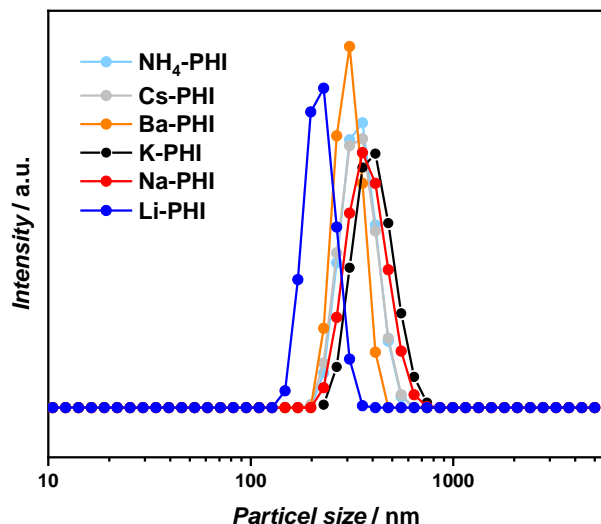


Figure S4.16: Diffusive light scattering experiment of aqueous *M*-PHI suspensions for particle size estimation.

Table S4.5: Average particle sizes of *M*-PHI estimated by diffusive light scattering.

Sample	Average particle size [nm]
K-PHI	1075±300
Na-PHI	915±240
Li-PHI	520±200
Cs-PHI	690±300
Ba-PHI	710±100
NH ₄ -PHI	950±300

The particle size estimation is only a description of particle sizes in aqueous suspension. For this measurement, the dispersivity of the particles is important. Therefore, the particle size might be different in solid powder. The measurement can only be used as rough estimation for particle sizes.

Estimation of water content in ambient samples

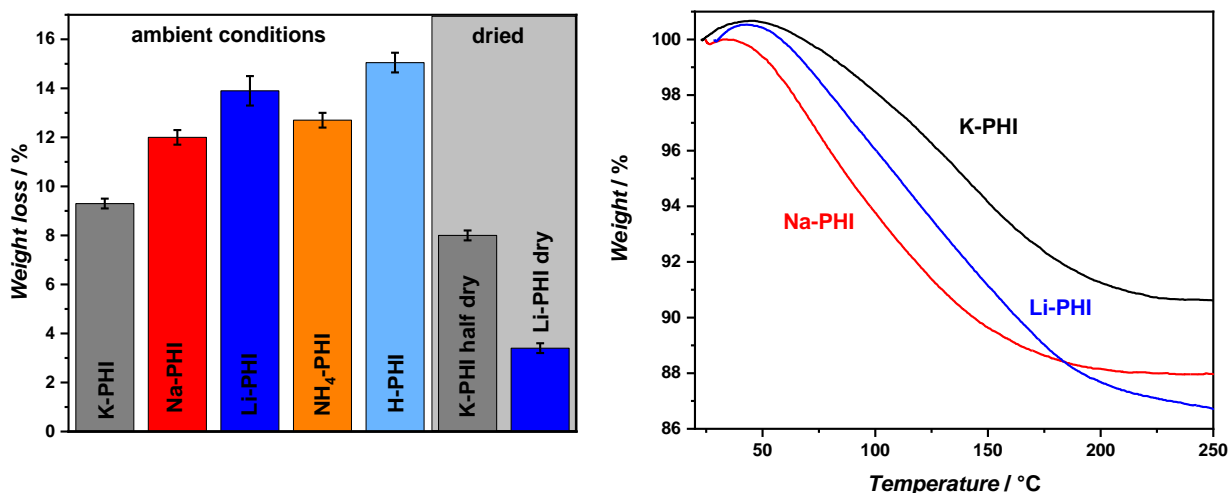


Figure S4.17: Thermogravimetric analysis (TGA) of various PHI compounds with different cations located in the polymer backbone. The heating rate was 1°C/min in inert gas atmosphere; K-PHI half dry (only dried overnight in vacuum oven) and Li-PHI dry (dried several days in vacuum oven and stored in the glove box) (left). Comparison of Li-, Na-, K-PHI weight loss in dependence of the temperature (right).

9.4.4. Electrochemical measurements

Electrochemical measurements in blocking and non-blocking configuration

Nevertheless, the alkali ion mobility in water free carbon nitrides could not be studied directly by impedance measurements where pure Li as an electrode was in contact to PHI, since carbon nitrides are known to irreversibly react with lithium while applying a current or heating up.^[52] We assume the hydration shell has a protecting function for the carbon nitride, preventing those irreversible reactions with Li in aqueous conditions, like described for other materials with Na already.^[53] Especially the ternary nitrogen in the center of heptazine rings irreversibly react to products like Li-CH=NR and Li-N=CR_2 (Figure S4.19). This irreversible reaction can also be observed in the symmetric non-blocking DC experiment Li|Li-PHI|Li (Figure S4.20). In those battery experiments the water in PHI was removed, so Li-ions could interact directly with the nitrogen atoms of carbon nitrides, since no hydration shell is present.^[54]

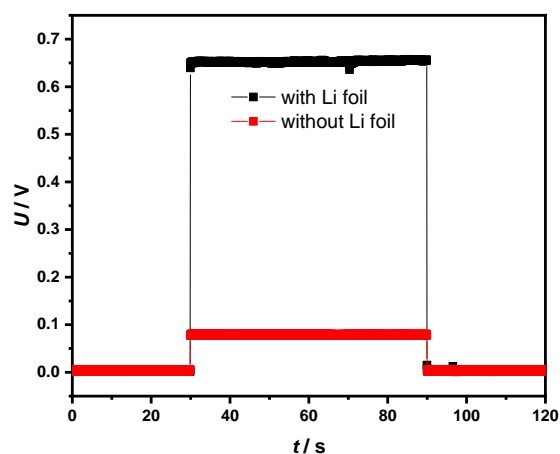


Figure S4.18: DC measurement of dry Li-PHI with Li foil as electrode contact material and without, by applying a current of 5 nA with a time resolution of 0.1 s. It can be seen that the conductivity is purely electronic and that the potential (and similarly the resistance) is higher when Li is used as contact material, pointing to decomposition or corrosion at the interface.

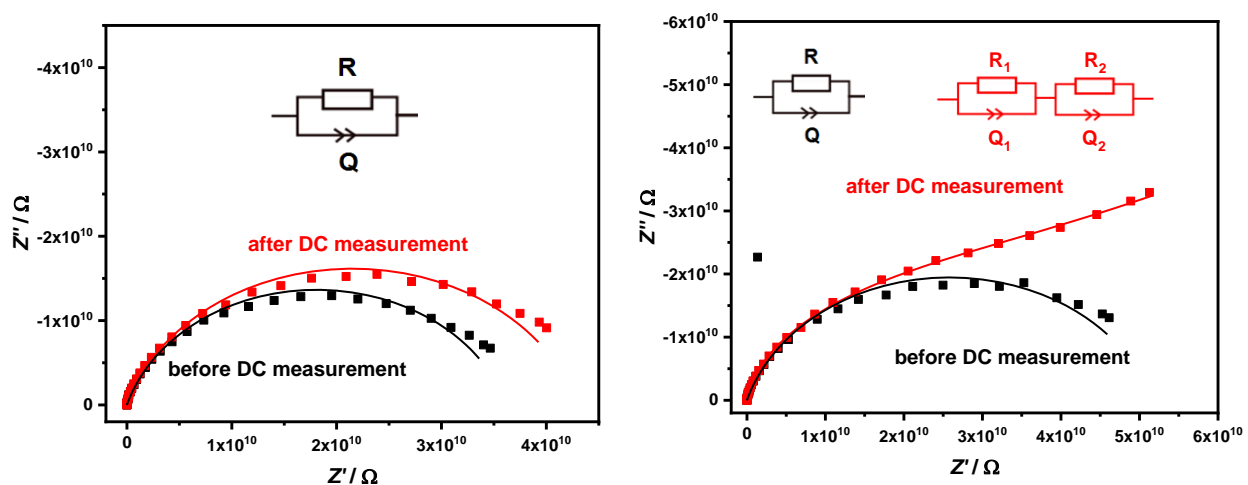


Figure S4.19: Nyquist plots of Li-PHI measured before and after DC measurements without Li contact (left) and with Li contact (right). The resistance is shifted without Li contacts by 13% (from $3.6 \times 10^{10} \Omega$ to $4.3 \times 10^{10} \Omega$) and in the case of Li contacts by 25% ($5.2 \times 10^{10} \Omega$ to $1.3 \times 10^{11} \Omega$).

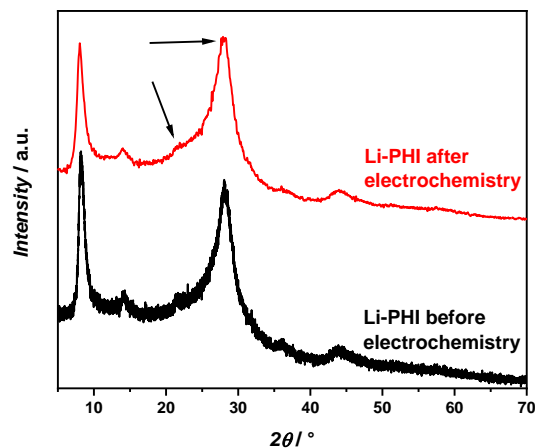


Figure S4.20: XRD analysis of Li-PHI before and after impedance and DC measurements with Li electrodes (surface of the pellet was scratched and used for XRD analysis). This is a literature known effect, where it can be found that Li decomposes Li-PHI by cycling.^[33]

Sample stability

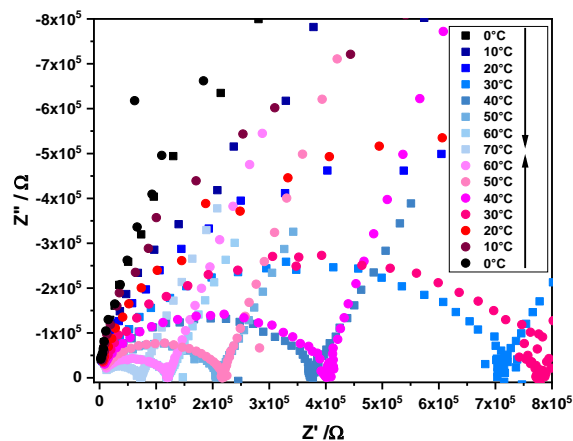


Figure S4.21: Temperature dependent measurement of Na-PHI with Au electrodes, started with heating the sample and followed by a cool down in temperature.

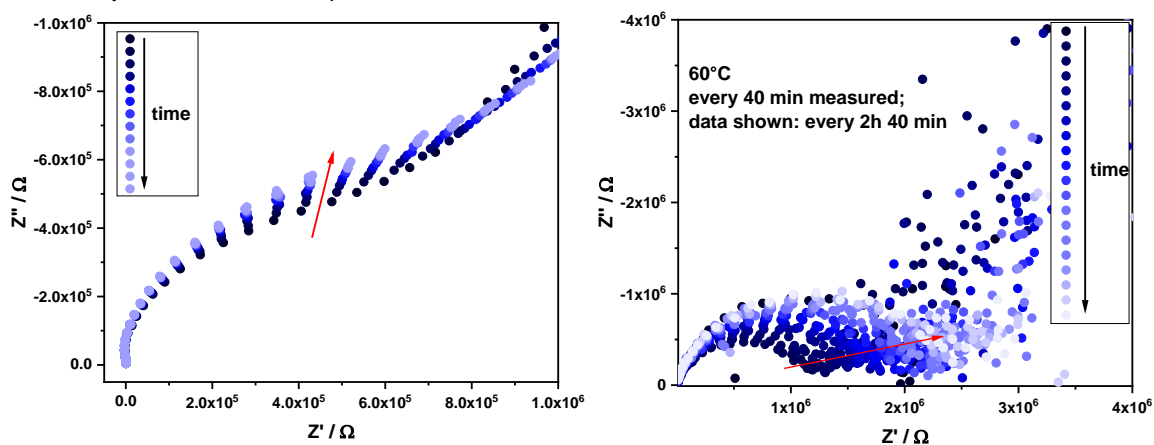


Figure S4.22: Time dependent impedance measurement of Na-PHI (at room temperature and C electrodes). Resistance shifts from 5.6×10^5 to $7.3 \times 10^5 \Omega$ (this causes a slight shift in conductivity from 2.5×10^{-6} to $1.9 \times 10^{-6} \text{ S/cm}$) (left). Time dependent measurement of Li-PHI at 60°C at C electrodes. The resistance shifts from 1.2×10^6 to $2.6 \times 10^6 \Omega$, which results in a shift of the conductivity from 8.9×10^{-7} to $4.1 \times 10^{-7} \text{ S/cm}$. Measurements were taken every 40 min (depicted measurements every 2 h 40 min) (right).

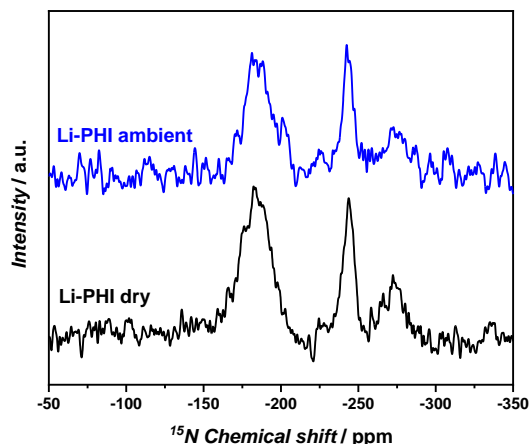
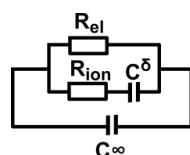


Figure S4.23: $\{^1\text{H}\}^{15}\text{N}$ CP NMR of Li-PHI dry and in comparison to Li-PHI at ambient conditions.

DC galvanostatic polarization and chemical diffusion theory



The initial jump in voltage (V_{init}) when applying a current (I) can be used to calculate the overall resistance (R_{ov}) by $V_{\text{init}} = IR_{\text{ov}}$. For a purely electronic conductor, the initial voltage jump is equal to the electronic conductivity. In the case of a mixed ionic and electronic conductor, the voltage will increase exponentially at the beginning, followed by a linear increase or saturation (V_s) due to the ionic motion (Figure S4.24). For shorter timescales the following approximation can be used to fit the data:

$$V = \frac{4}{\pi^{3/2}} \sqrt{\frac{t}{\tau^\delta}} \quad [55]$$

At the saturation voltage only electrons flow anymore, so that R_{el} (the resistance of electrons flowing) and hence R_{ion} (the resistance of ions moving) can be extracted from this value.^[56, 57] The chemical capacity describes the ability of a material to give away or take up ionic components such as alkali ions. This capacity C^δ can be calculated from $\tau^\delta = R^\delta C^\delta$, with $R^\delta = \frac{L}{A} \frac{\sigma_{\text{ion}} + \sigma_{\text{el}}}{\sigma_{\text{ion}} \sigma_{\text{el}}} = R_{\text{ion}} + R_{\text{el}}$ and $\tau^\delta =$ time scale of polarization.^[58, 59] Due to the external electric field force, an ionic concentration gradient is building up due to ion blocking electrodes. τ^δ can be extracted from the slope in the initial time range in a plot of the square root of time against the voltage in a constant current polarization experiment. For longer timescales, an exponential fitting is necessary to gain τ^δ in a plot of time against $\log(V)$ ($V = V_s [1 - \exp(-t/\tau^\delta)]$).^[56, 57]

To extract the overall resistance of the pellet, the DC polarization experiment has to be measured at high enough time resolution. The time steps between the potential measurements should be smaller than the time constant estimated from impedance measurement, where the semi-circle is approaching the x axis again. For this purpose a special potentiostat for high speed measurements was used (1 data point per 0.0001 s).

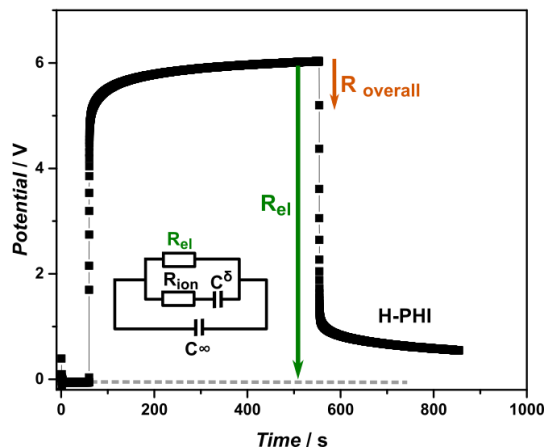


Figure S4.24: DC polarization experiment of H-PHI as an example with fitting to extract the overall (R_{overall}) and the electronic resistance (R_{el}).

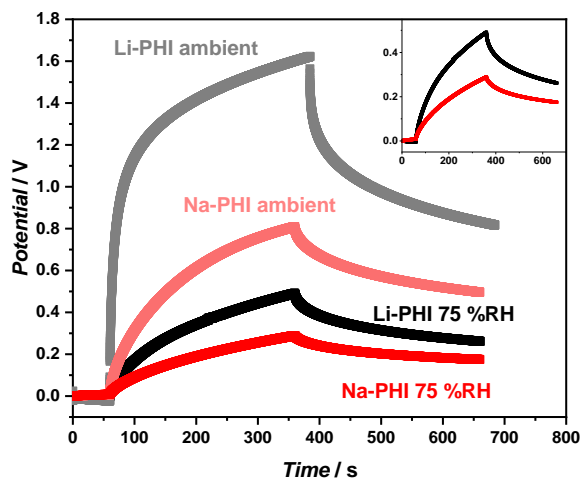


Figure S4.25: Polarization DC experiments of Li- and Na-PHI in ambient and 75 %RH environment with 2 nA applied current.

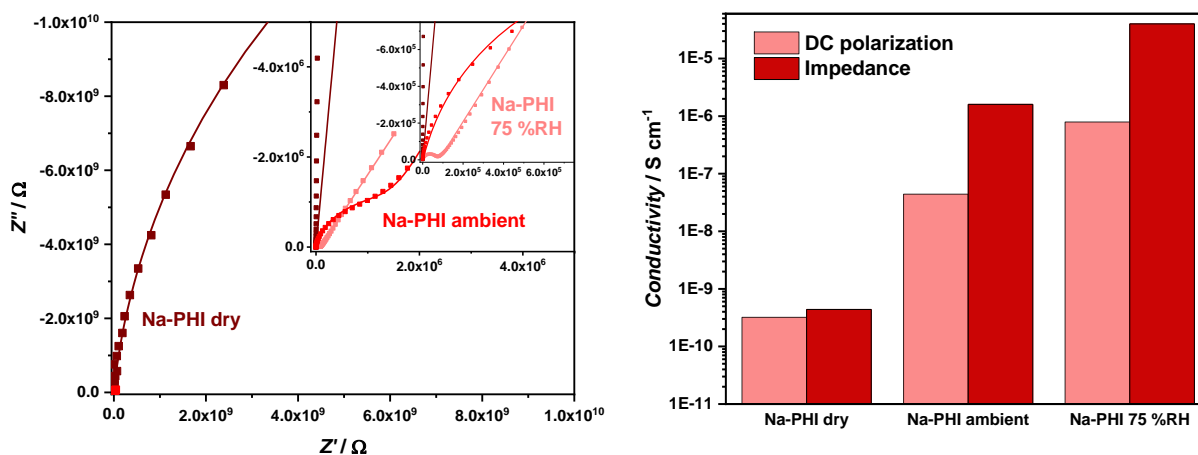


Figure S4.26: Nyquist plot of Na-PHI dry, ambient and 75 %RH environment (left) and comparison of conductivity of Na-PHI dry, ambient and at 75 %RH measured with impedance and DC (right).

Table S4.6: Comparison of conductivity values obtained from dry, ambient and 75 %RH environment for Na-PHI, Li-PHI and K-PHI. The conductivity values extract from DC measurements may vary from impedance data, since the time resolution in DC experiments was only 0.03 s, which is partially not fast enough to resolve all processes.

Sample	Conductivity DC [S cm^{-1}]	Conductivity impedance [S cm^{-1}]
Na-PHI dry	3.2×10^{-10}	4.4×10^{-10}
Na-PHI ambient	4.4×10^{-8}	$1.6 \times 10^{-6} - 2.7 \times 10^{-7}$
Na-PHI 75 %RH	7.9×10^{-7}	$4.0 \times 10^{-5} - 4.0 \times 10^{-6}$
Li-PHI dry	-	3.9×10^{-10}
Li-PHI ambient	2.1×10^{-8}	6.7×10^{-8}
Li-PHI 75 %RH	3.8×10^{-7}	8.8×10^{-7}
K-PHI dry	2.7×10^{-10}	$8.0 \times 10^{-10} - 2.0 \times 10^{-11}$
K-PHI ambient	1.7×10^{-8}	8.3×10^{-8}
K-PHI 75 %RH	-	$1.0 \times 10^{-5} - 1.0 \times 10^{-6}$

The DC measurement of Li-PHI at dry state was not possible to measure, caused by the high resistance of the sample, which reached the detection limit of the potentiostat.

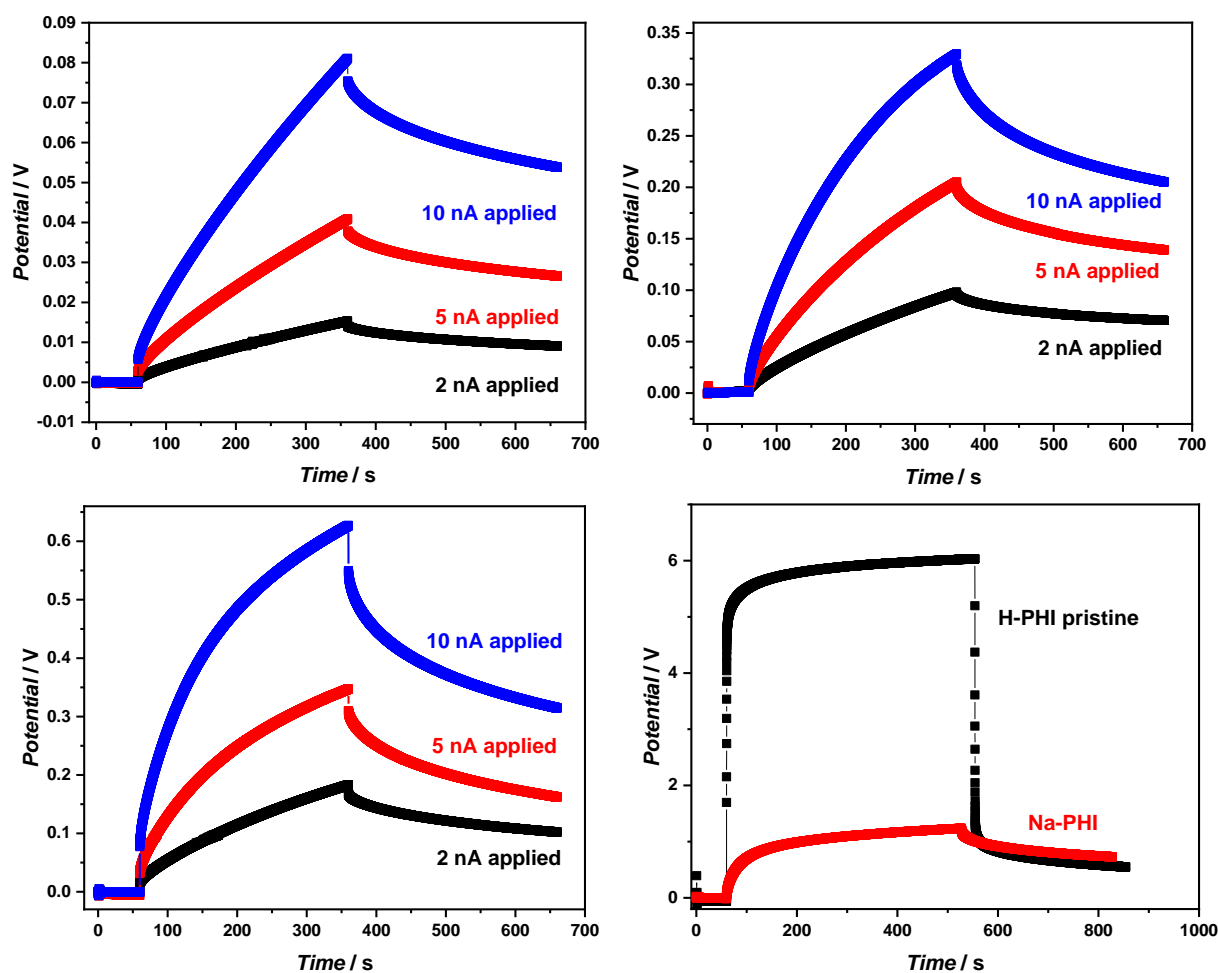


Figure S4.27: DC measurements of K-PHI (top left), Na-PHI (top right) and Li-PHI (bottom left) with 2, 5 and 10 nA applied current with a time resolution of 0.0001 s. DC measurement of H-PHI (bottom right) at 2 nA applied current showing less ionic contribution to conductivity than alkali ion containing PHI (e.g. Na-PHI shown here as comparison) (measured at 0.1 s time resolution).

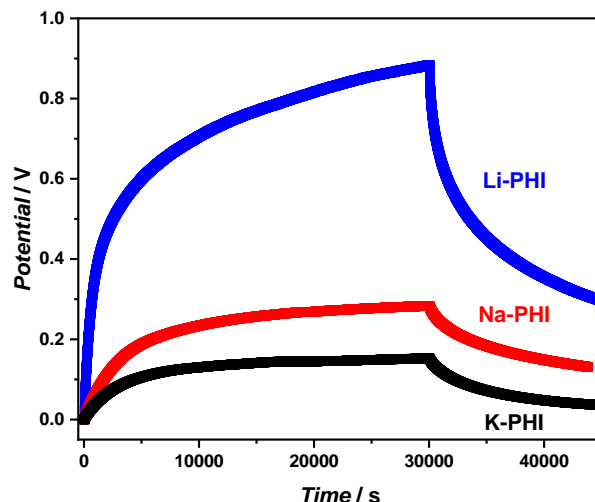


Figure S4.28: DC measurements of Li-PHI, Na-PHI and K-PHI with 2 nA applied current for 30000 s to estimate the electrical contribution to the resistance (0.1 s).

In general it can be seen from the DC measurements that the polarization is asymmetric for the region where current is applied initially compared to the voltage decay after the applied current is set to zero again. This points to different kinetics between “charging” the system and the decay. As it was described in a previous paper of our group,^[3] PHI can store electrons on the heptazine units by applying a current or illuminating.

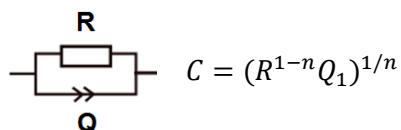
Table S4.7: Ionic, electronic and overall conductivity of K-PHI, Na-PHI, Li-PHI and H-PHI. The time resolution of the DC measurements was only 0.1 s, so that faster measurements are needed to deconvolute the faster processes as well and reach similar values as in impedance.

	K-PHI [S cm^{-1}]	Na-PHI [S cm^{-1}]	Li-PHI [S cm^{-1}]	H-PHI [S cm^{-1}]
σ_{overall}	$1.7 (\pm 3.0) \times 10^{-8}$	$1.5 (\pm 1.0) \times 10^{-7}$	$4.5 (\pm 1.0) \times 10^{-8}$	1.0×10^{-9}
σ_{el}	$2.5 (\pm 5.0) \times 10^{-10}$	$1.7 (\pm 7.0) \times 10^{-9}$	$5.0 (\pm 5.0) \times 10^{-10}$	1.9×10^{-10}
σ_{ion}	$1.7 (\pm 3.0) \times 10^{-8}$	$1.5 (\pm 1.0) \times 10^{-7}$	$4.5 (\pm 1.0) \times 10^{-8}$	7.5×10^{-10}
$\sigma_{\text{impedance}}$	$4.8 (\pm 12.0) \times 10^{-8}$	$5.1 (\pm 3.0) \times 10^{-6}$	$1.1 (\pm 1.0) \times 10^{-7}$	3.6×10^{-9}

It can be clearly seen from the DC polarization experiments that the conductivity of bare H-PHI, i.e. in absence of any alkali ion, shows a 1-2 orders of magnitude lower conductivity. Additionally, the shape of the DC curve of H-PHI is different in comparison to alkali-PHI, since a higher contribution of electronic conductivity to the overall conductivity can be observed (Table S4.7). The result also displays that protons in H-PHI are not likely to, or only poorly, contribute to the overall conductivity and therefore can be neglected in alkali ion containing PHI materials.

Impedance measurements

The capacitance C is calculated using the following formula with the resistance R [Ω], n the exponent value of the constant phase element and Q the constant phase element [$F\ s^{-n}$] of the fitting of the impedance data with the following equivalent circuit diagram, for the first semi-circle^[60]:



$$C = (R^{1-n} Q_1)^{1/n}$$

In a previous paper of our group, PHI is described to behave as pseudocapacitor.^[3] Out of this reason, the dielectric constant for the bulk process was calculated according to the following formula^[61, 62]:

$$C = \frac{A \varepsilon \varepsilon_0}{d}$$

Where C is the capacitance [F], A is the area of the electrodes contacting the pellet [cm^2], d the distance between the electrodes or the pellet thickness [cm] and ε_0 being the permittivity of free space [$8.85 \times 10^{-14}\ F\ cm^{-1}$].

In the case of aqueous solutions a permittivity of ε around 80 is expected, arising from water already. For polymeric and organic systems, the permittivity decreases to ε values between 2-5.^[63, 64] For poly(ethylene oxide), dielectric constants of the bulk properties with values of up to 14 have been reported.^[61] The dielectric constant is expected to increase with temperature, if the process is based on ionic conduction.^[65]

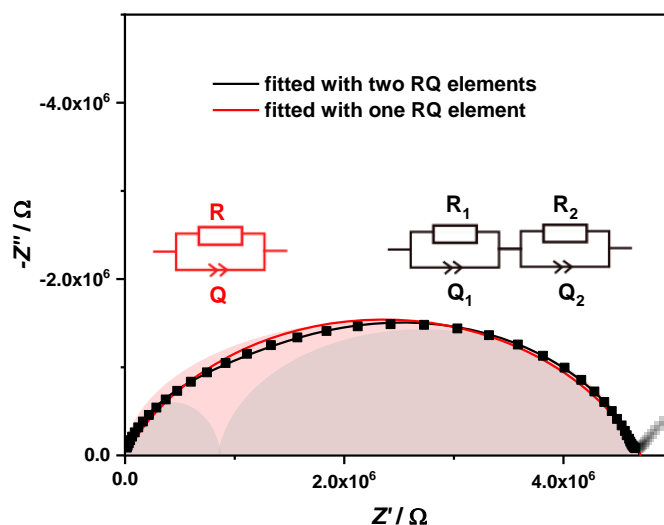


Figure S4.29: Impedance data of K-PHI with different fits of one RQ or two RQ elements (Humidity: 30 %RH).

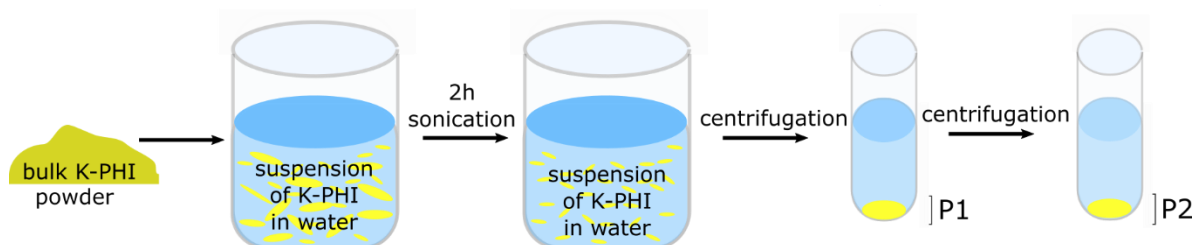
Table S4.8: Fitting parameter and calculated values for K-PHI impedance data fitted by an equivalent circuit diagram containing one or two RQ elements in comparison.

Elements	Fit parameters of one RQ element	Fit parameters of two RQ elements
R_1	$4.7 \times 10^6 \Omega$	$7.0 \times 10^5 \Omega$
CPE_1	$9.0 \times 10^{-11} F$	$1.6 \times 10^{-11} F$
α_1	0.74	0.92
R_2	-	$4.0 \times 10^6 \Omega$
CPE_2	-	$8.3 \times 10^{-11} F$
α_2	-	0.79
Calculated values		
C_1	$5.9 \times 10^{-12} F$	$6.0 \times 10^{-12} F$
C_2	-	$9.9 \times 10^{-12} F$
ϵ_1	16.2	16.6
ϵ_2	-	27.2

In polycrystalline samples with anisotropic conductivity mechanisms the first semi-circle in impedance spectra can be fitted with two RQ elements according to Kim *et al.* [66] to deconvolute the anisotropy of conduction in the material. The low dielectric constant points to two bulk for both processes. From the impedance measurements a rough estimation of the two different conduction pathways can be extracted at room temperature: $\sigma_1 = 1.4 \times 10^{-6} S cm^{-1}$ and $\sigma_2 = 2.4 \times 10^{-7} S cm^{-1}$ ($\sigma_1 = 5.8 \times \sigma_2$). The difference in conductivity between the in-plane and out-of-plane measurement in LiCl intercalated PTI was reported to be 65 times. [67] Hence, similar range would be expected also for PHI materials. It should be stated that these are only estimations and therefore, they can be used as lower limits for the different anisotropic process. The overall or average conductivity was extracted by impedance measurements with just fitting one semi-circle at the high frequency values. When also the low frequency values were included to the fit 2 semi-circles in total were used; one for the first semi-circle giving the overall conductivity and therefore neglecting the anisotropy and another huge one for the contact resistance.

Effect of particle size and pellet diameter on conductivity

PHI material with different particle sizes was obtained by the procedure shown in Scheme S4.1. Those different particle sizes were separated by centrifugation, dried and used for pellet preparation, respectively. The particle size separation by sonication and centrifugation was analyzed in a previous paper by our group already [3, 68] and did not show any changes in the potassium amount in the K-PHI particles.



Scheme S4.1: Depiction of PHI particle separation according to their size (P1 contains big particles, whereas P2 consists only of small particles).

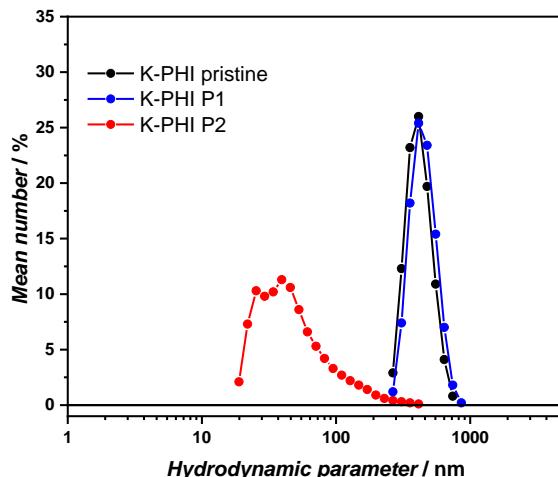


Figure S4.30: Particle size distribution of K-PHI measured by DLS measurements.

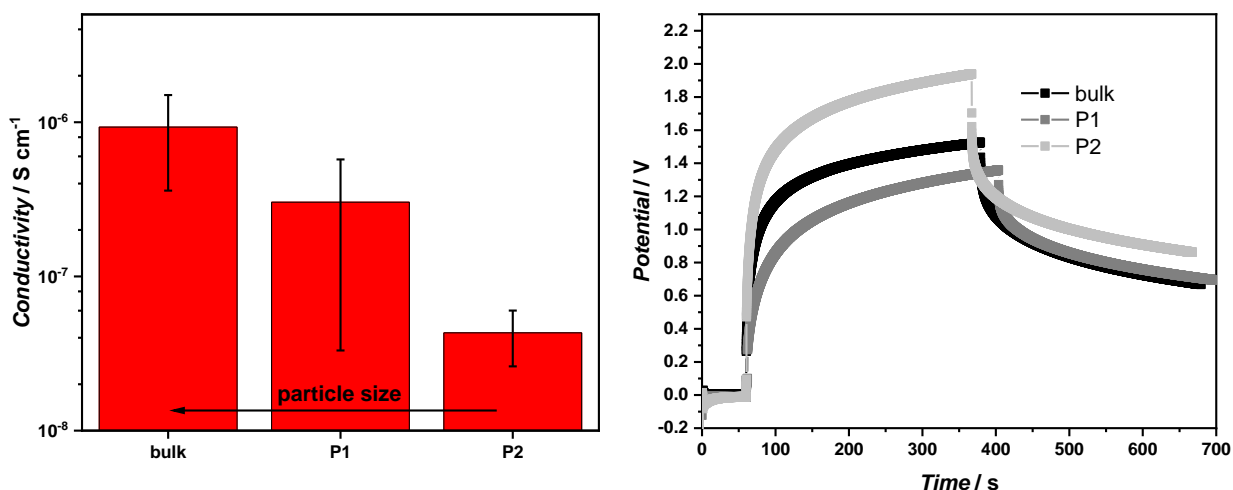


Figure S4.31: Conductivities of K-PHI bulk, P1 and P2 containing pellets, estimated by impedance analysis (left). DC analysis of K-PHI bulk, P1 and P2 pellets, showing no change in curve shape with decreasing particle size (right). This hints to a bulk ionic conductivity mechanisms in PHI.

Impedance measurements on pellets with different particles and crystallite sizes of PHI confirmed a bulk process, since bigger crystallite and particles sizes result in higher conductivity (Figure S4.31).^[69] To estimate further, if smaller particle sizes also affect the density of the pellet, the theoretical density was estimated from the unit cell of the crystal structure, reported earlier by our group^[2] – it is around $1.95\text{--}1.97\text{ g cm}^{-3}$. This calculation is based on the assumption that in every PHI pore a potassium ion with 7 water molecules as a hydration shell is located. Since this is not necessarily the case in the real sample this theoretical value might be off, and should only be handled as a rough estimation. The pressed pellets have in average a density of $\sim 1.69\text{ g cm}^{-3}$ (86% of the theoretical density), with an experimental error of 10%. This is also the case for pellets pressed with different particles sizes, but the density of the pellet is decreasing with decreasing particle size (Table S4.9). In Na-PHI and Li-PHI the theoretical density is around 1.97 g cm^{-3} and 1.92 g cm^{-3} respectively.

Table S4.9: Comparison of K-PHI particle sizes as well as Na-, and Li-PHI and their density in the pressed pellet as absolute values and in comparison to the theoretical density.

Material	Density [g cm^{-3}]	Density [%]
K-PHI-bulk	1.69	86
K-PHI P1	1.62	82
K-PHI P2	1.49	75
Na-PHI	1.66	84
Li-PHI	1.59	83

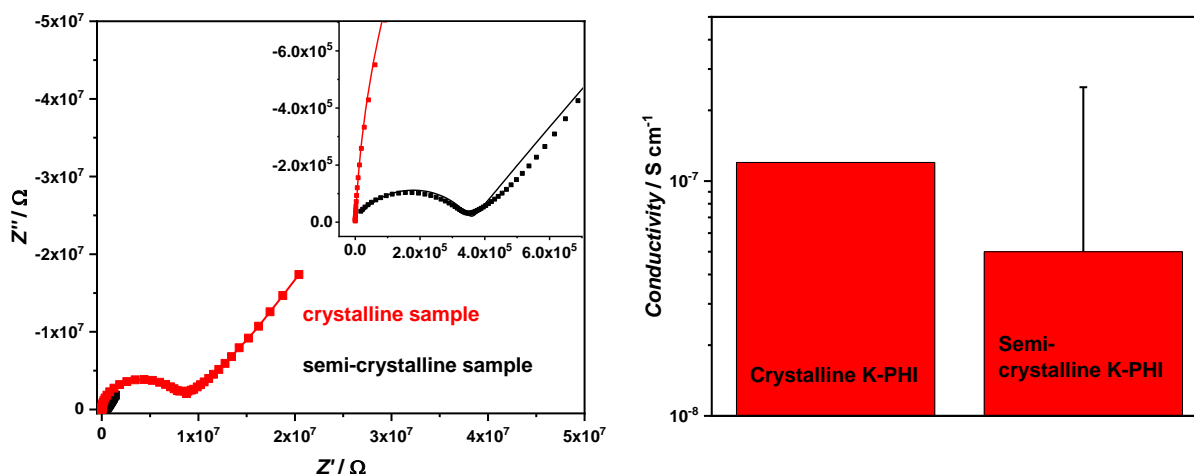


Figure S4.32: Nyquist plot of crystalline K-PHI and equivalent circuit diagram measured in ambient conditions, which was used for fitting (left). Comparison of conductivity of crystalline and a semi-crystalline K-PHI material in a pellet with no preferred particle orientation (right).

From a different synthesis route via ampule synthesis as described in a previous paper of our group ^[2], crystalline K-PHI can be obtained. This material has a slightly bigger crystallite size of 100 nm than the semi-crystalline material (20 nm) and can be used to study the impact of crystallite size on conductivity. In Figure S4.32 it can be seen that the conductivity of the crystalline sample is comparable to the one of the semi-crystalline material.

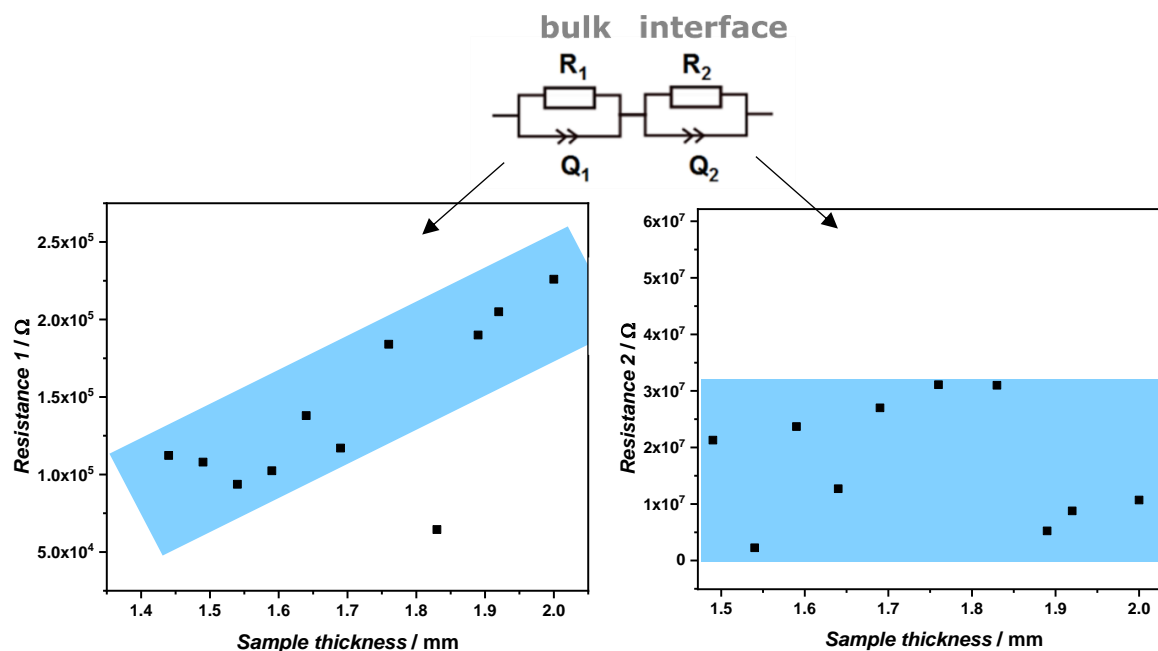


Figure S4.33: Dependence of the resistance (R_1 left and R_2 right) and the pellet thickness in K-PHI for the analysis if a bulk or a grain boundary process is dominant in the material (here pointing to a bulk conductivity process).

Also, impedance measurements depending on the thickness of the pellet point towards bulk conductivity, since the resistance of the first semi-circles is scaling linearly with pellet thickness (Figure S4.33). For a grain boundary based conductivity mechanism, no effect on the semi-circle would be expected.^[70]

The changes of the first RQ element as function of the pellet diameter can also be plotted to monitor the change in capacitance and the resulting dielectric constants. The obtained values vary only by a factor of 2 with no obvious trend, which is not a significant change and within the normal measurement errors. However, a trend is visible for the conductivity, the value also changes only by a factor of 2, which might also be due to different contact between electrodes and pellets by uneven polishing of the pellet.

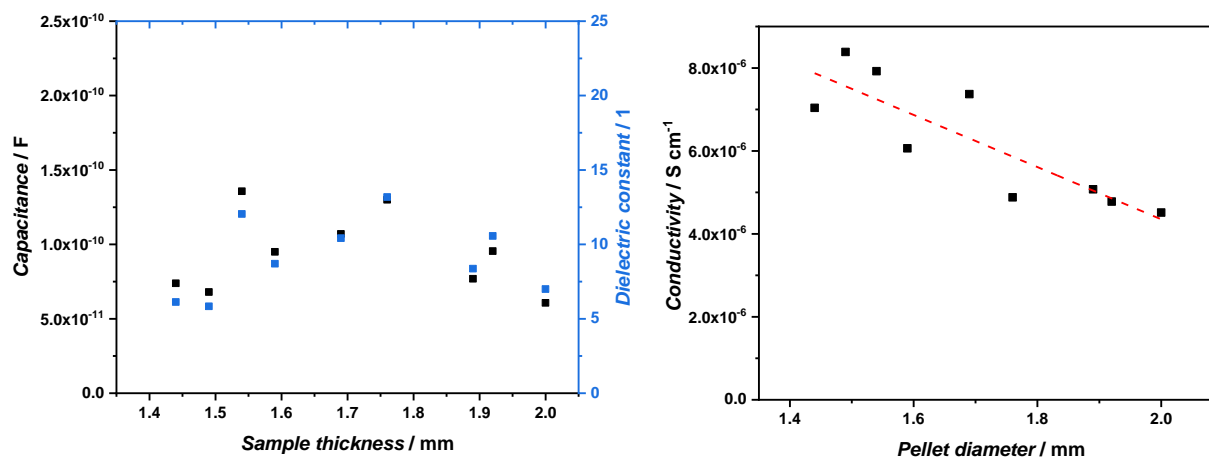


Figure S4.34: Dependence of capacitance and dielectric constant (left) and conductivity (right) of the pellet thickness of K-PHI.

9.4.5. Humidity dependent electrochemical analysis

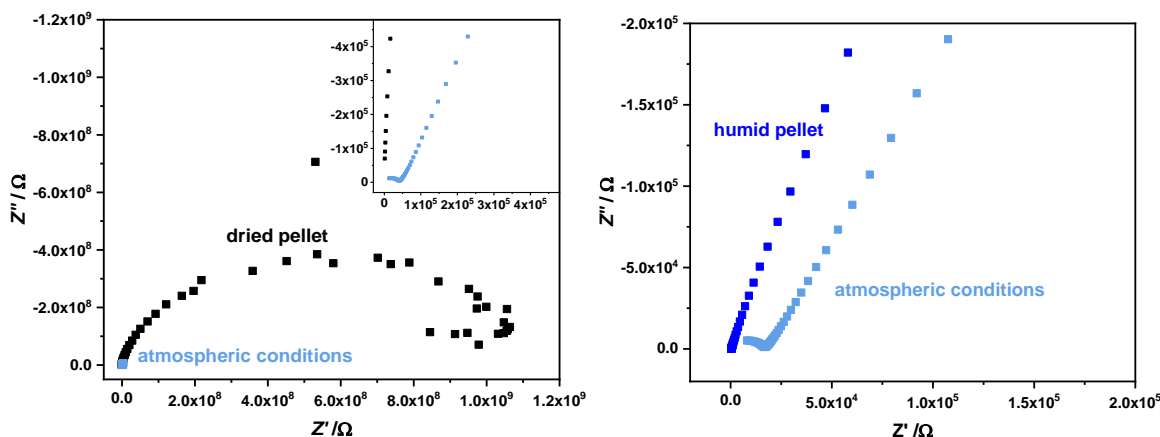


Figure S4.35: Nyquist plot of K-PHI in dried and in ambient conditions with insets to visualize the sample measured in atmospheric conditions (left). Nyquist plot of K-PHI in ambient conditions and as wetted pellet (right).

The diffusion constant of ions can be estimated from conductivity data by using the Nernst-Einstein-equation:

$$D^{\sigma} = \frac{\sigma_{imp} k_B T}{n z^2 e^2}$$

With σ_{imp} = conductivity determined by impedance spectroscopy [$S\ m^{-1}$], n = concentration of diffusing species [m^{-3}] (are mobile for ionic conductivity), z = charge number of diffusion species, e = elemental charge [C], k_B = Boltzmann constant [$kg\ m^2\ s^{-2}\ K^{-1}$] and T = temperature [K].^[59, 62, 71, 72]

Assuming a lithium loading of 1.63 wt% in Li-PHI, as measured by elemental analysis, the concentration of diffusion species is in average $2.60 \times 10^{27}\ m^{-3}$. When calculating the lithium loading from the data obtained from structure fitting by material studios[®], as described before ($a=b= 12.4\ \text{\AA}$, $c= 3.2\ \text{\AA}$, $\alpha=\beta=\gamma=90^\circ$), a value of $2.04 \times 10^{27}\ m^{-3}$ can be obtained, which is close to the estimated value extracted from elemental analysis.

The same assumption can be made for K-PHI and Na-PHI with $a=b= 12.78\ \text{\AA}$, $c= 4.31\ \text{\AA}$, $\alpha=\beta=109.6^\circ$ and $\gamma=120^\circ$ ^[2] resulting in a theoretical potassium or sodium loading of $1.90 \times 10^{27}\ m^{-3}$. This value is in good agreement with the value obtained from elemental analysis of $2.44 \times 10^{27}\ m^{-3}$. For diffusion coefficient analysis the concentration of diffusing species estimated by elemental analysis was used, since this is the actual concentration in the samples.

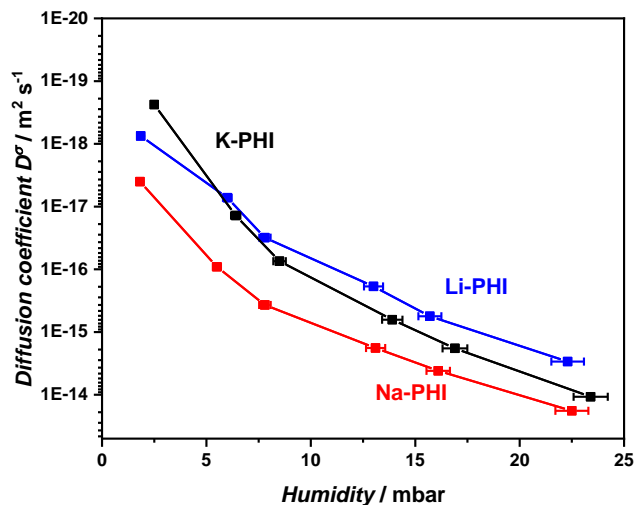


Figure S4.36: Diffusions coefficient D^o of Na-, Li-, and K-PHI coated with Ru, estimated from impedance measurements in dependence of humidity.

Table S4.10: Comparison of conductivity values obtained for Na-PHI with steel electrodes or Ru coated at steel electrodes showing no difference in conductivity values obtained.

Contact material	Conductivity DC [$S cm^{-1}$]	Conductivity impedance [$S cm^{-1}$]
Steel electrode	$1.5 (\pm 1.0) \times 10^{-7}$	$5.1 (\pm 3.0) \times 10^{-6}$
Ru coated at steel electrode	3.2×10^{-7}	2.4×10^{-6}

Table S4.11: Comparison of conductivity and diffusion coefficient of Na-, K- and Li-PHI at humid conditions (pellets were pressed with one drop of deionized water).

Sample	Conductivity impedance [$S cm^{-1}$]	Diffusion coefficient [$m^2 s^{-1}$]
Na-PHI humid	5.0×10^{-4}	4.1×10^{-12}
K-PHI humid	1.7×10^{-4}	1.4×10^{-12}
Li-PHI humid	6.0×10^{-5}	4.9×10^{-13}

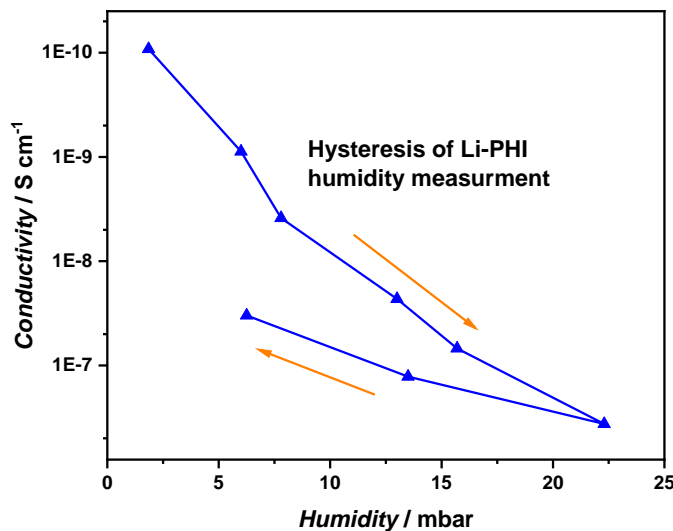


Figure S4.37: Hysteresis of humidity dependent conductivity measurement of Li-PHI.

Table S4.12: Capacitance and dielectric constant values of K-PHI at different temperature and humidity.

Temperature [°C]	Humidity [mbar]	Capacitance [10^{-12} F]	Dielectric constant
145	0	3.3	9.1
122	0	3.2	8.9
106	0	3.2	8.6
92	0	3.1	8.4
77	0	2.3	6.5
63	0	2.1	5.7
49	0	2.1	5.8
35	2.73	4.0	10.9
35	6.72	5.8	16.0
35	8.66	6.0	16.7
35	16.98	5.8	15.9
35	23.30	5.6	15.4

The estimated dielectric constant, which is extracted from the fitted capacity value in the impedance data, is decreasing with temperature at 0 mbar humidity. The sample pellet was pre-dried two day in vacuum at 145°C. At roughly 50°C the dielectric constant reaches a value of 5-6, which is in the expected range for polymer based systems^[63, 64] and close to the calculated value for fully condensed and melon-type carbon nitrides (4.6-7.2).^[73] According to literature the behavior of increasing dielectric constant with temperature clearly point to an ionic based conduction mechanism,^[65] which is in good agreement to our previous results.

By increasing the humidity stepwise, a simultaneous increase in the dielectric constant is observed. Above a humidity of 6.72 mbar the dielectric constant levels out at a value between 15 and 16. This higher value is most probably caused by the water located in the pores, which also assists the formation of a cation hydration shell.

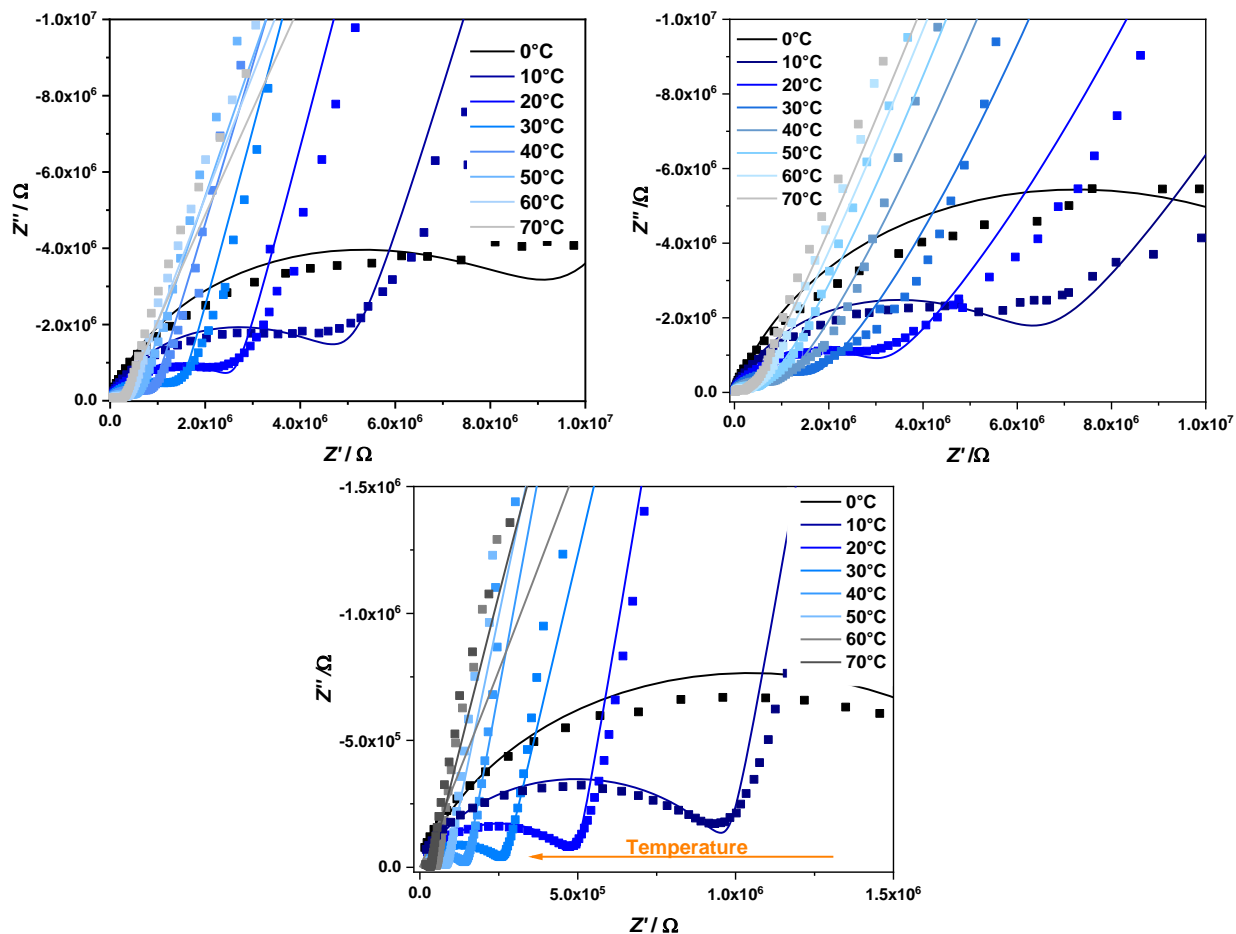


Figure S4.38: Temperature dependent measurement of K-PHI (top left), Li-PHI (top right) and Na-PHI (bottom) with carbon foil at steel electrodes under ambient conditions.

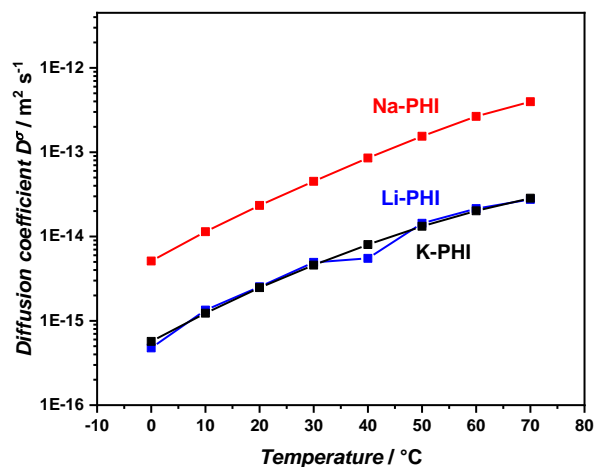


Figure S4.39: Diffusion coefficient of Na-, Li-, and K-PHI, estimated from impedance measurements by Nernst-Einstein equation dependent on the temperature. Errors of the values are too small to be seen; a systematic error of 7% was assumed, resulting in a variance in impedance measurements and concentration of diffusion species.

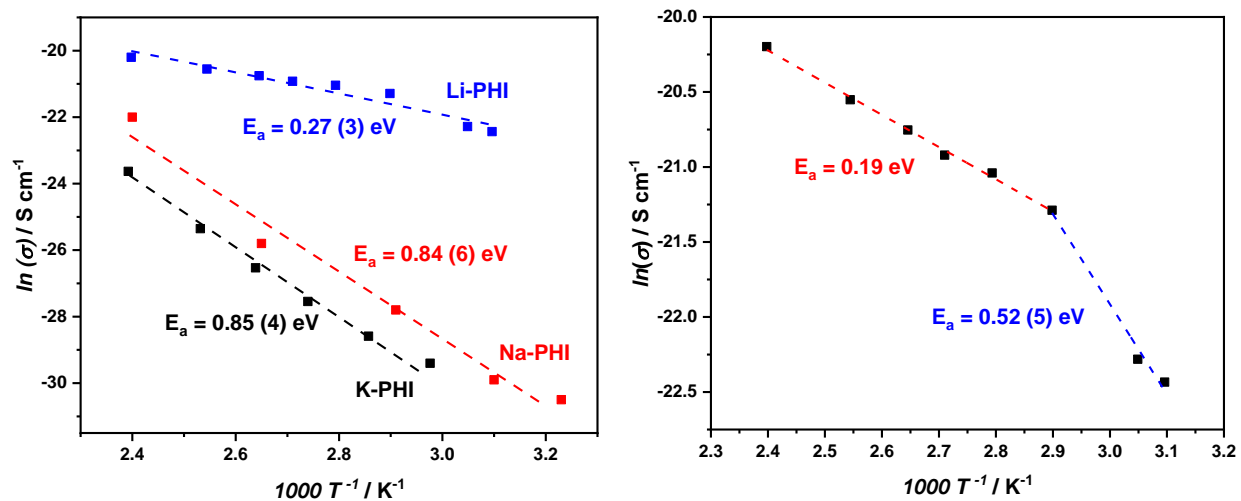


Figure S4.40: Arrhenius plot of dry K, Na- and Li-PHI in a temperature range of 40-145°C, with conductivity most likely being influenced by electron motion rather than ions (left). Zoom in to Li-PHI behavior at higher temperatures (right).

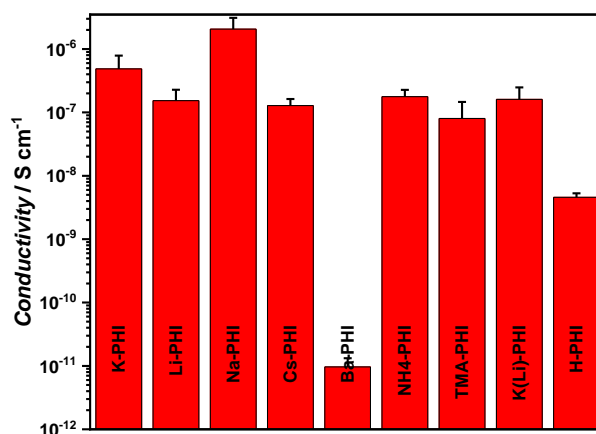


Figure S4.41: Overview of overall conductivities of different PHI materials at ambient conditions with various cations measured by impedance analysis.

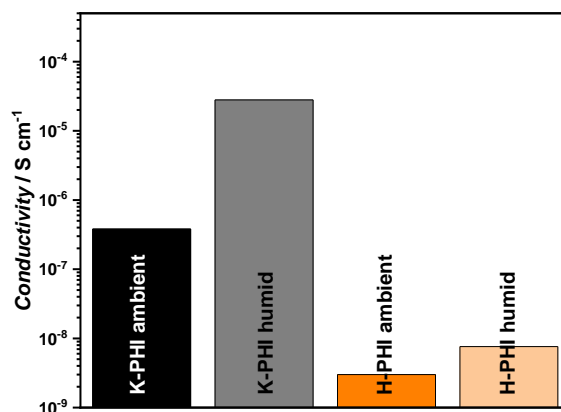


Figure S4.42: Comparison of conductivity values for dry and humid K-PHI as well as H-PHI measured by impedance spectroscopy.

An increase in conductivity by wetting H-PHI and K-PHI can be seen in both materials (Figure S4.42). From this result it cannot be excluded that at a certain humidity value the proton condition is also contributing to the overall conductivity. As described in literature the proton conductivity is enhanced if more water is present.^[74] For melon-type carbon nitrides, water molecules are adsorbed at the surface via double hydrogen bonding, which then enhances the proton conduction at the surface of the particle (similar to a grain boundary conduction). A similar effect may occur in PHI materials at high humidity, since the pores are filled with water, so the particle surface is hydrated.

9.4.6. NMR analysis

Dynamics of cations from PFG and NMR relaxation time measurements

From PFG NMR data tracer diffusion coefficients (D^{tr}) can be extracted. Nevertheless, reliable diffusion coefficients can only be extracted for values larger than $10^{-13} \text{ m}^2\text{s}^{-1}$, since signal to noise ratio is not high enough otherwise. Out of this reason, all the data shown in the following were used as an upper limit for diffusion and conductivity. For this diffusion process, an activation energy for long-range ion diffusion can be estimated by plotting the extracted diffusion coefficients in an Arrhenius plot (Figure S4.43). This value fits quite well the activation energy obtained from impedance spectroscopy ($0.50 (\pm 0.1) \text{ eV}$) also probing long-range ion mobility.

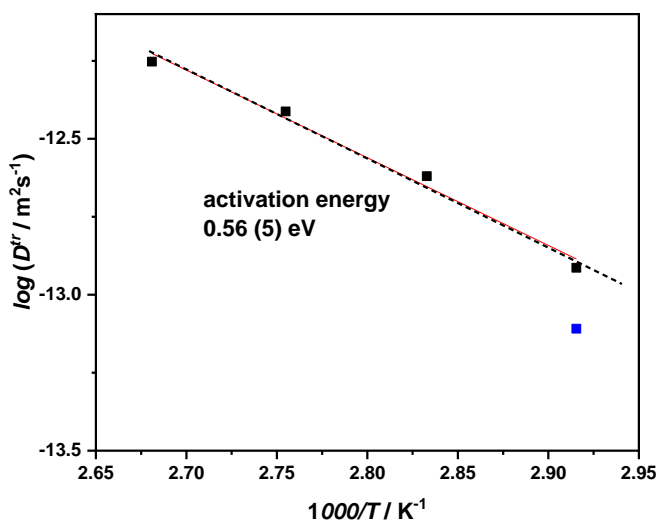


Figure S4.43: Arrhenius plot of ^7Li -ssNMR (PFG) of temperature dependence of Li tracer diffusion in Li-PHI under ambient conditions. The blue point is not considered for the fitting.

The conductivity of ions can be calculated out of PFG NMR data (by using the Nernst-Einstein-equation):

$$\sigma_{NMR} = \frac{D^{tr} n z^2 e^2}{k_B T}$$

With D^{tr} = diffusion coefficient [$\text{m}^2 \text{ s}^{-1}$], n = concentration of the diffusing species [m^{-3}] (mobile for ionic conductivity), z = charge number of diffusion species, e = elemental charge [C], k_B = Boltzmann constant [$\text{kg m}^2 \text{ s}^{-2} \text{ K}^{-1}$] and T = temperature [K].^[71] As described before the concentration of diffusion species is in average $2.60 \times 10^{27} \text{ m}^{-3}$ estimated by elemental analysis.

Table S4.13: Conductivities calculated from diffusion coefficient of PFG NMR at different temperatures for Li-PHI.

Temperature [K]	Diffusion coefficient [$\text{m}^2 \text{s}^{-1}$]	Conductivity [S cm^{-1}]
343	1.2×10^{-13}	1.3×10^{-5}
353	2.4×10^{-13}	2.6×10^{-5}
363	3.9×10^{-13}	4.2×10^{-5}
373	5.6×10^{-13}	6.0×10^{-5}

To get some insight in the diffusion mechanism, the Haven ratio (H_R) can be calculated ^[59, 75]:

$$H_R = \frac{D^{tr}}{D^\sigma}$$

With D^{tr} being the tracer diffusion coefficient and D^σ the conductivity diffusion coefficient. The Haven ratio at 70°C is around 4.3. When extrapolating the tracer diffusion coefficient to 303 K ($D^{tr} = 1.09 \times 10^{-14} \text{ m}^2 \text{ s}^{-1}$) a H_R of 2.2 (or inverse Haven ratio of 0.45) is obtained. These values suggest an ion conduction mechanism with solvated ions where the mobile ions do not interact strongly with each other.^[76] Such a correlation factor would point to 1D transport,^[59, 75] which is consistent with the 1D pore channels of PHI. Additional to the Haven ratio the correlation factor (f) can be estimated by:

$$D^{tr} = f D^{uc}$$

The uncorrelated diffusion coefficient was extracted from analysis of the NMR line broadening and is only meaningful at a temperature of 229 K. The tracer diffusion coefficient at 229 K is extracted from the fit in Figure S46 with a value of $1.14 \times 10^{-17} \text{ m}^2 \text{ s}^{-1}$. Together with an uncorrelated diffusion coefficient for 1D diffusion ($D^{uc} = 3.4 \times 10^{-16} \text{ m}^2 \text{ s}^{-1}$ (at 229 K)), a correlation factor of 0.034 can be estimated. This is in good agreement with the theoretical value for a one-dimensional diffusion mechanism in a 1D chain, where the correlation factor is close to 0.^[59, 77] For diffusion in a 2D lattice (2d squares or hexagonal) based on vacancy hopping a correlation factor of 0.46-0.56 is expected. The result for Li-PHI hints to a 1D transport of the alkali ions in the pore channels along the c direction.

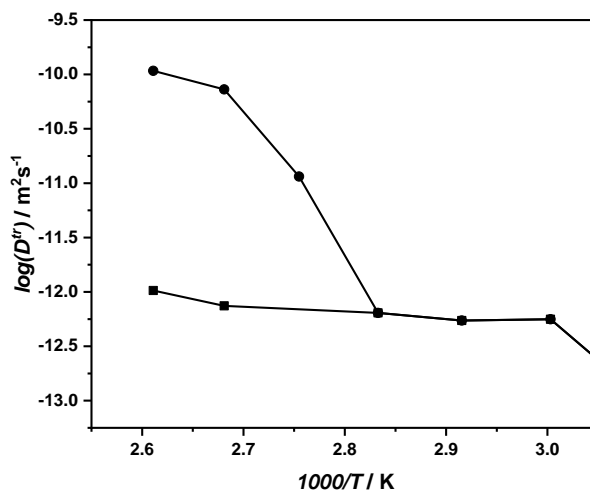


Figure S4.44: Arrhenius plot of ^7Li -ssNMR (PFG) of temperature dependence of Li tracer diffusion in Li-PHI at 75 %RH environment. At a temperature above 80°C two distinct diffusion coefficients are observed, probably due to two different transport mechanism, which are enabled at higher temperature and humid environment.

Two distinct diffusion coefficients are reported in literature for polymer based systems.^[78-80] There, a slower and a faster diffusion component for Li ions was found in an electrolyte mixture of polymer and liquid. The fast ion mobility was correlated to the diffusion of Li in the liquid, within the pores of the polymer, whereas the slower motion is due to Li-ions interacting with the polymer. The same might apply to PHI. Since under ambient conditions only one diffusion coefficient was obtained by PFG NMR, an additional fast diffusion pathway at 75 %RH due to more water molecules being present in the pores might be formed.

Similar results were reported^[53] for a nanostructured ion conducting polymer based on perfluorosulfonate, showing two different ion mobility processes, where increasing the humidity from 55 %RH to 100 %RH results in an enhanced ionic conductivity of 1-2 orders of magnitude (10^{-3} S m^{-1} with $D = 1.5 \times 10^{-11} \text{ m}^2 \text{ s}^{-1}$ and $5.3 \times 10^{-13} \text{ m}^2 \text{ s}^{-1}$). This is in line with the values we found for Li-PHI at 75 %RH. The higher mobility of alkaline ions at higher humidity can also be caused by an additional transport mechanism becoming more likely. This process might be comparable to an alkali ion transport in bulk water, which is in agreement with an increasing dielectric constant.

Another explanation for the two diffusion coefficients is the existence of anisotropy in the sample, which can cause a kink in diffusion coefficients at higher temperatures due to different ionic pathways in the pellet, caused by different oriented particles in the pellet.^[81] Nevertheless, this behavior as well as the fact that two distinct diffusion coefficients are only visible above 80°C is not understood completely and should be investigated further.

When combining the information of humidity dependant electrochemical and NMR measurements with water sorption data (taken from ^[2]), it is possible that capillary condensation in pores of PHI is occurring. The water sorption data show a type II isotherm, with the major adsorption occurring in the low pressure range and monolayer-multilayer adsorption afterwards. This behaviour is typical for material with a strong adsorbate-adsorbent interaction, which is further underlined by the hysteresis of adsorption and desorption data.^[82] The capillary condensation in pores at increasing humidity might add an additional transport possibility for the hydrated cations, which could explain an additional diffusion in PFG NMR and similar activation energies for the ion transport in Na-, K-, Li-PHI. For an estimation if capillary condensation is occurring the Kelvin equation can be used:^[83]

$$\ln\left(\frac{p}{p_0}\right) = -\frac{2\gamma V_M}{rRT}$$

with p the vapour partial pressure, p_0 the saturated vapour pressure, γ the surface tension, V_M the molar volume of the liquid, r the radius of the pore, R the universal gas constant and T the temperature. When taking the onset of the increase of the K-PHI isotherm for water sorption a radius of pores of roughly 0.8-2.1 nm can be extracted. In pores with a smaller radius capillary condensation might occur already at comparable low humidity values (of roughly 25 %RH) and is therefore likely to happen in the structural pores of PHI (with a radius of 0.38 nm).

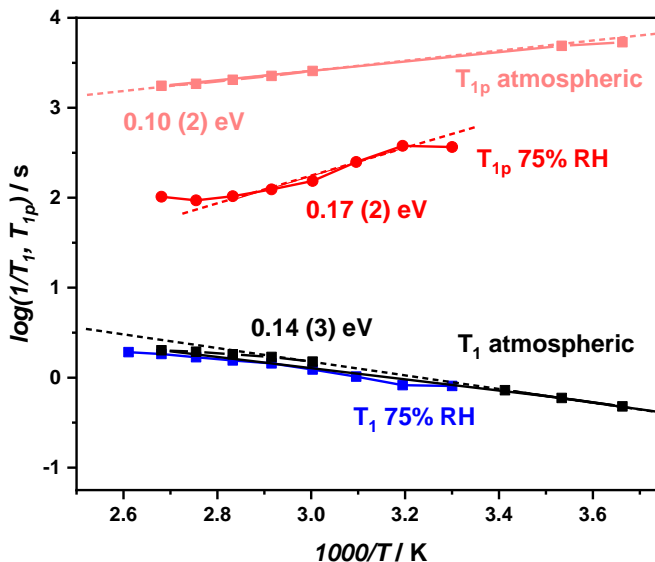


Figure S4.45: ^7Li -ssNMR spin-lattice relaxometry Li ion diffusion in Li-PHI at atmospheric and 75 %RH conditions. Dashed lines are fitted to curves to estimate activation energies for diffusion processes.

The activation energies estimated from T_1 relaxation experiments did not change with humidity, whereas the T_{1p} relaxometry revealed a different behavior with a higher activation energy of 0.17 eV at 75 %RH in comparison to ambient conditions (0.10 eV) (Figure S4.45), which might be caused by a higher degree of dissociation of water molecules^[46] in a hydrated lithium ion at higher humidity, which can be detected by T_{1p} measurements. The ion motion at humid conditions is hindered more at 10^5 s^{-1} time scales in T_{1p} relaxometry, since some of the water molecules in the hydration shell have to be rearranged for the motion in the pore channels for longer timescale motion. This effect is too slow to be tracked by the T_1 experiments, which are sensitive on the ns time scale. Due to the comparable high hydration energy this process is hindered and might be an explanation why sodium is more mobile in the PHI pore channels than lithium.

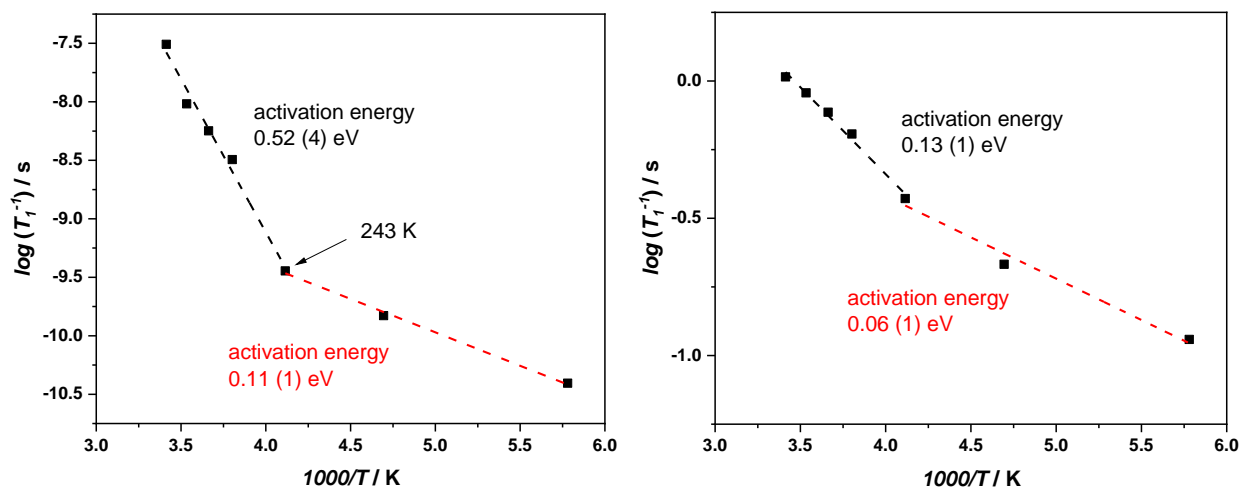


Figure S4.46: ^{23}Na - and ^1H -ssNMR spin-spin relaxometry in Na-PHI under ambient conditions. Dashed lines are fitted to curves to estimate activation energies for diffusion processes.

Spin-spin relaxation experiments can only be performed when the ion diffusion is fast enough to effect spin-spin relaxation. Values below 10^4 s^{-1} jump rates are typically not detectable anymore in NMR.^[84] Since PHI is at the boarder of this value, the analysis of those relaxation timescales was excluded. Instead, spin-lattice relaxation measurements (T_1 and $T_{1\rho}$) of Li-PHI and Na-PHI were performed for ^7Li , ^{23}Na and ^1H . By freezing of water within the pores the long-range motion of ions is hindered, hence only fast rotational or short-range motions are still possible. ^{23}Na and ^1H T_1 relaxometry on Na-PHI under ambient conditions in a temperature range of 293-173 K showed also two distinct regions below and above 243 K, confirming the result of water-assisted ion transport (Figure S4.46). A similar trend is seen for Li-PHI where the activation energy of Li ion motion below 240 K is decreasing. The decrease of activation energy below the water freezing point was already described in literature for boron doped carbon nitride films and is caused by the formation of ice in the compound.^[85]

Table S4.14: Comparison of diffusion coefficients and activation energies of diffusion processes at ambient conditions of Li-, Na- and K-PHI. Numbers in italics are just upper limits for diffusion coefficients and have a high uncertainty, since they were at the detection limit of the instrument.

	D [$\text{m}^2 \text{s}^{-1}$] at T [K]; Ea [eV] Li-PHI	D [$\text{m}^2 \text{s}^{-1}$] at T [K]; Ea [eV] Na-PHI	D [$\text{m}^2 \text{s}^{-1}$] at T [K]; Ea [eV] K-PHI
Dry D^σ	$7.5(\pm 5.0) \times 10^{-19}$ at 308	$4.0(\pm 3.0) \times 10^{-18}$ at 308	$2.3(\pm 2.0) \times 10^{-19}$ at 308
Dry Ea^σ	-	-	0.85 (± 0.02)
Ambient D^σ	$5.0(\pm 0.7) \times 10^{-15}$ at 303	$4.5(\pm 0.7) \times 10^{-14}$ at 303	$4.5(\pm 0.7) \times 10^{-15}$ at 303
Ambient Ea^σ	0.50 (± 0.01)	0.46 (± 0.03)	0.48 (± 0.01)
Ambient D^{uc}	$3.4(\pm 3.0) \times 10^{-16}$ at 229	$3.7(\pm 4.0) \times 10^{-16}$ at 206	-
Ambient Ea^{uc}	0.37 (± 0.01)	0.33 (± 0.01)	-
Ambient D^{tr}	<i>$< 1.2 \times 10^{-13}$ at 343</i>	-	-
Ambient Ea^{tr}	<i>0.56 (± 0.05)</i>	-	-
Ambient Ea^{T1}	0.14 (± 0.03)	0.22 (± 0.02)	-
Ambient Ea^{T1r}	0.10 (± 0.02)	-	-

Analysis of static NMR line shapes

Temperature dependent static ^7Li , ^{23}Na and ^1H NMR measurements were performed for Li- and Na-PHI in a temperature range of 173-373 K. By analyzing the full width at half maximum (FWHM) several estimates regarding the ion diffusion can be drawn. The correlation time τ_c characterizes the jump rate for a specific atom, and in a situation of exchange between different states correlates with the FWHM ($\Delta\omega \cdot \tau_c \approx 1$). The correlation time describes the time of an ion to jump between two points with a distance a , e.g. between two crystal positions or layers. The Einstein-Smoluchowski equation can be used for the extraction of an uncorrelated diffusion coefficient D^{uc} :

$$D^{uc} = \frac{a^2}{2b \cdot \tau_c}$$

a describes the mean jump distance/mean square displacement (in PHI we assumed it to be the stacking distance of 3.2 Å

or to be more accurate 3.17 Å for Na-PHI and 3.18 Å for Li-PHI) and b describes the dimensionality of the ion mobility ($b = 1$ for 1D, 2 for 2D, 3 for 3D).^[59, 86-88] In PHI, a one-dimensional ion conductivity within the pores is expected, as also observed by the correlation factor, in line with the 1D transport mechanism found in PTI.^[67] For Li-PHI a diffusion coefficient of $D^{\text{uc}} = 3.4 (\pm 0.1) \times 10^{-16} \text{ m}^2 \text{ s}^{-1}$ (at 229 K) is obtained. A 3 direction ion transport, as in a cubic system, would lead to $D^{\text{uc}} = 1.1 (\pm 0.1) \times 10^{-16} \text{ m}^2 \text{ s}^{-1}$ (at 229 K).

The activation energy of the jump can also be estimated by the Waugh and Fedin equation:

$$E_a = 1.6 \times 10^{-3} \cdot T_c$$

where T_c is the onset temperature of motional averaging of the respective atom.^[86] At low temperatures, the line is broad, which is likely due to several factors, namely un-averaged dipole-dipole interactions, interaction of the quadrupole ^7Li with the electrical field gradient at different coordination sites of Li, or some anisotropy in chemical shift.^[89] When the temperature is increasing, the Li ions start moving more rapidly, which averages the dipole-dipole interactions. At the onset of line narrowing for Li-PHI at 229 K the estimated correlation time is $\tau_c \approx 1.5 \times 10^{-4} \text{ s}$ (Figure 7.4c).

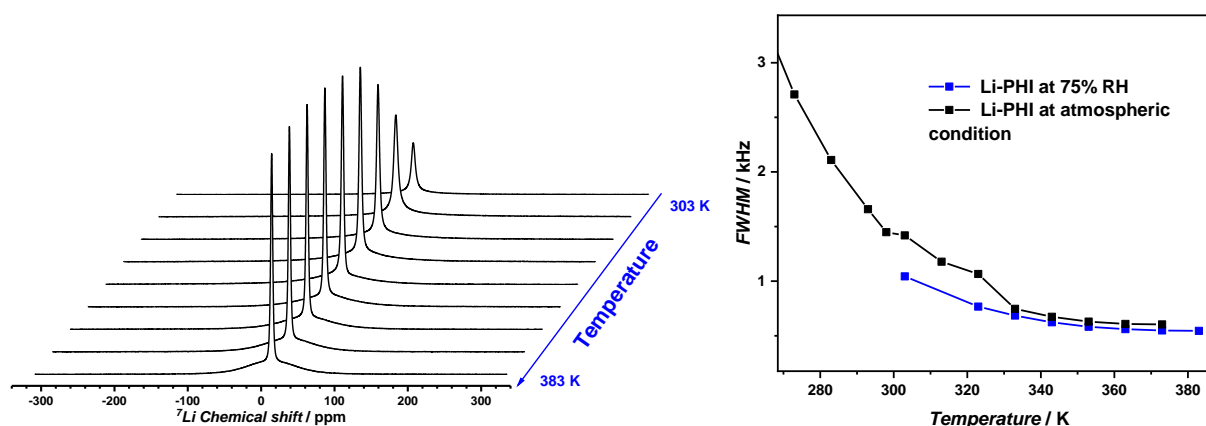


Figure S4.47: ^7Li -ssNMR static measurements of Li-PHI at different temperature at 75 %RH. Temperature dependence of full width at half maximum (FWHM) of Li-PHI at 75 %RH (blue line) and atmospheric conditions (black line).

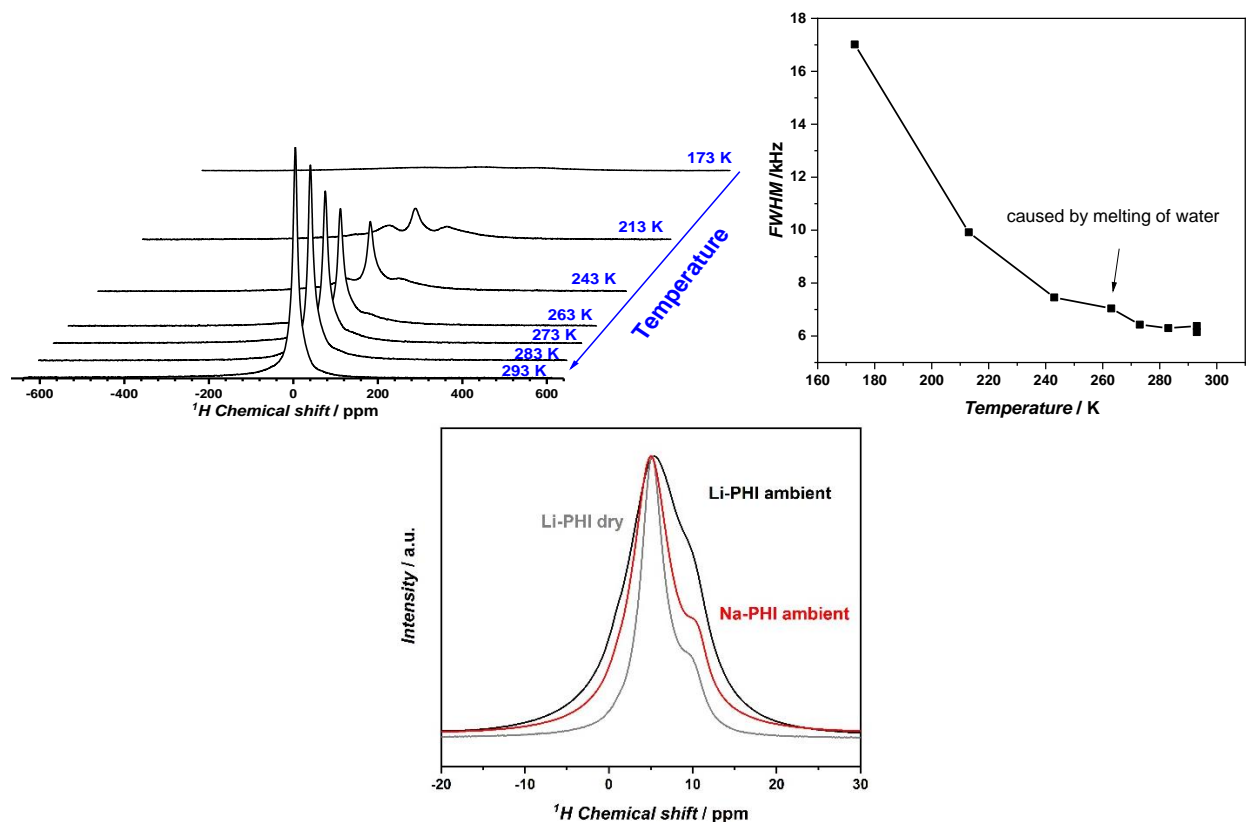


Figure S4.48: ^1H -ssNMR static measurements and line-shape analysis of Na-PHI at different temperatures under ambient conditions. Temperature dependence of full width at half maximum (FWHM) of Na-PHI (top). ^1H MAS NMR of Li- and Na-PHI at ambient and Li-PHI dry condition for comparison (bottom).

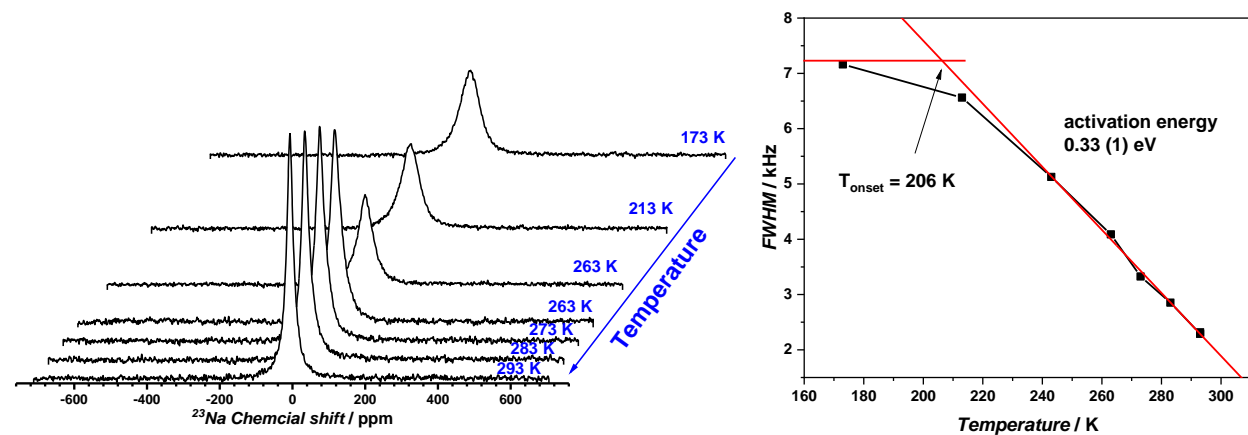


Figure S4.49: ^{23}Na -ssNMR static measurements and line-shape analysis of Na-PHI at different temperatures under ambient conditions. Temperature dependence of full width at half maximum (FWHM) of Na-PHI.

9.4.7. Quantum-chemical calculations

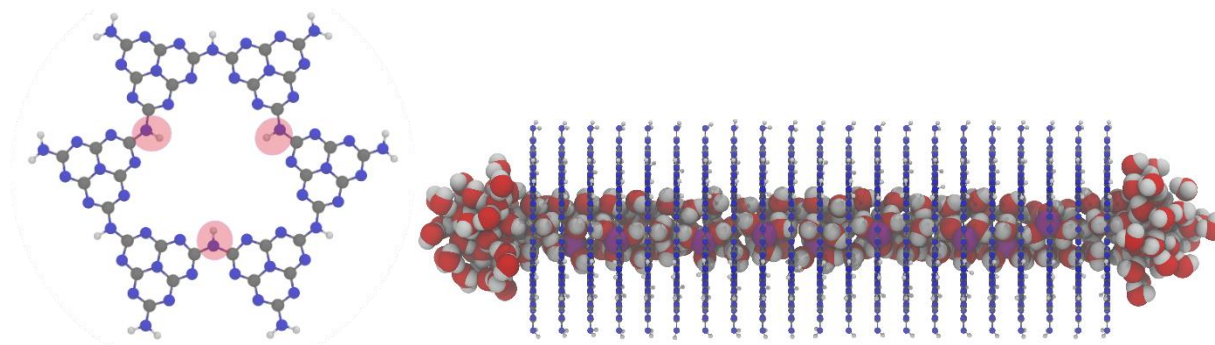


Figure S4.50: Single 2D PHI pore, with highlighted deprotonation possibilities of imide positions (left). Modeled PHI pore canal, side view across the pore canal showing water and ions within the pore (right).

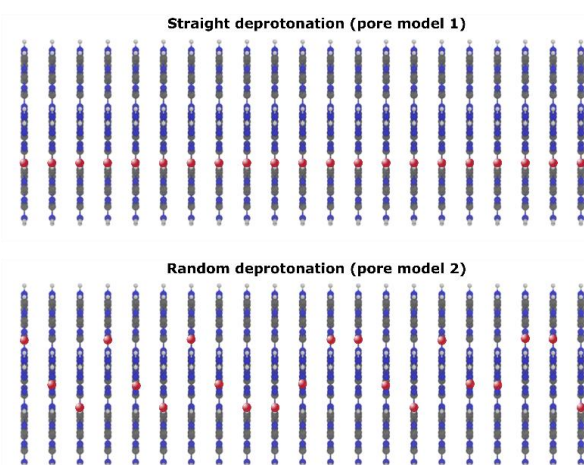


Figure S4.51: Two models for M-PHI used for subsequent MM/MD simulations and quantum-chemical calculations. A stack of 21 2D PHI pores are stacked as a defect-free eclipsed stacking. Red balls illustrate the deprotonated position of the imide bridge for each layer, resulting in three different orientations per pore. Top: Straight deprotonation pattern (pore model 1), all deprotonated imide bridges are located on top of each other. Bottom: Random deprotonation pattern (pore model 2), deprotonated imide bridges alternate through the layers in a random fashion.

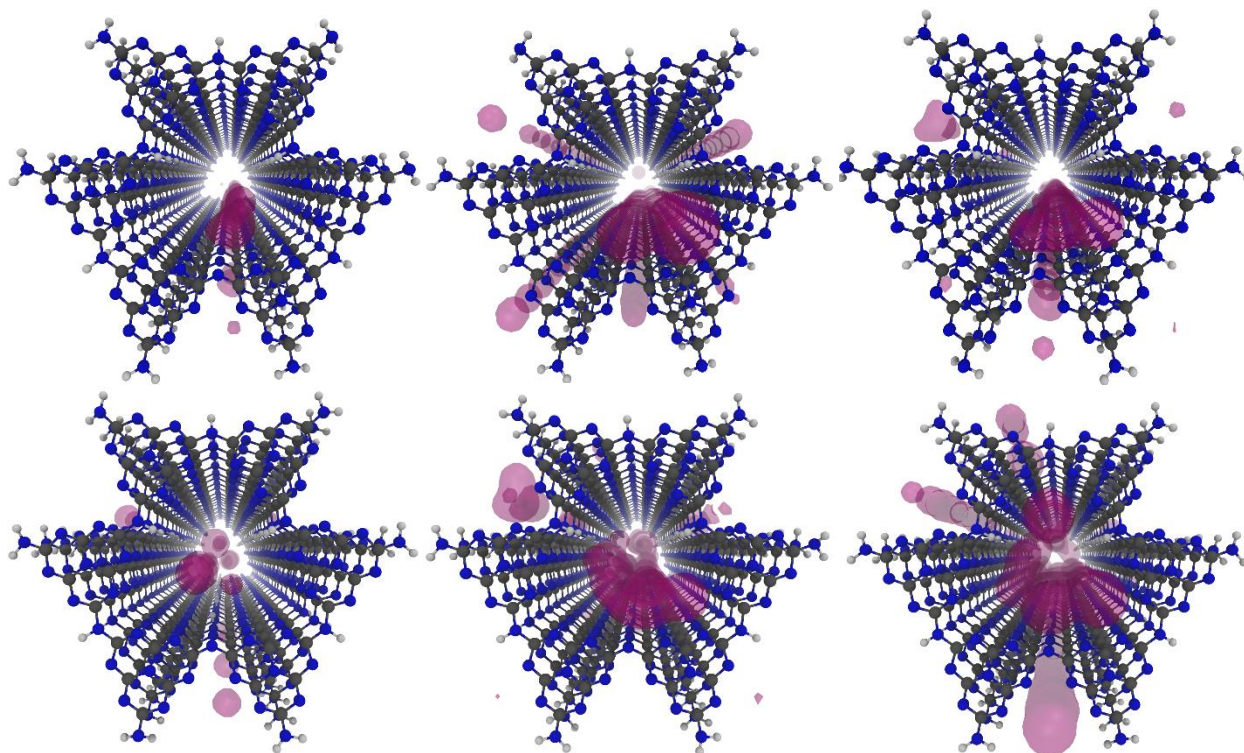


Figure S4.52: Visualization of alkali ion positions as mass densities calculated from corresponding MM/MD trajectories in a PHI channel in a perfectly eclipsed stacking for Li-, Na- and K-PHI (left to right). Top: pore model 1, Bottom: pore model 2.

In addition to the deprotonation pattern, the radius of the hydrated ions and the interaction strength of the ions with the backbone are important parameters for the conductivity.

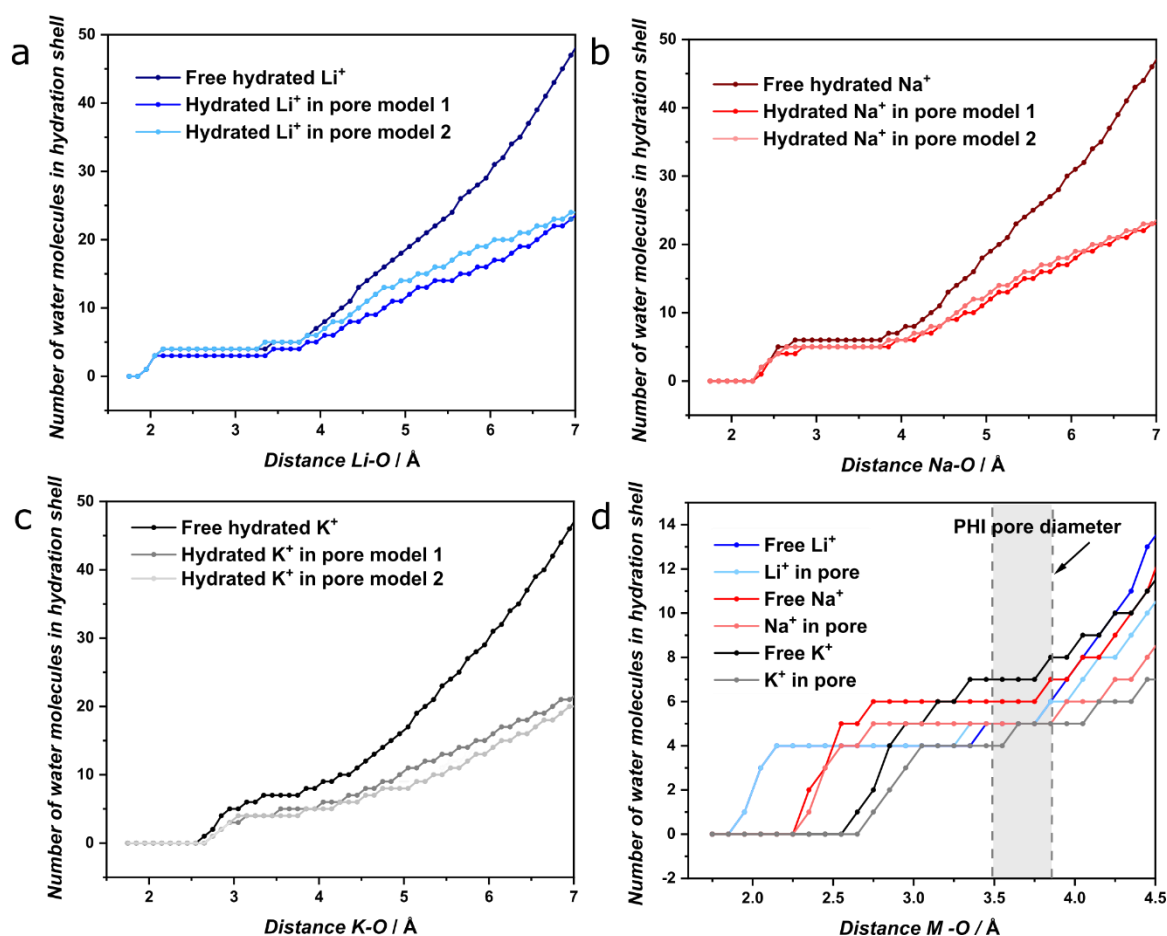


Figure S4.53: Radial distribution function [g(r)] data from MM/MD simulations for Ion-Water distances, using the oxygen atom in water. Analysis of the hydration shell of free ions as well as ions located in PH1. a) Li⁺, b) Na⁺, c) K⁺. d) Comparison of free ions and the pore model 2 for Li, Na and K. Grey area depicts the most probable hydration state in the PH1 pores, since 3.8 Å is the actual pore size of a PH1 pore.

Different deprotonation patterns (straight and random) were used in the simulated eclipsed stacking pore channels, to study the different interaction energy of the (partially) solvated ion in the PH1 pore channels. As experimental conditions are most probably in between the two model systems used, the effect of the different deprotonation models are compared to obtain the best possible insight in the conductivity mechanism in the modeled PH1 pore. The straight deprotonation pore model can be understood as model system to compare the pure interaction energies between different components. The randomly deprotonated pore model was simulated to best describe the conditions in a synthesized sample. Individual interactions are summarized in the following: Pore-ion interaction (Figure S4.55), water-ion interaction in the PH1 pore channel (Figure S4.54) and pore-water interaction (Figure S4.56).

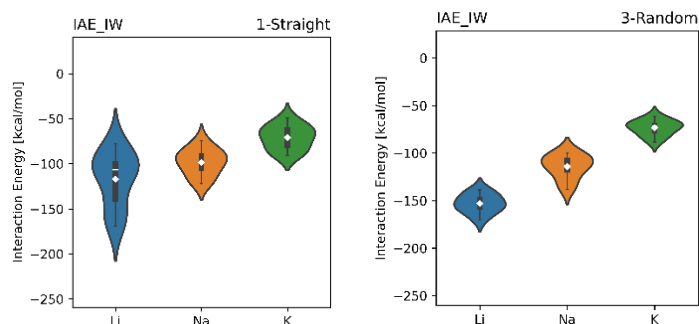


Figure S4.54: Interaction energy of Li-, Na- or K-ions with the water shell in the PHI pore channels in different deprotonation patterns in an eclipsed stacking system, obtained on PBE0-D3/Def2-TZVP^[24-27] level of theory. Pore model 1 on the left, pore model 2 on the right.

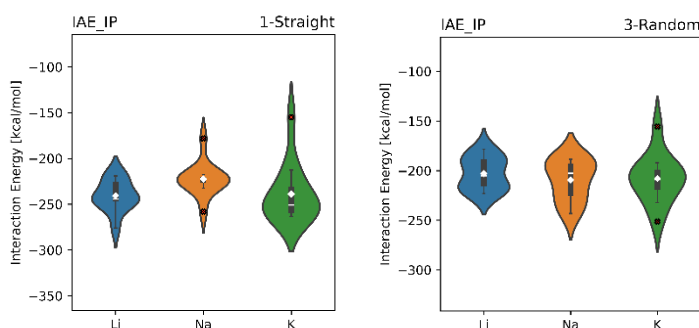


Figure S4.55: Interaction energy of Li-, Na- or K-ions with the PHI backbone in an eclipsed stacking system, obtained on PBE0-D3/Def2-TZVP^[24-27] level of theory. Pore model 1 on the left, pore model 2 on the right.

Table S4.16: Comparison of interaction energy of free solvated ions in water and the interaction energy of the ion and the water shell in the PHI pore channels.

Sample	E of free solvated ion [kcal/mol]	E of solvated ion in model 1 [kcal/mol]	E of solvated ion in model 2 [kcal/mol]
Li ⁺ (H ₂ O) _x	-172	-117	-153
Na ⁺ (H ₂ O) _x	-146	-98	-114
K ⁺ (H ₂ O) _x	-114	-71	-73

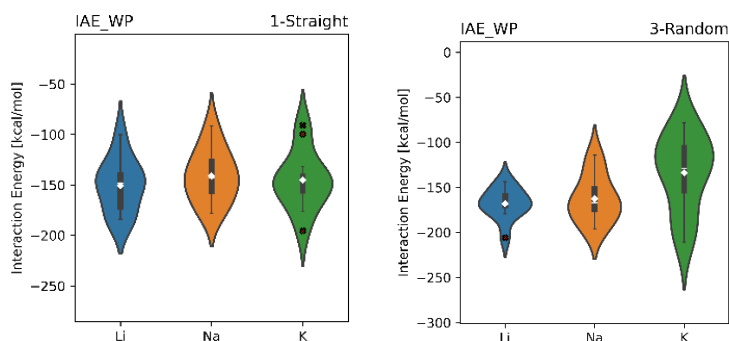


Figure S4.56: Interaction energy of water shell around the ions and the PHI backbone in different deprotonation patterns in an eclipsed stacking system, obtained on PBE0-D3/Def2-TZVP^[24-27] level of theory. Pore model 1 on the left, pore model 2 on the right.

9.4.8. Photocatalytic activity

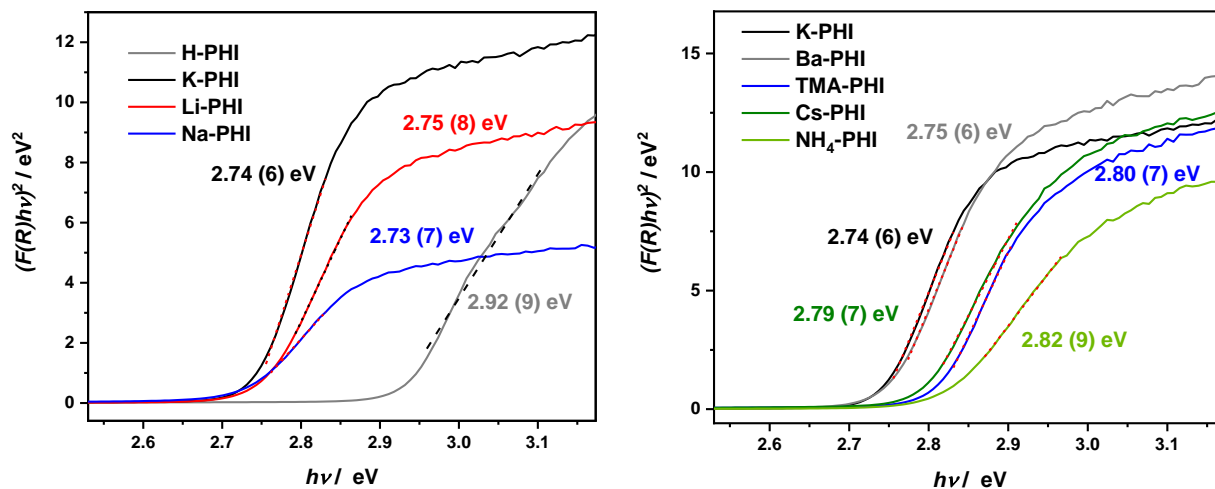


Figure S4.57: Tauc plot of different cation containing PHI structures Cs-, Ba-, TMA-, Li-, Na-, NH₄- and K-PHI to determine the optical band gap.

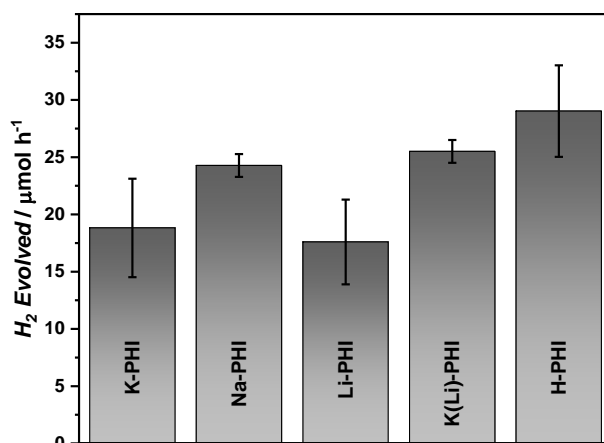


Figure S4.58: Photocatalytic hydrogen evolution rate of PHI materials with various cations and H-PHI in comparison. The photocatalysis experiments were performed with aqueous PHI suspension in presence of 10 vol% methanol as donor and Pt as co-catalyst. The Pt was photo-deposited in-situ from H₂PtCl₆ and the amount was optimized (*M*-PHI 8 wt% Pt and H-PHI 2 wt% Pt).^[1, 2, 22]

By changing the counterion within the pores other properties are changed as well, which are affecting the photocatalytic properties, such as stacking or optical bandgap. In H-PHI the optical bandgap is slightly increased (2.9 eV)^[2, 22] in comparison to e.g. K-PHI (2.7 eV). Besides the presence of protons in H-PHI is enhancing the photocatalytic hydrogen evolution. Since it does not contain any mobile cation in the pores and the structure is changed in comparison to K-PHI,^[2] H-PHI was excluded for the comparison of photocatalytic activity with ionic conductivity. Besides, also in the K(Li)-PHI sample, potassium exchange in Li-PHI again, a slight protonation was observed, maybe due to an increase amount of stacking defaults, which might favor the washing of alkaline ion.

Table S4.16: Color change of H-PHI when illuminated in an aqueous suspension in presence of 10 vol% MeOH and 0.5 M MCl_x . (100 mW cm^{-2} , AM 1.5 G).

Salt added to H-PHI	Photocharging (blue color) during illumination
LiCl	Yes
NaCl	Yes
KCl	Yes
TMACl	No
NH_4Cl	Yes
CsCl	Yes
$BaCl_2$	No
DI water	No

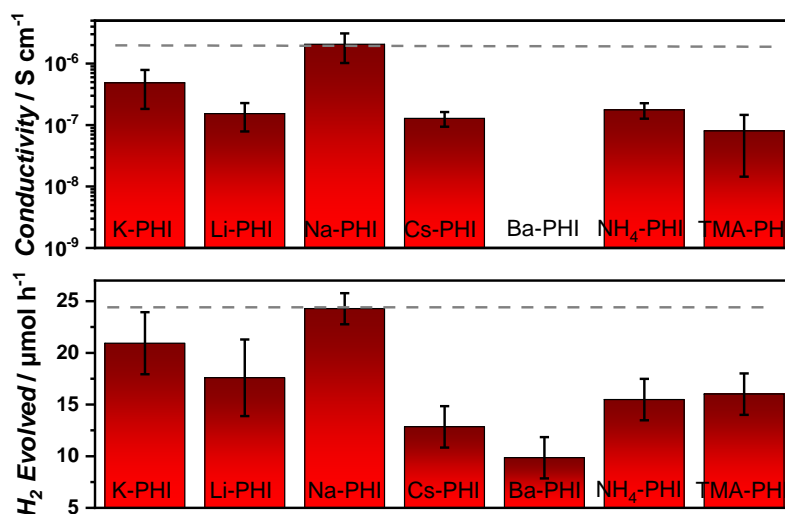


Figure S4.59: Comparison of conductivity and photocatalytic hydrogen evolution rate of PHI materials with various cations. The photocatalysis experiments were performed with aqueous PHI suspension in presence of 10 vol% methanol as donor and Pt as co-catalyst. The Pt was photo-deposited *in-situ* from H_2PtCl_6 and the amount was optimized (8 wt% Pt).^[2]

Analysis of PHI after photocatalysis

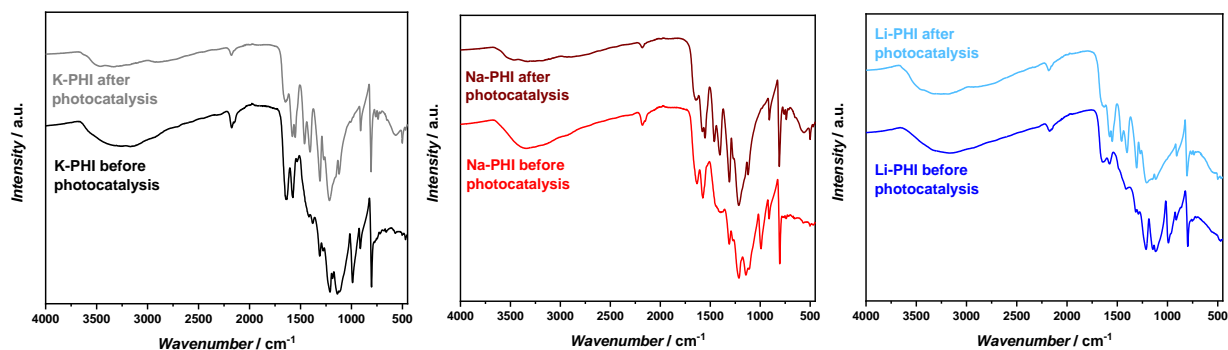


Figure S4.60: FT-IR analysis of K-PHI (left), Na-PHI (middle) and Li-PHI (right) before and after photocatalysis. Only minor changes, probably originating from partial protonation can be observed.

Table S4.17 Elemental analysis of alkali ion concentration before and after photocatalysis in *M*-PHI.

Sample	Amount alkali ion before photocatalysis [wt%]	Amount alkali ion after photocatalysis [wt%]	Relative amount of alkaline ion after photocatalysis [%]
Li-PHI	1.63	0.18	11.0
Na-PHI	4.96	0.25	5.0
K-PHI	9.70	0.73	7.6

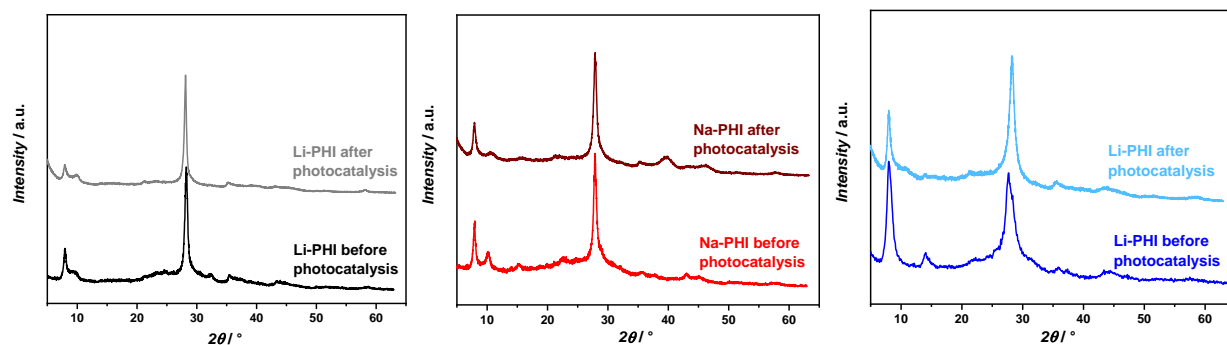


Figure S4.61: PXR D analysis of K-PHI (left), Na-PHI (middle) and Li-PHI (right) before and after photocatalysis. Only smaller changes point to a slight increase in disorder.

9.4.9. PL and electrochemical analysis under illumination

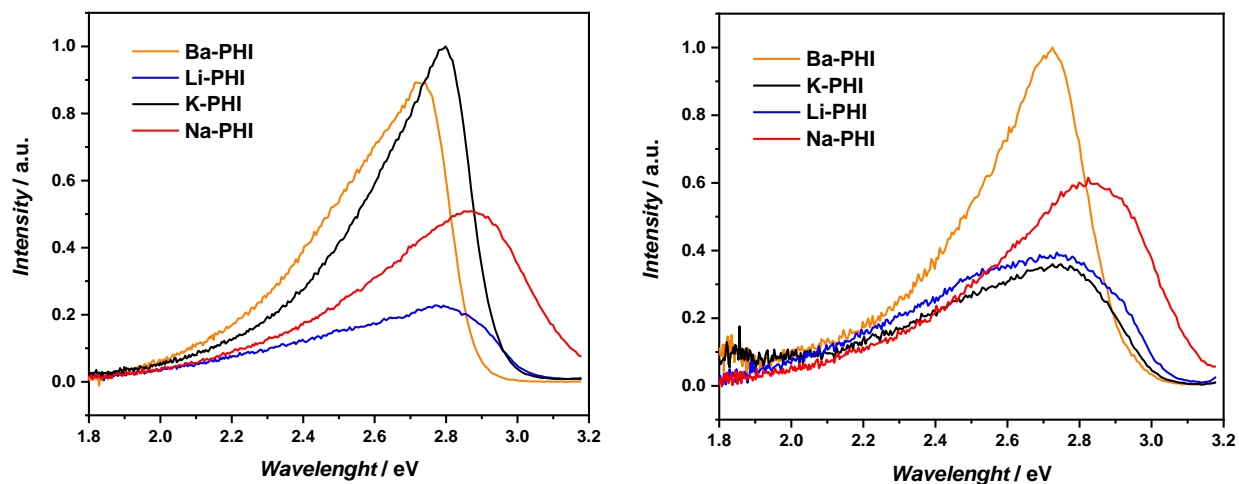


Figure S4.62: PL spectra of K- (black), Na- (red), Li- (blue) and Ba-PHI (orange) in aqueous suspensions (left) and in aqueous suspension with 10 vol% MeOH and 8 wt% Pt (right).

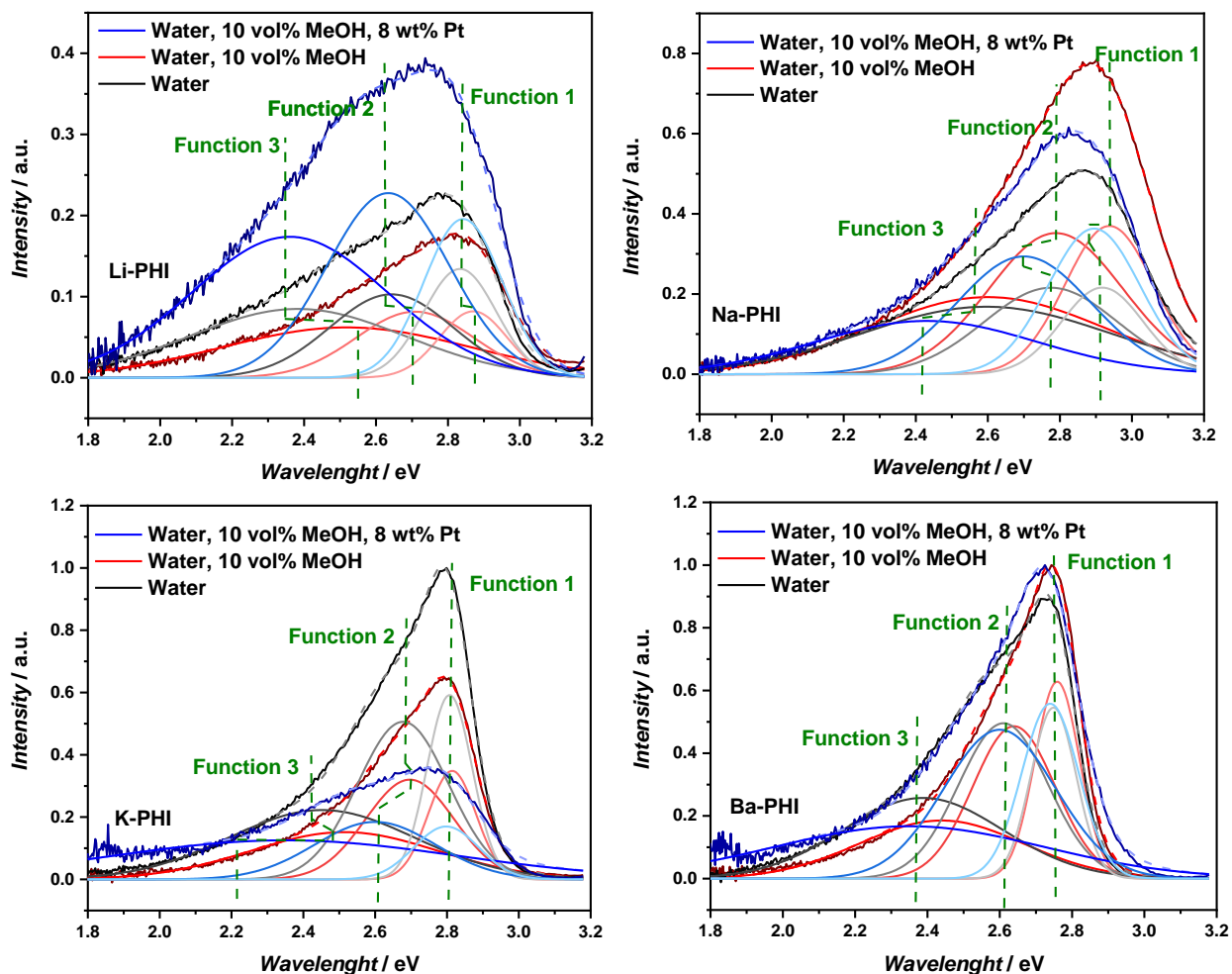


Figure S4.63: PL intensity, fitted with three Gaussian functions to deconvolute the spectrum. Li- (top left), Na- (top right), K- (bottom left) and Ba-PHI (bottom right) in aqueous suspensions, aqueous suspension with 10 vol% MeOH and in addition in presence of photo-deposited Pt (at 100 mW cm^{-2} , AM 1.5 G).

Table S4.18: Lifetimes of photo-generated charges estimated by PL time dependent measurements of Li-, Na-, K- and Ba-PHI in aqueous suspensions (white), aqueous suspension with 10 vol% MeOH (light grey) and in addition in presence of photo-deposited Pt (at 100 mW cm^{-2} , AM 1.5 G) (dark grey). For fitting an exponential and a Γ decay function were used.

Sample	T_{exp} [ns]	A_{exp} [%]	T_{mode} [ns]	A_{mode} [%]
Li-PHI	0.15 ± 0.01	87 ± 2	0.52 ± 0.05	13 ± 2
Na-PHI	0.20 ± 0.03	61 ± 11	0.45 ± 0.09	39 ± 11
K-PHI	0.16 ± 0.01	81 ± 4	0.49 ± 0.11	19 ± 4
Ba-PHI	0.16 ± 0.01	86 ± 1	0.84 ± 0.02	14 ± 1
Li-PHI	0.13 ± 0.01	85 ± 1	0.42 ± 0.03	15 ± 1
Na-PHI	0.29 ± 0.03	60 ± 2	0.52 ± 0.13	40 ± 2
K-PHI	0.11 ± 0.01	81 ± 1	0.30 ± 0.02	19 ± 1
Ba-PHI	0.14 ± 0.01	86 ± 1	0.62 ± 0.34	14 ± 1
Li-PHI	0.16 ± 0.01	85 ± 1	0.48 ± 0.03	15 ± 1
Na-PHI	0.28 ± 0.02	73 ± 2	0.49 ± 0.03	27 ± 2
K-PHI	0.13 ± 0.02	64 ± 1	0.40 ± 0.10	36 ± 1
Ba-PHI	0.10 ± 0.01	72 ± 1	0.20 ± 0.01	28 ± 1

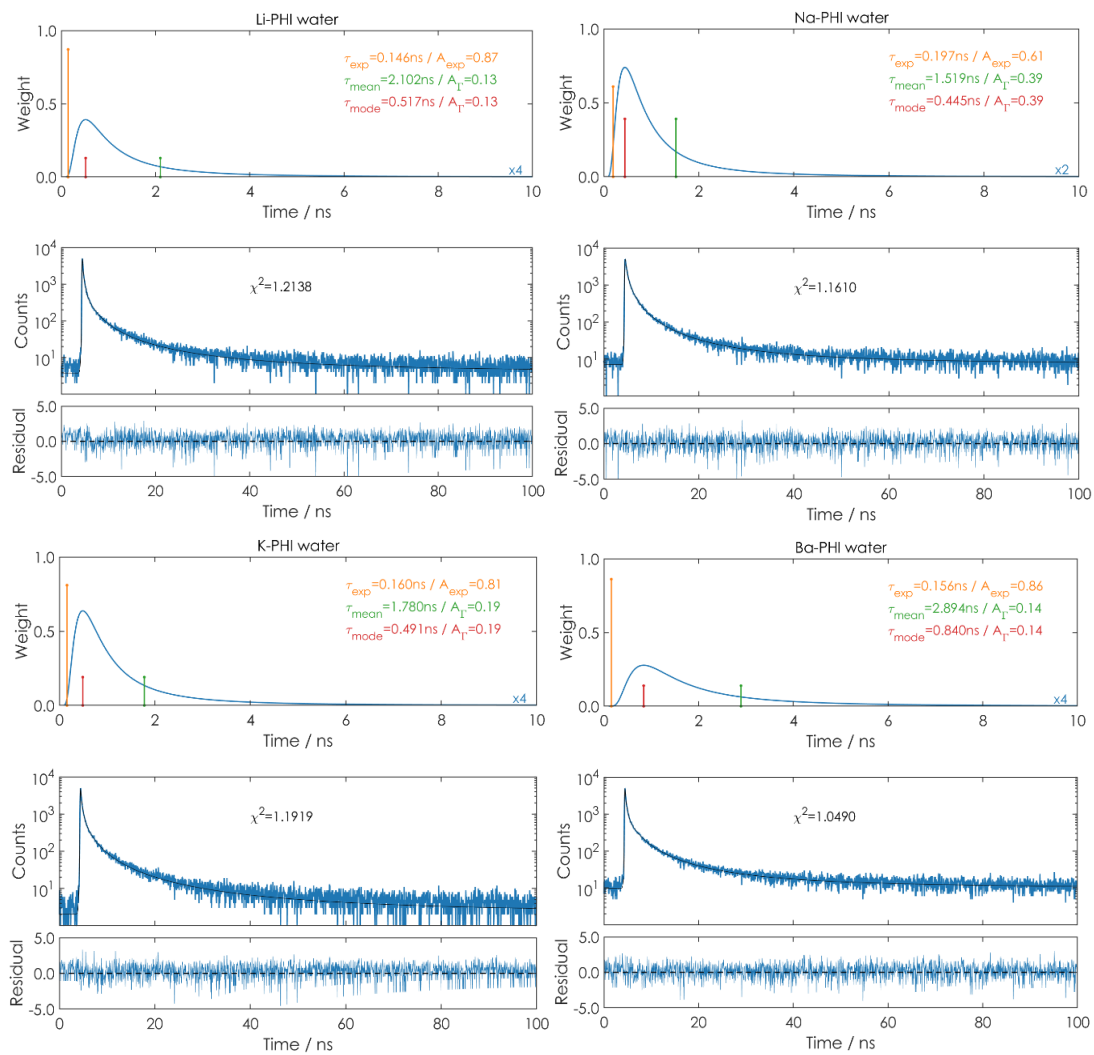


Figure S4.64: PL lifetime measurements and fittings of Li-, Na-, K- and Ba-PHI in the presence of water. Lifetime were extracted by fitting the signal decay with a convolution of a mono exponential and a Γ distribution, denoted by τ_{exp} and τ_{mode} , respectively.

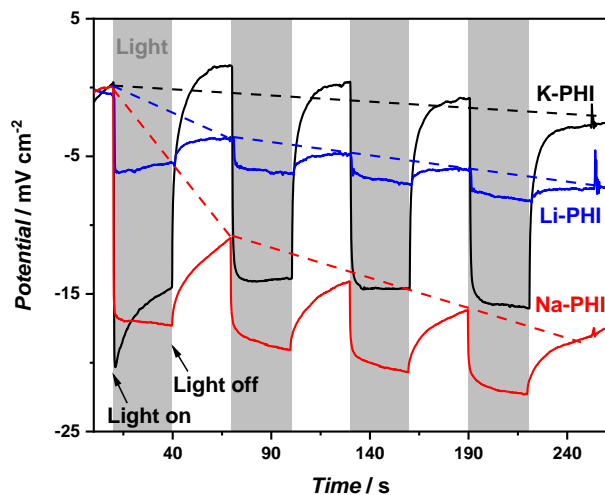


Figure S4.65: Photopotential of K- Li- and Na-PHI pellets at ambient conditions on the left side (illuminated with AM 1.5 G, 100 mW cm^{-1}) measured at open circuit potential. Dashed lines are included to guide the eye of the potential drop over four illumination and dark (relaxation) cycles.

9.4.10. Bibliography

- [1] V. W.-h. Lau, I. Moudrakovski, T. Botari, S. Weinberger, M. B. Mesch, V. Duppel, J. Senker, V. Blum, B. V. Lotsch, *Nat. Commun.* **2016**, 7 (1), 12165.
- [2] H. Schlomberg, J. Kröger, G. Savasci, M. W. Terban, S. Bette, I. Moudrakovski, V. Duppel, F. Podjaski, R. Siegel, J. Senker, R. E. Dinnebier, C. Ochsenfeld, B. V. Lotsch, *Chem. Mater.* **2019**, 31 (18), 7478-7486.
- [3] F. Podjaski, J. Kröger, B. V. Lotsch, *Adv. Mater.* **2018**, 30 (9), 1705477.
- [4] P. J. Chupas, X. Qiu, J. C. Hanson, P. L. Lee, C. P. Grey, S. J. L. Billinge, *J. Appl. Crystallogr.* **2003**, 36 (6), 1342-1347.
- [5] M. Kandiah, M. H. Nilsen, S. Usseglio, S. Jakobsen, U. Olsbye, M. Tilset, C. Larabi, E. A. Quadrelli, F. Bonino, K. P. Lillerud, *Chem. Mater.* **2010**, 22 (24), 6632-6640.
- [6] C. J. Wright, X.-D. Zhou, *J. Synchrotron Radiat.* **2017**, 24 (2), 506-508.
- [7] P. Juhas, T. Davis, C. L. Farrow, S. J. L. Billinge, *J. Appl. Crystallogr.* **2013**, 46 (2), 560-566.
- [8] P. F. Peterson, E. S. Bozin, T. Proffen, S. J. L. Billinge, *J. Appl. Crystallogr.* **2003**, 36 (1), 53-64.
- [9] S. J. L. Billinge, C. L. Farrow, *J. Phys.: Condens. Matter* **2013**, 25 (45), 454202.
- [10] X. Yang, P. Juhas, C. Farrow, S. Billinge, *arXiv: Materials Science* **2014**, 1402.3163.
- [11] E. Lorch, *J. Phys. C: Solid State Phys.* **1969**, 2 (2), 229-237.
- [12] A. Coelho, *J. Appl. Crystallogr.* **2018**, 51 (1), 210-218.
- [13] A. A. Coelho, P. A. Chater, A. Kern, *J. Appl. Crystallogr.* **2015**, 48 (3), 869-875.
- [14] E. O. Stejskal, J. D. Memory, *High Resolution NMR in the Solid State*, Oxford University Press, Oxford, **1994**, 189.
- [15] K. J. D. MacKenzie, M. E. Smith, *Multinuclear Solid-State Nuclear Magnetic Resonance of Inorganic Materials*, Elsevier Science, **2002**.
- [16] A. Bielecki, D. P. Burum, *J. Magn. Reson., Ser A* **1995**, 116 (2), 215-220.
- [17] K. H. Robin, D. B. Edwin, M. C. d. M. Sonia, G. Robin, G. Pierre, *Pure Appl. Chem.* **2001**, 73 (11), 1795-1818.
- [18] J. E. Tanner, *J. Chem. Phys.* **1970**, 52 (5), 2523-2526.
- [19] E. O. Stejskal, J. E. Tanner, *J. Chem. Phys.* **1965**, 42 (1), 288-292.
- [20] A. C. Fogarty, A. C. Jones, P. J. Camp, *Phys. Chem. Chem. Phys.* **2011**, 13 (9), 3819-3830.
- [21] J. Kröger, A. Jiménez-Solano, G. Savasci, P. Rovó, I. Moudrakovski, K. Küster, H. Schlomberg, H. A. Vignolo-González, V. Duppel, L. Grunenberg, C. B. Dayan, M. Sitti, F. Podjaski, C. Ochsenfeld, B. V. Lotsch, *Adv. Energy Mater.* **2021**, 11 (6), 2003016.
- [22] V. W.-h. Lau, V. W.-z. Yu, F. Ehrat, T. Botari, I. Moudrakovski, T. Simon, V. Duppel, E. Medina, J. K. Stolarczyk, J. Feldmann, V. Blum, B. V. Lotsch, *Adv. Energy Mater.* **2017**, 7 (12), 1602251.
- [23] V. W.-h. Lau, D. Klose, H. Kasap, F. Podjaski, M.-C. Pignié, E. Reisner, G. Jeschke, B. V. Lotsch, *Angew. Chem. Int. Ed.* **2017**, 56 (2), 510-514.
- [24] M. Ernzerhof, G. E. Scuseria, *J. Chem. Phys.* **1999**, 110 (11), 5029-5036.
- [25] C. Adamo, V. Barone, *J. Chem. Phys.* **1999**, 110 (13), 6158-6170.
- [26] S. Grimme, J. Antony, S. Ehrlich, H. Krieg, *J. Chem. Phys.* **2010**, 132 (15), 154104.
- [27] A. Schäfer, C. Huber, R. Ahlrichs, *J. Chem. Phys.* **1994**, 100 (8), 5829-5835.
- [28] J. P. Perdew, K. Burke, M. Ernzerhof, *Phys. Rev. Lett.* **1996**, 77 (18), 3865-3868.
- [29] K. Eichkorn, F. Weigend, O. Treutler, R. Ahlrichs, *Theor. Chem. Acc.* **1997**, 97 (1), 119-124.
- [30] A. M. Burow, M. Sierka, F. Mohamed, *J. Chem. Phys.* **2009**, 131 (21), 214101.
- [31] L. Grajciar, *J. Comput. Chem.* **2015**, 36 (20), 1521-1535.
- [32] A. M. Burow, M. Sierka, *J. Chem. Theory Comput.* **2011**, 7 (10), 3097-3104.
- [33] R. Łazarski, A. M. Burow, L. Grajciar, M. Sierka, *J. Comput. Chem.* **2016**, 37 (28), 2518-2526.
- [34] R. Łazarski, A. M. Burow, M. Sierka, *J. Chem. Theory Comput.* **2015**, 11 (7), 3029-3041.
- [35] R. Ahlrichs, M. Bär, M. Häser, H. Horn, C. Kölmel, *Chem. Phys. Lett.* **1989**, 162 (3), 165-169.
- [36] TURBOMOLE V7.3 2018, a development of University of Karlsruhe and Forschungszentrum Karlsruhe GmbH, 1989-2007, TURBOMOLE GmbH, since 2007; available from <http://www.turbomole.com>.
- [37] J. Wang, W. Wang, P. A. Kollman, D. A. Case, *J. Mol. Graphics Modell.* **2006**, 25 (2), 247-260.
- [38] <http://www.ks.uiuc.edu/Research/namd/> (accessed August 2020).

- [39] J. C. Phillips, R. Braun, W. Wang, J. Gumbart, E. Tajkhorshid, E. Villa, C. Chipot, R. D. Skeel, L. Kalé, K. Schulten, *J. Comput. Chem.* **2005**, *26* (16), 1781-1802.
- [40] J. Wang, R. M. Wolf, J. W. Caldwell, P. A. Kollman, D. A. Case, *J. Comput. Chem.* **2005**, *26* (1), 114-114.
- [41] J. Kussmann, C. Ochsenfeld, *J. Chem. Phys.* **2013**, *138* (13), 134114.
- [42] J. Kussmann, C. Ochsenfeld, *J. Chem. Theory Comput.* **2015**, *11* (3), 918-922.
- [43] E. R. Nightingale, *J. Phys. Chem.* **1959**, *63* (9), 1381-1387.
- [44] S. Ringe, E. L. Clark, J. Resasco, A. Walton, B. Seger, A. T. Bell, K. Chan, *Energ. Environ. Sci.* **2019**, *12* (10), 3001-3014.
- [45] P. Atkins, J. de Paula, *Atkins' physical chemistry*, Oxford University Press, New York, **2002**.
- [46] A. F. Holleman, E. Wiberg, N. Wiberg, *Lehrbuch der anorganischen Chemie*, Walter de Gruyter, **2007**.
- [47] K. J. Mallikarjunaiah, R. Damle, K. P. Ramesh, *Solid State Nucl. Magn. Reson.* **2008**, *34* (3), 180-185.
- [48] S. Kubota, S. Ozaki, J. Onishi, K. Kano, O. Shirai, *Anal. Sci.* **2009**, *25* (2), 189-193.
- [49] T. Kumeda, H. Tajiri, O. Sakata, N. Hoshi, M. Nakamura, *Nat. Commun.* **2018**, *9* (1), 4378.
- [50] J. Mähler, I. Persson, *Inorg. Chem.* **2012**, *51* (1), 425-438.
- [51] A. G. Stack, J. R. Rustad, *J. Phys. Chem. C* **2007**, *111* (44), 16387-16391.
- [52] G. M. Veith, L. Baggetto, L. A. Adamczyk, B. Guo, S. S. Brown, X.-G. Sun, A. A. Albert, J. R. Humble, C. E. Barnes, M. J. Bojdys, S. Dai, N. J. Dudney, *Chem. Mater.* **2013**, *25* (3), 503-508.
- [53] X. Guo, S. Theissen, J. Claussen, V. Hildebrand, J. Kamphus, M. Wilhelm, B. Luy, G. Guthausen, *Macromol. Chem. Phys.* **2019**, *220* (2), 1800350.
- [54] S. Gope, S. Malunavar, A. J. Bhattacharyya, *ChemistrySelect* **2018**, *3* (19), 5364-5376.
- [55] J. Maier, *Solid State Electrochemistry: Measurement Techniques and Applications*. In *Physical Chemistry of Ionic Materials*, Wiley, **2004**, 399-499.
- [56] A. Senocrate, T.-Y. Yang, G. Gregori, G. Y. Kim, M. Grätzel, J. Maier, *Solid State Ion.* **2018**, *321*, 69-74.
- [57] G. Y. Kim, A. Senocrate, T.-Y. Yang, G. Gregori, M. Grätzel, J. Maier, *Nat. Mater.* **2018**, *17* (5), 445-449.
- [58] C. Wagner, *Prog. Solid State Chem.* **1975**, *10*, 3-16.
- [59] H. Mehrer, *Diffusion in Solids: Fundamentals, Methods, Materials, Diffusion-Controlled Processes*, Springer Berlin Heidelberg, **2007**.
- [60] I. V. Krasnikova, M. A. Pogosova, A. O. Sanin, K. J. Stevenson, *Chem. Mater.* **2020**, *32* (6), 2232-2241.
- [61] A. J. Bhattacharyya, J. Fleig, Y.-G. Guo, J. Maier, *Adv. Mater.* **2005**, *17* (21), 2630-2634.
- [62] E. Barsoukov, J. R. Macdonald, *Impedance Spectroscopy: Theory, Experiment, and Applications*, Wiley, **2005**.
- [63] G. Maier, *Prog. Polym. Sci.* **2001**, *26* (1), 3-65.
- [64] V. F. Lvovich, *Impedance Spectroscopy: Applications to Electrochemical and Dielectric Phenomena*, Wiley, **2015**.
- [65] E. D. Wachsman, E. Society, E. S. Meeting, *Solid-state Ionic Devices II: Ceramic Sensors : Proceedings of the International Symposium*, Electrochemical Society, **2001**.
- [66] Y. Kim, D.-K. Shin, E.-C. Shin, H.-H. Seo, J.-S. Lee, *J. Mater. Chem.* **2011**, *21* (9), 2940-2949.
- [67] Y. Noda, C. Merschjann, J. Tarábek, P. Amsalem, N. Koch, M. J. Bojdys, *Angew. Chem. Int. Ed.* **2019**, *58* (28), 9394-9398.
- [68] J. Kröger, A. Jiménez-Solano, G. Savasci, V. W. h. Lau, V. Duppel, I. Moudrakovski, K. Küster, T. Scholz, A. Gouder, M.-L. Schreiber, F. Podjaski, C. Ochsenfeld, B. V. Lotsch, *Adv. Funct. Mater.* **2021**, *31* (28), 2102468.
- [69] X. Chen, P. M. Vereecken, *Adv. Mater. Interf.* **2019**, *6* (1), 1800899.
- [70] A. Morata, G. Dezanneau, A. Tarancon, F. Peiro, J. R. Morante In *Simulation of the influence of particle size distribution and grain boundary resistance on the electrical response of 2D polycrystals*, Conference on Electron Devices, 2-4 Feb. 2005; pp 225-228.
- [71] T. Holzmann, L. M. Schoop, M. N. Ali, I. Moudrakovski, G. Gregori, J. Maier, R. J. Cava, B. V. Lotsch, *Energ. Environ. Sci.* **2016**, *9* (8), 2578-2585.
- [72] S. Lunghammer, D. Prutsch, S. Breuer, D. Rettenwander, I. Hanzu, Q. Ma, F. Tietz, H. M. R. Wilkening, *Sci. Rep.* **2018**, *8* (1), 11970.

- [73] S. Melissen, T. Le Bahers, S. N. Steinmann, P. Sautet, *J. Phys. Chem. C* **2015**, *119* (45), 25188-25196.
- [74] V. K. Tomer, N. Thangaraj, S. Gahlot, K. Kailasam, *Nanoscale* **2016**, *8* (47), 19794-19803.
- [75] N. M. Vargas-Barbosa, B. Roling, *ChemElectroChem* **2020**, *7* (2), 367-385.
- [76] V. Bocharova, A. P. Sokolov, *Macromolecules* **2020**, *53* (11), 4141-4157.
- [77] A. Kuhn, O. Gerbig, C. Zhu, F. Falkenberg, J. Maier, B. V. Lotsch, *Phys. Chem. Chem. Phys.* **2014**, *16* (28), 14669-14674.
- [78] P. M. Richardson, A. M. Voice, I. M. Ward, *Int. J. Hydrogen Energy* **2014**, *39* (6), 2904-2908.
- [79] J. J. Hernandez, H. Zhang, Y. Chen, M. Rosenthal, M. D. Lingwood, M. Goswami, X. Zhu, M. Moeller, L. A. Madsen, D. A. Ivanov, *Macromolecules* **2017**, *50* (14), 5392-5401.
- [80] H. Park, P. P. M. Schleker, Z. Liu, N. Kowalew, T. Stamm, R. Schlögl, R.-A. Eichel, S. Heumann, J. Granwehr, *J. Phys. Chem. C* **2019**, *123* (41), 25146-25156.
- [81] J. Maier, *Kinetics and Irreversible Thermodynamics*. In *Physical Chemistry of Ionic Materials*, Wiley, **2004**, 268-398.
- [82] Y. Byun, S. H. Je, S. N. Talapaneni, A. Coskun, *Chem.– Eur. J.* **2019**, *25* (44), 10262-10283.
- [83] F. Cao, D. Li, R. Deng, L. Huang, D. Pan, J. Wang, S. Li, G. Qin, *RSC Adv.* **2015**, *5* (103), 84587-84591.
- [84] M. Wilkening, W. Küchler, P. Heitjans, *Phys. Rev. Lett.* **2006**, *97* (6), 065901.
- [85] H. Aoki, H. Shima, C. Kimura, T. Sugino, *Diamond Relat. Mater.* **2007**, *16* (4), 1300-1303.
- [86] A. Senocrate, I. Moudrakovski, G. Y. Kim, T.-Y. Yang, G. Gregori, M. Grätzel, J. Maier, *Angew. Chem. Int. Ed.* **2017**, *56* (27), 7755-7759.
- [87] J. Langer, V. Epp, P. Heitjans, F. A. Mautner, M. Wilkening, *Phys. Rev. B* **2013**, *88* (9), 094304.
- [88] A. Kuhn, S. Dupke, M. Kunze, S. Puravankara, T. Langer, R. Pöttgen, M. Winter, H.-D. Wiemhöfer, H. Eckert, P. Heitjans, *J. Phys. Chem. C* **2014**, *118* (49), 28350-28360.
- [89] A. Kuhn, P. Sreeraj, R. Pöttgen, H.-D. Wiemhöfer, M. Wilkening, P. Heitjans, *J. Am. Chem. Soc.* **2011**, *133* (29), 11018-11021.

9.5. List of abbreviation

4-MBA	4-methylbenzyl alcohol
AM 1.5 G	Air mass 1.5 global
ATP	Adenosine triphosphate
BET	Brunauer-Emmet-Teller
CB	Conduction band
CN _x	Carbon nitrides
CP	Cross polarization
CPPI	Cross polarization with polarization inversion
D ^σ	Conductivity diffusion coefficients
D ^{tr}	Tracer diffusion coefficients
D ^{uc}	Uncorrelated tracer diffusion coefficient
DC	Direct current
DCDA	Dicyandiamide
DFT	Density functional theory
DI	Deionized water
DLS	Diffusive light scattering
DNI	Direct normal irradiation
DQ-SQ	Double quantum – single quantum
E _a	Activation energy
E _f	Fermi energy
E _{Redox}	Reduction potential
E _{ph}	Photopotential
E _{f,n} or E _{f,p}	Quasi-Fermi levels of electrons or holes
ED	Electron diffraction
EIS	Electrochemical impedance spectroscopy
EPR	Electron paramagnetic resonance
FFT	Fast Fourier transformed
FT-IR	Fourier-transformed infrared spectroscopy
FWHM	Full width half maximum
g-C ₃ N ₄	Graphitic carbon nitride
GC	Gas chromatograph
GHI	Global horizontal irradiation
HEP	Hydrogen evolution photocatalytic system
HER	Hydrogen evolution reaction
HETCOR	Heteronuclear correlation
HOMO	Highest occupied molecular orbital

HR	High resolution
HSQC	Heteronuclear single quantum coherence
INEPT	Insensitive nuclei enhanced polarization transfer
LUMO	Lowest unoccupied molecular orbital
MAS	Magic-angle-spinning
Mel	Melamine
MeOH	Methanol
NADP	Nicotinamide adenine dinucleotide phosphate
OCP	Open circuit potential
OEP	Oxygen evolution photocatalytic system
OER	Oxygen evolution reaction
PDF	Pair distribution function
PFG NMR	Pulsed field gradient nuclear magnetic resonance
PHI	Poly(heptazine imide)
M/ Ba/ Cs/ H/ K/ Li/ Na/ NH ₄ / TMA-PHI	Cation/ barium/ cesium/ proton/ potassium/ lithium/ sodium/ ammonium/ tetramethylammonium containing PHI
PL	Photoluminescence
PTI	Poly(triazine imide)
PXRD	Powder X-ray diffraction
RH	Relative humidity
SAED	Selected area electron diffraction
SEM	Scanning electron microscopy
ssNMR	Solid state nuclear magnetic resonance
STH	Solar to hydrogen
TAS	Transient absorption spectroscopy
TEM	Transmission electron microscopy
TEoA	Triethanolamine
TGA	Thermogravimetric analysis
UPS	Ultraviolet photoelectron spectroscopy
UV-Vis	UV and visible light spectroscopy
VB	Valence band
XPS	X-ray photoelectron spectroscopy

9.6. List of figures

- Figure 1.1:** Depiction of average irradiation over a year, which reaches the earth surface when looking at the global horizontal irradiation and b) the direct normalized irradiation. c) Solar spectrum at atmospheric condition; air mass 1.5 global (AM 1.5 G) at 48.2° tilted surface. Numbers in brackets describe the percentage amount of light up to the specific wavelength in comparison to the total light intensity. 2
- Figure 1.2:** Infrastructure of solar driven hydrogen evolution on a direct way in photocatalysis and indirect via photovoltaics producing electricity, which can be transferred into hydrogen by electrolysis. Hydrogen gas can be used to power up power plants, houses or vehicles for transport by fuel cell technology, converting hydrogen either directly into power, or via fuel cells into electricity. 3
- Figure 1.3:** Light-induced charge separation and recombination in a semiconductor. I, Photo-induced charge generation and possible immediate recombination, II, charge carrier separation, III, transport of electrons and holes to the surface and transfer to a co-catalyst where the oxidation or reduction reaction is taking place, IV, bulk or surface recombination during charge transport, V, electron trapping in trap states located within the optical band gap. 4
- Figure 1.4:** a) Band alignment of a semiconductor-electrolyte interface in the dark. Here an *n*-type semiconductor is shown, which is not in contact with the electrolyte. b) When semiconductor and list of electrolyte are brought in contact a space charge layer is formed with bands upward banding and the Fermi-level (E_F) of the semiconductor is aligned with the redox-potential ($E_{F(\text{redox})}$) of the electrolyte. c) During illumination E_F is modified and better described by quasi-Fermi levels of electrons ($E_{F,n}$) and holes ($E_{F,p}$) that are continuously formed. Their difference describes the photopotential (E_{ph}). 7
- Figure 1.5:** a) Charge trapping in semiconductors after photoexcitation. b) Possibilities of radiative (black, error) or non-radiative (grey errors) charge carrier recombination after photoexcitation of the semiconductor. I) Direct radiative recombination, II) Auger recombination, III) Non-radiative trap-assisted recombination (Shockley-Read-Hall). 9
- Figure 1.6:** Energy scheme of required potentials for water splitting at pH 7. Blue arrows show the overpotentials, describing the additional energy required to drive the reactions, which depend on the material used. 10
- Figure 1.7:** Two compartment photocatalysis reaction with redox-mediator for overall water splitting, with an oxygen evolution photocatalytic system (OEP), electron mediator, and hydrogen evolution photocatalytic system (HEP). 12

Figure 1.8: Dependence of photocatalyst concentration on photocatalytic rate. I) linear increase of rate; II) constant rates with optimal concentration range at the onset of the plateau; III) decrease of reaction rate, due to light penetration depth reduction or IV) reaction rates remain constant. 13

Figure 2.1: Synthesis procedure for various carbon nitrides. 1D melon is obtained by heating the precursors (urea, dicyandiamide or cyandiamide) to 500-600°C in the absence of a salt melt. When a salt melt is present the 2D carbon nitrides PTI or PHI are formed, with pore fillings depending on the synthesis conditions. Besides, fully condensed structure of triazine-based systems (TGCN) and heptazine-based systems (g-C₃N₄) were reported, however, the existence of fully condensed g-C₃N₄ is still debated and lacking experimental evidence. Blue arrow highlights the synthesis routes, which will be discussed in more detail in Chapter 4 in combination with structural analysis. 21

Figure 2.2: Structure of PTI/Li⁺Cl⁻. a) Crystal structure with unit cell of PTI/Li⁺Cl⁻ view along c-axis and b) view along a,b plane. c) Single crystal shape and facets of PTI/Li⁺Cl⁻ grown by ionothermal synthesis. d) SEM image of single crystals. 22

Figure 2.3: a) In-plane structure of melon viewed from the top and b) PHI template by melamine, view along c-axis and c) along a,b plane. 23

Figure 2.4: Schematic description of process in photocatalytic hydrogen evolution reactions on heptazine-based materials. a) Postulated proton-coupled electron transfer process for heptazine molecules. b) Exciton based process for carbon nitrides with exciton formation after illumination. Light blue arrows depict internal conversion, dark blue arrows the exciton recombination possibilities and green arrows the exciton dissociation possibilities. 25

Figure 2.5: Effect of the addition of reaction components triethanolamine (TEoA) and H₂PtCl₆ in different orders to photo-deposit Pt on carbon nitrides (if no TEoA is present, the photo-deposition is conducted in absence of another electron donor). A complex formation of triethanolamine and Pt⁴⁺ is possible. 27

Figure 2.6: Timescales for different light-induced processes in carbon nitrides, analyzed by ultrafast spectroscopic measurements. 29

Figure 2.7: Reported tuning parameters on the molecular/structural and morphological level in the bulk and at the interface in order to boost photocatalytic hydrogen evolution with melon. 30

Figure 2.8: Defect-introducing strategies for carbon nitrides, including the formation of a) vacancies (here the most common N vacancies are shown), b) functional or termination groups and c) elemental doping. The most commonly used elements for doping are depicted with their predicted position for replacing atoms in the heptazine backbone or by coordinating between heptazine units. Most defect studies were performed on melon-type carbon nitrides. 32

- Figure 2.9:** Morphology tuning used for melon-based carbon nitrides to boost photocatalysis. Ranging from 0D quantum dots, via 1D nanofibres, nanowires or nanorods and nanotube, to 2D nanosheets and nanoribbons and 3D porous materials. 35
- Figure 2.10:** Exciton diffusion in between the layers is orders of magnitude faster than within one layer of melon. 37
- Figure 2.11:** Donor-acceptor function of carbon nitrides, where only the a) donor or b) the acceptor is absorbing light and charge carriers are transferred to the respective other part. c) Heterojunction formed between melon-type carbon nitride and PTI, where both material absorb sun light and both charge carrier types are shuttled. 38
- Figure 2.12:** Solar battery and “dark photocatalysis” application enabled by K-PHI due to stable photo-reduced, blue state after illuminating K-PHI with light <450 nm. After discharging and prior to illumination, K-PHI is yellow and changes its color to blue during illumination. 40
- Figure 2.13:** Photo-induced reactions catalyzed by carbon nitrides (1D melon-type and 2D PHI) including CO₂ reduction, N₂ fixation, antibacterial reactions, waste water treatment, pollutant degradation and synthesis of organic molecules like e.g. drugs. 42
- Figure 3.1:** Structure-activity-relationships in 2D PHI are disentangled to intermediate processes in the photocatalytic process. The detailed study of each tuning possibilities of carbon can be used to optimize the catalyst design. From light absorption, to exciton diffusion, charge trapping and hence charge transfer at the surface and catalytic reaction (from left top to right top) the timescales on which those processes occur are increasing. 52

9.7. List of publications

Publications that are part of this thesis

Structural insights into poly(heptazine imide): A light-storing carbon nitride material for dark photocatalysis

Hendrik Schlomberg, Julia Kröger, Gökçen Savasci, Maxwell W. Terban, Sebastian Bette, Igor Moudrakovski, Viola Duppel, Filip Podjaski, Renée Siegel, Jürgen Senker, Robert E. Dinnebier, Christian Ochsenfeld and Bettina V. Lotsch

Chem. Mater. **2019**, *31*, (18), 7478-7486. DOI:10.1021/acs.chemmater.9b02199

Interfacial engineering for improved photocatalysis in a charge storing 2D carbon nitride: Melamine functionalized poly(heptazine imide)

Julia Kröger, Alberto Jiménez-Solano, Gökçen Savasci, Petra Rovó, Igor Moudrakovski, Kathrin Küster, Hendrik Schlomberg, Hugo A. Vignolo-González, Viola Duppel, Lars Grunenberg, Cem B. Dayan, Metin Sitti, Filip Podjaski, Christian Ochsenfeld and Bettina V. Lotsch

Adv. Energy Mater. **2021**, *11*, (6), 2003016. DOI:10.1002/aenm.202003016

Morphology tuning in porous, 2D carbon nitrides: How the particle structure affects charge transport and photocatalysis

Julia Kröger, Alberto Jiménez-Solano, Gökçen Savasci, Vincent-W.h. Lau, Viola Duppel, Igor Moudrakovski, Kathrin Küster, Tanja Scholz, Marie-Luise Schreiber, Filip Podjaski, Christian Ochsenfeld and Bettina V. Lotsch

Adv. Funct. Mater. **2021**, *31*, (28), 2102468. DOI:10.1002/adfm.202102468

Conductivity mechanism in ionic 2D carbon nitrides: from hydrated ion motion to enhanced photocatalysis

Julia Kröger, Filip Podjaski, Gökçen Savasci, Alberto Jiménez-Solano, Igor Moudrakovski, Maxwell W. Terban, Sebastian Bette, Viola Duppel, Markus Joos, Alessandro Senocrate, Robert Dinnebier, Christian Ochsenfeld and Bettina V. Lotsch

Submitted

Publications that are not part of this thesis

Toward an aqueous solar battery: Direct electrochemical storage of solar energy in carbon nitrides

Filip Podjaski, Julia Kröger and Bettina V. Lotsch

Adv. Mater. **2018**, 30, (9), 1705477. DOI:10.1002/adma.201705477

Von der Jahrmarktattraktion zur Energiequelle: Kohlenstoffnitride

Hendrik Schlomberg, Filip Podjaski, Julia Kröger and Bettina V. Lotsch

Nachr. Chem. **2018**, 66, 1157-1161. DOI:10.1002/nadc.20184065088

Carbon nitride-based light-driven microswimmers with intrinsic photocharging ability

Varun Sridhar, Filip Podjaski, Julia Kröger, Alberto Jiménez-Solano, Byung-Wook Park, Bettina V. Lotsch and Metin Sitti

Proc. Natl. Acad. Sci. U.S.A., **2020**, 117, (40), 24748-24756. DOI:10.1073/pnas.2007362117

Polymer photocatalysts for solar-to-chemical energy conversion

Tanmay Banerjee, Filip Podjaski, Julia Kröger, Bishnu Biswal and Bettina V. Lotsch

Nat. Rev. Mater. **2021**, 6, 168-190. DOI:10.1038/s41578-020-00254-z

Biocompatible carbon nitride-based light-driven microswimmer propulsion in biological and ionic media with responsive on-demand drug delivery

Varun Sridhar, Filip Podjaski, Yunus Alapan, Julia Kröger, Lars Grunenberg, Vimal Kishore, Bettina V. Lotsch and Metin Sitti

Submitted

Patent

Electrochemical device, batteries, methods for harvesting light and storing electrical energy and detection methods

Filip Podjaski, Bettina V. Lotsch, Julia Kröger, Andreas Gouder, Hendrik Schlomberg,

International application PCT/EP2019/050448

9.8. International conference presentations

Conference on molecular nanostructures

Ascona, Switzerland, 05.-10.05.2017

Poster: *Graphitic carbon nitrides for photocatalytic hydrogen evolution*

6th international conference on semiconductor photochemistry

Oldenburg, Germany, 11.-14.09.2017

Poster: *Heptazine-based 2D carbon nitrides for photocatalytic hydrogen evolution*

Catalysis Science and Technology **Poster Prize**

Materials, Characterization, and Catalysis

Zurich, Switzerland, 15.-16.01.2018

Poster: *Heptazine-based 2D carbon nitrides for photocatalytic water reduction*

680th WE Heraeus-Seminar on 'Materials Development for automotive propulsion'

Bad Honnef, Germany, 14.-17.10.2018

Poster: *Towards enhanced photocatalytic hydrogen evolution by carbon nitrides with a true 2D topology*

27th Lecture conference on photochemistry

Online conference, 14.-15.09.2020

Talk: *Interfacial engineering in a truly 2D carbon nitride poly(heptazine imide) for photocatalytic hydrogen evolution*

International conference on resource chemistry

Online conference, 08.-09.03.2021

Poster: *Multifunctional & sustainable 2D carbon nitrides for green hydrogen production and direct solar energy storage*

Wiley-VCH **1th Poster Prize**